

Dissertation zur Erlangung des Doktorgrades
der Fakultät Chemie und Pharmazie
der Ludwig-Maximilians-Universität München

**Electrolytic Synthesis
and Structural Chemistry
of Intermetallic Phases
with Polar Metal-Metal Bonding**

Frank Tambornino

aus

Bocholt, Deutschland

2016

Erklärung

Diese Disstertation wurde im Sinne von §7 der Promotionsordnung vom 28. November 2011 von Herrn Prof. Dr. W. Schnick betreut.

Eidesstattliche Versicherung

Diese Dissertation wurde eigenständig und ohne unerlaubte Hilfe erarbeitet.

München, 20.10.2016

.....
Frank Tambornino

Dissertation eingereicht am 20.10.2016

1. Gutachter Prof. Dr. Wolfgang Schnick

2. Gutachter Prof. Dr. Dirk Johrendt

Mündliche Prüfung am 19.12.2016

to my family

It is the mark of an educated mind
to be able to entertain a thought
without accepting it.
— Aristotle

Mein ganz besonderer Dank gilt Herr Prof. W. Schnick für die Möglichkeit, die Dissertation in seinem Arbeitskreis anzufertigen.

Prof. Dirk Johrendt danke ich für die Bereitschaft, das Koreferat für diese Arbeit zu übernehmen.

Prof. Dr. O. Oeckler, Prof. Dr. A. Hartschuh, Prof. Dr. K. Karaghiosoff und Prof. Dr. T. Klapötke danke ich für ihre Bereitschaft, als Teil der Prüfungskommission für die mündliche Prüfung zur Verfügung zu stehen.

Mein ganz spezieller Dank gilt Dr. Constantin Hoch für die intensive Betreuung, die Überlassung dieses spannenden Themas und dafür, dass er mir immer mit Rat und Tat zur Seite stand. Du warst und bist eine Inspiration!

Ebenso danke ich allen meinen Praktikanten, Jonny Sappl, Philipp Bielec, Arthur Hafner, Felix Pultar, Sabine Hübner, Minh Trung Cong, Tobias Giftthaler und Kuno Schwärzer, die mich mit großem Eifer unterstützen.

Herrn Christian Minke gilt mein Dank für das Suchen so manchen NMR-Signals bei höchsten Verschiebungen, Herrn Thomas Miller für die Betreuung der IPDS-Geräte und Herrn Wolfgang Wünschheim für die Rechnerbetreuung und Hilfe bei jedwedem Computerproblem.

Frau Olga Lorenz danke ich ganz herzlich für ihre organisatorischen Tätigkeiten und Hilfsbereitschaft bei allen Arten von Problemen.

Meinen ehemaligen und aktuellen Laborkollegen Florian Pucher, Sebastian Schneider, Alexey Marchuk, Matthias Wörsching, Eva-Maria Bertschler, Simon Kloß, Philipp Bielec, Sebastian Vogel und Sebastian Wendl danke ich für die wahnsinnig tolle Zeit in D2.110.

Natürlich danke ich auch allen bisher unerwähnten Mitgliedern der AKs Schnick, Hoch, Lotsch und Oeckler für allerlei Tips, Ratschläge und die hervorragende Zusammenarbeit.

Danken möchte ich auch Pamela "Pam" Hathway, Thomas Riffelmacher, Simon Peschke, Philipp Schmid und Daniel Terwilliger für die Stunden gemeinsamen "Lernens" während des Bachelorstudiums. Mein spezieller Dank gebührt Simon Peschke, Philipp Schmid und Daniel Terwilliger für die wöchentlichen mittäglichen Besprechungen über Chemie und alle anderen Aspekte des Lebens.

Mein allergrößter Dank geht jedoch an meine Eltern, meinen Bruder Philipp und meine Freundin Steffi: Ohne euch wäre diese Arbeit nie entstanden.

Contents

1	Introduction	1
1.1	Historical Aspects on Discovery and Ethymology of Mercury	1
1.2	Amalgams of the Less-Noble Metals	3
1.3	Polar Metal-Metal Bonding	7
2	Aims and Scope of this Work	13
3	Results	15
3.1	Methods	15
3.1.1	Synthetic Methods	15
3.1.2	Analytical Methods	18
3.1.3	Quantum-Mechanical Calculations	20
3.2	Metal Iodide Solvates	22
3.2.1	Single Crystal Structures	22
3.2.2	Redetermination of $[\text{EuCl}_2(\text{H}_2\text{O})_6]\text{Cl}$	43
3.3	Lanthanide Amalgams	49
3.3.1	The Mercury-richest Europium Amalgam $\text{Eu}_{10}\text{Hg}_{55}$	50
3.3.2	The $\text{Gd}_{14}\text{Ag}_{51}$ Structure Type and its Relation to Some Complex Amalgam Structures	63
3.3.3	Synthesis and characterization of $\text{La}_{11+x}\text{Hg}_{45-x}$ and $\text{RE}_{11}\text{Hg}_{44.5}$ ($\text{RE} = \text{Nd}, \text{Sm}$) as hettotypes of the $\text{Sm}_{11}\text{Cd}_{45}$ structure type	87
3.3.4	Crystal Structure of $\text{Yb}_{11}\text{Hg}_{54}$	105
3.3.5	Crystal Structures of the REHg , REHg_2 and REHg_3 Amalgams	110
3.4	Alkali and alkaline earth metal amalgams	115
3.4.1	Bad Metal Behaviour in the New Hg-Rich Amalgam KHg_6 with Polar Metallic Bonding	116
3.4.2	NMR Investigations on the Li Amalgams Li_3Hg , LiHg and LiHg_3	133
3.4.3	$\text{AHg}_{11-x}\text{In}_x$	139
3.5	Electrolyses on Mercury-Free Cathode Materials	145
3.5.1	Electrocrystallization – A Synthetic Method for Intermetallic Phases with Polar Metal–Metal Bonding	146
3.5.2	$\text{Li}_3\text{Ga}_{14-x}\text{Sn}_x$ with $x \approx 1$	171
4	Discussion	175
4.1	Syntheses	176
4.1.1	Syntheses I: Preparative Electrocrystallisation	176
4.1.2	Syntheses II: Distillation Method	183
4.2	Evaluation of Crystal Structures and Measures of Complexity	185
4.2.1	Metal Iodide Solvate Structures as Decorated Variants of Simple Sphere Packings	185

4.2.2	Amalgams	192
4.3	Polar Intermetallics – Aspects of Chemical Bonding	199
4.3.1	What is a Polar Metal?	199
4.3.2	Polarity in Amalgams	199
4.3.3	Structures Derived from the BaHg ₁₁ Structure Type	208
4.3.4	Polarity in Li ₃ Ga ₁₄ and Li ₃ Ga ₁₃ Sn	212
5	Conclusion	221
5.1	DMF Solvates of Metal Iodides as Educts for Electrocrystallisation	221
5.2	Electrolysis on Unary, Binary and Ternary Reactive Cathodes	221
5.3	Crystal Structures of Hg-rich Amalgams	222
5.4	Evaluation of Polarity in Amalgams and Related Phases	223
6	Outlook	225
A	Crystallographic Data	227
B	Performed Experiments	241
C	Curriculum Vitae	251

1. Introduction

Quecksilber und Quecksilberverbindungen sind für Lebewesen *nicht essentiell* (der Mensch enthält normalerweise kein Quecksilber) [...]

Holleman, Wiberg: "Lehrbuch der Anorganischen Chemie", 102. ed., de Gruyter, Berlin, New York, page 1497, footnote 11.

It is impossible not to be captivated by the beauty of mercury. As the only metal liquid at room temperature it exhibits a shiny, silvery lustre. If pure, it does not wet a glass surface, forms little droplets with very low viscosity and was therefore named "liquid silver".^[1] A puddle of pure mercury is a perfect mirror.

In compounds, mercury predominantly exhibits oxidation states +1 (e.g. Hg_2Cl_2) and +2 (e.g. HgCl_2). The former always exhibit dimercury cations with a covalent bond $[\text{Hg} - \text{Hg}]^{2+}$. The latter always occur as monoatoms dications as they are a closed-shell species akin to noble gases with electron configuration $[\text{Xe}]4f^{14}5d^{10}$. Due to relativistic effects the 6s electrons are lowered in energy leading to a series of unusual effects: Mercury is liquid at room temperature, in contrast to its lighter homologues it is a noble-metal and due to its high electronegativity and electron affinity it is prone to formation of covalent bonds.

As all salts and organic compounds of mercury are highly toxic its use has been reduced. However, because of its unusual properties it is still of high interest to chemists which are just as fascinated by it as ancient civilisations.

1.1. Historical Aspects on Discovery and Ethymology of Mercury

Mercury is one of the elements known to ancient civilizations, the others being gold, silver, copper, iron, lead, tin, and sulphur.^[2] It occurs naturally in its metallic state as droplets together with its ore Cinnabar (HgS). Cinnabar was already used for its bright scarlet colour as the pigment 'vermilion' in wall paintings in the neolithic village of Çatalhöyük in modern-day Turkey (Fertile Crescent) in 7000–8000 BC. Its use for embalming was known at least since the Pre-Pottery Neolithic B (ca. 7600 – 6000 BC, Fertile Crescent), possibly in context of burial rituals.^[3] Its first use on European ground, also in context of preservation of human bones, dates



Figure 1.1.: Cinnabar (HgS) on calcite in bedrock (Nevada, USA).

back to ca. 5000 BC ('La Velilla', Palencia, Spain).^[4] Since then, cinnabar was used for colouring and/or ritual purposes by high cultures of Ancient Egypt, Indus Valley Civilisation and Chinese Shang dynasty.^[2,5]

Elemental mercury was discovered in an Egyptian tomb ceremonial cup at Kurna dating back between 1500–1600 BC.^[6,7] Whether the Egyptians had knowledge of isolation of mercury from cinnabar or whether they used mercury droplets commonly found together with cinnabar is not known. The first written account of knowledge of elemental mercury is found in ancient Greek texts. Although Aristotle (384 – 322 BC) had knowledge of mercury (ἄργυρος ὁ χυτός, 'liquid silver'), the first instructions on synthesis from Cinnabar were given by his successor Theophrastus (ca. 371 – ca. 287 BC) in his book 'On Stones'.^[8,9] He stated that mercury "*is made when cinnabar mixed with vinegar is ground in a copper vessel with a pestle made of copper*". Most likely a copper amalgam was obtained, purification by filtration and distillation was known little later as both Dioscorides (40–90 AD) and Pliny the elder (23 – 79 AD) describe those methods.^[10] This description given by Theophrastus is the earliest written account of the synthesis of a metal from its ore.^[9,11]

First applications of mercury are described by Dioscorides (40–90 AD), Pliny the elder (23 – 79 AD) and Vitruv (80-70 – ca. 15 BC) who used it to gild silver and copper by fire-gilding (lat. *inaurare*).^[10–12] They give detailed instructions for the isolation of gold from used clothing. Common to all processes is the use of gold amalgam which readily forms upon combining the elements.

In the middle ages, chemistry on mercury was commonly either of medical or alchemical nature.^[13] Agricola lists several methods for preparation and refinement of mercury^[14]. It was widely used as auxiliary reagent in mining and metallurgy and the cold amalgamation process for silver refinement (1571/72). Hot amalgamation as a superior process for silver refinement was invented by A. A. Barba in 1640.^[2]

A breakthrough in the use of amalgams took place shortly after the Voltaic pile was presented to the general public.^[15] The process of electrolysis on a mercury cathode was crucial for the works of Berzelius (Stockholm) and Davy (London) who independently performed electrolyses in 1806.^[16–22] Both connected a small pool of mercury (cathode) to small amounts of wet salts (anode) which they placed on top of each other. Amalgam formation was observed and the elements sodium (from Na₂CO₃ and NaHCO₃) and potassium (from K₂CO₃) were discovered after distillative removal of mercury. By following this idea of distilling off the mercury from the amalgams a number of elements were discovered over the next years.

The word "*amalgam*" most likely originates from Greek μαλακός (malakós, "soft") which verbifies into μαλάσσω (malássō, "to soften"). The direct connection to kneadable gold amalgam is obvious.^[23] A similar root word μάλαγμα (málagma, "gold") is also found in Arabic الْمَلْغَم (al-malḡam, "emollient poultice or unguent for sores") which points towards the use of mercury for various skin diseases.^[24] In old Latin language, *amalgama* directly translates to "mercury alloy", its use transferred to modern day chemistry through the middle ages.

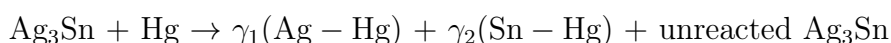
The element symbol Hg originates from the Greek ὑδραργυρος (*hydrargyros* from ὕδωρ = water and αργυρος = silver), the English *mercury* was chosen by the antique Romans

following the Greek's adjunction of the metal with the god Hermes, the vivid messenger of the gods, and adapting it to its Roman analogue, the god Mercurius.

1.2. Amalgams of the Less-Noble Metals

Amalgams of less noble metals are the respective metallic mercury-containing compounds of the alkali, alkaline earth and rare earth elements. An overview of the literature reported alkali metal amalgams is given in Table 1.1, of alkaline earth metal amalgams in Table 1.2 and of rare earth metal amalgams in Table 1.3.

"Amalgam" is a general term, it makes no distinction between line phases, solid solutions or border solubilities and was used well before knowledge on crystal structures was present. A naturally occurring amalgam is Ag_2Hg_3 (Moschellandsbergite). Together with Ag_3Sn it forms a substantial amount of the amalgam filling in dentistry, the rest of which is the γ phase of the Sn-Hg system.^[25] Dental amalgam was used since 1826, its current form contains silver 40–70%, tin 12–30% and copper 12–24%. It may also include indium 0–4%, palladium 0.5% and zinc up to 1%.^[26–28] Its widespread use is due to its low toxicity, easy availability and superior mechanical properties; after combining the educts it is kneadable and solidifies after a short time span.



Alkali metal amalgams are intermediate products of synthesis of sodium hydroxide and chlorine in Castner cells patented in 1894.^[29] The process involves electrolysis of a saturated brine between a shallow stream of mercury (cathode) and an assembly of graphite or iron anodes. During electrolysis, chlorine forms at the anodes, while sodium is reduced at and dissolved in mercury. The amalgam is then reacten with water in a decomposer to liberate concentrated sodium hydroxide solution.

After discovery of X-ray diffraction, the crystal structure of mercury was characterised in 1922,^[30] the two modifications of HgS in 1924/25.^[31,32] Coloradoite (HgTe)^[33] as the first intermetallic mercury mineral and LiHg as the first synthetic amalgam were characterised shortly after.^[34] All three Li amalgams were first examined in the 1930s,^[34,35] followed by Mg amalgams in 1940s (see refs. in Table 1.2). During the 1950s, the first Na, K, Sr and Ba amalgams were structurally characterised (see refs. in Tables 1.1 and 1.2) and as the first rare earth metal amalgams $RE\text{Hg}$ ($RE = \text{La, Ce, Pr, Nd}$) appeared.^[36]

Although reports on rare earth amalgam structures are scarce, it was already known at that time that rare earth metals readily form amalgams. As early as 1928 it was tried to separate the rare earth metals from one another by formation of their amalgams.^[37] Focussing on electrolytic processes from aqueous solutions of their respective acetates, amalgams of La, Nd, Ce, Sm and Y were reported on.^[38] Subsequent studies focused on the separation of Eu and Yb from their respective neighbours.^[39–43] It was found that the properties of the liquid or kneadable amalgams were too similar for a clean separation of the rare earth metals and fractionated crystallisation was developed as a superior process.

The 1960s and 1970s were dominated by reports on structures of alkaline earth and rare earth metal amalgams, only one new alkali metal amalgam (CsHg)^[44] was reported on. There were no new reports on rare earth metal amalgams after 1979, however, during the late 1980s reports on alkali and alkaline metal amalgams increased again, focusing on more complex structures of amalgams with higher Hg content.

In recent years, reports on amalgams of less noble metals were scarce, but new structures are continuously reported on, again focusing on complex structures and synthesis of mercury-rich amalgams. Amalgams with broad composition ranges are being reinvestigated with modern X-ray diffraction methods. Sodium amalgam, an intermediate product in the "amalgam process", was formerly addressed as NaHg_x (with $x = 5-6$). Recent investigations show that the actual composition is Na₁₁Hg₅₂.^[45, 46]

Alkali and alkaline earth metal amalgams show a distinct trend. The dimension of a mercury sublattice depends on the mercury content. Amalgams with low mercury content form isolated "mercuride ions", e.g. in α -Na₃Hg.^[47] Small Hg clusters with four ([Hg₄]^{δ-} squares)^[44, 48, 49] or eight atoms ([Hg₈]^{δ-} cubes) are found in CsHg and Rb₁₅Hg₁₆, respectively.^[50] Sheets and chains of negatively polarised mercury atoms are present in NaHg₂ (AlB₂ structure type, also the high pressure modification of KHg₂)^[51, 52] and A₂Hg₇ (A = K, Rb).^[53] Further increase of the Hg content leads to extended sublattices of negatively polarised mercury with embedded atoms of less noble metals, e.g. AHg₁₁ and Cs₂Hg₂₇.^[54, 55]

Table 1.1.: Graphical summary of the known alkali metal amalgams including space group type (SG), short description of main structural features and complexity measures (IG, IG_{bits} and IG_n, see chapter 4.2). Top to bottom: increasing Hg content, black boxes: crystal structure reported, grey box: high pressure polymorph.

	Li	Na	K	Rb	Cs	SG	Structure features	IG	IG _{bits}	IG _n
Li ₃ Hg ^[34, 35]	■					<i>Fm</i> $\bar{3}$ <i>m</i>	Li ₃ Bi structure type, ccp arrangement of Hg	1.500	6.000	0.750
α -Na ₃ Hg ^[47]	■	■				<i>P6</i> ₃ / <i>mmc</i>	Na ₃ As structure type, hcp arrangement of Hg	1.500	12.000	0.500
β -Na ₃ Hg ^[56]	■	■				<i>R</i> $\bar{3}$ <i>m</i>	modified Li ₃ Bi structure type			
α -Na ₈ Hg ₃ ^[52]	■	■				<i>R</i> $\bar{3}$ <i>c</i>	In ₃ Yb ₈ structure type	2.561	112.666	0.469
β -Na ₈ Hg ₃ ^[52]	■	■				<i>R</i> $\bar{3}$ <i>c</i>	Stacking variant of the In ₃ Yb ₈ structure type			
Na ₃ Hg ₂ ^[57, 58]	■	■				<i>P4</i> ₂ / <i>mmm</i>	unique, square planar [Hg ₄] ^{δ^-} clusters	1.922	38.439	0.445
LiHg ^[34, 35]	■					<i>Pm</i> $\bar{3}$ <i>m</i>	CsCl structure type	1.000	2.000	1.000
NaHg ^[49, 57]	■					<i>Cmcm</i>	Unique, puckered sheets of [Hg ₄] ^{δ^-} -rectangles	1.500	12.000	0.500
AHg ^[44, 49, 50]	■					<i>P</i> $\bar{1}$	KHg structure type, square planar [Hg ₄] ^{δ^-} clusters	2.000	16.000	0.667
Rb ₁₅ Hg ₁₆ ^[48]			■	■		<i>I4</i> ₁ / <i>a</i>	Unique, square planar [Hg ₄] ^{δ^-} and cubes of [Hg ₈] ^{δ^-} present	3.083	191.160	0.518
K ₅ Hg ₇ ^[59]			■	■		<i>Pbcm</i>	Unique, extended sheets of 5- and 6-membered Hg rings	3.085	148.078	0.552
AHg ₂ ^[57, 60]			■	■		<i>P6</i> / <i>mmm</i>	AlB ₂ structure type	0.918	2.755	0.579
AHg ₂ ^[51, 52]			■	■		<i>Imma</i>	CeCu ₂ structure type. Also with Sr, Ba.	0.918	5.510	0.355
LiHg ₃ ^[34, 35]	■					<i>P6</i> ₃ / <i>mmc</i>	Ni ₃ Sn structure type	0.811	6.490	0.270
A ₂ Hg ₇ ^[53]			■	■		<i>P</i> $\bar{3}$ <i>m1</i>	<i>trans</i> -connected chains of rhombohedrally distorted cubes			
K ₃ Hg ₁₁ ^[61]			■	■		<i>Immm</i>	Defect BaAl ₄ structure type	2.379	33.303	0.625
A ₅ Hg ₁₉ ^[61, 62]			■	■		<i>I4</i> / <i>m</i>	Defect BaAl ₄ structure type	2.168	52.039	0.473
A ₇ Hg ₃₁ ^[61]			■	■		<i>P6</i> / <i>mmm</i>	Ba ₇ Cd ₃₁ structure type, extended Hg partial structure. Also with Ba.	2.765	113.356	0.516
Na ₁₁ Hg ₅₂ ^[45, 46]			■	■		<i>P</i> $\bar{6}$	Unique, 3x3x1 superstructure of Gd ₁₄ Ag ₅₁ .	6.942	3936.056	0.759
KHg ₆ ^[63]			■	■		<i>Pnma</i>	BaHg ₆ structure type. Obviously also with Ba.	2.807	78.606	0.584
A ₃ Hg ₂₀ ^[61]			■	■		<i>Pm</i> $\bar{3}$ <i>n</i>	Rb ₃ Hg ₂₀ structure type.	1.892	87.025	0.343
AHg ₁₁ ^[54]			■	■		<i>Pm</i> $\bar{3}$ <i>m</i>	BaHg ₁₁ structure type. Obviously also with Ba.	1.981	71.323	0.383
Cs ₂ Hg ₂₇ ^[55]			■	■		<i>Im</i> $\bar{3}$	Unique	2.746	238.909	0.426
Total number	3	8	9	7	5					

Table 1.2.: Graphical summary of the known alkaline earth metal amalgams including space group type (SG), short description of main structural features and complexity measures (IG, IG_{bits} and IG_n, see chapter 4.2). Top to bottom: increasing Hg content, black boxes: crystal structure reported.

	Be	Mg	Ca	Sr	Ba	SG	Structure features	IG	IG _{bits}	IG _n
Mg ₃ Hg	■					<i>R</i> 32	Unique	2.646	63.510	0.577
Ca ₃ Hg ^[64]		■				<i>I</i> 4̄3 <i>m</i>	Unique	1.561	24.980	0.390
AE ₃ Hg ^[65, 66]			■			<i>Pnma</i>	Fe ₃ C structure type	1.500	24.000	0.375
AE ₂ Hg ^[66]		■				<i>Pnma</i>	Co ₂ Si structure type	1.585	19.020	0.442
Mg ₂ Hg			■			<i>I</i> 4/ <i>mmm</i>	MoSi ₂ structure type	1.585	19.020	0.442
Ba ₂ Hg ^[67]				■		<i>I</i> 4/ <i>mmm</i>	CuZr ₂ structure type	0.918	2.755	0.579
Mg ₅ Hg ₃ ^[68]		■				<i>P</i> 6 ₃ / <i>mcm</i>	Mn ₅ Si ₃ structure type	1.561	24.980	0.390
Ca ₅ Hg ₃ ^[66]			■			<i>I</i> 4/ <i>mcm</i>	Cr ₅ B ₃ structure type	1.750	28.000	0.438
AE ₃ Hg ₂ ^[65, 66]				■		<i>P</i> 4/ <i>mbm</i>	Si ₂ U ₃ structure type	1.522	15.219	0.458
AEHg ^[66, 69, 70]		■				<i>Pm</i> 3 <i>m</i>	CsCl structure type	1.000	2.000	1.000
CaHg ₂ ^[66]			■			<i>P</i> 3̄ <i>m</i>	Cd ₂ Ce structure type	0.918	2.755	0.579
CaHg ₂ ^[71]				■		<i>P</i> 6/ <i>mmm</i>	CaHg ₂ structure type	0.918	2.755	0.579
SrHg ₂ ^[65]					■	<i>Imma</i>	CeCu ₂ structure type	0.918	5.510	0.355
Ca ₄ Hg ₉ ^[72]			■			<i>I</i> 4/ <i>mcm</i>	Al ₄ Cu ₉ structure type	2.834	147.364	0.497
AEHg ₃ ^[71]				■		<i>P</i> 6 ₃ / <i>mnc</i>	Ni ₃ Sn structure type	0.811	6.490	0.270
Ba ₇ Hg ₃₁ ^[67]					■	<i>P</i> 6/ <i>mmm</i>	Ba ₇ Cd ₃₁ structure type	2.765	113.356	0.516
Sr ₁₃ Hg ₅₈ ^[65]					■	<i>P</i> 6 ₃ / <i>mnc</i>	Cd ₅₈ Gd ₁₃ structure type, also with La.	3.719	528.049	0.520
AE ₁₁ Hg ₅₄ ^[73]				■		<i>P</i> 6̄	Formerly Ca ₁₄ Hg ₅₁ or CaHg _{3.6} .	4.141	269.156	0.640
Ba ₂₀ Hg ₁₀₃ ^[74]					■	<i>F</i> 4̄3 <i>m</i>	Binary variant of the Ba ₂₀ Cd ₄ Hg ₉₉ structure type	3.750	461.283	0.540
BaHg ₆ ^[75]					■	<i>Pnma</i>	BaHg ₆ structure type	2.807	78.606	0.584
SrHg ₈ ^[76]				■		<i>Pnma</i>	Unique	4.170	300.235	0.676
AEHg ₁₁ ^[54]					■	<i>Pm</i> 3 <i>m</i>	BaHg ₁₁ structure type	1.981	71.323	0.383
Total number	0	5	12	9	6					

Table 1.3.: Graphical summary of the known rare earth metal amalgams. Dark grey: dystectica; grey: peritectica; light grey: unknown thermal behaviour; white: no reports on structure.^[77-91] *: Synthesized in this work; #: Structure type assigned, no reported refinement of crystallographic data; §: Assumed from thermoanalytical measurements; [1] Also Ce₁₀Hg₄₃, [2] Also La₁₃Hg₅₈, full refinement.

RE =	Sc	Y	La	Ce	Pr	Nd	Pm	Sm	Eu	Gd	Tb	Dy	Ho	Er	Tm	Yb	Lu
REHg	#	#	#	*	#	#		§	#	#	#	#	#	#	#	#	#
REHg ₂		#	#	#	§	#		*	#	#	#	#	#	#		#	
REHg ₃	*	*	*	#	*	§		§	#	*	#	*	*	*	*	*	*
REHg ₄		§	§	§	§	§		§		§							
RE ₁₁ Hg ₄₅		§	*	#[1]	#	*		*		#				§			
"REHg _{6.5} "			§[2]	§	§	§			*		§					*	

1.3. Polar Metal-Metal Bonding

The term "polar metal" is multiply defined in literature and used in different contexts. It describes for example electron localisation between two different metal atoms in a direct bonding interaction. This describes a polar covalent bond between two metal atoms, mostly within a multinuclear complex or organometallic compound. In another context, the term is used for description of the height of the Schottky barrier within the contact of a semiconductor and a metal. A third context originates from symmetry considerations where polarity is a symmetry element in the sense of a polar axis.

In this work, the term "polar metal" or "polar metal-metal bonding" will be used to describe the gradual transition of a metallic bond to an ionic bond, analogous to the transformation from covalent to ionic bonding. This is emphasised by the van-Arkel-Ketelaar triangle. Figure 1.2 shows the triangle first proposed by van Arkel, the three fundamental interatomic interactions located on the vertices: Ionic (CsF), covalent (F₂) and metallic (Sn).^[92] Along the edges compounds are located supposed to show the gradual transfer from one bonding modus to another. Ketelaar extended the triangle

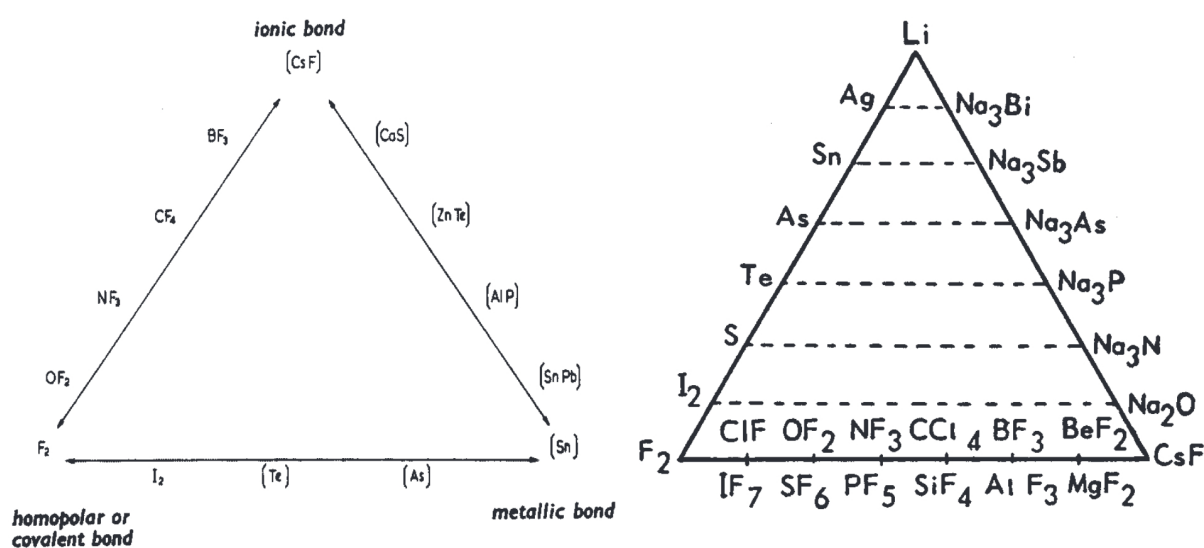


Figure 1.2.: Bond-type triangles as proposed by van Arkel (left) and Ketelaar (right).^[92, 93]

by making use of the space inside the triangle (horizontal lines) and adding compounds along these.^[93]

Since the initial proposal of the van-Arkel-Ketelaar triangle, it was modified numerous times with emphasis on different aspects.^[94] All authors use electronegativity difference ($\Delta\chi$) and average electronegativity (χ_{av}) of binary compounds as coordinate system. However, quantification is difficult as many compounds exhibit characteristics of all three bonding modi involved. Thus, the van-Arkel-Ketelaar triangle is a considerable oversimplification of the "true" bonding in those materials.^[94] Despite its shortcomings, the triangle is still useful to make rough estimations on the nature of compounds and of course for teaching purposes.

Polar metals often show "bad metal" behaviour. Following the Drude model, electric conductance σ is dependent on the lifetime τ of scattering events. Those take place on lattice vibration (temperature dependence) and disorder, as electrons are strongly influenced by kinks, impurities and grain boundaries. Other dependences include the free electron concentration n , the effective electron (or hole) mass m^* and elementary charge q : $\sigma = nq^2\tau/m^*$. In metallic conductors, the scattering rate of electrons on phonons increases with increasing temperature resulting in a linear dependence. According to Heisenberg's uncertainty principle, a minimum lifetime limit τ_{\min} implies a minimum metallic conductance σ_{MIR} which is called Mott-Ioffe-Regel limit. For metals with conductivities lower than this limit, non-physically high scattering rates are calculated, and thus should by theory be insulating. Most metals melt before reaching this limit, however, "bad metals" reach and can exceed this limit.^[95-97]

Strong electron correlation leading to bad metal behaviour has shown to procure interesting magnetic properties, unconventional superconductivity and non-classical temperature dependence of the resistance.^[98,99] Polar metal-metal bonding unlocks potential for new combinations of electric and magnetic properties. Describing the degree of polarity within a metallic system calls for quantitative approaches both in theory and experiment. Concepts dealing with polar metallic systems are scarce when compared with the widespread concepts describing and quantifying ionic contributions within a polar covalent system.

References

- [1] A. F. Holleman, N. Wiberg, G. Fischer, *Lehrbuch der Anorganischen Chemie*, Walter de Gruyter, Berlin, New York, 102nd edition (2007).
- [2] H. M. Leicester, *Discovery of the Elements*, Journal of chemical education, Easton, 7th edition (1968).
- [3] Y. Goren, A. Goring-Morris, I. Segal, *J. Archaeol. Sci.*, **28**(7), 671–690 (2001).
- [4] J. Martín-Gil, F. J. Martín-Gil, G. Delibes-de Castro, P. Zapatero-Magdalenó, F. J. Sarabia-Herrero, *Experientia*, **51**(8), 759–761 (1995).
- [5] K.-H. Schlote, *Chronologie der Naturwissenschaften*, Wissenschaftlicher Verlag Harri Deutsch GmbH, Frankfurt am Main, 1st edition (2002).

- [6] P. W. D'Itri, F. M. D'Itri, *Mercury contamination: a human tragedy*, Wiley, New York (1977).
- [7] J. M. Stillman, *The Story of Early Chemistry*, D. Appleton and Co., New York City (1924).
- [8] Aristotle, H. D. P. Lee, *Aristotle: Meteorologica*, Harvard University Press (1952).
- [9] E. R. Caley, J. F. C. Richards, Theophrastus, *Theophrastus on stones: Introduction, Greek text, English translation, and commentary*, The Ohio State University, Columbus (1956).
- [10] P. Dioscorides, J. M. Riddle, *De Materia Medica*, Univ. of Texas Pr., 1st edition (1986).
- [11] Pliny, H. Rackham, *Natural History, Book XXXIV*, Harvard University Press, 1st edition (1952).
- [12] Vitruvius, F. Granger, *De architectura, VII*, Harvard University Press, 1st edition (1934).
- [13] A. Greenberg, *From alchemy to chemistry in picture and story*, Wiley-Interscience, New Jersey, 1st edition (2007).
- [14] G. Agricola, H. C. Hoover, H. L. Hoover, *De Re Metallica*, Dover Publications, 1st edition (1950).
- [15] A. Volta, *Philos. Trans. R. Soc. London*, **90**, 403–431 (1800).
- [16] W. Cruickshank, *Philos. Mag. J. Sci.*, **4**, 187–191 (1800).
- [17] W. Cruickshank, *Philos. Mag. J. Sci.*, **4**, 254–264 (1800).
- [18] J. W. Ritter, *Beyträge zur nähern Kenntniss des Galvanismus und der Resultate seiner Untersuchung*, Frommann, Jena (1805).
- [19] J. W. Ritter, *Physisch-Chemische Abhandlungen in chronologischer Folge*, Reclam, Leipzig (1806).
- [20] C. J. T. Grotthuß, *Mémoire sur la décomposition de l'eau et des corps qu'il tient en dissolution à l'aide de l'électricité galvanique*, Rom (1805).
- [21] H. Davy, *Philos. Trans. R. Soc. London*, **97**, 1–56 (1807).
- [22] J. J. Berzelius, *Föreläsningar i Djurkemien*, Carl Delen, Stockholm (1806).
- [23] W. W. Skeat, *An etymological dictionary of the English language*, Oxford Clarendon Press, Oxford (1835).
- [24] F. Johnson, F. Meninski, J. Richardson, C. Wilkins, *A dictionary, Persian, Arabic and English*, W.H. Allen, London (1852).
- [25] C. W. Fairhurst, J. B. Cohen, *Acta Crystallogr. B*, **28(2)**, 371–378 (1972).
- [26] G. Ryge, C. W. Fairhurst, C. M. Fischer, *Int. Dent. J.*, **11(2)**, 1–5 (1961).

- [27] G. V. Black, *Dent. Cosmos*, **37**, 553–557 (1895).
- [28] R. Bharti, K. Wadhvani, A. Tikku, A. Chandra, *J Conserv. Dent.*, **13(4)**, 204 (2010).
- [29] H. Y. Castner, *US-Patent No. 528322* (1894).
- [30] C. S. Barrett, *Acta Crystallogr.*, **10(1)**, 58–60 (1957).
- [31] W. M. Lehmann, *Z. Kristallogr.*, **60(1-6)** (1924).
- [32] H. E. Buckley, *Miner. Mag.*, **20(110)**, 382–392 (1925).
- [33] W. H. Zachariasen, *Nor. geol. Tidsskr.*, **8(3)**, 5 (1926).
- [34] E. Zintl, G. Brauer, *Z. Phys. Chem.*, **20**, 245–271 (1933).
- [35] E. Zintl, A. Schneider, *Z. Elektrochem. Angew. Phys. Chem.*, **41(11)**, 771–774 (1935).
- [36] A. Iandelli, R. Ferro, *Atti Accad. Nazl. Lincei, Rend., Classe Sci. Fis., Mat. Nat.*, **10**, 48–52 (1951).
- [37] J. W. Neckers, H. C. Kremers, *J. Am. Chem. Soc.*, **50(4)**, 950–954 (1928).
- [38] E. E. Jukkola, L. F. Audrieth, B. S. Hopkins, *J. Am. Chem. Soc.*, **56(2)**, 303–304 (1934).
- [39] H. N. McCoy, *J. Am. Chem. Soc.*, **63(2)**, 7–8 (1937).
- [40] H. N. McCoy, R. P. Hammond, *J. Am. Chem. Soc.*, **64(4)**, 1009–1009 (1942).
- [41] J. K. Marsh, *J. Chem. Soc.*, **53(9)**, 8–10 (1943).
- [42] J. K. Marsh, *J. Chem. Soc.*, **53(9)**, 531–335 (1943).
- [43] T. Moeller, H. E. Kremers, *Industrial & Engineering Chemistry Analytical Edition*, **17(12)**, 798–800 (1945).
- [44] H.-J. Deiseroth, A. Strunck, *Angew. Chem.*, **99(7)**, 701–702 (1987); b) H.-J. Deiseroth, A. Strunck, *Angew. Chem. Int. Ed.*, **26(7)**, 687–688 (1987).
- [45] W. Hornfeck, C. Hoch, *Acta Crystallogr. B*, **71(6)**, 752–767 (2015).
- [46] C. Hoch, A. Simon, *Angew. Chem.*, **124(13)**, 3316–3319 (2012); b) C. Hoch, A. Simon, *Angew. Chem. Int. Ed.*, **51(13)**, 3262–3265 (2012).
- [47] H.-J. Deiseroth, M. Rochnia, *Z. Anorg. Allg. Chem.*, **620(10)**, 1736–1740 (1994).
- [48] H.-J. Deiseroth, A. Strunck, *Angew. Chem.*, **101(9)**, 1286–1287 (1989); b) H.-J. Deiseroth, A. Strunck, *Angew. Chem. Int. Ed.*, **28(9)**, 1251–1252 (1989).
- [49] H.-J. Deiseroth, A. Stupperich, R. Pankaluoto, N. E. Christensen, *Z. Anorg. Allg. Chem.*, **597(1)**, 41–50 (1991).
- [50] H.-J. Deiseroth, A. Strunck, W. Bauhofer, *Z. Anorg. Allg. Chem.*, **575(1)**, 31–38

- (1989).
- [51] H.-J. Deiseroth, *Prog. Solid State Chem.*, **25(1-2)**, 73–123 (1997).
- [52] H.-J. Deiseroth, A. Strunck, W. Bauhofer, *Z. Anorg. Allg. Chem.*, **558(1)**, 128–136 (1988).
- [53] E. Biehl, H.-J. Deiseroth, *Z. Anorg. Allg. Chem.*, **625(8)**, 1337–1342 (1999).
- [54] E. Biehl, H.-J. Deiseroth, *Z. Anorg. Allg. Chem.*, **625(7)**, 1073–1080 (1999).
- [55] C. Hoch, A. Simon, *Z. Anorg. Allg. Chem.*, **634(5)**, 853–856 (2008).
- [56] H.-J. Deiseroth, M. Rochnia, *Angew. Chem.*, **105(10)**, 1556–1558 (1993); b) H.-J. Deiseroth, M. Rochnia, *Angew. Chem. Int. Ed.*, **32(10)**, 1494–1495 (1993).
- [57] J. W. Nielsen, N. C. Baenziger, *Acta Crystallogr.*, **7(3)**, 277–282 (1954).
- [58] A. V. Tkachuk, A. Mar, *Acta Crystallogr. E*, **62(6)**, i129–i130 (2006).
- [59] E. J. Duwell, N. C. Baenziger, *Acta Crystallogr.*, **13(6)**, 476–479 (1960).
- [60] E. J. Duwell, N. C. Baenziger, *Acta Crystallogr.*, **8(11)**, 705–710 (1955).
- [61] E. Todorov, S. C. Sevov, *J. Solid State Chem.*, **149(2)**, 419–427 (2000).
- [62] E. Biehl, H.-J. Deiseroth, *Z. Anorg. Allg. Chem.*, **625(3)**, 389–394 (1999).
- [63] F. Tambornino, C. Hoch, *J. Alloys Compd.*, **618**, 299–304 (2015).
- [64] M. Pušelj, Z. Ban, *Croat. Chem. Acta*, **51(1)**, 75–79 (1978).
- [65] G. Bruzzone, F. Merlo, *J. Less-Common Met.*, **35(1)**, 153–157 (1974).
- [66] G. Bruzzone, F. Merlo, *J. Less-Common Met.*, **32(2)**, 237–241 (1973).
- [67] G. Bruzzone, F. Merlo, *J. Less-Common Met.*, **39(2)**, 271–276 (1975).
- [68] G. Brauer, R. Rudolph, *Z. Anorg. Allg. Chem.*, **248(4)**, 405–424 (1941).
- [69] G. Brauer, W. Haucke, *Z. Phys. Chem.*, **33**, 304–310 (1936).
- [70] R. Ferro, *Acta Crystallogr.*, **7(11)**, 781 (1954).
- [71] A. Iandelli, A. Palenzona, *Atti Accad. Nazl. Lincei, Rend., Classe Sci. Fis., Mat. Nat.*, **8**, 164–168 (1964).
- [72] Z. Ban, M. Pušelj, *Z. Naturforsch. B*, **35(12)**, 1594–1595 (1980).
- [73] A. V. Tkachuk, A. Mar, *Inorg. Chem.*, **47(4)**, 1313–8 (2008).
- [74] M. Wendorff, C. Röhr, *Z. Naturforsch. B*, **67**, 893–906 (2012).
- [75] M. Wendorff, C. Röhr, *J. Alloys Compd.*, **546**, 320–328 (2013).
- [76] A. V. Tkachuk, A. Mar, *Dalton Trans.*, **39(30)**, 7132–5 (2010).
- [77] C. Guminski, *J. Phase Equilib.*, **14(1)**, 97–99 (1993).

- [78] C. Guminski, *J. Phase Equilib.*, **14(3)**, 382–387 (1993).
- [79] C. Guminski, *J. Phase Equilib.*, **16(1)**, 86–91 (1995).
- [80] C. Guminski, *J. Phase Equilib.*, **16(1)**, 73–76 (1995).
- [81] C. Guminski, *J. Phase Equilib.*, **16(2)**, 181–185 (1995).
- [82] C. Guminski, *J. Phase Equilib.*, **16(1)**, 77–80 (1995).
- [83] C. Guminski, *J. Phase Equilib.*, **16(2)**, 186–192 (1995).
- [84] C. Guminski, *J. Phase Equilib.*, **16(3)**, 276–276 (1995).
- [85] C. Guminski, *J. Phase Equilib.*, **16(5)**, 448–453 (1995).
- [86] C. Guminski, *J. Phase Equilib.*, **16(6)**, 526–526 (1995).
- [87] C. Guminski, *J. Phase Equilib.*, **16(5)**, 454–458 (1995).
- [88] C. Guminski, *J. Phase Equilib.*, **14(3)**, 391–392 (1993).
- [89] C. Guminski, *J. Phase Equilib.*, **16(2)**, 193–196 (1995).
- [90] C. Guminski, *J. Phase Equilib.*, **16(5)**, 459–459 (1995).
- [91] C. Guminski, *J. Phase Equilib.*, **16(4)**, 348–352 (1995).
- [92] A. E. van Arkel, *Molecules and Crystals*, Butterworths, London (1949).
- [93] J. A. A. Ketelaar, *Chemical Constitutions - An Introduction to the Theory of the Chemical Bond*, Elsevier, Amsterdam, London, New York (1958).
- [94] T. L. Meek, L. D. Garner, *J. Chem. Educ.*, **82(2)**, 325 (2005).
- [95] O. Gunnarsson, M. Calandra, J. E. Han, *Rev. Modern Phys.*, **75(4)**, 1085–1099 (2003).
- [96] N. E. Hussey, K. Takenaka, H. Takagi, *Philos. Mag.*, **84(27)**, 2847–2864 (2004).
- [97] R. Jaramillo, S. D. Ha, D. M. Silevitch, S. Ramanathan, *Nature Physics*, **10(4)**, 304–307 (2014).
- [98] X. Deng, J. Mravlje, R. Žitko, M. Ferrero, G. Kotliar, A. Georges, *Phys. Rev. Lett.*, **110(8)**, 1–5 (2013).
- [99] V. J. Emery, S. A. Kivelson, *Phys. Rev. Lett.*, **74(16)**, 3253–3256 (1995).

2. Aims and Scope of this Work

The aim of this work is to investigate polar metal-metal bonding on the basis of synthesis and characterisation of new compounds, quantification of the electron transfer from the electropositive to the electronegative element as the ultimate goal. Mercury-rich amalgams of less noble metals (alkali, alkaline earth and rare earth metals) serve as model systems for polar metallic bonding. As those compounds often decompose peritectically at low temperatures, they are synthesised by electrocrystallisation at low temperatures. Their structures as well as their properties are characterised on the basis of X-ray crystallography, magnetic measurements, NMR investigations and band structure calculations.

The emphasis on experimental work is the development of an electrolytic approach. DMF solvate complexes of metal iodides serve as educts and will be structurally characterised before employment. Electrocrystallisation is expanded from Hg as cathode material to Ga and low melting eutectics of Ga/Sn, InHg and GalInStan. The outcome of the reactions gives insight into the reaction mechanisms. As electrolysis at high temperatures ($> 150\text{ }^{\circ}\text{C}$) is currently not feasible, a distillation method as a complementary approach for higher temperatures is developed.

The products are subject to structural analysis by single-crystal and powder diffraction methods. Mercury-rich amalgams often show high structural complexity which is rationalised and quantified by complexity measures. The role of disorder phenomena on the complexity of the crystal structures is investigated. Band structure calculations including Bader analysis lead to understanding of the underlying principles of chemical bonding.

Investigations for quantification of the electron transfer are performed on Li amalgams as model systems. A combination of synthesis, NMR Knight shift measurements and band structure calculations in combination with electrical conduction measurements is employed. The question if Bader charges can satisfactorily be used for the quantification of polarity is addressed.

3. Results

3.1. Methods

3.1.1. Synthetic Methods

The first section of the following chapter contains the procedures of the synthetic methods used in this work: Electrocrystallisation as a pathway toward metallic compounds with low peritectic decomposition temperatures, especially amalgams of less noble metals, distillation processes as a complementary high-temperature method and solvate syntheses of the educts (metal iodide solvates) for electrolysis. The second part contains the analytical methods: Single crystal and powder X-ray diffraction methods and subsequent refinement of data, elemental analysis, determination of physical properties with magnetic, electrical conductance, thermoanalytical and nuclear magnetic resonance measurements. Quantum mechanical calculations were used to gain insight into bonding modi of the substances in question.

Electrolysis

Electrolysis was performed in a specifically manufactured glass apparatus (see Figure 3.1). Anode and cathode compartments are separated by a glass frit and mantled in order to provide a constant reaction temperature with an external thermostat. Filling and operation of the unit is possible under inert gas conditions with a Schlenk attachment. If necessary, the product can be separated from the cathode, isolated and washed with dry DMF under inert gas with the aid of an internal glass frit located directly under the cathode.

The anode consisted of a Pt foil or a W rod sealed in a glass tube. The cathode design has to be adjusted to the respective cathode material. It is important that only the cathode material itself and not the connecting wires are in contact with the electrolyte to prevent secondary cathode reactions. For Hg-containing cathodes (e.g. Hg, $\text{In}_{1-x}\text{Hg}_x$ with $x \approx 1$), an amalgamated

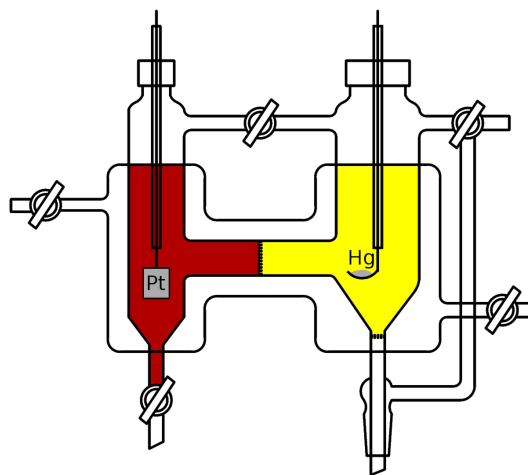


Figure 3.1.: Electrolysis chamber suitable for isothermic electrocrystallisation under inert gas conditions.

copper spoon was used, for Ga containing cathodes (e.g. Galinstan, $\text{Ga}_{0.8}\text{Sn}_{0.2}\dots$) a glass spoon with a Pt wire was used (see Figure 3.2).

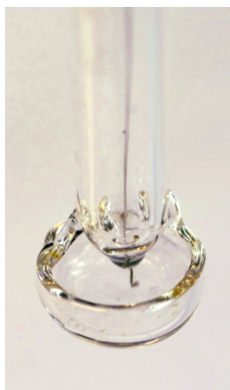


Figure 3.2.: Glass spoon with Pt wire.

A solution of an Iodide $M^{x+}I_x$ (M = electropositive metal, $x = 1-3$) in N,N -dimethyl formamide (DMF) served as electrolyte. DMF has high polarity ($\mu = 3.8$ D), a low melting and a high boiling temperature (liquid range: -61 to $+153$ °C) and thus offers a wide operating range. If the solubility of the salt was lower than $1 \text{ mol} \cdot \text{l}^{-1}$, a deposit of the salt was placed under the anode to resupply educt upon consumption during electrolysis. Iodides were preferred as they are generally highly soluble in DMF and show anodic formation of iodine allowing visual reaction observation. In contrast to bromides, chlorides and complex fluoride containing anions (BF_4^- , PF_6^-), the anode materials (Pt, W) and the glass container are inert toward iodine.

A typical electrolytic synthesis can be performed as follows: The electrolysis chamber is assembled and evacuated three times (pressure $< 1 \cdot 10^{-3}$ mbar) for 15 min and subsequently flooded with argon. In a Schlenk tube, the respective iodide is dissolved in dry DMF and the resulting solution degassed in high vacuum to remove residual traces of water. In an argon stream, the electrolysis chamber is filled with the electrolyte through the anode chamber and electrodes are installed. The thermostat is connected and the chamber is held at the desired temperature for 30 minutes prior to electrolysis. The temperature difference between the medium and the electrolyte normally is ≤ 5 °C. Electrolysis is started by applying a terminal voltage of 3–15 V for 1–72 h.

After completion, the thermostat is disconnected and the electrolysis chamber allowed to cool/warm to room temperature. For isolation, the chamber is emptied from solvent in an argon stream and the cathode washed with dry DMF. The product is then transferred to an argon-filled Schlenk tube and subsequently dried from residual DMF in high vacuum. Further manipulation is performed in an argon-filled glovebox.

Distillation Process

The synthesis of several amalgams was performed by combining high-temperature annealing and subsequent distillation. Mercury (10 eq.) and RE (RE = rare earth metal) are placed in borosilicate glass ampoules ($l = 25$ cm) with constrictions at $l = 10$ and $l = 20$ cm (see Figure 3.3). The ampoule is evacuated to a pressure below $1 \cdot 10^{-3}$ mbar and sealed. The lower part of the ampoule up to the constriction is put in a furnace in an upright position and heated to 300 °C for 12 h while the upper part is cooled in air to room temperature.

This allows the reaction of the educts to proceed in refluxing mercury. After cooling to room temperature, furnace and ampoule are turned in a horizontal position and the lower part up to the constriction is heated to 100 °C, allowing the mercury surplus to be distilled off. The product is isolated by sealing off the mercury filled part, further handling of the products is performed in an argon-filled glovebox.

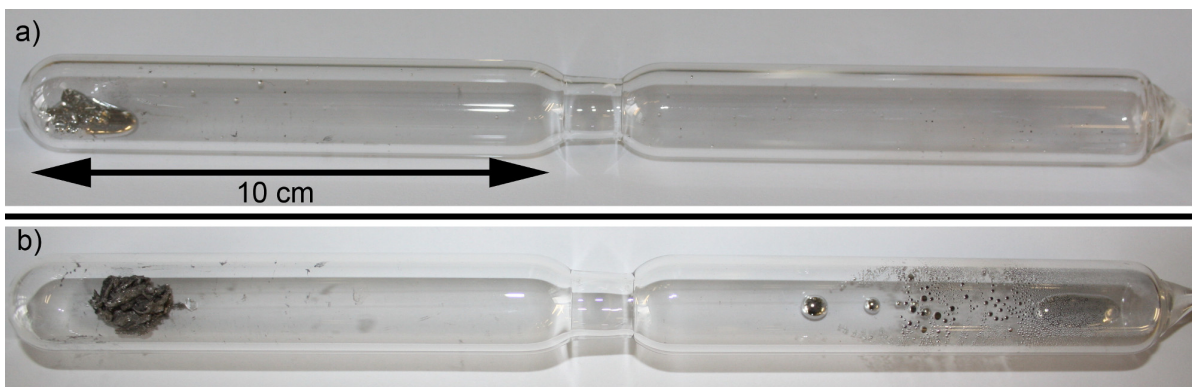


Figure 3.3.: Borosilicate glass ampoules used for distillation processes. Above: *RE* (*RE* = rare earth metal) and Hg sealed under vacuum. Below: *RE* amalgam (product, left) and surplus Hg (right) after the distillation operation. To isolate the product, the ampoule is separated into two parts by melting at the constriction.

Solvate Syntheses

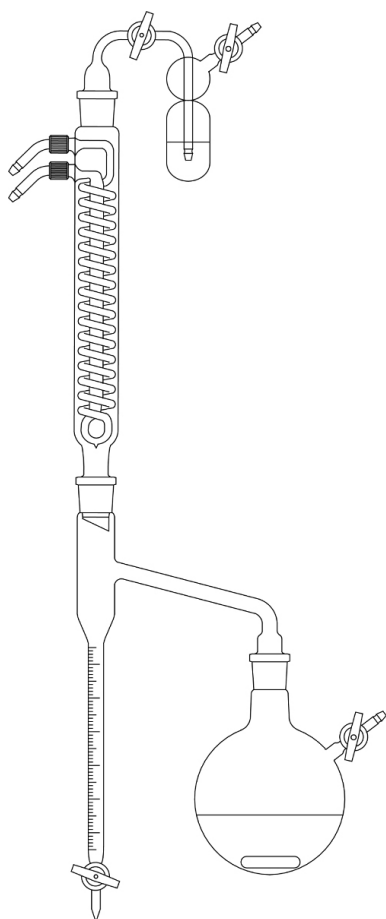


Figure 3.4.: Setup for synthesis of DMF solvates consisting of Schlenk flask, water separator, reflux condenser and bubble counter.

Alkali metal iodides were used as purchased. Prior to electrolysis a saturated solution of the respective iodide in DMF was prepared and degassed in high-vacuum.

DMF Solvates of EuI_3 and ScI_3 were prepared starting from the trivalent oxides. Small portions of the oxides were added to concentrated aqueous HCl at reflux conditions ($\approx 80^\circ\text{C}$) until only minor residuals of the oxides remained. Those were dissolved by addition of sufficient concentrated HCl until a clear, colourless solution was obtained. After cooling to room temperature, the solvent was removed under reduced pressure until the chloride hydrates were obtained.

DMF solvates of all other metal iodides were prepared from the respective chloride hydrates. The hydrates were dissolved in ice-cooled DMF (0°C) until a concentrated solution was obtained. A stoichiometric amount of a cooled saturated solution of KI in DMF was added. A metathesis reaction yielded phase-pure KCl as precipitate (solubility $< 0.1 \text{ g}\cdot\text{L}_{\text{DMF}}^{-1}$) isolated by filtration.

The remaining solution of the respective iodides in DMF was dried in a modified Dean-Stark apparatus (see Figure 3.4). The apparatus was evacuated and subsequently flooded with argon (3 times). A mixture of the water-containing iodide solutions in DMF and toluene (50 ml) was stirred and refluxed at 150°C for 3–5 h. During this period, the water was separated from the reaction mixture by azeotropic distillation and the process was allowed to continue until water separation ceased. After all water was

separated toluene was removed. In a constant argon stream (3–5 bubbles per minute) the reaction mixture was cooled to room temperature, the product was washed with a small portion of ice-cold DMF and isolated by standard Schlenk technique.

3.1.2. Analytical Methods

The following sections give an overview of the analytical methods employed in this work. Single crystal X-ray diffractometry was used to determine the crystal structures of compounds, powder X-ray diffractometry was used to confirm the crystal structure models from single crystal diffractometry and check for additional phases. Chemical composition was determined by ICP-AES chemical analysis. Potential low-temperature superconductivity and magnetical ordering was checked for by SQUID or AC susceptometer measurements. To compare the products to other metals and semimetals, electrical conductance measurements were performed. Thermoanalytical measurements were performed to determine melting/decomposition temperatures or to find ideal temperatures for tempering.

Single Crystal Diffractometry

Single crystals insensitive toward moisture or air were mounted on top of glass fibers. Specimens sensitive toward air and moisture were handled under dry paraffin oil (dried over potassium sand). Single crystals were isolated and transferred in Lindemann capillaries (inner diameter 0.1–0.3 mm, filled with dry paraffin oil), and sealed immediately.

The crystals were mounted on a one-circle Stoe IPDS1 diffraction system (Stoe IPDS, Stoe & Cie, Darmstadt) equipped with an image plate detector, graphite monochromator (Ag- K_{α} or Mo- K_{α} radiation) or a Bruker D8 Quest diffractometer system equipped with a CMOS detector, microfocus X-ray tube (Mo- K_{α} radiation), Goebel mirror optics and cooling system (Oxford cryo systems).

Collection, integration and correction of data was performed with device-native software (STOE and Bruker).^[1,2]

Structure solution and refinement Structure solution was performed with direct methods (SHELXS-97). Structure refinement was performed by the full-matrix least-squares method implemented in SHELXL-97. Initial visualisation (Pluton), checks for additional symmetry (Addsym & Newsym), absorption correction (AbsTomp, MulScanAbs, AbsSphere; IPDS data only), standardisation of cell metrics and atomic positions (StructureTidy) were performed with the programs implemented in the PLATON package.

Powder Diffraction

X-ray powder diagrams were recorded on a transmission powder diffractometer system (Stoe STADI-P, Stoe & Cie, Darmstadt, Mo $K_{\alpha 1}$ radiation, curved Ge[111] monochromator) to check for additional phases and Rietveld refinement. Representative portions

of the products were ground and sealed in capillaries with inner diameter of 0.1–0.5 mm, depending on the absorption coefficients of the samples. Some samples were diluted with diamond powder to account for either strong absorption or high ductility.

During Rietveld refinement (Topas Academic), peak shapes were modelled with a fundamental parameters approach (direct convolution of source emission profiles, axial instrument contributions) and a double-Voigt approach to compensate size-strain effects. A shifted Chebychev polynomial was applied for background modelling. Careful absorption correction was performed by assuming a cylindrical sample with a packing density of 0.5 – 0.7. If necessary, preferred orientation was corrected by spherical harmonics function (order no higher than 4) or a March-Dollase function.

Magnetic Measurements

Magnetic measurements on polycrystalline samples were either performed with a commercial SQUID magnetometer (MPMS-XL5, Quantum Design, Inc.) or a self-manufactured *ac* susceptometer.^[3]

The SQUID magnetometer operates in a temperature range from 1.8 K to 400 K with external fields up to 50 kOe. The fully automated differential dual-coil *ac* susceptometer operates in the temperature range 3.4 K – 320 K with alternating magnetic fields up to 8 Oe and frequencies between 100 Hz and 10 kHz. Sample amounts of about 20 to 50 mg were loaded into gelatine capsules and fixed in a straw as sample holder. The output data files were processed directly in ORIGIN.^[4] Data were corrected for sample holder and core diamagnetism.

Electric Conductance Measurements

One of the following methods was applied:

Electrical resistances were measured by the van-der-Pauw method.^[5] The samples were cold-pressed into pellets ($\varnothing = 6$ mm, thickness 1 mm) and fixed on a brass sample carrier using the epoxy resin Stycast TM 2850FT (EMERSON & CUMING, catalyst Tetraethylenepentamine), and copper wires (LAKESHORE, Quad-TwistT-Cryogenic wire 36 AWG) were fixed to the surface of the sample by silver conductive paint.

Temperature-dependent measurements of the *dc* resistances between 10 K and 300 K were performed with a closed-cycle He cryostat (Cold Head, CTI CRYOGENICS, Model 22 CP) connected to a temperature controller (LAKESHORE, Model 331) with a silicon diode temperature sensor. Data logging was performed by the program LEITMESS. Primary data evaluation and interpretation was performed with ORIGIN.^[4]

DSC

Differential scanning calorimetry (DSC) measurements were performed to determine decomposition/transformation temperatures of the samples (about 20 mg of material) in O-ring sealed (Vitron Rubber W.0.22") Fe containers (Perkin Elmer Large Volume Cap-

sules, capacity 60 μL). A nitrogen flow of 20 mL per minute was applied on a Linseis PT 10 DSC device calibrated with pure indium and zinc standards at a heating rate of $5\text{ }^\circ\text{C}\cdot\text{min}^{-1}$. Evaluation of data was performed with the device's own software.^[6]

Melting temperatures

Melting temperatures were either measured by DSC (see above) or estimated visually with a Büchi melting-point B-450 device. In a glove box, the substance was put in a glass capillary, temporarily sealed with grease, brought on air and sealed immediately. The melting temperature was roughly determined with a heating rate of $10\text{ }^\circ\text{C}\cdot\text{min}^{-1}$. Then, three measurements were performed with a heating rate of $0.1\text{ }^\circ\text{C}\cdot\text{min}^{-1}$ in a narrow temperature interval and the values were averaged.

Elemental Analysis (ICP-AES)

ICP-AES (Inductively coupled plasma – atomic emission spectroscopy) served as elemental analysis for all elements except halogenes and Cs, C, H, N, O. Small amounts ($\approx 1\text{ mg}$) were dissolved in analytical grade acid, diluted and sprayed into an argon plasma ($T \approx 10.000\text{ K}$). Positions and intensities of spectral lines were used for quantification, the error is within 5 %. Samples were measured and evaluated on a Varian Vista RL CCD simultaneous ICP–AES spectrometer.

Solid-State NMR

Solid-state NMR spectra of ^7Li and ^{199}Hg were acquired on a BRUKER AVANCE-III 500 spectrometer, with a static magnetic field of $B_0 = 11.7\text{ T}$. A commercial static probe was used for the measurements, with custom-made solenoid coils oriented perpendicular to the magnetic field. The number of transients required for a good quality spectrum was of the order of one hundred for ^7Li and several ten thousands for ^{199}Hg , with recycle delays between 1 and 4 s. Chemical shifts were reported relative to the secondary reference of the ^1H -NMR resonance of 1% $\text{Si}(\text{CH}_3)_4$ in CDCl_3 .

3.1.3. Quantum-Mechanical Calculations

Quantum-mechanical calculations were performed with the program package Wien2k.^[7] It uses the FP-LAPW method (Full Potential Linearized Augmented Planes Waves) including all electrons of the system instead of omitting core electrons and using pseudopotentials. All electron models are considered as standard for the numerical accuracy of solid-state DFT and supposed to yield most reliable values for a given functional as long as numerical accuracy is achieved, usually by means of large basis sets and dense k -meshes.^[8,9] This is especially useful for calculations of heavy elements to account for relativistic effects and f -electrons which can exhibit unusual behaviour.

Calculations were either performed on a PC (64 bit operating system (Linux Mint 16 Cinnamon) and a quad-core processor (Intel Core i5-3470 CPU @ 3.20GHz x 4) equipped

with 32GiB RAM) or on the LRZ Linux cluster (Leibniz Supercomputing Centre, dual socket octo-core AMD Opteron Magny Cours (2.0 GHz) processors, varying number of cores and allocated RAM).

If not mentioned otherwise, exchange correlations were calculated with standard PBE-GGA approximation.^[10] It was chosen because of its good results for a wide range of elements/compounds and as it is widely used it ensues comparability with other calculations from literature.^[11] Convergence criteria were charge convergence ≤ 0.0001 eV and charge distance ≤ 0.00001 eV.

Total and partial density of states (tDOS and pDOS) were determined by means of the modified tetrahedron method.^[7] Quantification of the topology of the electron density was performed according to Bader's 'Atoms in molecules' theory.^[12]

References

- [1] STOE & Cie GmbH, *X-Area: IPDS Control Software Version 1.39* (2006).
- [2] Bruker-AXS, *APEX2, Version 2014.11-0* (2014).
- [3] M. C. Tegel, *Iron Pnictide superconductors*, Phd thesis, LMU Munich (2011).
- [4] OriginLab, *Origin, Version 6.1* (2007).
- [5] L. J. van der Pauw, *Philips Res. Repts.*, **13**, 1–9 (1958).
- [6] PerkinElmer, *Pyris - Instrument Managing Software, Version 11* (2012).
- [7] P. Blaha, K. Schwarz, G. Madsen, D. Kvasnicka, J. Luitz, *An Augmented Plane Wave Plus Local Orbitals Program for Calculating Crystal Properties* (2013).
- [8] K. Lejaeghere, G. Bihlmayer, T. Bjorkman, P. Blaha, S. Blugel, V. Blum, D. Caliste, I. E. Castelli, S. J. Clark, A. Dal Corso, S. de Gironcoli, T. Deutsch, J. K. Dewhurst, I. Di Marco, L. Genovese, P. Giannozzi, M. Giantomassi, S. Goedecker, X. Gonze, O. Granas, E. K. U. Gross, A. Gulans, F. Gygi, D. R. Hamann, P. J. Hasnip, N. A. W. Holzwarth, D. Iu an, D. B. Jochym, F. Jollet, D. Jones, G. Kresse, K. Koepnik, E. Kucukbenli, S. Lubeck, M. Marsman, N. Marzari, U. Nitzsche, L. Nordstrom, T. Ozaki, L. Paulatto, W. Poelmans, M. I. J. Probert, M. Richter, S. Saha, M. Scheffler, M. Schlipf, K. Schwarz, S. Sharma, F. Tavazza, P. Thunstrom, A. Tkatchenko, M. Torrent, D. Vanderbilt, M. J. van Setten, V. Van Speybroeck, J. M. Wills, J. R. Yates, G.-X. Zhang, *Science*, **351(6280)**, 1415 (2016).
- [9] P. Haas, F. Tran, P. Blaha, *Phys. Rev. B*, **79(8)**, 1–10 (2009).
- [10] J. P. Perdew, K. Burke, M. Ernzerhof, *Phys. Rev. Lett.*, **77(18)**, 3865–3868 (1996).
- [11] G. I. Csonka, J. P. Perdew, A. Ruzsinszky, P. H. T. Philipsen, S. Lebègue, J. Paier, O. A. Vydrov, J. G. Ángyán, *Phys. Rev. B*, **79(15)**, 1–14 (2009).
- [12] R. F. W. Bader, *Atoms in Molecules*, John Wiley & Sons, Ltd, Chichester, UK (2002).

3.2. Metal Iodide Solvates

3.2.1. Single Crystal Structures

For electrocrystallisation it is convenient to use the metal iodide solvates as educts rather than the respective solvate free metal iodides. Preparation of the latter is often tedious as their syntheses require complicated devices and/or high temperatures. The respective solvates are much easier obtained at mild reaction conditions close to room temperature. Also, they are often obtained in one-pot reactions, further simplifying the procedure. Principal reaction pathways are: (1) Recrystallisation of a metal iodide hydrate from DMF. (2) Reaction of a metal with aqueous HI in DMF. (3) Direct reaction between a metal and iodide in DMF solvent. (4) Solution metathesis reaction between a metal chloride and KI in DMF.

The metal iodide solvates have been characterised in detail by single crystal and powder diffraction methods to get knowledge on the employed educts of electrocrystallisation. Their crystal structures were elucidated and put into context with motifs of close packed structures. The following chapter contains the unpublished results of the structural investigations. Additional data is compiled in the supplementary material chapter A.

[Li(DMF)₄]I

Pale yellow single crystals of good quality were yielded by dissolving 0.5 g portions of LiI (acros organics, 99 %) in dry DMF (100 ml, Fischer Chemical, HPLC grade) and subsequent degassing of the saturated solution in high vacuum. Dissolving LiI led to temperatures as high as 80 °C with local overheating of DMF (boiling point = 154 °C) originating from the high solvation enthalpy. The colour is probably due to minor iodine contamination already present in the educt:

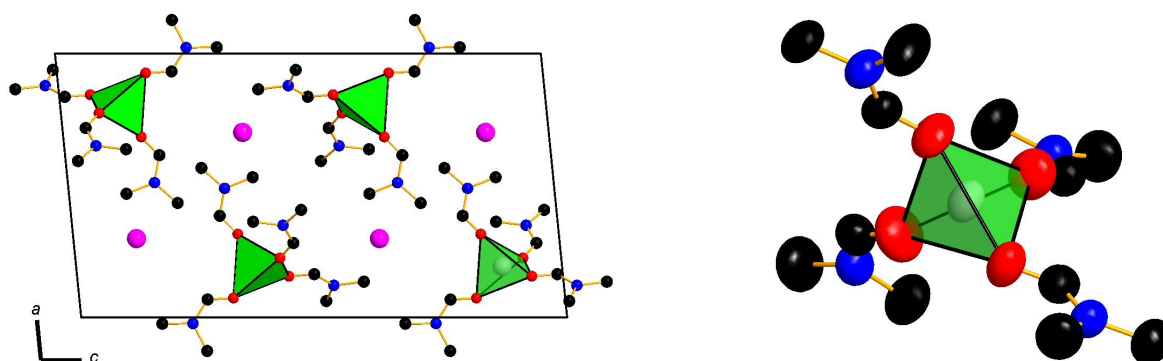
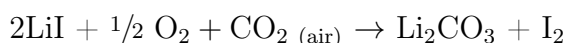


Figure 3.5.: The crystal structure of [Li(DMF)₄]I. I: magenta; Li: grey; C: black; O: red, N: blue. Left: View of the unit cell along [010]. Right: Li is coordinated by four O atoms of DMF molecules. Ellipsoids are drawn at a 75% probability level, H atom positions are omitted for clarity.

The resulting anhydrous saturated solution was allowed to cool to room temperature and within minutes pale yellow block-shaped and hygroscopic crystals formed. A suitable crystal was selected and centred on a STOE IPDS 1 diffraction system. For additional details on data collection and treatment see Tables 3.3, A.2 and A.3. Indexing yielded a monoclinic cell with systematic absence conditions leading to extinction symbol $P 1 2_1/c 1$ (unique axis b), indicating space group $P2_1/c$. Solution yielded heavy atom positions (iodine), all other atoms were subsequently located by analysis of the difference Fourier map during refinement. No additional symmetry was found. All atoms except H were treated with anisotropic thermal displacement parameters, H atom positions were refined with rigid-model constraints. Residual electron densities were in close proximity to I and thus treated as termination effects.

[Li(DMF)₄]I crystallises in space group $P2_1/c$ with four formula units in the unit cell and one crystallographic position for both Li and I atoms, and two crystallographically independent DMF molecules (see Table 3.1). Li atoms are coordinated by oxygen atoms of four DMF molecules. The resulting tetrahedron is distorted, angles (see Table A.3) range from $\angle_{\text{O-Li-O}} = 103.3(4)^\circ$ to $113.7(4)^\circ$. Distances (table A.2) range from $d_{\text{Li-O}} = 1.892(9)$ Å to $1.948(8)$ Å (see Table A.3) in accordance with similar coordination compounds (e.g. Li(H₂NCONH)).^[1,2]

Table 3.1.: Standardised^[3] fractional atomic coordinates and equivalent isotropic displacement parameters /Å² for [Li(DMF)₄]I. U_{eq} is defined as $1/3$ of the trace of the orthogonalized U_{ij} tensor. Standard deviations in units of the last digit are given in parentheses. All atoms occupy the general position with Wyckoff number 4e.

Atom	x	y	z	U_{eq}	Atom	x	y	z	U_{eq}
Li1	0.8067(5)	0.1254(10)	0.1233(3)	0.077(12)	H9C	0.1650	0.1950	0.1103	0.146
I1	0.29887(3)	0.59299(4)	0.129986(13)	0.0901(2)	O5	0.6837(3)	0.0551(6)	0.1605(2)	0.127(2)
O1	0.7744(3)	0.3414(5)	0.0788(2)	0.1125(11)	N5	0.5108(3)	0.0779(5)	0.1784(2)	0.0805(9)
N1	0.6504(3)	0.5662(5)	0.0657(2)	0.0748(9)	C13	0.6146(4)	0.0649(7)	0.1935(2)	0.0902(13)
C1	0.5932(5)	0.6908(9)	0.0251(3)	0.115(2)	H13A	0.6371	0.0631	0.2337	0.108
H1A	0.6136	0.6700	-0.0139	0.172	H13B	0.6229	-0.0444	0.2173	0.108
H1B	0.6111	0.8132	0.0369	0.172	C14	0.4684(5)	0.0956(8)	0.1182(2)	0.112(2)
H1C	0.5168	0.6724	0.0253	0.172	H14A	0.5270	0.1022	0.0938	0.167
C2	0.6372(5)	0.5857(9)	0.1266(2)	0.116(2)	H14B	0.4258	0.2042	0.1133	0.167
H2A	0.6671	0.4817	0.1477	0.174	H14C	0.4241	-0.0078	0.1069	0.167
H2B	0.5616	0.5952	0.1316	0.174	C15	0.4338(5)	0.0797(10)	0.2221(3)	0.129(2)
H2C	0.6739	0.6933	0.1415	0.174	H15A	0.4704	0.0526	0.2602	0.194
C3	0.7171(4)	0.4454(7)	0.0485(2)	0.0870(13)	H15B	0.3789	-0.0098	0.2121	0.194
H3A	0.7212	0.4378	0.0081	0.104	H15C	0.4011	0.1976	0.2230	0.194
H3B	0.7664	0.5140	0.0266	0.104	O7	-0.0738(3)	0.1501(5)	0.18277(14)	0.0969(10)
O3	0.1562(3)	0.0481(4)	-0.06427(13)	0.0936(9)	N7	0.0227(3)	0.1501(5)	0.2712(2)	0.0791(9)
N3	0.1221(3)	0.1296(5)	0.0266(2)	0.0742(9)	C22	-0.0673(4)	0.1449(6)	0.2361(2)	0.0793(11)
C7	0.0625(5)	0.2898(7)	0.0079(3)	0.1056(2)	H22A	-0.1316	0.1364	0.2537	0.095
H7A	0.0546	0.2955	-0.0344	0.159	H22B	-0.1098	0.2469	0.2477	0.095
H7B	0.1008	0.3953	0.0234	0.159	C23	0.0238(5)	0.1417(8)	0.3343(2)	0.100(2)
H7C	-0.0076	0.2858	0.0221	0.159	H23A	-0.0485	0.1550	0.3450	0.150
C8	0.1646(3)	0.0231(6)	-0.0113(2)	0.0798(11)	H23B	0.0682	0.2377	0.3519	0.150
H8A	0.2036	-0.0777	0.0033	0.096	H23C	0.0525	0.0266	0.3481	0.150
H8B	0.1350	-0.0969	-0.0058	0.096	C24	0.1264(4)	0.1590(10)	0.2476(3)	0.119(2)
C9	0.1355(4)	0.0905(7)	0.0892(2)	0.0973(14)	H24A	0.1608	0.0423	0.2512	0.179
H9A	0.1838	-0.0105	0.0965	0.146	H24B	0.1712	0.2476	0.2691	0.179
H9B	0.0666	0.0611	0.1024	0.146	H24C	0.1160	0.1931	0.2068	0.179

[Na(DMF)₃]I

Colourless single crystals of good quality were obtained by dissolving NaI (VWR chemicals, 99.5 %) in dry DMF (100 ml, Fischer Chemical, HPLC grade) under inert gas conditions until a saturated solution was obtained. The solvation enthalpy is negative

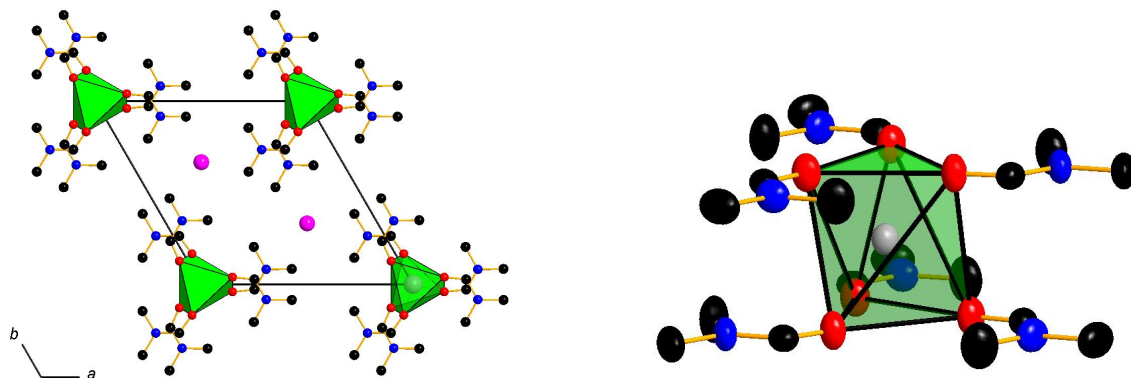


Figure 3.6.: The crystal structure of $[\text{Na}(\text{DMF})_3]\text{I}$. I: magenta; Na: green; C: black; O: red, N: blue. Left: View of the unit cell along $[001]$. Stacking of DMF molecules along $[001]$ is in gauche conformation to maximise packing density. Right: Na atoms are coordinated by six O atoms of DMF molecules. Ellipsoids are drawn at a 75% probability level, H atom positions are omitted for clarity.

and the solution reached a temperature of ca. $50\text{ }^\circ\text{C}$. The saturated solution was allowed to cool to room temperature. After 24 h, colorless block-shaped crystals several millimeters in length had formed. A suitable crystal was selected and measured on a STOE IPDS 1 diffraction system. For additional details on data collection and treatment see Table 3.3.

Hexagonal symmetry with extinction symbol $P - - c$ paired with absence of inversion (Wilson statistics) led to possible space groups $P6_3mc$ and $P\bar{6}2c$. Solution and initial refinement was performed in $P6_3mc$, checks for additional symmetry with Platon^[4] revealed the final space group $P\bar{6}2c$. All atoms except H were treated with anisotropic thermal displacement parameters, H atom positions were refined with rigid-model constraints. Twin refinement was applied to account for an inversion twin with approximate ratio of 30:70. The single crystal structure model and phase purity were confirmed by Rietveld refinement (see Figure 3.7 and Tables 3.2 and 3.4).

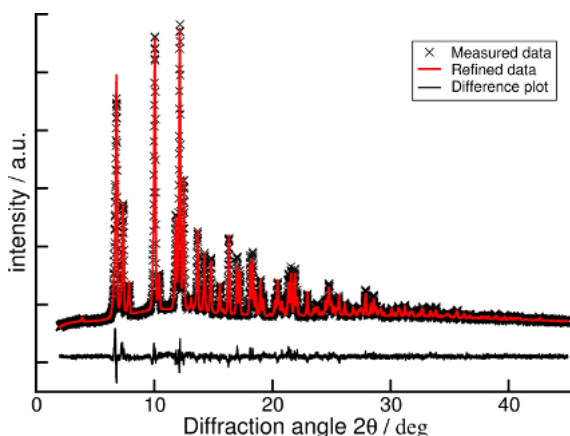


Figure 3.7.: Results of a Rietveld refinement of $[\text{Na}(\text{DMF})_3]\text{I}$. Refined parameters are compiled in Tables 3.2 and 3.4.

Table 3.2.: Results of the Rietveld refinement of $[\text{Na}(\text{DMF})_3]\text{I}$.

Formula	$[\text{Na}(\text{DMF})_3]\text{I}$
Z	2
Crystal system	hexagonal
Space group	$P\bar{6}2c$
Lattice parameters [\AA , \AA^3]	$a = 11.9005(4)$ $c = 6.4999(3)$ $V = 797.23(6)$
Density (X-ray) [g/cm^3]	1.65132(13)
Radiation	$\text{MoK}\alpha_1$
Parameters	42
Background parameters	12
R values	$R_p = 0.05138$ $R_{wp} = 0.06614$ $\chi^2 = 1.412$

The crystal structure is built from singular crystallographically independent Na and I atoms, together with three DMF molecules per asymmetric unit belonging to one crystallographic site (see Figure 3.6.) Na is coordinated by six oxygen atoms of DMF molecules, the resulting octahedron is slightly distorted ($\angle_{\text{O-Na-O}} = 79.929^\circ$ and 87.527° (see Tables A.4 and A.5)). The Na–O distances ($d_{\text{Na-O}} = 2.432(2)$ Å) are equal due to equivalent crystallographic positions and lie within the expected range.^[5] DMF molecules are oriented parallel to the *ab* plane, each coordinating two Na atoms as bridging ligand (see Figure 3.6) resulting in chains of face-sharing octahedra along [001]. The I atoms are located in voids between the DMF molecules.

Table 3.3.: Crystallographic data, details of the data collection and structure determination for $[\text{Li}(\text{DMF})_4]\text{I}$ and $[\text{Na}(\text{DMF})_3]\text{I}$.

		$[\text{Li}(\text{DMF})_4]\text{I}$	$[\text{Na}(\text{DMF})_3]\text{I}$
Crystal system		monoclinic	hexagonal
Space group		$P2_1/c$ (No. 13)	$P6_2c$ (No. 190)
Lattice parameters [Å, Å ³]			
	<i>a</i>	12.430(7)	11.918(2)
	<i>b</i>	7.364(2)	11.918(2)
	<i>c</i>	22.783(11)	6.5263(9)
	β	95.69(6)	
	<i>V</i>	2075(2)	802.8(2)
<i>Z</i>		4	2
Density (X-ray) [g/cm ³]		1.377	1.540
Diffractometer		— STOE IPDS 1 —	
Radiation		— Mo- K_α —	
Measurement temperature		— room temperature —	
Abs. coeff. $\mu_{\text{MoK}\alpha}$ [mm ⁻¹]		1.557	2.023
ϑ range for refinement [°]		2.91 – 25.00	3.42 – 24.99
Index range		$-14 \leq h \leq 14,$ $-8 \leq k \leq 8,$ $-27 \leq l \leq 27$	$-14 \leq h, k \leq 14,$ $-7 \leq l \leq 7$
No. of observed reflections		12977	10076
No. of ind. refl.		3456	506
No. of ind. refl. with ($I \leq 2\sigma(I)$)		2340	449
R_{int}		0.0828	0.0606
R_σ		0.0561	0.0198
Corrections		— Lorentz, polarisation, absorption —	
Absorption correction		— multiscan ^[6] —	
Structure solution		— SHELXS97 ^[7] —	
Structure refinement		— SHELXL97 ^[7] —	
No. of least-squares parameters		208	39
Goodness of fit on F^2		0.896	1.024
$R1/wR2$			
	For $I \geq 2\sigma(I)$	0.0415 / 0.1003	0.0187 / 0.0450
	For all data	0.0592 / 0.1072	0.0226 / 0.0457
res. electron density [e ⁻ ·Å ⁻³]		0.426 / -0.376	0.245 / -0.269

Table 3.4.: Top: Standardised^[3] fractional atomic coordinates and equivalent isotropic displacement parameters /Å² for [Na(DMF)₃]I as yielded by single crystal X-ray diffractometry. U_{eq} is defined as 1/3 of the trace of the orthogonalized U_{ij} tensor. Standard deviations in units of the last digit are given in parentheses. **Bottom:** Standardised^[3] fractional atomic coordinates and isotropic displacement parameters B_{iso} / pm² for [Na(DMF)₃]I as yielded by powder X-ray diffractometry.

Atom	Wyckoff number	x	y	z	U_{eq}	Atom	Wyckoff number	x	y	z	U_{eq}
Na1	2a	0	0	0	0.0403(4)	O1	6h	0.1673(2)	0.0398(2)	1/4	0.0495(8)
I1	2d	2/3	1/3	1/4	0.059(2)	C2	6h	0.2048(5)	0.3504(5)	1/4	0.072(2)
N1	6h	0.0826(4)	0.3475(3)	1/4	0.0473(9)	H2A	12i	0.1902	0.2644	0.2714	0.108
C1	6h	0.0847(5)	0.4696(4)	1/4	0.0635(13)	H2B	12i	0.2585	0.4061	0.3580	0.108
H1A	12i	0.0988	0.5033	0.1130	0.095	H2C	12i	0.2472	0.3827	0.1206	0.108
H1B	12i	0.1533	0.5298	0.3373	0.095	C3	6h	0.2645(4)	0.0278(4)	1/4	0.042(9)
H1C	12i	0.0033	0.4568	0.2997	0.095	H3A	12i	0.3146	0.0752	0.3689	0.050
H3B	12i	0.3146	0.0752	0.1311	0.050						

Atom	Wyckoff number	x	y	z	B_{iso}	Atom	Wyckoff number	x	y	z	B_{iso}
N1	6h	0.072(2)	0.341(2)	1/4	1.9(3)	O1	6h	0.167(9)	0.044(9)	1/4	4.4(4)
C1	6h	0.075(2)	0.461(2)	1/4	4.2(6)	C2	6h	0.197(2)	0.355(2)	1/4	4.9(5)
C3	6h	0.266(2)	0.035(2)	1/4	5.8(6)	I1	2d	2/3	1/3	1/4	4.63(8)
						Na1	2a	0	0	0	3.3(2)

[La(DMF)₉]I₃

LaCl₃·7H₂O (Chem Pur, 99.9 % metal basis) was dissolved in dry DMF (100 ml, Fischer Chemical, HPLC grade) until a saturated solution was obtained. A solution metathesis reaction was performed by addition of a stoichiometric amount of a saturated solution of KI in DMF, no temperature changes were observed for both processes. Subsequent azeotropic distillation resulted in an anhydrous solution of [La(DMF)₉]I₃ in DMF and upon cooling to room temperature, pale yellow and hygroscopic crystals formed. A suitable crystal was selected and mounted on a STOE IPDS 1 diffraction system. For additional details on data collection and treatment see Table 3.7.

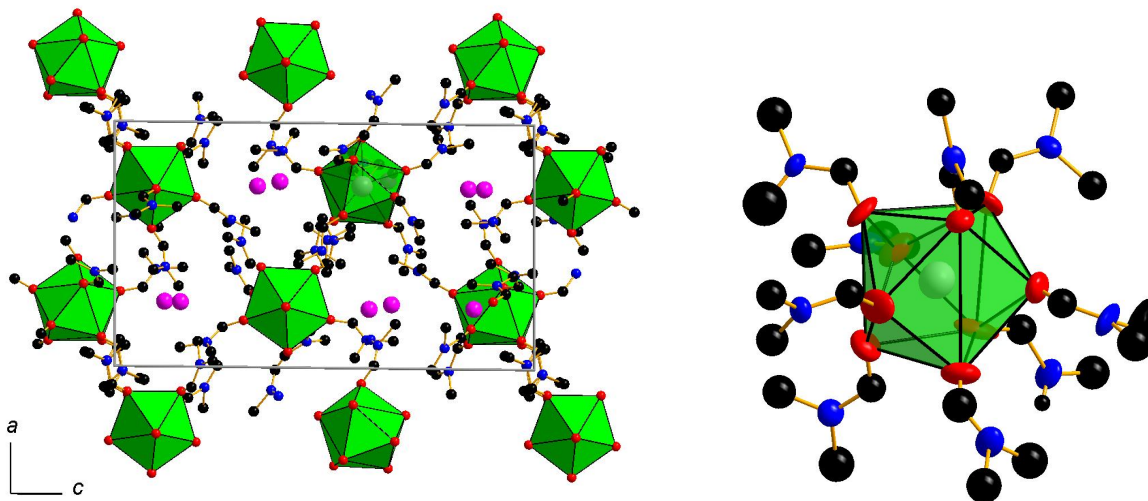


Figure 3.8.: The crystal structure of [La(DMF)₉]I₃. I: magenta; La: grey; C: black; O: red, N: blue. Left: Unit cell of [La(DMF)₉]I₃ along [010]. Right: La atoms are coordinated by O atoms of nine DMF molecules. Ellipsoids are drawn at a 75% probability level, H atom positions are omitted for clarity.

Indexing, absence of systematic extinction conditions and Wilson statistics indicated triclinic crystal system including inversion symmetry leading to space group $P\bar{1}$. Solution

succeeded in $P\bar{1}$ and yielded all heavy atom positions, upon refinement DMF molecules were identified from difference Fourier maps. All atoms except H were treated with anisotropic thermal displacement parameters, H atom positions were refined with rigid-model constraints. No additional symmetry was found. The single crystal structure and phase purity were confirmed by Rietveld refinement (see Figure 3.9 and Table 3.5).

$[\text{La}(\text{DMF})_9]\text{I}_3$ crystallises in space group $P\bar{1}$ with four formula units in the unit cell. There are two crystallographically independent La and six I sites and nine inequivalent DMF molecules per unit cell. La is coordinated by O atoms of nine DMF molecules forming a distorted tricapped trigonal prism. Distances (see Table A.6) range from $d_{\text{La-O}} = 2.33(2)$ Å to $2.62(2)$ Å. Other coordination compounds with La show similar interatomic distances and also tend to form large coordination spheres with up to 9 ligands due to the large ionic radius of La^{3+} .^[8,9]

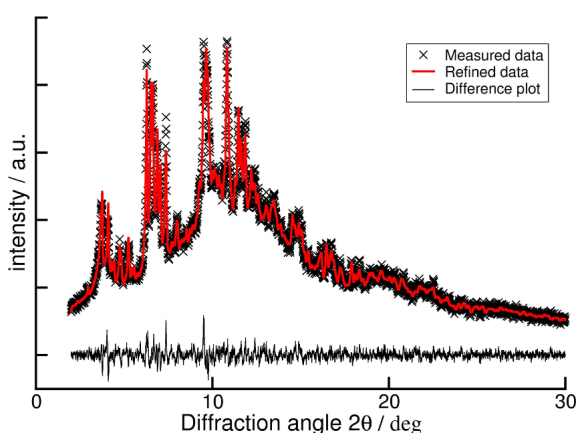


Figure 3.9.: Rietveld refinement of $[\text{La}(\text{DMF})_9]\text{I}_3$. Final refinement parameters are compiled in Table 3.5.

Table 3.5.: Results of the Rietveld refinement of $[\text{La}(\text{DMF})_9]\text{I}_3$.

Formula	$[\text{La}(\text{DMF})_9]\text{I}_3$
Z	4
Crystal system	triclinic
Space group	$P\bar{1}$
Latt. parameters [Å], [°]	$a = 12.986(2)$ $b = 17.199(3)$ $c = 22.083(3)$ $\alpha = 91.549(9)$ $\beta = 90.447(9)$ $\gamma = 95.107(9)$
Density (X-ray) [g/cm ³]	1.593(4)
Unit cell volume [Å ³]	4909(1)
Radiation	MoK α_1
Parameters	118
R values	$R_p = 0.02249$ $R_{wp} = 0.02890$ $\chi^2 = 1.420$

Table 3.6.: Standardised^[3] fractional atomic coordinates and equivalent isotropic displacement parameters /Å² for $[\text{La}(\text{DMF})_9]\text{I}_3$. U_{eq} is defined as $1/3$ of the trace of the orthogonalized U_{ij} tensor. Standard deviations in units of the last digit are given in parentheses. All atoms occupy the general position with Wyckoff number 2i.

Atom	x	y	z	U_{eq}	Atom	x	y	z	U_{eq}
I1	0.26035(13)	0.03525(11)	0.65935(8)	0.1047(6)	H19C	0.11580	0.17730	1.14370	0.2380
I2	0.23405(13)	-0.24825(12)	0.34807(8)	0.1118(6)	C193	0.061(3)	0.316(2)	1.229(2)	0.167(12)
I3	0.2406(2)	-0.51250(13)	0.60619(10)	0.1391(8)	H19D	-0.00620	0.31500	1.21010	0.2510
I4	0.2644(2)	0.47985(11)	1.15694(8)	0.1206(7)	H19E	0.10750	0.35580	1.21260	0.2510
I5	0.24532(13)	-0.25478(11)	0.85546(9)	0.1151(6)	H19F	0.05400	0.32610	1.27200	0.2510
I6	0.26547(2)	0.03027(11)	1.11928(9)	0.1145(6)	O21	0.103(2)	0.1927(13)	0.9700(11)	0.161(8)
La1	0.25709(8)	0.21289(7)	0.41064(5)	0.0594(3)	C211	0.076(2)	0.146(2)	1.0065(12)	0.092(7)
La2	0.23770(8)	0.27459(7)	0.91204(5)	0.0615(4)	H211	0.12640	0.12290	1.02810	0.1100
O11	0.2981(2)	0.1118(11)	0.3326(8)	0.153(8)	N21	-0.021(2)	0.1239(12)	1.0180(8)	0.097(6)
C111	0.31(2)	0.046(2)	0.3195(12)	0.108(8)	C212	-0.050(2)	0.063(2)	1.0600(13)	0.130(9)
H111	0.26670	0.00520	0.33060	0.1300	H21A	0.01060	0.03890	1.07190	0.1950
N11	0.396(2)	0.0288(10)	1.2906(7)	0.079(5)	H21B	-0.09920	0.02420	1.04090	0.1950
C112	0.475(2)	0.079(2)	1.2733(13)	0.134(10)	H21C	-0.08090	0.08550	1.09500	0.1950
H11A	0.48070	0.07510	1.23000	0.2010	C213	-0.108(3)	0.154(2)	0.988(2)	0.168(12)
H11B	0.53830	0.06510	1.29150	0.2010	H21D	-0.12920	0.19830	1.01140	0.2520
H11C	0.46280	0.13100	1.28580	0.2010	H21E	-0.16480	0.11400	0.98470	0.2520
C113	0.408(2)	-0.051(2)	1.2741(12)	0.119(8)	H21F	-0.08770	0.17070	0.94860	0.2520
H11D	0.34200	-0.08180	1.27610	0.1780	O22	0.3348(14)	0.4021(9)	0.9265(8)	0.122(6)
H11E	0.45610	-0.07170	1.30160	0.1780	C221	0.339(2)	0.461(2)	0.9624(12)	0.095(7)
H11F	0.43420	-0.05470	1.23370	0.1780	H221	0.30850	0.45420	0.99970	0.1140
O12	0.1501(12)	0.0869(10)	0.4320(7)	0.106(5)	N22	0.3840(13)	0.5316(10)	0.9529(7)	0.081(5)
C121	0.151(2)	0.0343(15)	0.4662(11)	0.081(6)	C222	0.394(2)	0.597(2)	0.9955(13)	0.131(9)
H121	0.18780	0.04460	0.50250	0.0970	H22A	0.32740	0.61630	1.00180	0.1960
N12	0.1065(11)	-0.0355(9)	0.4570(7)	0.069(5)	H22B	0.44100	0.63850	0.97990	0.1960

C122	0.112(2)	-0.1004(14)	0.5010(11)	0.102(7)	H22C	0.42080	0.58110	1.03320	0.1960
H12A	0.18400	-0.10550	0.51090	0.1530	C223	0.431(2)	0.5493(2)	0.8962(13)	0.134(10)
H12B	0.08160	-0.14890	0.48310	0.1530	H22D	0.44310	0.50120	0.87470	0.2010
H12C	0.07610	-0.08810	0.53720	0.1530	H22E	0.49670	0.58010	0.90310	0.2010
C123	-0.048(2)	0.0521(16)	0.5945(12)	0.119(9)	H22F	0.38660	0.57830	0.87260	0.2010
H12D	0.01910	0.03370	0.58920	0.1780	O23	0.308(2)	0.271(2)	0.8065(8)	0.173(10)
H12E	-0.08220	0.02640	0.62790	0.1780	C231	0.351(2)	0.245(2)	0.7623(14)	0.119(9)
H12F	-0.04070	0.10780	0.60250	0.1780	H231	0.34690	0.19060	0.75780	0.1430
O13	0.3763(12)	0.1218(9)	0.4559(9)	0.117(6)	N23	0.398(2)	0.2826(10)	0.7221(10)	0.112(7)
C131	0.426(2)	0.1150(14)	0.5035(12)	0.099(7)	C232	0.446(2)	0.257(2)	0.6645(14)	0.147(11)
H131	0.38930	0.11570	0.53960	0.1180	H23A	0.51840	0.27480	0.66480	0.2210
N13	0.5225(12)	0.1073(9)	0.5067(8)	0.072(5)	H23B	0.41220	0.27980	0.63120	0.2210
C132	0.426(2)	-0.0889(19)	0.438(2)	0.157(12)	H23C	0.43670	0.20110	0.66020	0.2210
H13A	0.42340	-0.03310	0.43630	0.2350	C233	0.409(4)	0.364(3)	0.731(2)	0.25(2)
H13B	0.35710	-0.11460	0.43640	0.2350	H23D	0.36200	0.38680	0.70440	0.3790
H13C	0.46450	-0.10670	0.40370	0.2350	H23E	0.47890	0.38430	0.72260	0.3790
C133	0.575(4)	0.118(3)	0.462(2)	0.25(2)	H23F	0.39300	0.37720	0.77220	0.3790
H13D	0.55480	0.16340	0.44240	0.3750	O24	0.4375(12)	0.2605(11)	0.9116(8)	0.123(6)
H13E	0.56380	0.07280	0.43530	0.3750	C241	0.509(2)	0.278(2)	0.8837(11)	0.097(7)
H13F	0.64650	0.12600	0.47380	0.3750	H241	0.50550	0.32320	0.86110	0.1160
O14	0.4092(13)	0.2658(13)	0.3488(9)	0.138(7)	N24	0.5933(13)	0.2448(11)	0.8796(10)	0.099(6)
C141	0.423(2)	0.329(2)	0.3231(13)	0.110(8)	C242	0.671(3)	0.283(2)	0.847(2)	0.176(13)
H141	0.36760	0.35960	0.31940	0.1320	H24A	0.66170	0.26890	0.80550	0.2640
N14	0.4878(14)	-0.3547(10)	0.6988(8)	0.084(5)	H24B	0.73670	0.26760	0.86130	0.2640
C142	0.399(2)	-0.318(2)	0.6891(14)	0.143(10)	H24C	0.66970	0.33850	0.85370	0.2640
H14A	0.41680	-0.26930	0.67020	0.2150	C243	0.606(3)	0.173(2)	0.907(2)	0.180(14)
H14B	0.36630	-0.30900	0.72700	0.2150	H24D	0.61860	0.18280	0.95030	0.2700
H14C	0.35260	-0.35150	0.66320	0.2150	H24E	0.66470	0.15000	0.89030	0.2700
C143	0.470(2)	-0.431(2)	0.7304(2)	0.162(12)	H24F	0.54490	0.13760	0.90160	0.2700
H14D	0.52680	-0.46220	0.72310	0.2420	O25	0.3056(12)	0.2680(13)	1.0134(7)	0.138(7)
H14E	0.40660	-0.45970	0.71520	0.2420	C251	0.322(2)	0.2782(14)	1.0675(12)	0.093(7)
H14F	0.46360	-0.42120	0.77310	0.2420	H251	0.27660	0.30730	1.08870	0.1110
O15	0.3997(13)	0.2821(9)	0.4779(9)	0.124(7)	N25	0.3965(13)	0.2534(12)	1.0989(8)	0.093(6)
C151	0.421(2)	0.344(2)	0.5092(10)	0.091(7)	C252	0.406(2)	0.263(2)	1.1622(13)	0.127(9)
H151	0.36950	0.37370	0.52320	0.1090	H25A	0.35320	0.29590	1.17660	0.1900
N15	0.521(2)	0.3668(11)	0.5220(8)	0.097(6)	H25B	0.47300	0.28900	1.17260	0.1900
C152	0.610(2)	0.330(2)	0.495(2)	0.150(11)	H25C	0.39650	0.21360	1.18060	0.1900
H15A	0.58580	0.28050	0.47700	0.2260	C253	0.462(2)	0.2016(14)	1.0695(11)	0.105(7)
H15B	0.66000	0.32380	0.52630	0.2260	H25D	0.43920	0.19090	1.02850	0.1570
H15C	0.64080	0.36410	0.46510	0.2260	H25E	0.46000	0.15330	1.09060	0.1570
C153	0.539(2)	0.441(2)	0.560(2)	0.155(12)	H25F	0.53250	0.22580	1.06970	0.1570
H15D	0.61260	0.45500	0.56520	0.2320	O26	0.1184(13)	0.3557(11)	0.9680(8)	0.131(6)
H15E	0.50860	0.43290	0.59930	0.2320	C261	0.078(2)	0.3823(14)	1.0105(11)	0.094(7)
H15F	0.50810	0.48250	0.54100	0.2320	H261	0.12200	0.39730	1.04300	0.1120
O16	0.1967(14)	0.2246(12)	0.5138(7)	0.133(7)	N26	-0.0182(14)	0.3941(11)	1.0192(9)	0.091(5)
C161	0.183(2)	0.2228(12)	0.5673(11)	0.080(6)	C262	0.056(3)	-0.429(2)	0.929(2)	0.201(2)
H161	0.22970	0.19480	0.58860	0.0960	H26A	0.11760	-0.39940	0.91690	0.3010
N16	0.1148(12)	-0.7456(9)	0.5994(7)	0.070(4)	H26B	0.00420	-0.43170	0.89790	0.3010
C162	-0.111(2)	-0.253(2)	0.3360(11)	0.105(7)	H26C	0.07120	-0.48160	0.93840	0.3010
H16A	-0.11490	-0.2030	0.32340	0.1570	C263	-0.086(3)	0.378(2)	0.975(2)	0.159(12)
H16B	-0.16980	-0.28590	0.31920	0.1570	H26D	-0.05160	0.35700	0.94070	0.2390
H16C	-0.04830	-0.27230	0.32220	0.1570	H26E	-0.11550	0.42490	0.96450	0.2390
C163	0.041(2)	-0.6992(14)	0.5720(11)	0.107(8)	H26F	-0.13960	0.33980	0.98810	0.2390
H16D	0.03880	-0.71000	0.52920	0.1600	O27	0.276(2)	0.1321(9)	0.9013(9)	0.132(7)
H16E	0.06230	-0.64450	0.57990	0.1600	C271	0.307(2)	0.0812(14)	0.9318(10)	0.078(6)
H16F	-0.02610	-0.71220	0.58870	0.1600	H271	0.30460	0.08790	0.97360	0.0940
O17	0.247(2)	0.3477(10)	0.4077(6)	0.124(7)	N27	0.343(2)	0.0202(12)	0.9108(9)	0.104(7)
C171	0.193(2)	0.402(2)	0.4322(14)	0.119(9)	C272	0.379(2)	-0.039(2)	0.9487(13)	0.133(10)
H171	0.16970	0.39390	0.47130	0.1430	H27A	0.44970	-0.04660	0.93900	0.2000
N17	0.1662(14)	-0.5272(10)	0.4065(9)	0.095(6)	H27B	0.33630	-0.08750	0.94190	0.2000
C172	0.116(2)	-0.470(2)	0.4343(14)	0.146(11)	H27C	0.37510	-0.02230	0.99040	0.2000
H17A	0.04490	-0.47400	0.42020	0.2190	C273	0.347(3)	0.015(3)	0.851(2)	0.209(2)
H17B	0.14920	-0.41950	0.42510	0.2190	H27D	0.33610	-0.03870	0.83720	0.3140
H17C	0.11700	-0.47630	0.47720	0.2190	H27E	0.41380	0.03740	0.83770	0.3140
C173	0.202(3)	-0.510(3)	0.337(2)	0.21(2)	H27F	0.29390	0.04410	0.83390	0.3140
H17D	0.14310	-0.52150	0.31080	0.3240	O28	0.163(2)	0.371(2)	0.8483(12)	0.201(2)
H17E	0.25550	-0.54240	0.32650	0.3240	C281	0.128(4)	0.396(3)	0.825(2)	0.161(2)
H17F	0.22710	-0.45560	0.33490	0.3240	N28	0.085(2)	0.448(2)	0.7857(10)	0.170(14)
O18	0.0644(11)	0.2336(11)	0.4126(8)	0.117(6)	C282	-0.005(3)	0.427(2)	0.755(2)	0.211(2)
C181	-0.011(2)	0.2074(16)	0.3823(12)	0.112(8)	H28A	0.01140	0.40820	0.71490	0.3170
H181	-0.00290	0.15960	0.36240	0.1350	H28B	-0.04400	0.47170	0.75190	0.3170
N18	-0.0932(2)	0.232(2)	0.373(2)	0.161(12)	H28C	-0.04430	0.38630	0.77560	0.3170
C182	-0.181(3)	0.201(2)	0.331(2)	0.174(13)	C283	0.169(4)	0.513(3)	0.789(2)	0.26(2)
H18A	-0.23120	0.16780	0.35350	0.2620	H28D	0.14880	0.55620	0.76690	0.3920
H18B	-0.15450	0.17040	0.29890	0.2620	H28E	0.23070	0.49460	0.77180	0.3920
H18C	-0.21430	0.24360	0.31550	0.2620	H28F	0.18200	0.52890	0.83050	0.3920
C183	-0.117(4)	0.298(4)	0.390(3)	0.42(5)	O29	0.101(2)	0.2064(14)	0.8418(11)	0.175(11)
H18D	-0.15120	0.31870	0.36060	0.6350	C291	0.085(3)	0.146(3)	0.8169(14)	0.19(2)
H18E	-0.05970	0.32850	0.39960	0.6350	H291	0.14180	0.11710	0.81020	0.2330
H18F	-0.15750	0.29310	0.42260	0.6350	N29	0.010(2)	-0.111(2)	0.2040(9)	0.117(8)
O19	0.1911(2)	0.2455(11)	0.3074(8)	0.136(7)	C292	0.897(3)	0.153(3)	0.802(2)	0.23(2)
C191	0.163(3)	0.221(2)	1.256(2)	0.152(12)	H29A	0.90970	0.20390	0.78440	0.3430
H191	0.19700	0.17820	1.24320	0.1820	H29B	0.87980	0.15920	0.84340	0.3430
N19	0.099(2)	0.2414(13)	1.2198(9)	0.108(7)	H29C	0.84030	0.12370	0.78030	0.3430
C192	0.079(2)	0.221(2)	1.155(2)	0.158(12)	C293	0.022(4)	-0.041(3)	0.233(2)	0.28(3)
H19A	0.10040	0.26530	1.13180	0.2380	H29D	-0.03860	-0.01360	0.22790	0.4140
H19B	0.00540	0.20740	1.14990	0.2380	H29E	0.08180	-0.01060	0.21880	0.4140
					H29F	0.03130	-0.04900	0.27620	0.4140

$[RE(DMF)_8]I_3$ with $RE = Sm, Gd, Er, Yb$

The compounds $[RE(DMF)_8]I_3$ ($RE = Sm, Gd, Er, Yb$) crystallise strictly isotypically. Synthesis and data collection is given for each compound individually, their crystal structures are discussed in the following paragraph. For additional details on data collection and treatment see Table 3.7.

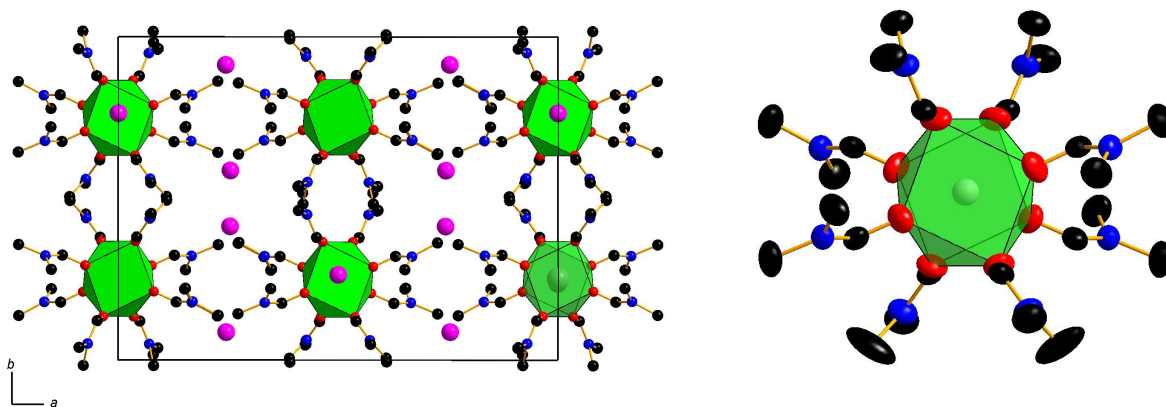


Figure 3.10.: The crystal structure of $[Er(DMF_8)]I_3$. I: magenta; Er: grey; C: black; O: red, N: blue. Left: Unit cell of $[Er(DMF_8)]I_3$ along $[001]$. Right: Er is coordinated by O atoms of eight DMF molecules forming a distorted cubic antiprism. Ellipsoids are displayed with 50% probability level, H atom positions are omitted for clarity.

$[Sm(DMF_8)]I_3$: $SmI_3 \cdot xH_2O$ ($x = 6-7$, Chem Pur, 99.9 % metal basis) was dissolved in anhydrous DMF (100 ml, Fischer Chemical, HPLC grade) until a saturated solution was obtained. A stoichiometric amount of a saturated solution of KI in DMF was added to perform a metathesis reaction. Subsequent azeotropic distillation resulted in an anhydrous solution of $[Sm(DMF_8)]I_3$ in DMF. Pale yellow crystals formed upon cooling of the solution, the crystals were very soft and hygroscopic. A suitable crystal was selected and mounted on a STOE IPDS 1 diffraction system. Indexing, systematic absence conditions and Wilson statistics indicated monoclinic crystal system with extinction symbol $C - c -$ with inversion symmetry leading to space group $C2/c$ (unique axis b). Solution yielded all heavy atom positions, refinement together with difference Fourier analysis yielded all DMF molecules. All atoms except H were treated with anisotropic thermal displacement parameters, H atom positions were refined with rigid-model constraints. No additional symmetry was found.

$[Gd(DMF_8)]I_3$: The synthesis was analogous to that of $[Sm(DMF_8)]I_3$ with the educt $GdCl_3 \cdot xH_2O$ ($x = 6-7$, Chem Pur, 99.9 % metal basis). Soft, pale yellow and hygroscopic crystals formed upon cooling of the solution. A suitable crystal was selected and mounted on a STOE IPDS 1 diffraction system. Indexing, systematic absences and Wilson statistics indicated monoclinic crystal system with extinction symbol $C - c -$ with inversion symmetry leading to space group $C2/c$ (unique axis b). Solution yielded all heavy atom positions, refinement together with difference Fourier analysis yielded DMF molecules. All atoms except H were treated with anisotropic thermal displacement pa-

rameters, H atom positions were refined with rigid-model constraints. No additional symmetry was found.

[Er(DMF₈)]I₃: The synthesis was analogous to that of [Sm(DMF₈)I₃] with the educt ErCl₃ · xH₂O ($x = 6-7$, Chem Pur, 99.9 % metal basis). Soft, pale magenta and moisture-sensitive crystals formed upon cooling of the solution. A suitable crystal was selected and mounted on a STOE IPDS 1 diffraction system. Indexing, systematic absences and Wilson statistics indicated monoclinic crystal system with extinction symbol $C - c -$ with inversion symmetry leading to space group $C2/c$ (unique axis b). Solution yielded all heavy atom positions, refinement together with difference Fourier analysis yielded all DMF molecules. All atoms except H were treated with anisotropic thermal displacement parameters, H atom positions were refined with rigid-model constraints. No additional symmetry was found. Residual electron density ($\leq 0.75 e^-$) was found in close proximity to Er and was thus treated as termination effect.

[Yb(DMF₈)]I₃: The synthesis was analogous to that of [Sm(DMF₈)I₃] with the educt YbCl₃ · xH₂O ($x = 6-7$, Chem Pur, 99.9 % metal basis). Soft, pale yellow and moisture sensitive crystals formed upon cooling of the solution. A suitable crystal was selected and mounted on a STOE IPDS 1 diffraction system. Upon examination of the reciprocal space it was revealed that two arbitrarily intergrown crystals were present and subsequently data was integrated separately for each individual. While essentially similar, only data of the first individual are discussed here. Indexing, systematic absences and Wilson statistics indicated monoclinic crystal system with extinction symbol $C - c -$ with inversion symmetry leading to space group $C2/c$ (unique axis b). Only few systematic absence violations were observed and can be explained by diffraction contribution of the second individual. Solution yielded all heavy atom positions, refinement together with difference Fourier analysis yielded DMF molecules. All atoms except H were treated with anisotropic thermal displacement parameters, H atom positions were refined with rigid-model constraints. No additional symmetry was found.

Crystal structures of [RE(DMF₈)I₃] with RE = Sm, Gd, Er, Yb The crystal structures of [RE(DMF₈)I₃] ($RE = \text{Sm, Gd, Er, Yb}$) are isotypical in space group $C2/c$ with four formula units per unit cell. There is one crystallographically independent RE site ($4e$), two I sites ($4e, 8f$) and four independent DMF molecules (all atoms on $8f$). RE is coordinated by the carbonyl oxygen atoms of eight DMF molecules forming a distorted square antiprism. The angle between the triangular planes of the "square" is approx. 12° , the rotation of the squares with respect to each other is $38.03(6)$ to $39.94(7)^\circ$.

[Sc(DMF₆)](I₃)₃

[Sc(DMF₆)](I₃)₃ was synthesised by dissolving Sc₂O₃ (smart elements 99.99 % metal basis) in fuming HCl (VWR chemicals) under reflux conditions followed by metathesis reaction with a saturated solution of KI (Sigma aldrich, 99 %) in DMF and subsequent azeotropic distillation (see chapter 3.1.1). During the last step the atmosphere was

contaminated with oxygen leading to partial oxidation of the I^- ions to I_2 , resulting in the formation of I_3^- ions.

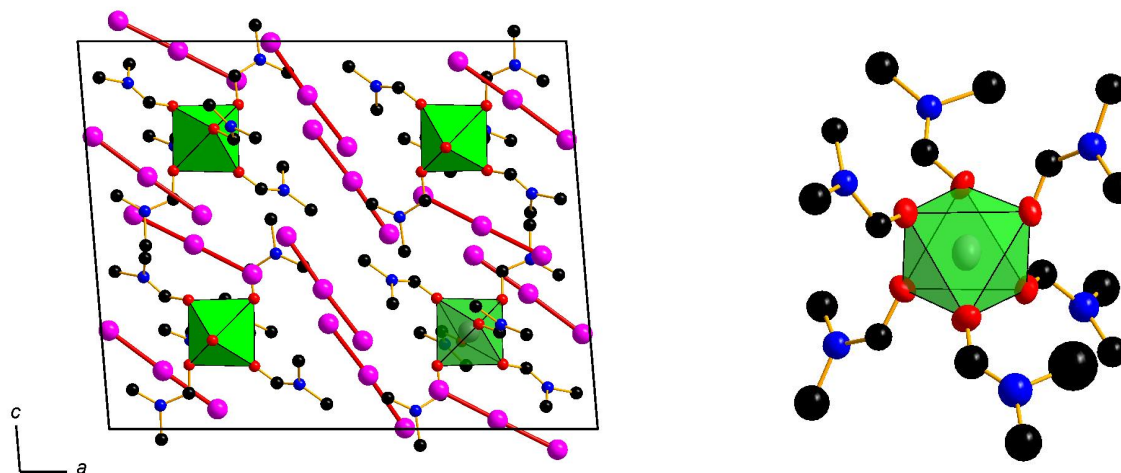


Figure 3.11.: The crystal structure of $[\text{Sc}(\text{DMF})_6](\text{I}_3)_3$. I: magenta; Sc: grey; C: black; O: red, N: blue, red bonds: I_3^- ions. Left: Unit cell of $[\text{Sc}(\text{DMF})_6](\text{I}_3)_3$ along $[010]$. Right: Sc is coordinated by the oxygen atoms of six DMF molecules forming a distorted octahedron. Ellipsoids are drawn with 75% probability level. H atom positions are omitted for clarity.

Upon storing the resulting deep red solution at room temperature for several months, crimson, platelike crystals sensitive toward moisture formed. A suitable crystal was selected and centred on a STOE IPDS diffraction system. For additional details on data collection and treatment see Table 3.8.

Indexing, systematic absence conditions and Wilson statistics indicated monoclinic crystal system with extinction symbol $P - 2_1/c -$ with inversion symmetry leading to space group $P2_1/c$. 5 systematic absence violations can be attributed to weak reflections originating from minor impurities on the crystal surface. Solution yielded all heavy atoms (Sc, I) including six O atoms surrounding Sc and erroneously assigned Fourier peaks in close proximity to I. From difference Fourier analysis, DMF molecules were found and assigned, no H atom positions were refined due to the poor data-to-parameter ratio. Sc, I, and O atoms were treated with anisotropic thermal displacement parameters, other atoms of the DMF molecules were treated with isotropic thermal displacement parameters. Absorption correction was performed with ABSTompa (Platon, 7 indexed crystal faces) to account for the highly anisotropic crystal shape.

The crystal structure consists of one crystallographically independent $[\text{Sc}(\text{DMF})_6]^{3+}$ ion and three I_3^- ions. All atoms occupy the general position 4e. The $[\text{ScO}_6]$ octahedron is slightly distorted with maximum distortions of $\Delta\angle_{\text{O-O-O}} \leq \pm 2^\circ$ and $d_{\text{Sc-O}} = 2.025(13) \text{ \AA}$ to $2.097(11) \text{ \AA}$ (see Table A.11).

The I_3^- ions deviate slightly from linearity with angles from $\angle_{\text{I-I-I}} = 177^\circ$ to 179° and distances from $d_{\text{I-I}} = 2.896(3)$ to $2.948(3) \text{ \AA}$, closest interionic distances range from $d_{\text{I-I}} = 3.912(3)$ to $3.967(3) \text{ \AA}$ (see Table A.10).

Table 3.7.: Crystallographic data, details of the data collection and structure determination for $[\text{La}(\text{DMF})_9]\text{I}_3$, $[\text{Sm}(\text{DMF})_8]\text{I}_3$, $[\text{Gd}(\text{DMF})_8]\text{I}_3$, $[\text{Er}(\text{DMF})_8]\text{I}_3$ and $[\text{Yb}(\text{DMF})_8]\text{I}_3$.

	$[\text{La}(\text{DMF})_9]\text{I}_3$	$[\text{Sm}(\text{DMF})_8]\text{I}_3$	$[\text{Gd}(\text{DMF})_8]\text{I}_3$	$[\text{Er}(\text{DMF})_8]\text{I}_3$	$[\text{Yb}(\text{DMF})_8]\text{I}_3$
Crystal system	triclinic				
Space group	$P\bar{1}$				
Lattice parameters [\AA , \AA^3]	a	22.831(11)	22.588(6)	22.441(2)	22.334(7)
	b	16.288(4)	16.403(7)	16.203(3)	16.212(3)
	c	11.801(5)	11.813(3)	11.7804(11)	11.787(2)
	α	91.88(2)			
	β	90.44(2)			
	γ	95.36(2)			
V	4871(1)	4319(3)	4316(2)	4216.3(10)	4199.2(17)
Z	4	4	4	4	4
Density (X-ray) [g/cm^3]	1.6068	1.729	1.740	1.797	1.814
Diffractometer	- STOE IPDS 1 -				
Radiation	Ag K_α				
Measurement temperature	- room temperature -				
Abs. coeff. [mm^{-1}]	1.413	3.549	1.988	4.233	4.479
ϑ range for refinement [$^\circ$]	2.07 - 25.90	2.45 - 25.00	2.68 - 25.00	3.04 - 24.99	2.47 - 25.00
Index range	-15 $\leq h \leq 15$, -20 $\leq k \leq 21$, -27 $\leq l \leq 27$	-27 $\leq h \leq 27$, -19 $\leq k \leq 19$, -14 $\leq l \leq 14$	-34 $\leq h \leq 34$, -24 $\leq k \leq 24$, -17 $\leq l \leq 17$	-26 $\leq h \leq 26$, -19 $\leq k \leq 19$, -13 $\leq l \leq 13$	-26 $\leq h \leq 26$, -19 $\leq k \leq 19$, -14 $\leq l \leq 14$
No. of observed reflections	42134	24607	31684	22679	14642
No. of ind. refl.	17562	3794	7733	3671	3642
No. of ind. refl. with ($I \leq 2\sigma(I)$)	4619	1807	5344	3042	2554
R_{int}	0.1051	0.3165	0.0635	0.0400	0.1191
R_σ	0.0853	0.1504	0.0463	0.0260	0.0760
Corrections	- Lorentz, polarisation, absorption -				
Absorption correction	- multiscan ^[6] -				
Structure solution	- SHELXS97 ^[7] -				
Structure refinement	- SHELXL97 ^[7] -				
No. of least-squares parameters	670	209	209	209	209
Goodness of fit on F^2	0.749	0.795	0.906	0.905	0.919
$R1/wR2$	0.0973 / 0.2045	0.0593 / 0.1355	0.0339 / 0.0744	0.0232 / 0.0577	0.0488 / 0.1103
res. electron density [$\text{e}^{-\text{\AA}^{-3}}$]	For all data	For all data	For all data	For all data	For all data
	1.633 / -1.232	1.554 / -1.342	0.824 / -0.838	0.750 / -0.687	2.675 / -2.460

Table 3.8.: Crystallographic data, details of the data collection and structure determination for $[\text{Zn}(\text{DMF})_2\text{I}_2]$, $[\text{CdI}_4][\text{Cd}(\text{DMF})_6]$, $RE_{12}(\text{DMF})_{24}(\mu_3 - \text{COOH})_8(\mu_3 - \text{OH})_{16}\text{I}_{12} \cdot 4\text{DMF}$ ($RE = \text{Nd}$, Eu), $[\text{Eu}(\text{H}_2\text{O})_4(\text{C}_3\text{H}_6\text{O})_4]\text{I}_3$, $[\text{Sc}(\text{DMF})_6]\text{I}_3$.

	$[\text{Zn}(\text{DMF})_2\text{I}_2]$	$[\text{CdI}_4][\text{Cd}(\text{DMF})_6]$	$RE_{12}(\text{DMF})_{24}(\mu_3 - \text{COOH})_8(\mu_3 - \text{OH})_{16}\text{I}_{12} \cdot 4\text{DMF}$ $RE = \text{Nd}$	$[\text{Eu}(\text{C}_3\text{H}_6\text{O})_4(\text{H}_2\text{O})_4]\text{I}_3$	$[\text{Sc}(\text{DMF})_6]\text{I}_3$
Crystal system	– monoclinic	– monoclinic	– tetragonal	– monoclinic	– monoclinic
Space group type	$C2/c$	$C2/c$	$I422$	$P2_1/c$	$P2_1/c$
Lattice parameters [\AA , \AA^3]	a 14.137(3)	22.1970(10)	$I422$ 21.881(3)	21.6340(10)	15.962(4)
	b 13.7104(17)	12.6383(5)	21.881(3)	21.6340(10)	13.378(4)
	c 15.915(3)	15.5521(8)	20.873(2)	21.0612(9)	13.615(3)
	β 111.33(2)	124.7440(11)	9994(2)	9857.3(8)	105.350(19)
V	2873.4(9)	3585.0(3)	2	2803.6(13)	4764.0(17)
Z	4	4	2	1	4
Density (X-ray) [g/cm^3]	2.086	2.298	1.971	1.964	2.207
Diffractometer	STOE IPDS 1	D8 Venture	– STOE IPDS 1	–	–
Radiation	$\text{Mo K}\alpha$	$\text{Mo K}\alpha$	$\text{Ag K}\alpha$	$\text{Mo K}\alpha$	$\text{Mo K}\alpha$
Measurement temperature	room temperature	100 K	– room temperature	–	–
Abs. coeff. $\mu_{\text{Ag}/\text{MoK}\alpha}$ [mm^{-1}]	5.984	4.677	2.646	1.518	5.565
ϑ range for refinement [$^\circ$]	2.14 – 24.99	3.920 – 80.548	1.81 – 24.02	1.83 – 20.00	2.32 – 25.00
Index range	$-16 \leq h \leq 16$,	$-40 \leq h \leq 40$,	$-19 \leq h \leq 31$,	$-26 \leq h \leq 26$,	$-16 \leq h \leq 18$,
	$-16 \leq k \leq 16$,	$-22 \leq k \leq 22$,	$-31 \leq k \leq 31$,	$-26 \leq k \leq 26$,	$-15 \leq k \leq 15$,
	$-18 \leq l \leq 18$	$-28 \leq l \leq 28$	$-29 \leq l \leq 29$	$-25 \leq l \leq 25$	$-16 \leq l \leq 16$
No. of observed reflections	18427	84604	39026	35408	17534
No. of ind. ref.	2532	11207	4369	4685	4923
No. of ind. ref. with ($I \leq 2\sigma(I)$)	1618	7988	1731	3043	1941
R_{int}	0.0672	0.0586	0.2126	0.1627	0.1685
R_σ	0.0592	0.0341	0.1506	0.1320	0.2268
Corrections			– Lorentz, polarisation, absorption	–	–
Absorption correction			– multiscan ^[6]	–	–
Structure solution / refinement			– SHELXS97 / SHELXL97 ^[7]	–	–
No. of least-squares parameters	122	172	185	253	166
Goodness-of-fit on F^2	0.768	1.102	0.757	0.973	0.969
$R1/wR2$	$I \geq 2\sigma(I)$	0.0298 / 0.0700	0.0418 / 0.0791	0.0741 / 0.0864	0.0479 / 0.0825
	all data	0.0509 / 0.0732	0.1008 / 0.1535	0.0979 / 0.1220	0.0825 / 0.1629
res. electron density [$\text{e}^{-\text{\AA}^{-3}}$]	0.784 / –0.642	3.122 / –2.143	1.117 / –2.612	0.832 / –0.970	0.609 / –1.017
					1.402 / –0.159

Table 3.9.: Standardised^[3] fractional atomic coordinates and equivalent isotropic displacement parameters /Å² for [Sm(DMF)₈]I₃, [Gd(DMF)₈]I₃, [Er(DMF)₈]I₃ and [Yb(DMF)₈]I₃. U_{eq} is defined as $1/3$ of the trace of the orthogonalized U_{ij} tensor. Standard deviations in units of the last digit are given in parentheses. All atoms occupy the general position with Wyckoff number 8*f*, only Sm, Gd, Er, Yb and their respective I2 positions occupy the site with Wyckoff number 4*e*.

Atom	x	y	z	U_{eq}	Atom	x	y	z	U_{eq}
Sm1	0	0.25060(5)	$3/4$	0.0516(3)	C6	0.2263(2)	0.1374(3)	1.0208(4)	0.0652(12)
Gd1	0	0.250487(13)	$3/4$	0.02865(5)		0.2261(4)	0.1374(7)	1.0198(9)	0.069(3)
Er1	0	0.250331(11)	$3/4$	0.02782(9)	H6A	0.2247	0.0857	1.0544	0.129
Yb1	0	0.25034(3)	$3/4$	0.0306(2)		0.2352	0.1187	0.9520	0.099
I1	0.24497(6)	0.08467(7)	0.69865(10)	0.0910(4)		0.2260	0.0918	1.0727	0.098
	0.24513(2)	0.08510(2)	0.69806(3)	0.06759(9)	H6B	0.2325	0.1166	0.9466	0.104
	0.245253(14)	0.08586(2)	0.69670(3)	0.06455(12)		0.2567	0.1711	1.0724	0.129
	0.24545(3)	0.08618(5)	0.69616(6)	0.0671(2)		0.2260	0.0931	1.0758	0.099
I2	0	0.23718(8)	$1/4$	0.0801(5)		0.2579	0.1752	1.0522	0.098
	0	0.23659(2)	$1/4$	0.05834(10)	H6C	0.2267	0.0925	1.0730	0.104
	0	0.23684(2)	$1/4$	0.05604(12)		0.2396	0.1341	0.9482	0.129
	0	0.23709(6)	$1/4$	0.0587(3)		0.2582	0.1754	1.0569	0.099
O1	0.0327(5)	0.1329(5)	0.6574(8)	0.081(3)		0.2333	0.1175	0.9476	0.098
	0.03397(14)	0.1332(2)	0.6601(2)	0.0599(7)		0.2578	0.1758	1.0492	0.104
	0.03463(13)	0.1341(2)	0.6647(3)	0.0522(7)	C7	-0.2281(7)	0.3561(11)	0.867(2)	0.091(5)
	0.0353(3)	0.1351(3)	0.6667(5)	0.055(2)		-0.2278(2)	0.3553(3)	0.8653(4)	0.0676(11)
O2	-0.0385(5)	0.3682(5)	0.6349(8)	0.082(3)		-0.2273(2)	0.3564(3)	0.8627(4)	0.0649(12)
	-0.03883(13)	0.3669(2)	0.6410(2)	0.0507(7)		-0.2269(4)	0.3552(7)	0.8605(9)	0.069(3)
	-0.03908(13)	0.3682(2)	0.6374(2)	0.0557(6)	H7A	-0.2294	0.3942	0.8044	0.137
	-0.0386(3)	0.3663(3)	0.6423(4)	0.052(2)		-0.2285	0.3931	0.8031	0.101
C1	-0.0408(6)	0.3830(7)	0.5323(12)	0.065(4)		-0.2283	0.3930	0.7983	0.097
	-0.0412(2)	0.3815(2)	0.5331(3)	0.0486(7)		-0.2307	0.3809	0.7862	0.104
	-0.0412(2)	0.3797(2)	0.5367(4)	0.0450(9)	H7B	-0.2382	0.3841	0.9325	0.137
	-0.0413(4)	0.3804(5)	0.5378(7)	0.047(2)		-0.2391	0.3830	0.9301	0.101
H1A	-0.0523	0.3320	0.4920	0.078		-0.2377	0.3863	0.9267	0.097
	-0.0540	0.3310	0.4939	0.058		-0.2344	0.3954	0.9163	0.104
	-0.0553	0.3288	0.4976	0.054	H7C	-0.2561	0.3126	0.8441	0.137
	-0.0552	0.3296	0.4982	0.057		-0.2557	0.3119	0.8419	0.101
H1B	-0.0002	0.3938	0.5228	0.078		-0.2558	0.3124	0.8417	0.097
	-0.0001	0.3905	0.5220	0.058		-0.2560	0.3113	0.8570	0.104
	0.0003	0.3872	0.5255	0.054	C8	-0.1535(8)	0.2802(9)	1.007(2)	0.093(5)
	0.0003	0.3884	0.5269	0.057		-0.1531(2)	0.2790(3)	1.0048(4)	0.0614(11)
C2	0.0498(6)	0.1181(7)	0.5666(13)	0.069(4)		-0.1534(2)	0.2789(3)	1.0069(4)	0.0651(11)
	0.0489(2)	0.1194(2)	0.5655(3)	0.0450(7)		-0.1528(5)	0.2791(7)	1.0035(8)	0.065(3)
	0.0488(2)	0.1204(2)	0.5692(3)	0.0426(8)	H8A	-0.1663	0.2240	0.9985	0.139
	0.0481(4)	0.1202(5)	0.5696(7)	0.043(2)		-0.1108	0.2777	1.0315	0.098
H2A	0.0810	0.1576	0.5615	0.083		-0.1689	0.2239	0.9959	0.092
	0.0783	0.1606	0.5547	0.054		-0.1100	0.2825	1.0334	0.097
	0.0783	0.1619	0.5583	0.051	H8B	-0.1739	0.3072	1.0611	0.139
	0.0772	0.1619	0.5559	0.052		-0.1685	0.2241	0.9981	0.098
H2B	0.0169	0.1320	0.5058	0.083		-0.1715	0.3079	1.0610	0.092
	0.0138	0.1295	0.5080	0.054		-0.1645	0.2222	0.9924	0.097
	0.0129	0.1312	0.5119	0.051	H8C	-0.1114	0.2820	1.0351	0.139
	0.0113	0.1298	0.5136	0.052		-0.1720	0.3068	1.0632	0.098
N1	0.0695(5)	0.0483(6)	0.5384(9)	0.061(3)		-0.1101	0.2769	1.0302	0.092
	0.07113(14)	0.0487(2)	0.5397(2)	0.0443(6)		-0.1751	0.3039	1.0571	0.097
	0.07035(14)	0.0495(2)	0.5420(3)	0.0426(7)	C9	0.1533(8)	0.2208(10)	1.109(2)	0.092(5)
	0.0699(3)	0.0490(4)	0.5438(5)	0.047(2)		0.1528(2)	0.2205(3)	1.1076(4)	0.0685(11)
N2	-0.0730(6)	0.4399(6)	0.4746(10)	0.073(3)		0.1518(2)	0.2205(3)	1.1070(4)	0.0657(12)
	-0.0733(2)	0.4397(2)	0.4761(3)	0.0524(7)	H9A	0.1512(5)	0.2202(7)	1.1065(8)	0.070(3)
	-0.0726(2)	0.4391(2)	0.4797(3)	0.0504(8)		0.1204	0.2570	1.0834	0.138
	-0.0727(3)	0.4389(4)	0.4808(6)	0.052(2)		0.1121	0.2396	1.0897	0.103
O3	-0.0777(5)	0.2958(6)	0.8474(9)	0.081(3)		0.1106	0.2390	1.0893	0.098
	-0.07711(12)	0.2938(2)	0.8488(2)	0.0558(6)	H9B	0.1079	0.2277	1.0950	0.105
	-0.07580(12)	0.2923(2)	0.8474(2)	0.0510(6)		0.1865	0.2518	1.1481	0.138
	-0.0752(3)	0.2918(4)	0.8473(5)	0.0487(14)		0.1791	0.2658	1.1288	0.103
C3	0.0798(8)	-0.0180(8)	0.6197(13)	0.083(5)		0.1780	0.2670	1.1278	0.098
	0.0802(2)	-0.0184(3)	0.6213(4)	0.0613(10)		0.1710	0.2729	1.1166	0.105
	0.0802(2)	-0.0177(2)	0.6236(4)	0.0573(11)	H9C	0.1420	0.1802	1.1595	0.138
	0.0795(5)	-0.0171(6)	0.6257(8)	0.058(2)		0.1562	0.1825	1.1703	0.103
H3A	0.1205	-0.0170	0.6582	0.124		0.1563	0.1822	1.1701	0.098
	0.1219	-0.0218	0.6543	0.092		0.1641	0.1870	1.1739	0.105
	0.1223	-0.0204	0.6573	0.086	C10	-0.1124(11)	0.4923(12)	0.528(2)	0.124(7)
	0.1222	-0.0231	0.6546	0.088		-0.1115(4)	0.4914(4)	0.5311(6)	0.126(4)
H3B	0.0717	-0.0693	0.5800	0.124		-0.1096(4)	0.4934(4)	0.5362(6)	0.113(3)
	0.0678	-0.0685	0.5825	0.092		-0.1089(7)	0.4944(9)	0.5387(11)	0.109(5)
	0.0681	-0.0686	0.5846	0.086	H10A	-0.1280	0.4617	0.5851	0.186
	0.0638	-0.0674	0.5890	0.088		-0.1506	0.4942	0.4847	0.189
H3C	0.0541	-0.0120	0.6753	0.124		-0.1174	0.4678	0.6056	0.170
	0.0568	-0.0091	0.6810	0.092		-0.1510	0.4901	0.5032	0.164
	0.0567	-0.0087	0.6831	0.086	H10B	-0.1445	0.5111	0.4699	0.186
	0.0587	-0.0051	0.6885	0.088		-0.0944	0.5451	0.5403	0.189
O4	0.0834(5)	0.2101(6)	0.8903(9)	0.086(3)		-0.1472	0.5037	0.4855	0.170
	0.08252(13)	0.2105(2)	0.8912(3)	0.0644(8)		-0.0952	0.5501	0.5324	0.164
	0.08027(12)	0.2110(2)	0.8911(3)	0.0573(7)	H10C	-0.0904	0.5386	0.5632	0.186
	0.0789(3)	0.2123(4)	0.8900(5)	0.054(2)		-0.1148	0.4694	0.6051	0.189
C4	-0.1281(7)	0.3242(8)	0.8255(12)	0.068(4)		-0.0886	0.5446	0.5549	0.170
	-0.1285(2)	0.3243(2)	0.8263(3)	0.0436(7)		-0.1044	0.4794	0.6186	0.164
	-0.1275(2)	0.3237(2)	0.8254(3)	0.0414(8)	C11	0.0933(9)	0.0368(9)	0.4304(14)	0.098(6)
	-0.1268(4)	0.3225(5)	0.8249(6)	0.043(2)		0.0914(3)	0.0369(3)	0.4313(4)	0.0699(12)
H4A	-0.1473	0.2982	0.7547	0.082		0.0902(2)	0.0375(3)	0.4334(4)	0.0647(12)
	-0.1479	0.2992	0.7554	0.052		0.0893(5)	0.0376(7)	0.4331(8)	0.066(3)
	-0.1475	0.2989	0.7538	0.050	H11A	0.0792	0.0801	0.3775	0.146
	-0.1468	0.2964	0.7541	0.051		0.0821	0.0844	0.3843	0.105

H4B	-0.1237	0.3818	0.8076	0.082	0.0804	0.0854	0.3858	0.097
	-0.1231	0.3814	0.8094	0.052	0.0757	0.0834	0.3836	0.099
	-0.1217	0.3815	0.8087	0.050	H11B 0.0802	-0.0151	0.3966	0.146
	-0.1210	0.3798	0.8061	0.051	0.0716	-0.0097	0.3930	0.105
C5	0.1348(7)	0.1774(7)	0.9085(13)	0.067(4)	0.0704	-0.0100	0.3952	0.097
	0.1331(2)	0.1787(2)	0.9076(3)	0.0463(7)	0.0721	-0.0125	0.3980	0.099
	0.1312(2)	0.1787(2)	0.9060(3)	0.0438(9)	H11C 0.1360	0.0379	0.4473	0.146
	0.1301(4)	0.1794(5)	0.9053(7)	0.046(2)	0.1340	0.0281	0.4446	0.105
H5A	0.1565	0.2013	0.8531	0.080	0.1332	0.0290	0.4468	0.097
	0.1551	0.2031	0.8524	0.056	0.1329	0.0344	0.4449	0.099
	0.1528	0.2038	0.8504	0.053	C12 -0.0754(8)	0.4548(10)	0.3534(13)	0.089(5)
	0.1521	0.2048	0.8506	0.055	-0.0738(2)	0.4522(3)	0.3531(4)	0.0674(11)
H5B	0.1291	0.1198	0.8885	0.080	-0.0737(2)	0.4516(3)	0.3566(4)	0.0657(12)
	0.1274	0.1218	0.8864	0.056	-0.0737(5)	0.4513(7)	0.3578(8)	0.066(3)
	0.1252	0.1212	0.8840	0.053	H12A -0.0502	0.4162	0.3237	0.133
	0.1237	0.1222	0.8821	0.055	-0.0501	0.4107	0.3248	0.101
N3	-0.1669(5)	0.3211(6)	0.8977(9)	0.060(3)	-0.0499	0.4097	0.3283	0.099
	-0.16723(12)	0.3217(2)	0.8970(2)	0.0424(6)	-0.0502	0.4089	0.3294	0.098
	-0.16657(13)	0.3219(2)	0.8949(3)	0.0398(7)	H12B -0.0619	0.5096	0.3425	0.133
	-0.1663(3)	0.3223(4)	0.8937(5)	0.041(2)	-0.0573	0.5048	0.3412	0.101
N4	0.1702(5)	0.1800(7)	1.0082(10)	0.068(3)	-0.0573	0.5049	0.3445	0.099
	0.16923(13)	0.1801(2)	1.0074(3)	0.0463(6)	-0.0566	0.5043	0.3458	0.098
	0.16808(13)	0.1797(2)	1.0056(3)	0.0437(7)	H12C -0.1156	0.4486	0.3134	0.133
	0.1675(3)	0.1787(4)	1.0054(5)	0.045(2)	-0.1143	0.4493	0.3129	0.101
C6	0.2277(7)	0.1392(11)	1.0220(13)	0.086(4)	-0.1147	0.4485	0.3162	0.099
	0.2271(2)	0.1382(3)	1.0245(4)	0.0660(11)	-0.1149	0.4490	0.3171	0.098

Table 3.10.: Standardised^[3] fractional atomic coordinates and equivalent isotropic displacement parameters / \AA^2 for $[\text{Sc}(\text{DMF})_6](\text{I}_3)_3$. U_{eq} is defined as $1/3$ of the trace of the orthogonalized U_{ij} tensor. Standard deviations in units of the last digit are given in parentheses. All atoms occupy the general position with Wyckoff number 4e.

Atom	x	y	z	U_{eq}	Atom	x	y	z	U_{eq}
Sc1	0.24733(14)	0.0021(2)	0.2487(2)	0.0686(9)	C21	0.2589(10)	0.3426(16)	0.3356(12)	0.118(7)
I1	0.01549(7)	0.36386(12)	0.25449(9)	0.1188(5)	C22	0.3477(11)	0.3852(19)	0.2512(14)	0.149(9)
I2	0.08586(7)	0.79532(11)	0.05250(9)	0.1186(6)	C23	0.3030(9)	0.2179(16)	0.2480(11)	0.089(6)
I3	0.11964(6)	0.35278(9)	0.15071(7)	0.0901(4)	N2	0.2994(7)	0.3156(12)	0.2806(8)	0.093(4)
I4	0.22498(7)	0.33832(12)	0.05195(9)	0.1212(5)	O6	0.3077(6)	0.0046(10)	0.1626(7)	0.103(4)
I5	0.39475(11)	0.2290(2)	0.4970(2)	0.2251(12)	C61	0.5505(13)	0.438(2)	0.435(2)	0.166(10)
I6	0.46083(7)	0.17373(12)	0.36089(10)	0.1314(6)	C62	0.3510(14)	0.004(2)	0.119(2)	0.138(9)
I7	0.5336(2)	0.1208(2)	0.22791(14)	0.2374(13)	C63	0.601(2)	0.351(4)	0.324(3)	0.29(2)
I8	0.68136(8)	0.14308(13)	0.10106(10)	0.1370(6)	N6	0.6033(10)	0.442(2)	0.3840(12)	0.141(7)
I9	0.79627(7)	0.17595(10)	0.02389(8)	0.1026(5)	O5	0.6821(5)	0.4623(8)	0.1636(7)	0.086(3)
O4	0.1743(5)	0.0448(8)	0.1661(7)	0.083(3)	C51	0.5755(10)	0.390(2)	0.0803(11)	0.112(7)
C41	0.0542(8)	0.0846(12)	0.1017(10)	0.083(5)	C52	0.3661(12)	0.573(2)	0.042(2)	0.161(9)
C42	0.1052(10)	0.397(2)	0.4736(13)	0.125(7)	C53	0.6844(10)	0.460(2)	0.0891(14)	0.105(7)
C43	0.1692(8)	0.0652(13)	0.0929(11)	0.080(5)	N5	0.6298(8)	0.4273(12)	0.0474(10)	0.109(5)
N4	0.1088(7)	0.0826(10)	0.0615(8)	0.084(4)	O1	0.7740(5)	0.3493(8)	0.2710(6)	0.083(3)
O3	0.1835(5)	0.0047(9)	0.3325(6)	0.087(3)	C11	0.1301(9)	0.633(2)	0.2560(11)	0.113(7)
C31	0.0378(10)	0.107(2)	0.4065(13)	0.130(8)	C12	0.2295(10)	0.651(2)	0.1831(12)	0.119(7)
C32	0.8982(10)	0.443(2)	0.0590(13)	0.132(8)	C13	0.1845(9)	0.793(2)	0.2499(11)	0.090(6)
C33	0.1362(10)	0.056(2)	0.3427(12)	0.092(6)	N1	0.1809(7)	0.6938(12)	0.2304(9)	0.097(5)
N3	0.0956(6)	0.0414(10)	0.3923(8)	0.079(4)	C21	0.2589(10)	0.343(2)	0.3356(12)	0.118(7)
O2	0.2642(5)	0.1546(9)	0.2739(7)	0.094(3)					

$[\text{Zn}(\text{DMF})_2\text{I}_2]$

$[\text{Zn}(\text{DMF})_2\text{I}_2]$ was synthesised by direct reaction of Zn powder (Ventron) with I_2 (acros organics, 99.5 %) in anhydrous DMF (Fischer Chemicals, HPLC grade). Zn powder was placed in a Schlenk flask and subsequently washed with diluted HCl (0.01 M) and degassed water (3 times). The slurry was dried in high vacuum. A solution of 0.9 eq. I_2 in DMF ($1 \text{ mol} \cdot \text{l}^{-1}$) was added and the mixture was stirred until all I_2 was consumed by Zn. The supernatant was decanted and collected, the remaining Zn residue was discarded.

The slightly yellow solution of ZnI_2 in DMF was concentrated in high vacuum at room temperature until crystallisation started. Subsequent cooling of the solution yielded large, block-shaped colourless crystals sensitive toward moisture. A suitable crystal was selected and centred on a STOE IPDS 1 diffraction system. For additional details on

data collection and treatment see Table 3.8. Indexing, systematic extinction conditions and Wilson statistics indicated monoclinic crystal system including inversion symmetry, unambiguously leading to space group $C2/c$. Solution succeeded in $C2/c$ and yielded all heavy atom positions (Zn, I) and the basic skeleton of DMF molecules. During refinement, atom types were assigned and hydrogen atoms were refined with rigid-model constraints. All atoms except H were treated with anisotropic thermal displacement parameters. No additional symmetry was found.

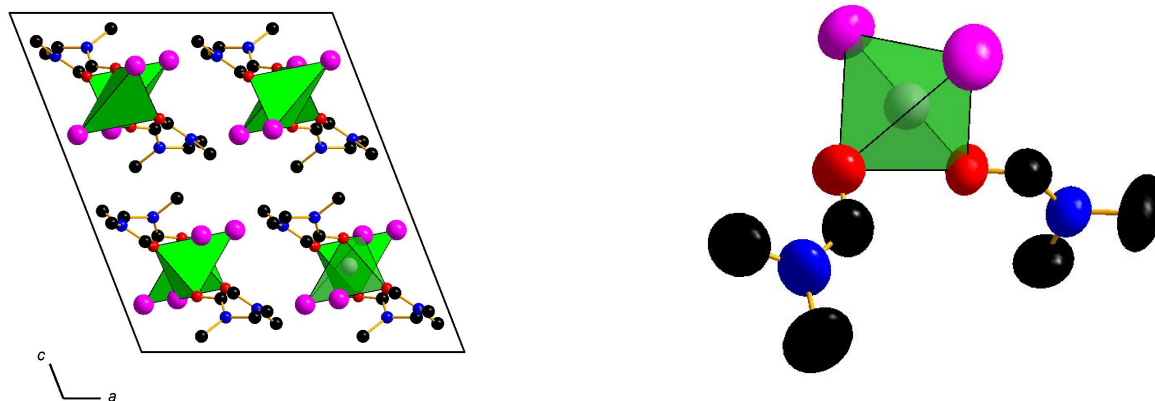


Figure 3.12.: The crystal structure of $[\text{Zn}(\text{DMF})_2\text{I}_2]$. I: magenta; Zn: grey; C: black; O: red, N: blue. Left: Unit cell of $[\text{Zn}(\text{DMF})_2\text{I}_2]$ along $[010]$. Right: Zn is coordinated by the oxygen atoms of two DMF molecules and two I^- ions, forming a distorted tetrahedron. Ellipsoids are drawn at a 75% probability level, H atom positions are omitted for clarity.

The crystal structure is composed of individual $[\text{Zn}(\text{DMF})_2\text{I}_2]$ molecules as shown in Figure 3.12 (right). There are eight formula units in the unit cell, each atom occupies the general position $8f$. Zn^{2+} is coordinated tetrahedrally with a small distortion attributed to the higher spatial demand of I^- in contrast to DMF. This leads to an enlarged angle $\angle_{\text{I}-\text{Zn}-\text{I}} = 122.10(3)^\circ$ and a compressed angle $\angle_{\text{O}-\text{Zn}-\text{O}} = 103.4(2)^\circ$ by comparison to the ideal value of 109.47° (see Tables A.13 and A.14).

Table 3.11.: **Top:** Standardised^[3] fractional atomic coordinates and equivalent isotropic displacement parameters $/\text{\AA}^2$ for $[\text{Zn}(\text{DMF})_2\text{I}_2]$. U_{eq} is defined as $1/3$ of the trace of the orthogonalized U_{ij} tensor. Standard deviations in units of the last digit are given in parentheses. All atoms occupy the general position with Wyckoff number $8f$.

Atom	x	y	z	U_{eq}	Atom	x	y	z	U_{eq}
Zn1	0.25470(4)	0.38587(4)	0.24775(4)	0.0588(2)	N1	0.0902(4)	0.2366(4)	0.3731(4)	0.0889(2)
I1	0.06366(3)	0.11414(4)	0.64018(3)	0.0909(2)	O1	0.1637(3)	0.3445(3)	0.3120(3)	0.0814(11)
I2	0.32548(3)	0.03522(3)	0.34361(3)	0.0793(2)	C4	0.2045(5)	0.1169(5)	0.0467(5)	0.091(2)
C1	0.0488(6)	0.3066(6)	0.4157(5)	0.114(2)	H4A	0.1933	0.0551	0.0699	0.137
H1A	0.0196	0.3592	0.3747	0.170	H4B	0.2025	0.1088	-0.0138	0.137
H1B	0.1015	0.3314	0.4685	0.170	H4C	0.1524	0.1619	0.0468	0.137
H1C	-0.0028	0.2764	0.4328	0.170	C5	0.3101(4)	0.2257(4)	0.1577(4)	0.0620(13)
C2	0.0627(10)	0.1336(6)	0.3801(10)	0.187(6)	H5A	0.3752	0.2432	0.1958	0.074
H2A	0.1002	0.1097	0.4397	0.281	H5B	0.3530	0.2734	0.1439	0.074
H2B	0.0786	0.0950	0.3367	0.281	C6	0.3926(5)	0.1011(6)	0.1023(6)	0.119(3)
H2C	-0.0088	0.1291	0.3685	0.281	H6A	0.4523	0.1391	0.1327	0.179
C3	0.1443(4)	0.2622(5)	0.3259(4)	0.081(2)	H6B	0.3869	0.0897	0.0411	0.179
H3A	0.1702	0.2125	0.3008	0.097	H6C	0.3973	0.0398	0.1327	0.179
H3B	0.1099	0.2341	0.2666	0.097	O2	0.2383(2)	0.2728(2)	0.1641(2)	0.0641(9)
N2	0.3023(3)	0.1545(3)	0.1027(3)	0.0609(10)					

[CdI₄][Cd(DMF)₆]

[CdI₄][Cd(DMF)₆] was synthesised by dissolving commercially available CdI₂ (Merck) in hot DMF (ca. 100 °C, Fischer Chemical, HPLC grade) until a saturated solution was obtained. Remaining solid CdI₂ was dissolved by dropwise addition of DMF. The resulting hot solution was degassed and allowed to cool to room temperature. Upon cooling, colourless, block-shaped crystals formed which were sensitive toward moisture and heat. Single crystal preparation and measurement at room temperature with STOE IPDS 1 devices failed due to recrystallisation of [CdI₄][Cd(DMF)₆] inside the capillary. Instead, a single crystal was mounted on a microgripper and centred on a Bruker D8 venture diffraction device equipped with cooling gas stream. Data collection was performed at 100 K. For additional details on data collection and treatment see Table 3.8.

Indexing, systematic extinction conditions and Wilson statistics indicated monoclinic crystal system including inversion symmetry, unambiguously leading to space group *C2/c*. Solution succeeded in *C2/c* and yielded all heavy atom positions (Cd, I) and all oxygen atoms of the DMF molecules. During refinement, atom positions of DMF molecules were assigned. Hydrogen atoms were refined by rigid body models. All atoms except H were treated with anisotropic thermal displacement parameters. No additional symmetry was found.

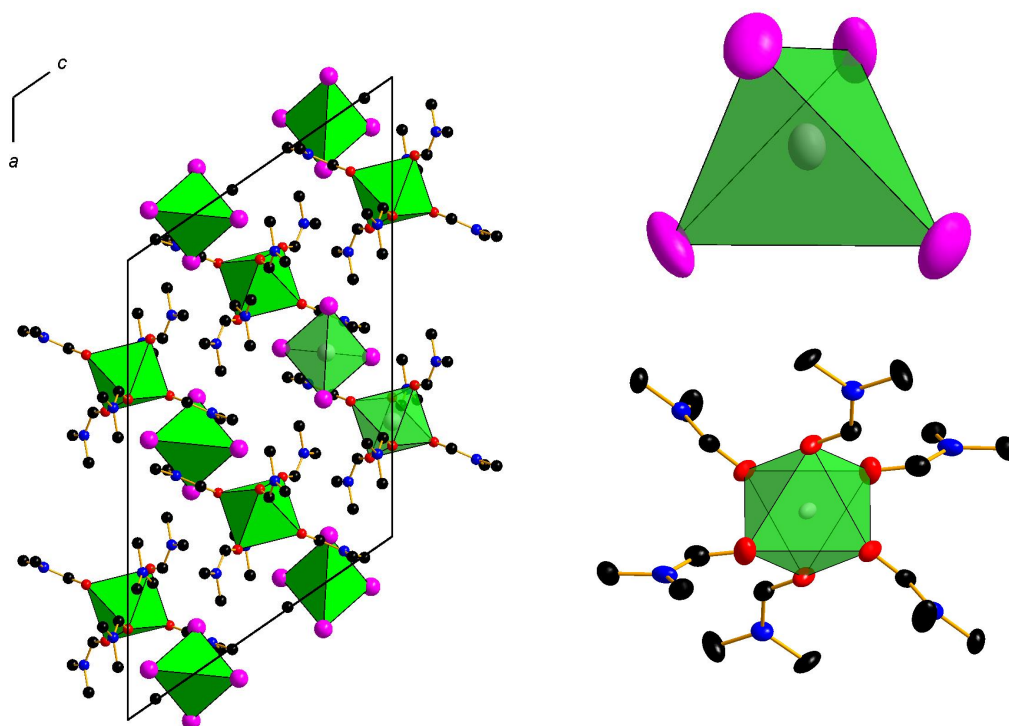


Figure 3.13.: The crystal structure of [CdI₄][Cd(DMF)₆]. I: magenta; Cd: grey; C: black; O: red, N: blue. Left: Unit cell of [CdI₄][Cd(DMF)₆] along [010]. Top right: Cd1 is coordinated by four I⁻ ions forming a tetrahedron. Bottom right: Cd2 is coordinated by oxygen atoms of six DMF molecules forming a distorted octahedron. Ellipsoids are drawn at a 75% probability level, H atom positions are omitted for clarity.

The crystal structure is composed of two crystallographically independent Cd sites. Cd1 is surrounded tetrahedrally by four I⁻, Cd2 is octahedrally surrounded by O atoms of six DMF molecules, resulting in an ionic packing following [CdI₄]⁻²[Cd(DMF)₆]²⁺. Both polyhedra show distortion caused by the spatial requirement of DMF. For additional details see chapter 4.2.1.

Table 3.12.: Top: Standardised^[3] fractional atomic coordinates and equivalent isotropic displacement parameters /Å² for [CdI₄][Cd(DMF)₆] at 100 K. U_{eq} is defined as $1/3$ of the trace of the orthogonalized U_{ij} tensor. Standard deviations in units of the last digit are given in parentheses. Wyckoff numbers are Cd1: 4e, Cd2: 4c, all other atoms: 8f.

Atom	x	y	z	U_{eq}	Atom	x	y	z	U_{eq}
Cd1	0	0.25358(3)	1/4	0.00926(8)	H5A	0.2137	0.1675	0.3968	0.032
Cd2	1/4	1/4	0	0.01370(9)	H5B	0.2521	0.1877	0.3394	0.032
I1	0.07763(2)	0.11760(2)	0.42020(2)	0.01712(8)	H5C	0.2891	0.2269	0.4547	0.032
I2	0.09738(2)	0.38189(2)	0.23986(3)	0.01881(8)	C6	0.2970(3)	0.4281(4)	0.2909(4)	0.0234(8)
C1	0.1190(3)	0.0845(4)	0.1482(4)	0.0222(8)	H6A	0.2510	0.4065	0.2778	0.035
H1A	0.1189	0.1591	0.1367	0.033	H6B	0.3349	0.3806	0.3403	0.035
H1B	0.1180	0.0729	0.2084	0.033	H6C	0.2938	0.4267	0.2267	0.035
H1C	0.0765	0.0527	0.0879	0.033	N2	0.2985(2)	0.0710(3)	0.4444(3)	0.0145(5)
C2	0.1301(3)	0.5630(4)	0.0376(5)	0.0288(10)	O3	0.3572(2)	0.2879(3)	0.1573(3)	0.0200(6)
H2A	0.1248	0.6181	0.0754	0.043	C7	0.3984(2)	0.2211(3)	0.2245(3)	0.0174(7)
H2B	0.1254	0.4953	0.0613	0.043	H7A	0.4136	0.1738	0.1911	0.021
H2C	0.0926	0.5704	-0.0358	0.043	H7B	0.3679	0.1795	0.2382	0.021
N1	0.1854(2)	0.0367(3)	0.1659(3)	0.0194(6)	N3	0.4591(2)	0.2453(3)	0.3182(3)	0.0173(6)
O1	0.1973(2)	0.4039(3)	-0.0004(3)	0.0209(6)	C8	0.4958(3)	0.1631(5)	0.1048(4)	0.0302(11)
O2	0.2050(2)	0.1677(3)	0.0848(3)	0.0281(7)	H8A	0.4461	0.1694	0.0842	0.045
C3	0.2215(3)	0.0804(4)	0.1313(4)	0.0219(8)	H8B	0.5146	0.0947	0.1353	0.045
H3A	0.2721	0.0866	0.1912	0.026	H8C	0.4971	0.1714	0.0446	0.045
H3B	0.2213	0.0292	0.0846	0.026	C9	0.5163(3)	0.3530(4)	0.1507(4)	0.0253(9)
C4	0.2285(2)	0.4902(3)	0.0344(3)	0.0168(7)	H9A	0.5390	0.3973	0.2117	0.038
H4A	0.2386	0.5163	-0.0148	0.020	H9B	0.4640	0.3560	0.1146	0.038
H4B	0.2756	0.4746	0.0986	0.020	H9C	0.5295	0.3773	0.1051	0.038
C5	0.2601(2)	0.1719(4)	0.4055(4)	0.0213(8)					

[Eu(H₂O)₄(C₃H₆O)₄]I₃

[Eu(H₂O)₄(C₃H₆O)₄]I₃ was synthesised by dissolving [Eu(DMF)₈]I₃ (2.603 g, 0.002 mmol) in acetone (50 ml, 1.22 mmol) and refluxing for 3.5 h at 60 °C. The resulting solution was allowed to cool to room temperature. Upon cooling pale yellow hygroscopic crystals formed. A suitable crystal was selected and mounted on a STOE IPDS 1 diffraction system. For additional details on data collection and treatment see Table 3.8. Indexing yielded a monoclinic metric with systematic absence conditions and Wilson statistics indicating space group $P2_1/b$. Solution and refinement were performed in the standardised setting $P2_1/c$.

[Eu(H₂O)₄(C₃H₆O)₄]I₃ crystallises in space group $P2_1/c$ with four formula units in the unit cell. Eu³⁺ ions are coordinated by oxygen atoms of four acetone and four water water molecules leading to a distorted quadratic antiprism as coordination geometry.

Eu₁₂C₉₂H₂₂₀O₆₀N₂₈I₁₂ and Nd₁₂C₉₂H₂₂₀O₆₀N₂₈I₁₂

The above compounds can be written as [RE₁₂(DMF)₂₄(μ₃-COOH)₈(μ₃-OH)₁₆]I₁₂·4DMF (RE = Nd, Eu). The Nd compound was synthesised by electrolytic decomposition of DMF (Fischer Chemical, HPLC grade) at 15 V in the presence of NdI₃ and subsequent storage of the resulting solution in air. Upon reaction, the colour of the solution changed from pale magenta (Nd³⁺ colour) to dark brown due to the formation of I₃⁻ ions on the

anode. After three months, the product was isolated as single crystals of irregular shape exceeding several millimetres in size. When mechanically manipulated the crystals were very soft. Characteristically for Nd, the crystals showed purple colour when exposed to natural light and appeared pale yellow under fluorescent light (pleochroism). The product was sensitive toward moisture.

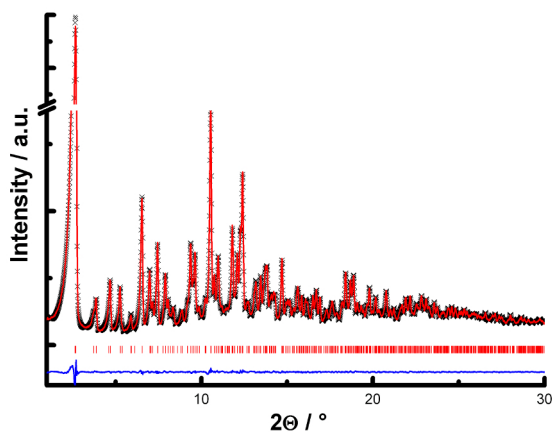


Figure 3.14.: Rietveld refinement of $\text{Eu}_{12}\text{C}_{92}\text{H}_{220}\text{O}_{60}\text{N}_{28}\text{I}_{12}$. Final refinement parameters are compiled in Table 3.13.

Table 3.13.: Results of the Rietveld refinement of $\text{Eu}_{12}\text{C}_{92}\text{H}_{220}\text{O}_{60}\text{N}_{28}\text{I}_{12}$.

Formula	$\text{Eu}_{12}\text{C}_{92}\text{H}_{220}\text{O}_{60}\text{N}_{28}\text{I}_{12}$
<i>Z</i>	2
Crystal system	tetragonal
Space group	<i>I422</i>
Latt. parameters [\AA , \AA^3]	$a = 21.8486(3)$ $c = 20.9863(5)$ $V = 10018.1(3)$
Density (X-ray) [g/cm^3]	1.8932(7)
Radiation	$\text{MoK}_{\alpha 1}$
Parameters	104
Background parameters	18
<i>R</i> values	$R_p = 0.02177$ $R_{wp} = 0.02758$ $\chi^2 = 1.863$

A suitable single crystal was selected and centred on a STOE IPDS diffraction system. For additional details on data collection and treatment see Table 3.8. Indexing, systematic absence conditions and Wilson statistics indicated a tetragonal unit cell without inversion center and extinction symbol $I---$. All heavy atom positions were found during structure solution in space group *I422* and were subsequently refined with anisotropic thermal displacement parameters. Difference Fourier analysis revealed the coordinating atoms and ions. Due to their unique structure, DMF molecules could be assigned unambiguously, as well as formiate anions. Hydroxide anions were assumed and refined to achieve charge balance.

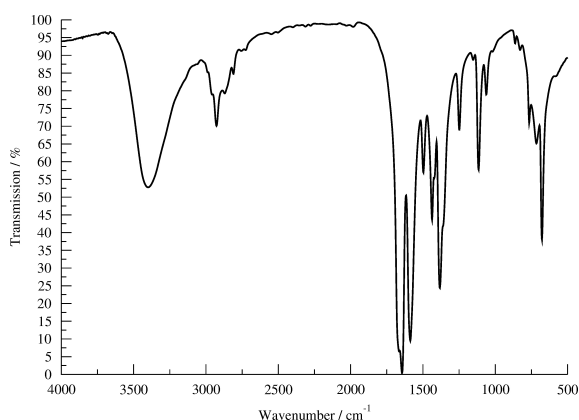


Figure 3.16.: FTIR spectrum of $\text{Eu}_{12}\text{C}_{92}\text{H}_{220}\text{O}_{60}\text{N}_{28}\text{I}_{12}$, measured with the KBr pellet method on a Spectrum BX II spectrometer (Perkin Elmer, Waltham MA, USA).

The free solvate DMF molecule displays a split position. The accuracy of the structure elucidation as well as phase purity of the product were confirmed by Rietveld refinement (see Figure 3.14 and Table 3.13).

The crystal structure of $[\text{Nd}_{12}(\text{DMF})_{24}(\mu_3\text{-COOH})_8(\mu_3\text{-OH})_{16}]\text{I}_{12} \cdot 4\text{DMF}$ consists of a space filling sodalite-type substructure in which iodine ions compose the truncated octahedra (see Fig 3.15a). The hexagonal faces of the sodalite-type cages are centred by further iodine atoms. Inside, $[\text{Nd}_{12}(\text{DMF})_{24}(\mu_3\text{-COOH})_8(\mu_3\text{-OH})_{16}]\text{I}_{12}$ and four additional DMF solvent molecules are located

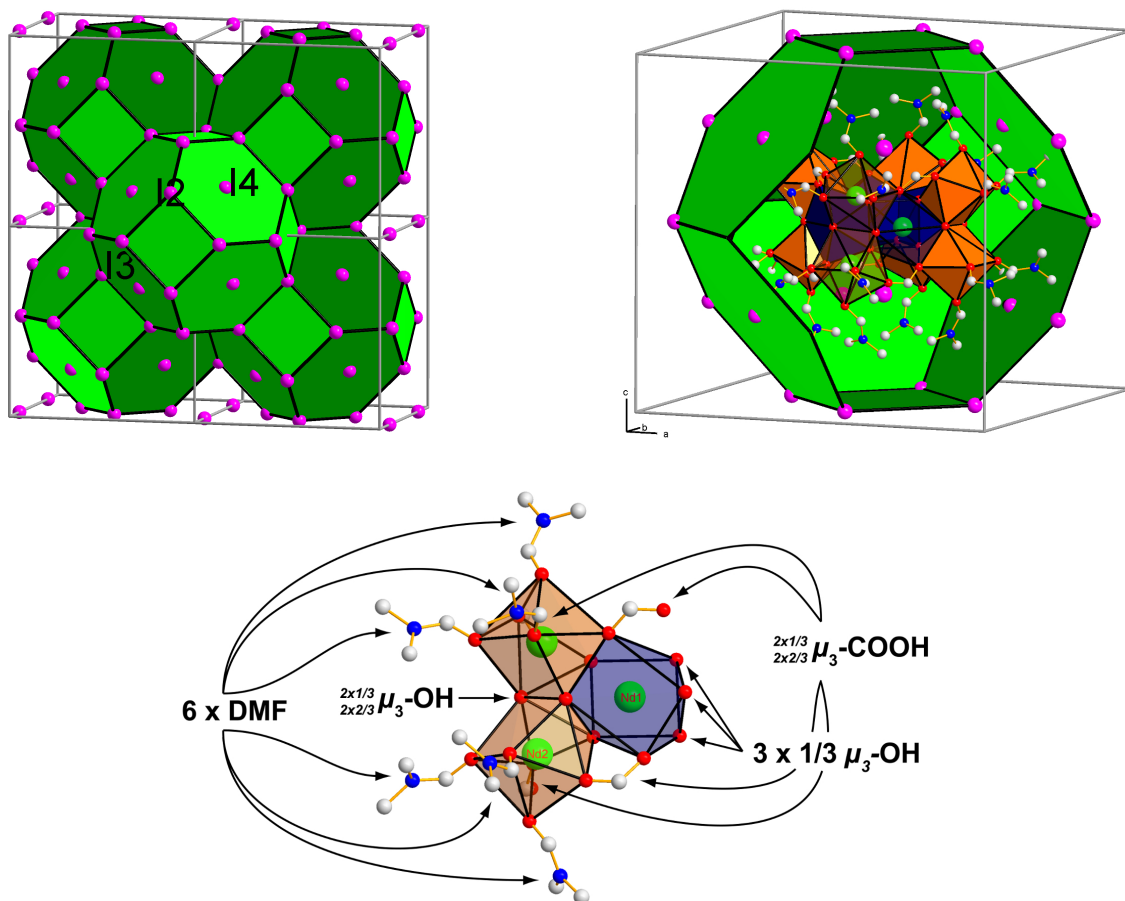


Figure 3.15.: The crystal structures of $RE_{12}C_{92}H_{220}O_{60}N_{28}I_{12}$ on the example of $RE = Eu$. a) Iodine ions build a framework with centring (I4) ions. b) A cut-open truncated octahedron shows the $[Nd_{12}(DMF)_{24}(\mu_3-COOH)_8(\mu_3-OH)_{16}]I_{12} \cdot 4DMF$ core. c) A detailed scheme of the coordination and connection of Nd.

(see Figure 3.15b). This core can be described as follows: Twelve Nd atoms occupy two crystallographically independent sites. These metal centres are coordinated by 56 oxygen atoms forming a $[Nd_{12}O_{56}]$ -core: 24 non-bridging DMF molecules, 16 μ_3 -bridging hydroxide ions and 8 μ_3 -bridging formate anions coordinate the Nd atom group on the outer surface. A detailed scheme is shown in Figure 3.15c.

A pseudocubic void capped at the top and bottom by additional iodine ions is formed (that do not contribute to the sodalite cage). Thus, a slightly distorted octahedron $[(Nd)_4(I)_2]$ occupies the centre and the vertices of the unit cell. Both crystallographically independent Nd positions are coordinated by distorted square antiprisms. Nd1 is connected via hydroxide and formate bridges to a total number of six neighbouring centres. Nd2 is shielded by three DMF ligands on one side, and connected via hydroxide and formate bridges to five additional Nd atoms.

The hydrogen atoms of the hydroxide ions could not be located by single crystal or powder diffraction methods. To get evidence for hydroxide ions FTIR data was collected (see Figure 3.16). The spectrum shows a broad band originating from hydroxide bonds between 3250 and 3650 cm^{-1} . Free solvate DMF connects with its aldehyde group to

one hydroxide group forming a hydrogen bond and leading to the broad peak at 3425 cm^{-1} . Free hydroxide, not exhibiting hydrogen bonding, is located at the centre of the pseudocubic void. All other signals are either part of DMF (coordinating DMF and solvate DMF), formiate ions or lattice vibrations.

Table 3.14.: Top: Standardised^[3] fractional atomic coordinates and equivalent isotropic displacement parameters / \AA^2 for $[\text{RE}_{12}(\text{DMF})_{24}(\mu_3\text{-COOH})_8(\mu_3\text{-OH})_{16}]\text{I}_{12} \cdot 4\text{DMF}$ ($\text{RE} = \text{Nd}, \text{Eu}$). U_{eq} is defined as $1/3$ of the trace of the orthogonalized U_{ij} tensor. Standard deviations in units of the last digit are given in parentheses.

Atom	Wyckoff	x	y	z	U_{eq}	Atom	Wyckoff	x	y	z	U_{eq}
	number						number				
Nd1	8g	0.09340(2)	0.09340(2)	0	0.0279(2)	H23A	16k	0.17640	0.06010	0.34990	
Eu1	8g	0.09180(2)	0.09180(3)	0	0.0284(2)	16k	16k	0.16240	0.07940	0.31390	
Nd2	16k	0.20910(2)	0.00770(2)	0.09600(2)	0.0351(2)	H23B	16k	0.11430	0.02510	0.34230	
Eu2	16k	0.20710(2)	0.00910(3)	0.09330(2)	0.0379(2)	16k	16k	0.10440	0.03810	0.30040	
I1	4e	0	0	0.2034(2)	0.0546(2)	H23C	16k	0.14390	0.05750	0.28300	
4e	0	0	0	0.2020(2)	0.0553(2)	16k	16k	0.13870	0.03320	0.36570	
I2	8i	0.2625(2)	0	$1/2$	0.0965(2)	O3	16k	0.2850(5)	0.0879(5)	0.1033(7)	0.0647(2)
8i	0.26140	0.0000(2)	$1/2$	0.0965(2)		16k	16k	0.2825(6)	0.0885(6)	0.1001(9)	0.0681(2)
I3	4d	0	$1/2$	$1/4$	0.0705(2)	N3	16k	0.3636(8)	0.1451(8)	0.1387(8)	0.0578(2)
4d	0.7316(2)	0.2316(2)	$1/4$	0.0845(2)		16k	16k	0.3612(11)	0.1428(9)	0.1362(11)	0.0836(2)
I4	8j	0.7303(2)	0.2303(2)	$1/4$	0.0738(2)	C31	16k	0.3058(12)	0.1306(12)	0.1357(13)	0.0482(2)
8j	0	$1/2$	$1/4$	0.0552(2)		16k	16k	0.309(3)	0.125(2)	0.135(2)	0.0805(2)
O1	16k	0.0459(5)	0.3062(5)	0.1003(8)	0.0702(2)	H31	16k	0.27830	0.15390	0.15940	
16k	0.0439(6)	0.3039(5)	0.1005(9)	0.0621(2)		16k	16k	0.28340	0.14170	0.16600	
N1	16k	0.1017(6)	0.3894(6)	0.1202(8)	0.0597(2)	C32	16k	0.3230(14)	0.1019(14)	0.317(2)	0.0784(2)
16k	0.1002(9)	0.3866(8)	0.117(2)	0.0576(2)		16k	16k	0.324(2)	0.103(2)	0.320(2)	0.0637(2)
C11	16k	0.0864(7)	0.3337(7)	0.1302(8)	0.0548(2)	H32A	16k	0.28560	0.12240	0.30600	
16k	0.085(2)	0.3324(9)	0.1253(12)	0.0505(2)		16k	16k	0.29490	0.07790	0.34260	
H11	16k	0.10710	0.31250	0.16220		H32B	16k	0.31390	0.06250	0.33460	
16k	0.10910	0.31040	0.15430			16k	16k	0.30320	0.12960	0.29110	
C12	16k	0.1475(9)	0.419(2)	0.1591(12)	0.0568(2)	H32C	16k	0.34740	0.09700	0.27890	
16k	0.1494(12)	0.4155(13)	0.1620(14)	0.0758(2)		16k	16k	0.35260	0.07690	0.29750	
H12A	16k	0.05950	0.37200	0.30630		C33	16k	0.407(2)	0.104(2)	0.115(2)	0.0984(2)
16k	0.05890	0.37060	0.30710			16k	16k	0.409(3)	0.107(2)	0.107(3)	0.1079(2)
H12B	16k	0.05230	0.33000	0.36670		H33A	16k	0.39130	0.06280	0.11860	
16k	0.06000	0.32240	0.36260			16k	16k	0.39950	0.10040	0.06320	
H12C	16k	0.17500	0.38910	0.17620		H33B	16k	0.44400	0.10690	0.13990	
16k	0.17180	0.38310	0.18310			16k	16k	0.44780	0.12840	0.11060	
C13	16k	0.0675(11)	0.425(2)	0.0749(11)	0.0684(2)	H33C	16k	0.41570	0.11260	0.07110	
16k	0.0652(14)	0.4260(12)	0.075(2)	0.0655(2)		16k	16k	0.41220	0.06760	0.12820	
H13A	16k	0.02780	0.40760	0.06900		O111	16k	0.0026(5)	0.1008(3)	0.0654(3)	0.0284(2)
16k	0.02320	0.41160	0.07260			16k	16k	0.0037(4)	0.0992(6)	0.0650(4)	0.0292(2)
H13B	16k	0.08870	0.42610	0.03460		O121	16k	0.0609(3)	0.2015(3)	0.0043(8)	0.0336(2)
16k	0.08330	0.42470	0.03320			16k	16k	0.0605(4)	0.1988(4)	0.0040(11)	0.0431(2)
H13C	16k	0.06320	0.46630	0.09080		C333	16k	0.1302(7)	0.1451(7)	0.1486(8)	0.0457(2)
16k	0.06580	0.46770	0.09030			16k	16k	0.132(2)	0.1456(11)	0.1455(11)	0.0531(2)
O2	16k	0.2173(6)	0.0202(7)	0.2117(7)	0.0876(2)	H333	16k	0.15350	0.14570	0.18580	
16k	0.2068(11)	0.0280(14)	0.2081(13)	0.0581(2)		16k	16k	0.15320	0.14270	0.18450	
N2	16k	0.018(2)	0.184(2)	0.3070(9)	0.0892(2)	O331	16k	0.0901(5)	0.1834(5)	0.1456(6)	0.0539(2)
16k	0.005(2)	0.1814(12)	0.297(2)	0.0531(2)		16k	16k	0.0881(6)	0.1834(6)	0.1438(8)	0.0550(2)
C21	16k	0.0234(11)	0.2114(11)	0.253(2)	0.0856(2)	O332	16k	0.1447(4)	0.1046(4)	0.1081(5)	0.0400(2)
16k	0.023(2)	0.2145(2)	0.243(3)	0.0937(2)		16k	16k	0.1438(5)	0.1060(4)	0.1046(7)	0.0376(2)
H21	16k	0.06120	0.22830	0.24310		O4	8g	0.1879(5)	0.1879(5)	0	0.0665(2)
16k	0.05890	0.23660	0.23480			8g	8g	0.1898(8)	0.1898(8)	0	0.0552(2)
C22	16k	0.0713(13)	0.1806(13)	0.345(2)	0.0523(2)	N4	8g	0.2601(8)	0.2601(8)	0	0.1047(2)
16k	0.052(3)	0.180(2)	0.339(2)	0.0910(2)		8g	8g	0.2610(12)	0.2610(12)	0	0.1095(2)
H22A	16k	0.10270	0.20590	0.32710		C41	16k	0.212(2)	0.229(2)	0.035(2)	0.0481(2)
16k	0.08920	0.19480	0.31930			16k	16k	0.210(2)	0.230(3)	0.031(2)	0.0973(2)
H22B	16k	0.08530	0.13900	0.34710		C42	16k	0.220(3)	0.305(3)	0.035(3)	0.0741(2)
16k	0.05790	0.13890	0.35410			16k	16k	0.259(2)	0.302(5)	0.051(3)	0.0810(2)
H22C	16k	0.06210	0.19450	0.38780		C43	16k	0.306(2)	0.291(2)	0.054(2)	0.0861(2)
16k	0.04180	0.20670	0.37430			16k	16k	0.311(3)	0.301(2)	0.071(3)	0.0796(2)
C23	16k	0.152(2)	0.035(2)	0.322(2)	0.0256(2)						
16k	0.144(2)	0.040(2)	0.321(3)	0.1079(2)							

References

- [1] M. Wenger, T. Armbruster, U. Bern, C. Bern, *Eur. J. Mineral.*, **3**, 387–399 (1991).
[2] H. Sawinski, R. Dronskowski, *Z. Naturforsch. B*, **69(6)**, 651–654 (2014).

- [3] L. M. Gelato, E. Parthé, *J. Appl Crystallogr.*, **20(2)**, 139–143 (1987).
- [4] Y. Le Page, *J. Appl Crystallogr.*, **20(3)**, 264–269 (1987).
- [5] R. M. Wood, G. J. Palenik, *Inorg. Chem.*, **38(17)**, 3926–3930 (1999).
- [6] A. L. Spek, *Acta Crystallogr. D*, **65(2)**, 148–155 (2009).
- [7] G. M. Sheldrick, *Acta Crystallogr. A*, **64(1)**, 112–122 (2007).
- [8] A. Trzesowska, R. Kruszynski, T. J. Bartczak, *Acta Crystallogr. B*, **60(2)**, 174–178 (2004).
- [9] R. D. Shannon, C. T. Prewitt, *Acta Crystallogr. B*, **25(5)**, 925–946 (1969).

The following chapter contains the published results for the single crystal structure determination and topological analysis of $[\text{EuCl}_2(\text{H}_2\text{O})_6]\text{Cl}$. $[\text{EuCl}_2(\text{H}_2\text{O})_6]\text{Cl}$ was synthesised from Eu_2O_3 as intermediate product during synthesis of $[\text{Eu}(\text{DMF}_8)]\text{I}_3$. The latter compound serves as educt for electrocrystallisation.

3.2.2. Redetermination of $[\text{EuCl}_2(\text{H}_2\text{O})_6]\text{Cl}$

Frank Tambornino, Philipp Bielec, Dr. Constantin Hoch*

* *Ludwig-Maximilians-Universität München, Butenandtstrasse 5-13, D-81377 München, Germany Correspondence e-mail: constantin.hoch@cup.uni-muenchen.de*

published in: *Acta Crystallogr. E* **70(6)** i27, (2014). DOI:10.1107/S160053681401030

Reprinted (adapted) with permission from International Union for Crystallography

The crystal structure of the title compound, hexaaqua-dichloridoeuropium(III) chloride, was redetermined with modern crystallographic methods. In comparison with the previous study [Lepert *et al.* (1983). *Aust. J. Chem.* **36**, 477–482], it could be shown that the atomic coordinates of some O atoms had been confused and now were corrected. Moreover, it was possible to freely refine the positions of the H atom positions and thus to improve the accuracy of the crystal structure. $[\text{EuCl}_2(\text{H}_2\text{O})_6]\text{Cl}$ crystallizes with the $\text{GdCl}_3 \cdot 6\text{H}_2\text{O}$ structure type, exhibiting discrete $[\text{EuCl}_2(\text{H}_2\text{O})_6]^+$ cations as the main building blocks. The main blocks are linked with isolated chloride anions via O—H \cdots Cl hydrogen bonds into a three-dimensional framework. The Eu^{3+} cation is located on a twofold rotation axis and is coordinated in the form of a Cl_2O_6 square antiprism. One chloride anion coordinates directly to Eu^{3+} , whereas the other chloride anion, situated on a twofold rotation axis, is hydrogen bonded to six octahedrally arranged water molecules.

Related literature

For previous structure determinations of the title compound see: Lepert *et al.* (1983); Bel'skii & Struchkov (1965). For the $\text{GdCl}_3 \cdot 6\text{H}_2\text{O}$ structure type and isotypic compounds, see: Marezio *et al.* (1961); Bell & Smith (1990); Burns & Peterson (1971); Graeber *et al.* (1966); Habenschuss & Spedding (1980); Hoch & Simon (2008); Junk *et al.* (1999); Reuter *et al.* (1994). For standardization of crystal data, see: Gelato & Parthe (1987).

Experimental

S1 Comment

$[\text{EuCl}_2(\text{H}_2\text{O})_6]\text{Cl}$ crystallizes with the $\text{GdCl}_3 \cdot 6\text{H}_2\text{O}$ structure type (Marezio *et al.*, 1961), like many metal trichloride hexahydrates $\text{MCl}_3 \cdot 6\text{H}_2\text{O}$ with $\text{M} = \text{Y}$ (Bell & Smith, 1990), Ce (Reuter *et al.*, 1994), Nd (Habenschuss & Spedding, 1980), Sm–Tm (Graeber *et al.*, 1966), Am, Bk (Burns & Peterson, 1971), and three bromide hexahydrates $\text{MBr}_3 \cdot 6\text{H}_2\text{O}$

with $M = \text{Pr, Dy}$ (Junk et al., 1999) and Eu (Hoch & Simon, 2008). The first structure determination of the title compound was performed on the basis of film data (Bel'skii & Struchkov, 1965) and without determination of the hydrogen atom positions. A first exact structure determination with all atomic positions was performed by Lepert *et al.* (1983). However, the published data contain errors in the atomic coordinates. We have thus redetermined the structure on the basis of modern area detector data.

The Eu^{3+} cation in $[\text{EuCl}_2(\text{H}_2\text{O})_6]\text{Cl}$ is located on a twofold rotation axis and is coordinated in form of a distorted square antiprism defined by six water molecules and two chloride anions (Fig. 1, Table 1). Hydrogen bonds $\text{O}-\text{H}\cdots\text{Cl}$ connect the $[\text{EuCl}_2(\text{H}_2\text{O})_6]^+$ cations with the Cl^- counter-anions to a three-dimensional framework (Fig 2). The complexing chloride anion Cl1 is surrounded by three, the isolated chloride anion Cl2 by six H atom positions (Figs. 3, 4), forming hydrogen bonds with $\text{Cl}\cdots\text{H}$ distances between 2.36 (4) and 2.54 (3) Å (Table 2) and are in good agreement with those in other chloride hydrates. The $\text{Eu}^{\text{III}}-\text{O}$ distances in $[\text{EuCl}_2(\text{H}_2\text{O})_6]\text{Cl}$ range from 2.3078(16) to 2.4620(18) Å and are comparable with those in $\text{EuCl}_3 \cdot 3\text{H}_2\text{O}$ (2.39-2.40 Å; Reuter et al., 1994), $\text{EuCl}_3 \cdot 6\text{H}_2\text{O}$ (2.39-2.43 Å; Graeber et al., 1966), or $\text{EuCl}(\text{OH})_2$ (2.35-2.44 Å; Demyanets et al., 1974) and also with those in $\text{EuBr}_3 \cdot 6\text{H}_2\text{O}$ (Hoch & Simon, 2008).

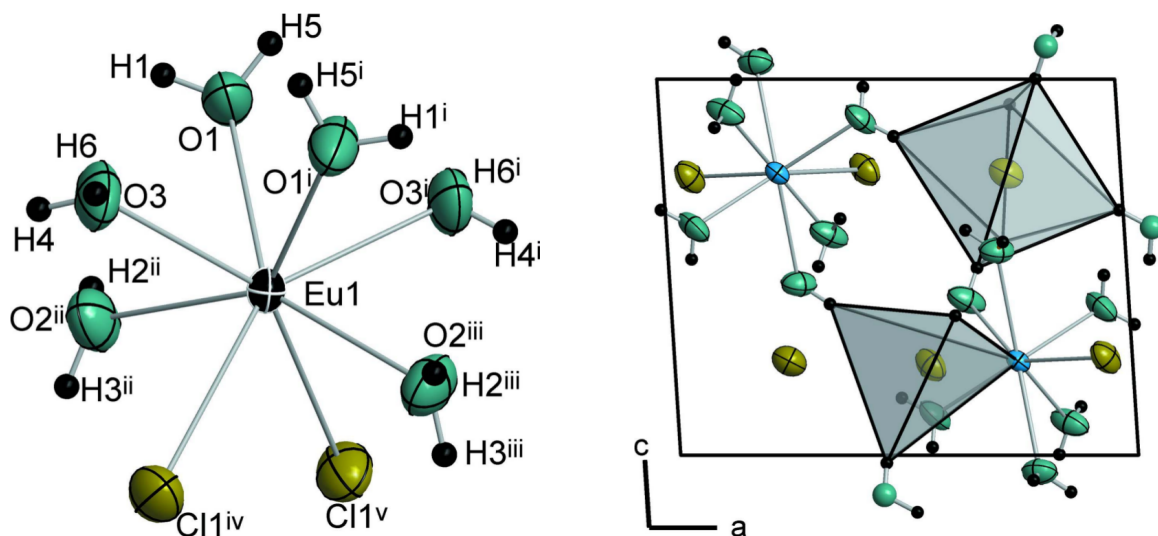
S1 Experimental

The title compound was obtained by adding small portions of commercially available Eu_2O_3 (Alfa Aesar, 99.99%) into concentrated aqueous HCl solution at 353 K until only minor amounts of undissolved Eu_2O_3 remained visible for several minutes. The surplus Eu_2O_3 finally was dissolved by dropwise addition of concentrated HCl to the solution until a clear colourless solution was obtained. The solution was allowed to cool to 293 K, yielding colourless single-crystal blocks of $[\text{EuCl}_2(\text{H}_2\text{O})_6]\text{Cl}$.

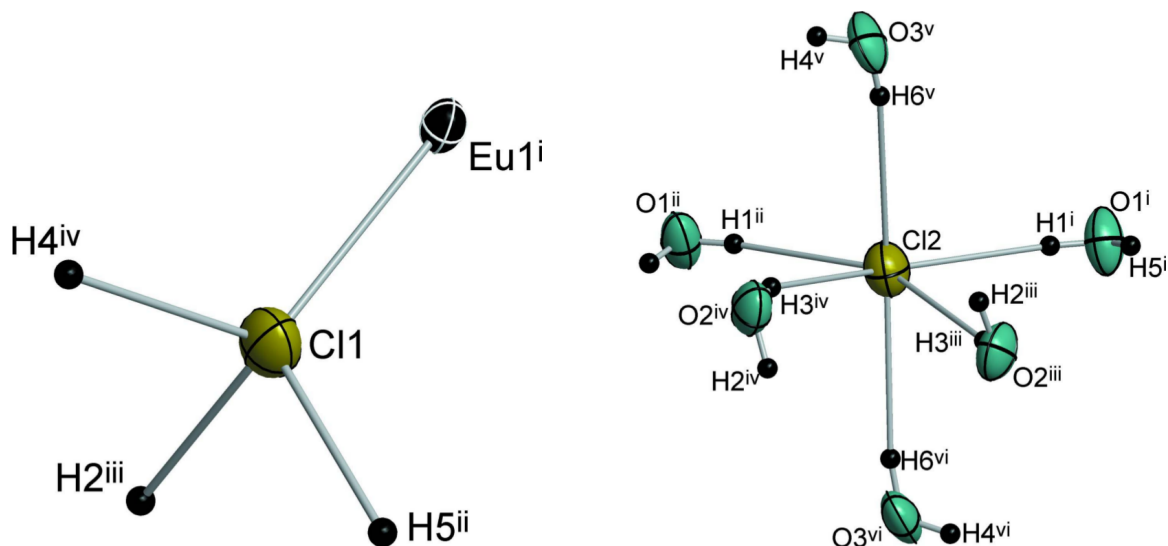
S1 Refinement

The positions of all hydrogen atoms were identified from the difference Fourier map and were freely refined, applying one common isotropic displacement parameter to all six H atom positions.

For better comparability of our structure model with the previous model by Lepert *et al.* (1983) we have used the same setting in space group $P2/n$. In the crystal structure description given by Lepert *et al.* (1983) several misspellings of the atomic positions were adopted into the databases. The published model leads to diverging refinements if taken as starting values. We have analysed the misspellings and give a conclusive assignment of the atomic positions. If standardized by the program *STRUCTURE-TIDY* (Gelato & Parthé, 1987), the comparison of our model with the one given by Lepert *et al.* (1983) shows, in addition to an origin shift of (0, 1/2, 0), that the y and z coordinates of atoms O1, O2 and O3 were permuted. In fact, $y(\text{O1})$ and $z(\text{O1})$ belong to $y(\text{O3})$ and $z(\text{O3})$, $y(\text{O2})$ and $z(\text{O2})$ belong to $y(\text{O1})$ and $z(\text{O1})$, and finally $y(\text{O3})$ and $z(\text{O3})$ belong to $y(\text{O2})$ and $z(\text{O2})$. If re-ordered in the given way, the refinement based on starting values from Lepert *et al.* (1983) lead to convergence in few cycles with satisfying results.



Left: Figure 1. The cationic $[\text{Eu}(\text{H}_2\text{O})_6\text{Cl}_2]^+$ unit in $[\text{Eu}(\text{H}_2\text{O})_6\text{Cl}_2]\text{Cl}$. Ellipsoids are drawn at 75% probability level. Hydrogen atoms are drawn as small black spheres with arbitrary radius. [Symmetry code: (i) $3/2 - x, y, 1/2 - z$; (ii) $x, y, -1 + z$; (iii) $3/2 - x, y, 3/2 - z$; (iv) $1 - x, -y, 1 - z$; (v) $1/2 + x, -y, -1/2 + z$]. **Right: Figure 2.** View along $[010]$ on the crystal structure of $[\text{Eu}(\text{H}_2\text{O})_6\text{Cl}_2]\text{Cl}$. Small black spheres represent H atom positions, blue ellipsoids represent Eu atoms, olive ellipsoids represent Cl atoms, turquoise ellipsoids represent O atoms. Grey polyhedra represent the coordination of H atom positions around Cl atoms.



Left: Figure 3. The coordination sphere of the coordinating Cl1 atom is a distorted tetrahedron built from three water molecules and one europium atom. The water molecules coordinate via hydrogen bonds. [Symmetry codes: (i) $1 - x, -y, 1 - z$; (ii) $1/2 + x, 1 - y, 1/2 + z$; (iii) $3/2 - x, y, 3/2 - z$; (iv) $x, y, 1 + z$]. **Right: Figure 4.** The coordination sphere of the anionic Cl2 atom consists of six water molecules coordinating via their hydrogen atoms forming a distorted octahedron. [Symmetry codes: (i) $3/2 - x, y, 1/2 - z$; (ii) $x, y, 1 + z$; (iii) $3/2 - x, 1 + y, 3/2 - z$; (iv) $x, 1 + y, z$; (v) $1 - x, 1 - y, 1 - z$; (vi) $1/2 + x, 1 - y, 1/2 + z$].

Hexaaquadichloridoeuropium(III) chloride.

<i>Crystal data</i>	
[EuCl ₂ (H ₂ O) ₆]Cl	$Z = 2$
$M_r = 366.41$	$F(000) = 348$
Monoclinic, $P 2/n$	$D_x = 2.441 \text{ Mg m}^{-3}$
Hall symbol: -P 2yac	AgK α radiation, $\lambda = 0.56083 \text{ \AA}$
$a = 9.6438(12) \text{ \AA}$	Cell parameters from 13548 reflections
$b = 6.5322(10) \text{ \AA}$	$\mu = 3.74 \text{ mm}^{-1}$
$c = 7.929(3) \text{ \AA}$	$T = 293 \text{ K}$
$\beta = 93.653(13)^\circ$	Stretched cuboid, clear colourless
$V = 498.4(2) \text{ \AA}^3$	0.23 x 0.20 x 0.18 mm
<i>Data collection</i>	
Stoe IPDS I diffractometer	13401 measured reflections
	1762 independent reflections
Radiation source: fine-focus sealed tube	1762 independent reflections
Graphite monochromator	$R_{\text{int}} = 0.043$
φ scan	$\theta_{\text{max}} = 25.5^\circ$, $\theta_{\text{main}} = 3.0^\circ$
Absorption correction: multi-scan	$h = -14 \rightarrow 14$
(MulScanAbs in PLATON, Spek, 2009)	$k = -10 \rightarrow 10$
$T_{\text{min}} = 0.425$, $T_{\text{max}} = 0.510$	$l = -11 \rightarrow 11$
<i>Refinement</i>	
Refinement on F^2	Secondary atom site location:
Least-squares matrix: full	difference Fourier map
$R[F^2 > 2\sigma F^2] = 0.015$	Hydrogen site location:
$wR(F^2) = 0.032$	inferred from neighbouring sites
$S = 1.03$	All H-atoms parameters refined
1762 reflections	$w = 1/[\sigma^2(F_o^2) + 0.015P]^2$
66 parameters	where $P = (F_o^2 + 2 F_c^2)/3$
0 restraints	$(\Delta/\sigma)_{\text{max}} < 0.001$
Primary atom site location: structure-invariant	$\Delta\rho_{\text{max}} = 0.63\text{e\AA}^{-3}$
direct methods	$\Delta\rho_{\text{min}} = -0.77\text{e\AA}^{-3}$

Fractional atomic coordinates and isotropic or equivalent isotropic displacement parameters (\AA^2)

	x	y	z	$U_{\text{iso}}^*/U_{\text{eq}}$
Eu1	0.7500	0.150918 (18)	0.2500	0.01345 (3)
Cl1	0.44156 (5)	0.16532 (7)	0.76010 (6)	0.02588 (9)
Cl2	0.85427 (18)	0.62387 (11)	0.7500	0.02813 (13)
O1	0.7500	0.4256 (2)	0.0872 (2)	0.0275 (3)
O2	0.78164 (18)	0.0484 (2)	0.9561 (2)	0.0263 (3)
O3	0.56055 (17)	0.3002 (2)	0.1060 (2)	0.0278 (3)
H1	0.827 (4)	0.454 (6)	0.001 (5)	0.051 (4)*
H2	0.846 (3)	0.084 (5)	0.902 (4)	0.035 (3)*
H3	0.766 (4)	-0.063 (7)	0.933 (5)	0.058 (5)*
H4	0.551 (4)	0.265 (6)	0.020 (5)	0.052 (5)*
H5	0.881 (4)	0.520 (5)	0.129 (5)	0.040 (3)*
H6	0.491 (4)	0.319 (6)	0.152 (5)	0.044 (4)*

 Atomic displacement parameters (\AA^2)

	U^{11}	U^{22}	U^{33}	U^{12}	U^{13}	U^{23}
Eu1	0.01398 (5)	0.01346 (5)	0.01244 (6)	0.000	-0.00293 (3)	0.000
Cl1	0.02417 (18)	0.02396 (18)	0.0286 (2)	-0.00652 (16)	-0.00541 (16)	0.00198 (17)
Cl2	0.0297 (3)	0.0305 (3)	0.0235 (3)	0.000	-0.0033 (2)	0.000
O1	0.0368 (8)	0.0229 (6)	0.0214 (8)	-0.0100 (6)	-0.0085 (6)	0.0038 (5)
O2	0.0336 (7)	0.0277 (7)	0.0175 (7)	-0.0047 (6)	-0.0001 (6)	-0.0039 (5)
O3	0.0250 (6)	0.0317 (7)	0.0250 (8)	0.0067 (5)	-0.0113 (6)	-0.0028 (5)

Special details

Geometry. All e.s.d.'s (except the e.s.d. in the dihedral angle between two l.s. planes) are estimated using the full covariance matrix. The cell e.s.d.'s are taken into account individually in the estimation of e.s.d.'s in distances, angles and torsion angles; correlations between e.s.d.'s in cell parameters are only used when they are defined by crystal symmetry. An approximate (isotropic) treatment of cell e.s.d.'s is used for estimating e.s.d.'s involving l.s. planes.

Refinement. Refinement of F^2 against ALL reflections. The weighted R -factor wR and goodness of fit S are based on F^2 , conventional R -factors R are based on F , with F set to zero for negative F^2 . The threshold expression of $F^2 > \sigma(F^2)$ is used only for calculating R -factors(gt) etc. and is not relevant to the choice of reflections for refinement. R -factors based on F^2 are statistically about twice as large as those based on F , and R -factors based on ALL data will be even larger.

Geometric parameters (\AA^2). Symmetry codes: (i) $-x+3/2, y, -z+1/2$; (ii) $x, y, z-1$; (iii) $-x+3/2, y, -z+3/2$; (iv) $-x+1, -y, -z+1$; (v) $x+1/2, -y, z-1/2$; (vi) $x-1/2, -y+1, z+1/2$; (vii) $x, y+1, z$; (viii) $-x+1, -y+1, -z+1$; (ix) $x, y, z+1$.

Eu1—O1	2.4618 (15)	O2—H3	0.76 (4)
Eu1—O1 ⁱ	2.4618 (16)	O2—H2	0.81 (3)
Eu1—O2 ⁱⁱ	2.4620 (18)	O3—H4	0.72 (4)
Eu1—O2 ⁱⁱⁱ	2.4620 (18)	O3—H6	0.79 (4)
Eu1—O3	2.3078 (16)	C11—H2	2.535 (4)
Eu1—O3 ⁱ	2.3078 (15)	C11—H4	2.3535 (4)
Eu1—C11 ^{iv}	2.7690 (12)	C11—H5 ^{vi}	2.36 (3)
Eu1—C11 ^v	2.7690 (12)	C12—H1 ⁱ	2.36 (4)
O1—H1	0.74 (4)	C12—H3 ^{vii}	2.5071 (4)
O1—H5	0.74 (4)	C12—H6 ^{viii}	2.53 (4)
Eu1—O1—H1	122 (3)	O1—Eu1—O2 ⁱⁱ	67.83 (6)
Eu1—O1—H1	122 (3)	O1i—Eu1—C11 ^{iv}	105.35 (5)
Eu1—O1—H5	121 (3)	O1—Eu1—C11 ^{iv}	145.35 (4)
Eu1—O1—H5	121 (3)	O2ii—Eu1—O2 ⁱⁱⁱ	148.45 (8)
Eu1 ^{ix} —O2—H2	124 (3)	O2ii—Eu1—C11 ^{iv}	83.83 (4)
Eu1 ^{ix} —O2—H2	124 (3)	O2iii—Eu1—C11 ^{iv}	72.65 (4)
Eu1 ^{ix} —O2—H3	117 (3)	O3i—Eu1—O1 ⁱ	76.70 (6)
Eu1 ^{ix} —O2—H3	117 (3)	O3—Eu1—O1 ⁱ	67.31 (6)
Eu1—O3—H4	112 (3)	O3i—Eu1—O2 ⁱⁱ	116.15 (7)
Eu1—O3—H4	112 (3)	O3—Eu1—O2 ⁱⁱ	77.82 (6)
Eu1—O3—H6	120 (3)	O3i—Eu1—O3	130.01 (8)
Eu1—O3—H6	120 (3)	O3i—Eu1—C11 ^{iv}	146.64 (4)
O1 ⁱ —Eu1—O1	86.43 (9)	O3—Eu1—C11 ^{iv}	78.18 (5)
O1 ⁱ —Eu1—O2 ⁱⁱ	140.68 (5)	C11iv—Eu1—C11 ^v	83.51 (2)

Hydrogen-bond geometry ($\text{\AA}, ^\circ$). Symmetry codes: (ii) $x, y, z-1$; (iii) $-x+3/2, y, -z+3/2$; (vi) $x-1/2, -y+1, z+1/2$; (viii) $-x+1, -y+1, -z+1$; (x) $x, y-1, z$.

$D-H \cdots A$	$D-H$	$H \cdots A$	$D \cdots A$	$D-H \cdots A$
O1—H1 \cdots C12 ⁱⁱ	0.74 (4)	2.36 (4)	3.081 (2)	166.08
O2—H2 \cdots C11 ⁱⁱⁱ	0.81 (3)	2.54 (3)	3.351 (2)	174.97
O2—H3 \cdots C12 ^x	0.76 (4)	2.51 (4)	3.2234 (19)	157.37
O3—H4 \cdots C11 ⁱⁱ	0.72 (4)	2.35 (4)	3.036 (2)	160.44
O1—H5 ^{vi} \cdots C11	0.74 (2)	2.36 (3)	3.095 (2)	173.89
O3—H6 \cdots C12 ^{viii}	0.79 (4)	2.53 (4)	3.310 (2)	170.66

3.3. Lanthanide Amalgams

The following chapter contains published as well as unpublished results of lanthanide amalgams examined in this work. $\text{Eu}_{10}\text{Hg}_{55}$ was synthesised by electrocrystallisation and is the mercury-richest Eu amalgam, the results were published in *Z. Anorg. Allg. Chem.*. It crystallises in a hettotype structure of the $\text{Gd}_{14}\text{Ag}_{51}$ structure type and the question arose whether the structure determination of the aristotype is correct or whether a twinning problem was overlooked, leading to higher pseudo-symmetry.

Following this chain of thought, the aristotype and three isotypical structures ($\text{RE}_{14}\text{Ag}_{51}$, $\text{RE} = \text{Y}, \text{Ce}, \text{Gd}, \text{Tb}$) were synthesised and examined in detail with the aid of single crystal and powder X-ray diffraction and HRTEM. Electric and magnetic properties were also investigated. We found the higher symmetry ($P6/m$) to be true and one crystallographic position half-occupied. The results were published in *J. Alloys Compd.*

Another hettotype of the $\text{Gd}_{14}\text{Ag}_{51}$ structure type is the crystal structure of $\text{Yb}_{11}\text{Hg}_{51}$, prepared by the distillation method (unpublished). In contrast to $\text{Eu}_{10}\text{Hg}_{55}$, $\text{Yb}_{11}\text{Hg}_{51}$ does not exhibit any mixed- or underoccupied positions, making the link between the higher symmetry aristotype and the more complex and lower symmetric crystal structure of $\text{Eu}_{10}\text{Hg}_{55}$.

Other phases synthesised by the distillation method are $\text{La}_{11+x}\text{Hg}_{45-x}$ and $\text{RE}_{11}\text{Hg}_{44.5}$ ($\text{RE} = \text{Nd}, \text{Sm}$). Both crystallise as hettotypes of the $\text{Sm}_{11}\text{Cd}_{45}$ structure type and show distinct mixed and underoccupied positions not present in the aristotype. A complete topological analysis along with quantum-chemical calculations was published in *J. Solid State Chem.*

The last part of this chapter contains unpublished results of lanthanide amalgams with general compositions REHg , REHg_2 and REHg_3 . They were synthesised by the distillation method and analysed by X-ray diffraction methods. Earlier results of structure analysis were confirmed, only SmHg_2 was found to crystallise in a second modification, unknown from previously published results.

3.3.1. The Mercury-richest Europium Amalgam $\text{Eu}_{10}\text{Hg}_{55}$

Frank Tambornino^[a] and Constantin Hoch^{*[a]}

* Dr. C. Hoch Fax: +49-89-2180-77440 E-Mail: constantin.hoch@cup.uni-muenchen.de

[a] Department of Chemistry Ludwig-Maximilians-Universität München Butenandtstr. 5-13, Haus D 81377 München, Germany

published in: *Z. Anorg. Allg. Chem.* **641**, 537–542 (2015).

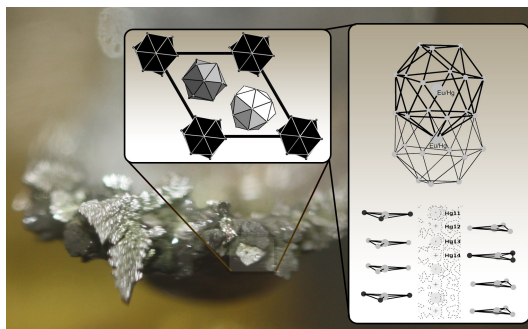
DOI:10.1002/zaac.201400561

Reprinted (adapted) with permission from *Zeitschrift für Anorganische und Allgemeine Chemie*. Copyright 2015 WILEY-VCH Verlag GmbH & Co. KGaA, Weinheim

– Dedicated to Professor Hans-Jörg Deiseroth on the Occasion of His 70th Birthday –

Abstract

The mercury-richest europium amalgam $\text{Eu}_{10}\text{Hg}_{55}$ was synthesized by isothermal electrocrystallization from a solution of $\text{EuI}_3 \cdot 8\text{DMF}$ in DMF on a reactive mercury cathode. The crystal structure shows remarkable complexity and polar metal–metal bonding. Closely related to the structures of mercury-rich amalgams $\text{A}_{11-x}\text{Hg}_{55+x}$ ($\text{A} = \text{Na}, \text{Ca}, \text{Sr}$), it shows underoccupied Hg positions along $[00z]$. $\text{Eu}_{10}\text{Hg}_{55}$ can be described as hettotype structure of the $\text{Gd}_{14}\text{Ag}_{51}$ structure type.



Introduction

Much work has been put into synthesis and crystallographic investigation of amalgams. Many structures of alkali metal amalgams have been described toward the end of the 20th century.^[1a–1c] In addition to the large number of binary amalgams, also the ternary amalgam $\text{NaK}_{29}\text{Hg}_{48}$ was synthesized and its crystal structure published.^[1d] However, information regarding the structures of mercury-rich amalgams is scarce due to peritectic decomposition temperatures as low as 12 °C and high moisture and air sensitivity. This makes their synthesis challenging and their analysis demanding.^[2a] In recent years, the amalgams $\text{Cs}_2\text{Hg}_{27}$ and $[\text{N}(\text{CH}_3)_4]\text{Hg}_8$ and the industrially important amalgam $\text{Na}_{11}\text{Hg}_{52}$ have been reported.^[2a–2c] With the help of a new preparative method we now have studied the amalgams of rare earth metals. Their crystal structures are mostly unknown. This is rather surprising considering the effort spent on the separation of the rare earth metals via electrolysis utilizing their amalgams in the 1930–50ies.^[3a–3e]

Europium amalgams with the compositions EuHg , EuHg_2 , and EuHg_3 were prepared by conventional solid state chemistry.^[4a–4d] The first mercury-rich Eu amalgams were synthesized by electrolysis with the aim of separating europium from other rare earth metals. McCoy was the first to describe the formation of an amalgam during the electrolysis of europium(III)-acetate in aqueous medium and reported on a compound with the approximate composition " Hg_{10}Eu ", which solidifies when the amalgam contains more than 1.38 wt-% Eu.^[3d] Merlo and Formasini applied the traditional solid state route and heated elemental mercury and europium in the proportion 4:1 in sealed pyrex tubes to 150–200 °C.^[3a] Their product (" $\text{EuHg}_{3.6}$ ") was analyzed by powder diffraction methods and assigned to the $\text{GdAg}_{3.6}$ structure type (later changed to $\text{Gd}_{14}\text{Ag}_{51}$ structure type).^[5a–5d] By performing the electrolysis introduced by McCoy and subsequently removing the surplus mercury by distillation Lyle and Westall yielded " $\text{EuHg}_{3.6}$ " for Mössbauer spectroscopic studies proposing Eu^{2+} as the prevailing oxidation state.^[6] No structure solution or refinement was attempted so the exact structure remained unknown. In this paper we report on the first single crystal structure determination of $\text{Eu}_{10}\text{Hg}_{55}$ and its relation to other intermetallic crystal structures.

Results and Discussion

Single Crystal Structure Description

$\text{Eu}_{10}\text{Hg}_{55}$ crystallizes in the hexagonal system in space group $P\bar{6}$ with $a = 13.595(5)$ and $c = 9.735(4)$ Å. The final R values and further information on collection and treatment of single crystal data can be found in Table 1. There are 20 crystallographic sites (4 Eu, 16 Hg), of which four Hg sites are underoccupied and one Eu site shows mixed occupancy with Hg.

In $\text{Eu}_{10}\text{Hg}_{55}$ europium is solely coordinated by Hg atoms. The coordination spheres around Eu1 and Eu2 (see Table 2 and Figure 1) (CN = 15) are tricapped hexagonal prisms with both basal and one rectangular face capped. Eu3 (see Table 2 and Figure 1) is also coordinated by 15 (or 16 considering the partial occupied Hg chain, see below)

Hg atoms. The position of (EuHg)41 (CN = 16) is of mixed occupancy with 50% Eu and 50% Hg. This position is coordinated by 15 Hg and one (EuHg)41 position in a coordination sphere best described as Frank-Kasper polyhedron with 16 vertices. The polyhedra around (EuHg)41 form interpenetrating pairs. These are stacked along [00z] sharing trigonal basal faces (see Figure 1d, e).

Table 1. Crystallographic data and details on data collection, structure solution, and refinement of $\text{Eu}_{10}\text{Hg}_{55}$ at 293 K.

Empirical sum formula	$\text{Eu}_{10+x}\text{Hg}_{55-x}$
Crystal system	hexagonal
Space group	$P\bar{6}$ (No. 174)
Lattice parameters ($T = 293$ K)	
$a / \text{\AA}$	13.595(5)
$c / \text{\AA}$	9.735(4)
$V / \text{\AA}^3$	15589.2(1)
Formula units Z	1
Calculated density ($\text{g}\cdot\text{cm}^{-3}$)	13.37
$F(000)$	5028
Absorption coefficient (mm^{-1})	79
Radiation, wavelength (\AA)	Ag-K α , 0.56086
Diffractometer	IPDS 1 ((Stoe & Cie, Darmstadt, Germany)
Data collection mode	φ -Scans, $0^\circ \leq \varphi \leq 200.4^\circ$, $\Delta\varphi = 1.2^\circ$
Corrections	Lorentz, polarisation, absorption (semiempirical)
Transmission factors T_{\min}/T_{\max}	0.003/0.063
Number of free parameters	118
Number of collected data	16654
Number of unique data	1469
Number of unique data with $I \geq 2\sigma(I)$	1033
$R_{\text{int}}/R(\sigma)$	0.1989/0.0878
Data range	$-18 \leq h, \leq 18$ $-18 \leq k, \leq 18$ $-12 \leq l, \leq 13$
Structure solution	direct methods ^[9]
Structure refinement	full matrix least-squares on F^2
Extinction coefficient	0.000028(12)
Final R values [$I \geq 2\sigma(I)$]	$R1 = 0.0461$ $wR2 = 0.0789$
Final R values (all data)	$R1 = 0.0770$ $wR2 = 0.0861$
Goodness of Fit	0.897
Residual electron density min./max ($\text{e}^- \cdot \text{\AA}^{-3}$)	-4.53 / 3.50
ICSD deposition number	428668

The mercury atoms are coordinated by both Eu and Hg. The resulting polyhedra can be grouped according to their shapes: First, a group of distorted icosahedra are around Hg4, Hg5, Hg6, Hg7 Hg8, Hg9, and Hg10 (Table 2, Figure 3). The second group of polyhedra around Hg1, Hg2, Hg11, Hg12, Hg13, Hg14, Hg15, and Hg16 are based on pentacapped trigonal prisms. Finally, Hg3 is coordinated irregularly with CN = 13. The coordination spheres are shown in Figure 3. According to their site symmetry the least regular polyhedra are formed around Hg1 to Hg6 (site symmetry 1), more regular polyhedra around Hg7–9 (site symmetry m..) and around Hg12, Hg13, Hg15

Table 2. Standardised fractional atomic coordinates and equivalent isotropic displacement parameters / \AA^2 for $\text{Eu}_{10}\text{Hg}_{55}$. U_{eq} is defined as $\frac{1}{3}$ of the trace of the orthogonalized U_{ij} tensor. Standard deviations in units of the last digit are given in parentheses.

Atom	Wyckoff site	x	y	z	Occ.	U_{eq}
Hg(1)	6l	0.05964(17)	0.22829(19)	0.3443(3)	1	0.0291(5)
Hg(2)	6l	0.28878(18)	0.43051(17)	0.3383(3)	1	0.0331(6)
Hg(3)	6l	0.13340(19)	0.4897(2)	0.1677(3)	1	0.0342(5)
Hg(4)	6l	0.2199(2)	0.1957(3)	0.1630(3)	1	0.0403(7)
Hg(5)	6l	0.4752(2)	0.38730(19)	0.2935(3)	1	0.0367(6)
Hg(6)	6l	0.39263(15)	0.11550(17)	0.2599(3)	1	0.0304(4)
Hg(7)	3k	0.5342(3)	0.2176(3)	1/2	1	0.0404(8)
Hg(8)	3j	0.3083(3)	0.4257(3)	0	1	0.0380(8)
Hg(9)	3j	0.5010(3)	0.0776(3)	0	1	0.0347(8)
Hg(10)	3j	0.4312(3)	0.2566(3)	0	1	0.0379(8)
Hg(11)	1a	0	0	0	0.492(10)	0.049(4)
Hg(12)	2g	0	0	0.1629(10)	0.508(10)	0.029(2)
Hg(13)	2g	0	0	0.3424(12)	0.492(10)	0.033(2)
Hg(14)	1b	0	0	1/2	0.508(10)	0.026(3)
Hg(15)	2h	1/3	2/3	0.3461(5)	1	0.0253(9)
Hg(16)	1c	1/3	2/3	0	1	0.046(2)
Eu(1)	3k	0.2694(3)	0.1985(3)	1/2	1	0.0205(8)
Eu(2)	3k	0.0767(3)	0.4623(3)	1/2	1	0.0193(8)
Eu(3)	3j	0.0307(3)	0.2424(4)	0	1	0.0236(9)
Eu(41)	2i	2/3	1/3	0.1817(4)	0.48(1) Eu	0.024(1)
Hg(42)	2i	2/3	1/3	0.1817(4)	0.52(1) Hg	0.024(1)

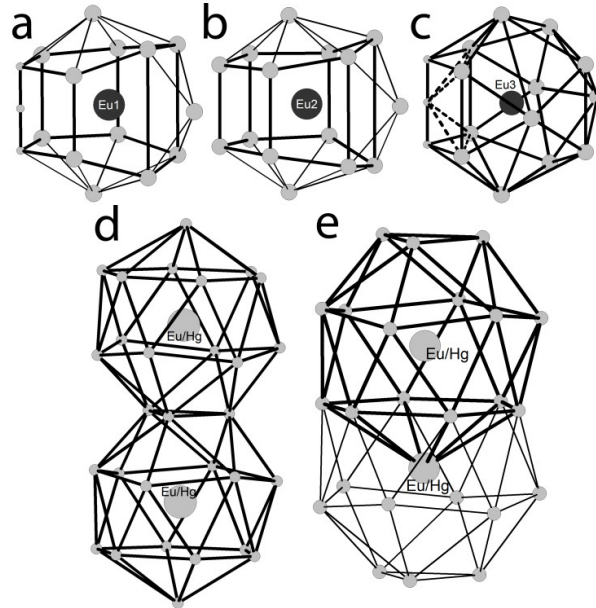


Figure 1. Polyhedra around Eu1 (a), Eu2 (b), and Eu3 (c) are shown. Additionally, two different representations of the interpenetrating pairs of the polyhedra around (EuHg)41 are shown (d, e). Color code: black: Eu; grey: Hg; small grey: underoccupied Hg, large dark grey: (EuHg)41. For details see text.

Table 3. Coefficients $U_{ij} / \text{\AA}^2$ of the anisotropic atomic displacement parameters for $\text{Eu}_{10}\text{Hg}_{55}$. U_{ij} is defined as $\exp\{-2\pi^2[U_{11}(ha^*)^2 + \dots + 2U_{12}hka^*b^*]\}$. Standard deviations in units of the last digit are given in parentheses.

Atom	U_{11}	U_{22}	U_{33}	U_{12}	U_{13}	U_{23}
Hg(1)	0.023(1)	0.037(1)	0.029(1)	-0.002(1)	-0.0005(9)	0.0171(9)
Hg(2)	0.028(1)	0.0212(9)	0.049(2)	-0.001(1)	-0.002(1)	0.0120(8)
Hg(3)	0.032(1)	0.038(1)	0.026(2)	-0.002(1)	-0.0038(9)	0.0121(9)
Hg(4)	0.044(2)	0.064(2)	0.028(2)	-0.004(2)	-0.002(1)	0.038(1)
Hg(5)	0.031(1)	0.027(1)	0.046(2)	-0.006(1)	0.011(1)	0.009(1)
Hg(6)	0.0264(9)	0.031(1)	0.032(1)	0.0033(9)	0.004(1)	0.0127(8)
Hg(7)	0.028(1)	0.031(2)	0.045(2)	0	0	0.002(1)
Hg(8)	0.031(2)	0.035(2)	0.044(3)	0	0	0.013(1)
Hg(9)	0.028(1)	0.037(2)	0.038(2)	0	0	0.014(1)
Hg(10)	0.031(2)	0.030(1)	0.044(2)	0	0	0.008(1)
Hg(11)	0.040(4)	U_{11}	0.07(1)	0	0	0.020(2)
Hg(12)	0.026(2)	U_{11}	0.036(5)	0	0	0.013(1)
Hg(13)	0.023(2)	U_{11}	0.055(7)	0	0	0.011(1)
Hg(14)	0.015(3)	U_{11}	0.050(8)	0	0	0.007(1)
Hg(15)	0.0226(9)	U_{11}	0.031(3)	0	0	0.0113(5)
Hg(16)	0.047(2)	U_{11}	0.043(5)	0	0	0.024(1)
Eu(1)	0.024(2)	0.020(2)	0.022(2)	0	0	0.015(2)
Eu(2)	0.017(2)	0.019(2)	0.020(2)	0	0	0.008(1)
Eu(3)	0.025(2)	0.027(2)	0.025(3)	0	0	0.018(2)
Eu(41)	0.021(1)	U_{11}	0.030(3)	0	0	0.0106(7)
Hg(42)	0.021(1)	U_{11}	0.030(3)	0	0	0.0106(7)

(site symmetry 3..). Ideal trigonal prisms form around Hg11, Hg15 and Hg16 according to their site symmetry 6.. .

A special feature of this structure is the partial occupied Hg chain along $[0,0,z]$. The electron density map (see Figure 2) shows discrete maxima with too close distances (1.53(1) to 1.74(2) Å) for a full occupancy.

Free refinement of the respective occupation factors results in underoccupation. Thus, two sets of mutually exclusive chains shifted toward one another by $z = 1/6$ form. One chain is constituted from Hg atoms at $z = 0, 0.3424(12), 0.6576(12)$ the second from Hg atoms at $z = 0.1629(10), \frac{1}{2}, 0.8371(10)$. The interatomic distances within one set of Hg atoms are in the range of 3.28(12)–3.33(19) Å and are well in agreement with normal Hg–Hg distances found in many amalgam structures. The relative proportions of the two sets of Hg chains can vary from crystal to crystal as we have found occupancies of 50:50 to 75:25, always resulting in an overall full occupation (see Table 2).

The total structure can be rationalised as hexagonal rod packing (Figure 4). The respective polyhedra around (EuHg)41, Hg15, and Hg16 together with the polyhedra around Hg11–14 form columns extending along $[001]$ by sharing common faces. Thus three subsets of hexagonal rod packings form, combining into one comprehensive set.

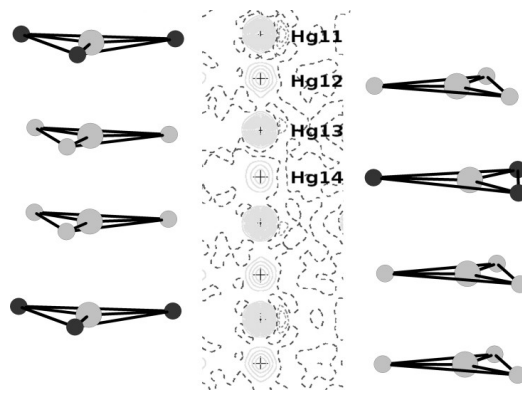


Figure 2. Display of the electron density F_{obs} (middle) and the two possible occupancy modes (right and left). Only one set, i.e. left or right, is allowed to assure reasonable interatomic distances between Hg atoms.

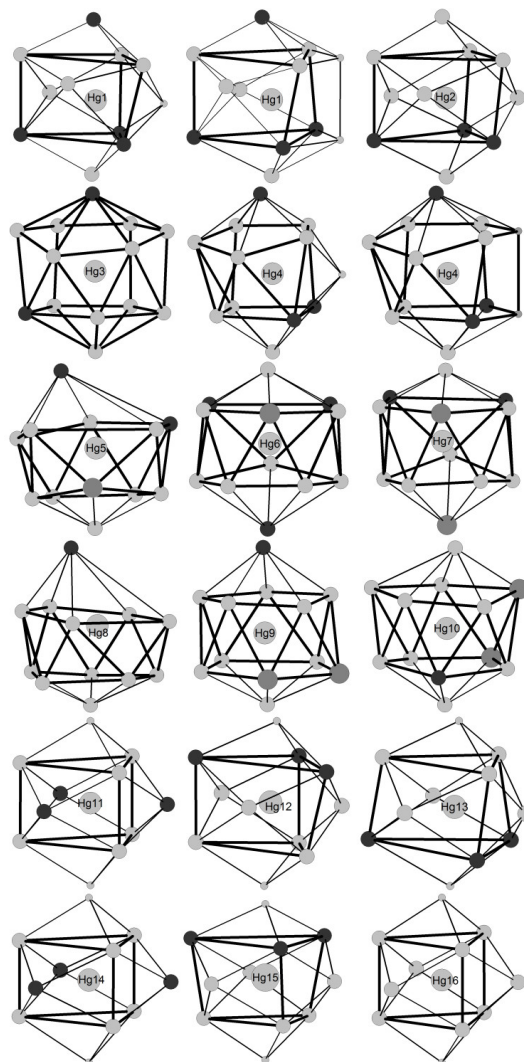


Figure 3. Polyhedra around all Hg atoms are shown. Polyhedra around Hg1, Hg2, and Hg11–16 are distorted pentacapped prisms, polyhedra around Hg3 and Hg5–10 are distorted icosahedra. The polyhedron around Hg4 is irregularly. Color code: black: Eu; grey: Hg; small grey: underoccupied Hg, large dark grey: (EuHg)41. For details see text.

Table 4. Results of the Rietveld refinement of $\text{Eu}_{10}\text{Hg}_{55}$

Empirical sum formula	$\text{Eu}_{10+x}\text{Hg}_{55-x}$ ($x = 0.1$)
Crystal system	hexagonal
Space group	$P\bar{6}$ (No. 174)
Lattice parameters ($T = 273$ K)	
a / Å	13.593(1)
c / Å	9.747(1)
V / Å ³	1559.7(2)
Density (X-ray) / $\text{g} \cdot \text{cm}^{-3}$	13.39(12)
Radiation, wavelength / Å	Mo-K α , 0.70930
Formula units Z	1
Monochromator	curved Ge single crystal
No. of parameters	90
R_p	0.01525
R_{wp}	0.01931
χ^2	1.046

Comparison to Related Structures

Several amalgams were initially described by the sum formula “ $\text{XHg}_{3.6}$ ” ($X = \text{Ca}, \text{Sr}, \text{Eu}, \text{Yb}$, “ $\text{GdAg}_{3.6}$ ” structure type).^[7a–7c] This assignment was later changed to the $\text{Gd}_{14}\text{Ag}_{51}$ structure type with space group symmetry $P6/m$. The $\text{Gd}_{14}\text{Ag}_{51}$ structure type has recently been reinvestigated.^[5d] Applying modern X-ray methods Tkachuk and Mar could show that some of the phases – namely $A_{11-x}\text{Hg}_{54+x}$ ($A = \text{Ca}, \text{Sr}; x = 0.08–0.5$) – crystallize closely related to the $\text{Gd}_{14}\text{Ag}_{51}$ type, but in space group $P\bar{6}$.^[8] This symmetry reduction leads to the ordering of a half occupied Ag hexagon into fully occupied Hg triangles (this holds for all amalgams in space group $P\bar{6}$, so far). Nevertheless, the amalgam structures show higher complexity introduced by different kinds of mixed and underoccupation phenomena. Furthermore, the $\text{Eu}_{10}\text{Hg}_{55}$ structure is closely related to the structure of $\text{Na}_{11}\text{Hg}_{52}$.^[2c] The latter exhibits a $3 \times 3 \times 1$ superstructure of the $\text{Eu}_{10}\text{Hg}_{55}$ unit cell (lattice parameters $a = 39.703(2)$ $c = 9.6180(5)$ Å). This leads to a ninefold larger unit cell, to 132 crystallographically independent positions and thus to a very complicated crystal structure. A comparison of all mentioned amalgam structures and the aristotype by means of complexity measures has been performed and discussed elsewhere.^[5d]

Conclusions

Phase pure samples of the mercury-richest europium amalgam $\text{Eu}_{10}\text{Hg}_{55}$ were synthesized by preparative isothermal electrocrystallization. Its crystal structure was investigated by modern crystallographic methods including single crystal and powder diffraction. The compound crystallizes in space group $P\bar{6}$ and exhibits close relation to other mercury-rich amalgams such as $A_{11-x}\text{Hg}_{54+x}$ ($A = \text{Ca}, \text{Sr}; x = 0.08\text{--}0.5$) and $\text{Na}_{11}\text{Hg}_{52}$. The former assignment of $\text{Eu}_{10}\text{Hg}_{55}$ to the $\text{Gd}_{14}\text{Ag}_{51}$ structure type is wrong. However, $\text{Gd}_{14}\text{Ag}_{51}$ represents the aristotype to all aforementioned amalgams. Other mercury-rich rare earth amalgams have been reported to crystallize similarly (“ $\text{YbHg}_{3.6}$ ”) or in a closely related cubic structure type ($A_{11}\text{Hg}_{45}$, $A = \text{La}, \text{Ce}, \text{Pr}, \text{Nd}, \text{Sm}, \text{Gd}$). Those are the topic of ongoing investigations.

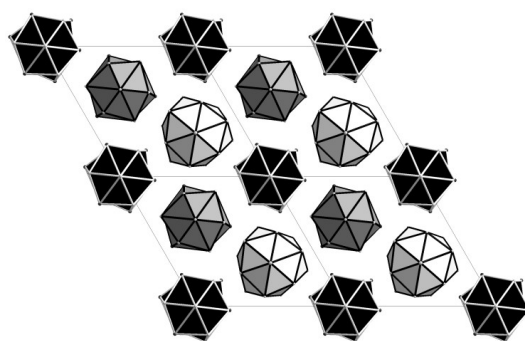


Figure 4. The hexagonal rod packing is shown with viewing direction along $[001]$. Black polyhedra form around Hg11–14, dark grey polyhedra around Hg15 and Hg16 and light grey polyhedra around (EuHg)41.

Experimental Section

Materials: The following reagents were used: N,N' -dimethyl formamide (DMF, Acros Organics, 99.5% for analysis, dried with molecular sieve 3 Å), Europium(III)oxide (Sigma Aldrich, 99.9% trace metal basis), hydrochloric acid (Sigma Aldrich, 37% in water), potassium iodide (Merck, 99.5% trace metal basis).

Preparation: $\text{EuI}_3 \cdot 8\text{DMF}$ was prepared as follows. Fuming HCl (20 mL) was boiled under reflux. Eu_2O_3 was added in portions (0.1 g) until a cloudy suspension did no longer dissolve within 30 min (total amount 10 g, 28.4 mmol). Subsequently, excess Eu_2O_3 was dissolved by dropwise addition of fuming HCl. After cooling to room temperature, water was removed under reduced pressure yielding a colorless crystalline product ($\text{EuCl}_3 \cdot 6\text{H}_2\text{O}$). $\text{EuCl}_3 \cdot 6\text{H}_2\text{O}$ was dissolved in DMF (150 mL) and a solution of potassium iodide (28.3 g, 170.15 mmol) in dry DMF (35 mL) was added. Immediately, a colorless precipitate formed. The precipitate was filtered off, washed with DMF and identified as phase-pure KCl by powder diffractometry. To the remaining solution toluene (50 mL) was added and an azeotropic distillation on a water separator under reflux conditions was carried out (180 °C oil bath temperature, 3 h). The pale yellow solution was allowed to cool to room temperature. Excess DMF was removed under reduced pressure

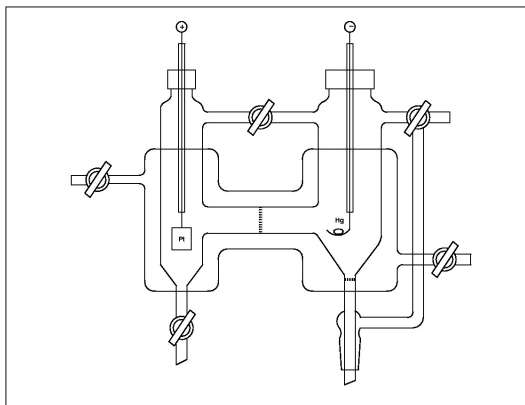


Figure 5. Detailed drawing of the electrolysis chamber used in the synthesis.

until pale yellow crystals formed. The product was collected under Schlenk conditions and identified as phase-pure $\text{EuI}_3 \cdot 8\text{DMF}$ by single crystal and powder diffraction (yield 53.3 g, 47.6 mmol, 84%).

The title compound was synthesized by preparative isothermal electrolysis under anhydrous conditions. For this purpose a saturated solution of $\text{EuI}_3 \cdot 8\text{DMF}$ in dry N,N' -dimethyl formamide (100 mL) was prepared and subsequently degassed in vacuum to remove traces of water and oxygen. The solution was transferred into the electrolysis chamber (see Figure 5). The chamber consisted of anode and cathode compartments separated by a porous glass frit. With the aid of a mantle surrounding the electrolysis chamber, the reaction could be performed at a constant temperature in the range from -30 to $+90$ °C. The electrolysis chamber was connected to a Schlenk line. The cathode chamber was equipped with a small glass frit to separate and wash the product from the electrolyte. The anode consisted of a platinum foil (1 cm^2) and the cathode of an amalgamated copper spoon with a single drop of mercury suspended in it. The solution was electrolyzed for 72 h at room temperature with a terminal voltage of 5 V. The product formed at the cathode was washed with dry DMF, dried in vacuo and subsequently handled in an argon-filled glovebox. $\text{Eu}_{10}\text{Hg}_{55}$ forms hard and brittle crystals of metallic luster which are highly sensitive toward air and moisture.

Single Crystal and Powder Diffraction Analysis: A suitable single crystal was selected under dry paraffin oil and sealed in a capillary ($d = 0.2 \text{ mm}$) filled with dry oil. The crystal was mounted on a Stoe IPDS1 diffraction system equipped with an image plate detector, graphite monochromator and Ag-K_α radiation. A second crystal was centred on a Bruker D8 Quest diffractometer equipped with a CMOS detector, microfocus X-ray tube (Mo-K_α radiation), Goebel mirror optics and cooling system. Data collection was performed at 100 K. Details on the measurement at 100 K can be found in the Supporting Information.

The data showed a primitive hexagonal metric with no systematic absences. Structure solution with SHELXS-97 in $P\bar{6}$ yielded most of the heavy atom positions.^[9] Subsequent structure refinement with SHELXL-97 yielded underoccupied positions and revealed mixed occupied sites. Heavy atom assignment was carried out by analysis of the atomic displacement parameters and interatomic distances. Checks for additional symmetry were performed with the PLATON package and revealed the final space group $P\bar{6}$.^[10a,10b] Fractional atomic coordinates in standardized setting and equivalent isotropic displacement parameters are compiled in Table 2, coefficients of the anisotropic displacement parameters can be found in Table 3. The residual electron densities were always in close proximity to heavy atom positions and thus were treated as termination effects.

Further details of the crystal structure investigations may be obtained from the Fachinformationszentrum Karlsruhe, 76344 Eggenstein-Leopoldshafen, Germany (Fax: +49-7247-808-666; E-Mail: crysdata@fiz-karlsruhe.de, http://www.fiz-karlsruhe.de/request_for_deposited_data.html) on quoting the depository number CSD-428668.

X-ray Powder Diagrams were recorded with a transmission powder diffractometer (Stoe STADI-P, Stoe, Darmstadt, Mo- $K_{\alpha 1}$ radiation, germanium monochromator) in Debye-Scherrer geometry and show the absence of further crystalline phases. Representative portions of the products were ground and sealed in capillaries with inner diameter of 0.1 mm. Rietveld refinement was performed with a fundamental parameter approach and a double Voigt approach to compensate size-strain effects (Figure 6, Table 4). A shifted Chebychev function with 20 parameters was applied for background modeling. Careful absorption correction was performed by taking the linear absorption coefficient, the capillary diameter and the packing density into account. Within small error margins, the refined structure model confirms the model from single crystal structure determination which was taken as starting values.

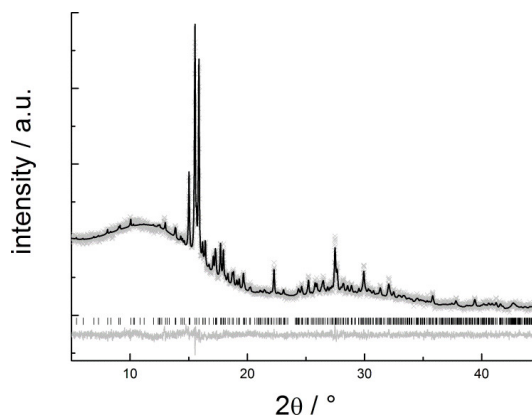


Figure 6. Rietveld refinement of $\text{Eu}_{10}\text{Hg}_{55}$. Light grey crosses display measured data, black line the refined model. Black bars indicate Bragg positions and the grey line displays the difference plot. Further data is compiled in Table 4.

Supporting Information (see footnote on the first page of this article): Crystallographic data and details on data collection, structure solution and refinement of $\text{Eu}_{10}\text{Hg}_{55}$ at 100 K, Standardised fractional atomic coordinates and equivalent isotropic displacement parameter \AA^2 for $\text{Eu}_{10}\text{Hg}_{55}$, coefficients U_{ij}/pm^2 of the anisotropic atomic displacement parameters for $\text{Eu}_{10}\text{Hg}_{55}$.

References

- [1] a) H. Deiseroth, A. Strunck, *Angew. Chem.* **1989**, *101*, 1286–1287; *Angew. Chem. Int. Ed. Engl.* **1989**, *28*, 1251–1252; b) H. Deiseroth, *Chem. Unserer Zeit* **1991**, *25*, 83–86; c) H. Deiseroth, *Prog. Solid State Chem.* **1997**, *1*, 73–123; d) H. Deiseroth, E. Biehl, *J. Solid State Chem.* **1999**, *142*, 177–184.
- [2] a) C. Hoch, A. Simon, *Z. Anorg. Allg. Chem.* **2008**, *5*, 853–856; b) C. Hoch, A. Simon, *Z. Anorg. Allg. Chem.* **2006**, *14*, 228–229; c) C. Hoch, A. Simon, *Angew. Chem.* **2012**, *124*, 3316–3319; C. Hoch, A. Simon, *Angew. Chem. Int. Ed.* **2012**, *51*, 3262–3265.
- [3] a) L. Yntema, *J. Am. Chem. Soc.* **1930**, *52*, 2782–2784; b) J. Marsh, *J. Chem. Soc.* **1942**, 523–526; c) J. Marsh, *J. Chem. Soc.* **1943**, 531–535; d) H. McCoy, H. Morris, P. Selwood, in: *Inorganic Syntheses* (Ed.: W. Fernelius) Wiley-VCH, Weinheim, **1946**, vol 2, pp. 65–69; e) E. Onstott, *J. Am. Chem. Soc.* **1959**, *81*, 4451–4458.
- [4] a) A. Iandelli, A. Palenzona, *J. Less-Common Met.* **1965**, *1*, 1–6; b) A. Iandelli, A. Palenzona, *J. Less-Common Met.* **1968**, *3*, 273–284; c) A. Iandelli, A. Palenzona, *Atti Accad. Naz. Lincei Rend. Cl. Sci. Fis. Mater. Nat.* **1964**, *37*, 165–168; d) F. Merlo, M. Fornasini, *J. Less-Common Met.* **1979**, *2*, 221–231.

- [5] a) S. Steeb, D. Godel, C. Löhr, *J. Less-Common Met.* **1968**, 2, 137–141; b) O. McMasters, K. Gschneidner Jnr, R. Venteicher, *Acta Crystallogr., Sect. B* **1970**, 9, 1224–1229; c) D. Bailey, G. Kline, *Acta Crystallogr., Sect. B* **1971**, 3, 650–653; d) F. Tambornino, J. Sappl, C. Hoch, *J. Less-Common Met.* **2015**, 618, 326–335.
- [6] S. Lyle, W. Westall, *J. Less-Common Met.* **1984**, 2, 265–272.
- [7] a) G. Bruzzone, F. Merlo, *J. Less-Common Met.* **1973**, 2, 237–241; b) G. Bruzzone, F. Merlo, *J. Less-Common Met.* **1974**, 2, 153–157; c) F. Merlo, M. Fornasini, *J. Less-Common Met.* **1979**, 221–231.
- [8] A. Tkachuk, A. Mar, *Inorg. Chem.* **2008**, 47, 1313–1318.
- [9] G. M. Sheldrick, *Acta Crystallogr., Sect. A* **2008**, 64, 112–122.
- [10] a) A. L. Spek, *Acta Crystallogr., Sect. D* **2009**, 65, 148–155; b) Y. Le Page, *J. Appl. Crystallogr.* **1987**, 20, 264–269.

Supplementary material

Table 1. Crystallographic data and details on data collection, structure solution, and refinement of $\text{Eu}_{10}\text{Hg}_{55}$ at 100K.

Empirical sum formula	$\text{Eu}_{10+x}\text{Hg}_{55-x}$ ($x = 0.1$)
Crystal system	hexagonal
Space group	$P\bar{6}$ (No. 174)
Lattice parameters ($T = 100\text{K}$, \AA , \AA^3)	$a = 13.595(5)$ $c = 9.735(4)$ $V = 15589.2(1)$
Formula units Z	1
Calculated density ($\text{g}\cdot\text{cm}^{-3}$)	13.603
$F(000)$	5028
Absorption coefficient (mm^{-1})	147.082
Diffractometer	D8Quest (Bruker)
Data collection mode	ω -scans and ϕ -scans
Corrections	Lorentz, polarisation, absorption (semiempirical)
Transmission factors T_{\min}/T_{\max}	0.0267/0.0743
Number of free parameters	119
Number of collected data	46076
Number of unique data	2148
Number of unique data with $I \geq 2\sigma(I)$	2002
$R_{\text{int}}/R(\sigma)$	0.336/0.0852
Data range	$-20 \leq h, \leq 20$ $-21 \leq k, \leq 20$ $-14 \leq l, \leq 14$
Structure solution	direct methods
Structure refinement	full matrix least-squares on F^2
Extinction coefficient	0.000035(6)
Final R values [$I \geq 2\sigma(I)$]	$R1 = 0.0655$ $wR2 = 0.1464$
Final R values (all data)	$R1 = 0.0734$ $wR2 = 0.1492$
Goodness of Fit	1.740
Residual electron density min./max ($\text{e}^- \cdot \text{\AA}^{-3}$)	$-3.725 / 4.297$
ISCD deposition number	428668

Table 2. Standardised fractional atomic coordinates and equivalent isotropic displacement parameters / \AA^2 for $\text{Eu}_{10}\text{Hg}_{55}$. U_{eq} is defined as $\frac{1}{3}$ of the trace of the orthogonalized U_{ij} tensor. Standard deviations in units of the last digit are given in parentheses.

Atom	x	y	z	Occ.	U_{eq}
Hg(1)	0.05919(13)	0.22283(15)	0.34527(16)	1	0.0159(3)
Hg(2)	0.28863(13)	0.43009(13)	0.33903(16)	1	0.0163(3)
Hg(3)	0.13431(13)	0.48958(14)	0.16909(14)	1	0.0154(3)
Hg(4)	0.22620(15)	0.20274(16)	0.16255(15)	1	0.0191(4)
Hg(5)	0.47688(14)	0.38864(14)	0.29199(19)	1	0.0196(3)
Hg(6)	0.39078(12)	0.11413(12)	0.25932(17)	1	0.0140(3)
Hg(7)	0.53532(18)	0.21516(18)	$\frac{1}{2}$	1	0.0186(4)
Hg(8)	0.30919(18)	0.42891(18)	0	1	0.0170(4)
Hg(9)	0.49999(18)	0.07518(18)	0	1	0.0158(4)
Hg(10)	0.43480(19)	0.25725(19)	0	1	0.0190(4)
Hg(11)	0	0	0	0.234(12)	0.043(7)
Hg(12)	0	0	0.1632(4)	0.766(12)	0.0162(10)
Hg(13)	0	0	0.3415(14)	0.234(12)	0.022(4)
Hg(14)	0	0	$\frac{1}{2}$	0.766(12)	0.0140(11)
Hg(15)	$\frac{1}{3}$	$\frac{2}{3}$	0.3465(3)	1	0.0132(5)
Hg(16)	$\frac{1}{3}$	$\frac{2}{3}$	0	1	0.046(2)
Eu(1)	0.2742(2)	0.2002(2)	$\frac{1}{2}$	1	0.0132(5)
Eu(2)	0.0764(2)	0.4607(2)	$\frac{1}{2}$	1	0.0113(5)
Eu(3)	0.0286(2)	0.2388(2)	0	1	0.0189(8)
Eu(41)	$\frac{2}{3}$	$\frac{1}{3}$	0.1818(3)	0.31 Eu	0.0146(8)
Hg(41)	$\frac{2}{3}$	$\frac{1}{3}$	0.1817(4)	0.69 Hg	0.0146(8)

Table 3. Coefficients U_{ij} / \AA^2 of the anisotropic atomic displacement parameters for $\text{Eu}_{10}\text{Hg}_{55}$. U_{ij} is defined as $\exp\{-2\pi^2[U_{11}(ha^*)^2 + \dots + 2U_{12}hka^*b^*]\}$. Standard deviations in units of the last digit are given in parentheses.

Atom	U_{11}	U_{22}	U_{33}	U_{12}	U_{13}	U_{23}
Hg(1)	0.0104(7)	0.0186(8)	0.0199(7)	-0.0007(5)	-0.0001(5)	0.0081(6)
Hg(2)	0.0120(7)	0.0093(7)	0.0276(8)	-0.0010(5)	-0.0007(5)	0.0053(6)
Hg(3)	0.0126(7)	0.0144(7)	0.0166(6)	-0.0007(5)	-0.0017(5)	0.0048(6)
Hg(4)	0.0200(8)	0.0257(9)	0.0202(8)	-0.0004(6)	0.0001(5)	0.0177(7)
Hg(5)	0.0139(7)	0.0113(7)	0.0280(8)	-0.0036(6)	0.0046(6)	0.0020(6)
Hg(6)	0.0099(6)	0.0130(7)	0.0198(7)	0.0000(5)	0.0002(5)	0.0061(5)
Hg(7)	0.0100(9)	0.0111(9)	0.0268(11)	0	0	-0.0006(7)
Hg(8)	0.0097(9)	0.0108(9)	0.0281(11)	0	0	0.0034(8)
Hg(9)	0.0101(9)	0.0112(9)	0.0259(10)	0	0	0.0050(8)
Hg(10)	0.0131(9)	0.0098(9)	0.0291(11)	0	0	0.0021(8)
Hg(11)	0.037(9)	U_{11}	0.054(16)	0	0	0.019(4)
Hg(12)	0.0113(12)	U_{11}	0.026(2)	0	0	0.0056(6)
Hg(13)	0.013(4)	U_{11}	0.042(9)	0	0	0.006(2)
Hg(14)	0.0072(13)	U_{11}	0.028(3)	0	0	0.0036(7)
Hg(15)	0.0080(7)	U_{11}	0.0237(14)	0	0	0.0040(3)
Hg(16)	0.0161(11)	U_{11}	0.025(2)	0	0	0.0080(5)
Eu(1)	0.0100(11)	0.0084(11)	0.0222(13)	0	0	0.0053(10)
Eu(2)	0.0057(11)	0.0067(11)	0.0207(13)	0	0	0.0025(9)
Eu(3)	0.0093(11)	0.0151(12)	0.0188(13)	0	0	0.0095(10)
Eu(41)	0.0115(9)	U_{11}	0.0207(14)	0	0	0.0057(5)
Hg(41)	0.0115(9)	U_{11}	0.0207(14)	0	0	0.0057(5)

3.3.2. The $\text{Gd}_{14}\text{Ag}_{51}$ Structure Type and its Relation to Some Complex Amalgam Structures

Frank Tambornino, Jonathan Sappl, Dr. Constantin Hoch*

* *Corresponding author. Tel.: +49 (0)89 2180 77421; fax: +49 (0)89 2180 77440. E-mail address: constantin.hoch@cup.uni-muenchen.de (C. Hoch).*

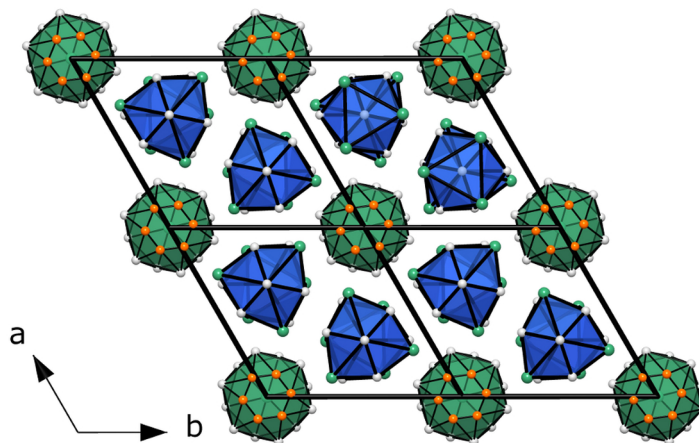
published in: *J. Alloys Compd.* **618**, 326–335 (2015).

DOI:10.1016/j.jallcom.2014.08.017

Reprinted (adapted) with permission from Journal of Alloys and Compounds. Copyright 2014 Elsevier B.V.

Abstract

A plethora of binary and ternary intermetallic compounds has been assigned to the $\text{Gd}_{14}\text{Ag}_{51}$ structure type, crystallising in the hexagonal system (space group $P6/m$, $a = 1264.30(18)$ pm, $c = 933.58(11)$ pm for $\text{Gd}_{14}\text{Ag}_{51}$). Starting in the late 1960s, much work has been invested in the structural elucidation of these crystal structures. However, reliable single crystal data are scarce, and most structure type assignments have been performed merely on the basis of powder data. We have redetermined four representatives of the binary $\text{RE}_{14}\text{Ag}_{51}$ structure type ($\text{RE} = \text{Y}, \text{Ce}, \text{Gd}, \text{Tb}$) with modern high-precision single crystal X-ray methods. The assignment of the $\text{Gd}_{14}\text{Ag}_{51}$ structure type to space group $P6/m$ was additionally verified by careful analysis of high resolution transmission electron micrographs. We emphasise the close relation of the $\text{Gd}_{14}\text{Ag}_{51}$ structure type to the structures of some recently described amalgams of similar composition focussing on disorder phenomena and structural complexity. Furthermore, we provide detailed information on synthesis as well as electrical and magnetic properties for $\text{Gd}_{14}\text{Ag}_{51}$, the parent compound of this structure family.



Introduction

Recently, the $\text{Gd}_{14}\text{Ag}_{51}$ structure type attracted new attention as several amalgams of the alkali and alkaline-earth metals were described in very closely related crystal structures. [1–3] As a consequence of the observation of disorder phenomena, the $\text{Gd}_{14}\text{Ag}_{51}$ structure type could be regarded either as archetype structure for these amalgams or as a possibly overlooked twinning problem. In this context, we found it worthwhile to revisit exemplary representatives of this large family of intermetallic compounds with modern crystallographic methods.

$\text{Gd}_{14}\text{Ag}_{51}$, the parent compound, was first described with the composition "GdAg₃" by Steeb and coworkers in 1968 [4]. On the basis of powder diffraction data it was assigned to the "Ag₃Pu" type. Both "GdAg₃" and "Ag₃Pu" later were reassigned to the $\text{Gd}_{14}\text{Ag}_{51}$ type [5]. Bailey and Kline performed the first single crystal structure refinement in 1970 and gave the actual composition as "GdAg_{3.6}", much closer to 51:14 (= 3.643) [6]. Later in the same year, $\text{RE}_{14}\text{Ag}_{51}$ with $\text{RE} = \text{Y}, \text{Nd}, \text{Sm}, \text{Gd}, \text{Tb}, \text{Dy}, \text{Ho}, \text{Er}$ were assigned to the $\text{Gd}_{14}\text{Ag}_{51}$ structure type on the basis of powder diffraction patterns [7]. Numerous phases followed: $\text{Th}_{14}\text{Ag}_{51}$ [8], several copper and gold compounds ($\text{M}_{14}\text{Cu}_{51}$ with $\text{M} = \text{Zr}, \text{Hf}, \text{Ce}$ [9,10], $\text{RE}_{14}\text{Au}_{51}$ with $\text{RE} = \text{Pr}, \text{Nd}, \text{Gd}, \text{U}$) [11–16], and also some amalgams $\text{RE}_{14}\text{Hg}_{51}$ with $\text{RE} = \text{Ca}, \text{Sr}, \text{Eu}, \text{Yb}$ [17–19], again on the basis of powder diffraction patterns. Ordered ternary variants include $\text{Gd}_{14}\text{Cu}_{48}\text{Ga}_3$, $\text{Tb}_{14}\text{Cu}_{48}\text{Ga}_3$ and $\text{Ca}_{14}\text{Au}_{46}\text{Sn}_5$ [20,21].

In 2008 the mercury-rich Ca and Sr amalgams were reinvestigated by Mar and coworkers with modern X-ray single crystal methods [1]. They reported the respective crystal structures in space group $P\bar{6}$ rather than $P6/m$ and described occurring disorder effects in detail. Mar et al. already marked out the close relation of the amalgam structures to the $\text{Gd}_{14}\text{Ag}_{51}$ structure type and possible problems with its space group assignment. Recently, we reinvestigated the mercury-richest Europium amalgam $\text{Eu}_{10}\text{Hg}_{55}$ and refined its structure from single crystal data. It crystallizes in space group $P\bar{6}$ in close relation both to the $\text{Gd}_{14}\text{Ag}_{51}$ and the $(\text{Ca}/\text{Sr})_{14}\text{Hg}_{51}$ crystal structures, however, differing in the respective disorder phenomena [3].

The structure of $\text{Na}_{11}\text{Hg}_{52}$ [2] shows a $(3 \times 3 \times 1)$ superstructure of the alkaline-earth metal amalgams, again in space group $P\bar{6}$ and with yet different disorder phenomena.

Thus, all named amalgams have similar structures differing among themselves in their respective disorder patterns and from the $\text{Gd}_{14}\text{Ag}_{51}$ structure type by the lower symmetric space group type. The reported $\text{Gd}_{14}\text{Ag}_{51}$ structure in space group $P6/m$ shows Ag atoms arranged in a hexagon around the sixfold axis with very short Ag–Ag distances and an occupation factor of $\frac{1}{2}$. This situation is never observed in the named amalgams. At equivalent Hg positions, ordered and fully occupied triangles occur, as they are described in space group $P\bar{6}$, where no sixfold point symmetry is present. As $P\bar{6}$ is a direct subgroup of $P6/m$, we reinvestigated the crystal structures of some $\text{Gd}_{14}\text{Ag}_{51}$ -type compounds in order to decide whether there was a crystallographic reason for finding higher symmetry in the $\text{Gd}_{14}\text{Ag}_{51}$ structure type or whether an overlooked twinning problem causes the equidistant hexagon of half-occupied silver atoms. Single crystal data were collected for $\text{RE}_{14}\text{Ag}_{51}$ ($\text{RE} = \text{Y}, \text{Ce}, \text{Gd}, \text{Tb}$). We refined the data in several space groups to compare the results. In addition, we recorded high-resolution transmission elec-

Table 1: Details for the preparation of the $RE_{14}Ag_{51}$ phases with $RE = Y, Ce, Gd, Tb$. Uniform heating rates of 80 K/h from room temperature to T_{\max} and cooling rates from $T_{\max}-70$ K to room temperature were applied. The intermediate cooling rate from T_{\max} to $T_{\max}-70$ K was 2 K/h in all cases.

Nominal composition	amount weighed [mg, mmol]				T_{\max} [K]
	$m(RE)$	$n(RE)$	$m(Ag)$	$n(Ag)$	
$Y_{14}Ag_{51}$	277.0	3.116	1223.2	11.340	1348
$Ce_{14}Ag_{51}$	396.2	2.828	1105.9	10.252	1348
$Gd_{14}Ag_{51}$	285.3	1.814	714.1	6.620	1273
$Tb_{14}Ag_{51}$	288.8	1.817	712.2	6.603	1273

tron microscopy (HRTEM) images for $Gd_{14}Ag_{51}$ in relevant orientations to rule out that the X-ray structure model of higher symmetry may be an effect of twinning in domains smaller than the X-ray coherence length.

Preparation and single crystal structure determination

Synthesis of the $RE_{14}Ag_{51}$ compounds was generally performed starting from elemental cerium, gadolinium, terbium and yttrium together with silver powder (Ce: smart-elements, 99.9%; Gd: smart-elements, 99.9%; Ag: chempur, 99.99%; Tb: smart-elements, 99.9%; Y: smart-elements, 99.9%). In an argon-filled glove box, the rare-earth metals were filed and filled in tantalum crucibles together with silver powder. The crucibles were sealed by arc welding. The containers were heated to $T_{\max} = 1273$ or 1348 K with a rate of 80 K/h and subsequently cooled to 70 K below T_{\max} with a rate of 2 K/h for crystallization and finally to room temperature with a rate of 80 K/h. For details see Table 1.

After cooling, the tantalum crucibles were opened in air. The products are stable toward room atmosphere over weeks. Suitable single crystals were selected under a stereo microscope. The crystals show metallic luster and irregular shape. Specimens suitable for X-ray investigations were mounted on top of glass fibers and centred on a one-circle goniometer with imaging plate (Stoe IPDS, Stoe & Cie, Darmstadt, AgK_{α} radiation, graphite monochromator).

The collected diffraction images showed primitive hexagonal patterns without any systematic extinctions in all cases. In Table 2 all possible space group candidates are assembled with their respective R_{int} values. Clearly all high Laue group candidates are ruled out by the averaging. From the remaining space group candidates all non-centrosymmetric groups are in contradiction with the Wilson statistics, and space group $P\bar{3}$ is not in agreement with the sixfold symmetry visible in the electron density plot calculated in space group $P1$ (Figure 1). The remaining space groups thus are $P\bar{6}$ and $P6/m$.

The structure solutions by direct methods [22] succeeded in space group $P\bar{3}$. Lowest possible symmetry was chosen in order not to overlook pseudo-symmetry. The structure solution yielded all atom positions. Atom assignment was carried out by analysis of the thermal displacement parameters as indicator for heavier (lanthanide) or lighter (silver)

Table2: A comparison of the R_{int} values for all possible space group candidates derived from the reflection statistics of a single crystal X-ray data set of $\text{Gd}_{14}\text{Ag}_{51}$.

Crystal system	trigonal			hexagonal	
Laue class	$\bar{3}$	$\bar{3}m1$	$\bar{3}1m$	$6/m$	$6/mmm$
R_{int}	0.087	0.527	0.531	0.091	0.533
Space group	$P3$	$P321$	$P312$	$P6$	$P622$
	$P\bar{3}$	$P3m1$	$P31m$	$P\bar{6}$	$P6mm$
		$P\bar{3}m1$	$P\bar{3}1m$	$P6/m$	$P\bar{6}2m$
					$P\bar{6}m2$
					$P6/mmm$

atoms. After anisotropic treatment of all thermal displacement parameters the atomic positions were checked for statistical mixed occupation or underoccupation. Only Ag5 (named Ag* by Bailey and Kline [6]) showed to be half-occupied within error margins after free refinement of the occupation factor (see Table A7). As too close next-neighbour distances suggested a mutually exclusive occupation of the six Ag5 positions in form of two disordered triangles, the occupation factor was fixed to be $\frac{1}{2}$ in the final refinement cycles. All other atomic positions were fully occupied and no mixed occupation could be detected. Checks for additional symmetry were performed using the platon [23,24] package and revealed the final space group $P6/m$. The possibility of a superstructure was also taken into consideration but no superlattice reflections had been observed. Refinements in the direct subgroup $P\bar{6}$ or $P6$ (loss of inversion symmetry) resulted in Flack parameters of 0.5 within small error margins, large correlation matrix elements for all parameters of those atom positions connected by an inversion center in space group $P6/m$ and much worse R values. Together with the analysis of F_{obs} maps calculated in space group $P1$ to rule out all symmetry biases (see Figure 1) showing all six Ag5 positions to have the same electron density which is about half of the one of all other Ag positions, $P6/m$ was chosen to be the "true" space group for the crystal structure description. The underoccupancy and the mutually exclusive occupation of atom positions in too close proximity cannot be resolved by symmetry reduction.

The final R values of the converged refinements and further information on collection and treatment of single crystal data can be found in Table 3, fractional atomic coordinates in standardised setting [25] and equivalent isotropic displacement parameters are compiled in Table A7, coefficients of the anisotropic displacement parameters can be found in Table A8. The residual electron densities were small and always in close proximity of the heavy atom positions and therefore regarded as termination effects. In the discussion, the refined structure of $\text{Gd}_{14}\text{Ag}_{51}$ is always referred to, being the parent compound of this structure type. Further information on data collection and structural details can be obtained by requesting the respective crystal information files (cif) from the Fachinformationszentrum Karlsruhe, D-76344 Eggenstein-Leopoldshafen, Germany (e-mail: crysdata@fiz-karlsruhe.de) on quoting the depository numbers CSD-427781 ($\text{Ce}_{14}\text{Ag}_{51}$), CSD-427782 ($\text{Gd}_{14}\text{Ag}_{51}$), CSD-427793 ($\text{Tb}_{14}\text{Ag}_{51}$) and CSD-427783 ($\text{Y}_{14}\text{Ag}_{51}$), the names of the authors and citation of the paper.

X-ray powder diagrams of the air and moisture stable and very brittle products were recorded on a transmission powder diffractometer (Stoe STADI-P, Stoe & Cie, Darm-

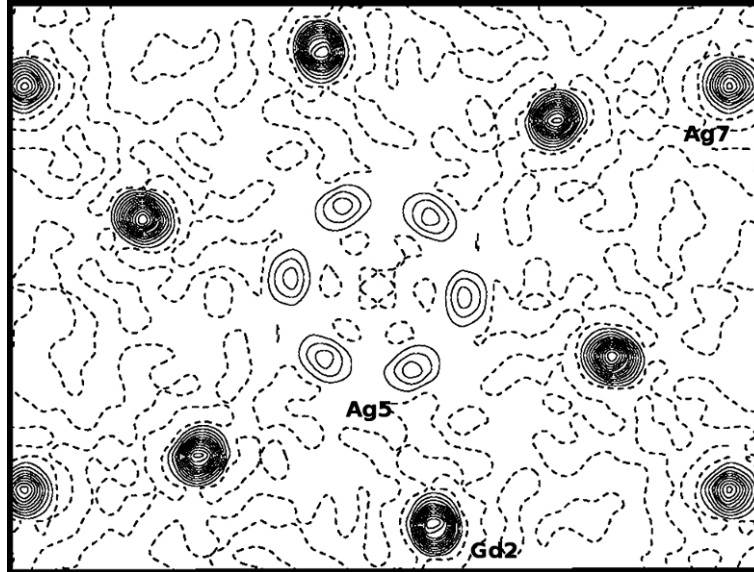


Fig. 1. Electron density map for $\text{Gd}_{14}\text{Ag}_{51}$. Plot of the observed electron density F_{obs} for $\text{Gd}_{14}\text{Ag}_{51}$ calculated in space group $P1$ with view along $[001]$ at a height of $z = 0$. In the center of the selected area six Ag5 atoms form a hexagon in which all atoms have only half the electron density as e. g. atom Ag7 shown in close proximity. The uniform electron density distribution calculated in space group $P1$ shows that the structure model in space group $P6/m$ with half-occupied Ag5 atoms is not a consequence of pseudosymmetry. The electron density map is drawn at a contour lines at a level of $25 \text{ e}^-/\text{\AA}^3$, the zero electron density level is marked as dashed lines.

stadt, $\text{MoK}_{\alpha 1}$ radiation, graphite monochromator) and show the absence of further crystalline phases. Representative portions of the products were ground and sealed in capillaries with inner diameter of 0.3 mm. Rietveld refinement was performed with a fundamental parameter approach and a double Voigt approach to compensate size-strain effects. A shifted Chebychev function with 12 parameters was applied for background modelling. Careful absorption correction was performed by taking the linear absorption coefficient, the capillary diameter and the packing density into account. Within small error margins, the refined structure model confirms the model from single crystal structure determination which was taken as starting values (see Figure 2). Further details on Rietveld refinements can be found in Table 4.

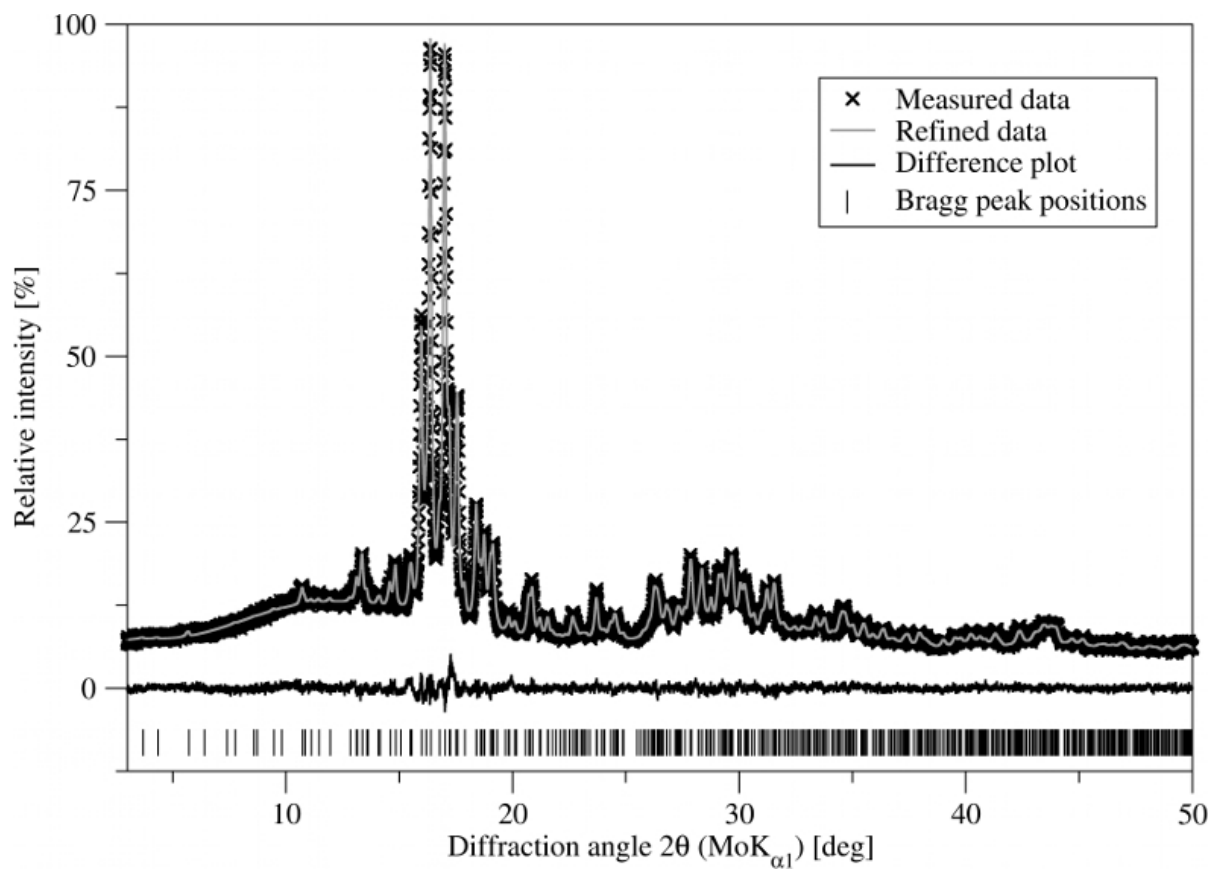


Fig. 2. Rietveld refinement of $Gd_{14}Ag_{51}$. Final refinement parameters are compiled in Table 4.

Table 3: Crystallographic data, details of the data collection and structure determination for $X_{14}Ag_{51}$ with $X = Y, Ce, Gd, Tb$.

	$Ce_{14}Ag_{51}$	$Gd_{14}Ag_{51}$	$Tb_{14}Ag_{51}$	$Y_{14}Ag_{51}$
Crystal system			hexagonal	
Space group			$P6/m$, (No. 175)	
Lattice parameters [pm]	a	1285.24(17)	1264.30(18)	1256.82(8)
	c	946.83(11)	927.54(11)	923.30(8)
Unit cell volume [10^6pm^3]		1354.5(3)	1292.4(3)	1263.05(16)
Z			– 1	
Density (X-ray) [g/cm^3]		9.15	7.88	8.87
Diffractometer			– STOE IPDS-I, $\text{AgK}\alpha$ radiation	
			– graphite monochromator	
Measurement temperature			– 295 K	
Absorption coefficient $\mu_{\text{AgK}\alpha}$ [mm^{-1}]		15.53	12.60	18.78
ϑ range for refinement [$^\circ$]		2.5 – 24.99	2.54 – 24.96	2.95 – 25.00
Index range		$-19 \leq h \leq 19$,	$-19 \leq h \leq 19$,	$-18 \leq h \leq 14$,
		$-19 \leq k \leq 19$,	$-19 \leq k \leq 19$,	$-18 \leq k \leq 18$,
		$-14 \leq l \leq 14$	$-13 \leq l \leq 14$	$-10 \leq l \leq 13$
No. of observed reflections		19967	16979	8190
No. of independent reflections		1712	1631	1581
No. of independent reflections with ($I \leq 2\sigma(I)$)		1111	1300	1439
R_{int}		0.1790	0.0733	0.1329
Corrections			– Lorentz, polarisation, absorption	
Absorption correction			– multiscan [23]	– none
Structure solution			– SHELXS97 [22]	– multiscan [23]
Structure refinement			– SHELXL97 [22]	
No. of free least-squares parameters			– 62	
Goodness-of-fit on F^2		0.995	0.983	1.123
$R1/wR2$		0.0462/0.1000	0.0246/0.0435	0.0314/0.0656
	For $I \geq 2\sigma(I)$	0.0860/0.1116	0.0396/0.0457	0.0511/0.0706
	For all data	3.63/–3.53	2.70/–2.49	3.23/–2.41
Max./min. residual electron density [$\text{e}^{-\text{Å}^{-3}}$]				5.13/–4.73

Table 4: Results of the Rietveld refinement of $\text{Gd}_{14}\text{Ag}_{51}$

Formula	$\text{Gd}_{14}\text{Ag}_{51}$
Z	1
Crystal system	hexagonal
Space group	$P6/m$ (No. 175)
Lattice parameters [pm]	$a = 1267.52(4)$ $c = 932.36(4)$
Density (X-ray) [g/cm^3]	9.8(1)
Unit cell volume [10^6pm^3]	1297.2(1)
Radiation	$\text{MoK}_{\alpha 1}$
Monochromator	curved Ge single crystal
Parameters	55
R values	$R_p = 0.03075$ $R_{wp} = 0.03937$ $\chi^2 = 1.185$

HRTEM investigations

Ground crystals of $\text{Gd}_{14}\text{Ag}_{51}$ were dispersed in absolute ethanol and drop-cast on copper grids coated with a holey carbon film (S166-2, Plano GmbH, Germany). All grids were fixed on a double-tilt holder. SAED, HRTEM and EDX measurements were performed on a Titan 80-300 (FEI, USA) with a field emission gun operated at 300 kV and equipped with a TEM TOPS 30 EDX spectrometer (EDAX, Germany). Images were recorded with an UltraScan 1000 camera (Gatan, USA, resolution: $2\text{k}\times 2\text{k}$). SAED and EDX measurements were also performed on a Jeol 2010 system (Jeol, Germany) with a heated LaB_6 emitter operated at 200 keV, equipped with a EDAX Apollo XLT EDX detector (EDAX, Germany). Images were recorded on a TemCam F216 camera (TVIPS, Germany, resolution: $2\text{k}\times 2\text{k}$). HRTEM and SAED data were evaluated with the programs Digital Micrograph [27] (including Fourier filtering of the HRTEM images), Process Diffraction 7 [28] and JEMS [29], EDX data were processed with ES Vision [30] and EDAX TEAM [31].

Electrical resistivity and magnetic susceptibility

Resistance measurements were carried out on a cold-pressed pellet (10 kN, \varnothing : 4 mm, thickness: 0.75 mm) of $\text{Gd}_{14}\text{Ag}_{51}$ powder. The van der Pauw technique (four-probe method) was applied [26]. The pellet was contacted with the aid of silver conductive paint. Currents of 0.5-0.8 mA were applied. The potential difference was measured as a function of the temperature upon cooling and heating (300 to 3.5 K).

Magnetic susceptibility measurements were carried out on powder samples of $\text{Gd}_{14}\text{Ag}_{51}$ on an AC susceptometer (self-built) [32]. Data were measured at 1333 Hz and 3 Oe.

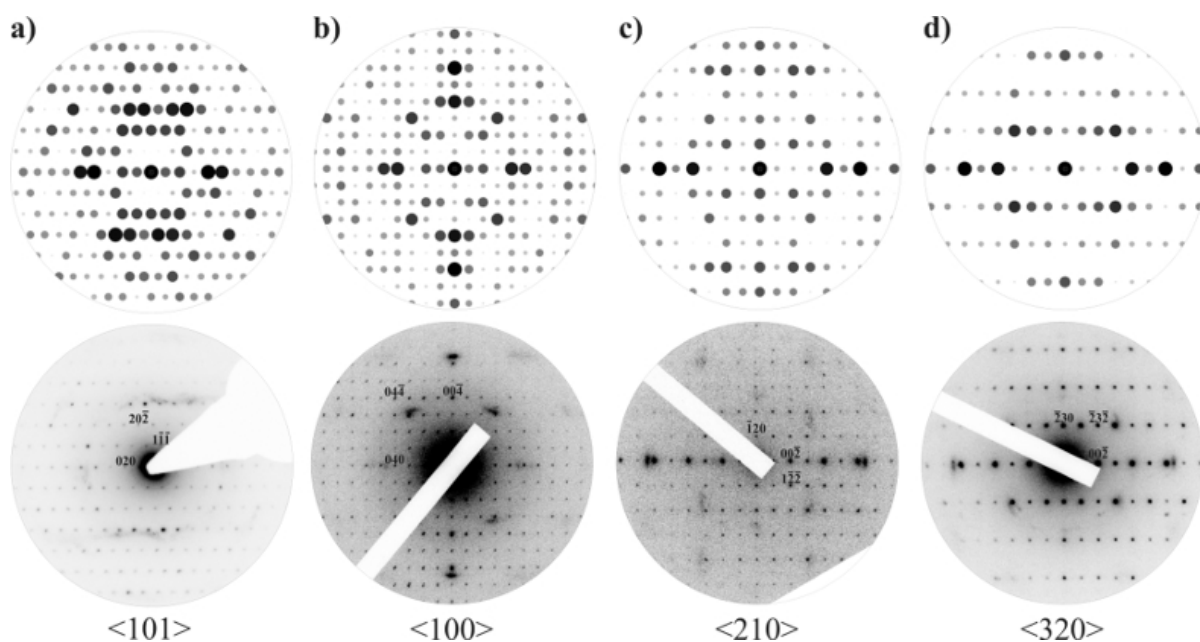


Fig. 3. Selected area electron diffraction (SAED) patterns of $\text{Gd}_{14}\text{Ag}_{51}$. Experimental (bottom) SAED patterns with corresponding simulations (top, based on the result of the single-crystal X-ray diffraction data) of $\text{Gd}_{14}\text{Ag}_{51}$ obtained from different crystallites, exemplary reflections in the selected plains are labeled with indices.

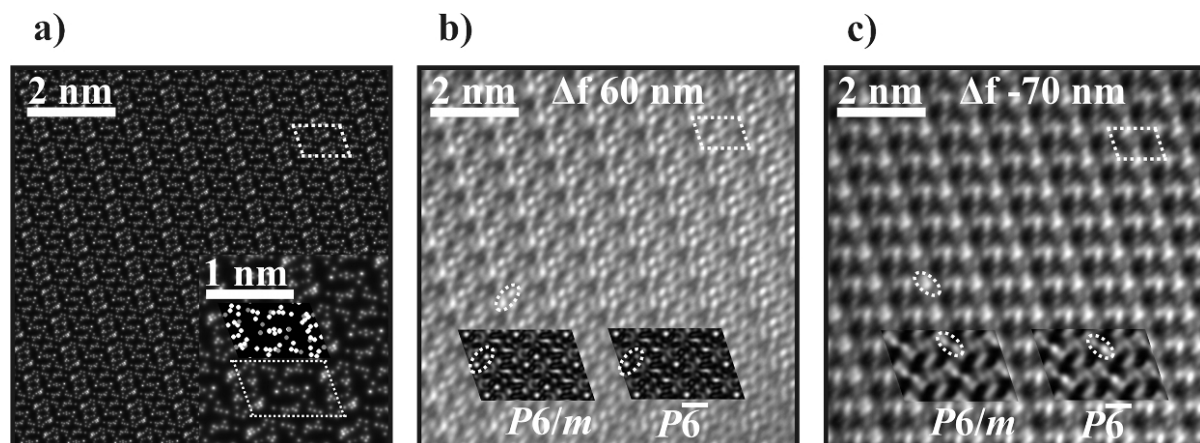


Fig. 4. High resolution transmission electron micrographs (HRTEM) of $\text{Gd}_{14}\text{Ag}_{51}$. Projected potential with enlarged inset (a) and HRTEM images with inserted image simulations in the correct ($P6/m$) and the competing ($P\bar{6}$) space group (b, c) along the $\langle 101 \rangle$ zone axis (accelerating voltage 300 keV, $C_s = 0.6$ mm, spread of focus = 3.6 nm, beam semi-convergence = 25 mrad, layer thickness five unit cells), inserted: defocus values 60 nm (b) and -70 nm (c), white dotted rhombus shows the dimension of the unit cell and white dotted ellipsoids mark the decisive contrast differences.

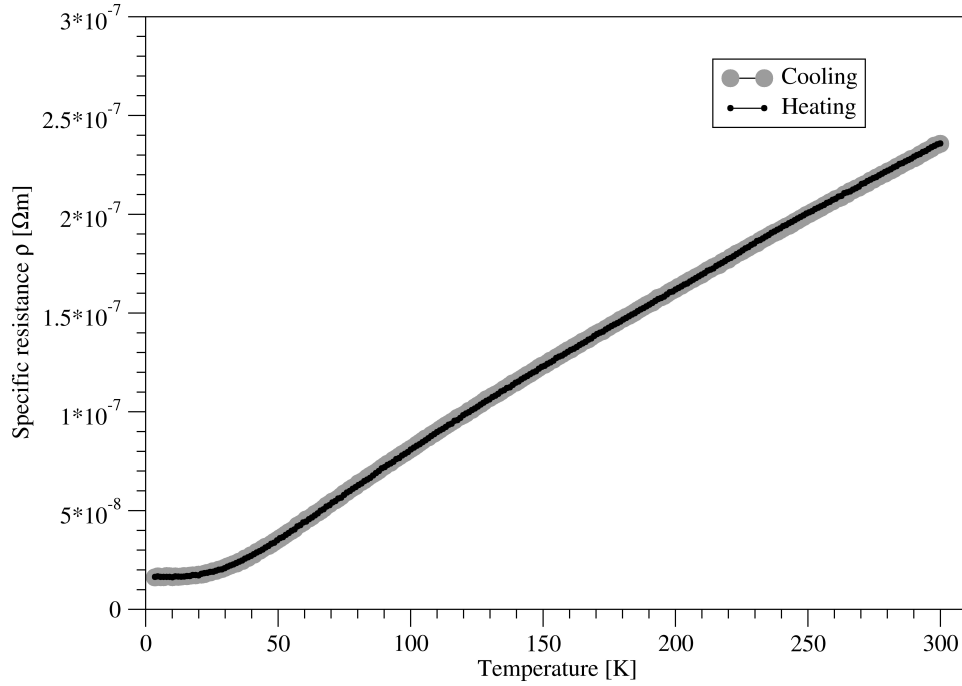


Fig. 5. Temperature-dependent specific resistivity of $\text{Gd}_{14}\text{Ag}_{51}$. Cooling curve: grey; reheating curve: black. The data show a linear decrease with decreasing temperature and an overall low specific resistivity, indicating good metal behaviour.

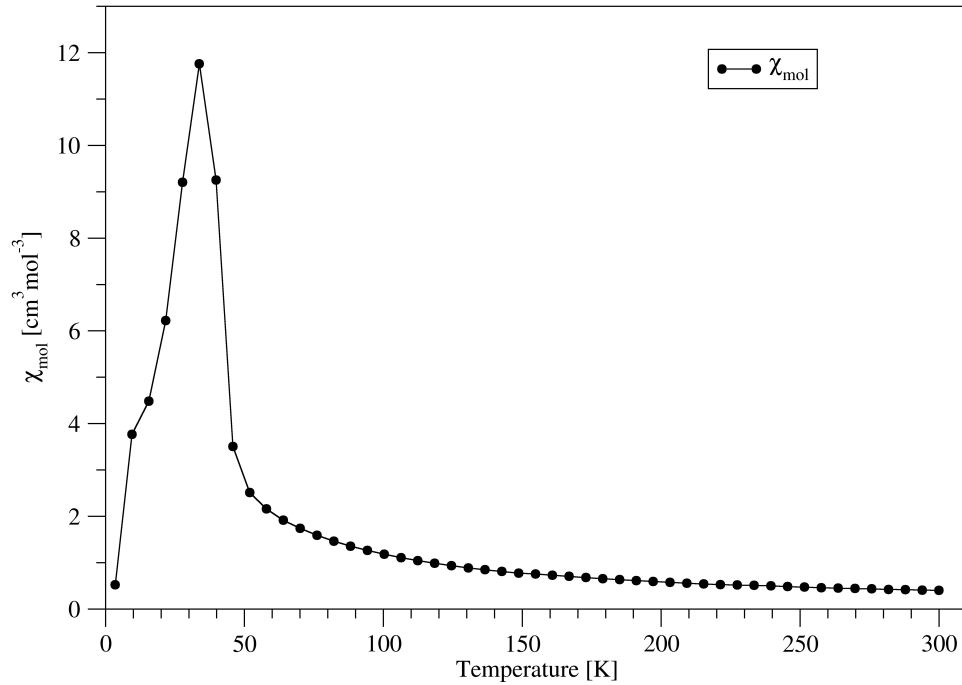


Fig. 6. Temperature-dependent magnetic susceptibility of $\text{Gd}_{14}\text{Ag}_{51}$. The data show a linear increase with decreasing temperature and an anomaly at 30 K, typical for a good metal with antiferromagnetic ordering at low temperatures.

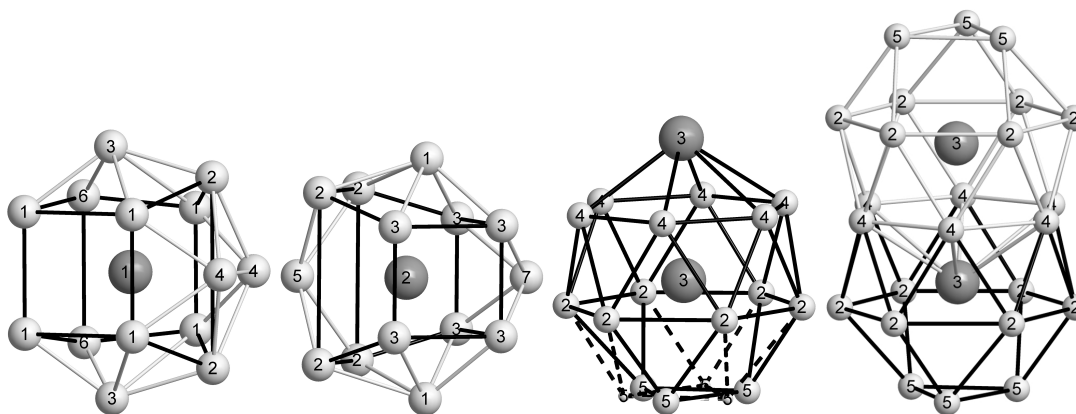


Fig. 7. Coordination polyhedra centred by Gd in $\text{Gd}_{14}\text{Ag}_{51}$. Polyhedra around Gd1 and Gd2 are derived from capped pentagonal prisms. The basal corpus is black, the capping grey. Gd3 centers a Frank-Kasper polyhedron. Note the two possible locations for the Ag5 atoms, indicated by dashed black lines. Two Frank-Kasper polyhedra around Gd3 interpenetrate to form pairs. Light grey spheres represent Ag atoms, dark grey spheres are drawn for Gd.

Results and discussion

Crystal structure description

$\text{Gd}_{14}\text{Ag}_{51}$, the parent compound of the structure type, crystallizes in the hexagonal space group $P6/m$ with $a = 1264.3(2)$ pm and $c = 933.5(2)$ pm. The structure contains three crystallographically independent Gd and seven Ag positions.

The first coordination sphere around Gd atoms is constituted only of Ag atoms. Figure 7 shows the coordination polyhedra around Gd1 and Gd2. Atom Gd1 has 14 Ag neighbours: six Ag1, two Ag2 and two Ag6 atoms form a distorted pentagonal prism, two Ag3 atoms cap the pentagonal basal faces and two Ag4 atoms cap adjacent rectangular faces. Atom Gd2 also is coordinated by 14 Ag atoms. Four Ag2 and six Ag3 atoms again form a distorted pentagonal prism, the basal faces being capped by two Ag1 atoms and two of the rectangular faces being capped by Ag7 and Ag5 atoms, respectively. The coordination of atom Gd3 is somewhat more complicated as shown in Figure 7. Gd3 is coordinated by three different silver sites (6 x Ag2, 6 x Ag4, 6 x Ag5 (half occupied, see below)) and an additional Gd3 atom, completing a coordination sphere best described as Frank-Kasper polyhedron with 16 vertices. It can also be rationalised as a Friauf polyhedron with capping of all hexagonal faces. Two interpenetrating polyhedra of this type surrounding two neighbouring Gd3 atoms form pairs which are further condensed via the faces formed by the half-occupied Ag5 hexagons to form columns along [001].

Silver atoms are coordinated by both gadolinium and silver atoms. All Ag coordination polyhedra can be grouped into two types. The ones of the first type are derived from an icosahedron (around Ag1, Ag2, Ag3 and Ag4, Figure 8), the ones of the second type are derived from capped trigonal prisms (around Ag5, Ag6 and Ag7, Figure 9). The distorted icosahedra are built from eight Ag and four Gd positions each, the capped trigonal prisms from eight Ag and three Gd atoms. The most distorted icosahedra are found around Ag1, Ag2 and Ag3, as they occupy general positions (Wyckoff position 12I).

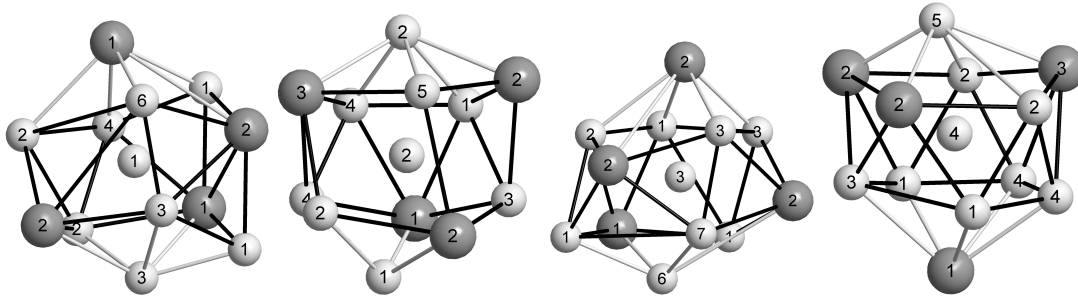


Fig. 8. Coordination polyhedra centred by Ag in $\text{Gd}_{14}\text{Ag}_{51}$ (1). Polyhedra around Ag1, Ag2, Ag3 and Ag4 are derived from icosahedra. The pentagonal antiprismatic base of the distorted icosahedra is drawn in black. Ag atoms are shown in light grey, Gd atoms in dark grey.

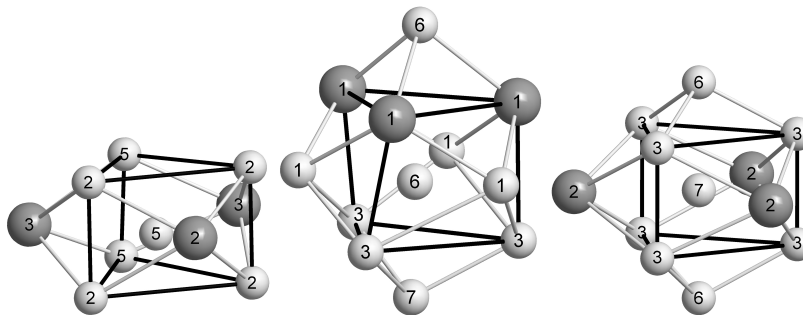


Fig. 9. Coordination polyhedra centred by Ag in $\text{Gd}_{14}\text{Ag}_{51}$ (2). Polyhedra around Ag5, Ag6 and Ag7 are derived from pentacapped trigonal prisms. The trigonal prismatic base is shown in black, the capping in grey. Ag atoms are shown in light grey, Gd atoms in dark grey.

The icosahedron around Ag4 and the trigonal prism around Ag5 each include a mirror plane (Wyckoff positions $6k$ and $6j$) rendering them somewhat closer to ideal shapes. Ag6 has point symmetry 3 (Wyckoff position $4h$). The least distorted polyhedron forms around Ag7 (Wyckoff position $2c$) with site symmetry $\bar{6}$.

Atom Ag5, situated close to the sixfold axis, has symmetry-equivalent neighbouring atoms in too close proximity (see Table A9). These atoms show sharp electron density maxima which can be refined as Ag atoms with only 50% occupation (see Figure 1 and Table A7). This results in two mutually exclusively orientated Ag5 triangles (Figure 7) with interatomic distances of 274.3(2)pm, well in agreement with those found in other Ag-rich intermetallics [33–36]. However, the threefold symmetry for the ordered model is not in agreement with the space group symmetry. Refinement in a lower symmetric space group shows no ordering of independent Ag5 positions and therefore no symmetry lowering from space group $P6/m$ is necessary, as can be seen from the electron density map calculated in space group $P1$ (see Figure 1). The effect of half-occupied Ag5 positions therefore is not due to an overlooked twinning problem, and the amalgam crystal structures with ordered triangle of fully occupied Hg atoms at topologically equivalent positions therefore belong to new structure types of lower symmetry.

The complete packing of the described polyhedra can best be rationalised starting from the Gd-centred polyhedra. The resulting representation of the total structure is given in Figure 12. The polyhedra do not fill space without empty wedges when condensed via common faces. The atomic positions of the three Gd sites form thinned and slightly

Table 5: Results of EDX measurements for various crystals of $\text{Gd}_{14}\text{Ag}_{51}$ in atom-%.

crystal	1	2	3	4	5	6	average	calc.
Ag(K)	78.4	79.0	74.2	77.7	79.3	77.3	77.7(17)	78.5
Gd(L)	21.6	21.0	25.8	22.3	20.7	22.7	22.3(17)	21.5

distorted hexagonal layers in different heights along [001] (Gd1 at $z = \frac{1}{2}$, Gd2 at $z = 0$ and Gd3 at $z \approx 0.3$, see Figure 10) and thus show the relation of this structure type with a hexagonal closest sphere packing.

Alternatively, the structure can be rationalised as hexagonal rod packing. The polyhedra around Gd3 at $(0, 0, 0)$ and Ag7 at $(\frac{1}{3}, \frac{2}{3}, 0)$ form columns extending along [001] by sharing common faces. In this picture, the comparison of the $\text{Gd}_{14}\text{Ag}_{51}$ structure type with the structures of related amalgams (see below) in space group $P\bar{6}$ is very clear: in Figure 11 the effect of symmetry loss can be seen in the ordering of the hexagons of half-occupied Ag atoms to triangles of fully occupied Hg atoms. The splitting of two symmetry-equivalent rods (around Ag7 in $\text{Gd}_{14}\text{Ag}_{51}$) into two independent but topologically very similar rods in the amalgams also is a consequence of the symmetry reduction.

Electron microscopy

Since the structure of $X_{14}\text{Ag}_{51}$ compounds can be fitted well in the two space groups $P6/m$ and $P\bar{6}$ (other possible candidates have been ruled out following the structure refinement on the basis of single crystal data, see above in section 2.1.) TEM investigations on different crystals of $\text{Gd}_{14}\text{Ag}_{51}$ were performed in order to verify the final structure model in space group $P6/m$. Good crystallinity and domains larger than 100 nm were observed. The SAED patterns were taken from thin areas to minimize dynamic electron scattering. The reflection positions and especially the reflection intensities match well with the SAED patterns simulated in space group $P6/m$ (Figure 3).

HRTEM simulations performed with the multislice method were compared to experimental data passing the Scherzer defocus (Figure 4) collected from thin areas of $\text{Gd}_{14}\text{Ag}_{51}$ crystals. The difference in weight between Ag and Gd does not have a relevant impact on special contrast features along the $\langle 101 \rangle$ direction in the projected potential (Figure 4 a). The atoms form streaks clearly visible both in the projected potential and the inserted structural projection and have their equivalents in HRTEM images and corresponding simulations. Significant features in the experimental HRTEM images correlate to features in simulated HRTEM images. Slight but explicit contrast differences within the critical chemical surrounding of the Ag5 atom (Figure 4 b, c; white dotted ellipsoids) provide evidence for the distinction between the two structure models in space groups $P6/m$ and $P\bar{6}$. In both defocus images, the model in space group $P\bar{6}$ results in double spots with one weaker and one stronger intensity, whereas the two spots with equal intensities resulting from the model in space group $P6/m$ match better with the recorded images.

The chemical composition of the product was confirmed by energy-dispersive X-ray (EDX) spectroscopy. No other elements except Ag and Gd were detected and the average composition is in good agreement with the composition $\text{Gd}_{14}\text{Ag}_{51}$ (Table 5).

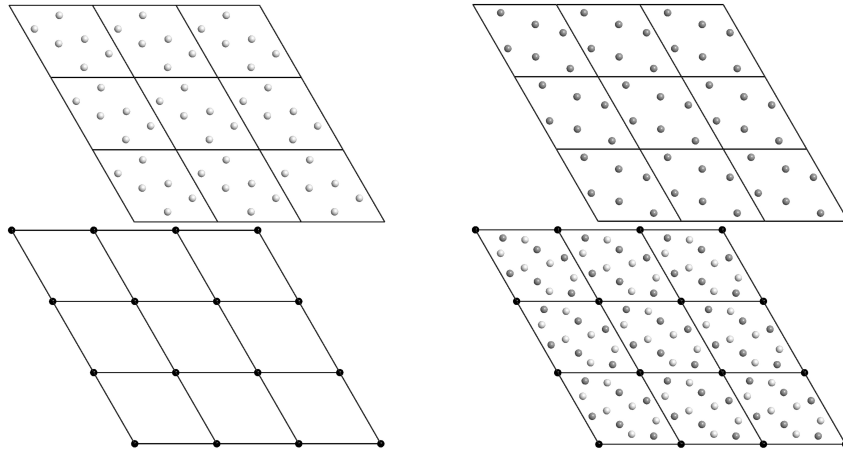


Fig. 10. Three sublattices of Gd1 (upper left, light grey, at $z = \frac{1}{2}$), Gd2 (upper right, dark grey, at $z = 0$) and Gd3 (lower left, black, at $z \approx 0.3$). They form thinned and slightly distorted hexagonal patterns. When combined in one picture (lower right), the relation to the hexagonal closest packing is clearly visible.

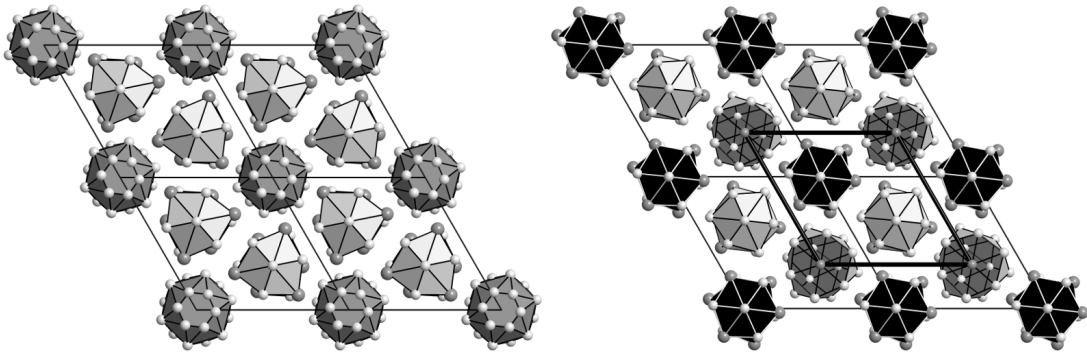


Fig. 11. View along the c axes of $\text{Gd}_{14}\text{Ag}_{51}$ (left) and $\text{Eu}_{10}\text{Hg}_{55}$ (right). The comparison clearly shows the differences of the two structures in space groups $P6/m$ ($\text{Gd}_{14}\text{Ag}_{51}$) and $P6$ ($\text{Eu}_{10}\text{Hg}_{55}$). In addition to an origin shift, the positions of the half-occupied hexagons of Ag5 atoms in $\text{Gd}_{14}\text{Ag}_{51}$ are ordered and fully occupied triangles of Hg atoms in $\text{Eu}_{10}\text{Hg}_{55}$. The orientation of the unit cell of the $P6/m$ model is given as black lines in the lower picture for direct comparison.

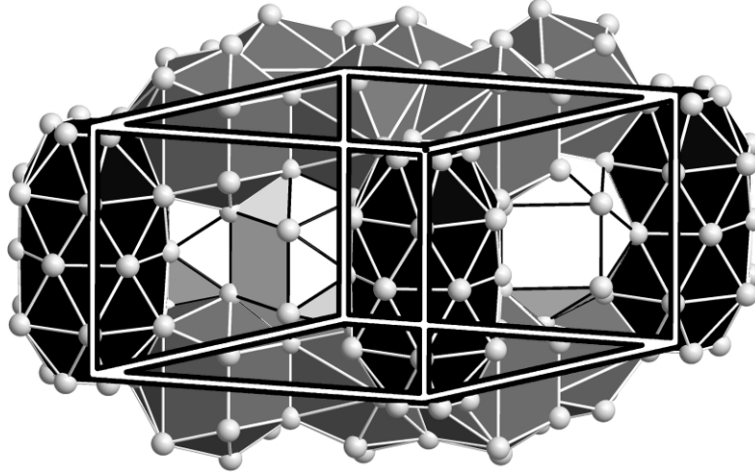


Fig. 12. The packing of Gd-centred polyhedra in $\text{Gd}_{14}\text{Ag}_{51}$. Grey polyhedra around Gd1, white polyhedra around Gd2 and black polyhedra around Gd3. The packing of the polyhedra is not space filling, kinks and voids remain in between the polyhedra.

Table 6: Complexity values for compounds derived from the $\text{Gd}_{14}\text{Ag}_{51}$ family. IG is the bit per atom, IG_{Bits} is the total information content of the unit cell, IG_n is the normalized information content.

Compound	IG	IG_{Bits}	IG_n
$\text{Gd}_{14}\text{Ag}_{51}$ [6]	3.101	210.850	0.509
$\text{Ca}_{11}\text{Hg}_{54}$ [1]	3.857	251.853	0.640
$\text{Eu}_{10}\text{Hg}_{55}$ [3]	4.233	275.159	0.703
$\text{Na}_{11}\text{Hg}_{52}$ [2]	6.942	3936.056	0.759
$\text{La}_{11}\text{Hg}_{45}$ [37]	3.797	425.287	0.558

Comparison with related structures

In 1973 and 1974 the amalgams $\text{Ca}_{14}\text{Hg}_{51}$ and $\text{Sr}_{14}\text{Hg}_{51}$ were assigned to the $\text{Gd}_{14}\text{Ag}_{51}$ structure type by Bruzzone and coworkers on the basis of powder diffraction patterns [18,19]. However, investigations by Mar and coworkers in 2008 showed that they crystallise in a closely related structure type with lowered symmetry, leading to an ordered occupation of those Hg atoms equivalent to the Ag5 position in $\text{Gd}_{14}\text{Ag}_{51}$ [1]. The symmetry is lowered from space group $P6/m$ to $P\bar{6}$. Removal of the mirror plane normal to the sixfold axis goes along with a loss of the inversion centre. In both $\text{Ca}_{14}\text{Hg}_{51}$ and $\text{Sr}_{14}\text{Hg}_{51}$ the position centering the Frank-Kasper polyhedron (Gd3 in $\text{Gd}_{14}\text{Ag}_{51}$) is mixed-occupied by Hg and Ca or Sr. A third amalgam with composition $\text{Eu}_{10}\text{Hg}_{55}$ [3] is of the same type, however, here in addition to the mixed occupancy of the position centering the Frank-Kasper polyhedron a split position of a Hg atom along $[0,0,z]$ occurs. Again, this structure shows space group symmetry $P\bar{6}$ with an ordered triangle formed by the atoms corresponding to the position of Ag5 in $\text{Gd}_{14}\text{Ag}_{51}$.

$\text{Na}_{11}\text{Hg}_{52}$ [2] is a further structure with close relation to the $\text{Gd}_{14}\text{Ag}_{51}$ structure type. It crystallizes in a $(3 \times 3 \times 1)$ superstructure with respect to the parent compound. From the 101 Hg and 30 Na positions in the unit cell of $\text{Na}_{11}\text{Hg}_{52}$, one single Hg position shows a mixed occupation with 50% Na. Other amalgams of the general composition

$X_{11}\text{Hg}_{45}$ ($X = \text{La}, \text{Ce}, \text{Pr}, \text{Nd}, \text{Sm}, \text{Gd}, \text{U}$) [37] crystallise in a cubic structure that can be derived from the hexagonal $\text{Gd}_{14}\text{Ag}_{51}$ structure type and exhibits the same structural basic building units. This structural relationship is topic of further investigations.

All these different yet closely related structures can be compared in terms of complexity values as introduced by Krivovichev [38]. All structures show high but comparable complexity. The various disorder phenomena in the amalgams contribute to an increase of their complexities in comparison with the one of $\text{Gd}_{14}\text{Ag}_{51}$, however, the effect of symmetry reduction from space group $P6/m$ to $P\bar{6}$ and the herewith related higher number of symmetry-independent atomic positions is by far more relevant. A huge increase in complexity for the same reason (symmetry reduction by enlargement of the unit cell in the sense of a *klassengleiche* subgroup) is found for the sodium amalgam. Here, only a minor disorder phenomenon is present, but there are 131 independent atomic positions, whereas $\text{Ca}_{14}\text{Hg}_{51}$, $\text{Sr}_{14}\text{Hg}_{51}$ and $\text{Eu}_{10}\text{Hg}_{55}$ have only 20 independent atom positions and $\text{Gd}_{14}\text{Ag}_{51}$ has 10. The crystal structure of $\text{Na}_{11}\text{Hg}_{52}$ is with this respect the most complex binary compound hitherto known not representing an approximant to a quasicrystalline structure [39].

Electrical and magnetic properties

The specific resistivity of $\text{Gd}_{14}\text{Ag}_{51}$ shows the typical behaviour of a metal and decreases with decreasing temperature, see Figure 5. The specific resistivity at room temperature ($2.25 \cdot 10^{-7} \Omega \cdot \text{m}$) is about one order of magnitude lower than the one of metallic silver ($1.59 \cdot 10^{-8} \Omega \cdot \text{m}$ [40]) and about one order of magnitude higher than the one of metallic gadolinium ($1.26 \cdot 10^{-6} \Omega \cdot \text{m}$ [41]). In contrast, the amalgams with closely related structures show typical "bad metal behaviour", as e. g. shown for $\text{Na}_{11}\text{Hg}_{52}$. This is consistent with the lower electronegativity difference between Ag and the rare-earth metals compared to the one between Hg and alkali, alkaline-earth or rare-earth metals. The low Joffe-Regel limit detected for $\text{Na}_{11}\text{Hg}_{52}$ also is in good agreement with the very low-symmetric and extremely complex structure with long translational periodicity.

At temperatures below 30 K, $\text{Gd}_{14}\text{Ag}_{51}$ the susceptibility of $\text{Gd}_{14}\text{Ag}_{51}$ shows a deviation from the behaviour of a simple pauli paramagnet which can be interpreted as antiferromagnetic ordering, see Figure 6. This has also been observed for $\text{Tb}_{14}\text{Ag}_{51}$ (27 - 27.9K) and $\text{U}_{14}\text{Au}_{51}$ (23K) [15,42].

Conclusions

We have shown that the $\text{Gd}_{14}\text{Ag}_{51}$ structure type can be assigned to space group $P6/m$ by single crystal X-ray structure analysis, careful analysis of the electron density map and TEM investigations. The observed effect of six symmetry equivalent, half-occupied and mutually exclusive Ag positions cannot be resolved by symmetry reduction and is an intrinsic feature of this structure type. The comparison of four single crystal refinements ($X_{14}\text{Ag}_{51}$ with $X = \text{Y}, \text{Ce}, \text{Gd}$ and Tb) shows that all compounds crystallise isotypically in the strict sense of the word. Recently occurred doubts on the few single crystal data

available in literature therefore can be outruled, also it is probable that all the structure type assignments based merely on powder diffraction data are correct.

A basic and prominent structure element in the $\text{Gd}_{14}\text{Ag}_{51}$ structure type is a rod formed by condensed pairs of two interpenetrating Frank-Kasper polyhedra with 16 Ag vertices and centred by Gd atoms. These rods are packed in a hexagonal rod packing topology. A class of related structures with general composition $X_{11}\text{Ag}_{45}$ crystallizes in a cubic structure type where these rods form a cubic packing. The same rods are also the prominent structure motifs in a number of amalgam structures. They can be regarded as hettotypes to the $\text{Gd}_{14}\text{Ag}_{51}$ aristotype as they crystallise in the direct subgroup $P\bar{6}$. Their respective structures show different kinds of disorder phenomena and higher complexity, mainly due to the lower space group symmetry. However, in all these slightly different structures, the Hg positions equivalent to Ag5 in $\text{Gd}_{14}\text{Ag}_{51}$ form ordered and fully occupied triangles. In contrast to these amalgams which show highly polarised metal-metal bonding due to the high differences in the electronegativities of Hg and alkali or alkaline-earth metal, $\text{Gd}_{14}\text{Ag}_{51}$ shows the typical behaviour of a good metal and antiferromagnetic ordering at low temperatures.

The reason for the lower symmetric amalgam structures showing ordered atomic positions may lie in the higher ionic contributions. The local Coulomb potentials lead to the formation of coordination spheres of negatively polarised Hg atoms surrounding the positively polarised less noble metals, and the ionic bonding contributions may favour structures with higher order in comparison to the primarily metallic bonding in $\text{Gd}_{14}\text{Ag}_{51}$ structure type compounds with low electronegativity differences and good metallic behaviour. Extensive studies to clarify the degree of electron transfer of the less noble metals to Hg in the amalgams and the resulting effects on the crystal structures are at the moment performed in our group both on the basis of quantum mechanical calculations and on NMR spectroscopic investigations. In addition, a new and unconventional approach to the rationalisation of highly complex crystal structures [43] may shed a light on local structural details, giving new impulse for the interpretation of the disorder phenomena of both $\text{Gd}_{14}\text{Ag}_{51}$ type structures and the related amalgams.

Acknowledgements

We would like to thank Gina Friederichs from Prof. Dr. Dirk Johrendts group at Ludwig-Maximilians-Universität München for the temperature-dependent measurements of the specific resistivity and the magnetic susceptibility of $\text{Gd}_{14}\text{Ag}_{51}$. We are especially grateful for the valuable contributions of Lukas Neudert who performed the electron microscopic studies.

References

- [1] A.V. Tkachuk, A. Mar, Alkaline-earth metal mercury intermetallics $\text{A}_{11-x}\text{Hg}_{54+x}$ ($\text{A} = \text{Ca}, \text{Sr}$), *Inorg. Chem.* 47 (2008) 1313–1318, <http://dx.doi.org/10.1021/ic7015148>.
- [2] C. Hoch, A. Simon, $\text{Na}_{11}\text{Hg}_{52}$ – Komplexität in einem polaren Metall, *Angew. Chem.* 124 (2012) 3316–3319, <http://dx.doi.org/10.1002/ange.201108064>; C. Hoch, A. Simon, $\text{Na}_{11}\text{Hg}_{52}$ – Komplexität in einem polaren Metall, *Angew. Chem. Int. Ed.* 51 (2012) 3262–3265, <http://dx.doi.org/10.1002/anie.201108064>.
- [3] F. Tambornino, C. Hoch, The Hg-richest europium amalgam, $\text{Eu}_{10}\text{Hg}_{55}$ *Z. Kristallogr. Suppl.* 32 (2013) 79–80.
- [4] S. Steeb, D. Godel, C. Löhr, On the structure of the compounds $\text{Ag}_3\text{R.E.}$ ($\text{R.E.} = \text{Y}, \text{La}, \text{Ce}, \text{Sm}, \text{Gd}, \text{Dy}, \text{Ho}, \text{Er}$), *J. Less Common Met.* 15 (1968) 137–141, [http://dx.doi.org/10.1016/0022-5088\(68\)90047-7](http://dx.doi.org/10.1016/0022-5088(68)90047-7).
- [5] O.J.C. Runnalls, The crystal structures of some intermetallic compounds of plutonium, *Can. J. Chem.* 34 (1956) 133–145, <http://dx.doi.org/10.1139/v56-017>.
- [6] D.M. Bailey, G.R. Kline, The crystal structure of $\text{GdAg}_{3.6}$, *Acta Crystallogr. B*27 (1971) 650–653, <http://dx.doi.org/10.1107/S0567740871002711>.
- [7] O.D. McMasters, K.A. Gschneidner Jr., R.F. Venteicher, Crystallography of the silver-rich rare-earth-silver intermetallic compounds, *Acta Crystallogr. B*26 (1970) 1224–1229, <http://dx.doi.org/10.1107/S0567740870003928>.
- [8] S. Cirafici, A. Palenzona, The phase diagram of the Th–Ag system, *J. Less Common Met.* 135 (1987) 1–4, [http://dx.doi.org/10.1016/0022-5088\(87\)90332-8](http://dx.doi.org/10.1016/0022-5088(87)90332-8).
- [9] J.P. Gabathuler, P. White, E. Parthe, $\text{Zr}_{14}\text{Cu}_{51}$ and $\text{Hf}_{14}\text{Cu}_{51}$ with $\text{GdAg}_{3.6}$ structure type, *Acta Crystallogr. B*31 (1975) 608–610, <http://dx.doi.org/10.1107/S0567740875003378>.
- [10] C. Allibert, W. Wong-Ng, S.C. Nyburg, $\text{CeCu}_{3.6}$, a disordered variant of $\text{Gd}_{14}\text{Ag}_{51}$ type, *Acta Crystallogr. C*40 (1984) 211–214, <http://dx.doi.org/10.1107/S0108270184003620>.
- [11] A. Saccone, M.L. Fornasini, D. Macció, S. Delfino, Phase equilibria in the Gd–Au system, *Intermetallics* 4 (1996) 111–119, [http://dx.doi.org/10.1016/0966-9795\(95\)00025-9](http://dx.doi.org/10.1016/0966-9795(95)00025-9).
- [12] A. Saccone, D. Macció, M. Giovannini, S. Delfino, The praseodymium-gold system, *J. Alloy Comp.* 247 (1997) 134–140, [http://dx.doi.org/10.1016/S0925-8388\(96\)02606-0](http://dx.doi.org/10.1016/S0925-8388(96)02606-0).
- [13] A. Saccone, D. Maccio, S. Delfino, R. Ferro, The neodymium-gold phase diagram, *Metall. Mater. Trans. A*30 (1999) 1169–1176, <http://dx.doi.org/10.1007/s11661-999-0266-7>.

- [14] H. Ott, E. Felder, A. Schilling, A. Dommann, F. Hulliger, Low-temperature properties of $U_{14}Au_{51}$, *Solid State Commun.* 71 (1989) 549–551, [http:// dx.doi.org/10.1016/0038-1098\(89\)90533-4](http://dx.doi.org/10.1016/0038-1098(89)90533-4).
- [15] F. Canepa, A. Palenzona, R. Eggenhoffner, Effects of the Th-substitution on the antiferromagnetic coupling and Kondo-like behaviour in the heavy-fermion system $U_{14}Au_{51}$, *Physica B* 176 (1992) 293–300, [http://dx.doi.org/10.1016/0921-4526\(92\)90234-J](http://dx.doi.org/10.1016/0921-4526(92)90234-J).
- [16] A. Schenck, M. Pinkpank, F. Gygax, K.-U. Neumann, K.R.A. Ziebeck, A. Amato, Magnetic properties of $U_{14}Au_{51}$: an exemplary study by muon spin-rotation spectroscopy, *J. Phys. Condens. Matter* 10 (1998) 8059–8082, [http:// dx.doi.org/10.1088/0953-8984/10/36/015](http://dx.doi.org/10.1088/0953-8984/10/36/015).
- [17] F. Merlo, M.L. Fornasini, Crystal structure of the $R_{11}Hg_{45}$ compounds ($R = La, Ce, Pr, Nd, Sm, Gd, U$), *J. Less Common Met.* 64 (1979) 221–231, [http://dx.doi.org/10.1016/0022-5088\(79\)90173-5](http://dx.doi.org/10.1016/0022-5088(79)90173-5).
- [18] G. Bruzzone, F. Merlo, The calcium–mercury system, *J. Less Common Met.* 32 (1973) 237–241, [http://dx.doi.org/10.1016/0022-5088\(73\)90091-X](http://dx.doi.org/10.1016/0022-5088(73)90091-X).
- [19] G. Bruzzone, F. Merlo, The strontium–mercury system, *J. Less Common Met.* 35 (1974) 153–157, [http://dx.doi.org/10.1016/0022-5088\(74\)90154-4](http://dx.doi.org/10.1016/0022-5088(74)90154-4).
- [20] R.V. Gumenyuk, Y.B. Kuzma, Crystal structure of $Gd_{14}Cu_{48}Ga_3$ and $Tb_{14}Cu_{48}Ga_3$, *Inorg. Mater.* 43 (2007) 135–137, <http://dx.doi.org/10.1134/S0020168507020070>.
- [21] Q. Lin, J.D. Corbett, $Ca_{14}Au_{46}Sn_5$: a colored $Gd_{14}Ag_{51}$ -type structure containing columns of well-differentiated hexagonal gold stars, *Inorg. Chem.* 50 (2011) 1808–1815, <http://dx.doi.org/10.1021/ic102243c>.
- [22] G.M. Sheldrick, A short history of SHELX, *Acta Crystallogr. A* 64 (2008) 112– 122. doi:01.1107/S0108767307043930.
- [23] A.L. Spek, Structure validation in chemical crystallography, *Acta Crystallogr. D* 65 (2009) 148–155, <http://dx.doi.org/10.1107/S090744490804362X>.
- [24] Y. Le Page, Computer derivation of the symmetry elements implied in a structure description, *J. Appl. Cryst.* 20 (1987) 264–269, <http://dx.doi.org/10.1107/S0021889887086710>; Y. Le Page, MISSSYM1.1 – a flexible new release, *J. Appl. Cryst.* 21 (1988) 983– 984, <http://dx.doi.org/10.1107/S0021889888007022>.
- [25] L.M. Gelato, E. Parthé, STRUCTURE TIDY – a computer program to standardize crystal structure data, *J. Appl. Cryst.* 20 (1987) 139–143, <http://dx.doi.org/10.1107/S0021889887086965>.
- [26] L.J. Van der Pauw, A method of measuring specific resistivity and hall effect of discs of arbitrary shape, *Philips Res. Rep.* 13 (1958) 1–9.
- [27] Digital Micrograph v3.6.1, Gatan Software Team, Pleasanton, USA, 1999. [28] J.L. Lábár, Consistent indexing of a (set of) single crystal SAED pattern(s) with the ProcessDiffraction program, *Ultramicroscopy* 103 (2005) 237–249, [http:// dx.doi.org/10.1016/j.ultramic.2004.12.004](http://dx.doi.org/10.1016/j.ultramic.2004.12.004).
- [29] JEMS v3.3425U2008, CIME-EPFL, Switzerland, 2008. [30] ES Vision v4.0.164, Emispec Systems Inc., Tempe, USA, 2002. [31] TEAM v3.4.1, EDAX AMETEK, Wiesbaden, Germany, 2013.
- [32] M.C. Tegel, Iron Pnictide Superconductors, Ph.D. Thesis, Ludwig-Maximilians-Universität München, 2011.
- [33] G. Bruzzone, M. Ferretti, F. Merlo, The Ba–Ag system, *J. Less Common Met.* 128 (1987) 259–264, [http://dx.doi.org/10.1016/0022-5088\(87\)90213-X](http://dx.doi.org/10.1016/0022-5088(87)90213-X).

- [34] G.J. Snyder, A. Simon, Crystal structure of Ag_7Ca_2 a new intermetallic structure type, *J. Alloy Comp.* 223 (1995) 65–69, [http://dx.doi.org/10.1016/0925-8388\(94\)01485-X](http://dx.doi.org/10.1016/0925-8388(94)01485-X).
- [35] L.D. Calvert, C. Rand, The crystal structure of Ag_8Ca_3 , *Acta Crystallogr.* 17 (1964) 1175–1176, <http://dx.doi.org/10.1107/S0365110X64003024>.
- [36] J.K. Brandon, R.Y. Brizard, W.B. Pearson, D.J.N. Tozer, c-Brasses with I and P cells, *Acta Crystallogr.* B33 (1977) 527–537, <http://dx.doi.org/10.1107/S0567740877003987>.
- [37] F. Merlo, M.L. Fornasini, Crystal structure of the $\text{R}_{11}\text{Hg}_{45}$ compounds (R=La, Ce, Pr, Nd, Sm, Gd, U), *J. Less Common Met.* 64 (1979) 221–231, [http://dx.doi.org/10.1016/0022-5088\(79\)90173-5](http://dx.doi.org/10.1016/0022-5088(79)90173-5).
- [38] S.V. Krivovichev, Topological complexity of crystal structures: quantitative approach, *Acta Crystallogr.* A68 (2012) 393–398, <http://dx.doi.org/10.1107/S0108767312012044>; S.V. Krivovichev, Which inorganic structures are the most complex?, *Angew Chem. Int. Ed.* 53 (2014) 654–661, <http://dx.doi.org/10.1002/anie.201304374>.
- [39] S.V. Krivovichev, Private Communication, 2014.
- [40] R.C. Weast, S.M. Shelby, *Handbook of Chemistry and Physics*, 48th ed., The Chemical Rubber Co., Ohio, 1968.
- [41] R.V. Colvin, A. Arajs, Electrical resistivity of polycrystalline gadolinium from 4 to 375 K, *Phys. Status Solidi* 4 (1964) 37–42, <http://dx.doi.org/10.1002/pssb.19640040104>.
- [42] P. Fischer, V. Pomjakushin, L. Keller, A. Daoud-Aladine, W. Sikora, A. Dommann, F. Hüliger, Antiferromagnetic three-sublattice Tb ordering in $\text{Tb}_{14}\text{Ag}_{51}$, *Phys. Rev.* B72 (2005) 134413, <http://dx.doi.org/10.1103/PhysRevB.72.134413>.
- [43] W. Hornfeck, B. Harbrecht, Multiplicative congruential generators, their lattice structure, its relation to lattice–sublattice transformations and applications in crystallography, *Acta Crystallogr.* A65 (2009) 532–542, <http://dx.doi.org/10.1107/S0108767309037088>; W. Hornfeck, Quantitative crystal structure descriptors from multiplicative congruential generators, *Acta Crystallogr.* A68 (2012) 167–180, <http://dx.doi.org/10.1107/S0108767311049853>.

Supplementary material

Table A.7 Standardised atom coordinates [25] and equivalent isotropic displacement parameters [pm^2] for $\text{Gd}_{14}\text{Ag}_{51}$ at 293 K. After free refinement of the site occupation factor of atom Ag5 it was set to 0.5 for final refinement. Standard deviations of the last digit are given in parentheses.

Atom	Wyckoff pos.	Site occup.	x	y	z	U_{equiv}
Ag1	12l	1	0.10451(4)	0.43889(4)	0.33144(5)	118.3(9)
Ag2	12l	1	0.26662(4)	0.07488(4)	0.23686(5)	122.4(9)
Ag3	12l	1	0.49423(4)	0.11557(4)	0.15256(5)	116.4(9)
Ag4	6k	1	0.05884(5)	0.23857(5)	$\frac{1}{2}$	88.2(11)
Ag5	6j	0.495(6)	0.0162(2)	0.13259(15)	0	260(6)
Ag6	4h	1	$\frac{1}{3}$	$\frac{2}{3}$	0.29815(9)	115.9(14)
Ag7	2c	1	$\frac{1}{3}$	$\frac{2}{3}$	0	138(2)
Gd1	6k	1	0.46871(4)	0.14014(4)	$\frac{1}{2}$	93.2(8)
Gd2	6j	1	0.11414(4)	0.39036(5)	0	158.9(10)
Gd3	2e	1	0	0	0.30708(8)	85.3(12)

Table A.8 Anisotropic displacement parameters [pm^2] for $\text{Gd}_{14}\text{Ag}_{51}$ at 293 K. Standard deviations of the last digit are given in parentheses.

Atom	U_{11}	U_{22}	U_{33}	U_{23}	U_{13}	U_{12}
Ag1	121.9(18)	89.8(17)	119.9(19)	15.0(14)	-14.5(15)	35.5(15)
Ag2	116.4(18)	115.4(18)	140(2)	16.2(16)	38.4(16)	61.6(16)
Ag3	91.3(18)	127.2(18)	112(2)	11.1(16)	-3.8(16)	40.4(15)
Ag4	72(2)	89(2)	0.0102(3)	0	0	39(2)
Ag5	573(13)	159(8)	113(8)	0	0	232(8)
Ag6	97.3(18)	97.3(18)	153(3)	0	0	48.7(9)
Ag7	135(3)	135(3)	146(5)	0	0	67.3(14)
Gd1	91.0(16)	93.1(17)	101.3(17)	0	0	50.5(13)
Gd2	123.3(18)	276(2)	92.3(18)	0	0	111.1(18)
Gd3	75.2(16)	75.2(16)	106(3)	0	0	37.6(8)

Table A.9 Selected interatomic distances [pm] for Gd₁₄Ag₅₁ at 293 K. Standard deviations of the last digit are given in parentheses.

Atom 1	Atom 2	Distance	Atom 1	Atom 2	Distance	Atom 1	Atom 2	Distance		
Ag1	Ag4	278.60(8)	Ag3	Ag6	285.93(6)	Ag6	Gd1	310.88(7)		
	Ag3	279.41(8)		Ag7	289.08(5)		Ag7	Ag6	278.35(9)	
	Ag6	290.31(5)		Ag3	299.79(9)			Ag3	289.08(6)	
	Ag2	293.27(6)		Ag1	299.87(6)			Gd2	319.34(8)	
	Ag3	299.87(8)		Gd2	317.10(6)			Gd1	Ag1	309.44(8)
	Ag2	302.35(9)		Gd2	324.10(9)				Ag6	310.88(6)
	Gd1	309.44(8)		Gd2	324.74(9)			Ag6	310.93(6)	
	Gd1	311.04(7)		Gd1	328.97(6)			Ag1	311.04(7)	
	Ag1	314.73(8)		Ag4	Ag4			272.16(11)	Ag1	316.20(8)
	Gd1	316.20(8)			Ag1			278.60(8)	Ag4	318.95(10)
Ag2	Gd2	316.87(6)	Ag2	Ag2	287.10(6)	Ag4		Ag4	323.82(7)	
	Ag5	276.34(13)		Ag2	289.62(7)		Ag3	328.97(6)		
	Ag3	277.21(8)		Gd1	318.95(7)		Ag2	333.70(7)		
	Ag4	287.10(6)		Gd1	323.82(10)		Gd2	Ag5	284.94(19)	
	Ag4	289.62(7)		Gd3	326.36(8)			Ag2	313.60(8)	
	Ag1	293.27(9)		Ag5	Ag5		158.39(24)	Ag1	316.87(6)	
	Ag5	298.76(20)			Ag5		274.34(22)	Ag3	317.10(8)	
	Ag2	301.13(9)		Ag2	276.34(18)		Ag7	319.43(6)		
	Ag1	302.35(7)		Gd2	284.94(19)		Ag3	324.10(9)		
	Gd3	308.18(7)		Ag2	298.76(13)		Ag3	324.74(7)		
Gd2	313.60(6)	Ag5	316.78(31)	Ag2	330.24(6)					
Gd2	330.24(8)	Gd3	327.53(13)	Gd3	Ag2	308.18(5)				
Gd1	333.70(7)	Ag6	Ag7		278.35(9)	Ag4	326.36(8)			
Ag3	Ag2		277.21(8)	Ag3	285.93(7)	Ag5	327.53(15)			
	Ag1	279.41(8)	Ag3	286.03(8)	Gd3	360.21(11)				
	Ag3	284.85(7)	Ag1	290.25(7)						

Table A.10 Standardised atom coordinates [25] and equivalent isotropic displacement parameters [pm²] for Y₁₄Ag₅₁ at 293 K. The occupation factor for Ag5 was set to 0.5. Standard deviations of the last digit are given in parentheses.

Atom	Wyckoff pos.	x	y	z	U_{equiv}
Ag1	12l	0.10422(6)	0.43934(6)	0.33222(7)	99.7(17)
Ag2	12l	0.26576(6)	0.07508(5)	0.23587(7)	117.8(18)
Ag3	12l	0.49359(5)	0.11552(6)	0.15231(6)	97.8(17)
Ag4	6k	0.05831(7)	0.23799(7)	$\frac{1}{2}$	71.2(19)
Ag5	6j	0.0053(3)	0.1279(2)	0	278(9)
Ag6	4h	$\frac{1}{3}$	$\frac{2}{3}$	0.30050(12)	96(2)
Ag7	2c	$\frac{1}{3}$	$\frac{2}{3}$	0	112(3)
Y1	6k	0.46817(8)	0.14010(8)	$\frac{1}{2}$	78(2)
Y2	6j	0.11416(9)	0.39088(10)	0	128(2)
Y3	2e	0	0	0.30832(18)	74(3)

Table A.11 Anisotropic displacement parameters [pm^2] for $\text{Y}_{14}\text{Ag}_{51}$ at 293 K. Standard deviations of the last digit are given in parentheses.

Atom	U_{11}	U_{22}	U_{33}	U_{23}	U_{13}	U_{12}
Ag1	131(3)	94(3)	54(3)	16.3(19)	-11.5(18)	40(2)
Ag2	146(3)	119(3)	99(3)	27.5(19)	61(2)	74(2)
Ag3	100(3)	131(3)	42(3)	10.3(18)	-3.6(17)	43(2)
Ag4	78(3)	95(3)	37(3)	0	0	41(3)
Ag5	710(20)	232(12)	33(9)	0	0	338(13)
Ag6	96(3)	96(3)	95(4)	0	0	48.2(14)
Ag7	126(4)	126(4)	83(6)	0	0	63.1(19)
Y1	103(4)	96(4)	41(4)	0	0	54(3)
Y2	125(4)	237(5)	27(4)	0	0	94(4)
Y3	83(4)	83(4)	54(6)	0	0	41.6(19)

Table A.12 Standardised atom coordinates [25] and equivalent isotropic displacement parameters [pm^2] for $\text{Ce}_{14}\text{Ag}_{51}$ at 293 K. The occupation factor for Ag5 was set to 0.5. Standard deviations of the last digit are given in parentheses.

Atom	Wyckoff pos.	x	y	z	U_{equiv}
Ag1	12l	0.07336(9)	0.26761(9)	0.23968(11)	150(2)
Ag2	12l	0.11499(9)	0.49523(9)	0.15324(11)	158(2)
Ag3	12l	0.33241(9)	0.43754(9)	0.32879(11)	162(2)
Ag4	6k	0.05981(11)	-0.17986(11)	$\frac{1}{2}$	122(3)
Ag5	6j	0.1053(3)	0.1382(3)	0	217(11)
Ag6	4h	$\frac{1}{3}$	$\frac{2}{3}$	0.7104(2)	153(3)
Ag7	2c	$\frac{1}{3}$	$\frac{2}{3}$	0	220(5)
Ce1	6k	0.14074(9)	0.46982(9)	$\frac{1}{2}$	125(2)
Ce2	6j	0.27494(11)	0.38960(13)	0	239(3)
Ce3	2e	0	0	0.30435(19)	118(3)

Table A.13 Anisotropic displacement parameters [pm^2] for $\text{Ce}_{14}\text{Ag}_{51}$ at 293 K. Standard deviations of the last digit are given in parentheses.

Atom	U_{11}	U_{22}	U_{33}	U_{23}	U_{13}	U_{12}
Ag1	169(4)	135(4)	149(4)	15(3)	12(3)	79(3)
Ag2	172(4)	123(4)	151(5)	-3(3)	4(4)	53(3)
Ag3	184(4)	130(4)	165(5)	24(3)	34(3)	74(3)
Ag4	106(5)	117(5)	136(6)	0	0	50(4)
Ag5	251(17)	123(14)	150(16)	0	0	-1(11)
Ag6	144(4)	144(4)	173(8)	0	0	72(2)
Ag7	242(7)	242(7)	175(12)	0	0	121(4)
Ce1	125(4)	122(4)	131(4)	0	0	64(3)
Ce2	247(5)	475(7)	117(5)	0	0	273(6)
Ce3	102(4)	102(4)	150(8)	0	0	51(2)

Table A.14 Standardised atom coordinates [25] and equivalent isotropic displacement parameters [pm^2] for $\text{Tb}_{14}\text{Ag}_{51}$ at 293 K. The occupation factor for Ag5 was set to 0.5. Standard deviations of the last digit are given in parentheses.

Atom	Wyckoff pos.	x	y	z	U_{equiv}
Ag1	12l	0.10429(6)	0.43913(5)	0.33190(7)	122.0(12)
Ag2	12l	0.26642(6)	0.07514(6)	0.23611(8)	132.2(13)
Ag3	12l	0.49401(6)	0.11560(6)	0.15249(7)	117.9(13)
Ag4	6k	0.05860(7)	0.23842(8)	$\frac{1}{2}$	95.4(16)
Ag5	6j	0.0097(3)	0.1300(2)	0	272(9)
Ag6	4h	$\frac{1}{3}$	$\frac{2}{3}$	0.29965(13)	121.0(19)
Ag7	2c	$\frac{1}{3}$	$\frac{2}{3}$	0	137(3)
Tb1	6k	0.46839(5)	0.13998(5)	$\frac{1}{2}$	100.4(11)
Tb2	6j	0.11409(5)	0.39071(6)	0	150.6(13)
Tb3	2e	0	0	0.30759(11)	88.1(16)

Table A.15 Anisotropic displacement parameters [pm^2] for $\text{Tb}_{14}\text{Ag}_{51}$ at 293 K. Standard deviations of the last digit are given in parentheses.

Atom	U_{11}	U_{22}	U_{33}	U_{23}	U_{13}	U_{12}
Ag1	129(3)	96(2)	118(3)	15(2)	-10(2)	38(2)
Ag2	137(3)	126(3)	143(3)	20(2)	47(2)	73(2)
Ag3	102(2)	128(2)	105(3)	11(2)	-2(2)	43(2)
Ag4	86(3)	99(3)	97(4)	0	0	43(3)
Ag5	640(20)	192(12)	85(11)	0	0	283(12)
Ag6	106(3)	106(3)	151(5)	0	0	53.1(13)
Ag7	139(4)	139(4)	132(7)	0	0	69(2)
Tb1	107(2)	106(2)	95(2)	0	0	58.7(18)
Tb2	128(2)	249(3)	85(3)	0	0	102(2)
Tb3	86(2)	86(2)	93(4)	0	0	42.8(11)

3.3.3. Synthesis and characterization of $\text{La}_{11+x}\text{Hg}_{45-x}$ and $\text{RE}_{11}\text{Hg}_{44.5}$ ($\text{RE} = \text{Nd}, \text{Sm}$) as hettotypes of the $\text{Sm}_{11}\text{Cd}_{45}$ structure type

Frank Tambornino, Kuno Schwärzer, Constantin Hoch*

* Corresponding author. Tel.: +49 (0)89 2180 77421; fax: +49 (0)89 2180 77440. E-mail address: constantin.hoch@cup.uni-muenchen.de (C. Hoch).

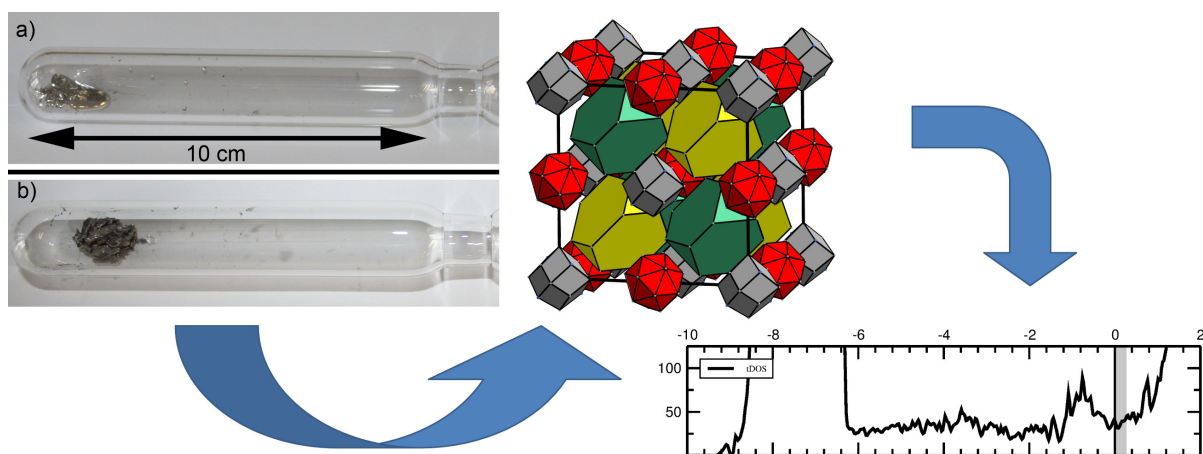
published in: *J. Solid State Chem.*, **242**, 162–169 (2016).

DOI:10.1016/j.jssc.2016.07.001

Reprinted (adapted) with permission from Journal of Solid State Chemistry. Copyright 2016 Elsevier B.V.

Abstract

The mercury-rich amalgams $\text{La}_{11+x}\text{Hg}_{45-x}$ and $\text{RE}_{11}\text{Hg}_{44.5}$ (space group $F\bar{4}3m$ (No. 216), $\text{La}_{11+x}\text{Hg}_{45-x}$: $a = 21.9342(19)$ Å, $\text{RE} = \text{Nd}$: $a = 21.7384(14)$ Å; $\text{RE} = \text{Sm}$: $a = 21.6555(4)$ Å), were synthesized by dissolving the respective rare earth metals in a mercury surplus and subsequently distilling off the excess. The compounds were characterized by single crystal and powder X-ray methods together with *ab-initio* band structure calculations. Both crystal structures deviate significantly and in different ways from their common aristotype, the $\text{Sm}_{11}\text{Cd}_{45}$ structure type. In $\text{La}_{11+x}\text{Hg}_{45-x}$ ($x = 0.7(1)$) two crystallographic sites show mixed occupancy, whereas in $\text{RE}_{11}\text{Hg}_{44.5}$ one of the Hg positions is fully unoccupied. Their band structures exhibit typical broad Hg *d* states at low energies, and a strong mixing of *s* and *p* states indicates a mercury sublattice with high connectivity.



Introduction

The structural chemistry of binary mercury-rich amalgams of less noble metals is versatile. Large unit cells in combination with low symmetry and disorder phenomena lead to structural complexity unexpected for binary compounds. A large number of alkali and alkaline earth metal amalgams are reported, but in comparison relatively little is known about lanthanoid metal amalgams. In contrast to amalgams with lower Hg content and simple structures ($REHg$ [1-3], $REHg_2$ [3, 4] and $REHg_3$ [2, 3, 5]), the structurally complicated mercury-rich amalgams are less understood. In addition to their high structural complexity, structure elucidation of mercury-rich amalgams is further hampered by extreme air and moisture sensitivity and remarkably high absorption effects. In previous work, we reinvestigated the crystal structure of $Eu_{14}Hg_{51}$ on the basis of single crystal data and could improve the previous structure model [6] by including a pronounced and unique defect pattern [7]. This amalgam is one example of a class of Hg-rich amalgams with composition close to $REHg_5$.

A group of amalgams with composition $RE_{11}Hg_{45}$ ($RE = Ce, Nd, Gd, Pr$, also U) [6], close to $REHg_4$, was assigned to the cubic $Sm_{11}Cd_{45}$ structure type (established 1979 by single crystal X-ray diffraction) [8] only on the basis of the respective powder X-ray diffraction patterns. A large number of cadmides – discovered prior to 1979 – with general composition $RE_{11}Cd_{45}$ ($RE = Y, Pr, Nd, Gd, Tb, Dy, Ho, Er, Tm, Lu$) were later on assigned to this structure type, again based on powder diffraction data [9–11]. Early descriptions of disorder phenomena in this structure type were given for $Gd_{9.08}Mg_{45.9}$ [12]. Ternary compounds show particular complexity ($(Ce_{4.726}Y_{4.920}Mg_{1.354})Mg_{43.98}$ and $Ce_{6.9}Y_{12.5}Mg_{92.2}$) [13, 14], but for the respective cadmides and mercurides no reports on disorder phenomena have been given so far.

Previously we have reinvestigated the $Gd_{14}Ag_{51}$ structure type and some of its amalgam representatives [7, 15]. We have found the aristotype structure to be correctly described in higher symmetry and the hettotypes showing lower space group symmetry in combination with individual disorder phenomena. As an analogous situation could be expected for the $Sm_{11}Cd_{45}$ structure family, we found it worthwhile to reinvestigate some of its representatives $RE_{11}Hg_{45}$ ($RE = La, Nd, Sm$). Here we present detailed X-ray structure analyses and the resulting new structure models with disorder phenomena leading to the actual compositions $La_{11+x}Hg_{45-x}$ with $x = 0.7(1)$ and $RE_{11}Hg_{44.5}$ ($RE = Nd, Sm$), respectively. The structures can be regarded as hettotypes of the $Sm_{11}Cd_{45}$ type, crystallizing in the same space group type but with specific mixed occupied atomic positions (La compound) or vacancies (Nd and Sm compound). Band structure calculations help gaining insight into bonding modi, but no electronic reason is found for the disorder phenomena.

Material and methods

Preparation

In an argon-filled glovebox, *RE* (*RE* = La: 1 g, 7.15 mmol, 99.99% metal base, smart elements; *RE* = Nd: 0.5 g, 3.47 mmol, 99.99% metal base, smart elements; *RE* = Sm: 0.5 g, 3.33 mmol, 99.99% metal base, smart elements) were mixed with 10 equivalents of mercury (distilled twice) in a glass ampoule (see Figure 1, total length 22 cm). The closed ampoule was brought to air, evacuated to a pressure below $1 \cdot 10^{-3}$ mbar and then sealed by fusing.

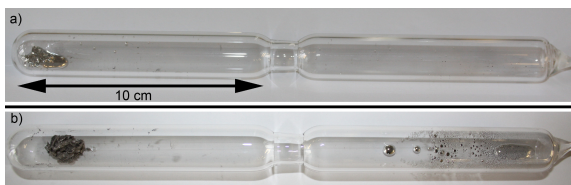


Fig. 1. Borosilicate glass ampoules for the synthesis of Hg-rich amalgams. Above: La and Hg sealed under vacuum, prior to reaction. Below: Product (left) and surplus Hg (right) after the distillation. To isolate the product, the ampoule is separated into two parts by sealing off at the central constriction.

The lower part of the ampoule up to the central constriction was placed in a vertical tube furnace in upright position and heated to ca. 300 ± 1 °C for 12 hours. The boiling mercury reacts with the educt metals to a liquid but viscous amalgam. The surplus mercury condensates at the air-cooled upper part of the ampoule outside the furnace, creating a Hg reflux. After cooling the ampoule to room temperature, furnace and ampoule were turned into a horizontal position and the lower part was heated to ca. 100 ± 1 °C. The surplus mercury was distilled into the cold part, see Figure 1b. The product was separated from the Hg by sealing off the mercury-filled part of the ampoule. This method yields polycrystalline material as well as single crystals and therefore has advantages over the standard technique of heating and tempering stoichiometric educt mixtures. The brittle amalgam crystals showed bright metallic luster, were very sensitive toward air and moisture and therefore handled in a glovebox or under dried paraffin oil.

Structure determination

Single crystal X-ray diffraction of $\text{La}_{11+x}\text{Hg}_{45-x}$

In a glovebox, small sample amounts were put in a petri dish and covered with dried paraffin oil. The sample was brought to air and suitable specimens of irregular shape were isolated and sealed in paraffin-filled glass capillaries ($\varnothing = 0.3$ mm). After centering the crystals on a IPDS1 diffractometer system (Stoe & Cie. GmbH, Darmstadt, Germany) equipped with an imaging plate and graphite-monochromatized Ag- $K\alpha$ radiation and determining the orientation matrix, data collection was performed in φ scan geometry with $\Delta\varphi = 0.8^\circ$. The intensities of the accessible part of the Ewald sphere were collected between 0 and 200.0 ° φ . Data were subsequently corrected for Lorentz, polarization and absorption effects (multiply-scanned symmetry equivalents [16]). Systematic absences (hkl only observed for $h+k$, $h+l$, $k+l$ and consequences on $0kl$, $h0l$ and $00l$ and on $h00$, $0k0$ and $00l$) together with Wilson statistics indicated face cen-

tering and absence of centrosymmetry, suggesting the possible space groups $F23$ (No. 196), $F432$ (No. 209) and $F43m$ (No. 216). Structure solution with direct methods succeeded in space group $F23$ and yielded all atom positions. Atom assignment was carried out by analysis of the thermal displacement parameters as indicator for heavier (Hg) or lighter (La) atoms. After anisotropic treatment of all thermal displacement parameters the atomic positions were checked for mixed occupancy. Only two positions (La10/Hg10, 0.23(10):0.77(10) and La13/Hg13, 0.49(18):0.51(18), see Table 2) showed significant mixed occupancy and were assumed to be overall fully occupied. Checking for additional symmetry (Platon package [20]) revealed the final space group $F\bar{4}3m$. The high $R_{\text{int}} = 0.1533$ is caused by a very thin layer of elemental mercury covering the crystal. Liquid mercury is a very efficient X-ray absorber, even in thin layers and hence influences reflection statistics, not in all cases mended by absorption correction algorithms. Further details on crystal structure, data collection, structure solution and refinement are compiled in Table 1, fractional atomic coordinates in standardized setting [21] and isotropic displacement parameters are compiled in Table 2, anisotropic displacement parameters for all atoms can be found in Table A5. Further details on the crystal structure investigations are available from Fachinformationszentrum Karlsruhe, 76344 Eggenstein-Leopoldshafen, Germany (fax. +49 (0)7247 808 666; e-mail: crysdata@fiz-karlsruhe.de; http://www.fiz-informationsdienste.de/en/DB/icsd/depot_anforderung.html) on quoting the deposition number CSD-431022.

Powder X-ray diffraction

Samples for powder diffraction studies on $\text{Nd}_{11}\text{Hg}_{44.5}$ and $\text{Sm}_{11}\text{Hg}_{44.5}$ were prepared in a glovebox by grinding the samples and sealing the powder in glass capillaries ($\varnothing = 0.3$ mm). To account for the high absorption coefficients, the sample was optically diluted with diamond powder, and data were collected in multiple subsequently added ranges between 2.0 and $70^\circ 2\theta$.

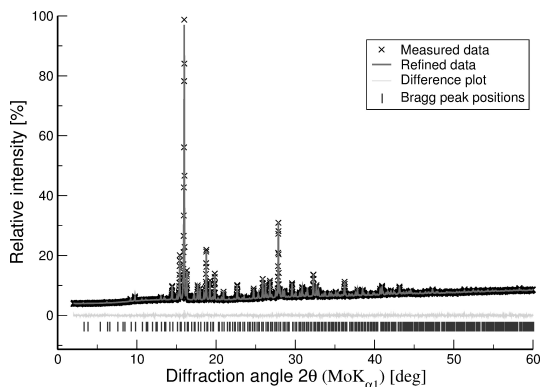


Fig. 2. Rietveld refinement of $\text{Sm}_{11}\text{Hg}_{44.5}$. Final refinement parameters are compiled in Table A4.

ratio was low due to high symmetry, common values for B_{iso} were refined for all Hg and all RE atoms. This allowed to check each atom individually for underoccupation by refining the respective occupation parameters. With high significance all atoms showed full

Data collection was performed on a diffractometer system with position-sensitive linear detector (Stadi P, Stoe & Cie. GmbH, Darmstadt, Germany, MYTHEN 2K detector) in Ge(111)-monochromatized Mo- $K\alpha 1$ radiation in Debye-Scherrer geometry. Rietveld refinements were performed with a fundamental parameter approach [17, 18], and a double-Voigt approach to compensate size-strain effects. A shifted Chebychev function was applied for background modelling. As starting values the single crystal structure model of $\text{La}_{11+x}\text{Hg}_{45-x}$ was applied after replacing La with either Nd or Sm and avoiding mixed positions. On all positions x , y , z were freely refined. As the data/parameter

Table 1: Crystallographic data and details on data collection, structure solution and refinement of $\text{La}_{11+x}\text{Hg}_{45-x}$.

Empirical sum formula	$\text{La}_{11+x}\text{Hg}_{45-x}$, $x = 0.7(1)$
Crystal system	cubic
Space group	$F\bar{4}3m$ (No. 216)
Lattice parameters (\AA , \AA^3)	$a = 21.934(2)$ $V = 10553(3)$
Formula units Z	8
Calculated density ($\text{g}\cdot\text{cm}^{-3}$)	13.231
Absorption coefficient (mm^{-1})	75.044
Radiation, wavelength (\AA)	Ag- $K\alpha$, 0.56086
Diffractometer	IPDS 1 (Stoe & Cie, Darmstadt, Germany)
Data collection mode	φ -Scans, $0^\circ \leq \varphi \leq 200^\circ$, $\Delta\varphi = 0.8^\circ$
Corrections	Lorentz, polarization, absorption [16]
Transmission factors T_{\min}/T_{\max}	0.005 / 0.031
Number of l.s. parameters	70
Number of collected data	31194
Number of unique data	1010
Number of unique data with $I \geq 2\sigma(I)$	808
R_{int}/R_σ	0.1533 / 0.0421
Data range	$-33 \leq h \leq 32$, ($2\theta_{\max} = 49.8^\circ$) $-33 \leq k, l \leq 33$
Structure solution	direct methods [19]
Structure refinement	full matrix least-squares on F^2 [19]
$R1$ ($I \geq 2\sigma(I)$)/ $R1$ (all data)	0.0428 / 0.0617
$wR2$ ($I \geq 2\sigma(I)$)/ $wR2$ (all data)	0.1174 / 0.1251
Residual electron density min/max ($\text{e}^- \cdot \text{\AA}^{-3}$)	-3.694/5.582
Extinction coefficient	0.0000072(15)

occupation. However, the thermal displacement parameter for Hg13 on 0,0,0 appeared to be unreasonably large ($>20 \text{ pm}^2$) during free refinement. After fixing to 2 pm^2 the occupation factor was refined freely and it became clear that this position is vacant. The atom was excluded from the list and a difference Fourier map (see Fig. A6) shows no residual electron density at this position. As a structural consequence, the neighbouring atom Hg8 relaxes toward this vacancy and thus gives further evidence for an actual unoccupied position as the shortened interatomic distances prohibit occupation ($d_{(0,0,0)\text{-Hg8}} = 2.2066(7)\text{\AA}$), see inset of Figure 4. A chemical analysis via ICP-AAS or EDX/WDX is unhelpful to prove the lower Hg content in $\text{RE}_{11}\text{Hg}_{44.5}$, as the powder may contain some Hg metal sticking to the surface of the crystallites, and the effect amounts to a difference of only 1.1 at.-% Hg in comparison with a structure with fully occupied position of Hg13.

Selected details on the results of the refinement are given in Table A4 and Figure 2. The atomic coordinates together with Wyckoff numbers and isotropic thermal displacement parameters U_{ij} are compiled in Tables A6 and A7. Further details can be obtained from Fachinformationszentrum Karlsruhe, 76344 Eggenstein- Leopoldshafen, Germany (fax. +49 (0)7247 808 666; e-mail: crysdata@fiz-karlsruhe.de;http://www.fiz-

Table 2: Standardized fractional atomic coordinates [21], Wyckoff numbers, equivalent isotropic displacement parameters (\AA^2) and site occupation factors as result of a single crystal structure refinement of $\text{La}_{11+x}\text{Hg}_{45-x}$. U_{eq} is defined as $\frac{1}{3}$ of the trace of the orthogonalized U_{ij} tensor. Standard deviations in units of the last digit are given in parentheses.

Atom	Wyckoff site	x	y	z	U_{eq}	s.o.f
Hg1	48h	0.04581(6)	x	0.64056(8)	0.0373(5)	1
La1	48h	0.07623(13)	x	0.26411(15)	0.0356(6)	1
Hg2	48h	0.07671(6)	x	0.76178(7)	0.0257(3)	1
Hg3	48h	0.16475(8)	x	0.01589(12)	0.0430(5)	1
Hg4	48h	0.18753(6)	x	0.50893(9)	0.0312(4)	1
Hg5	48h	0.20458(6)	x	0.89269(11)	0.0351(4)	1
Hg6	24g	0.09583(14)	$\frac{1}{4}$	$\frac{1}{4}$	0.0388(6)	1
Hg7	24f	0.16275(12)	0	0	0.0291(5)	1
Hg8	16e	0.0761(2)	x	x	0.0541(10)	1
Hg9	16e	0.16150(9)	x	x	0.0322(6)	1
Hg10	16e	0.33370(11)	x	x	0.046(2)	0.77(10)
La10	16e	0.33370(11)	x	x	0.046(2)	0.23(10)
Hg11	16e	0.41279(7)	x	x	0.0275(5)	1
La2	16e	0.65678(11)	x	x	0.0212(7)	1
La3	16e	0.91140(11)	x	x	0.0224(7)	1
Hg12	4d	$\frac{3}{4}$	$\frac{3}{4}$	$\frac{3}{4}$	0.0323(12)	1
La4	4c	$\frac{1}{4}$	$\frac{1}{4}$	$\frac{1}{4}$	0.0196(13)	1
La5	4b	$\frac{1}{2}$	$\frac{1}{2}$	$\frac{1}{2}$	0.0190(13)	1
Hg13	4a	0	0	0	0.049(4)	0.5(2)
La13	4a	0	0	0	0.049(4)	0.5(2)

informationsdienste.de /en/DB/icsd/depot_anforderung.html) on quoting the deposition numbers CSD-431027 (Sm compound) and CSD-431028 (Nd compound).

Band structure calculations

DFT calculations of the electronic band structure were performed for the hypothetical fully ordered structure model $\text{La}_{11}\text{Hg}_{45}$ with the program package Wien2k [23], applying the FP-LAPW method. Lattice parameters and atomic positions were used as the results of single crystal analysis, see Tables 1 and 2. The exchange correlation was taken account of by the generalized gradient approximation, GGA [24], and muffin-tin radii were set to 132.29 pm (2.5 a. u., $R_{\text{mt}} \cdot K_{\text{max}} = 8$) for all atoms. The cut-off energy was set to -6 Ry, and 343 k-points of the Brillouin zone (20 thereof in the irreducible wedge of the Brillouin zone) were calculated in a 7x7x7 Monkhorst-Pack grid. K-meshes with higher density would be favourable with respect to higher resolution. Due to the high calculation power needed for large structures with mixed occupation we were not able to perform larger calculations within reasonable times with our means. Handling of the mixed positions would have to be accounted for by modeling superstructures with reduced symmetry and ordered positions. However, this was not practicable with our means for $\text{La}_{11+x}\text{Hg}_{45-x}$, as the crystal structure exhibits 448 atoms per unit cell. Therefore we decided to calculate the electronic structure based on a model without mixed positions and assumed all mixed positions to be fully occupied by Hg (Hg/La10 and HgLa/13).

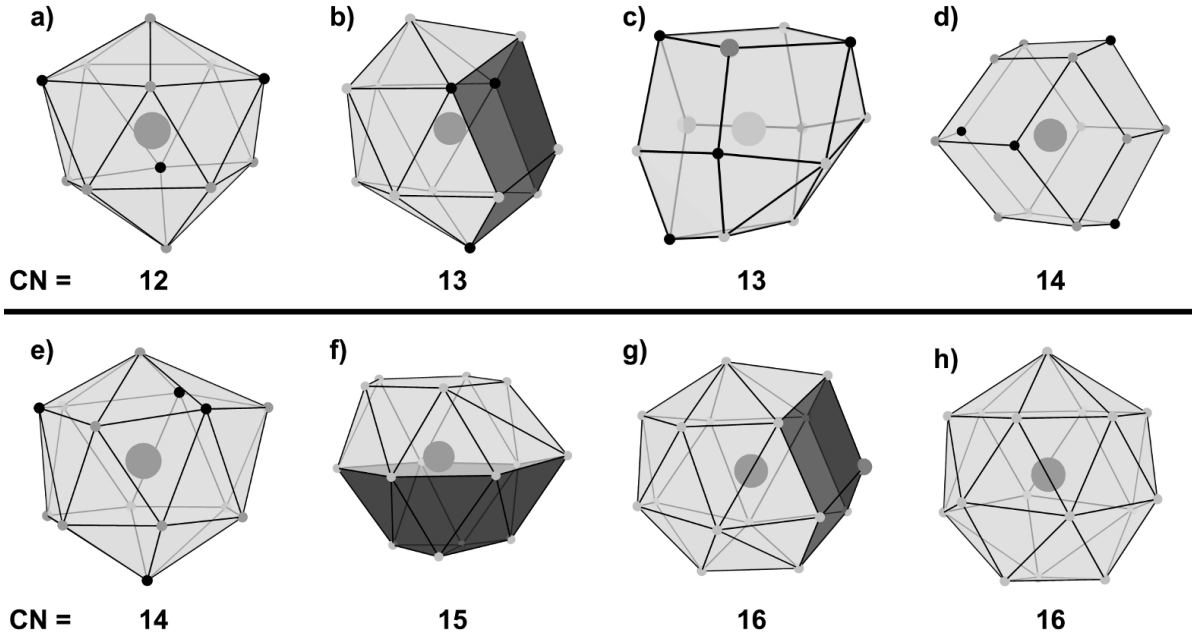


Fig. 3. Representative coordination polyhedra for $\text{La}_{11+x}\text{Hg}_{45-x}$ around a) Hg1, b) Hg3, c) Hg6, d) Hg8, e) Hg11, f) La1, g) La3, h) La2. Small black spheres: La atoms, small grey spheres: Hg atoms, medium sized grey spheres: mixed occupancy La/Hg. The full set of coordination polyhedra for all atoms can be found in Table 3.

Results and discussion

Crystal structure description

$\text{La}_{11+x}\text{Hg}_{45-x}$ crystallizes in the cubic system with space group $F\bar{4}3m$ (No. 216, $a = 21.9342(19)$ Å). 17 independent crystallographic sites build the structure (5 La, 12 Hg), of which two Hg sites show mixed occupancy with La.

The crystal structure of $\text{La}_{11+x}\text{Hg}_{45-x}$ can be built from eight different polyhedra coordinating the individual atomic sites. Describing the structure via coordination polyhedra of individual atoms emphasizes the ionic picture of a highly polar intermetallic phase in the sense of $[\text{La}^{\delta+}]_{11+x}[\text{Hg}^{\delta-}]_{45-x}$, where the lanthanum cations are coordinated only by mercury anions (see Figure 3f-h). The Hg atoms (3a-e) are coordinated by both La and Hg atoms, according to the sum formula, and La atoms show a clear tendency to avoid direct contacts due to the Coulomb repulsion of $\text{La}^{\delta+}$ cations. The coordination polyhedra are shown by representative examples in Figure 3. Coordination numbers for La are 14–16, for Hg they range from 12 to 14. Icosahedra and rhombic dodecahedra are prevailing with a total number of eight (see Table 3 and Figure 3a,b). Hg often shows icosahedric coordination in Hg-rich amalgams, as can also be seen here for Hg1,2,4,5. Hg9,10,13 and La4 show rhombic dodecahedral coordination. Two further polyhedra (around Hg6,7) can be derived from a rhombic dodecahedron by removing one vertex and thus decreasing the number of coordinating atoms to 13 (see Figure 3c). Five Frank-Kasper polyhedra with coordination number 14 (bicapped hexagonal antiprism, see Figure 3e) and coordination number 16 (capped truncated tetrahedron, see 3h) coor-

dinate the atomic sites of Hg8,11,12 and La2,5, respectively. Two less common polyhedra form around Hg3 and La3 which may be described as "Centaur"-like polyhedra. (Here we adapt the term usually applied to a polyhedron consisting of half a cube and half an icosahedron, in analogy to the mythical hybrid creature of horse and man. [25, 26] In our cases the two halves of the "Centaur"-like polyhedra are derived from a rhombic dodecahedron and a Frank-Kasper polyhedron.) The coordination polyhedron around Hg3 can be described as a Centaur-like polyhedron consisting of parts of a rhombic dodecahedron (see the three dark grey rhombic faces in Figure 3b) and of an icosahedron (16 light grey triangular faces, $\frac{4}{5}$ of an icosahedron). La3 is surrounded by another type of Centaur-like polyhedron where rhombic faces (dark grey in Figure 3g) are combined with 22 triangular faces (light grey, $\frac{9}{10}$ of a Frank-Kasper polyhedron), resulting in coordination number 16. A special polyhedron with coordination number 15 surrounds La1. It is best described as conjunction of two cupolae with a common sixfold basal plane. One cupola displays a five-membered (light grey in Figure 3f), the other cupola a four-membered cap (dark grey). Combination of these different polyhedra leads to a complicated structure description as all of them will interpenetrate.

In an alternative picture, the topology of the atomic arrangement in the crystal structure of $\text{La}_{11+x}\text{Hg}_{45-x}$ can be described by augmenting the most special positions of this highly symmetric structure by their respective environment, starting from the coordination polyhedra above and adding concentric next-neighbor polyhedra [22]. The atomic positions with highest site symmetry ($\bar{4}3m$) are La/Hg13 with Wyckoff site 4a (see Table 2), La5 (4b), La4 (4c) and Hg12 (4d). The mixed occupied site

Table 3: Compilation of the coordination polyhedra in $\text{La}_{11+x}\text{Hg}_{45-x}$. Representative examples are shown in Figure 3.

polyhedron	CN	centering atoms
icosahedron	12	Hg1, Hg2, Hg4, Hg5
mono-truncated rhombic dodecahedron	13	Hg6, Hg7
Centaur 1	13	Hg3
rhombic dodecahedron	14	Hg9, Hg10, Hg13, La4
bicapped hexagonal antiprism	14	Hg8, Hg11
xenomorphic bicupola	15	La1
Centaur 2	16	La3
Frank-Kasper	16	Hg12, La2, La5

La/Hg13 is coordinated by a slightly distorted rhombic dodecahedron (La and Hg atoms occupying the non-equivalent vertices). These dodecahedra are arranged in the unit cell in the topology of a cubic closest packing, see Figure 4 (left). All octahedral voids in this fcc motif are filled by regular Frank-Kasper polyhedra with 16 vertices (4 Hg11, 12 Hg1) around La5. Half of the tetrahedral voids is occupied by La4, centering a slightly distorted rhombic dodecahedron (4 La10/Hg10 with mixed occupancy, 4 Hg9 and 4 Hg6). This is further coordinated by a cuboctahedron (12 La1) interlaced with an additional truncated tetrahedron (12 Hg3, see Figure 4c). The second half of the tetrahedral voids is occupied by Hg12, surrounded by tetra-capped truncated tetrahedron (Frank-Kasper polyhedron with CN = 16 from 4 La2 and 12 Hg5), further surrounded by a cuboctahedron (12 Hg2) interlaced with an additional truncated tetrahedron (12 Hg4, see Figure 4d). Thus, the most special atomic positions and their first and next coordinations build the motif a hierarchical variant of the Fe_3Al structure type with rhombic

dodecahedra and Frank-Kasper polyhedra on the octahedrally coordinated and truncated tetrahedra on the tetrahedrally coordinated positions.

$\text{Nd}_{11}\text{Hg}_{44.5}$ and $\text{Sm}_{11}\text{Hg}_{44.5}$ also crystallize in the cubic system in the same space group type $F\bar{4}3m$ (No. 216, Nd compound: $a = 21.7384(14)$ Å, and Sm compound: $a = 21.6555(4)$ Å). There are only 16 independent crystallographic sites (5 RE , 11 Hg), none of which show mixed or reduced occupancy. The structures deviate from the $\text{La}_{11+x}\text{Hg}_{45-x}$ structure with regard to two aspects: (1) The position of Hg13 (0,0,0) in $\text{La}_{11+x}\text{Hg}_{45-x}$ is vacant in $RE_{11}\text{Hg}_{44.5}$, leading to a considerable relaxation of the surrounding rhombic dodecahedron which collapses toward a tetrahedral entity (4 Hg8, see Figure 4 insert), and (2) no atomic site in $RE_{11}\text{Hg}_{44.5}$ shows any significant mixed occupancy. However, as displacement factors and site occupation factors tend to correlate during Rietveld refinement, mixed occupancy can not entirely be excluded. The electron density map for $RE_{11}\text{Hg}_{44.5}$ (see Figure A6 in the Supplemental Material) supports this finding and shows sharp electron density maps for all atoms, no electron density at (0,0,0) and the relaxation of Hg8 in its direct vicinity.

$\text{Nd}_{11}\text{Hg}_{45}$ and $\text{Sm}_{11}\text{Hg}_{45}$ are isotypic and can be regarded, together with $\text{La}_{11+x}\text{Hg}_{45-x}$, as hettotypes of the $\text{Sm}_{11}\text{Cd}_{45}$ structure type, however, all compounds crystallize with the same space group $F\bar{4}3m$ (No. 216). The differences in the crystal structure are not due to symmetry reduction but disorder phenomena like mixed occupancy and voids. This is on the one hand an analogy but also a distinct difference to the aristotype $\text{Gd}_{14}\text{Ag}_{51}$ and its hettotype amalgam structures, e.g. $\text{Eu}_{10}\text{Hg}_{55}$ [7]. The aristotype space group symmetry $P6/m$ is reduced to $P\bar{6}$ and a disorder in the aristotype (half occupied Ag positions in a hexagon) is ordered (fully occupied Hg positions in a triangle). At the same time new disorder phenomena comparable to the mixed occupancies described above is introduced in the hettotypes.

Aspects of chemical bonding

The band structure of $\text{La}_{11}\text{Hg}_{45}$, the hypothetical structure with fully ordered occupation of all positions, has been calculated with the full-potential linearized augmented plane wave (FP-LAPW) method implemented in the WIEN2k code [23]. The results are summarized as total density of states (tDOS) for the whole structure and partial density of states (pDOS) for each crystallographically independent position (see Figure 5). The grey shaded area corresponds to the electron count of the hypothetical phase with $\text{La}_{11+x}\text{Hg}_{45-x}$ with $x = 0-1$. We assume that the overall features of the DOS only marginally change within this composition range, merely the Fermi level is adjusted to account for a different electron count in the unit cell.

The tDOS shows $\text{La}_{11}\text{Hg}_{45}$ to be metallic with no (pseudo) band gaps or other distinct features near the Fermi level. Broad Hg d levels between -9 and -6 eV indicate strong binding interactions of the Hg atoms forming a $[\text{Hg}]^{\delta-}$ sublattice, a situation well known from other Hg-rich amalgams [27]. The electronic states of the La atoms are scattered leading to narrow unpronounced states in this range. From -6 eV up to the Fermi level, s and p states of mainly Hg atoms mix and spread over the whole range. Above -1 eV La states become significantly more pronounced which can also be seen in the tDOS. However, due to the low absolute number of La atoms in comparison to Hg atoms, the

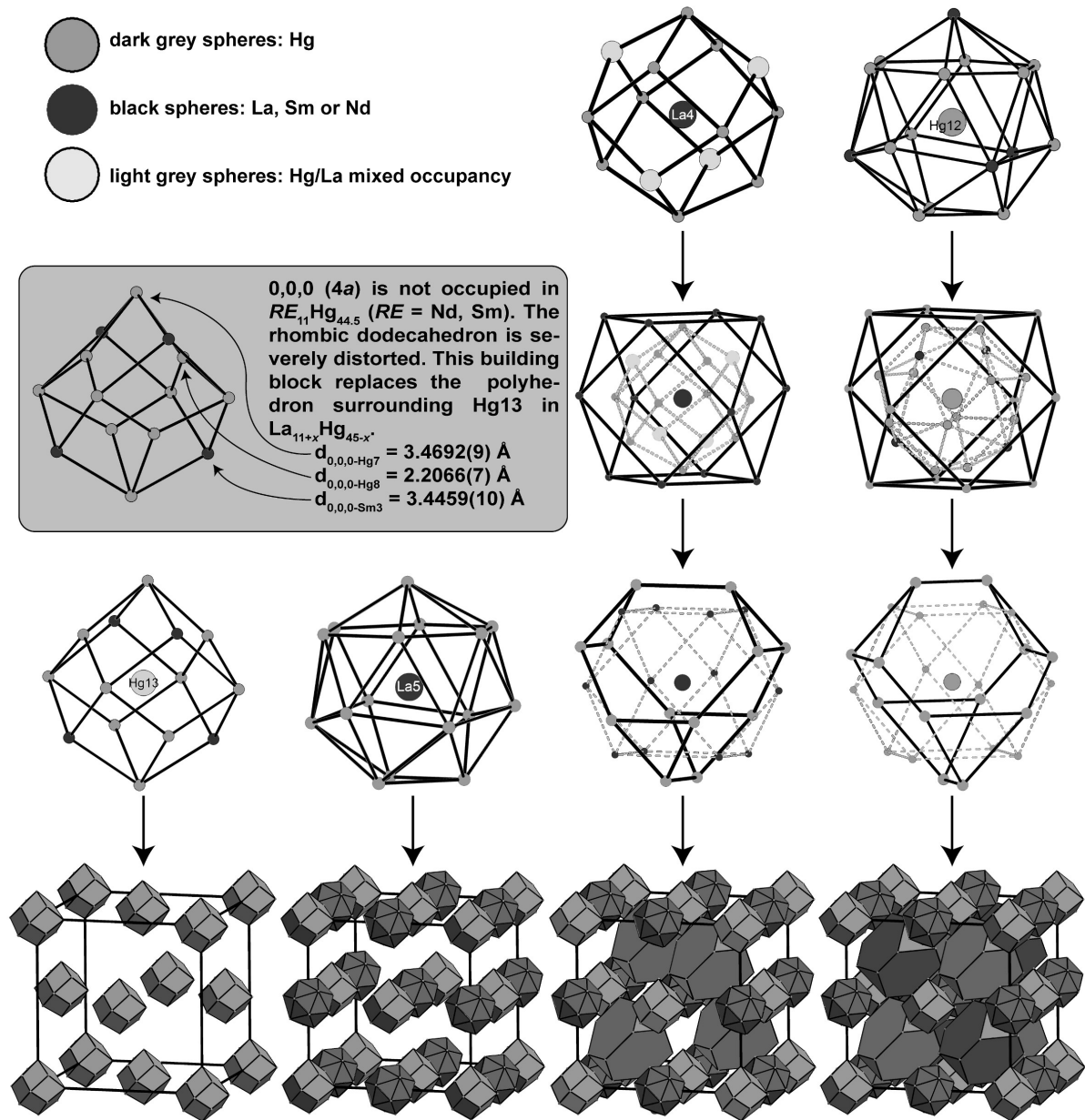


Fig. 4. Topologic relation of the $La_{11+x}Hg_{45-x}$ and $RE_{11}Hg_{44.5}$ ($RE = Nd, Sm$) crystal structures to the Fe_3Al structure type in the sense of hierarchical variants. The insert shows the coordination of the void at $(0,0,0)$ in $RE_{11}Hg_{44.5}$ ($RE = Nd, Sm$) and the resulting relaxation of its direct surrounding, leading to a collapsed rhombic dodecahedron. See text for details.

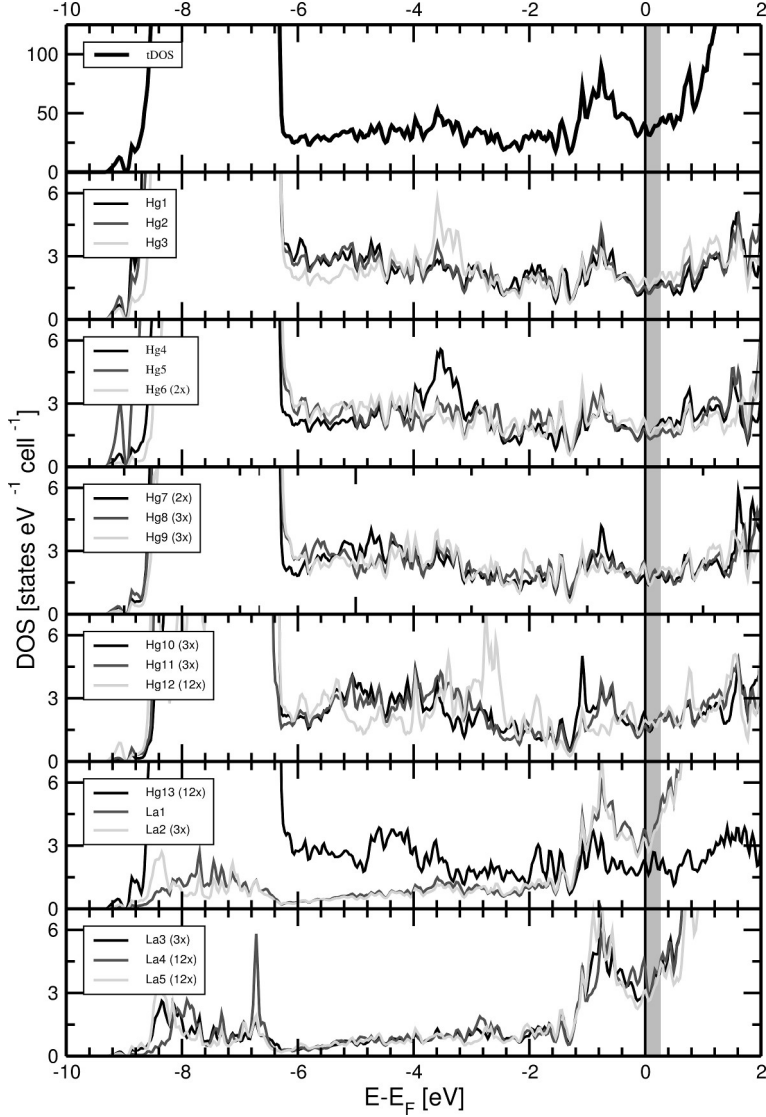


Fig. 5. Total density of states (tDOS) and partial density of states calculated for $\text{La}_{11}\text{Hg}_{45}$. E_F (solid vertical line) is set as the energy reference at 0 eV. The grey shaded area corresponds to the electron count in the hypothetical phase width $\text{La}_{11+x}\text{Hg}_{45-x}$ with $x = 0-1$.

tDOS is still largely dominated by Hg states. At the current level the electronic band structure does not account for the mixed occupancy of two crystallographic sites. No pronounced pseudogaps are found within the grey shaded area which corresponds to the electron count in the hypothetical phase width $\text{La}_{11+x}\text{Hg}_{45-x}$ with $x = 0-1$. We have calculated the Bader charges for all atomic positions (see Table A8), and it is obvious that all La atoms have an equally distributed positive charge. Also the negative charge on the Hg atoms does not differ widely, ranging from -0.26 to -0.53. The atom positions Hg10 and Hg13 which show mixed occupation appear inconspicuous. The equal charge distribution and the partial but considerable electron transfer has previously been observed for other amalgams of less noble metals, e. g. KHg_6 [28]. This homogeneous delocalisation of the negative partial charge over the Hg substructure is the consequence of high electronegativity difference and the endergonic electron affinity of Hg.

Conclusions

Hg-rich amalgams of the less noble metals show interesting structural diversity. As mercury is the only noble metal with a positive electron affinity and hence no pronounced tendency toward anion formation, the electron transfer induced by the high electronegativity difference is always incomplete. The polarity of the metal-metal bonding in these amalgams is highest for the Hg-rich phases as a larger Hg sublattice can delocalize the negative partial charge more efficiently. Intermetallic systems with high polarity can show interesting electric behavior due to strong scattering of the conduction electrons at the Coulombic potentials located at the positively polarized atoms of the less noble metals. Especially low Ioffe-Regel limit resistances often are the consequence. Synthesis and crystallographic characterization of the Hg-richest amalgams is complicated, and knowledge on these phases is scarce. The amalgams connected with the $\text{Sm}_{11}\text{Cd}_{45}$ structure type show interesting features with respect to polar structure motifs ($\text{Hg}^{\delta-}$ anions form discrete coordination polyhedra around $\text{La}^{\delta+}$ cations) and at the same time structural motifs common to classic intermetallic phases (Frank-Kasper polyhedra, high packing density). However, the band structure clearly shows all features of good metallic behavior. There is a large family of amalgams of less noble metals with compositions MHg_x with $4 \leq x \leq 5$. They can be derived from the $\text{Gd}_{14}\text{Ag}_{51}$ structure type or, as in the presented cases, from the $\text{Sm}_{11}\text{Cd}_{45}$ structure type. The individual representatives $A_{11-x}\text{Hg}_{55-x}$ ($A = \text{Na}, \text{Ca}, \text{Sr}, \text{Eu}$) and $RE_{11(+x)}\text{Hg}_{45-x}$ ($RE = \text{La}, \text{Nd}, \text{Sm}$) differ in their respective disorder phenomena. The mixed occupation patterns always occur in a singular way, and hitherto no electronic reasons have been found. For the most complicated structure of $\text{Na}_{11-x}\text{Hg}_{55-x}$ a detailed topological evaluation [29] points toward geometric reasons for the observed disorder phenomena, however, this has so far not been performed for the other representatives. Future work will reveal whether geometric reasons can be identified in all known cases or whether configurational entropic effects may be attributed for the observed disorder phenomena. The latter would imply a low probability to find a representative of the structure types in question with no disorder at all. As a large number of lanthanides and actinides were reported to form similar amalgams of composition $RE_{11}\text{Hg}_{45}$ ($RE = \text{Ce}, \text{Gd}, \text{Pr}, \text{U}$) but mixed occupancies or other complications were never reported, we strongly encourage to look further into the matter of this interesting part of intermetallic chemistry.

Acknowledgements

We thank Prof. Dr. Wolfgang Schnick for his longstanding and generous financial support.

References

- [1] A. Iandelli, A. Palenzona, Atomic size of rare earths in intermetallic compounds. MX compounds of CsCl type *J. Less Common Met.* 9 (1965), 1-6. DOI: 10.1016/0022-5088(65)90028-7
- [2] H. R. Kirchmayr Gitterkonstanten und Strukturen der Verbindungen DyHg, HoHg, ErHg; DyHg₂, HoHg₂, ErHg₂; DyHg₃, HoHg₃ und ErHg₃ *Monatsh. Chem.* 95 (1964), 1667-1670. DOI: 10.1007/BF00901725
- [3] A. Iandelli, A. Palenzona, Crystal chemistry of intermetallic compounds In: *Handbook on the Physics and Chemistry of Rare Earths*, Vol.2, Chapter 13, Elsevier B. V. (1979), pp. 1-54. DOI: 10.1016/S0168-1273(79)02004-3
- [4] A. Iandelli, A. Palenzona On the occurrence of the MX₂ phases of the rare earths with the IB, IIB and IIIB group elements and their crystal structures *J. Less Common Met.* 15 (1968), 273-284. DOI: 10.1016/0022-5088(68)90186-0
- [5] A. Palenzona MX₃ intermetallic phase of the rare earths with Hg, In, Tl, Pb *J. Less Common Met.* (1966), 290-292. DOI: 10.1016/0022-5088(66)90031-2
- [6] F. Merlo, M. L. Fornasini, Crystal structure of the R₁₁Hg₄₅ compounds (R = La, Ce, Pr, Nd, Sm, Gd, U), *J. Less Common Met.* 64 (1979), 221-231. DOI: 10.1016/0022-5088(79)90173-5
- [7] F. Tambornino, C. Hoch, The mercury-richest europium amalgam Eu₁₀Hg₅₅, *Z. Anorg. Allg. Chem.* 641 (2015), 537-542. DOI: 10.1002/zaac.201400561
- [8] M. L. Fornasini, B. Chabot, E. Parthé, The crystal structure of Sm₁₁Cd₄₅ with γ -brass and α -Mn clusters, *Acta Crystallogr. B*34 (1978), 2093-2099. DOI: 10.1107/S0567740878007505
- [9] R. Ryba, P. K. Kejriwal, R. Elmendorf, The partial yttrium-cadmium phase diagram, *J. Less Common Met.* 18 (1969), 419-422. DOI: 10.1016/0022-5088(69)90011-3
- [10] G. Bruzzone, M. L. Fornasini, F. Merlo, Rare-earth intermediate phases with cadmium, *J. Less Common Met.* 30 (1973), 361-375. DOI: 10.1016/0022-5088(73)90147-1
- [11] G. Bruzzone, M. L. Fornasini, F. Merlo, The gadolinium-cadmium system, *J. Less Common Met.* 25 (1971), 295-301. DOI: 10.1016/0022-5088(71)90153-6
- [12] M. L. Fornasini, P. Manfrinetti, K. A. Gschneidner Jr, GdMg₅: a Complex Structure with a Large Cubic Cell, *Acta Crystallogr. C*42 (1986), 138-141. DOI: 10.1107/S0108270186097019
- [13] H. Flandorfer, A. Kostikas, C. Godart, M. Giovannini, R. Ferro, A. Saccone, P. Rogl, On the magnetic and valence properties of Ce-Mg-Y compounds, *J. Alloys Compd.* 240 (1996), 116-123. DOI: 10.1016/0925-8388(96)02244-X
- [14] T.-S. You, Y. Jung, M.-K. Han, G. J. Miller, The Y_{5-x}Mg_{24+x} (1.08(4) ≤ x ≤ 1.30(1)) series and a ternary derivative Ce_{6.9}Y_{12.5(7)}Mg_{92.2}: A comparison of their crystal and electronic structures, *J. Solid State Chem.* 204 (2013), 170-177. DOI: 10.1016/j.jssc.2013.05.037
- [15] F. Tambornino, J. Sappl, C. Hoch, The Gd₁₄Ag₅₁ structure type and its relation to some complex amalgam structures, *J. Alloys Compd.* 618 (2015), 326-335. DOI: 10.1016/j.jallcom.2014.08.017
- [16] R. H. Blessing, An empirical correction for absorption anisotropy, *Acta Crystallogr. A*51 (1995), 33-38. DOI: 10.1107/S0108767394005726
- [17] H. M. Rietveld, A profile refinement method for nuclear and magnetic structures, *J. Appl. Cryst.* 2 (1969), 65-71. DOI: 10.1107/S0021889869006558
- [18] A. Coelho, *Topas Academic Version 4.1*, Coelho Software, Brisbane, 2007.

- [19] G. M. Sheldrick, A short history of SHELX, *Acta Crystallogr.* A64 (2007), 112-122. DOI: 10.1107/S0108767307043930
- [20] A. L. Spek, Structure validation in chemical crystallography, *Acta Crystallogr.* D65 (2009), 148-155. DOI: 10.1107/S090744490804362X
- [21] L. M. Gelato, E. Parthé, Structure Tidy - a computer program to standardize crystal structure data, *J. Appl. Cryst.* 20 (1987), 139-143. DOI: 10.1107/S0021889887086965
- [22] M.L. Fornasini, B. Chabot and E. Parthé, The crystal structure of $\text{Sm}_{11}\text{Cd}_{45}$ with γ -brass and α -Mn clusters, *Acta Crystallogr. B* 34 (1978) 2093-2099. DOI: 10.1107/S0567740878007505.
- [23] P. Blaha, K. Schwarz, G. K. H. Madsen, D. Kvasnicka, and J. Luitz, WIEN2k: An augmented plane wave + local orbitals program for calculating crystal properties, Technische Universität Wien, Austria (2001).
- [24] J. P. Perdew, K. Burke, and M. Ernzerhof, Generalized gradient approximation made simple *Phys. Rev. Lett.* 77 (1996), 3865. DOI: 10.1103/PhysRevLett.77.3865
- [25] D. Raschke, Zur Untersuchung fehlgeordneter Strukturen mit dem optischen Diffraktometer OPDIRA und über die Struktur des quaternären Fluoridchlorids $\text{Ba}_9\text{Cd}_{13}\text{F}_{43}\text{Cl}$, PhD Thesis, University of Stuttgart, Germany 1985.
- [26] S. Lidin and A.-K. Larsson, A structural description of β - K_2SO_4 , *Acta Chem. Scand.* 45 (1991), 856-859. DOI: 10.3891/acta.chem.scand.45-0856
- [27] M. Wendorff and C. Röhr, The new barium mercuride BaHg_6 and ternary indium and gallium derivatives, *J. Alloys Compd.* 546 (2013), 320-328. DOI: 10.1016/j.jallcom.2012.07.101.
- [28] F. Tambornino, C. Hoch, Bad metal behaviour in the new Hg-rich amalgam KHg_6 with polar metallic bonding, *J. Alloys Compd.* 618 (2015), 299-304. DOI: 10.1016/j.jallcom.2014.08.173
- [29] W. Hornfeck, C. Hoch, Structural chemistry and number theory amalgamized: crystal structure of $\text{Na}_{11}\text{Hg}_{52}$, *Acta Crystallogr.* B71 (2015), 752-767. DOI: 10.1107/S205252061501673X

Supplementary Information

Table A5: Coefficients U_{ij} (\AA^2) of the anisotropic atomic displacement parameters for $\text{La}_{11+x}\text{Hg}_{45-x}$. U_{ij} is defined as $\exp\{-2\pi^2[U_{11}(ha^*)^2+\dots+2U_{12}hka^*b^*]\}$. Standard deviations in units of the last digit are given in parentheses.

Atom	U_{11}	U_{22}	U_{33}	U_{23}	U_{13}	U_{12}
Hg1	0.0455(7)	U_{11}	0.0210(6)	-0.0006(4)	U_{23}	-0.0218(8)
La1	0.0353(9)	U_{11}	0.0363(13)	-0.0052(8)	U_{23}	0.0082(11)
Hg2	0.0277(5)	U_{11}	0.0217(6)	-0.0001(3)	U_{23}	-0.0068(6)
Hg3	0.0440(7)	U_{11}	0.0409(11)	-0.0087(6)	U_{23}	0.0023(9)
Hg4	0.0338(5)	U_{11}	0.0262(7)	0.0013(4)	U_{23}	0.0028(6)
Hg5	0.0252(5)	U_{11}	0.0547(11)	-0.0020(5)	U_{23}	0.0009(5)
Hg6	0.0254(11)	0.0456(10)	U_{22}	-0.0026(12)	0	0
Hg7	0.0245(9)	0.0314(7)	U_{22}	0.0104(8)	0	0
Hg8	0.0541(10)	U_{11}	U_{11}	0.0062(13)	U_{23}	U_{23}
Hg9	0.0322(6)	U_{11}	U_{11}	-0.0017(6)	U_{23}	U_{23}
Hg10	0.046(2)	U_{11}	U_{11}	-0.0107(9)	U_{23}	U_{23}
La10	0.046(2)	U_{11}	U_{11}	-0.0107(9)	U_{23}	U_{23}
Hg11	0.0275(5)	U_{11}	U_{11}	-0.0049(5)	U_{23}	U_{23}
La2	0.0212(7)	U_{11}	U_{11}	0.0003(7)	U_{23}	U_{23}
La3	0.0224(7)	U_{11}	U_{11}	0.0000(7)	U_{23}	U_{23}
Hg12	0.0323(12)	U_{11}	U_{11}	0	0	0
La4	0.0196(13)	U_{11}	U_{11}	0	0	0
La5	0.0190(13)	U_{11}	U_{11}	0	0	0
Hg13	0.049(4)	U_{11}	U_{11}	0	0	0
La13	0.049(4)	U_{11}	U_{11}	0	0	0

Table A6: Standardised fractional atomic coordinates^[3] and isotropic displacement parameters (\AA^2) as a result of the Rietveld refinement of $\text{Sm}_{11}\text{Hg}_{44.5}$.

Atom	Wyckoff	x	y	z	B_{iso}
Hg1	48h	0.0464(3)	x	0.6398(4)	1.66(4)
Sm1	48h	0.0755(4)	x	0.2654(6)	1.18(9)
Hg2	48h	0.0776(3)	x	0.7633(5)	1.66(4)
Hg3	48h	0.1589(3)	x	0.0208(5)	1.66(4)
Hg4	48h	0.1871(3)	x	0.5096(4)	1.66(4)
Hg5	48h	0.2044(3)	x	0.8942(4)	1.66(4)
Hg6	24g	0.0967(5)	$\frac{1}{4}$	$\frac{1}{4}$	1.66(4)
Hg7	24f	0.1613(6)	0	0	1.66(4)
Hg8	16e	0.0588(4)	x	x	1.66(4)
Hg9	16e	0.1608(4)	x	x	1.66(4)
Hg10	16e	0.3342(4)	x	x	1.66(4)
Hg11	16e	0.4123(5)	x	x	1.66(4)
Sm2	16e	0.6566(6)	x	x	1.18(9)
Sm3	16e	0.9088(6)	x	x	1.18(9)
Hg12	4d	$\frac{3}{4}$	$\frac{3}{4}$	$\frac{3}{4}$	1.66(4)
Sm4	4c	$\frac{1}{4}$	$\frac{1}{4}$	$\frac{1}{4}$	1.18(9)
Sm5	4b	$\frac{1}{2}$	$\frac{1}{2}$	$\frac{1}{2}$	1.18(9)

Table A7: Standardised fractional atomic coordinates^[3] and isotropic displacement parameters (\AA^2) as a result from the Rietveld refinement of $\text{Nd}_{11}\text{Hg}_{44.5}$.

Atom	Wyckoff	x	y	z	B_{iso}
Hg1	48h	0.04735(7)	x	0.6398(12)	2.60(13)
Nd1	48h	0.08142(9)	x	0.264(2)	2.1(2)
Hg2	48h	0.0788(10)	x	0.765(2)	2.60(13)
Hg3	48h	0.16223(7)	x	0.0241(12)	2.60(13)
Hg4	48h	0.18706(8)	x	0.5106(11)	2.60(13)
Hg5	48h	0.20588(7)	x	0.8918(13)	2.60(13)
Hg6	24g	0.093(2)	$\frac{1}{4}$	$\frac{1}{4}$	2.60(13)
Hg7	24f	0.168(2)	0	0	2.60(13)
Hg8	16e	0.05853(9)	x	x	2.60(13)
Hg9	16e	0.1601(9)	x	x	2.60(13)
Hg10	16e	0.3275(9)	x	x	2.60(13)
Hg11	16e	0.413(2)	x	x	2.60(13)
Nd2	16e	0.6544(14)	x	x	2.1(2)
Nd3	16e	0.907(2)	x	x	2.1(2)
Hg12	4d	$\frac{3}{4}$	$\frac{3}{4}$	$\frac{3}{4}$	2.60(13)
Nd4	4c	$\frac{1}{4}$	$\frac{1}{4}$	$\frac{1}{4}$	2.1(2)
Nd5	4b	$\frac{1}{2}$	$\frac{1}{2}$	$\frac{1}{2}$	2.1(2)

Table A4: Details on data collection and results of the Rietveld refinement of $\text{Nd}_{11}\text{Hg}_{44.5}$ and $\text{Sm}_{11}\text{Hg}_{44.5}$

Formula	$\text{Nd}_{11}\text{Hg}_{44.5}$	$\text{Sm}_{11}\text{Hg}_{44.5}$
Z	8	
Crystal system	cubic	
Space group	$F\bar{4}3m$ (No. 216)	
Lattice parameters (\AA , \AA^3)	$a = 21.7384(14)$ $V = 10272(2)$	$a = 21.6555(4)$ $V = 10155(5)$
Calc. density ($\text{g}\cdot\text{cm}^3$)	13.60(3)	13.83(7)
Radiation, wavelength (\AA)	Mo-K α 1, 0.70926	
Monochromator	curved Ge [111]	
Data collection geometry	Debye-Scherrer	
Least-squares parameters	50	53
R values	$R_{\text{exp}} = 0.04608$ $R_{\text{p}} = 0.03436$ $R_{\text{wp}} = 0.04381$ $\chi^2 = 0.951$ $R_{\text{Bragg}} = 0.0086$	$R_{\text{exp}} = 0.02351$ $R_{\text{p}} = 0.01879$ $R_{\text{wp}} = 0.02238$ $\chi^2 = 1.062$ $R_{\text{Bragg}} = 0.0064$

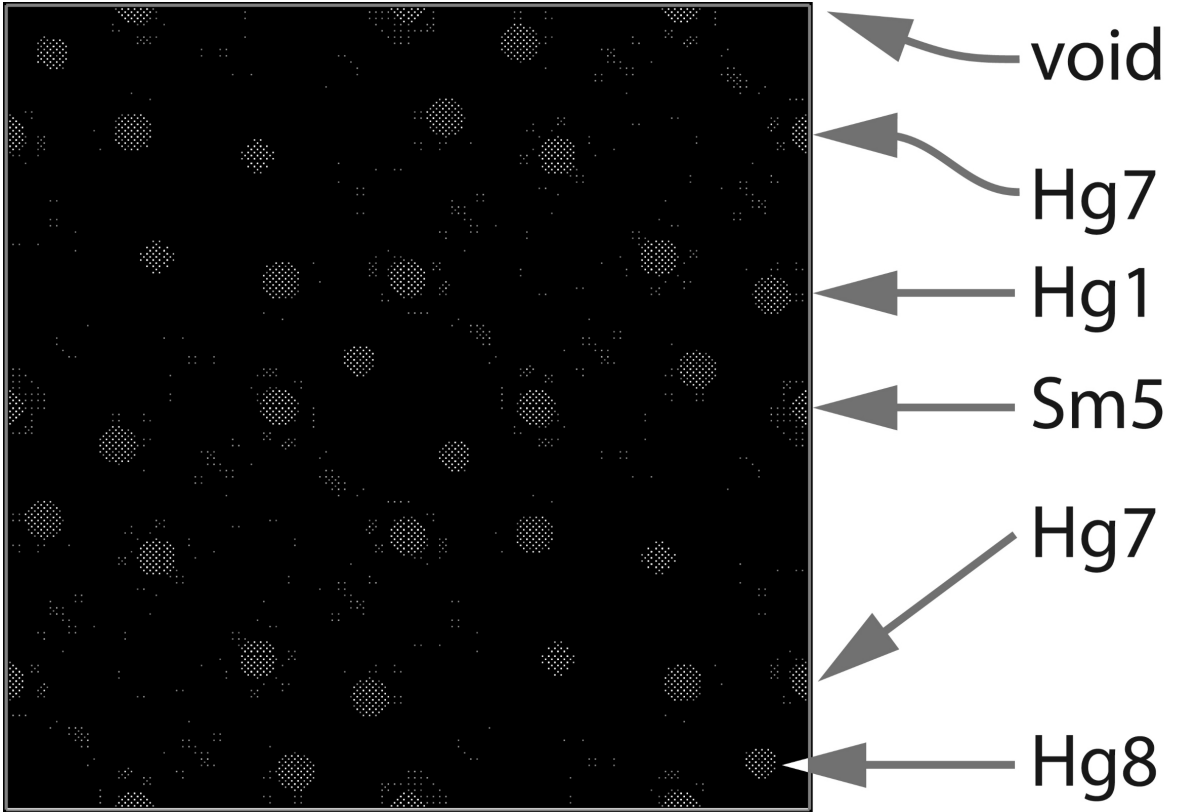


Fig. A6. Electron density map F_{obs} of the ab plane of $\text{Sm}_{11}\text{Hg}_{44.5}$ with sheet thickness $\Delta c=0.05$ at height $c=0$. It clearly shows no electron density in the void $(0,0,0)$. Also, the position of Hg8 is clearly shifted toward $(0,0,0)$ further confirming the unoccupied position.

Table A7: Bader charges calculated for $\text{La}_{11}\text{Hg}_{45}$.

Atom	Bader charge	Site multiplicity	Charge incl. multiplicity
Hg1	-0.351	48	-16.834
Hg2	-0.416	48	-19.968
Hg3	-0.360	48	-17.282
Hg4	-0.335	48	-16.092
Hg5	-0.263	48	-17.445
Hg6	-0.263	24	-6.319
Hg7	-0.494	24	-11.867
Hg8	-0.263	16	-4.213
Hg9	-0.340	16	-5.448
Hg10	-0.533	16	-8.521
Hg11	-0.450	16	-7.205
Hg12	-0.288	4	-1.153
Hg13	-0.322	4	-1.290
La1	+1.466	48	+70.356
La2	+1.462	16	+23.395
La3	+1.449	16	+23.183
La4	+1.441	4	+5.763
La5	+1.431	4	+5.722
Hg total			-133.538
La total			+128.420
Diff. total			-5.118
Diff. %			3.8

3.3.4. Crystal Structure of $\text{Yb}_{11}\text{Hg}_{54}$

Reacting elemental Yb with Hg (10 eq.) at 300 °C in vacuum and subsequent distillation of the mercury surplus yielded $\text{Yb}_{11}\text{Hg}_{54}$ as silver metallic lustrous crystals, sensitive toward air and moisture. A suitable single crystal was isolated and mounted on a STOE IPDS 1 diffraction system. For additional details on data collection and refinement see Table 3.16.

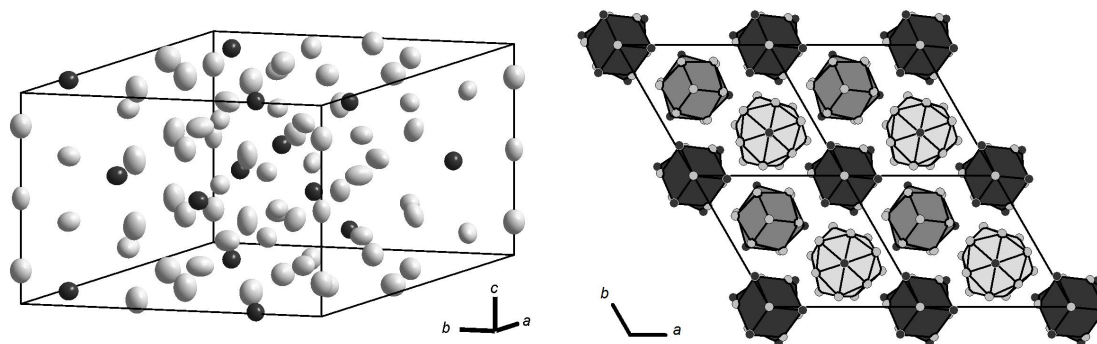


Figure 3.17.: Left: Unit cell of $\text{Yb}_{11}\text{Hg}_{54}$ with anisotropic displacement ellipsoids for all atoms drawn at a 99% probability level. Right: Hexagonal rod packing with viewing direction along $[001]$. Black polyhedra form around Hg11 and Hg13, dark grey around Hg12 and Hg14 and light grey around Yb4. Yb: dark grey; Hg: light grey.

Reflections of the accessible part of a whole Ewald sphere were collected. Indexing showed hexagonal metric and no systematic absences were detected. Wilson statistics indicated no centrosymmetry. Solution in $P\bar{6}$ yielded all atom positions. During refinement, correct atoms were assigned using displacement parameters and subsequently refined with anisotropic thermal displacement parameters. Residual electron density was in close proximity of atomic position and were thus treated as termination effects. Checks for additional symmetry were performed and showed no higher symmetry.

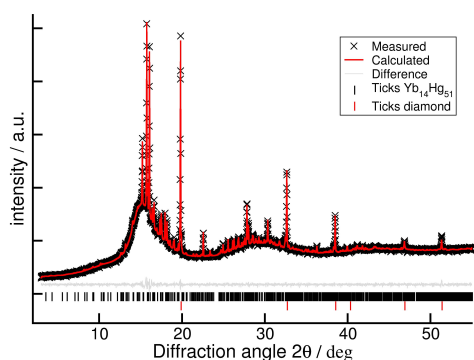


Figure 3.18.: Results of the Rietveld refinement of $\text{Yb}_{11}\text{Hg}_{54}$.

Table 3.15.: Results of the Rietveld refinement of $\text{Yb}_{11}\text{Hg}_{54}$.

Formula	$\text{Yb}_{11}\text{Hg}_{54}$
Z	1
Crystal system	hexagonal
Space group	$P\bar{6}$
Lattice parameters [Å , Å^3]	$a = 13.4242(2)$ $c = 9.6163(2)$ $V = 1500.78(6)$
Density (X-ray) [g/cm^3]	14.0910(6)
Radiation	$\text{MoK}\alpha_1$
Parameters	136
Background parameters	65
R values	$R_p = 0.00537$ $R_{wp} = 0.00715$ $\chi^2 = 1.578$

$\text{Yb}_{11}\text{Hg}_{54}$ crystallises in the hexagonal system with space group $P\bar{6}$ ($a = 13.4242(2) \text{ \AA}$, $c = 9.6163(2) \text{ \AA}$). There are four crystallographically independent Yb sites and 14 Hg sites. No mixed or underoccupied positions were detected.

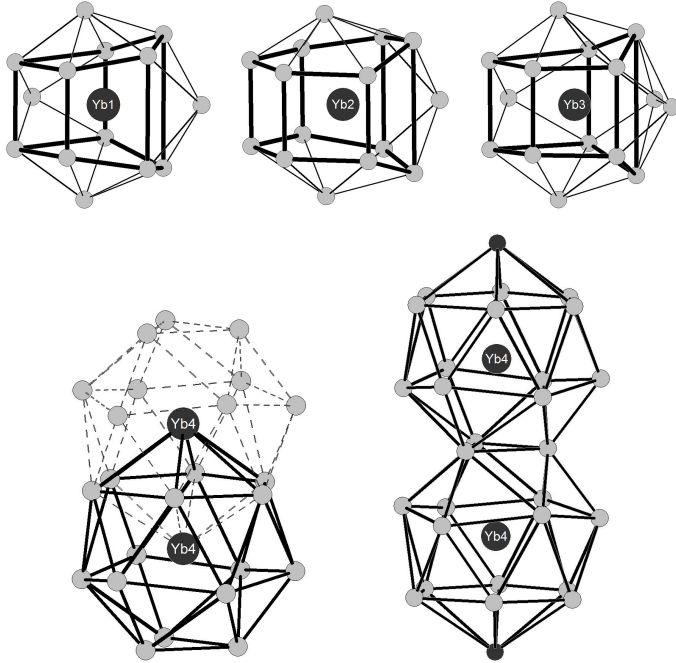


Figure 3.19.: Polyhedra around Yb atoms in $\text{Yb}_{11}\text{Hg}_{54}$. Polyhedra around Yb1–3 can be derived from capped pentagonal or hexagonal prisms. The polyhedron surrounding Yb4 is a Frank-Kasper polyhedron (CN=16) forming interpenetrating pairs. Yb: dark grey; Hg: light grey.

In $\text{Yb}_{11}\text{Hg}_{54}$ Yb is solely coordinated by Hg atoms. The coordination spheres can be derived from capped prisms (see Figure 3.19). Around Yb1 (CN=14) a pentagonal prism forms with both basal faces and two non-neighbouring side faces capped. Around Yb2 (CN=15) a hexagonal prism forms with both basal faces and one side face capped. Around Yb3 (CN=15) a pentagonal prism forms with both basal faces capped. The latter shows additional capping of two neighbouring faces and one further, non-neighbouring side face. Yb4 is coordinated by 15 Hg and one Yb (Yb4) position in a coordination sphere best described as Frank-Kasper polyhedron with 16 vertices. These polyhedra form interpenetrating pairs, where the centre of one polyhedron is also the vertex of the interpenetrating one. The pairs are stacked along $[00z]$ sharing trigonal basal faces (see Figure

3.19)

Most Hg atoms are coordinated by both Yb and Hg with the exception of Hg14, which is solely coordinated by Hg. The resulting polyhedra can be grouped according to their shapes: Polyhedra around Hg1–2, Hg8, and Hg11–14 are derived from capped prisms, polyhedra around Hg4, Hg6–7 and Hg9–10 are distorted icosahedra. Unique are the polyhedra surrounding Hg3 and Hg5.

Pentacapped trigonal prisms form around Hg2 and Hg11–14. Both basal and all three side faces are capped. In both polyhedra around Hg1 and Hg8 the two basal and two side faces of trigonal prisms are capped by one atom each. One side face, however, is capped by two atoms, indicated by dashed lines in Figure 3.20. The difference between them is the orientation. While the pair coordinating Hg1 is parallel to $[001]$, the pair coordinating Hg8 is perpendicular to $[001]$ with vector $[0.1107 \ 0.9938 \ 0]$.

Hg3 is surrounded by two different cupolae. The "top" is a hexagonal pyramid and the "bottom" is a pentagonal pyramid and can be seen as a part of an icosahedron, resulting in $\text{CN} = 13$ (see Figure 3.20). It can be seen that the "front" also resembles

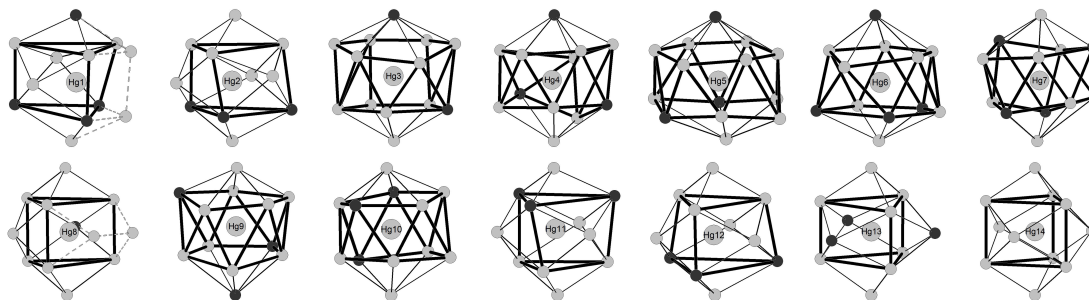


Figure 3.20.: Polyhedra around all Hg atoms in $\text{Yb}_{11}\text{Hg}_{54}$. Polyhedra around Hg1–2, Hg8, and Hg11–14 are derived from capped prisms, polyhedra around Hg4, Hg6–7 and Hg9–10 are distorted icosahedra. The polyhedron around Hg3 and Hg5 are more irregular. Yb: black; Hg: light grey.

an icosahedron, but in the "back" rectangular faces are present due to the enlarged coordination number. Hg5 is surrounded by a hexagonal antiprism with both basal faces capped.

According to their site symmetry the least regular polyhedra are formed around Hg1 to Hg6 (site symmetry 1), more regular polyhedra around Hg7–10 (site symmetry $m..$) and around Hg11 and Hg12 (site symmetry $3..$). Ideal trigonal prisms form around Hg13, and Hg14 according to their site symmetry $6..$

The whole structure can be rationalised as hexagonal rod packing of stacked polyhedra as shown in Figure 3.17. Each type of polyhedra (around Hg11 and Hg13; Hg12 and Hg14; Yb4) is stacked along $[00z]$, thus forming rods. Again, each type of rod packs in a hexagonal pattern. All three types of rods are telescoped so the voids are filled and a dense packing is yielded.

$\text{Yb}_{11}\text{Hg}_{54}$ crystallises as hettotype of the $\text{Gd}_{14}\text{Ag}_{51}$ structure type. In contrast to other hettotypes of the $\text{Gd}_{14}\text{Ag}_{51}$ structure type ($A_{11-x}\text{Hg}_{55+x}$ ($A = \text{Ca}, \text{Sr}$)^[1], $\text{Eu}_{10}\text{Hg}_{55}$ and $\text{Na}_{11}\text{Hg}_{52}$ ^[2]) $\text{Yb}_{11}\text{Hg}_{54}$ does not show mixed or underoccupied positions but exhibits a fully ordered structure.

Table 3.16.: Crystallographic data, details of the data collection and structure determination for $\text{Yb}_{11}\text{Hg}_{54}$.

Empirical sum formula	$\text{Yb}_{11}\text{Hg}_{54}$
Crystal system	hexagonal
Space group	$P\bar{6}$, (No. 174)
Lattice parameters (T = 293K)	
$a / \text{\AA}$	13.3998(15)
$c / \text{\AA}$	9.6072(9)
$V / \text{\AA}^3$	1493.9(3)
Formula units / Z	1
Calculated density [$\text{g}\cdot\text{cm}^{-3}$]	14.156
$F(000)$	5090
Absorption coefficient [mm^{-1}]	84.677
Radiation, wavelength [\AA]	$\text{AgK}\alpha$ 0.56086
Diffractometer	STOE IPDS-I
Corrections	Lorentz, polarisation, absorption (semiempirical)
Transmission factors T_{\min}/T_{\max}	0.0026/0.024
Number of free parameters	112
Number of collected data	31084
Number of unique data	4870
Number of unique data with ($I \geq 2\sigma(I)$)	3754
$R_{\text{int}}/R_{\sigma}$	0.1150/0.0712
Data range	$-22 \leq h \leq 21,$ $-22 \leq k \leq 22,$ $-15 \leq l \leq 15$
Structure solution	direct methods, SHELXS97 ^[3]
Structure refinement	full matrix least-squares on F^2 , SHELXL97 ^[3]
Extinction coefficient	0.000242(13)
Final R values $I \geq 2\sigma(I)$	$R1 = 0.0428$ $wR2 = 0.0649$
Final R values (all data)	$R1 = 0.0683$ $wR2 = 0.0705$
Goodness of Fit	0.994
Residual electron density min./max [$\text{e}^{-}/\text{\AA}^{-3}$]	4.431/−3.496

Table 3.17.: Standardised fractional atomic coordinates and equivalent isotropic displacement parameters /Å² for Yb₁₁Hg₅₄ as yielded by single crystal X-ray diffractometry. U_{eq} is defined as $\frac{1}{3}$ of the trace of the orthogonalized U_{ij} tensor. Standard deviations in units of the last digit are given in parentheses.

Atom	Wyckoff number	x	y	z	U_{eq}
Hg1	6l	0.78199(7)	0.83830(7)	0.65475(8)	0.01847(14)
Hg2	6l	0.14426(7)	0.71448(7)	0.65569(11)	0.0260(2)
Hg3	6l	0.35756(9)	0.87152(8)	0.82899(9)	0.0248(2)
Hg4	6l	0.97796(7)	0.77192(7)	0.83776(9)	0.0110(2)
Hg5	6l	0.60812(8)	0.08240(7)	0.70191(10)	0.0210(2)
Hg6	6l	0.72682(7)	0.61154(6)	0.73844(7)	0.01796(13)
Yb1	3k	0.92697(11)	0.72585(11)	1/2	0.0148(2)
Yb2	3k	0.54256(12)	0.61760(11)	1/2	0.0166(2)
Hg7	3k	0.53233(10)	0.21641(10)	1/2	0.0222(2)
Yb3	3j	0.21050(11)	0.97606(12)	0	0.0151(2)
Hg8	3j	0.12407(12)	0.69415(13)	0	0.0271(2)
Hg9	3j	0.49928(11)	0.08113(11)	0	0.0240(2)
Hg10	3j	0.43937(10)	0.26186(11)	0	0.0211(2)
Yb4	2i	2/3	1/3	0.80261(13)	0.0137(3)
Hg11	2g	0	0	0.8430(2)	0.0228(3)
Hg12	2h	1/3	2/3	0.6547(2)	0.0233(3)
Hg13	1b	0	0	1/2	0.0174(3)
Hg14	1c	1/3	2/3	0	0.0279(5)

3.3.5. Crystal Structures of the $REHg$, $REHg_2$ and $REHg_3$ Amalgams

$REHg_3$

By reaction of rare earth metals with mercury at 300 °C in vacuum and subsequent removal of surplus mercury by distillation the following 1:3 phases have been synthesised: $ScHg_3$, YHg_3 , $LaHg_3$, $NdHg_3$, $GdHg_3$, $DyHg_3$, $HoHg_3$, $ErHg_3$, $TmHg_3$ and $LuHg_3$ (rare earth metals obtained from smart elements, 99.99 % metal basis, Hg double distilled). $LiHg_3$ crystallises isotypically but has been synthesised by electrocrystallisation and is discussed in chapter 3.4.2.

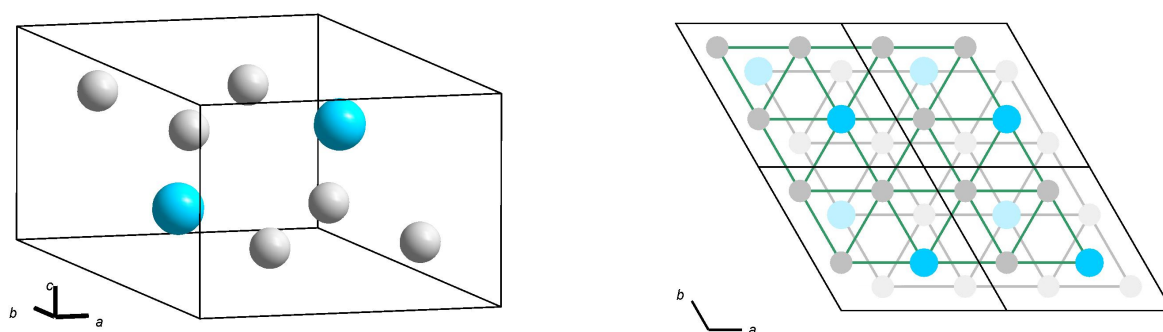


Figure 3.21.: Left: Unit cell of $GdHg_3$, representative for all 1:3 phases. Right: View on the crystal structure of $GdHg_3$ along the $[001]$, the lower layer is transparent. Gd: light blue, Hg: grey.

All products were characterized by powder diffractometry and subsequent Rietveld refinements. The diffractograms are compiled in Figure 3.22, the data in Table 3.18. In the syntheses of $GdHg_3$ and $DyHg_3$, traces of a side phase were observed, the main reflection can be assigned to $Gd_{11}Hg_{45}$ or $Dy_{11}Hg_{45}$, respectively. However, due to the low percentage of side phases, their structural parameters could not be refined. The structures are isotypic to the low-temperature phase of Ni_3Sn ($P6_3/mmc$). Hg occupies the $6h$ position ($x, 2x, 1/4$) and RE the $2c$ position ($1/3, 2/3, 1/4$). The structure can be rationalised as decorated hexagonal closest packing with hexagonal layers $[REHg_3]$. They are stacked along c according to $-A-B-A-B-$ with anti-cuboctahedral coordination of all atoms. RE elements are coordinated by Hg atoms only, Hg atoms have a mixed coordination.

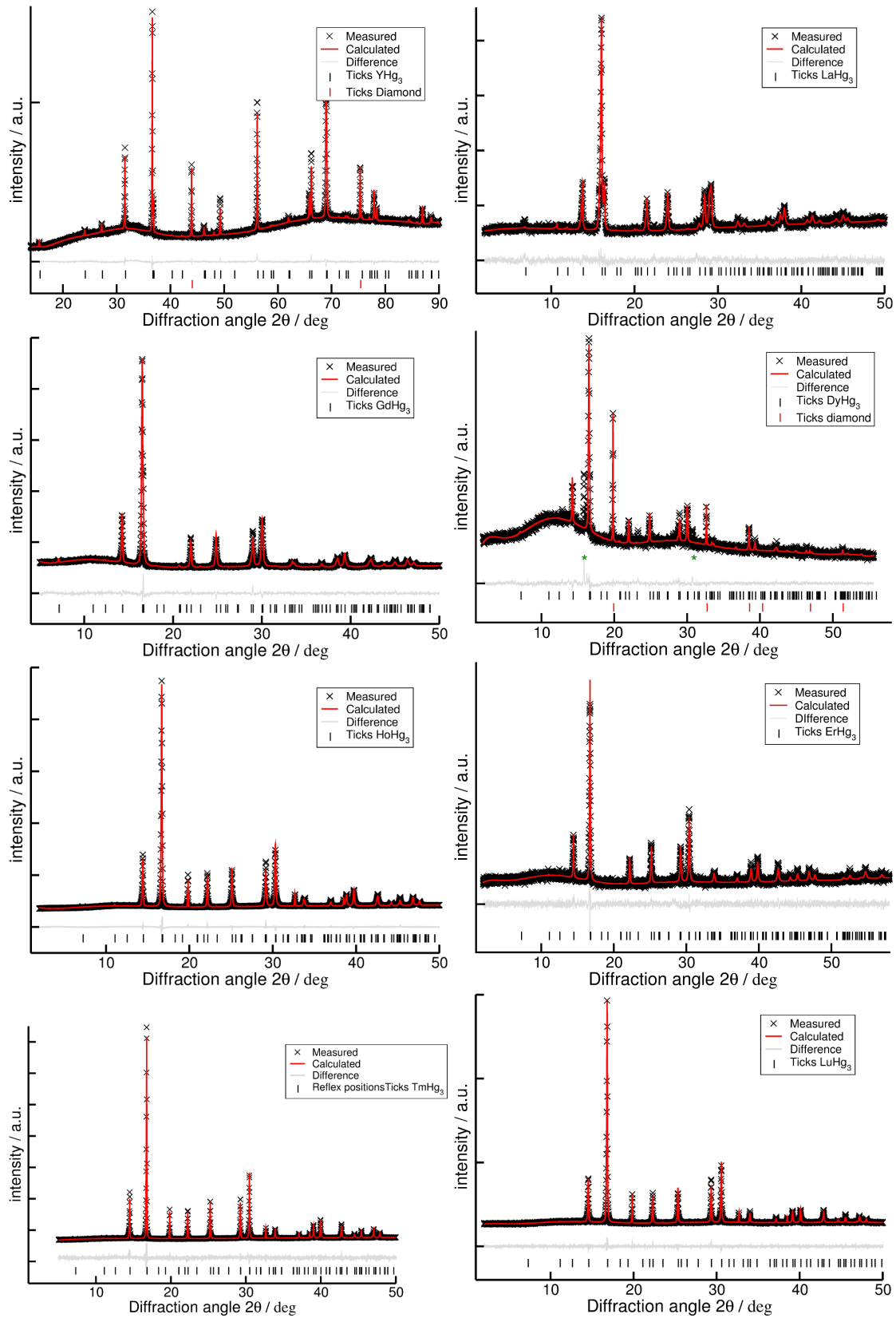


Figure 3.22.: Rietveld refinements (from left to right, top to bottom): YHg_3 , LaHg_3 , GdHg_3 , DyHg_3 , HoHg_3 , ErHg_3 , TmHg_3 and LuHg_3 . Refinement parameters are compiled in Table 3.18.

Table 3.18.: Results of the Rietveld refinements of YHg_3 , LaHg_3 , GdHg_3 , GdHg_3 , DyHg_3 , HoHg_3 , TmHg_3 , LuHg_3 and YbHg_3 . Refined powder patterns are shown in Figure 3.22. All structures crystallise isotypically. Isotropic displacement parameters are given in \AA^2 . Standard deviations in units of the last digit are given in parentheses.

Formula		YHg_3	LaHg_3	GdHg_3	GdHg_3	DyHg_3
Z				– 2 –		
Crystal system				– hexagonal –		
Space group				– $P6_3/mmc$ –		
Latt. parameters						
[\AA , \AA^3]	$a =$	6.5479(2)	6.8231(8)	6.596(4)	6.595(5)	6.595(10)
	$c =$	4.8779(1)	4.9693(6)	4.899(4)	4.899(4)	4.902(9)
	$V =$	181.12(2)	200.35(5)	184.63(3)	184.47(2)	184.63(7)
ρ (X-ray) [g/cm^3]		12.664(7)	12.277(3)	13.65(2)	13.67(2)	13.79(5)
Radiation		$\text{CuK}_{\alpha 1}$		– $\text{MoK}_{\alpha 1}$ –		
Parameters		42	21	27	45	33
R values	$R_p =$	0.02795	0.04005	0.01982	0.02145	0.04427
	$R_{\text{wp}} =$	0.03738	0.04984	0.02740	0.03158	0.06195
	$\chi^2 =$	1.238	0.909	1.306	1.173	1.179
	x	0.835(2)	0.841(4)	0.839(3)	0.839(8)	0.838(2)
Hg1	y	0.165(2)	0.159(4)	0.161(3)	0.161(8)	0.162(2)
	z	$1/4$	$1/4$	$1/4$	$1/4$	$1/4$
	B_{iso}	6.18(5)	2.00(11)	1.46(6)	1.6(2)	2.5(3)
	x	$1/3$	$1/3$	$1/3$	$1/3$	$1/3$
RE1	y	$2/3$	$2/3$	$2/3$	$2/3$	$2/3$
	z	$1/4$	$1/4$	$1/4$	$1/4$	$1/4$
	B_{iso}	7.28(11)	1.9(4)	1.3(2)	0.4(5)	3(2)
Formula		HoHg_3	ErHg_3	TmHg_3	YbHg_3	LuHg_3
Z				– 2 –		
Crystal system				– hexagonal –		
Space group				– $P6_3/mmc$ –		
Latt. parameters						
[\AA , \AA^3]	$a =$	6.5311(13)	6.5092(2)	6.49615(8)	6.603(3)	6.474(4)
	$c =$	4.8744(14)	4.8641(4)	4.86436(10)	5.027(2)	4.854(3)
	$V =$	180.04(2)	178.48(3)	177.77(5)	189.69(2)	176.12(2)
ρ (X-ray) [g/cm^3]		14.143(7)	14.310(3)	14.398(5)	13.566(13)	14.64(2)
Radiation				– $\text{MoK}_{\alpha 1}$ –		
Parameters		33	26	28	26	33
R values	$R_p =$	0.01797	0.05942	0.02788	0.02914	0.02910
	$R_{\text{wp}} =$	0.02749	0.07548	0.02479	0.03923	0.03757
	$\chi^2 =$	1.388	1.033	1.472	1.370	1.071
	x	0.829(3)	0.833(2)	0.832(8)	0.8283(5)	0.829(5)
Hg1	y	0.171(3)	0.166(2)	0.168(8)	0.1717	0.171(5)
	z	$1/4$	$1/4$	$1/4$	$1/4$	$1/4$
	B_{iso}	2.54(5)	1.22(12)	2.00(14)	6.47(7)	2.93(8)
	x	$1/3$	$1/3$	$1/3$	$1/3$	$1/3$
RE1	y	$2/3$	$2/3$	$2/3$	$2/3$	$2/3$
	z	$1/4$	$1/4$	$1/4$	$1/4$	$1/4$
	B_{iso}	0.81(10)	1.9(5)	1.4(4)	2.11(8)	1.3(2)

SmHg₂

Reaction of Sm with Hg (10 eq.) at 300 °C and subsequent distillation at the same temperature in vacuum yielded SmHg₂. The substance is grey, lacklustre, hard, brittle and sensitive toward air and moisture. X-ray powder diffraction and Rietveld refinement were performed (see Figure 3.24 and Table 3.19). The Rietveld refinement shows relatively large residual values, which can be attributed to the high absorption coefficient.

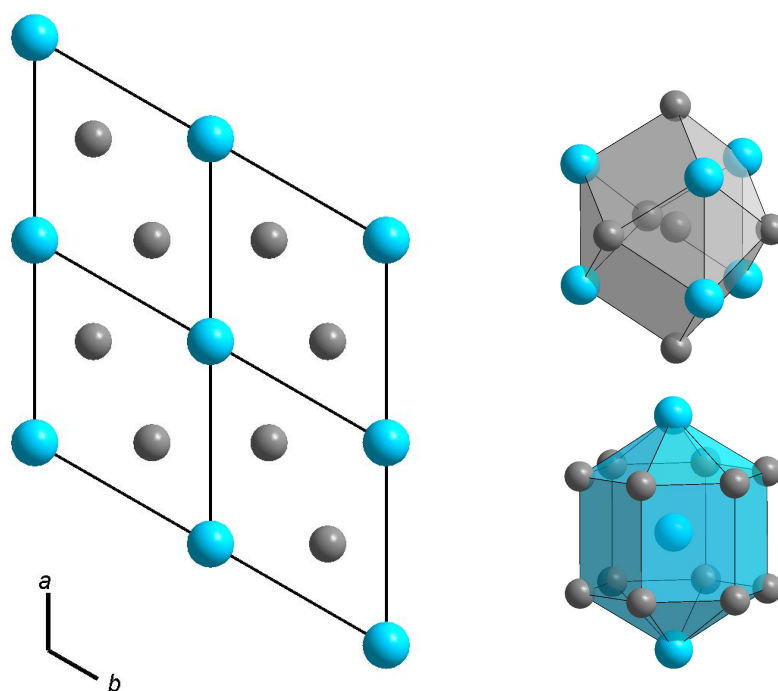


Figure 3.23.: The structure of SmHg₂ is shown. Sm: light blue, Hg: grey. Left: 2x2x1 super cell of SmHg₂ viewed along [001]. Top right: coordination of Hg1, bottom right: coordination around Sm1.

The structure crystallises isotypic to AlB₂ (*P6/mmm*) in the hexagonal crystal system. Sm atoms occupy the vertices of the unit cell (1a; 0,0,0), Hg occupies the 2d position (1/3,2/3,1/2). Hg atoms are arranged in layers. The topology of a Hg layer is the same as in graphite. Each Hg is equidistant from three other Hg atoms ($d_{\text{Hg-Hg}_{\text{intra}}}$ = 2.8167(2) Å), the next nearest neighbours is a set of six Sm atoms forming a trigonal prism ($d_{\text{Hg-Sm}}$ = 3.3151(2) Å). The next layers are only slightly further distant than the Sm prism ($d_{\text{Hg-Hg}_{\text{inter}}}$ = 3.4964(4) Å). Sm is coordinated by Hg ($d_{\text{Sm-Hg}}$ = 3.3151(2) Å) with its next Sm neighbour only little further away ($d_{\text{Sm-Sm}_{\text{inter}}}$ = 3.4964(4) Å) thus forming a hexagonal prism with both basal faces capped.

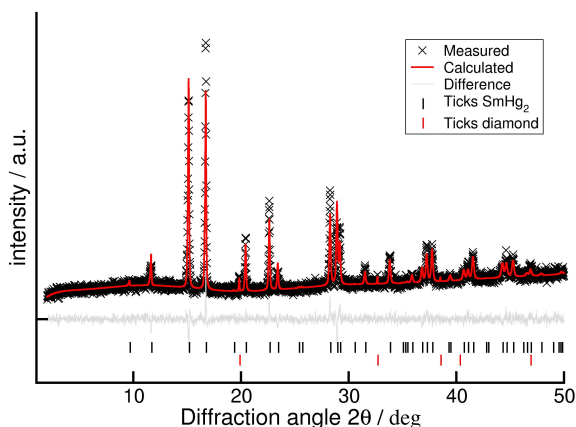


Figure 3.24.: Results of a Rietveld refinement of SmHg_2

Table 3.19.: Results of a Rietveld refinement of SmHg_2 .

Formula	SmHg_2
Z	1
Crystal system	hexagonal
Space group	$P6/mmm$
Latt. param. [\AA , \AA^3]	$a = 4.8786(4)$ $c = 3.4964(4)$ $V = 72.07(2)$
Density (X-ray) [g/cm^3]	12.708(3)
Radiation	$\text{MoK}\alpha_1$
Parameters	32
Background parameters	12
R values	$R_p = 0.05792$ $R_{wp} = 0.07373$ $\chi^2 = 0.927$

Table 3.20.: Standardised fractional atomic coordinates and equivalent isotropic displacement parameters $/\text{\AA}^2$ for SmHg_2 as yielded by powder X-ray diffractometry. Standard deviations in units of the last digit are given in parentheses.

Atom	Wyckoff number	x	y	z	B_{iso}
Sm1	1a	0	0	0	0.71(2)
Hg1	2d	$1/3$	$2/3$	$1/2$	0.79(2)

References

- [1] A. V. Tkachuk, A. Mar, *Inorg. Chem.*, **47**(4), 1313–8 (2008).
- [2] C. Hoch, A. Simon, *Angew. Chem.*, **124**(13), 3316–3319 (2012); b) C. Hoch, A. Simon, *Angew. Chem. Int. Ed.*, **51**(13), 3262–3265 (2012).
- [3] G. M. Sheldrick, *Acta Crystallogr. A*, **64**(1), 112–122 (2007).

3.4. Alkali and alkaline earth metal amalgams

The following chapter contains published as well as unpublished results of alkali metal amalgams examined in this work. Seeds of KHg_6 were synthesised by electrocrystallisation together with KHg_{11} as side phase. Phase-pure samples of KHg_6 were synthesised by using the seeds for crystal growth by tempering stoichiometric mixtures of KHg_{11} and elemental potassium. Band structure calculations showed considerable but incomplete electron transfer from potassium to the electronegative sublattice, resulting in "bad metal" behaviour as shown by electric resistance measurements. These results were published in *J. Alloys Compd.*.

No experimental work was done on alkaline earth metal amalgams but their crystal structures known from literature are essential for the understanding of some of the new amalgam structures discussed here.

To gain deeper insight into the electron transfer, NMR Knight shift studies in combination with band structure calculations were performed on the three Li amalgams Li_3Hg , LiHg and LiHg_3 , which still have to be published. ^7Li as well as ^{199}Hg are NMR active cores and allowed for complementary monitoring of the s electron density at Fermi level. With increasing mercury content of the amalgams, the NMR shift was lowered for ^7Li and increased for ^{199}Hg . It was shown that with increasing mercury content a shift in the energy of bands occurs which is in accordance with increased positive partial charge on Li and that Knight shift measurements are a convenient tool for monitoring the degree of polarisation of the metal-metal bonding.

The last part of this chapter contains unpublished results of electrolyses on HgIn cathodes with KI- and RbI-containing electrolytes. In both cases the incorporation of In in the BaHg_{11} aristotype structure was observed leading to compositions $\text{AHg}_{11-x}\text{In}_x$ ($A = \text{K}$: $x \approx 1$, Rb : $x \approx 6$). The geometric implications by incorporation of In were examined. Band structure calculations showed no electronic reason for the incorporation of In on particular crystallographic sites, the features of the tDOS of the aristotype and hettotype are similar.

3.4.1. Bad Metal Behaviour in the New Hg-Rich Amalgam KHg_6 with Polar Metallic Bonding

Frank Tambornino, Dr. Constantin Hoch*

* *Corresponding author. Tel.: +49 (0)89 2180 77421; fax: +49 (0)89 2180 77440. E-mail address: constantin.hoch@cup.uni-muenchen.de (C. Hoch).*

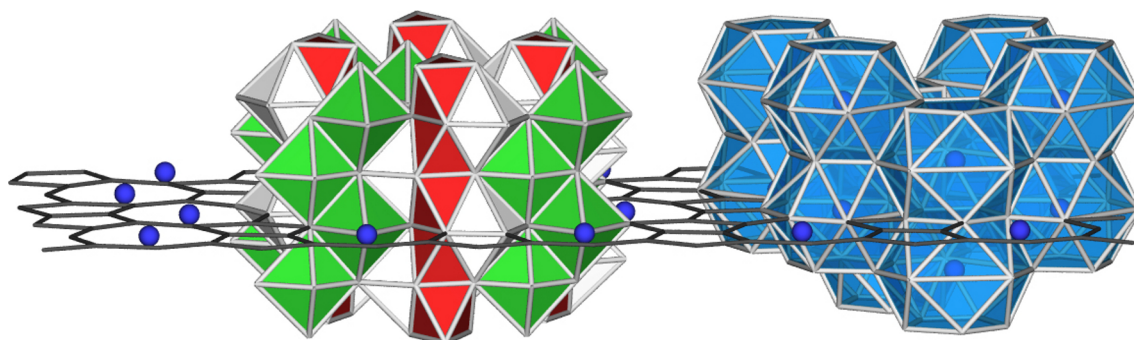
published in: *J. Alloys Compd.*, **618**, 299–304 (2015).

DOI:10.1016/j.jallcom.2014.08.173

Reprinted (adapted) with permission from Journal of Alloys and Compounds. Copyright 2014 Elsevier B.V.

Abstract

The new mercury-rich amalgam KHg_6 crystallizes with the BaHg_6 structure type (orthorhombic, space group $Pnma$ (No. 62), $a = 13.394(9) \text{ \AA}$, $b = 5.270(3) \text{ \AA}$, $c = 10.463 \text{ \AA}$). It was prepared by electrolysis of a solution of KI in N,N' -Dimethylformamide at 343 K at a reactive Hg cathode. The structure of KHg_6 shows motifs of ionic packing, covalent Hg cluster formation and metallic properties. KHg_6 decomposes peritectically at 443 K. The combination of alkali metals with a noble metal with moderate electron affinity results in the formation of polar metal-metal bonding with considerable but incomplete electron transfer from the electropositive to the electronegative sublattice, resulting in typical "bad metal behaviour", illustrated by resistance and susceptibility measurements and quantum theoretical calculations.



Introduction

Amalgams of less noble metals have been studied extensively in the second half of the 20th century. Early thermoanalytical studies in the binary system K–Hg [1] reported the existence of Hg-rich phases with tentative compositions of KHg_{11} , KHg_9 , KHg_4 , KHg_3 , $\text{KHg}_{2.7}$, KHg_2 and K_5Hg_7 . The composition of the Hg-richest phase KHg_{11} (BaHg_{11} structure type [2]) was confirmed by crystallographic investigations [3], as well as the ones of KHg_2 [4] and K_5Hg_7 [5]. The composition KHg_4 is close to those of K_7Hg_{31} [6] ($\text{KHg}_{4.4}$), K_3Hg_{11} [6] ($\text{KHg}_{3.7}$) and K_2Hg_7 [7] ($\text{KHg}_{3.5}$), however, no phases with compositions close to KHg_9 , KHg_3 or $\text{KHg}_{2.7}$ have been reported so far.

The crystal structures of most amalgams have been thoroughly studied, however, their respective physical properties remain widely unknown. Band structure calculations on these polar amalgams are scarce due to the typically large and low symmetric structures. Those examples available in literature [8] show considerable but incomplete electron transfer from the less noble metal to the mercury sublattice. As the electron affinity of mercury is insufficient for the formation of Zintl-analogous $[\text{Hg}_n]^{m-}$ anions, partially negative polarised $[\text{Hg}_n]^{\delta-}$ networks with equal charge distribution over all Hg atoms are the more favourable consequence. Ongoing NMR experiments on Li_3Hg , LiHg and LiHg_3 [9,10] in our group reveal that the charge transfer is generally more pronounced in the Hg-richer amalgams as a larger Hg sublattice can delocalise the negative charge more efficiently. The negatively polarised Hg sublattice in polar amalgams tends to cluster formation as $\text{Hg}^{\delta-}$ is formally analogous to early p-group elements. In a number of amalgams with rather low Hg content Hg–Hg–Hg bond angles close to 90° corresponding to σ_p -type bonds can be found in $[\text{Hg}_4]$ squares or $[\text{Hg}_8]$ cubes [11–14]. If the negative charge is delocalised over a larger number of Hg atoms, d contributions get more dominant and the bond angles show larger values resulting in icosahedra or larger polyhedra [15,16]. Following an ionic approach, $[\text{Hg}_n]^{\delta-}$ clusters can be described as negatively charged coordination spheres surrounding the positively charged cations of the less noble metals. However, most Hg-rich amalgam structures can alternatively be described by motifs from closest sphere packings, emphasising their metallic character. Amalgams of less noble metals thus show contributions from ionic, covalent and metallic bonding at the same time. The interplay of the three bonding types leads to typical "bad metal behaviour", e. g. high specific resistance, low Ioffe-Regel limit.

The unusual combination of structural motifs and physical properties from both metallic and ionic bonding may lead to interesting materials. High-efficiency thermoelectrics depend on good electric conductivity, a typical metallic property, in conjunction with low thermal conductivity, a typical property of ionic compounds. Amalgams, in addition, might fulfil other commonly proposed prerequisites for good thermoelectric materials, such as heavy atoms, "rattling cages", high correlation of the electrons and rather low densities of state at the Fermi level. In addition, the interplay of covalent and ionic structure motifs with those of a metallic sphere packing typically leads to complicated structures of low symmetry and long translational periods, and the Ioffe-Regel limit resistances are reached already at low temperatures.

The chemical preparation of amalgams of less noble metals suffers from various problems, and knowledge on the Hg-richest phases is especially scarce. The main reason is

the typically very low peritectic decomposition temperatures for the Hg-rich amalgams ($\text{Cs}_2\text{Hg}_{27}$: +12 °C [17]). In the most inauspicious cases, these combine with high reaction enthalpies resulting from the electronegativity differences and high kinetic contributions to the seed formation at low reaction temperatures to a total inhibition of phase formation, even when long tempering times are applied [18]. A novel approach to phase-pure samples in gram scale of these hitherto elusive phases has shown useful in the recent years. The isothermal electrocrystallisation is a cathodic reduction process with metallic Hg as the reactive cathode and the less noble metal in form of a solution of the respective iodide in an aprotic, polar solvent. In the past years, this method yielded phases like $\text{Cs}_2\text{Hg}_{27}$, $\text{Na}_{11}\text{Hg}_{52}$, $[\text{N}(\text{CH}_3)_4]\text{Hg}_8$ or $\text{Eu}_{10}\text{Hg}_{55}$ [17–20] and many others.

Here we report on preparation, crystal structure and physical properties of the new Hg-rich potassium amalgam KHg_6 with polar metal-metal bonding and the characteristic "bad metal" behaviour.

Material and methods

Preparation and single crystal structure determination

KHg_6 was prepared by electrolysing 100 ml of a saturated solution of dry KI in abs. *N,N'*-Dimethylformamide (DMF) with a single drop of Hg suspended in an amalgamated copper spoon as cathode and a Pt foil (ca. 1 cm²) as anode at 341, 345, 349, and 353 K. A glass apparatus suitable for isothermal electrocrystallisation has been presented previously [17,19], allowing the performance of the electrolysis under Schlenk conditions and at constant temperatures between -223 and +473 K. Due to inner resistance of the electrolysis chamber, a terminal voltage of 7.0 V had to be applied. Maximal currents of 10 mA could be detected during the process taking about 12 h to total consumption of the mercury. After electrolysis, the products were scraped from the copper spoon under argon without removing it from the electrolysis chamber, washed with small portions of fresh DMF and then transferred to Schlenk tubes and dried under vacuum.

Prior to the preparation of the electrolysis solution, KI was dried by heating to 473 K under vacuum for several hours. DMF was dried over CaH_2 and distilled under inert atmosphere.

When performed at room temperature, the electrolysis yields pure KHg_{11} , in accordance with the phase diagram for the system K–Hg [1]. Its decomposition temperature is given to 338 K, however, when the electrolysis is performed at 341 - 353 K, the products still showed the presence of KHg_{11} in X-ray powder diffractograms with fractional amounts KHg_6 : KHg_{11} of about 0.6 : 0.4 according to Rietveld refinements. This may be due to kinetic hindering of the seed formation. Pure samples of KHg_6 were prepared from mixtures of KHg_{11} (3.75 g, 1.67 mmol) prepared previously via electrolysis together with metallic potassium (52.7 mg, 1.43 mmol) in proportions according to the composition KHg_6 . The thoroughly homogenised mixture was tempered after adding a small amount of electrolytically grown KHg_6 seeds at 358 K for 62 h. A rocking-curve temperature program of 358 ± 5 K with rocking intervals of 5 min was applied in order to improve the single crystal quality by Ostwald ripening. According to X-ray powder diffractometry,

the samples consisted from pure KHg_6 , however, small traces of KHg_{11} could be detected in the susceptibility measurements (see Figs. 1 and 2).

The addition of a small amount of KHg_6 seeds is essential as KHg_6 cannot be obtained by directly reacting Hg with K in the required amounts by tempering. This was verified by reacting a mixture of potassium and mercury with nominal composition KHg_6 (1.0000 g Hg, 4.99 mmol, 32.5 mg K, 0.83 mmol) in a closed tantalum ampoule with the following temperature program: $\text{RT} \xrightarrow{10\text{K/h}} 473 \text{ K}$ (12 h), then fast cooling in ice water, followed by $\text{RT} \xrightarrow{10\text{K/h}} 373 \text{ K}$ (2 weeks) $\xrightarrow{10\text{K/h}} \text{RT}$. In the X-ray powder diffractogram of the sample all intensities could be indexed with the pattern of KHg_{11} .

KHg_6 forms brittle, dark metallic crystals of irregular shape and is very sensitive toward air and traces of moisture. KHg_{11} also is air- and moisture-sensitive, but not to the same extent than KHg_6 . Suitable single crystals of irregular shape were isolated under dry paraffin oil and sealed in capillaries ($\varnothing = 0.1 \text{ mm}$) filled with dry paraffin oil. After centering the crystals on the one-circle goniometer of a IPDS1 diffractometer system (Stoe & Cie. GmbH, Darmstadt, Germany) equipped with imaging plate and graphite-monochromatised $\text{Ag-K}\alpha$ radiation, the metric was determined from 20 orientation images. Final data collection was performed in φ scan geometry with $\Delta\varphi = 1.2^\circ$ and $0 \leq \varphi \leq 200.4^\circ$. Data were corrected for Lorentz, polarisation and absorption effects [21–23]. Further details on crystal structure, data collection, structure solution and refinement are compiled in Table A1, fractional atomic coordinates in standardised setting [24] and isotropic displacement parameters are compiled in Tables A2 and A6, anisotropic displacement parameters for all atoms can be found in Table A3. Further details on the crystal structure investigations are available from Fachinformationszentrum Karlsruhe, 76344 Eggenstein-Leopoldshafen, Germany (fax. +49 (0)7247 808 666; e-mail: crysdata@fiz-karlsruhe.de; http://www.fiz-informationsdienste.de/en/DB/icsd/depot_anforderung.html) on quoting the deposition number CSD-427001.

Samples for powder diffraction were prepared by grinding the brittle samples in a glove-box and sealing the powder samples in glass capillaries ($\varnothing = 0.2 \text{ mm}$). To account for the high absorption coefficients, data were collected in many subsequently added ranges in the range $2.0^\circ \leq 2\vartheta \leq 70^\circ$. Data collection was performed on a diffractometer system with position-sensitive linear detector (Stadi P, Stoe & Cie. GmbH, Darmstadt, Germany) in $\text{Ge}(111)$ -monochromatised $\text{Mo-K}\alpha 1$ radiation. Rietveld refinements were performed with a fundamental parameter approach [25], a double Voigt approach to compensate size-strain effects. A shifted Chebychev function was applied for background modelling (24 parameters were refined) and a LeBail-Jouanneaux function for profile modelling. Further details on the results of the refinement are given in Table A4 and in Fig. 1.

Specific resistance and susceptibility measurements

Temperature dependent measurements of the electric conductivity were performed with a Cryovac cryostat between 290 and 3 K on cold-pressed polycrystalline sample pellets. The van-der-Pauw 4-point technique (current generator Keithley 2400 SourceMeter, voltmeter Hewlett-Packard 43420A Nanovoltmeter) was applied with a current of 1 mA.

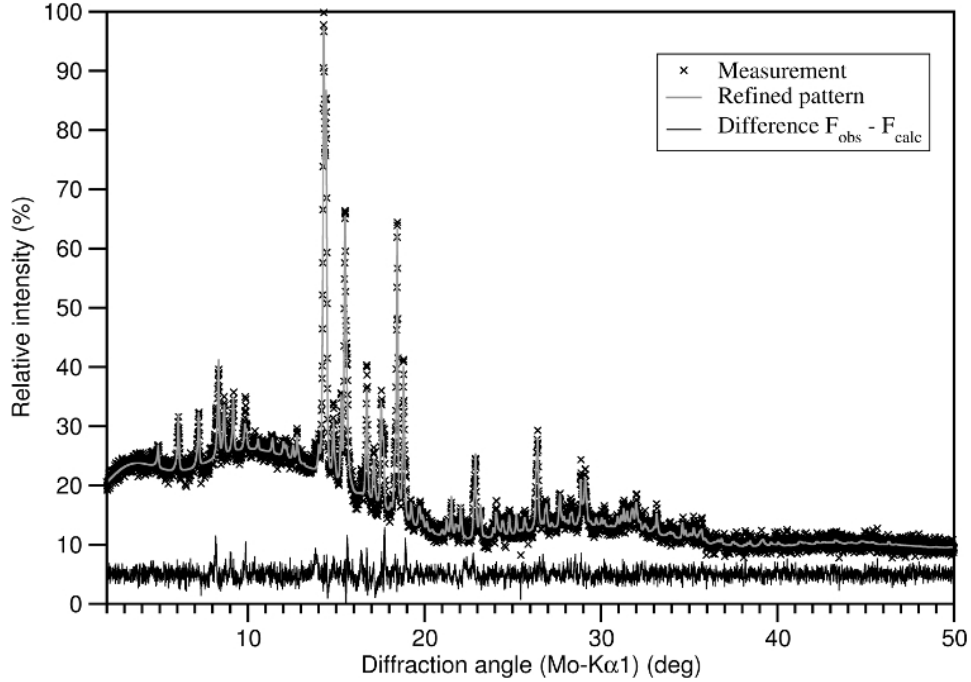


Figure 1. Rietveld refinement of KHg_6 . The powder diffraction pattern of a KHg_6 sample shows no additional crystalline phases. The strong diffuse background is caused by glass powder added to dilute the highly absorbing sample.

Susceptibility measurements were performed on a fully automated AC susceptometer (self-built) [26]. Data were measured at 1333 Hz and 3 Oe. The sample was cooled to 1.8 K without applying an external field, then heated to 5 K in a field of 3 Oe (shielding effect) and subsequently cooled to 1.8 K (Meissner effect).

Thermoanalysis

17.0 mg of KHg_6 powder were filled under argon in a tight-sealed steel crucible (Perkin Elmer steel crucibles 60 μl) and transferred into a differential scanning calorimeter (Linseis High Performance DSC PT10, Linseis Messgeräte GmbH, Selb, Germany). The sample was heated at a rate of 5 $\text{K}\cdot\text{min}^{-1}$ to $T_{\text{max}} = 200$ $^{\circ}\text{C}$. The heating was performed under streaming nitrogen (20 $\text{ml}\cdot\text{min}^{-1}$) and an empty steel crucible was used as reference. The endothermic effect with onset at 443 K indicates the incongruent melting of the sample (Fig. 3) which is in good agreement with the published phase diagram [1].

Band structure calculations

DFT calculations of the electronic band structure were performed with the program package Wien2000 [27], applying the full-potential linear augmented plane wave (FP-LAPW) method. The exchange and correlation functional of Perdew, Burke and Ernzerhof [28] with a generalised gradient approximation (GGA) was applied. The muffin-tin radii were set to 121.7 pm (2.3 a. u.) and the number of basis functions was determined by the value of $R_{\text{mt}} \cdot K_{\text{max}} = 8$ with K_{max} as the largest k vector. The separation energy was

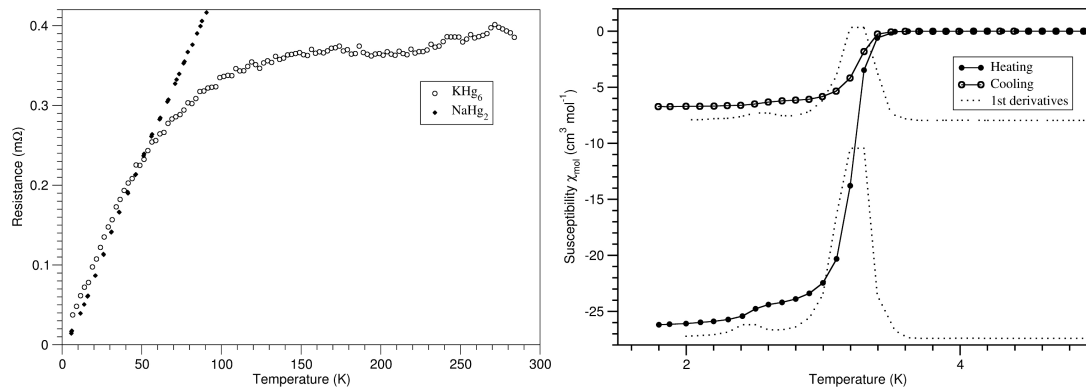


Figure 2. Above: Temperature dependence of the resistance of KHg_6 (cooling from room temperature). In comparison to NaHg_2 [18], KHg_6 shows strong deviation from ideal metallic behaviour and a low Ioffe-Regel limit resistance. Below: Susceptibility measurement of KHg_6 . KHg_6 becomes superconductive at 3.22 K. A weak additional signal occurs at 2.45 K and belongs to T_C of KHg_{11} impurities [3].

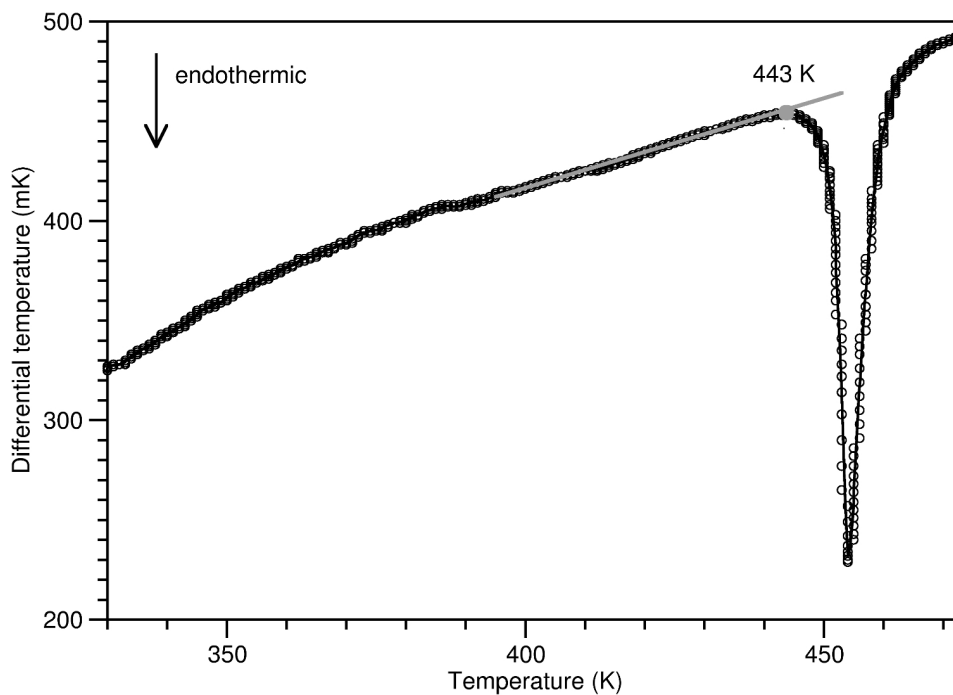


Figure 3. Differential scanning calorimetry showing the incongruent melting point of KHg_6 at 443 K.

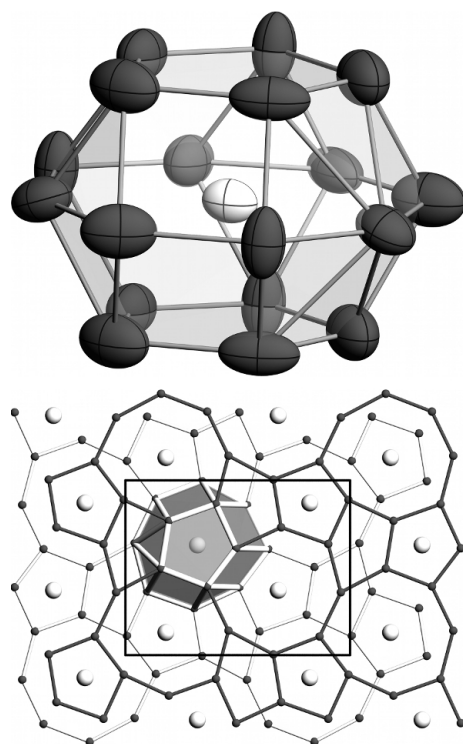


Figure 4. Above: coordination polyhedron of 18 Hg atoms around potassium. All ellipsoids (dark grey: Hg, light grey: K) have been drawn at a probability level of 90%. Below: Projection along [010] on the Hg nets and the formation of the [KHg₁₈] polyhedra. The dark grey nets lie at $y = \frac{1}{4}$, the light grey nets at $y = \frac{3}{4}$.

set to -6 Ry. 816 k points in the Brillouin zone (108 thereof in the irreducible Brillouin zone) were calculated in a 6x17x8 Monkhorst-Pack grid.

Results and Discussion

The new amalgam KHg₆ crystallizes isotypically to BaHg₆ [29] in the orthorhombic system (space group *Pnma*, No. 62, $a = 13.410(8)$, $b = 5.269(3)$, $c = 10.459(7)$ Å). The structure can be described as an arrangement of layers of condensed planar $(8^25)_4(5^28)_4$ Hg sheets consisting of eight- and five-membered rings. The layers are stacked along [010] in an ...ABA... sequence. The larger eight-membered rings of one layer are capped by five-membered rings of adjacent layers on both sides, resulting in an 18-fold coordination for the potassium atoms centering the eight-membered rings (see Fig. 4). Within a single layer, strong covalent Hg–Hg bonds are present (286.0 to 308.5 pm), whereas between two adjacent layers the Hg–Hg bonds are much weaker (322.3 to 423.9 pm; selected interatomic distances are compiled in Table A5).

Interatomic K–Hg distances range from 345.7(8) to 408.0(13) pm (see Table A5) and are in good agreement with those found in other potassium amalgams [3–7]. The structure description via [KHg₁₈] coordination polyhedra and covalent Hg–Hg bonding accounts for the ionic contributions in the structure by emphasising the coordination of negatively

charged Hg atoms surrounding the positively charged alkali metal atom according to $\text{K}^+[\text{Hg}_6]^-$.

As many other Hg-rich amalgams, however, this structure can also be deduced from motifs of a closest sphere packing, thus emphasising the metallic character of the compound.

The atoms Hg(1), Hg(3), Hg(5) and Hg(6) together with K(1) build a zig-zag chain of *cis*-edge-sharing octahedra. A second chain of *trans*-face-sharing octahedra is built from the atoms Hg(1), Hg(2) and Hg(5), and a third chain of *trans*-corner-sharing octahedra from the atoms Hg(1), Hg(2), Hg(4), Hg(5) and Hg(6). For atom labels and crystallographic sites see Table A2. All three chains extend along the *b* direction and share common Hg atoms to form a layer of octahedra (see Fig. 5). Each chain is an individual cut-out from a closest sphere packing, however, as the octahedra have different connection patterns and orientations, the sum of all three chains does not belong to one common closest sphere packing for the KHg_6 structure.

As a consequence of the interplay of ionic, covalent and metallic bonding contributions, KHg_6 shows a characteristic "bad metal" behaviour. The complex dependence of the specific resistance with temperature (see Fig. 2) shows metallic behaviour. At temperatures above 50 K the resistance deviates from linear behaviour, and converges toward a low Ioffe-Regel saturation resistance [30].

KHg_6 becomes superconducting when cooled below $T_C = 3.22$ K (see Fig. 2). The transition temperature is lower than the one of pure Hg ($T_C = 4.19$ K) [31] and higher than the one of the Hg-richest amalgam KHg_{11} ($T_C = 2.45$ K) [3]. Traces of this amalgam were still present in the sample used for susceptibility measurements, leading to a weak additional signal.

The DFT calculations of the total density of states (see Fig. 7) shows no pronounced minimum at the Fermi energy, i. e. neither a band gap nor pseudo-band gaps occur. This is in agreement with the overall metallic behaviour of KHg_6 and in very good agreement with details of the chemical bonding extensively described for BaHg_6 [29]. The partial DOS for K(1) show mostly p-state contributions below the Fermi level, however, the electron transfer is incomplete and s-states still contribute significantly to the density of states at the Fermi level. Bader charges have been calculated (see Table A7), emphasising this bonding situation with a charge for K of +0.87. The charge distribution for the Hg atoms is almost homogeneous, ranging from -0.09 for Hg(1) to -0.17 for Hg(3). This is in good agreement with the fact that Hg(3) shows the shortest distances to its neighbours.

Conclusions

KHg_6 is a new metallic amalgam with considerable ionic bonding contributions. The interplay of ionic, metallic and covalent bonding leads to interesting electric properties. The low Ioffe-Regel limit resistance can be interpreted as a consequence of small scattering length of the conducting electrons in a complex crystal structure, however, most of the intermetallic systems showing comparable behaviour have even more complex structures. We have found a new and prolific synthetic route toward intermetallic phases with high Coulomb contributions. Future investigations are aimed at the elucidation of the

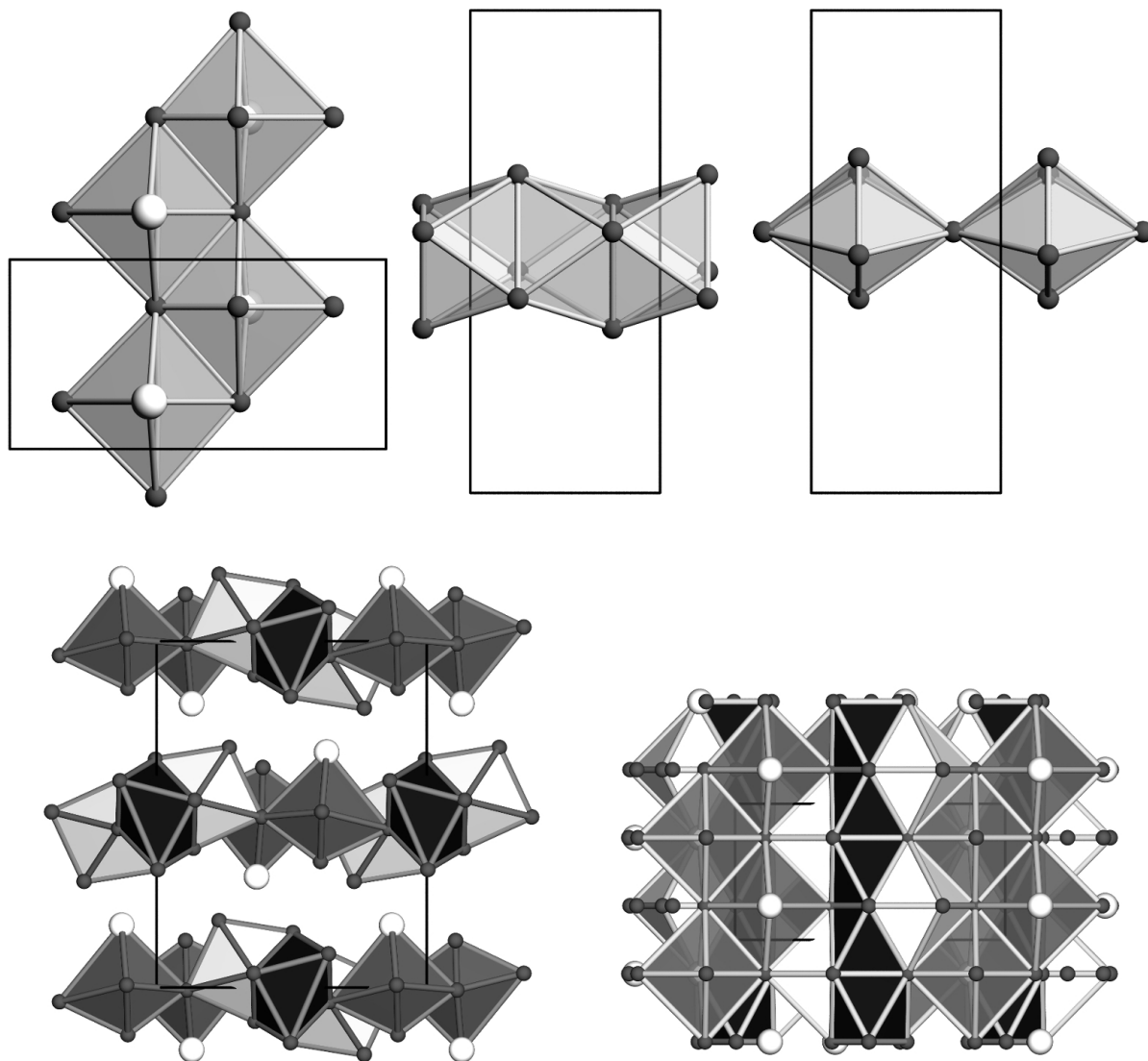


Figure 5. Upper row: three different chains of octahedra present in the structure of KHg_6 and their respective orientation in the unit cell (projected along $[100]$ for the first and along $[001]$ for the other two chains). Lower left and right: Connection of the three chain systems (chain 1: middle grey, chain 2: dark grey, chain 3: bright grey) to a sheet-like structure in two different projections of the unit cell (left: projection along $[010]$, right: projection along $[100]$).

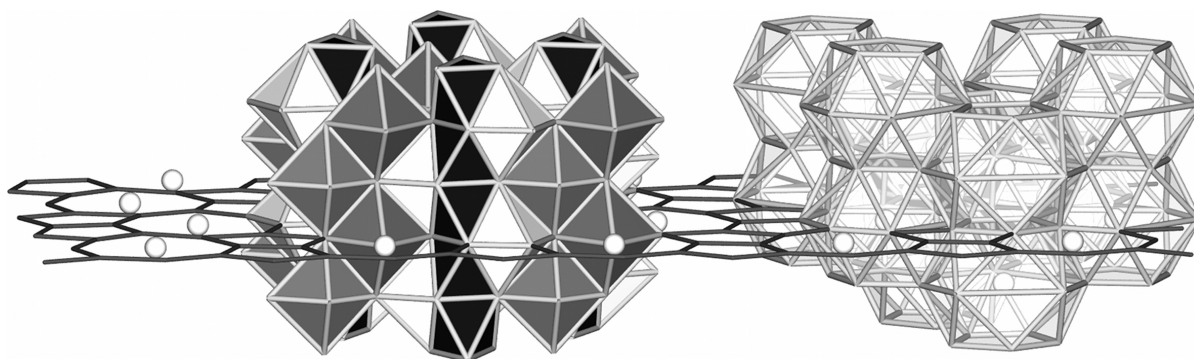


Figure 6. Synoptic view of the two complementary crystal structure descriptions via $[\text{KHg}_5]$ and $[\text{Hg}_6]$ octahedra chains (left) or by $[\text{KHg}_{18}]$ coordination polyhedra (left) and planar Hg nets.

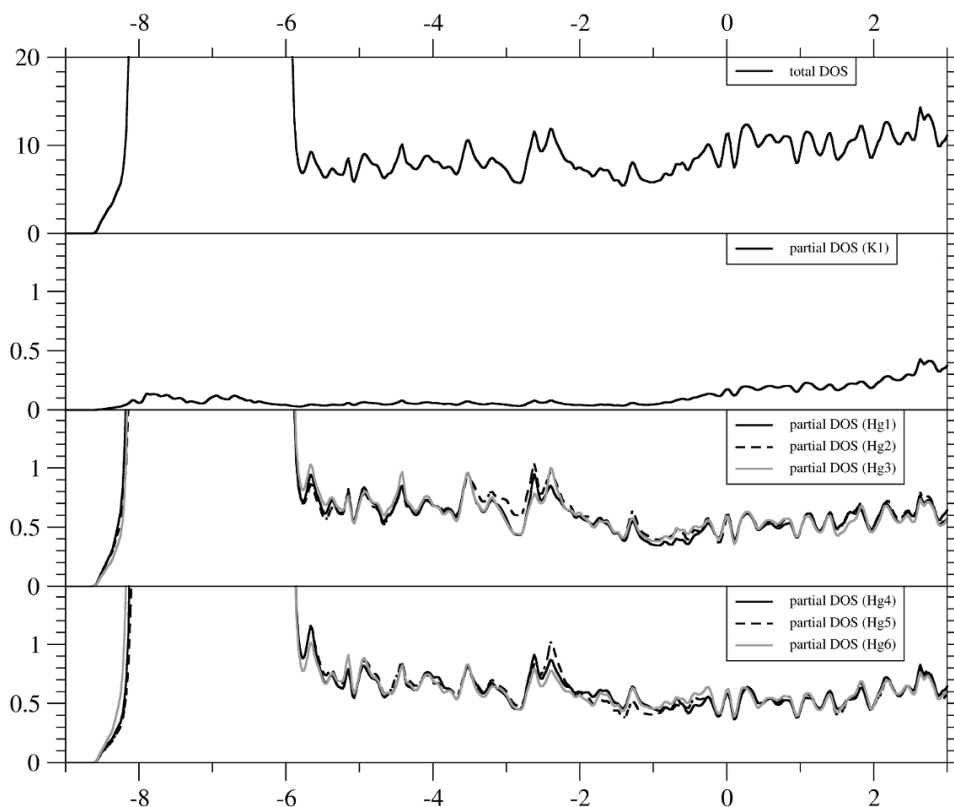


Figure 7. Plot of the total density of states in KHg_6 and the partial densities of states for atoms K(1) and Hg(1)-(6) in KHg_6 .

interplay of crystal structure, band structure and physical properties, as e. g. electric resistance and thermal conductivity with respect to thermoelectric behaviour.

Acknowledgements

We thank Dr. Reinhard Kremer, Eva Brücher and Gisela Siegle from Max-Planck-Institut für Festkörperforschung Stuttgart (Germany) for recording the temperature-dependent specific resistance and Prof. Dr.-Ing. Caroline Röhr from Albert-Ludwigs-Universität Freiburg im Breisgau (Germany) for her kind help with band structure calculations on amalgam systems. The susceptibility measurements have been performed by Gina Friederichs in the group of Prof. Dr. Dirk Johrendt at Ludwig-Maximilians-Universität München (Germany). DTA measurements were performed in collaboration with the group of Prof. Dr. Thomas M. Klapötke at LMU München.

References

- [1] T.B. Massalski (Ed.), Binary Phase Diagrams, second ed., ASM International, Materials Park, Ohio, USA, 1990.
- [2] G. Peyronel, Gazz. Chim. Ital. 82 (1952) 679.

- [3] E. Biehl, H.J. Deiseroth, *Z. Anorg. Allg. Chem.* 625 (1999) 1073.
- [4] E.J. Duwell, N.C. Baenziger, *Acta Crystallogr.* 8 (1955) 705.
- [5] E.J. Duwell, N.C. Baenziger, *Acta Crystallogr.* 13 (1960) 476.
- [6] E. Todorov, S.C. Sevov, *J. Solid State Chem.* 149 (2000) 419.
- [7] E. Biehl, H.J. Deiseroth, *Z. Anorg. Allg. Chem.* 625 (1999) 1337.
- [8] H.J. Deiseroth, in: M. Driess, H. Nöth (Eds.), *Molecular Clusters of the Main Group Elements*, Wiley-VCH, Weinheim, Germany, 2003.
- [9] F. Tambornino, C. Hoch, T. Bräuniger, in preparation.
- [10] E. Zintl, G. Brauer, *Z. Phys. Chem. B20* (1933) 245; E. Zintl, A. Schneider, *Z. Elektrochem.* 41 (1935) 771; H. Pauly, A. Weiss, H. Witte, *Z. Metallk.* 59 (1968) 554.
- [11] H.J. Deiseroth, A. Strunck, *Angew. Chem.* 101 (1989) 1286.
- [12] E.J. Duwell, N.C. Baenziger, *Acta Crystallogr.* 8 (1955) 705.
- [13] H.J. Deiseroth, A. Strunck, W. Bauhofer, *Z. Anorg. Allg. Chem.* 575 (1989) 31; H.J. Deiseroth, A. Strunck, *Angew. Chem.* 99 (1987) 701.
- [14] J.W. Nielson, N.C. Baenziger, *Acta Crystallogr.* 7 (1954) 277; A.V. Tkachuk, A. Mar, *Acta Crystallogr.* E62 (2006) i129.
- [15] H.J. Deiseroth, *Prog. Solid State Chem.* 25 (1997) 73.
- [16] J. Köhler, M.-H. Whangbo, *Solid State Sci.* 10 (2008) 444.
- [17] C. Hoch, A. Simon, *Z. Anorg. Allg. Chem.* 634 (2008) 853.
- [18] C. Hoch, A. Simon, *Angew. Chem.* 124 (2012) 3316; C. Hoch, A. Simon, *Angew. Chem. Int. Ed.* 51 (2012) 3262.
- [19] C. Hoch, A. Simon, *Z. Anorg. Allg. Chem.* 632 (2006) 2288.
- [20] F. Tambornino, C. Hoch, *Z. Kristallogr. Suppl.* 13 (2012) 79.
- [21] IPDS control software X-Area v. 1.39, Stoe & Cie. GmbH, Darmstadt, Germany, 2006.
- [22] X-RED, Data Reduction for STADIP and IPDS, Version 1.31, 2005, Stoe & Cie., Darmstadt, Germany.
- [23] X-SHAPE, Crystal Optimization for Numerical Absorption Correction Version 2.07, 2005, Stoe & Cie., Darmstadt, Germany.
- [24] L.M. Gelato, E. Parthé, *J. Appl. Cryst.* 20 (1987) 139.
- [25] A. Coelho, Topas Academic Version 4.1, Coelho Software, Brisbane, 2007.
- [26] M.C. Tegel, Iron Pnictide superconductors, Ph.D. Thesis, Ludwig-Maximilians-Universität München, 2011.
- [27] P. Blaha, K. Schwarz, G.K.H. Madsen, D. Kvasnicka, J. Luitz, WIEN2k, An Augmented Plane Wave and Local Orbitals Program for Calculating Crystal Properties, Technische Universität Wien, Austria, 2006.
- [28] J.P. Perdew, K. Burke, M. Ernzerhof, *Phys. Rev. Lett.* 77 (1996) 3865.
- [29] M. Wendorff, C. Röhr, *J. Alloys Compd.* 546 (2013) 320.

- [30] A.F. Ioffe, A.R. Regel, in: A.F. Gibson, F.A. Kroger, R.E. Burgess (Eds.), *Prog. Semicond.*, vol. 4, Heywood, London, 1960, p. 237.
- [31] L. Bergmann, C. Schaefer (Eds.), *Lehrbuch der Experimentalphysik*, seventh ed., vol. 2, Walter de Gruyter, Berlin, 1987, p. 786.
- [32] G.M. Sheldrick, A short history of SHELX, *Acta Crystallogr. A* 64 (2008) 112–122.

Supplementary information

Table A.1: Crystallographic data and details on data collection, structure solution and refinement of KHg_6 .

Empirical sum formula	KHg_6
Crystal system	orthorhombic
Space group	$Pnma$ (No. 62)
Lattice parameters (\AA , \AA^3)	$a = 13.410(8)$ $b = 5.269(3)$ $c = 10.459(7)$ $V = 739.1(8)$
Formula units Z	4
Calculated density ($\text{g}\cdot\text{cm}^{-3}$)	11.167
Absorption coefficient (mm^{-1})	68.154
Radiation, wavelength (\AA)	$\text{Ag-K}\alpha$, 0.56086
Diffractometer	IPDS 1 ((Stoe & Cie, Darmstadt, Germany)
Data collection mode	φ -Scans, $0^\circ \leq \varphi \leq 200.4^\circ$, $\Delta\varphi = 1.2^\circ$
Corrections	Lorentz, polarisation, absorption
Transmission factors T_{\min}/T_{\max}	0.0098/0.0725
Number of l.s. parameters	44
Number of collected data	6020
Number of unique data	798
Number of unique data with $I \geq 2\sigma(I)$	392
$R_{\text{int}}/R(\sigma)$	0.2018/0.1077
Data range	$-17 \leq h, \leq 17$, $2\theta_{\max} = 41.9^\circ$ $-6 \leq k, \leq 6$ $-13 \leq l, \leq 13$
Structure solution	direct methods [32]
Structure refinement	full matrix least-squares on F^2 [32]
$R1$ ($F_o^2 \geq 2\sigma(F_o^2)$)/ $R1$ (all data)	0.0517/0.1250
$wR2$ ($F_o^2 \geq 2\sigma(F_o^2)$)/ $wR2$ (all data)	0.925/0.1089
Residual electron density min./max ($\text{e}^- \cdot \text{\AA}^{-3}$)	2.424/-2.504
Extinction coefficient	0.00070(8)
ICSD deposition number	427001

Table A.2: Standardised fractional atomic coordinates [24] and equivalent isotropic displacement parameters (pm^2) for KHg_6 . All atoms occupy sites with the Wyckoff position $4(c)$ ($x, 1/4, z$). U_{eq} is defined as $\frac{1}{3}$ of the trace of the orthogonalised U_{ij} tensor. Standard deviations in units of the last digit are given in parentheses.

Atom	x	y	z	U_{eq}
K(1)	0.3203(8)	1/4	0.3702(12)	380(20)
Hg(1)	0.0410(2)	1/4	0.3597(2)	539(6)
Hg(2)	0.0974(3)	1/4	0.6356(3)	681(8)
Hg(3)	0.1357(2)	1/4	0.1068(2)	551(7)
Hg(4)	0.3067(2)	1/4	0.7314(3)	615(8)
Hg(5)	0.3410(2)	1/4	0.0044(3)	657(8)
Hg(6)	0.5074(2)	1/4	0.6114(3)	511(6)

Table A.3: Coefficients U_{ij} (pm^2) of the anisotropic atomic displacement parameters for KHg_6 . U_{ij} is defined as $\exp\{-2\pi^2[U_{11}(ha^*)^2 + \dots + 2U_{12}hka^*b^*]\}$. $U_{12} = U_{23} = 0$ in all cases due to site symmetry. Standard deviations in units of the last digit are given in parentheses.

Atom	U_{11}	U_{22}	U_{33}	U_{13}
K(1)	460(70)	340(40)	330(50)	-100(50)
Hg(1)	486(16)	733(14)	397(14)	61(11)
Hg(2)	1040(30)	528(12)	480(15)	-106(16)
Hg(3)	930(20)	350(10)	369(14)	-54(12)
Hg(4)	825(18)	357(10)	664(17)	396(15)
Hg(5)	686(17)	540(12)	746(18)	-302(14)
Hg(6)	386(15)	480(11)	666(17)	-6(12)

Table A.4: Details to the Rietveld refinement of KHg_6 .

Empirical sum formula	KHg_6
Crystal system	orthorhombic
Space group	$Pnma$ (No. 62)
Lattice parameters (\AA , \AA^3)	$a = 13.3850(20)$ $b = 5.2636(7)$ $c = 10.4519(20)$ $V = 736.4(2)$
Formula units	4
Calculated density ($\text{g}\cdot\text{cm}^{-3}$)	11.874
Absorption coefficient (mm^{-1})	143.01
Radiation, wavelength (\AA)	Mo- $K\alpha_1$, 0.70930
Diffractometer	Stadi P ((Stoe & Cie, Darmstadt, Germany)
Detector	linear position-sensitive detector
Monochromator	curved Ge(111)
Data collection geometry	Debye-Scherrer
Sample	capillary ($\varnothing = 0.2$ mm)
No. of background parameters	24
No. of profile parameters	36
R_p	2.089
R_{exp}	2.347
wR_p	2.704
GooF on χ^2	1.152

Table A.5: Selected interatomic distances (pm) in KHg_6 . The cutoff for next neighbours was set to 400 pm for the Hg atoms and to 450 pm for the K atom. Standard deviations in units of the last digit are given in parentheses.

Atoms		distance	Atoms		distance				
Hg(1)	–	Hg(3)	293.3(4)	Hg(5)	–	Hg(4)	289.3(5)		
		Hg(2)	298.9(4)			Hg(3)	295.6(5)		
		Hg(5)	303.5(4)			Hg(1)	303.5(4)		
		Hg(2)	322.3(3) (2x)			Hg(2)	308.5(3) (2x)		
		Hg(5)	342.5(3) (2x)			Hg(1)	342.5(3) (2x)		
		Hg(4)	359.3(3) (2x)			K(1)	368.5(9) (2x)		
		K(1)	374.4(13)			Hg(2)	373.6(5)		
		Hg(6)	375.4(3) (2x)			K(1)	384.0(13)		
		K(1)	381.6(13)			Hg(6)	–	Hg(3)	286.0(4)
		Hg(2)	–					Hg(6)	290.4(5)
Hg(4)	297.9(5)			Hg(4)	296.8(4)				
Hg(1)	298.9(4)			Hg(3)	325.9(3) (2x)				
Hg(5)	308.5(3) (2x)			K(1)	351.2(8) (2x)				
Hg(1)	322.3(3) (2x)			Hg(6)	352.3(4) (2x)				
Hg(5)	373.6(5)			K(1)	355.7(12)				
K(1)	376.6(10) (2x)			Hg(1)	375.4(3) (2x)				
K(1)	408.0(13)			K(1)	–			Hg(4)	345.7(8) (2x)
Hg(3)	–							Hg(6)	286.0(4)
						Hg(1)	293.3(4)	Hg(6)	355.7(12)
		Hg(5)	295.6(5)			Hg(3)	366.1(9) (2x)		
		Hg(4)	303.9(2) (2x)			Hg(5)	368.5(9) (2x)		
		Hg(6)	325.9(3) (2x)			Hg(3)	370.4(12)		
		K(1)	366.1(9) (2x)			Hg(1)	374.4(12)		
		K(1)	370.4(12) (2x)			Hg(2)	376.6(10) (2x)		
		Hg(4)	–			Hg(5)	289.2(5)	Hg(4)	377.9(13)
						Hg(6)	296.8(4)	Hg(1)	381.6(13)
				Hg(2)	297.9(5)	Hg(5)	384.0(13)		
Hg(3)	303.9(2) (2x)			Hg(2)	408.0(13)				
K(1)	345.7(8) (2x)			Hg(3)	423.9(13)				
Hg(1)	359.3(3) (2x)								
K(1)	377.9(13)								

Table A.6: Standardised fractional atomic coordinates [24] and equivalent isotropic displacement parameters (pm^2) for KHg_6 as result of the Rietveld refinement. All atoms occupy sites with the Wyckoff position $4(c)$ ($x, 1/4, z$). All atoms were refined with isotropic displacement parameters B_{eq} . Standard deviations in units of the last digit are given in parentheses.

Atom	x	y	z
K(1)	0.3280(21)	1/4	0.3850(36)
Hg(1)	0.0080(6)	1/4	0.1298(10)
Hg(2)	0.0993(6)	1/4	0.6277(13)
Hg(3)	0.1356(6)	1/4	0.6099(10)
Hg(4)	0.3036(8)	1/4	0.7211(10)
Hg(5)	0.3374(9)	1/4	0.0077(9)
Hg(6)	0.5356(7)	1/4	0.6513(10)

Table A.7: Bader charges for all atoms in KHg_6 .

Atom	charge
K(1)	+0.87
Hg(1)	-0.09
Hg(2)	-0.11
Hg(3)	-0.17
Hg(4)	-0.15
Hg(5)	-0.12
Hg(6)	-0.15

3.4.2. NMR Investigations on the Li Amalgams Li_3Hg , LiHg and LiHg_3

Introduction

The binary phase diagram Li–Hg was the topic of thermoanalytical studies of the early 20th century. The reported phases LiHg_6 , LiHg_2 and Li_2Hg were never characterised in crystallographic studies and most probably are non-existent. The mercury-richest Li amalgam LiHg_3 was prepared 1900 by electrolysis and subsequent crystallisation at low temperature.^[1] In 1911, LiHg and Li_3Hg were observed during thermoanalytic studies and their crystal structures were assigned to simple crystal structure types based on Debye-Scherrer patterns.^[2,3] No refinement of powder or single crystal data was performed. As Li amalgams present a structurally simple series from Hg-poor to Hg-rich compounds and both Hg and Li show convenient NMR activity, this system was chosen for systematic investigations on the quantification of polarity in intermetallic compounds via NMR methods, corroborated by *ab-initio* band structure calculations and measurement of physical properties.

The Knight shift is the shift in NMR signals in metallic systems and originates from the hyperfine coupling of the nuclear spin with the spin of conduction electrons. Electrons in orbitals with non-zero probability at the core site (*s* electrons) have the highest influence. In first approximation, *s* electrons can be regarded as the only influence on the Knight shift. For many metallic systems Knight shift measurements have been reported: NMR resonance for liquid Hg was observed in 1959, Knight shift for single-crystalline Hg was reported in 1968.^[4,5] Subsequent NMR studies on metallic Hg focused on expanded films or Hg in porous materials.^[6–8] In only two instances, Knight shift measurements for Hg in intermetallic compounds have been performed: the mixed crystal series $\text{NaHg}_{1-x}\text{Tl}_x$ ($x = 0.1–0.9$) and $\text{Hg}_{1-x}\text{Cd}_x\text{Te}$ ($x = 0.2–0.28$).^[9,10] Only in the latter case, Hg NMR shifts were discussed and put into context with band structure calculations. In contrast, information on lithium NMR is abundant. The Knight shift of metallic lithium was reported in 1949.^[11] Since then, lithium NMR has become a powerful tool in both inorganic and organic chemistry. Main focuses lie on ionic lithium compounds (solution or solid state) and covalently bonded lithium in organometallic compounds.^[12–15] Recently, *in-situ* NMR monitoring of lithium ion batteries has gained reasonable attention.^[16–19] However, studies on intermetallic compounds are less common. Herzog-Cance focussed on the temperature dependent mobility of lithium in Li_2Ga_7 , but no detailed discussion of the bonding situation is given.^[20] Menetrier focussed on the Knight shift in a number of Li–Sn compounds showing nonclassical Zintl-like behaviour.^[21] Band structure calculations were correlated with the observed ^7Li Knight shift. However, complementary Sn NMR was not reported on. No systematic combined NMR investigation of both the electropositive and the electronegative elements has been reported so far.

Sample preparation and crystallographic characterization

For the preparation of Li_3Hg and LiHg , suitable amounts of Li (abcr 99.9%) and Hg (double distilled) were mixed in an argon filled glovebox and sealed in steel crucibles by mechanical pinching and folding. The sealed crucibles were heated under Ar atmosphere to 575 K over the course of 10 h, held at elevated temperature for 48 h and subsequently

Table 3.22.: Results of the Rietveld refinement of LiHg₃ and LiHg.

Formula		LiHg ₃	LiHg
<i>Z</i>		2	1
Crystal system		hexagonal	cubic
Space group type		<i>P6₃/mmc</i> (194)	<i>Pm$\bar{3}m$</i> (221)
Lattice parameters [\AA , \AA^3]	<i>a</i> =	6.23608(9)	3.29140(9)
	<i>c</i> =	4.79217(9)	
	<i>V</i> =	161.39(6)	35.656(3)
Density (X-ray) [g/cm ³]		12.5258(4)	9.6648(8)
Radiation		– MoK α_1 –	
Monochromator		– curved Ge single crystal –	
Parameters		32	24
Background Parameters		– 18 –	
<i>R</i> values	<i>R_p</i> =	00.1609	0.02187
	<i>R_{wp}</i> =	0.02404	0.03089
	χ^2 =	1.718	1.798

cooled to room temperature within 10 h. The highly air- and moisture-sensitive products were isolated and handled under argon. For details on preparation see Table 3.21.

LiHg₃ was prepared by isothermal preparative electrolysis, see chapter 3.1.1. As electrolyte, a solution of lithium iodide (5 g, 37.4 mmol, Acros Organics 99.999%) in dry DMF (DMF, 100 ml, dried over molecular sieve 3 \AA , Fischer Chemical, HPLC grade) was used. Electrolysis was

performed at room temperature with terminal voltage 5 V over the course of 12 h, yielding crystal needles several millimetres in length. The crystals were washed with dry DMF, dried in high vacuum and further handled in an argon-filled glovebox.

Suitable single crystals of irregular shape (Li₃Hg) or needles (LiHg₃) were isolated and sealed in capillaries ($\varnothing = 0.1$ mm) filled with dry paraffin oil. After centering on the one-circle goniometer of a IPDS1 diffractometer system (Stoe & Cie. GmbH, Darmstadt, Germany) equipped with imaging plate and graphite-monochromatised Ag-K α radiation (Li₃Hg) or Mo-K α radiation (LiHg₃), the metric was determined from 11 orientation images. Final data collection was performed in φ scan geometry. Data were corrected for Lorentz, polarisation and absorption effects.^[22]

Phase purity of the samples was confirmed by X-ray powder diffractometry (Stoe STADI-P, Stoe & Cie, Darmstadt, MoK α_1 radiation, graphite monochromator). Small amounts were ground and sealed in glass capillaries ($\varnothing = 0.2$ mm). Data from Rietveld refinements were used for band structure calculations (see Tables 3.22 and 3.23).

Table 3.21.: Details on preparation of Li₃Hg and LiHg.

Nominal composition	amount weighed			
	<i>m</i> (Li) [mg]	<i>n</i> (Li) [mol]	<i>m</i> (Hg) [mg]	<i>n</i> (Hg) [mol]
Li ₃ Hg	0.945	135.493	9.6595	45.164
LiHg	0.3345	48.18	9.6655	48.18

Crystal structures

The three Li amalgams crystallise in simple and highly symmetric structure types. Reported structures^[3,23] were verified and all structural parameters defined more precisely by least-squares refinement on the basis of single crystal and powder diffraction data.

The Hg-richest amalgam in this series, LiHg₃, is isotypic with the Ni₃Sn structure type and can be described as a colouring variant of the hcp packing (see also REHg₃ with RE = Y, La, Gd, Dy, Ho, Er, Tm, Yb, Lu; chapter 3.3.5).^[24] The hexagonal unit cell shows an *a/c*-ratio of 1.302, close to the one of the aristotype (*a/c*-ratio: 1.247) and thus considerably shorter than the ideal ratio of $\sqrt{8}/3 = 1.633$. Both Li and Hg are coordinated by twelve atoms in anticuboctahedral environment. Li atoms occupy sites 2*c* with site symmetry $\bar{6}m2$ and Hg occupies sites 6*h* with site symmetry *mm*2. Li is solely coordinated by Hg, Hg is coordinated by 8 Hg and 4 Li. This reflects the high polarity in the sense of Li⁺[Hg^{δ-}]₃. The high site symmetry is important with respect to NMR signal shape.

LiHg crystallises with the CsCl structure type (in intermetallic chemistry often referred to as β' phase). Li and Hg form commutative cubic primitive sublattices and are coordinated by twelve atoms (eight atoms of the alternate and six of the identical element) in rhombic dodecahedra with highest cubic point symmetry (Li and Hg: 1*a*, $m\bar{3}m$).

The Hg-poorest amalgam Li₃Hg crystallises with the AlFe₃ structure type,^[25] a colouring variant of the bcc packing with 2x2x2-fold unit all with respect to bcc. It can also be described as a NaCl-type lattice from Hg (4*a*, $m\bar{3}m$) and Li1 (4*b*, $m\bar{3}m$) with Li2 occupying all tetrahedral interstices (8*c*, $\bar{4}3m$). Due to the high cubic point symmetry, NMR signals are expected to be sharp for all crystallographic sites.

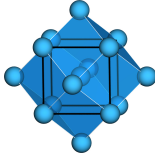
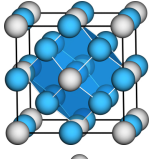
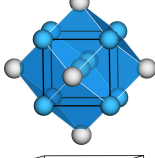
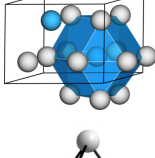
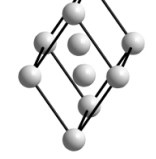
NMR spectroscopy - ⁷Li

⁷Li solid state NMR signals for Li₃Hg, LiHg and LiHg₃ were recorded for the first time, elemental Li was used as metallic reference^[28] and [Li(DMF)]₄I as cationic reference (1.24 ppm). All shifts are positive and with the exception of [Li(DMF)]₄I, well out of range for usual cationic lithium (see Table 3.24).^[29] Elemental Li shows the highest shift (265.1 ppm), consistent with literature.^[28] In the Li-richest compound Li₃Hg the shift is lower (203.2 ppm). This trend continues (LiHg (101.7 ppm) to LiHg₃ (72.9 ppm)) with the Hg-richest compound exhibiting the lowest shift.

NMR spectroscopy - ¹⁹⁹Hg

¹⁹⁹Hg solid state NMR signals for Li₃Hg, LiHg and LiHg₃ have been recorded for the first time, elemental mercury was used as metallic reference.^[4,30] The shifts of mercury (22480 ppm), LiHg (4500 ppm) and LiHg₃ (17172 ppm) are well out of the range of ionic mercury compounds. Li₃Hg exhibits the smallest shift (1680 ppm). The findings are consistent with the results shown for the ⁷Li measurements in the sense of ionic bonding contributions.

Table 3.23.: The crystal structures of lithium,^[26] Li₃Hg, LiHg, LiHg₃ and mercury.^[27] Lithium atoms: blue, mercury atoms: grey

Sum formula	Unit cell	Structure type	Space group type	Lattice parameters / Å	Z	Wyckoff numbers
Li		W	$Fm\bar{3}m$ (No. 221)	$a = 3.509$	2	Li1: 2a
Li ₃ Hg		AlFe ₃	$Fm\bar{3}m$ (No. 225)	$a = 6.561$	4	Hg1: 4a Li1: 4b Li2: 8c
LiHg		CsCl	$Fm\bar{3}m$ (No. 225)	$a = 3.286$	1	Hg1: 1a Li1: 1b
LiHg ₃		Ni ₃ Sn	$P6_3/mmc$ (No. 194)	$a = 6.240$ $c = 4.794$	2	Hg1: 6h Li1: 2c
Hg		Hg	$R\bar{3}m$ (No. 166)	$a = 3.025$ $\alpha = 70.74^\circ$	3	Hg1: 1a

Electric resistance measurements

Temperature-dependent measurements of the electric conductivity were performed with a Cryovac cryostat between 290 and 3 K on cold-pressed polycrystalline sample pellets. The van-der-Pauw 4-point technique (current generator Keithley 2400 SourceMeter, voltmeter Hewlett-Packard 43420A Nanovoltmeter) was applied with a current of 1 mA. Specific electric resistance as a function of temperature for the three lithium amalgams is shown in Figure 3.26.

Table 3.24.: ⁷Li- and ¹⁹⁹Hg-NMR shifts observed for lithium, Li₃Hg, LiHg, LiHg₃ and mercury

	Li	Li ₃ Hg	LiHg	LiHg ₃	Hg
⁷ Li /ppm	265.1	203.2	101.7	72.9	—
¹⁹⁹ Hg /ppm	—	1680	4500	17172	22480

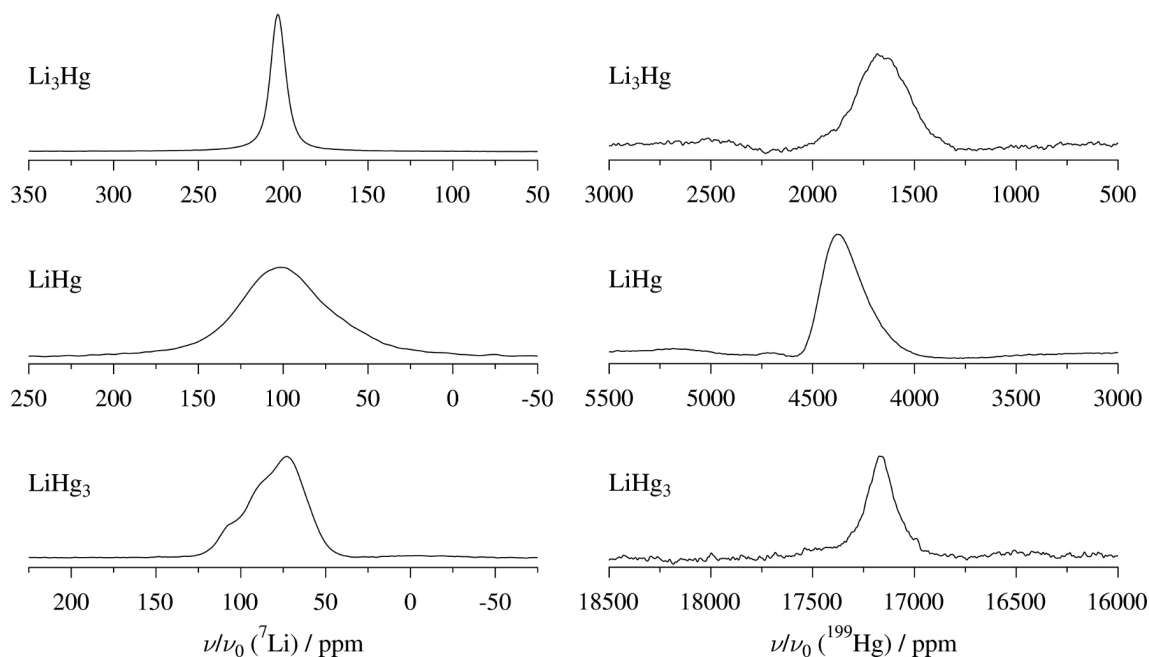


Figure 3.25.: ^{199}Hg and ^7Li NMR signals for Li_3Hg , LiHg and LiHg_3 .

Computational details

All structural parameters used for the calculations were either taken from literature (Li and Hg)^[26,27] or were the result of structural refinements (Li_3Hg , LiHg and LiHg_3). Calculations were carried out with the WIEN2k package by means of the full-potential linearized augmented plane wave algorithm (FP-LAPW).^[31] For the modeling of the band structure and for optimizing the conditions for mercury rich amalgams, three different functionals were applied: PBE-GGA,^[32] unscreened hybrid PBE0^[33] and the Yukawa screened PBE0.^[34] To achieve straightforward comparable results, the calculation for the different compounds were carried out as similar as possible. Therefore, all Muffin-Tin radii R_{mt} were set to 2.5 a.u. (132.3 pm), and the number of basis functions $R_{\text{mt}} \cdot k_{\text{max}}$ was set to 8 with k_{max} as largest k vector. Details on the calculations are compiled in Table 3.25. In order to reduce the computational time when utilising unscreened PBE0 and YS-PBE0 potentials, those computations were performed with a reduced k-mesh as implemented in the WIEN2k code.^[31] Fat-band plots are compiled in Figure 4.20.

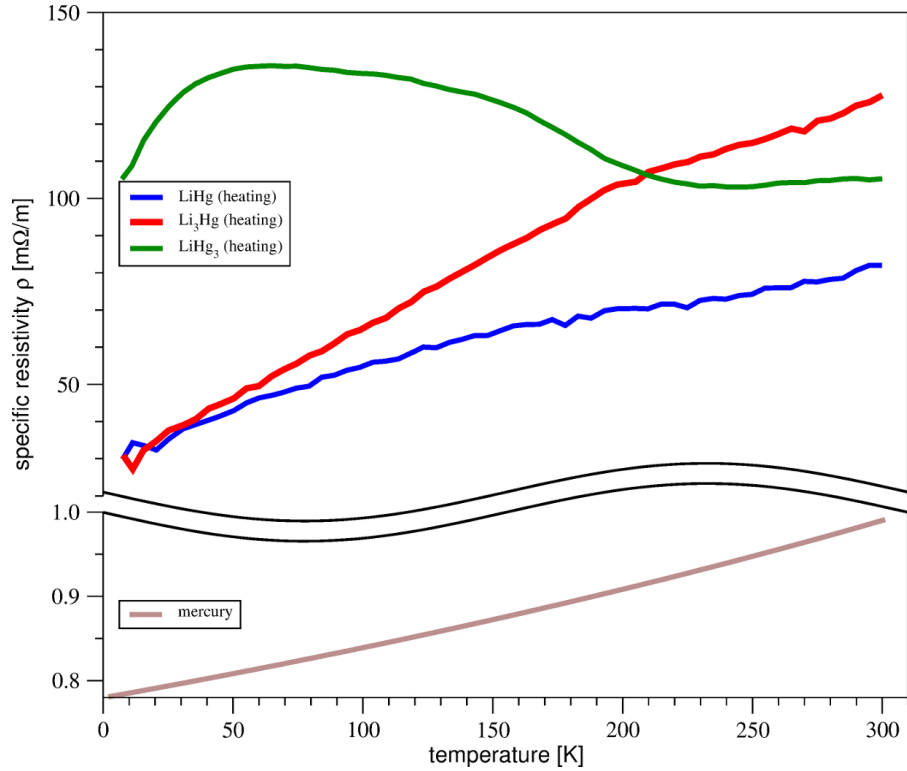


Figure 3.26.: Measured specific resistances for the amalgams in question and mercury as comparison. Data for heating from 2 K to 300 K are shown.

Table 3.25.: Computational details for the calculation of the electronic structures of lithium, Li_3Hg , LiHg , LiHg_3 and mercury.

		Li	Li_3Hg	LiHg	LiHg_3	Hg
crystal data		see Tables 3.23 and 3.22				
PBE	$R_{\text{mt}}/\text{a.u.}$	2.5	2.5	2.5	2.5	2.5
	$R_{\text{mt}} \cdot k_{\text{max}}$	8	8	8	8	8
	k-points/BZ	1728	1728	1728	1728	512
	k-Points/IBZ	68	72	126	133	512
	Monkhorst-Pack-Grid	$12 \times 12 \times 12$	$12 \times 12 \times 12$	$12 \times 12 \times 12$	$12 \times 12 \times 12$	$8 \times 8 \times 8$
PBE0	$R_{\text{mt}}/\text{a.u.}$	2.5	2.5	2.5	2.5	2.5
	$R_{\text{mt}} \cdot k_{\text{max}}$	8	8	8	8	8
	k-points/BZ	27	27	27	27	27
	k-Points/IBZ	27	27	27	27	27
	reduced MP-Grid	$3 \times 3 \times 3$	$3 \times 3 \times 3$	$3 \times 3 \times 3$	$3 \times 3 \times 3$	$3 \times 3 \times 3$
#of bands	100	75	75	100	75	
YS-PBE	R_{mt}	2.5	2.5	2.5	2.5	2.5
	$R_{\text{mt}} \cdot k_{\text{max}}$	8	8	8	8	8
	k-points/BZ	27	8	27	8	27
	k-Points/IBZ	27	8	27	8	27
	reduced MP-Grid	$3 \times 3 \times 3$	$2 \times 2 \times 2$	$3 \times 3 \times 3$	$2 \times 2 \times 2$	$3 \times 3 \times 3$
#of bands	100	100	75	100	75	

3.4.3. $\text{AHg}_{11-x}\text{In}_x$

$\text{KHg}_{11-x}\text{In}_x$

A saturated solution of KI (Sigma Aldrich, 99.0 % metal basis) in DMF (100 ml, Fischer Organic, HPLC grade) was electrolysed on a liquid HgIn electrode. The electrode material was prepared by dissolving elemental In (smart elements, 99.999 %) in Hg (double distilled) at room temperature. Electrolysis parameters: T = room temperature, U = 3.5 V, duration = 24 h, electrode material: HgIn in a glass spoon contacted with Pt wire. The electrolytic process yielded a mixture of $\text{KHg}_{11-x}\text{In}_x$ ($x \approx 1$) and KIn_4 in a 85:15 ratio as grey microcrystalline powder. The product mixture was air- and moisture-sensitive, and upon exposure with water formation of metallic Hg (or HgIn) and KOH was observed. A powder X-ray diffractogram was collected and subsequently refined, see Table 3.26 and Figure 3.27.

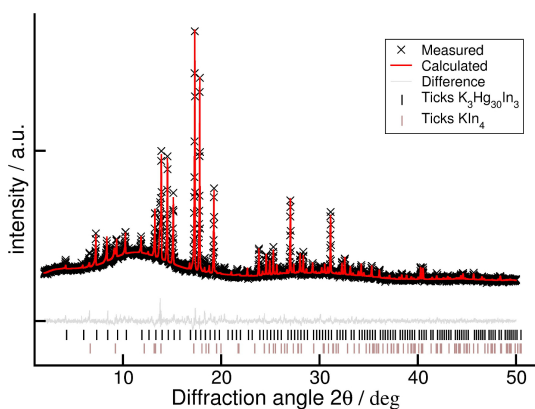


Figure 3.27.: Results of the Rietveld refinement of $\text{KHg}_{11-x}\text{In}_x$ with $x \approx 1$.

Table 3.26.: Results of the Rietveld refinement of $\text{KHg}_{11-x}\text{In}_x$ with $x \approx 1$.

Formula	$\text{K}_3\text{Hg}_{30}\text{In}_3$	KIn_4
Phase fraction	85%	15%
Z	1	4
Crystal system	cubic	tetragonal
Space group	$Pm\bar{3}m$	I/mmm
Lattice parameters [\AA , \AA^3]	a 9.7112(3)	a 4.762(2)
	c —	c 12.323(12)
	V 915.85(7)	V 279.5(4)
Density [g/cm^3]	11.69(5)	7.961(10)
Radiation	— $\text{MoK}\alpha_1$ —	
Parameters	— 48 —	
Background par.	— 18 —	
R values	$R_p = 0.02380$	
	$R_{wp} = 0.03265$	
	$\chi^2 = 1.281$	

Thermal displacement parameters were constrained to be equal for all Hg atoms. Subsequent freeing of one thermal displacement parameter for Hg at a time was performed to check for mixed occupation. For Hg4/In4 a smaller value indicated less electrons and thus mixed occupancy with In. This, however, does not entirely exclude the possibility of mixed Hg/In positions for Hg1–Hg3. Refinement of KIn_4 was performed with very few parameters as it was only present with 15 wt% and many reflections with small intensities were unobserved. Thermal displacement factors were not refined and set to $B_{\text{iso}} = 1$. Least-squares parameters refined were both lattice parameters, one atomic position (x of In2) and one peak broadening effect (integral breadth crystallite size approach, 4 parameters) leading to only 7 parameters for this phase.

Both crystal structures KHg_{11} and KIn_4 have previously been described.^[35] The crystal structures were validated within small error margins.

Table 3.27.: Standardised fractional atomic coordinates, site occupation factors and isotropic displacement parameters / \AA^2 for $\text{K}_3\text{Hg}_{30}\text{In}_3$ and KIn_4 . Standard deviations in units of the last digit are given in parentheses.

Atom	Wyckoff number	x	y	z	s.o.f.	B_{iso}
$\text{K}_3\text{Hg}_{30}\text{In}_3$						
K1	3d	1/2	0	0	1	2.62(13)
Hg1	1b	1/2	1/2	1/2	1	3.91(11)
Hg2	8g	0.1554(3)	0.1554(3)	0.1554(3)	1	3.91(11)
Hg3	12i	0.3428(3)	0.3428(3)	0	1	3.91(11)
Hg4	12j	0.2622(4)	0.2622(4)	1/2	0.72(3)	4.3(2)
In4	12j	0.2622(4)	0.2622(4)	1/2	0.18(3)	4.3(2)
KIn_4						
K1	2a	0	0	0	1	1
In1	4d	0	1/2	1/4	1	1
In2	4e	0	0	0.435(3)	1	1

$\text{RbHg}_{11-x}\text{In}_x$

A saturated solution of RbI (ChemPur, 99.9 %) in DMF (100 ml, Fischer Organic, HPLC grade) was electrolysed on a liquid HgIn electrode. The electrode material was prepared by dissolving equal atomic amounts of elemental In (smart elements, 99.999 % metal basis) and Hg (double distilled) at room temperature. Electrolysis parameters: T = room temperature, U = 3.5 V, duration = 24 h, electrode material: HgIn dispersed in a glass spoon contacted with Pt wire. The electrolytic process yielded a grey microcrystalline powder sensitive toward air and moisture. A powder diffractogram was collected and subsequently refined, see Table 3.28 and Figure 3.28. The product was identified as $\text{RbHg}_{11-x}\text{In}_x$ with $x \approx 6.2(3)$. Elemental analysis (ICP-AES) confirmed the composition (Rb:Hg:In \approx 1:6:6) within small error margins.

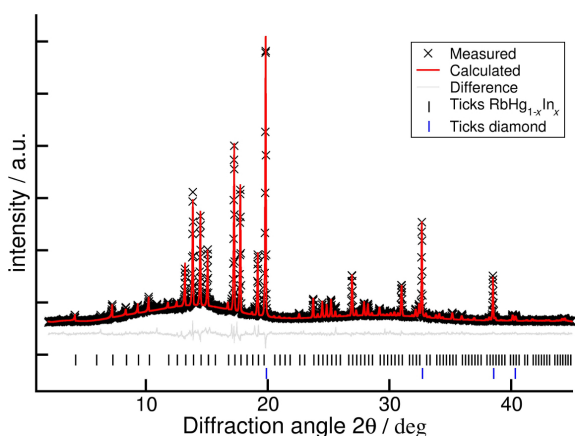


Figure 3.28.: Results of the Rietveld refinement of $\text{RbHg}_{11-x}\text{In}_x$ with $x \approx 6.2(3)$.

Table 3.28.: Results of the Rietveld refinement of $\text{RbHg}_{11-x}\text{In}_x$ with $x \approx 6.2(3)$.

Formula	$\text{RbHg}_{11-x}\text{In}_x$
Z	4
Crystal system	cubic
Space group	$Pm\bar{3}m$
Lattice parameters [\AA , \AA^3]	$a = 9.7538(3)$ $V = 927.93(7)$
Density [g/cm^3]	8.56(12)
Radiation	– Mo $\text{K}_{\alpha 1}$ –
Parameters	– 41 –
Background par.	– 19 –
R values	$R_{\text{exp}} = 0.0097$ $R_p = 0.01577$ $R_{\text{wp}} = 0.02297$ $\chi^2 = 2.303$

RbHg_{11-x}In_x crystallises in the BaHg₁₁ type ($Pm\bar{3}m$, $a = 9.7538(3)$ Å), all Hg positions shows mixed occupancy with In in varying amounts. This led to various complications during Rietveld refinement which were dealt with as follows: Prior to measurement, the substance was mixed with diamond (approx. 90 wt%) to lower the overall absorption. The absorption was accounted for by modelling a cylindrical shape ($\varnothing_{\text{outer}} = 0.3$ mm, $\varnothing_{\text{inner}} = 0.28$ mm), the packing density was set to 0.7. Isotropic thermal displacement parameters were constrained for all Hg/In mixed positions, the parameter for Rb was refined and gave a value similar to the formerly mentioned. Site occupation parameters of each Hg/In position were constrained to be fully occupied.

If every position was assumed to be occupied by Hg only, thermal displacement of Rb became negative, indicating too many electrons present. Assuming every position to be fully occupied by In, thermal displacement of Rb became unreasonably large. Free refinement of site occupation factors together with thermal displacement factors led to strong correlation and was thus avoided. χ^2 is rather high despite the good fit due to long measurement (72 h) and the resulting superior counting statistics (see R_{exp} , Table 3.28). It is noteworthy that the refinement is fragile and minor changes may result in large deviations from the reported values. For further discussion see chapter 4.3.3.

Table 3.29.: Standardised fractional atomic coordinates, site occupation factors and equivalent isotropic displacement parameters /Å² for RbHg_{11-x}In_x. Standard deviations in units of the last digit are given in parentheses.

Atom	Wyckoff number	x	y	z	s.o.f.	B_{iso}
Rb1	3d	0	0	1/2	1	2.2(4)
Hg1	1b	1/2	1/2	1/2	0.88(7)	2.98(13)
In1	1b	1/2	1/2	1/2	0.12(7)	2.98(13)
Hg2	8g	0.1548(3)	x	x	0.49(5)	2.98(13)
In2	8g	0.1548(3)	x	x	0.51(5)	2.98(13)
Hg3	12i	0.2646(3)	1/2	x	0.38(5)	2.98(13)
In3	12i	0.2646(3)	1/2	x	0.62(5)	2.98(13)
Hg4	12j	0.3458(3)	x	0	0.65(5)	2.98(13)
In4	12j	0.3458(3)	x	0	0.35(5)	2.98(13)

References

- [1] W. Kerp, W. Böttger, *Z. Anorg. Allg. Chem.*, **25(1)**, 1–71 (1900).
- [2] G. J. Zukowsky, *Z. Anorg. Allg. Chem.*, **71(1)**, 403–418 (1911).
- [3] E. Zintl, A. Schneider, *Z. Elektrochem. Angew. Phys. Chem.*, **41(11)**, 771–774 (1935).
- [4] W. Knight, A. Berger, V. Heine, *Annals of Physics*, **8(2)**, 173–193 (1959).
- [5] R. Weinert, R. Schumacher, *Phys. Rev.*, **172(3)**, 711–717 (1968).
- [6] V. S. Kasperovich, E. V. Charnaya, C. Tien, C. S. Wur, *Phys. Solid State*, **45(9)**, 1802–1807 (2003).

- [7] W. W. Warren, F. Hensel, *Phys. Rev. B*, **26(10)**, 5980–5982 (1982).
- [8] U. El-Hanany, W. W. Warren, *Phys. Rev. Lett.*, **34(20)**, 1276–1279 (1975).
- [9] P. C. Schmidt, W. Baden, N. Weiden, A. Weiss, *Phys. Stat. Sol. A*, **92**, 205–212 (1985).
- [10] J. Shi, M. Wessels, J. H. Ross, *Phys. Rev. B*, **48(12)**, 8742–8746 (1993).
- [11] W. Knight, *Phys. Rev.*, **76(8)**, 1259–1260 (1949).
- [12] H. Günther, D. Moskau, P. Bast, D. Schmalz, *Angew. Chem.*, **99(12)**, 1242–1250 (1987); b) H. Günther, D. Moskau, P. Bast, D. Schmalz, *Angew. Chem., Int. Ed.*, **26**, 1212 (1987).
- [13] H. Günther, *J. Bras. Chem. Soc.*, **10(4)**, 241–262 (1999).
- [14] H. J. Reich, *J. Org. Chem.*, **77(13)**, 5471–5491 (2012).
- [15] D. Johnels, G. Harald, in R. Luisi, V. Capriati (editors), *Lithium Compounds in Organic Synthesis: From Fundamentals to Applications*, John Wiley & Sons, Inc., London (2014).
- [16] C. P. Grey, Y. J. Lee, *Solid State Sci.*, **5(6)**, 883–894 (2003).
- [17] C. P. Grey, N. Dupré, *Chem. Rev.*, **104**, 4493–4512 (2004).
- [18] N. M. Trease, T. K. Köster, C. P. Grey, *Electrochem. Soc. Inter.*, **20**, 69–73 (2011).
- [19] F. Blanc, M. Leskes, C. P. Grey, *Accounts of Chemical Research*, **46(9)**, 1952–1963 (2013).
- [20] M. Tillard-Charbonnel, C. Belin, M. H. Herzog-Cance, *Eur. J. Solid State Inorg. Chem.*, **25**, 329 (1988).
- [21] E. Bekaert, F. Robert, P. E. Lippens, M. Ménétrier, *J. Phys. Chem. C*, **114(14)**, 6749–6754 (2010).
- [22] A. L. Spek, *Acta Crystallogr. D*, **65(2)**, 148–155 (2009).
- [23] E. Zintl, G. Brauer, *Z. Phys. Chem.*, **20**, 245–271 (1933).
- [24] P. Rahlfs, *Metallwirtschaft, Metallwissenschaft, Metalltechnik*, **16**, 343–345 (1937).
- [25] A. J. Bradley, A. H. Jay, *Proc. R. Soc. A*, **125**, 339–357 (1932).
- [26] A. Hull., *Phys. Rev.*, **10(6)**, 661–696 (1917).
- [27] C. S. Barrett, *Acta Crystallogr.*, **10(1)**, 58–60 (1957).
- [28] R. Schumacher, N. VanderVen, *Phys. Rev.*, **144(1)**, 357–360 (1966).
- [29] D. M. Grant, R. K. Harris, *Encyclopedia of Nuclear Magnetic Resonance, 8 Volume Set*, Wiley, 1st edition (1996).
- [30] W. E. Blumberg, B. Telephone, J. Eisinger, R. G. Shulman, M. Hill, **26(7)**, 1187–

1194 (1965).

- [31] P. Blaha, K. Schwarz, G. Madsen, D. Kvasnicka, J. Luitz, *An Augmented Plane Wave Plus Local Orbitals Program for Calculating Crystal Properties* (2013).
- [32] J. P. Perdew, K. Burke, M. Ernzerhof, *Phys. Rev. Lett.*, **77(18)**, 3865–3868 (1996).
- [33] C. Adamo, V. Barone, *J. Chem. Phys.*, **110(13)**, 6158 (1999).
- [34] F. Tran, P. Blaha, *Phys. Rev. B*, **83(23)**, 235118 (2011).
- [35] E. Biehl, H.-J. Deiseroth, *Z. Anorg. Allg. Chem.*, **625(7)**, 1073–1080 (1999).

3.5. Electrolyses on Mercury-Free Cathode Materials

The following chapter contains published as well as unpublished results of electrolyses with emphasis on mercury-free cathode materials. In the first part, electrocrystallisation as a new synthetic method toward intermetallic phases is presented and has been published in *Inorg. Chem.*. After an introduction focussing on historical aspects of electrolysis, the techniques, prerequisites, limitations and overall aptness of electrocrystallisation are presented. Products as yielded by electrolysis on elemental (Hg or Ga), binary (Ga/Sn eutectic, HgIn) and ternary (Ga/In/Sn eutectic) cathode systems are investigated. Literature-known compounds previously synthesised by classical solid state methods were reproduced by electrocrystallisation ($\text{Li}_3\text{Ga}_{14}$, NaGa_4 , $\text{K}_8\text{Ga}_8\text{Sn}_{38}$). In addition, the new binary main group element compound CsIn_{12} was synthesised utilising Hg as inert solvent for In in a HgIn cathode material.

Electrolysis on GaInStan yielded $\text{Li}_3\text{Ga}_{14-x}\text{Sn}_x$ with incorporation of Sn on only one crystallographic site, among side phases LiGa, LiIn and In. The compound $\text{Li}_3\text{Ga}_{13}\text{Sn}$ was synthesised phase-pure by electrolysis on a GaSn eutectic cathode material and investigated by single crystal and powder X-ray methods. Band structure calculations for $\text{Li}_3\text{Ga}_{14}$ and $\text{Li}_3\text{Ga}_{13}\text{Sn}$ were performed and showed the adjustment of Fermi energy by incorporation of Sn as electron donor. For $\text{Li}_3\text{Ga}_{14}$ the total DOS at Fermi level is high whereas $\text{Li}_3\text{Ga}_{13}\text{Sn}$ shows a small band gap indicating semiconducting behaviour. The results are not yet published.

3.5.1. Electrocrystallization – A Synthetic Method for Intermetallic Phases with Polar Metal–Metal Bonding

Frank Tambornino, Jonathan Sappl, Felix Pultar, Trung Minh Cong, Sabine Hübner, Tobias Gifftthaler, Constantin Hoch*

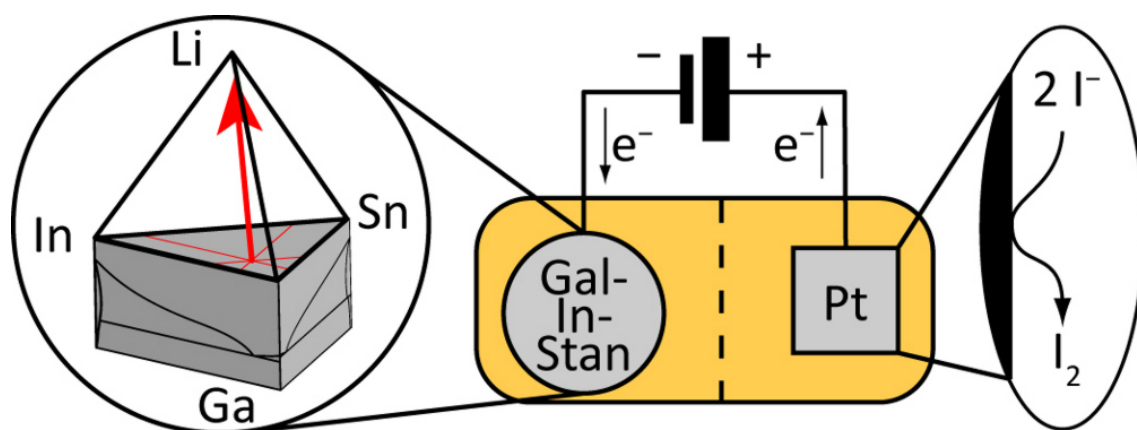
* *Corresponding author. Tel.: +49 (0)89 2180 77421; fax: +49 (0)89 2180 77440. E-mail address: constantin.hoch@cup.uni-muenchen.de (C. Hoch).*

published in: *Inorg. Chem.*, (2016).
DOI: 10.1021/acs.inorgchem.6b02068

Reprinted (adapted) with permission from *Inorganic Chemistry*. Copyright 2016

Abstract

Isothermal electrolysis is a convenient preparation technique for a large number of intermetallic phases. A solution of the salt of a less noble metal is electrolysed on a cathode consisting of a liquid metal or intermetallic system. This yields crystalline products at mild reaction conditions in few hours. We show the aptness and the limitations of this approach. First, we give an introduction into the relevance of electrolytic synthesis for chemistry. Then we present materials and techniques our group has developed for electrocrystallization useful for electrochemical syntheses in general. Subsequently, we discuss different phase formation eventualities and propose basic rationalization concepts, illustrated with examples from our work. The scope of this report is to present electrocrystallisation as a well-known yet underestimated synthetic process, especially in intermetallic chemistry. For this purpose we adduce literature examples ($\text{Li}_3\text{Ga}_{14}$, NaGa_4 , $\text{K}_8\text{Ga}_8\text{Sn}_{38}$), technical advice, basic concepts and new crystal structures only available by this method: $\text{Li}_3\text{Ga}_{13}\text{Sn}$ and CsIn_{12} .



Electrocrystallization has recently proven especially helpful in our work concerning synthesis of intermetallic phases with polar metal-metal bonding, especially Hg-rich amalgams of less-noble metals. With the term "polar metal-metal bonding" we describe phases where the constituting elements have large electronegativity difference and yet

show incomplete electron transfer from the less-noble to the nobler metal. This distinguishes polar intermetallic phases from classical Zintl phases where the electron transfer is virtually complete. Polar metallic phases can show "bad metal behavior" and interesting combinations of ionic and metallic properties. Amalgams of less-noble metals are preeminent representatives for this class of intermetallic phases as Hg is the only noble metal with endothermic electron affinity and thus a very low tendency toward anion formation. To illustrate both the aptness of the electrocrystallization process and our interest in polar metals in the above-mentioned sense, we present amalgams but also Hg-free intermetallics.

1. Introduction

1.1. Electrolysis as an Old Preparative Method

Shortly after Alessandro Volta had presented the Voltaic pile,¹ the first experimentalists exploited the new electric power for preparative chemistry and invented electrolysis.^{2–6} Protagonists were Jöns Jacob Berzelius (Stockholm) and Humphry Davy (London), independently and contemporaneously publishing first results of electrolytic reactions in 1806.^{7,8} In close correspondence and with the highest estimation toward the contributions of their respective colleague,⁹ they pioneered the fundamental works on electricity by Michael Faraday.¹⁰ Both Davy and Berzelius employed a small pool of liquid mercury as cathode on which they placed small portions of common salts. The salt was moisturized and touched with a wire attached to the anode of the Voltaic pile. As they both observed (Davy about half a year later than Berzelius) the formation of amalgams, they concluded that this was due to a metallic "base" to the respective salts. As Berzelius chose natron (NaHCO_3) and "caustic kali" (KOH) for his experiments while Davy took soda (Na_2CO_3) and potash (K_2CO_3), the same elements subsequently were baptized *sodium* and *potassium* in Anglo-Saxon and by Lavoisier's instigation in french-speaking countries or *natrium* and *kalium* in several continental european countries, propagated by Berzelius' student F. Wöhler. Davy followed the idea of distilling off the mercury from the amalgams, yielding the pure metals. The discovery of a number of elements is nowadays intimately connected with him whereas Berzelius' contributions faded into background.

1.2. Industrial electrolytic processes

The most energy-consuming technical process in chemical industry is the amalgam process, one of the three technical realizations of the chloralkali electrolysis for the production chlorine and soda lye from brine.^{11,12} Other technically relevant electrolytic processes focus mainly on anodic oxidation (e. g. production of peroxodisulfate) or on reduction of a metal cation from solution or melt (e. g. aluminum production; raffination of copper, gallium, and others). Thus, a considerable number of basic materials for chemical industry and everyday life are connected to electrolytic preparation processes.

1.3. Electrolysis in Chemical Research

In organic chemistry a number of both electrolytic oxidations and reductions are in use:¹³ Kolbe electrolysis may be the most common of them. However, despite the long history of electrolysis it is only scarcely used nowadays in preparative chemical research. Electrolysis is particular suitable for explorative chemistry as its fundamental parameters (current density, potentials, concentrations, temperature etc.) are readily controllable with the highest precision.

Isothermal electrocrystallization offers a possibility to explore binary phase diagrams in a way complementary to conventional solid state thermochemistry. Consider a phase diagram like that for the binary system Na–Hg (see Figure 1).

A phase with tentative composition "NaHg₅" was first detected in early thermochemical studies. A conventional attempt, mixing Na and Hg in the desired ratio and then heating the mixture over the liquidus temperature, does not result in formation of this phase. Due to its peritectic decomposition temperature of 157 °C the sample must be cooled quickly below this decomposition temperature and then tempered slightly below it for a long time. Now, the high reaction enthalpy caused by large electronegativity differences of Na and Hg ($EN(\text{Na}) = 0.93$,

$EN(\text{Hg}) = 1.93$ according to the Pauling scale)¹⁵ comes into play. Adding even small portions of sodium to mercury results in a vigorous reaction, a flash and local heating over the boiling point of mercury (357 °C). Even rapid cooling will result in NaHg₂ formation, and a remaining surplus of mercury. Subsequent tempering of the mixture of NaHg₂ and Hg below 157 °C does not yield "NaHg₅", most probably due to kinetic hindering of seed formation at low temperatures. This phase with actual composition Na_{11+x}Hg_{52-x} ($x \approx 0.19$) can easily be obtained as single-phase crystalline material by electrocrystallization. Here, the process starts, at a given temperature below the peritectic decomposition temperature, with a solution of a Na salt in a polar, aprotic solvent and pure Hg as a cathode. Na⁺ cations are reduced at and dissolved in the Hg cathode and slowly increase the Na concentration in the liquid amalgam until the liquidus in the phase diagram is reached. The corresponding solid phase, "NaHg₅", will crystallize, and a mercury-richer liquid remains until all liquid material has been consumed. Subsequently, the electrolysis stops as Na diffusion ceases. If the terminal voltage is held

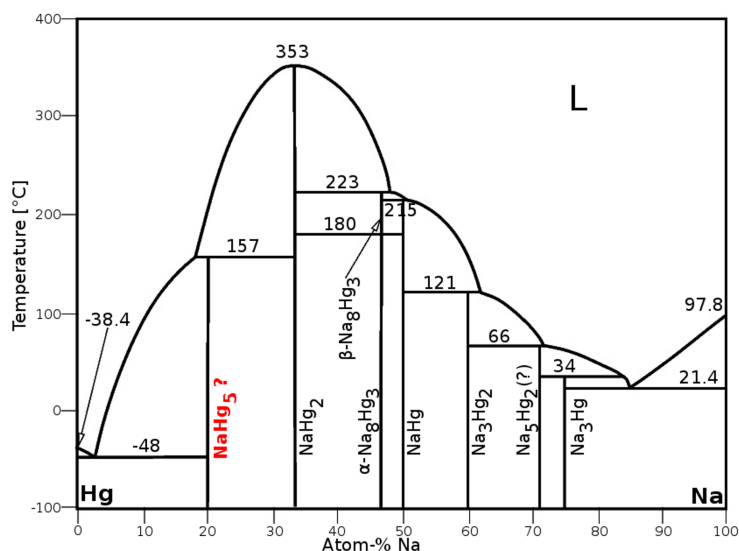


Figure 1 Phase diagram of the binary system Na–Hg, modified version of ref 14.

constant, no sodium deposition will take place. Details for the electrolytic preparation and the crystal structure of $\text{Na}_{11}\text{Hg}_{52}$ have been given previously.^{16,17}

Amalgams of less-noble metals (alkali, alkaline earth, and lanthanoid metals) are interesting examples for intermetallic phases with polar metal-metal bonding. As a larger Hg sublattice is more effective in delocalizing a negative charge Hg-rich amalgams show highest polarization. The example of the phase diagram Na–Hg illustrates the preparative problem common to all systems of Hg with a less-noble metal: the inconvenient combination of high reaction enthalpies and low decomposition temperatures. This may be the reason why there is scarce knowledge on structures of the Hg-richest amalgams despite decades of crucial and extensive studies on the less Hg-rich phases.

1.4. Hg-Free Cathode Systems for Preparative Electrolysis

As electrocrystallization relies on a liquid metallic cathode material, not only Hg but also Ga and a number of binary and multinary metallic alloys and eutectics can be chosen as educts. The temperature range is limited by freezing and boiling temperature of the employed solvent. In the following we present a number of possible combinations and give details on requirements and the technical limits of the process. The main part of this publication will deal with the different possible reaction pathways following from the application of a binary or multinary liquid cathode and electrolyzing a less noble metal into it. A binary cathode system offers three possibilities: (1) Adding a third metal by reduction from solution leads to a ternary intermetallic phase. (2) The metal from solution will only form an intermetallic phase with one of the two cathode components, and the other serves as solvent for the latter. (3) The metal from solution forms two individual binary compounds with the cathode components. There are chemical tendencies deciding which of these three pathways will be followed, and we show representative examples.

2. Results and Discussion

2.1. Prerequisites and Limitations of Electrocrystallization: Apparative Requirements, Electrode Construction, Electrolyte Composition, and Feasible Cathode Systems

In order to perform a preparative electrolysis reaction under controlled conditions, we have constructed the electrolysis chamber shown in Figure 2. The anode consists of a Pt wire, Pt foil, or W rod.

The cathode design has to be adjusted to the respective cathode material. For Hg, a simple amalgamated copper spoon (see Figure 2, upper left) with a single drop of mercury suspended in it was applied. For other metals or multinary systems, a perforated Teflon block with an internal tungsten plate appeared to give the best results (see Figure 2, lower left). The anode and cathode compartments are separated by a glass frit and mantled in order to provide a constant reaction temperature with the aid of an external thermostat. As many of the phases we study are very sensitive toward traces of water and oxygen, the setup was designed to work under Schlenk conditions. The product can

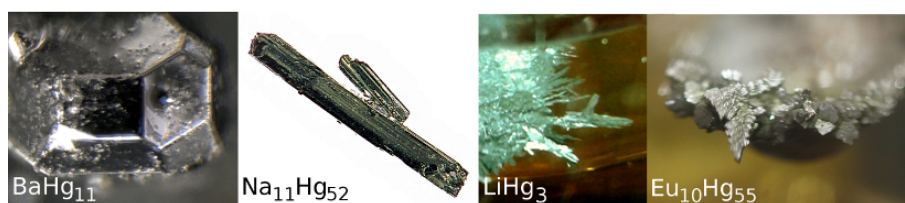
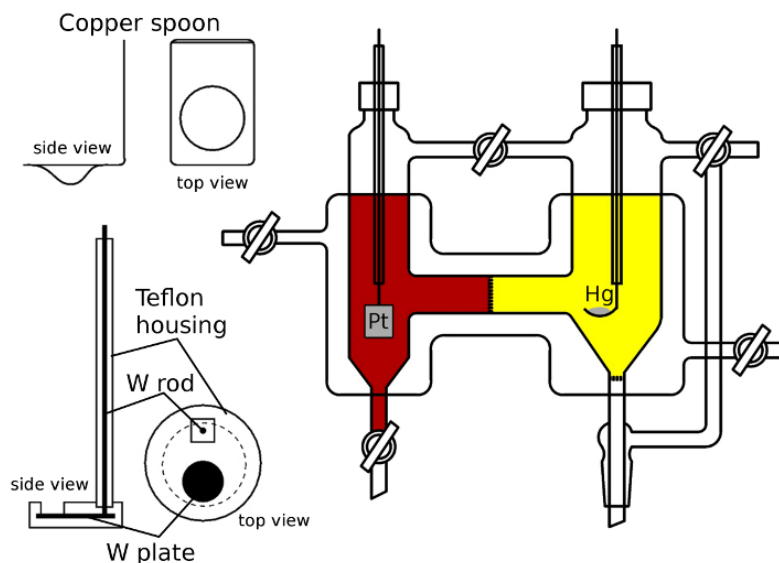


Figure 2: Electrolysis chamber suitable for isothermic electrocrystallization under inert conditions, and two different cathode constructions. Some amalgam crystals are shown below.

be separated from the cathode inside the apparatus, filtered off the remaining electrolyte solution and washed with fresh solvent on a small glass frit right beneath the cathode. The presented setup may be completed by a reference electrode for registration not only of terminal voltages but also of the actual electrode potentials, hence enabling a quantitative reaction control.

A suitable solvent for electrocrystallization has a preferably large liquid range, has high polarity in order to dissolve salts in sufficiently high concentrations, can easily be dried and purified, and shows chemical stability and also redox inertness with respect to the rather high electrode potentials. The salts of less-noble metals should be chosen with regard to their solubility in the given solvent and to the reactivity of the oxidation products of the anion toward solvent or the product when the oxidation product diffuses from the anode compartment toward the cathode. The salts have to be thoroughly dried prior to use in order to prevent H_2 formation at the cathode. Our preferred electrolyte is a solution of the anhydrous iodide of a less noble metal in *N,N*-dimethylformamide. DMF has high polarity ($\mu = 3.8$ D) and a low melting and a high boiling temperature (liquid range from -61 to $+153$ °C),¹⁵ and thus offers a wide operating range. We have chosen the iodides as the anodic formation of iodine, and subsequently, triiodide is preferable to the formation of the strong oxidizing agents bromine or chlorine from bromides or chlorides, and because of the generally very high solubility of iodides in DMF. In addition, the strong color of iodine or triiodide in DMF solution immediately detects the onset of the reaction. The anode materials are insensitive toward iodine.

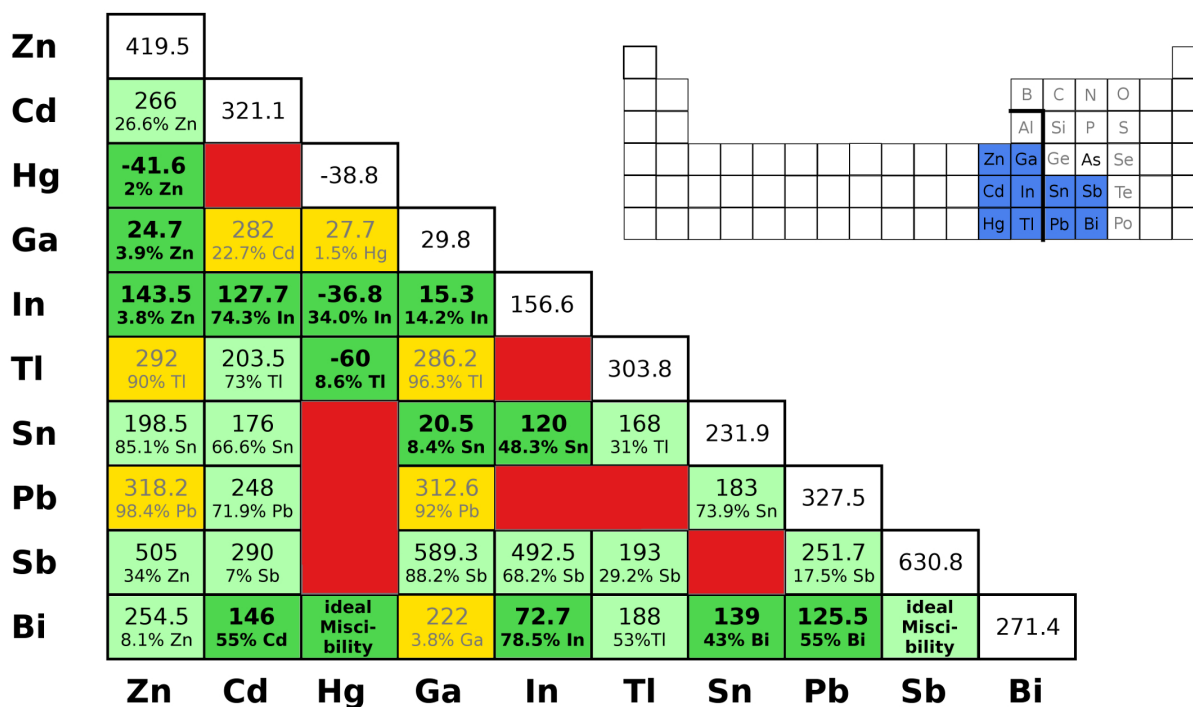


Figure 3.29.: Melting points of the lowest melting metals and their binary eutectics. Refer to text for color coding.

Drying or preparing anhydrous metal iodides can be complicated. In comparison to NaI which can be dried simply by heating in a vacuum, LaI_3 as a typical example is difficult to synthesize as pure binary compound. At this point, employing DMF as solvent shows another advantage: as DMF is a well-coordinating solvent, complexes of the general composition $\text{MI}_x \times y \text{DMF} = [\text{M}(\text{DMF})_y]\text{I}_x$ can be easily prepared by dissolving a hydrate $\text{MI}_x \times y \text{H}_2\text{O}$ in boiling DMF, removing the water by azeotropic distillation with toluene as entrainer, and subsequently crystallizing the solvate complex by cooling the solution. This works with very high yield as the temperature dependence of the solubility of most metal iodides in DMF is high. The respective metal iodide solvate complexes are isolated as crystalline material; the purity can be confirmed by e.g. X-ray powder diffraction, and then the material is taken for the electrolysis. By this simple procedure, elaborate and time-consuming syntheses of of anhydrous binary metal iodides can be avoided.

The choice of a cathode material is limited by its melting point with respect to the boiling temperature of the electrolyte's solvent. If DMF is employed, all intermetallic systems with melting points below ca. 150 °C are suitable. Metals with low melting points or low-melting binary eutectics typically are gathered around the Zintl border. In Figure 3 all binary systems and their respective eutectics are compiled. Only the few fields marked in red show no miscibility of the respective elements. Yellow marked fields show miscibility gaps. Fields marked in dark green show homogeneous phases that are liquid within the temperature range for liquid DMF. Light green fields could be of interest if the solvent was changed from DMF to a suitable and redox-inert ionic liquid or salt melt.

Table 1: Amalgams of Less-Noble Metals Prepared by Electrocrystallization^a

amalgam	T	terminal voltage
[N(CH₃)₄]Hg₈ ²²	-30 °C	10 V
LiHg ₃ ²³	20 °C.	5 V
Na₁₁Hg₅₂ ^{16,17}	50 °C	4.5 V
KHg₆ ²⁴	70 °C	7 V
K ₃ Hg ₁₁ ²⁵	100 °C	6 V
RbHg ₁₁ ²⁶	20 °C	7 V
Cs₂Hg₂₇ ²⁷	2 °C	6 V
Cs ₃ Hg ₂₀ ²⁵	20 °C	6 V
SrHg ₁₁ ²⁶	0 °C	5 V
BaHg ₁₁ ²⁶	0 °C	5 V
Eu₁₀Hg₅₅ ²⁸	20 °C	5 V
ErHg ₃ ²⁹	20 °C	7 V

^aNew amalgam phases from our work are emphasized in bold face.

2.2. Electrocrystallization on Elemental Cathode Systems: Pure Hg or Ga as Cathode Material

The simplest case is the employment of a pure element as reactive cathode material. When a metal cation from the electrolyte solution is reduced at the reactive cathode a binary intermetallic phase will be formed. It will be the phase with highest content of the cathode metal marked in the respective binary phase diagram, if the reaction temperature is chosen below the deepest respective decomposition or melting temperature. The cathode metal must be liquid for the electrolysis to enable diffusion of the reduced metal into the bulk, and Hg and Ga are the only metals that are liquid between the freezing and boiling points of DMF. By electrolysis of a solution of the iodides of alkali, alkaline earth or lanthanoid metals in DMF on a liquid Hg as cathode material, a number of crystalline Hg-rich amalgams could be prepared over the past years, see Table 1. The analogous reactions with liquid Ga consequently yield Ga-rich gallides. In the system Li–Ga, for example, the Ga-richest phase is Li₃Ga₁₄,^{18,19} and in the system Na–Ga it is NaGa₄,¹⁰ both reported in the literature. Indeed, in the respective electrocrystallizations, these phases are the only ones observed, see Figure 4. The crystal structure of Li₃Ga₁₄ could be redetermined, and the literature model was confirmed from powder data by Rietveld refinement. A compilation of improved crystallographic parameters, details on data collection and structure determination as well as selected geometric parameters are compiled in the Supporting Information. NaGa₄ crystallizes with the BaAl₄ structure type.^{20,21}

2.3. Binary Cathode Materials with One Metal Acting as Solvent for the Other: Liquid Hg/In Mixtures as Cathode Material

At room temperature, Hg and In show miscibility over a wide composition range Hg_xIn_{1-x} with $0 \leq x \leq 0.66$.¹⁴ We have prepared a liquid solution of indium in mercury with composition 1:1 (melting point: -19 °C) and performed an electrolysis of a CsI solution

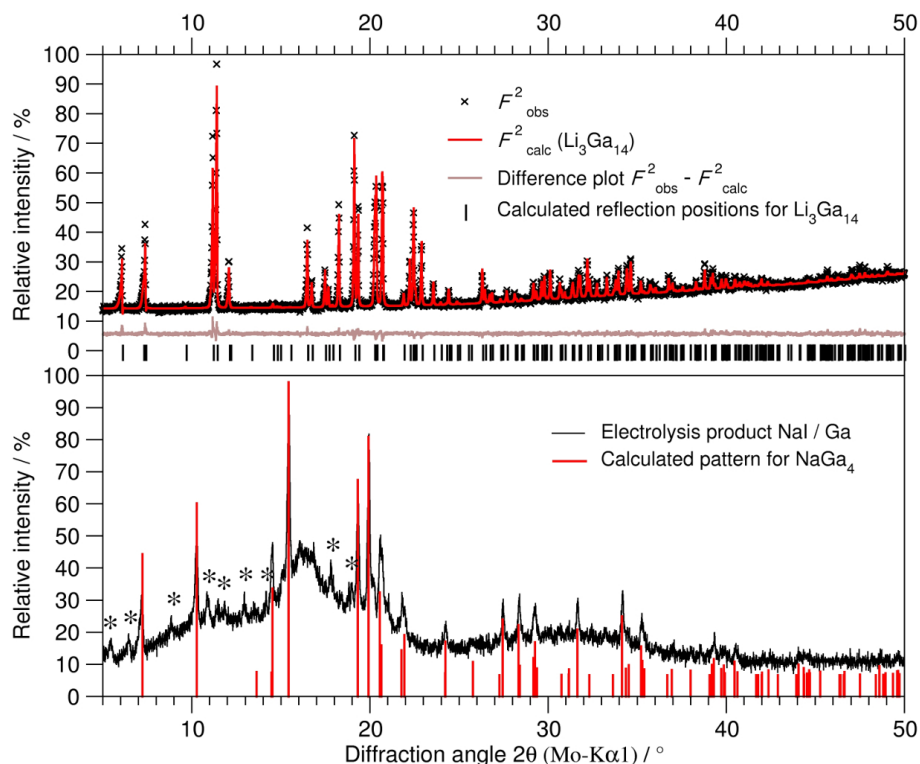


Figure 4: Powder diffraction patterns of the electrolysis products of a solution of LiI in DMF (above, as a result from Rietveld refinement) and a solution of NaI in DMF (below) on liquid Ga electrodes. In the lower diffractogram small maxima marked with asterisks originate from oxidic impurities. The diffuse background is due to a thin layer of liquid Ga.

in DMF on it. As a result, we observed that liquid Hg remained and a new phase, CsIn₁₂ with hitherto unknown crystal structure had formed. The difference in reactivity of Hg versus In is most probably due to their very different electron affinities: indium has an exothermic electron affinity of -0.38 eV, whereas mercury shows endothermic electron affinity with $+1.56$ eV.³⁰ This large difference results in a clear reactivity difference, and indium is expected to be reduced first. If the voltage is chosen appropriately (in our case: 5 V terminal voltage), the electrolysis stops when all indium is consumed and a subsequent amalgam formation is suppressed. Our synthetic approach suggests that CsIn₁₂ is the In-richest phase in the system Cs–In and was overlooked in previous thermoanalytic studies.¹⁴ According to our observations, CsIn₁₂ does not decompose or melt up to 300 °C.

CsIn₁₂ forms xenomorphic crystals with pronounced pseudocubic twinning from electrolysis. Crystal quality is considerably improved by tempering the electrolytic product under argon at 300 °C; however, the crystal structure could not be solved and refined from single crystal data due to multiple merohedric twinings. The structure model shown below therefore was refined from powder data with the Rietveld method, and the starting values were extracted from symmetry relation considerations starting from the NaZn₁₃ structure type as aristotype,^{31,32} identified from the twinned crystals. The pseudocubic data sets could be solved and refined in space group $Fm\bar{3}c$, the space group of the aristotype NaZn₁₃; however, additional reflections in the diffraction patterns were observed and systematic elongations of a group of In atoms pointed toward a superstruc-

Table 2: Crystallographic Details as Results of a Rietveld Refinement of CsIn₁₂

empirical formula	CsIn ₁₂	
cryst syst	orthorhombic	
space group	<i>Pnn2</i> (No. 34)	
<i>Z</i>	4	
lattice params	<i>a</i> / Å	14.2100(7)
	<i>b</i> / Å	14.2095(7)
	<i>c</i> / Å	13.9994(7)
	<i>V</i> / Å ³	2826.7(2)
density / g·cm ⁻³	6.559(5)	
radiation, wavelength / Å	MoK α 1, 0.70930	
diffractometer syst	Stoe Stadi P	
detector	Mythen 2K	
no. of l.s. params	127	
no. of background params	24	
<i>R</i> values	<i>R</i> _p	0.02699
	<i>R</i> _{wp}	0.03935
	<i>R</i> _{Bragg}	0.03196
	<i>R</i> _{exp}	0.00755
	<i>R</i> _{exp'}	0.03889
	χ^2 (GOF)	5.214

ture with lower symmetry. The powder patterns from phase-pure samples could not be indexed with the cubic structure model. Subsequent symmetry reduction followed the group-subgroup relations shown in Figure S2 in the Supporting Information. The powder pattern could only be fully indexed in a structure model in space group *Pnn2*, resulting in Rietveld refinements with satisfactory residual values and a reasonable structure model. Details on the Rietveld refinements in all possible space group candidates are compiled in the Supporting Information. The symmetry reduction is necessary to give room for considerable structural distortions: The four crystallographic Cs sites in CsIn₁₂ are topologically equivalent and show 24-fold coordination in a chiral polyhedron of In atoms best described as a strongly distorted rhombicuboctahedron. A rotation of the square faces of a regular rhombicuboctahedron of 28.7° would lead to a chiral polyhedron called a "snub cube"³³ (Kepler first named this Archimedean polyhedron *cubus simus*)³⁴ consisting of squares and isosceles triangles. In CsIn₁₂ the square faces are rotated only by 8.7°, resulting in a hybrid between snub cube and rhombicuboctahedron. In NaZn₁₃ a cubic primitive arrangement of snub cubes leads to interstitial icosahedric voids centred by an additional Zn atom. In CsIn₁₂ the distorted rhombicuboctahedra result in interstitial cuboctahedra not occupied by further In atoms, hence the difference in the respective compositions. A direct comparison of the two structures is shown in Figure 5. Basic crystallographic information and atomic coordinates are given in Tables 2 and 3. Further details on data collection and crystal structure can be obtained free of charge by requesting the crystal information file (cif) from Fachinformationszentrum Karlsruhe, D-76344 Eggenstein-Leopoldshafen, Germany (e-mail: crysdata@fiz-karlsruhe.de) on quoting the depository number CSD-431738, the names of the authors and citation of this paper.

Table 3: Fractional Atomic Coordinates, Wyckoff Numbers and Isotropic Thermal Displacement Parameters $B_{\text{iso}} / \text{\AA}^2$ as a Result of a Rietveld Refinement of CsIn_{12}

Atom	Wyckoff position	x	y	z	B_{iso}
Cs1	2a	0	0	0.063(5)	6.2(6)
Cs2	2a	0	0	0.583(5)	6.2(6)
Cs3	2b	0	1/2	0.548(4)	6.2(6)
Cs4	2b	0	1/2	0.037(4)	6.2(6)
In1	4c	0.082(2)	0.423(2)	0.804(5)	3.7(2)
In2	4c	0.913(2)	0.416(2)	0.308(6)	3.7(2)
In3	4c	0.411(2)	0.392(2)	0.805(5)	3.7(2)
In4	4c	0.586(2)	0.398(2)	0.306(5)	3.7(2)
In5	4c	0.364(2)	0.885(3)	0.818(6)	3.7(2)
In6	4c	0.607(2)	0.883(2)	0.314(5)	3.7(2)
In7	4c	0.111(2)	0.865(2)	0.785(5)	3.7(2)
In8	4c	0.910(2)	0.880(2)	0.326(5)	3.7(2)
In9	4c	0.208(2)	0.588(2)	0.417(5)	3.7(2)
In10	4c	0.722(2)	0.599(2)	0.636(5)	3.7(2)
In11	4c	0.733(2)	0.387(3)	0.191(5)	3.7(2)
In12	4c	0.224(2)	0.395(2)	0.928(5)	3.7(2)
In13	4c	0.400(2)	0.277(2)	0.480(5)	3.7(2)
In14	4c	0.601(2)	0.011(2)	0.650(5)	3.7(2)
In15	4c	0.614(2)	0.778(3)	0.145(5)	3.7(2)
In16	4c	0.412(2)	0.723(2)	0.970(5)	3.7(2)
In17	4c	0.245(2)	0.129(2)	0.139(5)	3.7(2)
In18	4c	0.734(2)	0.084(3)	0.976(5)	3.7(2)
In19	4c	0.737(2)	0.908(3)	0.484(5)	3.7(2)
In20	4c	0.215(2)	0.913(3)	0.640(5)	3.7(2)
In21	4c	0.012(2)	0.199(2)	0.166(4)	3.7(2)
In22	4c	0.127(2)	0.213(2)	0.939(5)	3.7(2)
In23	4c	0.019(2)	0.698(2)	0.430(4)	3.7(2)
In24	4c	0.891(2)	0.723(3)	0.783(4)	3.7(2)

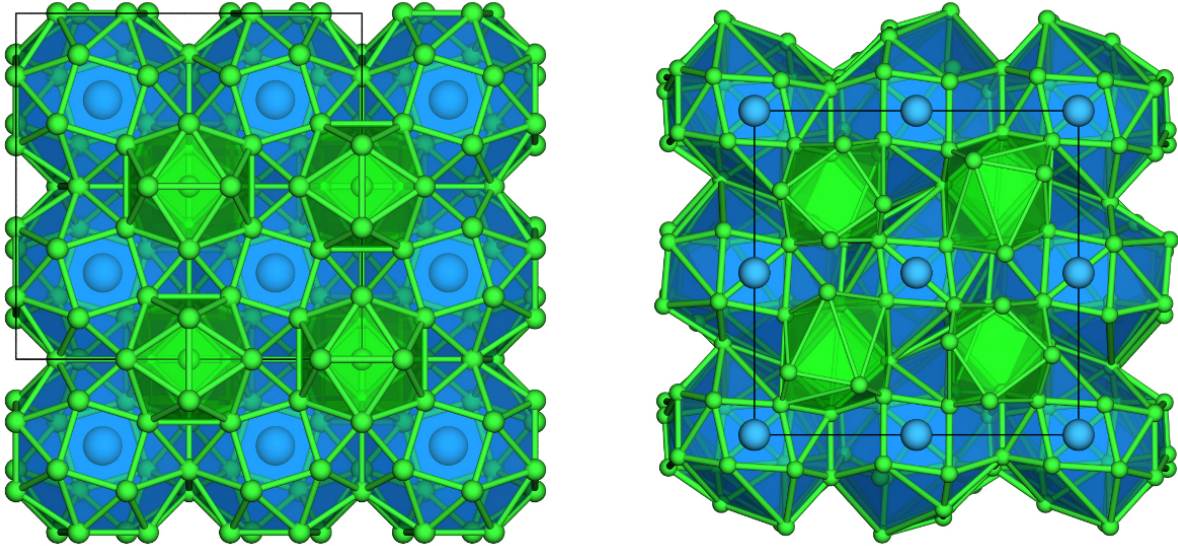


Figure 5: Comparison of the crystal structures of NaZn_{13} (left) and CsIn_{12} (right). Distortion of the regular coordination polyhedra in NaZn_{13} is realized by symmetry reduction from $Fm\bar{3}c$ (NaZn_{13}) to $Pnn2$ (CsIn_{12}).

2.4. Ternary Intermetallic Phases by Electrolysis on a Binary Cathode Material: Liquid Ga/Sn Mixtures as Cathode Material

Ga and Sn both have exothermic electron affinities (-0.30 and -1.20 eV, respectively) and form a eutectic mixture with melting point 20.5 °C at composition $\text{Ga}_{91.6}\text{Sn}_{8.4}$. The liquidus runs almost linear from the eutectic point to the melting point of pure Sn (232.0 °C).¹⁴ Electrolysis on a liquid Ga/Sn cathode with composition 7:3 therefore took place at a temperature of 70 °C. Gallium and tin both are located close to the Zintl border, with Ga on the left and Sn on the right of it. Accordingly, tin forms numerous classical Zintl anions $[\text{Sn}_x]^{n-}$, but for gallides the formal structural separation into cationic and anionic building units is only true for rare examples. We therefore found it interesting to check whether the reaction of a less noble metal with this mixture would lead to two binaries (a nonclassical gallide Zintl phase and a classical stannide Zintl phase) or a more complicated ternary phase. On the basis of the respective electron affinities, the electrolysis of a Sn/Ga alloy should be expected to form a binary stannide first. However, the electrolysis of a solution of KI in DMF on an electrode of composition Ga:Sn = 7:3 resulted in the formation of single-phase clathrate-I-type $\text{K}_8\text{Ga}_8\text{Sn}_{38}$.³⁵ Although the product contains much more Sn than the pristine electrode material, some elemental β -Sn remained unreacted. The powder diagram of the product is shown in Figure 6. The binary clathrate K_8Sn_{44} along with a number of analogous alkali metal tetrelides is a Zintl phase according to the formulation $[\text{K}^+]_8[\text{Sn}^-]_8[\text{Sn}^0]_{36}\square_2$: Removing a Sn atom from a tetrahedral network renders the four neighboring Sn atoms trivalent and according to the Zintl concept they carry one negative charge each. To compensate for eight positive charges from eight K cations, two Sn atoms have to be removed, creating eight negatively charged trivalent Sn atoms.

The separation of the clathrate network into uncharged and negatively charged Sn atoms has previously been shown by ^{118}Sn Mössbauer spectroscopy on $\text{Rb}_8\text{Sn}_{44}\square_2$.³⁶ The atomic positions of the trivalent stannide anions can alternatively be occupied by four-valent and hence negatively charged Ga^- anions without creating vacancies, as in $\text{K}_8\text{Ga}_8\text{Sn}_{38}$. A large number of analogous clathrate structures has been synthesised and characterized over past decades as this group of compounds shows a number of interesting properties, ranging from superconductivity to thermoelectric behavior.³⁷ The electrocrystallization technique offers an easy access to new multinary representatives of intermetallic clathrates.

2.5. Multinary Cathode Materials Resulting in a Mixture of Different Binary Products: Liquid Ga/In/Sn Mixtures as Cathode Material

If multinary cathode systems are taken into consideration (see the compendium of low melting systems in Table 4; this list is not intended to be exhaustive), a plethora of intermetallic systems that are liquid at feasible temperatures are open to be explored with electrocrystallization. Multinary cathode materials interact after the same pattern shown above. The products can be a quaternary (or higher multinary) intermetallic phase, or a mixture of different binary compounds. One of the components can also act as inert solvent for the others. We present the result of an electrolysis of a LiI solution on a "Galinstan" cathode as representative example.

Electrolysis of a LiI solution on the ternary mixture "Galinstan" as cathode material (Ga:In:Sn = 62.5:21.5:16.0 weight-%) leads to the formation of several binary lithium compounds. The polycrystalline product after a three-day electrolysis with 5 V terminal voltage consisted of LiGa, LiIn, Li₃Ga₁₄ and some residual elemental indium. LiGa and LiIn crystallize with the NaTl structure type with Ga and In forming diamond-analogous anionic frameworks, respectively. Rietveld refinement showed mixed occupation Ga/Sn for one of the crystallographic Ga positions, and a significant enlargement of the lattice parameters of the phase LiIn indicates incorporation of Sn as well. Due to the insufficient X-ray contrast of In and Sn the mixed occupation could not be quantified by refinement. Also the phase Li₃Ga₁₄ shows some incorporation of Sn following Li₃Ga_{14-x}Sn_x, so in strict meaning these phases are multinary as well. In this Li–Ga–In–Sn system, the occurrence of two lithium gallides with different ratios Li:Ga seems to be in contradiction with the stated general "rule" that for a given temperature only

one, the Ga-richest, phase would be expected to form. This is strictly speaking only true for an electrocrystallization on elemental gallium. When the ternary eutectic Galinstan is employed, Ga depletion in the cathode material during electrolysis has to be taken into account, as well as different solubilities of products in changing cathode materials, lattice energies, and kinetic effects concerning seed formation. Phase formation hence is multicausal and not in all cases predictable. A differentiation of the possible influences would call for time-dependent experiments in order to reveal which phases are formed initially and which phases are formed subsequently.

2.6. Limiting Factors for Electrocrystallization

There are limits to this method resulting from the low reaction temperatures, as observed in e.g., the binary system Fe–Ga: When a solution of FeI₂·6 DMF in DMF is electrolyzed on Ga at 70 °C, the respective phase diagram (see Figure 7) would suggest the formation of FeGa₃ as the Ga-richest phase.⁴³ However, we observed the deposition of metallic Fe on the surface of liquid Ga. The suppression of phase formation is most probably due to the extremely low solubility of Fe in Ga at low temperature. A heterogeneous mixture of

Table 4: Some Multinary Intermetallic Eutectics and Low-Melting Systems with the Respective Melting Points and Chemical Compositions

system	melting point [°C]	composition [wt-%]
"Galinstan" ³⁸	11	59.6:26:14.4
Ga/In/Sn		
Ga/Sn/Zn	17	82:12:6
"French eutectic"		
Bi/Pb/Sn/In/Cd	46.9	41:22.1:10.6:18.1:8.2
"Cerrolow 117" ³⁹		
Bi/Pb/Sn/In/Cd	47.2	44.7:22.6:8.3:19.1:5.3
"Cerrolow 136" ³⁹		
Bi/Pb/Sn/In/Cd	58	49:18:12:21
"Field's metal" ⁴⁰		
Bi/In/Sn	62	32.5:51:16.5
"Wood's metal" ⁴⁰		
Bi/Pb/Sn/Cd	70	50:25:12.5:12.5
"Lipowitz's eutectic" ⁴⁰		
Bi/Pb/Sn/Cd	74	50:27:13:10
"Guthrie's metal"		
Bi/Pb/Sn/Cd	71.1	47.4:19.4:20:13.3
"Onion's eutectic" ⁴¹ ,		
"Lichtenberg's metal"	92	50:20:30
Bi/Pb/Sn		
"Rose's metal" ⁴⁰ ,		
"D'Arcet's metal" ⁴⁰	95	50:25:25
Bi/Pb/Sn		
"Newton's metal" ⁴⁰		
Bi/Pb/Sn	98	50:30:20
"Malotte's metal" ⁴²		
Bi/Pb/Sn	123	46.1:19.7:34.2
Bi/Sn/Zn	130	56:40:4

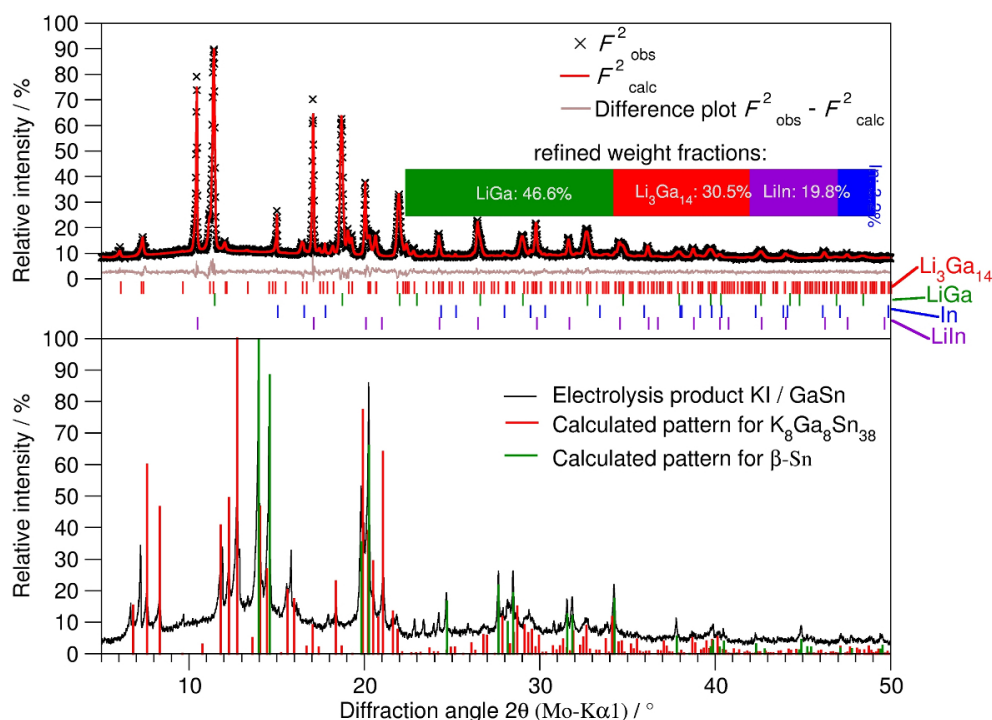


Figure 6: Powder diffraction pattern and Rietveld refinement of the products of an electrolysis of LiI solution on Galinstan (above) and of the product of an electrolysis of a KI solution on a mixture of Ga and Sn (below). Reflections of an unknown decomposition product are marked with asterisks.

the two metals is formed as a consequence. In order to initialize the reaction of the two metals, it would be necessary to heat the mixture to considerably higher temperatures at which a homogeneous melt with higher Fe content is formed (to dissolve 10 at.-% Fe in Ga at least 800 °C have to be reached). Spontaneous phase formation occurs in systems with less steep liquidus curves, see e.g., the system Na–Hg in Figure 1 in comparison.

A similar problem occurs if a reaction product shows extremely low solubility in the cathode metal. The product will then form a thin, passivating surface layer, preventing the progression of the reaction. This has been observed for ammonium amalgams from substituted ammonium cations $[NR_4]^+$ with larger substituents than $R = CH_3$.²²

3. Conclusion

Three different cases can be expected when employing a multinary cathode system for electrocrystallization experiments: (1) one metal can serve as solvent for a second one. (2) From a cathode material consisting of N elements one product phase with $N+1$ constituents can be formed. (3) From a cathode material consisting of N elements $N+1$ binary product phases (or other less complex products than in case 2) can be formed. The first case occurs when the reactivity and electron affinities of the two metals in the cathode material are very different. The difference between cases 2 and 3 is due to structural and chemical reasons. We presented the example of an electrolysis of a KI solution on a Ga/Sn cathode where the formation of $K_8Ga_8Sn_{38}$ was observed. The crystal structure of this ternary clathrate provides chemically different crystallographic

sites, favoring four-valent network positions for Sn atoms, and trivalent positions for Ga. This chemical difference of the available crystallographic sites favors the formation of one ternary instead of several binary phases. As a result of the electrolysis of a LiI solution on a Ga/Sn/In electrode we present the formation of several binary compounds, according to case 2. Although for $\text{Li}_3\text{Ga}_{14}$ and LiIn Sn inclusion was observed we would like to discern the resulting solid solutions clearly from a ternary phase as e.g., the clathrate above. In $\text{Li}_3\text{Ga}_{14}$ and LiIn a chemical separation of the available crystallographic sites is not as clear as in the clathrate, and therefore, no favorable ternary phases is available. Obviously, the quaternary system Li–Ga–Sn–In does not hold a quaternary phase, at least not one being stable under the given conditions.

There is an additional, systematically different way to synthesize ternary (or multi-ary) phases via electrocrystallization we have not probed yet: A solution containing two (or more) different less-noble metal salts can be electrolyzed on a single-element cathode, and the formation of a ternary compound can result. The necessary condition would be that the elements in solution have the same electrochemical potential. This can be achieved according to the Nernst equation by adjusting the respective concentrations of the metals in solution. As an example, two elements with similar standard potentials, e.g., Na and K, should give a ternary Na/K amalgam. With inclusion of a multinary cathode material in this approach the preparative scope of electrocrystallization would be expanded even further.

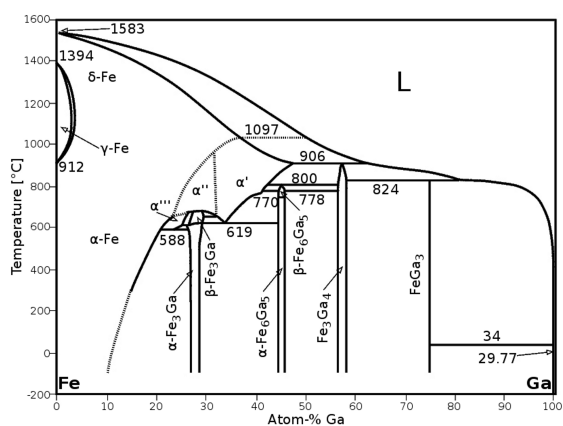


Figure 7: Phase diagram of the binary system Fe–Ga, modified version of ref 14.

Electrocrystallization has proven to be a convenient way for the synthesis of intermetallic compounds. Compounds with low peritectic decomposition temperatures are in general difficult to synthesize via standard solid state preparation techniques. Here, electrocrystallization offers the opportunity to obtain these compounds conveniently as phase-pure material with high crystallinity. With an isothermal increase of the amount of one element via cathodic reduction in the cathode element a phase diagram can be scanned in a complementary way to conventional thermochemical phase analysis. Thus, electrocrystallization can reveal in particular those phases overlooked in conventional thermo-analytical studies.

Studies on new intermetallic systems are of interest in their own behalf. We have had a great benefit from electrocrystallization for studies on intermetallic systems with highly polar metal-metal bonding. However, the impact of intermetallic phases is much higher: They are widely employed as catalysts and as precursor compounds for, e.g., the preparation of oxidic or nitridic systems. Oxidation of NaTl was shown to yield Na_3TlO_2 ⁴⁴, and a number of SiAlON-based luminophors are prepared by nitridation of multinary intermetallics.^{45,46} With this regard, electrocrystallization could help in the production of new intermetallic precursor systems for further chemical modification and may provide a wide application range beyond intermetallic chemistry.

4. Experimental Section

4.1 Cathode Materials

All metals were used in high purities. Hg was purified from all less noble impurities by treatment with half-concentrated HNO₃ and from all remaining impurities by filtration and subsequent double distillation in vacuum at 120 °C. Ga was used as purchased, also tin and indium (99.999%, Smart-Elements GmbH, Wien, Austria). Binary and ternary intermetallic cathode materials were synthesised according to the available binary phase diagrams. In the Supporting Information the synthesis conditions for all intermetallic cathode materials are summarized. The respective syntheses are simple and straightforward.

The employment of a low melting alkali metal as "cathode" metal and the salt of a noble metal could in principle be used for preparative purposes, however, this setting would of course constitute a galvanic cell with spontaneous exothermic reaction difficult to regulate.

4.2 Electrolyte

N,N-Dimethylformamide was chosen as solvent for the electrolyte solutions according to its electrochemical stability, its strictly aprotic character and its high polarity. DMF was purified and dried by distillation and degassing at elevated temperatures. The alkali metal iodides were used as purchased (LiI, NaI, KI, RbI, CsI 99.9% from abcr GmbH, Karlsruhe, Germany), without further purification. Alkaline earth metal iodides were synthesised from the respective commercially available chloride hydrates by dissolution in DMF and addition of NaI dissolved in DMF. As NaCl has very low solubility in DMF it precipitates and can be filtered off. The resulting solution of alkaline earth metal iodide still contains water from the starting material which is eliminated by either azeotropic distillation with toluene as entrainer or by degassing in vacuum at 120 °C. The solutions were either directly taken as electrolyte, or the earth alkaline iodide was isolated by evaporation of DMF in vacuum in the form of its DMF solvate as crystalline material, e.g., [Ba(DMF)₈]I₂. Solvate complexes of the lanthanoid metal iodides LnI₃ were synthesised in DMF by reaction of the metal with iodine, or by adding aqueous concentrated HI to the lanthanoid metal oxide or carbonate. The resulting solutions were dried in the same way as described for the alkaline earth metals. Evaporation of the solvent leads to the isolation of solvate complexes [Ln(DMF₈)]I₃ or, only in the case of La, [La(DMF₉)]I₃. For electrocrystallization, the solutions had concentrations between 0.1 and 1 mol L⁻¹.

4.3 Electrocrystallization Conditions

The apparatus shown in Figure 2 was thoroughly dried by heating in vacuum, and then the electrolyte solution was inserted under argon. The anode (Pt foil or W rod) was inserted, and then the amalgamated copper spoon with a single Hg drop was inserted, or the Teflon inset with the intermetallic cathode material was placed inside the device

and in contact with the external voltage source. With the aid of an external temperature control perfusing a heating/cooling liquid through the glass mantle a chosen temperature was adjusted for about 1 h before starting the electrolysis. As the design of the electrolysis chamber does not include a reference electrode only terminal voltages but not the actual electrode potentials could be adjusted. The terminal voltages depend not only on the electrode potentials, but also on ohmic resistance of the electrolyte, temperature, electrode distance and other parameters. In order to find the minimum voltage at which a redox reaction starts, the voltage was increased slowly until the formation of iodine at the anode indicated the onset of the process. Typical values for terminal voltages were 2 to 7 V. The electrolyses were stopped when all liquid cathode material had been consumed, typically after 2 – 24 h. After removal of the electrolyte the product was washed with small portions of pure DMF and dried in vacuum inside the electrolysis apparatus. The crystalline products were isolated under strict inert gas conditions and characterized by powder X-ray diffraction or single crystal X-ray diffraction.

4.4 Powder X-ray Diffraction

Samples for X-ray powder diffraction measurements were prepared in an argon-filled glove-box. The powder samples were ground in agate mortars, in cases of ductile samples under addition of diamond powder. The hygroscopic samples were sealed in glass capillaries (inner diameter of 0.1 to 0.5 mm, Hilgenberg, Malsberg, Germany). Measurements were performed in Debye-Scherrer geometry on a STADI P diffractometer system (Stoe & Cie GmbH, Darmstadt, Germany) with Ge-111-monochromatized $\text{CuK}\alpha 1$ or $\text{MoK}\alpha 1$ radiation. Intensities were collected with a MYTHEN detector (Dectris, Baden, Switzerland). For phase identification the detected diffraction pattern was compared to patterns calculated from single-crystal data. Rietveld refinements were performed with a fundamental parameter approach⁴⁷ and a double Voigt model was used to compensate size-strain effects. The background was modeled with shifted Chebychev functions, and the profiles were modeled with LeBail-Jouanneaux functions.

4.5 Single crystal X-ray diffraction

A small portion of the air- and moisture-sensitive reaction products was covered with paraffin oil dried over K metal and brought to air. Suitable specimens for single crystal X-ray structure analysis were selected under a microscope and sealed in paraffin-filled capillaries with inner diameter of 0.1 mm (Hilgenberg, Malsberg, Germany). The crystals were mounted either on a one-circle diffractometer system IPDS 1 (Stoe & Cie GmbH, Darmstadt, Germany) with graphite-monochromatized $\text{MoK}\alpha$ or $\text{AgK}\alpha$ radiation, and an image plate detector or on a three-circle diffractometer system D8 QUEST (Bruker AXS, Karlsruhe, Germany) with Göbel mirror optics, $\text{MoK}\alpha$ radiation, and a CCD detector. After a quality check and determination of the orientation matrix on the basis of a set of preliminary exposure frames intensity data of at least half of the accessible part of the Ewald sphere were collected at room temperature (φ and ω scans) and subsequently corrected for Lorentz, polarization and absorption effects.^{48,49} Structure solution was performed with direct methods in all cases; structure refinement on F^2 was performed with full-matrix least-squares cycles.⁵⁰

Supporting information

The Supporting Information is available free of charge on the ACS Publications website at DOI 10.1021/acs.inorgchem.6b02068.

Preparation of cathode materials. Crystallographic data and Rietveld refinement results for $\text{Li}_3\text{Ga}_{14}$ and for the electrolysis product of Galinstan as cathode material with LiI solution in DMF. Details on structure solution and refinement, crystallographic data, symmetry relations and Rietveld refinement results for CsIn_{12} (PDF)

The authors declare no competing financial interest.

Acknowledgement

The authors thank Thomas Miller, Wolfgang Wünschheim and Christian Minke from the Department of Chemistry at LMU München for technical support. C.H. is much obliged to Professor Dr. Wolfgang Schnick at LMU München for his longstanding financial support and for a most fruitful research environment.

References

- (1) Volta, A. On the electricity excited by the mere contact of conducting substances of different kinds. *Philos. Trans. R. Soc. London* **1800**, *90*, 403–431.
- (2) Nicholson, W.; Carlisle, A.; Cruickshank, W. Experiments on galvanic electricity. *Philos. Mag. J. Sci.* **1800**, *7*, 337–350.
- (3) Ritter, J. W. *Beyträge zur nähern Kenntniss des Galvanismus und der Resultate seiner Untersuchung*; Frommann, Jena, 1805.
- (4) Ritter, J. W. Neue Versuche und Bemerkungen über den Galvanismus. *Ann. Phys.* **1805**, *19*, 1–44.
- (5) Ritter, J. W. *Physisch-Chemische Abhandlungen in chronologischer Folge*; Reclam, Leipzig, 1806.
- (6) Grotthuß, C. J. T. *Mémoire sur la décomposition de l'eau et des corps qu'il tient en dissolution à l'aide de l'électricité galvanique*; Rom, 1805.
- (7) Davy, H. On some chemical agencies of electricity (Bakerian Lecture of 1807). *Phil. Trans. Roy. Soc. (London)* **1807**, *97*, 1–56.
- (8) Berzelius, J. J. *Föreläsningar i Djurkemien*; Carl Delén, Stockholm, 1806.
- (9) Berzelius, J. J. *Traité de Chimie*; Firmin Diderot Frères, Paris, 1831; Vol. 1; p 164.
- (10) Ross, S. Faraday consults the scholars: the origins of the terms of electrochemistry. *Notes Rec. R. Soc. London* **1961**, *16*, 187–220.
- (11) O'Brien, T. F.; Bommaraju, T. V.; Hine, F. *Handbook of Chlor-Alkali Technology*; Springer, New York, 2005.
- (12) Moussallem, I.; Jörrisen, J.; Kunz, U.; Pinnow, S.; Turek, T. Chlor-alkali electrolysis with oxygen depolarized cathodes: history, present status and future prospects. *J. Appl. Electrochem.* **2008**, *38*, 1177–1194.

- (13) Popp, F. D.; Schultz, H. P. Electrolytic reduction of organic compounds. *Chem. Rev.* **1962**, *62*, 19–40.
- (14) T. B. Massalski, P. R. S., H. Okamoto, Ed. *Binary alloy phase diagrams*, 2nd ed.; ASM International, Materials Park, Ohio, 1990.
- (15) Linde, D. R., Ed. *CRC Handbook of Physics*, 90th ed.; Taylor and Francis, Boca Raton, 2010.
- (16) Hoch, C.; Simon, A. Na₁₁Hg₅₂ - Komplexität in einem polaren Metall. *Angew. Chem.* **2012**, *124*, 3316–3319.
- (17) Hoch, C.; Simon, A. Na₁₁Hg₅₂ - complexity in a polar metal. *Angew. Chem. Int. Ed.* **2012**, *51*, 3262–3265.
- (18) Belin, C.; Ling, R.-G. The unexpected lithium-deficient phase of Li₃Ga₇: Synthesis and X-ray structure of Li₃Ga₁₄. *J. Solid State Chem.* **1982**, *45*, 290–292.
- (19) Stoehr, J.; Schäfer, H. Ga-Clusterverbände im Li₃Ga₁₄. *Rev. Chim. Minér.* **1982**, *19*, 122–127.
- (20) Bruzzone, G. The D13 structure type in intermetallic compounds. *Acta Crystallogr.* **1969**, *B25*, 1206–1207.
- (21) Andress, K. R.; Alberti, E. Röntgenographische Untersuchung der Legierungsreihe Al-Ba. *Zeitschr. Metallk.* **1935**, *27*, 126–128.
- (22) Hoch, C.; Simon, A. Tetramethylammoniumamalgam [N(CH₃)₄]Hg₈. *Z. Anorg. Allg. Chem.* **2006**, *632*, 2288–2294.
- (23) Zintl, E.; Schneider, A. Röntgenanalyse der Lithiumamalgame. *Z. Elektrochem.* **1935**, *41*, 771–774.
- (24) Tambornino, F.; Hoch, C. Bad metal behaviour in the new Hg-rich amalgam KHg₆ with polar metallic bonding. *J. Alloys Compd.* **2015**, *618*, 299–304.
- (25) Todorov, E.; Sevov, S. C. Synthesis and structure of the alkali metal amalgams A₃Hg₂₀ (A = Rb,Cs), K₃Hg₁₁, Cs₅Hg₁₉, and A₇Hg₃₁ (A = K,Rb). *J. Solid State Chem.* **2000**, *149*, 419–427.
- (26) Biehl, E.; Deiseroth, H.-J. Darstellung, Strukturchemie und Magnetismus der Amalgame MHg₁₁ (M: K, Rb, Ba, Sr). *Z. Anorg. Allg. Chem.* **1999**, *625*, 1073–1080.
- (27) Hoch, C.; Simon, A. Cs₂Hg₂₇, das quecksilberreichste Amalgam - ein naher Verwandter der Bergman-Phasen. *Z. Anorg. Allg. Chem.* **2008**, *634*, 853–856.
- (28) Tambornino, F.; Hoch, C. The mercury-richest europium amalgam, Eu₁₀Hg₅₅. *Z. Anorg. Allg. Chem.* **2015**, *641*, 537–542.
- (29) Palenzona, A. MX₃ intermetallic phase of the rare earths with Hg, In, Tl, Pb. *J. Less-Comm. Met.* **1966**, *10*, 290–292.
- (30) Simons, J. H.; Seward, R. P. Slow electron scattering and the apparent electron affinity of mercury. *J. Chem. Phys.* **1938**, *6*, 790.
- (31) Ketelaar, J. The crystal structure of alloys of zinc with the alkali and alkaline earth metals and of cadmium with potassium. *J. Chem. Phys.* **1937**, *5*, 668.
- (32) Wendorff, M.; Röhr, C. Polar binary Zn/Cd-rich intermetallics: Synthesis, crystal and electronic structure of A(Zn/Cd)₁₃ (A = al- kali/alkaline earth) and Cs_{1.34}Zn₁₆. *J. Alloys Compd.* **2006**, *421*, 24–34.
- (33) Coxeter, H. S. M.; Longuet-Higgins, M. S. L.; Miller, J. C. P. Uniform polyhedra. *Phil. Trans. Royal Soc. London Ser. A* **1954**, *246*, 401–450.

- (34) Kepler, J. *Harmonices Mundi libri V*; Johann Planck, Linz (Austria), 1619.
- (35) Tanaka, T.; Onimaru, T.; Suekuni, K.; Mano, S.; Fukuoka, H.; Yamanaka, S.; Takabatake, T. Interplay between thermoelectric and structural properties of type-I clathrate $K_8Ga_8Sn_{38}$ single crystals. *Phys. Rev. B* **2010**, *81*, 165110–1–165110–6.
- (36) Hoch, C.; Niemeyer, D.; Röhr, C. Rb/Cs-Stannide: ASn , $A_{12}Sn_{17}$, $A_8Sn_{44}\square_2$ - Strukturelle und Mössbauerspektroskopische Untersuchungen. *Z. Kristallogr. Suppl.* **2000**, *17*, 165.
- (37) Shevelkov, A. V.; Kovnir, K. In *Structure and Bonding*; Fässler, T., Ed.; Zintl Clathrates; Springer, Berlin, Heidelberg, 2011; Vol. 139 (Zintl Phases); pp 97–142.
- (38) van Ingen, G. N.; Kapteijn, J.; Meijering, J. L. On the system gallium-indium-tin. *Script. Metallurg.* **1970**, *4*, 733–736.
- (39) White, G. K.; Meeson, P. J. *Experimental Techniques in Low-Temperature Physics*, 4th ed.; Oxford University Press, 2002.
- (40) Lipowitz, A. In *Polytechnisches Journal*; Dingler, E. M., Ed.; Über Wood's leichtflüssiges Metall; G. Cotta, Stuttgart, 1860; Vol. 158; pp 376–377.
- (41) Jenson, W. B. Ask the historian - Onions fusible alloy. *J. Chem. Ed.* **2010**, *87*, 1050–1051.
- (42) Parker, S. P. *McGraw-Hill Dictionary of Scientific and Technical Terms*, 6th ed.; The McGraw-Hill Companies, 2003.
- (43) Okamoto, H. The Fe-Ga (iron-gallium) system. *Bull. Alloy Phase Diag.* **1990**, *11*, 576–577.
- (44) Wagner, G.; Hoppe, R. Neue Synthesewege zu Metalloxiden: Na_3TiO_2 aus $NaTi$ und Na_2O_2 . *J. Less Common Met.* **1986**, *120*, 225–237.
- (45) Watanabe, H.; Kijima, N. Nitridation of AEAlSi for production of $AEAlSiN_3$: Eu^{2+} nitride phosphors (AE = Ca, Sr). *J. Ceram. Soc.(Jap.)* **2009**, *92*, 641–648.
- (46) Wang, T.; Yang, J.; Mo, Y.; Bian, L.; Song, Z.; Liu, Q. L. Synthesis, structure and tunable red emissions of $Ca(Al/Si)_2N_2(N_{1-x}O_x)$: Eu^{2+} prepared by alloy-nitridation method. *J. Luminesc.* **2013**, *137*, 173–179.
- (47) Coelho, A. Topas Academic Version 4.1. Coelho Software, Brisbane, 2007.
- (48) X-Area: IPDS control software Version 1.39. STOE Cie. GmbH, Darmstadt, Germany, 2006.
- (49) APEX2, Version 2014.11-0. Bruker-AXS, Madison, Wisconsin, USA, 2014.
- (50) Sheldrick, G. M. A short history of SHELX. *Acta Crystallogr.* **2008**, *A64*, 112–122.

Supplementary information

Contents

- 1 Preparation of cathode materials
- 2 Rietveld refinement results
- 3 Details on Rietveld refinement of CsIn₁₂

Preparation of cathode materials

Mercury

Mercury was purified from less noble impurities by vigorous stirring under half-concentrated HNO₃ until colorless and insoluble Hg₂(NO₃)₂ started to form. Solid impurities were removed by filtering through paper. Subsequently, the mercury was distilled twice in vacuum at 120°C.

Gallium

Gallium was used as purchased (99.999%, smart-elements GmbH, Wien, Austria).

Galinstan

Galinstan was prepared from the elements. Suitable amounts of gallium, indium and tin (Ga:In:Sn = 59.6:26:14.4 wt%) were combined in a 2mL Micro Tube with Lip Seal Screw Cap & Loop under air. Reaction of the metals proceeded at room temperature by vigorously shaking the educts in the container. During reaction the mixture cooled under room temperature indicative for the formation of the eutectic.

Mercury/Indium

Mercury was purified as mentioned above. Indium (99.999%, smart-elements GmbH, Wien, Austria) was used as purchased. One equivalent of Mercury was put in a glass vial and small chunks of Indium (total amount of one equivalent) were added. The vial was gently shaken until all indium was dissolved. In contrast to mercury, which is non-wetting toward glass, the Hg:In = 1:1 mixture covers the vial.

Table S1: Crystallographic details as results of a Rietveld refinement on $\text{Li}_3\text{Ga}_{14}$. The graphical result of the refinement is shown in the main text, see Figure 4 (top).

Empirical formula	$\text{Li}_3\text{Ga}_{14}$
Crystal system	trigonal
Space group	$R\bar{3}m$, No. 166
Lattice parameters / \AA , \AA^3	$a = 8.4535(2)$ $c = 16.8229(4)$ $V = 1041.13(3)$
Formula units Z	3
Calculated density / $\text{g}\cdot\text{cm}^{-3}$	4.770(2)
Diffractometer	STADI P (Stoe & Cie., Darmstadt, Germany)
Detector	MYTHEN 2K (Dectris Ltd., Baden-Daettwil, Switzerland)
Data collection	Debye-Scherrer geometry, glass capillary $\varnothing = 0.2$ mm, step width = 0.015° , exposure time = 50 s/step
Radiation, wavelength / \AA	$\text{MoK}_{\alpha 1}$, 0.70930
Number of l. s. parameters	33
Number of background parameters	12
R values	$R_p = 0.01215$ $R_{wp} = 0.01627$ $R_{\text{Bragg}} = 0.00587$ χ^2 (Goof) = 1.242

Rietveld refinements

3. Details on Rietveld refinement of CsIn_{12}

The structure refinement was performed on powder data with the Rietveld method (see below for graphical results), starting with idealized parameters derived from the aristotype structure of NaZn_{13} (see below). The powder diffraction patterns were recorded in $\text{Mo K}\alpha 1$ radiation on a STADI P system (Stoe & Cie., Darmstadt, Germany) with a MYTHEN 2K detector (Dectris Ltd., Baden, Switzerland) in Debye-Scherrer geometry (capillary diameter: 0.1 mm, step width: 0.015° , exposure time: 500 s/step). The finely ground powder was diluted with diamond powder (red ticks in the Rietveld plots below) to optimize absorption effects. All Cs atoms are topologically identical and therefore were refined with one common isotropic thermal displacement parameter, so were all Indium atoms.

A series of refinements shows that symmetry reduction to space group $Pnn2$ is necessary to get full accordance of data and structure model. In all higher space groups a number of reflections remains unindexed. Further symmetry reduction to $P222$ or monoclinic subgroups of $Pnn2$ was checked but gave no improvement. The final refinement of the $Pnn2$ structure model with 24 In sites and 4 Cs sites gives a good agreement of calculated

Table S2: Standardised fractional atomic coordinates, isotropic displacement parameters / \AA^2 and site occupation factors for $\text{Li}_3\text{Ga}_{14}$.

Atom	Wyckoff position	x	y	z	B_{iso}	s.o.f.
Ga1	6c	0	0	0.0789(3)	1.19(11)	1
Ga2	18h	0.5066(2)	-x	0.1971(2)	0.75(5)	1
Ga3	18h	0.4387(2)	-x	0.0512(2)	0.89(6)	1
Li1	18h	0.4795(4)	-x	0.3812(6)	1.00	0.5

Table S3: Crystallographic details as results of a Rietveld refinement on the electrolysis product of Galinstan as cathode material with LiI solution. The graphical result of the refinement is shown in the main text, see Figure 6 (top).

Empirical formula		$\text{Li}_3\text{Ga}_{14-x}\text{Sn}_x$	LiGa	LiIn	In
Proportion by weight		30.5 %	46.6 %	19.8 %	3.2 %
Crystal system		trigonal	cubic	cubic	tetragonal
Space group		$R\bar{3}m$	$Fd\bar{3}m$	$Fd\bar{3}m$	$I4/mmm$
Lattice parameters / \AA , \AA^3	a	8.4539(2)	6.1822(4)	6.7666(4)	3.2579(4)
	c	16.8236(4)			4.9450(3)
	V	797.23(6)	236.28(4)	309.82(5)	52.49(2)
Formula units Z		3	8	8	2
Calculated density / $\text{g}\cdot\text{cm}^{-3}$		1.6513(1)	4.3100(8)	5.0(7)	7.264(3)
Diffractometer		— STADI P (Stoe & Cie., Darmstadt, Germany) —			
Detector		— MYTHEN 2K (Dectris Ltd., Baden-Daettwil, Switzerland) —			
Data collection		— Debye-Scherrer geometry, — — glass capillary $\varnothing = 0.2$ mm, — — step width = 0.015° , exposure time = 100 s/step —			
Radiation, wavelength / \AA		— $\text{MoK}\alpha_1$, 0.70930 —			
Number of l. s. parameters		— 60 for all phases combined —			
Number of background parameters		— 12 —			
R values		— $R_p = 0.02298$ — — $R_{wp} = 0.03315$ —			
		$R_{\text{Bragg}} = 0.01417$	0.01228	0.00509	0.02310
		— χ^2 (GooF) = 1.556 —			

and observed intensities. The resulting structure model shows very strong distortions in comparison with the aristotype structure of NaZn_{13} (see Figure 5 in the main text).

Table S4: Standardised fractional atomic coordinates, isotropic displacement parameters / \AA^2 and site occupation factors for $\text{Li}_3\text{Ga}_{14-x}\text{Sn}_x$ as result from a Rietveld refinement of the electrolysis product of Galinstan as cathode material with LiI solution. Standard deviations in units of the last digit are given in parentheses.

Atom	Wyckoff position	x	y	z	B_{iso}	s.o.f.
Ga1	6c	0	0	0.0742(8)	1.5(5)	0.56(6)
Sn1	6c	0	0	0.0742(8)	1.5(5)	0.44(6)
Ga2	18h	0.5008(7)	-x	0.1996(6)	2.7(4)	1
Ga3	18h	0.4399(6)	-x	0.0470(7)	0.60(5)	0.95(3)
Li1	18h	0.404(2)	-x	0.381(5)	1.00	0.5

Table S5: Standardised fractional atomic coordinates and isotropic displacement parameters / \AA^2 for LiGa as result from a Rietveldrefinement of the electrolysis product od Galinstan as cathode material with LiI solution. Standard deviations in units of the last digit are given in parentheses.

Atom	Wyckoff position	x	y	z	B_{iso}
Ga1	8a	1/2	1/2	1/2	1.52(8)
Li1	8b	0	0	0	7.5(8)

Table S6: Standardised fractional atomic coordinates and isotropic displacement parameters / \AA^2 for LiIn as result from a Rietveld refinement of the electrolysis product od Galinstan as cathode material with LiI solution. Standard deviations in units of the last digit are given in parentheses.

Atom	Wyckoff position	x	y	z	B_{iso}
In1	8a	1/2	1/2	1/2	1.97(10)
Li1	8b	0	0	0	6.5(8)

Table S7: Standardised fractional atomic coordinates and isotropic displacement parameters / \AA^2 for In as result from a Rietveld refinement of the electrolysis product od Galinstan as cathode material with LiI solution. Standard deviations in units of the last digit are given in parentheses.

Atom	Wyckoff position	x	y	z	B_{iso}
In1	2a	0	0	0	4(1)

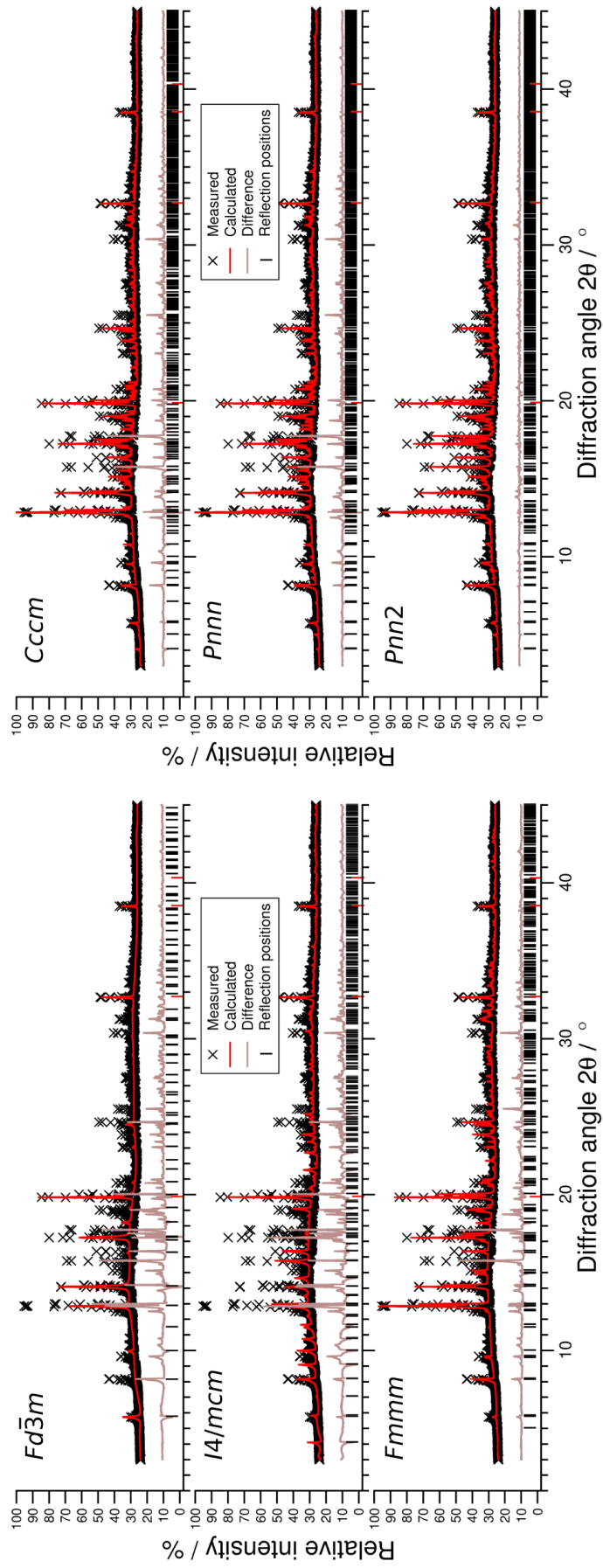


Figure S1: Rietveld refinements of $CsIn_{12}$ in space groups $Fd\bar{3}m$, $I4/mcm$, $Fmmm$, $Cccm$, $Pnnn$ and $Pnn2$.

3.5.2. $\text{Li}_3\text{Ga}_{14-x}\text{Sn}_x$ with $x \approx 1$

$\text{Li}_3\text{Ga}_{13-x}\text{Sn}_x$ with $x \approx 1$ was prepared by electrolyzing 100 ml of a saturated solution of LiI (acros organics, 99 % metal basis) in dry DMF (100 ml, Fischer Organic, HPLC grade). The cathode consisted of a Ga-Sn solution (92.9 at% Ga (smart elements, 99.999 % metal basis), 7.1 at% Sn (alfa aesar, 99.999 % metal basis)) with the approximate melting point 55 °C.^[1] In order to obtain a homogeneously molten cathode material, the temperature was brought to and held at 80 °C. Electrolysis proceeded at this temperature and a terminal voltage of 3.5 V. After electrolysis, the solid product was washed with dry DMF, transferred to a Schlenk tube and subsequently dried in high vacuum. Further manipulation was carried out in an argon-filled glovebox.

Samples for powder and single crystal diffraction were prepared as stated in chapter 3.1.2. Indexing of single crystal data revealed two individua, both with hexagonal symmetry, rhombohedral centring and similar lattice parameters. The individua were integrated and refined separately. Only individuum 1 is further discussed as the second individuum showed too few independent reflections. Structure solution and refinement succeeded in space group $R\bar{3}m$. Heavy atom positions were result of solution, difference Fourier analysis revealed the Li positions. All positions were checked for mixed/underoccupation. Ga(3)/Sn(3) show mixed occupancy of 50%, the Li position is only half occupied.

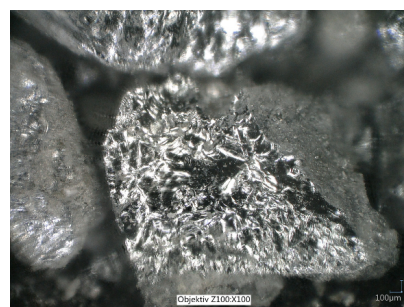
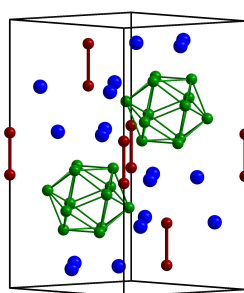


Figure 3.30.: Left: Excerpt of the crystal structure of $\text{Li}_3\text{Ga}_{13-x}\text{Sn}_x$ (Li: blue; Ga: green; Ga/Sn: red). Emphasis on dumbbell (red bonds) and icosahedra (green bonds) is shown, gallium atoms from icosahedra extending in adjacent cells have been omitted for clarity. Right: Optical microscope photograph of $\text{Li}_3\text{Ga}_{13}\text{Sn}$.

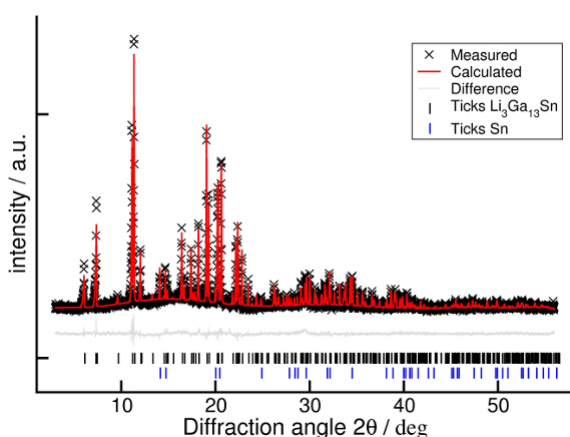


Figure 3.31.: Results of a Rietveld refinement of $\text{Li}_3\text{Ga}_{13-x}\text{Sn}_x$.

Table 3.30.: Results of a Rietveld refinement of $\text{Li}_3\text{Ga}_{13-x}\text{Sn}_x$. For atomic parameters see Table A.20.

Formula	$\text{Li}_3\text{Ga}_{13-x}\text{Sn}_x$ $x \approx 1$
Z	3
Crystal system	trigonal
Space group	$R\bar{3}m$
Lattice parameters [Å , Å^3]	$a = 8.48096(2)$ $c = 16.89013(4)$ $V = 1052.09(5)$
Density (X-ray) [g/cm^3]	4.88(2)
Radiation	$\text{MoK}\alpha_1$
Parameters	40
Background parameters	18
R values	$R_p = 0.2988$ $R_{wp} = 0.04025$ $\chi^2 = 1.381$

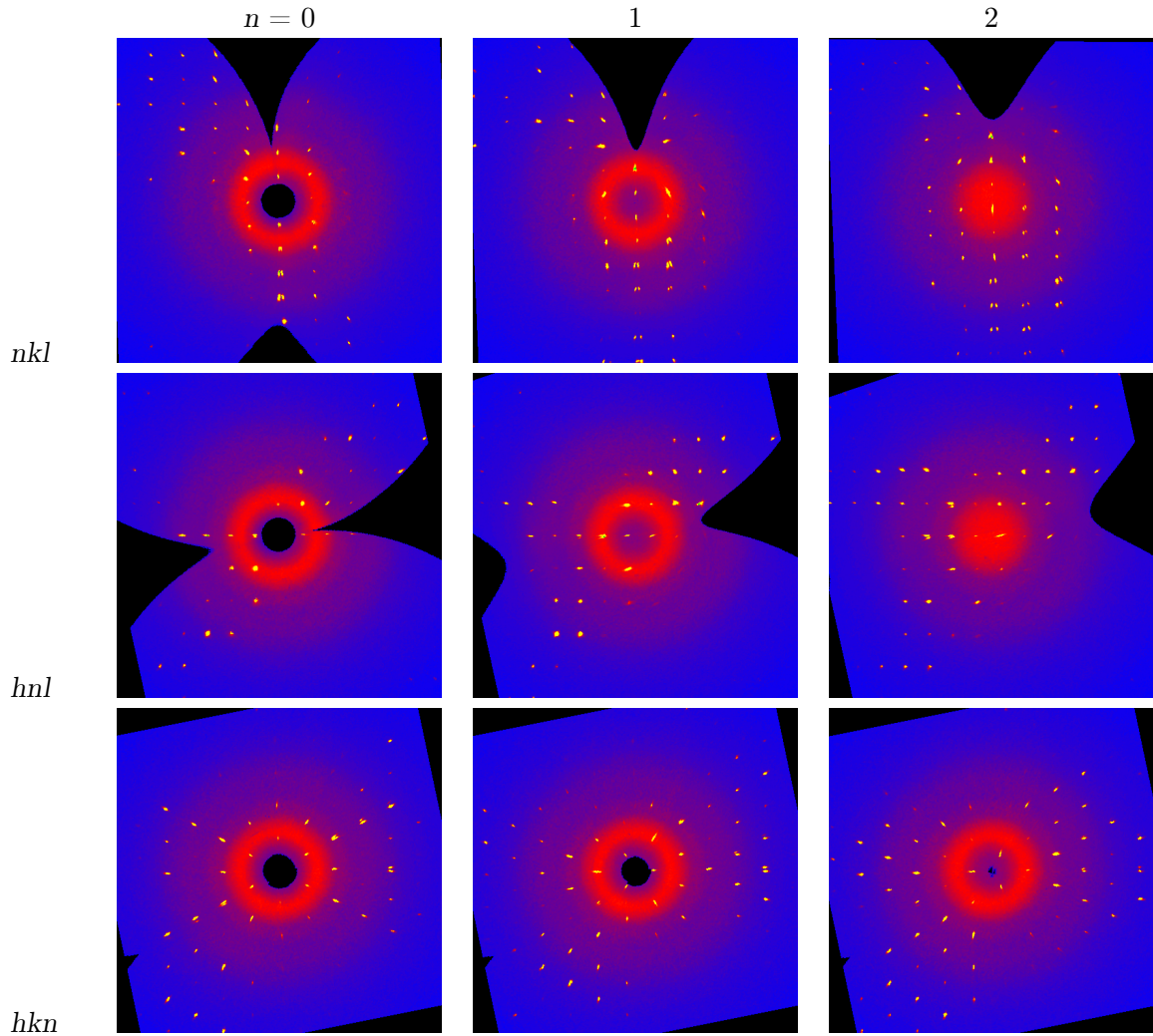


Figure 3.32.: Calculated precession images of a single crystal X-ray measurement of $\text{Li}_3\text{Ga}_{13-x}\text{Sn}_x$.

The parent compound $\text{Li}_3\text{Ga}_{14}$ has previously been reported on by Stör and Schäfer^[2] and was reproduced by electrolysis. $\text{Li}_3\text{Ga}_{13-x}\text{Sn}_x$ crystallizes in the trigonal space group $R\bar{3}m$ with 3 formula units in the unit cell. There are three crystallographically independent gallium sites, one shows mixed occupancy with Sn (Ga:Sn = 1:1). Ga(2) and (3) form an icosahedron, Ga(1)/Sn(1) builds a dumbbell-like motif. The only Li site is statistically half-occupied forming triangles as structural motif. To assess whether the mixed/underoccupations are statistical or of ordered nature, calculated precession images are shown in Figure 3.32, showing no distinct diffuse intensity distribution.

The crystal structure of $\text{Li}_3\text{Ga}_{13-x}\text{Sn}_x$ can topologically be derived from Heusler-type phases (see Figure 3.33). If the centroids of the dumbbells, icosahedra and triangles are substituted by "atoms", icosahedra and dumbbell centroids build a cubic face centred motif each, the distortion from ideal 90° being 7.3° . Centroids of lithium triangles occupy all tetrahedral voids. Furthermore, the space group type of Heusler phases ($Fm\bar{3}m$) is a direct supergroup of $R\bar{3}m$ (index [i2]) illustrating the relationship.

Table 3.31.: Crystallographic data, details of the data collection and structure determination for $\text{Li}_3\text{Ga}_{13-x}\text{Sn}_x$.

empirical sum formula	$\text{Li}_3\text{Ga}_{13-x}\text{Sn}_x$
crystal system	trigonal
space group	$R\bar{3}m$
Lattice param. [\AA , \AA^3]	a 8.458(2)
	c 16.829(3)
	V 1038.2(3)
	Z 3
calc. density ($\text{g}\cdot\text{cm}^3$)	5.151
Abs. coeff. (mm^{-1})	14.314
Radiation (\AA)	Mo-K α 1
Diffractionmeter	IPDS 1 (Stoe & Cie, Germany)
Corrections	Lorentz, polar., absorption
No. of collected data	5076
No. of unique data	487
with $I \geq 2\sigma(I)$	443
$R_{\text{int}}/R_{\sigma}$	0.0613/0.0247
Structure solution	direct methods ^[3]
Structure refinement	full matrix least-squares on F^2 ^[3]
$R1 (I \geq 2\sigma(I))/R1$ (all)	0.0299/0.0343
$wR2 (I \geq 2\sigma(I))/wR2$ (all)	0.0673/0.0685
Res. electron dens.	1.195/-1.475

Table 3.32.: Standardised fractional atomic coordinates and equivalent isotropic displacement parameters U_{eq} for $\text{Li}_3\text{Ga}_{13-x}\text{Sn}_x$ from single crystal data. U_{eq} is defined as $1/3$ of the trace of the orthogonalized U_{ij} tensor. Standard deviations in units of the last digit are given in parentheses.

Atom	Wyckoff number	x	y	z	U_{eq}
Ga1	18h	0.4383(3)	0.5617(3)	0.0498(2)	0.0035(9)
Ga2	18h	0.5022(3)	0.4978(3)	0.1971(2)	0.0041(11)
Ga3	6c	$2/3$	$1/3$	0.2534(4)	0.011(2)
Sn3	6c	$2/3$	$1/3$	0.2534(4)	0.011(2)
Li1	18h	0.225(5)	0.450(11)	0.02(4)	0.7(5)

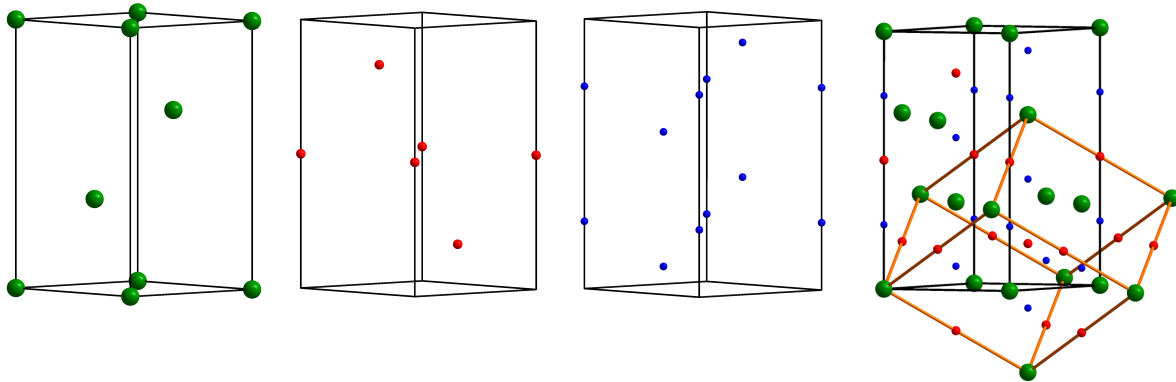


Figure 3.33.: From left to right: Centroids of $[\text{Ga}_{12}]$ icosahedra (green), centroids of $[\text{Ga}/\text{Sn}_2]$ dumbbells (red), centroids of (Li_3) triangles (blue) and the assembled structure with pseudocubic unit cell (orange bars).

DFT calculations were performed as stated in chapter 3.1.2. Muffin-Tin radii were set to 121.7 pm (2.3 a. u., $R_{\text{mt}} \cdot K_{\text{max}} = 8$) for all atoms, the cut-off energy was set to -6 Ry, and 816 k-points of the Brillouin zone (108 thereof in the irreducible Brillouin zone) were calculated in a $6 \times 17 \times 8$ Monkhorst-Pack grid. Plots of the density of states are compiled in Figure 4.27.

References

- [1] T. B. Massalski, *Binary Alloy Phase Diagrams*, ASM International, Materials Park, Ohio, USA, 2nd edition (1990).
- [2] J. Stöhr, H. Schäfer, *Z. Anorg. Allg. Chem.*, **474(3)**, 221–225 (1981).
- [3] G. M. Sheldrick, *Acta Crystallogr. A*, **64(1)**, 112–122 (2007).

4. Discussion

The first part of the following chapter contains a comparative discussion of the employed synthetic methods. Electrolysis on different cathode materials is evaluated with modified Born-Haber cycles. The paths through the respective phase diagrams are assessed for unary, binary and ternary cathode materials. Crystallisation of multiple products from binary and ternary cathode materials is rationalised as well as the employment of Hg as solvent for In. Electrocrystallisation is compared with the distillation approach, similarities and differences are put into context.

The second part contains the evaluation of the obtained crystal structures. Metal iodide solvate structures are rationalised as decorated variants of simple sphere packings. The relations are further illustrated by group-subgroup schemes with the aid of Bärnighausen trees. The crystal structures of the synthesised amalgams are evaluated and put into context with literature-known crystal structures. A structure-field diagram for mercury-rich compounds with composition from AHg_5 to AHg_{11} is proposed. In addition, the crystal structures are analysed by means of complexity measures to quantify multiple disorder phenomena.

The third part contains discussions related to chemical bonding in polar metals. After clarification of the term "polar metal", polarity in amalgams is evaluated. The band structures of three Li amalgams is examined in detail and correlated with the Knight shift measurements of both ^7Li and ^{199}Hg . NMR shifts of ^7Li are put into context with data from literature and compiled in a scheme. Electric conductance is discussed on the Li amalgams and on KHg_6 , model systems for polar metals, and on $\text{Gd}_{14}\text{Ag}_{51}$ as a metallic reference.

The bonding polarity in $\text{Li}_3\text{Ga}_{14}$ and $\text{Li}_3\text{Ga}_{13}\text{Sn}$ is the subject of the fourth part. The crystal structure is described with the aid of Wade formalism and band structure calculations reveal the importance of the underoccupation of the Li site and rationalise the incorporation of Sn on one Ga site. NMR measurements show predominantly Li^+ as an indicator for high polarity. In combination with the discussions on structures derived from the BaHg_{11} structure type, Bader charges are critically evaluated.

4.1. Syntheses

4.1.1. Syntheses I: Preparative Electrocrystallisation

Historical remarks

Liquid mercury as reactive cathode material was first used by Davy and Berzelius.^[1,2] Small amounts of wet salts were contacted to a pool of liquid mercury and a Voltaic pile was used to perform electrolysis.^[3] Metal ions of the respective salts are reduced at and dissolved in the liquid cathode and later isolated by evaporation of Hg. The idea of mercury as auxiliary agent was taken up again – over one hundred years later – during the second world war, the background being separation of rare earth metals.^[4–13] However, preparative electrolysis was not employed for synthesis of intermetallic compounds, the first target-oriented syntheses were performed only recently (also within this work).^[14–16] For a detailed description of the experimental procedure see chapter 3.1.1.

Basic mechanism of electrocrystallisation

Preparative electrolysis on metallic cathodes offers a unique way of synthesis, fundamentally different from classic solid state methods. The latter processes rely on a defined educt ratio and variation of the temperature. In contrast, electrolysis is isothermal (i.e. no temperature variation) and the composition varies over time. This is illustrated on the basis of a binary phase diagram (see Figure 4.1). Classical solid state synthesis (indicated by a green arrow) shows constant composition and variation of the temperature. Electrocrystallisation (indicated by red arrows) starts at pure Hg (or any other liquid metal electrode), with an isothermal change of composition over time.

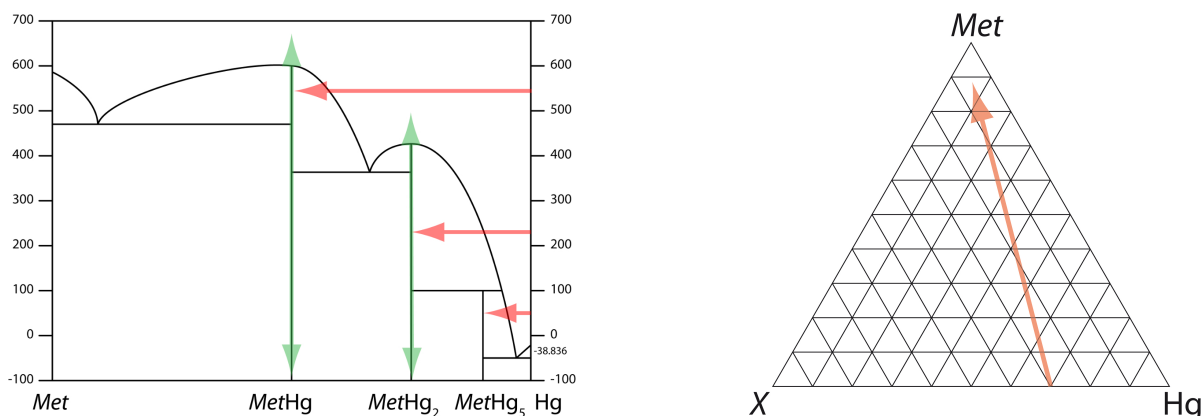


Figure 4.1.: Left: Hypothetical binary *Met*-Hg phase diagram, typical for the combination of Hg with an electropositive element (*Met*). Two dystectica (*MetHg* and *MetHg₂*) and one peritectic phase (*MetHg₅*) are shown. Right: An isothermal section of the hypothetical ternary X-*Met*-Hg phase diagram is shown (*Met*: electropositive element, X: other metal). Red arrows indicate electrolytic processes, green arrows classic solid state synthesis.

During the electrolytic process, ions (Met^{n+}) are reduced to the metallic state and dissolved in the cathode material. As the cathode is enriched with *Met*, one moves horizon-

tally through the phase diagram. When the composition reaches the liquidus curve, the two-phase area is entered: the corresponding solid phase is depleted and a mercury-rich liquid phase retains as cathode. Subsequently, the whole cathode is consumed by this process ideally yielding a phase-pure sample. Reaction ceases as the mobility of atoms in solids is not high enough for the reaction to proceed.

This method is especially valuable for synthesis of compounds melting incongruently at low temperatures. Classical methods rely on high cooling rates and tempering below the peritectic point. At low temperatures this is not feasible as the mobility of atoms is negligible, e.g. in $\text{Cs}_2\text{Hg}_{27}$ below $12\text{ }^\circ\text{C}$.^[14] Isothermal preparative electrocrystallisation provides synthetic access to these phases as crystallisation occurs below decomposition temperature from a liquid phase (increased mobility).

When a binary system is used as cathode, the electrolytic reduction of a metal from solution either yields a ternary product, two binary products or one metal serves as solvent for a binary product. Independent of the outcome of the reaction, the electrolytic process can be visualised with a ternary phase diagram as shown in Figure 4.1, right. On a hypothetical cathode with composition " X_7Hg_3 ", a solution of *Met*-iodide is electrolysed. During the reaction, the amount of *Met* in the cathode material is increased, the *X*:Hg ratio remains the same. A solid product precipitates when a liquidus curve is reached and the process terminates when all liquid cathode material is consumed. As there are several degrees of freedom (composition, temperature), different products can form either simultaneously or in succession, deviating from the red path in the depicted ternary phase diagram.

Figure 4.3 shows a sketch of the elemental processes involved in the electrolytic crystallisation process. It is based on the well-known Born-Haber cycle, including an "initial state" (prior electrolysis), a state highest in energy (top), a "final state" (right, after successful electrolysis) and an "intercepted state" (left, unsuccessful attempt). The left and right part of the Figure differ in the applied terminal potential.

The initial state consists of elemental Hg (cathode), solvated $\text{Met}_{\text{DMF}}^{n+}$ and I_{DMF}^- (in DMF, electrolyte). Desolvation and adsorption to the electrodes are the first steps. Next,

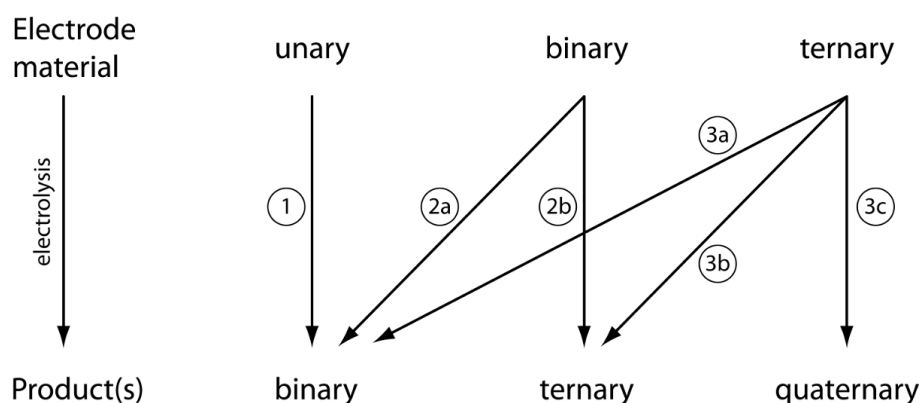


Figure 4.2.: Basic paths for electrolysis. Unary cathode materials: Only binary products are obtained (1). Binary cathode materials: either two binary (2a) or one ternary (2b) product forms. Ternary cathode materials: either several binary (3a), several ternary (3b) or one quaternary (3c) product forms.

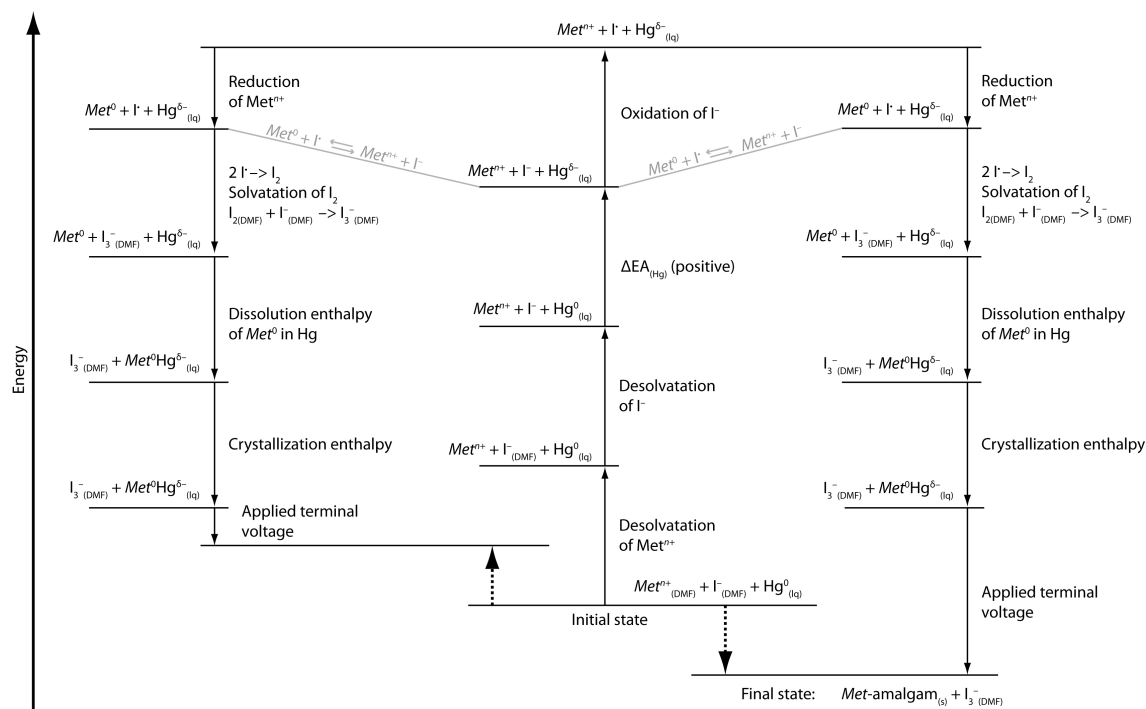


Figure 4.3.: Overview of elemental reactions involved in electrocrystallisation.

the endothermic electron affinity of Hg is considered, pushing the system in a higher energy state.^[17] (If one was to modify the scheme for metallic cathodes with negative electron affinities, the direction of the arrow is to be reversed making this partial reaction exergonic.) To reach the state highest in energy, I^{-} is oxidised to I^{\cdot} (radical).

The first exergonic reaction is the reduction of Met^{n+} to Met^0 as every ionization energy is positive and so every electron affinity of cations is negative. (The upper states of both sides show a simplified Born-Haber cycle for the system Met^0 -iodine. The grey reaction path connects both sides, the hypothetical Met^0I at lowest energy, respectively.) Recombination of two I^{\cdot} , subsequent reaction with additional I^{-} to I_3^{-} and solvation comes next, completing all reaction parts involving iodine. Most metals react with/dissolve in Hg exothermically so this partial reaction is considered exergonic. As stated above, dissolution of Met^0 in Hg is an essential part of the process as the absence of solubility renders the reaction stagnant through passivation. Upon supersaturation of Hg with Met^0 the liquidus of the system Hg- Met is reached and solidification occurs. Lattice energy makes this exergonic, however, strong heat effects are not observed because the process is slow and heat transport from the electrode is good through DMF. The last contribution is the applied terminal voltage (ATV). If the ATV is too low, the "final state" is energetically disfavoured with respect to the initial state. If one sets the ATV high enough, reaction can proceed.

Limitations of the scheme are: (1) Kinetic effects leading to overvoltage, seed formation or decreased speed of the reaction are not considered, (2) detailed reactions on the electrodes (adsorption, desorption, Helmholtz double layer, polarization) are omitted for clarity (3) the scheme is not suited for quantification as *all* other energies have to be known to quantify *one* unknown energy of the cycle.

Electrolysis with unary, binary and ternary reactive cathode materials

Unary electrodes Compounds with peritectic and dystectic melting points can be synthesised with electrocrystallisation, only the highest melting dystectic of a given phase diagram cannot be overcome. In this work the following compounds were synthesised starting from unary electrode materials. Amalgams: LiHg_3 (see chapter 3.4.2), KHg_{11} and KHg_6 (see chapter 3.4.1) and $\text{Eu}_{10}\text{Hg}_{55}$ (see chapter 3.3.1); Gallides: $\text{Li}_3\text{Ga}_{14}$ and NaGa_4 (see chapter 3.5.1).

Binary electrodes Electrolysis of LiI on a binary Ga-Sn cathode (see Figure 4.4) yields $\text{Li}_3\text{Ga}_{13}\text{Sn}$. Figure 4.4 shows an isothermal section of the ternary phase diagram Li-Ga-Sn including literature-known binary and ternary phases (black) and the new phase $\text{Li}_3\text{Ga}_{13}\text{Sn}$ (red). Two different electrolytic synthesis pathways are indicated by arrows. Pale blue: Electrolysis performed in this work (see chapter 3.5.2) starting from Ga-Sn eutectic with 8% Sn and melting point 55 °C yields $\text{Li}_3\text{Ga}_{13}\text{Sn}$; Purple: hypothetical electrolysis starting from GaSn (melting point 130 °C), leading to LiGaSn as product. In both cases the Ga:Sn ratio remains the same for the educt and the product.

Formation of a ternary phase during electrolysis on a binary cathode is one of the possible outcomes. Another one is the formation of a binary phase with the second electrode

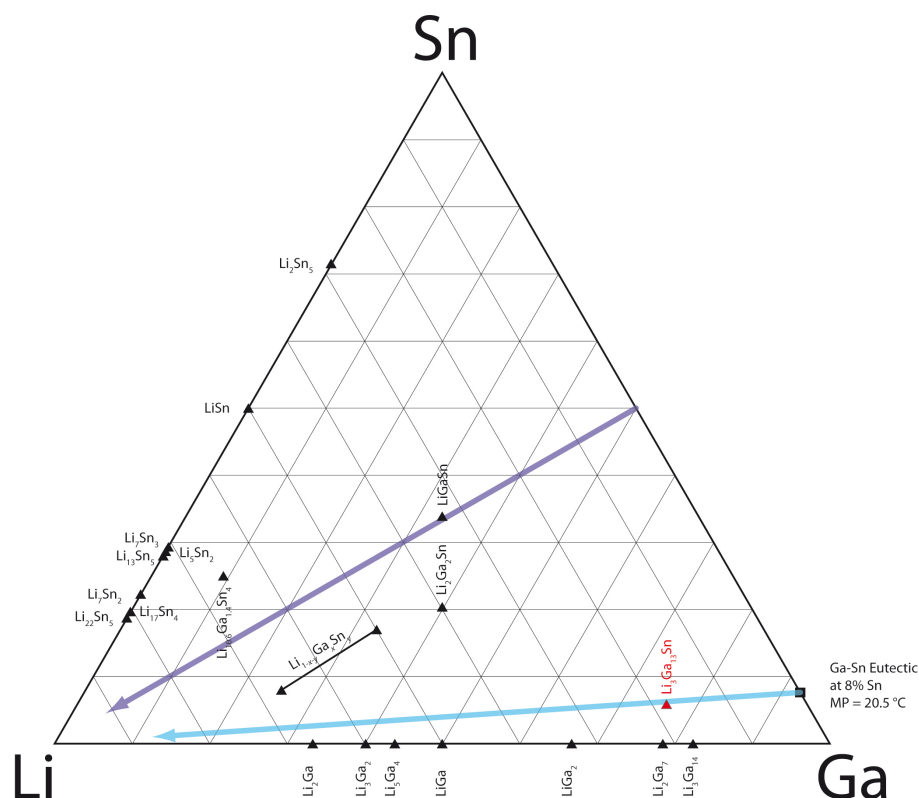


Figure 4.4.: Ternary phase diagram of Li-Ga-Sn. Literature known phases are black, the new phase in red. Literature is compiled in Table 4.1. The pathway of the performed electrolysis is shown in light blue, another possible pathway leading to LiGaSn is shown in purple.

ingredient serving as inert solvent. This was observed when CsI was electrolysed on a HgIn cathode (see chapter 3.5.1). The process yielded CsIn₁₂ and elemental Hg. Analogous to the description given above, this outcome can be rationalised by a modified Born-Haber scheme (see Figure 4.5). The left part of the scheme shows the formation of CsIn₁₂, the right part the suppressed formation of a Cs amalgam. Both sides differ by the electron affinity of Hg (positive, endothermic) with respect to In (negative, exothermic). It is immediately clear that additional formation of a Cs amalgam would require a higher terminal voltage, which was prevented in this case.

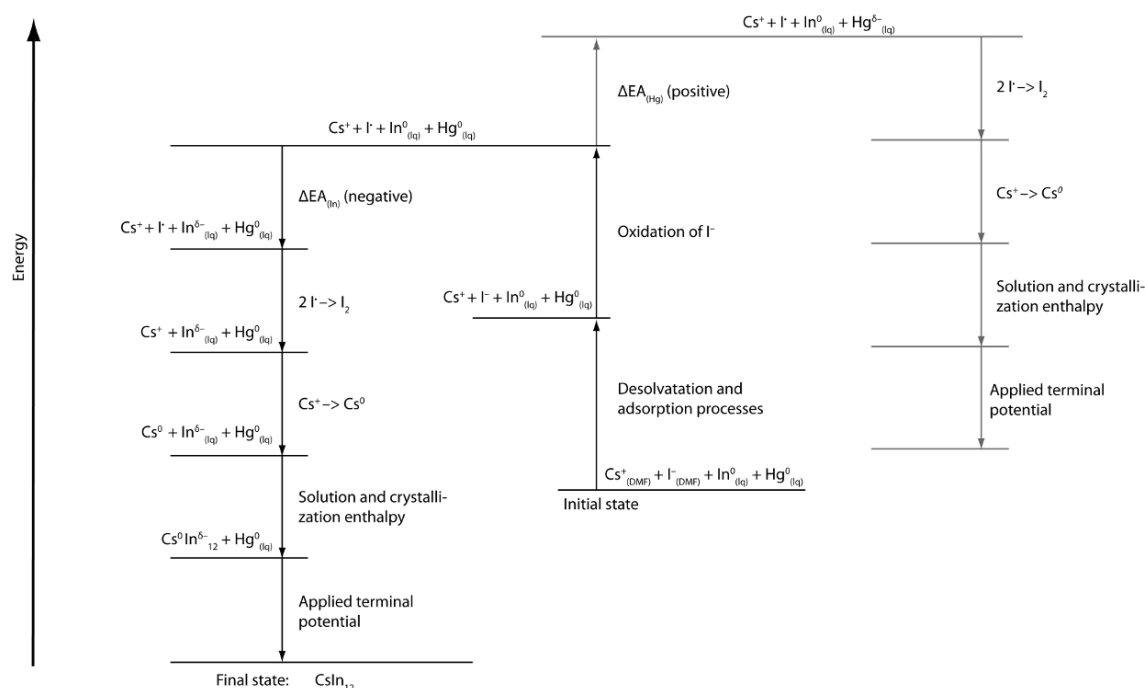


Figure 4.5.: Elemental reactions for the electrolysis of CsI on HgIn as cathode material. Black: Observed formation of CsIn₁₂. grey: Hindered formation of a Cs amalgam.

Ternary electrodes A third possible outcome of electrolysis on multinary cathode materials is the observation of demixing and formation of multiple binary phases. This was observed for electrolysis of LiI on GaInStan as ternary cathode material (see chapter 3.5.1). The graphical illustration of the electrolytic pathway in a quaternary phase diagram is difficult. It is schematically presented in Figure 4.7, however, known phases have been omitted for clarity. The basal plane is an isothermal section of the ternary phase diagram of Ga–In–Sn with the intersection of the red lines at the eutectic (GaInStan, electrode material) and the red arrow indicating change in composition during electrolysis. No quaternary phase but several simple other phases were yielded: LiGa 46.6wt%, Li₃Ga_{14-x}Sn_x 30.5wt% ($x \approx 1$), LiIn 19.8wt% (with substantial amounts of Sn on the In position) and In 3.2wt% (wt% determined by Rietveld refinement, see chapter 3.5.1). A detailed description of formation is impossible without a full evaluation of the ternary phase diagram which lies beyond the scope of this thesis. However, we make a proposal by considering the respective binary phase diagrams (see Figure 4.6) and the observed phase formation.

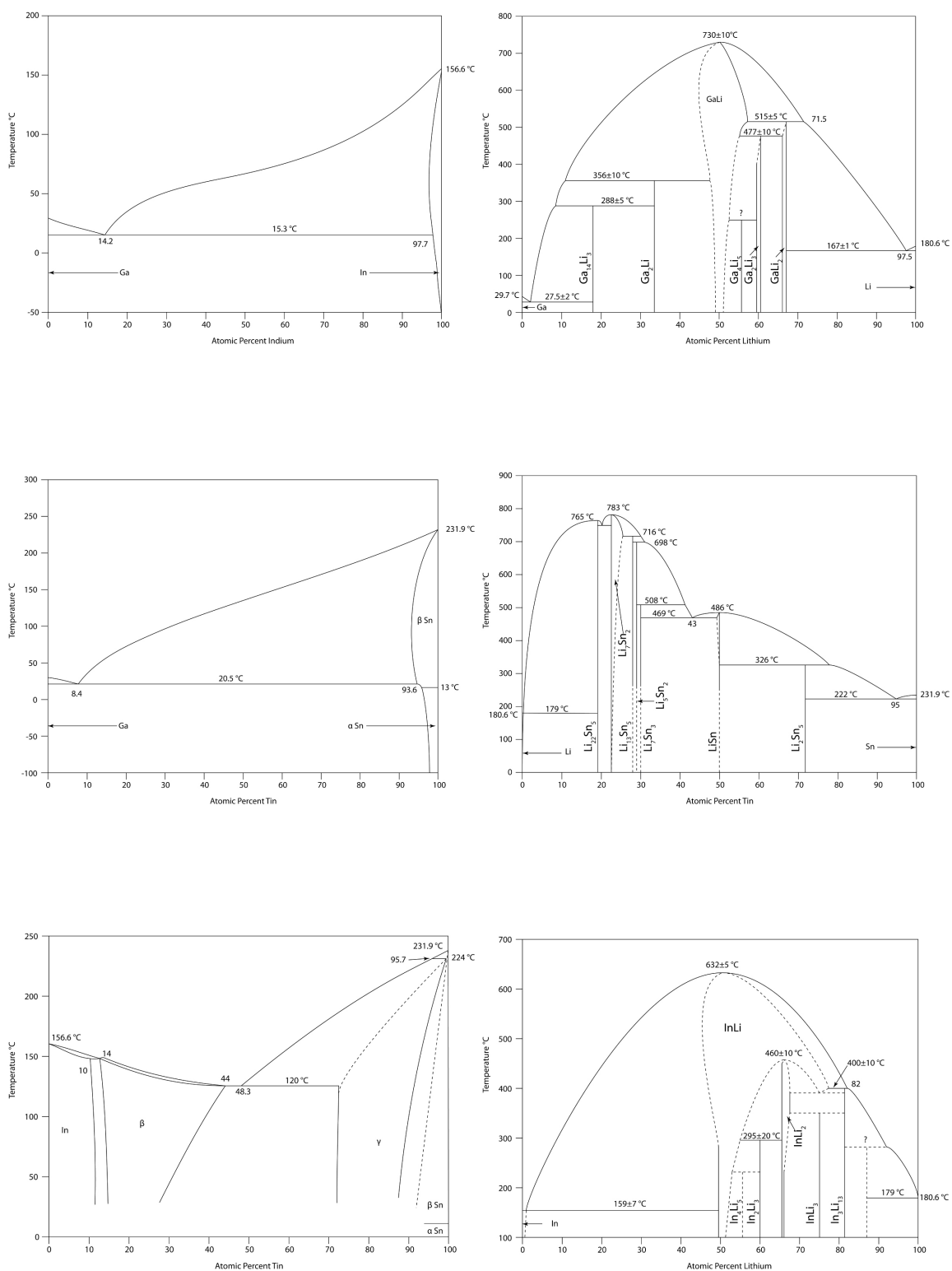


Figure 4.6.: Binary phase diagrams for Ga-In, Ga-Li, Ga-Sn, Sn-Li, In-Sn and In-Li (left to right, top to bottom).^[18]

Perfect liquid miscibility is observed for Ga–Sn and Ga–In (see Figure 4.6). The phase diagram In–Sn is a non-classical Hume-Rothery system without pronounced dystectica, an eutectic is observed 48.3 at% Sn, constituted by the β and γ phases. This indicates small binding interactions between the three constituents, resulting in the especially low melting GaInStan eutectic. Phase diagrams Ga–Li and In–Li show a pronounced dystectic for the respective phases LiGa and LiIn which are the highest melting phases in the respective systems. Other known phases melt incongruently at lower temperatures, indicating high energy of formation for LiGa and LiIn compared to other phases (thermodynamic sink). Thus, formation of LiGa and LiIn is highly favoured. In addition, both LiGa and LiIn show large phase width, possibly extending into the ternary and quaternary phase diagrams. In contrast, the Li–Sn diagram shows formation of non-classical Zintl phases with two dystectica. LiSn shows small phase width and melts 280 K lower than $\text{Li}_{22}\text{Sn}_5$.^[19,20] One concludes the formation of LiSn being hampered, other Li–Sn phases are more likely to form.

Table 4.1.: References for the compounds depicted in Figure 4.4.

Substance	Lit.	Substance	Lit.	Substance	Lit.	Substance	Lit.
$\text{Li}_{22}\text{Sn}_5$	[20]	Li_7Sn_3	[21]	Li_5Ga_4	[22]	$\text{Li}_{10.6}\text{Ga}_{1.4}\text{Sn}_4$	[23]
$\text{Li}_{17}\text{Sn}_4$	[24]	LiSn	[19]	LiGa	[25]	$\text{Li}_{1-x-y}\text{Ga}_x\text{Sn}_y$	[23]
Li_7Sn_2	[26]	Li_2Sn_5	[27]	LiGa_2	[18]	$\text{Li}_2\text{Ga}_2\text{Sn}$	[28]
$\text{Li}_{13}\text{Sn}_5$	[29]	Li_2Ga	[30]	Li_2Ga_7	[31]	LiGaSn	[28]
Li_5Sn_2	[32]	Li_3Ga_2	[30]	$\text{Li}_3\text{Ga}_{14}$	[31]	$\text{Li}_3\text{Ga}_{13}\text{Sn}$	this work

Binary phase diagrams can be used to minimise the number of phases likely to form. Electrocrystallisation stops when a solid phase is formed. In the Ga–Li and In–Li phase diagrams the solid phases GaLi and LiIn are the highest melting, making the Li-rich parts of the phase diagrams inaccessible by electrolysis. Possible Li-poor products are GaLi, $\text{Li}_3\text{Ga}_{14}$ and LiIn. Li_2Sn_5 as a Sn-rich phase does not form because Sn is more likely to be incorporated in other phases forming more easily (e.g. LiIn with Sn on the In position), the reaction most likely stops at the dystectic InLi.

Phase formation during electrolysis of a LiI solution on a GaInStan cathode can be rationalised as follows: First Li^+ is reduced forming a quaternary metallic solution with Ga, In and Sn. Further enrichment of the cathode material with Li leads to co-crystallisation of LiGa and LiIn while formation of $\text{Li}_3\text{Ga}_{14}$ is hindered by high In content. A possible reason is the increased solubility of this phase when In is present in the cathode, as indicated by the Li–In phase diagram. As the cathode is depleted in Ga (In and Sn to a lesser degree), In becomes insoluble in the cathode segregating as element (minor side phase). A Ga-rich

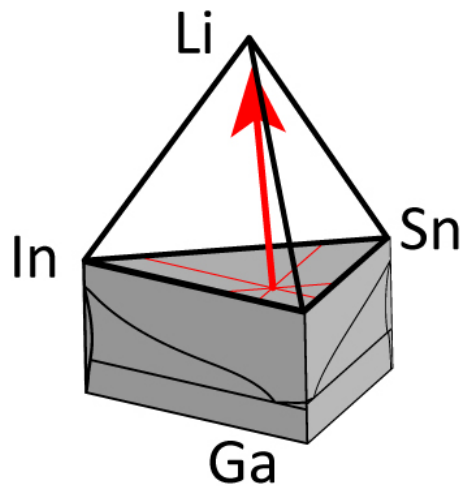


Figure 4.7.: Quaternary phase diagram of the system Ga–In–Sn–Li. The intersection of red lines shows the GaInStan eutectic, the red arrow the change in composition during the electrolysis.

electrode with additional Sn remains equivalent to the electrolysis of LiI on a Ga-Sn electrode (see above). $\text{Li}_3\text{Ga}_{14}$ forms (with Sn on one position) and the reaction stops.

4.1.2. Syntheses II: Distillation Method

A complementary preparation method is the distillative synthesis of amalgams (presented in chapter 3.3.3). In this chapter we will describe and discuss the distillation process and put it into context with electrocrystallisation.

Experimental procedure

An electropositive metal is mixed with a mercury surplus of at least 10 equivalents. This mixture is put into borosilicate glass ampoules ($l \approx 20$ cm) with a constriction at half length (see Figure 3.3). Evacuation to $p \leq 1 \cdot 10^{-3}$ mbar is followed by sealing the ampoule. It is then put upright into an oven, with the upper part above the constriction. The lower part is heated to 300 °C, the top part air-cooled. Hg vaporises in the lower part, condenses on the air-cooled part and flows back into the heated part. Essentially, the reaction is performed in refluxing mercury.

In all cases the reaction can be observed *before* the ampoule is heated. Adding powders of elemental lanthanides to mercury immediately leads to an exothermal reaction, heating the mixture to temperatures as high as 100 °C. After cooling, a sludge of a solid amalgam in surplus mercury is formed. *If this is not observed, the powdered less electronegative reactant may have developed a thin oxide layer, preventing the reaction at room temperature. Proceed with extreme caution!* It is possible that upon heating the reaction may not take place until high temperatures are reached. Subsequently, the instating reaction is extremely exergonic and may melt the ampoule *leading to implosion*. If no reaction is observed at room temperature, the experiment has to be aborted and the reactants dissolved in half-concentrated HNO_3 .

When the reaction mixture is homogenous, heating is ceased and the ampoule allowed to cool to room temperature. Afterwards the oven including the ampoule is turned horizontally and heated to 100 °C. This allows the surplus mercury to be distilled into the cold part of the ampoule, which, again, is air-cooled. This is the point where the constriction becomes essential. It prevents the distilled mercury from flowing back into the reaction mixture and is thus removed from the reaction. After completion the ampoule is allowed to cool to room temperature and the product-containing part of the ampoule is separated from the Hg-containing part by sealing at the constriction, resulting in phase-pure amalgam and freshly distilled mercury.

Reaction mechanism and difference to electrocrystallisation

The preparation can be divided into steps: (1) Dissolution of the electropositive metal in Hg. (2) Complete reaction of the starting materials at elevated temperature. (3) Crystallisation of the desired amalgam. (4) Removal of surplus mercury at low temperature. The Hg-richest amalgam stable at given conditions (100 °C, $p \leq 1 \cdot 10^{-3}$ mbar) is

obtained. Analogous to electrolysis, the distillation process is rationalised by evaluation of the respective binary phase diagrams. During electrocrystallisation, a metallic reactive cathode is enriched with a metal by reducing it from solution. This results in an horizontal movement through the phase diagram as shown in Figure 4.1 (left). During distillation, one also moves horizontally through the phase diagram. Usually, temperatures required for distillation are higher than for electrocrystallisation. Distillation only works when a substantial vapour pressure of Hg over the component mixture is achieved, thus requiring higher temperatures. Therefore, electrocrystallisation is appropriate for syntheses of amalgams with especially low stability ranges. Figure 4.8 shows the vapour pressure/temperature phase diagram of Hg.^[33] Melting, boiling and critical points are shown. For comparison: Ampoules employed in the experiments of this work are stable to a pressure of 10 bar (≈ 800 K / 525 °C) which is well above the required temperature.

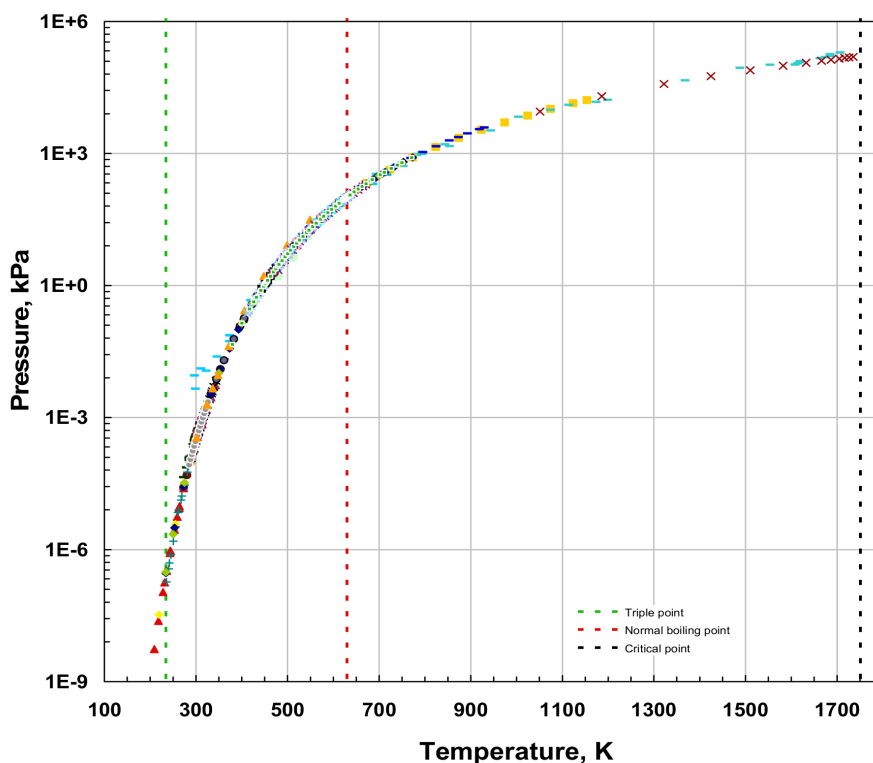


Figure 4.8.: Experimental vapour pressure data for Hg. Modified Figure taken from NIST Interagency/Internal Report (NISTIR) - 6643.^[33]

At the reaction temperature (300 °C) the vapour pressure of Hg is 2000 mbar and thus mercury is boiling in the evacuated ampoule (10^{-3} mbar). This allows the reaction to proceed and a solution of an amalgam in Hg is obtained. For distillation the temperature is lowered to 100 °C corresponding to a vapour pressure of 3 mbar. Hg is no longer boiling but still shows substantial vapour pressure allowing for good transport through the gas phase. For comparison: 50 °C and 0 °C correspond to p_{Hg} of 0.5 mbar and 0.0015 mbar, respectively. Distillation at those temperatures is not feasible as the vapour pressures are too low for a substantial Hg transport along the length of the ampoule. In conclusion, the distillation method is useful to obtain amalgams with high decomposition temperatures, whereas electrocrystallisation is especially useful for the synthesis of amalgams with unusually low decomposition temperatures.

4.2. Evaluation of Crystal Structures and Measures of Complexity

Quantification of the vague term "complexity" is possible with the definition of complexity measures.^[34,35] For a long time, complexity in crystal structures was regarded as "largely a qualitative, frequently intuitive, notion".^[36] This is in contrast to the frequent use of the term and related terminology to describe structures, e.g. "complicated structure", "the most complex structure", "complex superstructure" or "a masterpiece of structural complexity".^[16,36,37] A new approach towards a numerical interpretation of complexity leading to quantifiable ratings provides important tools for comparison of structures and was developed recently.^[34,35] Within this new method, structures are deconstructed and adapted to information theory concepts, more precisely graph theory: total crystal structure (graph), atoms as vertices (nodes) and chemical bonds as edges (links).

The structural information content of one crystal structure per reduced unit cell is IG in [bits/atom] and is calculated as the sum of the number of crystallographic orbits k and the probability of occurrence of the atom on the i th orbit p_i . The total information content IG_{Bits} (in [bits/unit cell]) is calculated by multiplying IG with the number of atoms in the unit cell. To make IG independent of the number of atoms, a normalised information content IG_n (unitless) is defined by division of IG by IG_{max} (the maximal information content with all non-equivalent atoms). Strong influence on the information content is imposed by the size of the unit cell and therefore the number of atoms in the unit cell. Structures with low symmetry are generally more complex as they exhibit more inequivalent crystallographic orbits than a unit cell similar in size but with higher in symmetry. Mixed positions introduce more complexity, they are treated as additional crystallographic orbits. Underoccupation is also treated as additional crystallographic orbit.^[34,35]

Another method of rationalising complex crystal structures, especially of coordination compounds, is to reduce the coordination moieties to spheres. The topology of the packing of those centroids can then be analysed topologically. Thus, complex structures can be reduced to and explained by simple sphere packings.

4.2.1. Metal Iodide Solvate Structures as Decorated Variants of Simple Sphere Packings

Preparative electrolysis as synthetic method often yields intermetallic compounds which are very sensitive towards air and moisture. A dry aprotic solvent is necessary. In order to dissolve the educts (iodides) it must be polar. In addition, the liquid range and electrochemical stability should be large and its viscosity low. *N,N*-dimethyl formamide (DMF) satisfies all requirements. It is liquid from $-61\text{ }^{\circ}\text{C}$ to $153\text{ }^{\circ}\text{C}$, very polar (3.86 D), of low viscosity (0.802 mPas), electrochemically stable up to $\approx 5\text{ V}$ and easy to dry over CaH_2 or by azeotropic distillation.

The starting material for electrolysis, usually an iodide, is dissolved in DMF, the resulting solution dried and used for electrolysis. However, some iodides are very expensive and it is convenient to synthesise the iodides in DMF as solvent yielding the respective

coordination compounds. Synthetic procedures were carried out as described in chapter 3.1.1.

DMF coordinates via its O atom in the sp^2 lone-pair direction. Coordination numbers range from 4 in $[\text{Li}(\text{DMF})_4]\text{I}$ to 9 in $[\text{La}(\text{DMF})_9]\text{I}_3$ (see Table 4.2), larger ions coordinating more DMF. The crystal structures of the resulting solvates can be rationalised as follows: Iodide and coordinated cations can be replaced by centroids which – in a first approximation – are spherical (see Figure 4.9). The centroids are packed in motifs known from simple sphere packings or hierarchical variants thereof.

$[\text{Li}(\text{DMF})_4]\text{I}$ is a decorated variant of the α -U structure type. Stacking of the hexagonal planes is similar in $[\text{Li}(\text{DMF})_4]\text{I}$ and α -U (see Figure 4.12, right). Despite this, there is no direct group-subgroup relation between the two structures, the similarity is merely topological.

$[\text{Na}(\text{DMF})_{6/2}]\text{I}$ is a decorated variant of the NiAs structure type with $[\text{Na}(\text{DMF})_{6/2}]^+$ occupying the Ni and I^- the As sites. The a/c ratio is 0.548, significantly less than in NiAs (1.39), indicating a severe compression of the structure along the c axis. This compression originates from stacking of the $[\text{Na}(\text{DMF})_{6/2}]^+$ octahedra forming rods along c sharing trigonal faces (see Figure 3.6) and thus employing DMF as μ_2 -bridging ligand.

Hierarchical variants of the hexagonal closest packing: $[\text{Sr}(\text{DMF})_7]\text{I}_2$, $[\text{Ba}(\text{DMF})_8]\text{I}_2$ and $[\text{La}(\text{DMF})_9]\text{I}_3$. The symmetry relation between the aristotype (Mg) and the respective hettotypes $[\text{Sr}(\text{DMF})_7]\text{I}_2$ and $[\text{Ba}(\text{DMF})_8]\text{I}_2$ is shown in Figure 4.10 (left). Symmetry reduction steps were chosen as follows: The initial hexagonal cell is converted to orthorhombic C centred with double volume and free y coordinate (set to the final value of 0.61, only small deviation from $2/3$). Reduction to monoclinic C is followed by tripling of the b axis, leading to a splitting of the $4e$ position into three $4e$ positions ($[\text{Ba}(\text{DMF})_8]\text{I}_2$).

Table 4.2.: Coordination compounds of iodides with DMF. ¹ Mixed coordination by DMF and Iodide. ² DMF as bridging ligand. ³ $RE = \text{Nd, Sm, Eu, Gd, Er, Yb}$

Compound	CN	Coordination polyhedron
$[\text{Li}(\text{DMF})_4]\text{I}$	4	tetrahedron
$[\text{Be}(\text{DMF})_4]\text{I}$	4	tetrahedron
$[\text{Zn}(\text{DMF})_2\text{I}_2]\text{I}$	4	tetrahedron ¹
$[\text{Na}(\text{DMF})_{6/2}]\text{I}$	6	octahedron ²
$[\text{Ca}(\text{DMF})_6]\text{I}_2$	6	octahedron
$[\text{Mg}(\text{DMF})_6]\text{I}_2$	6	octahedron
$[\text{Cd}(\text{DMF})_6][\text{CdI}_4]$	6	octahedron ¹
$[\text{Sc}(\text{DMF})_6](\text{I}_3)_3$	6	octahedron
$[\text{Sr}(\text{DMF})_7]\text{I}_2$	7	augm. trig. prism
$[\text{Ba}(\text{DMF})_8]\text{I}_2$	8	square antiprism
$[\text{RE}(\text{DMF})_8]\text{I}_3$	8	square antiprism ³
$[\text{La}(\text{DMF})_9]\text{I}_3$	9	tricap. trig. prism

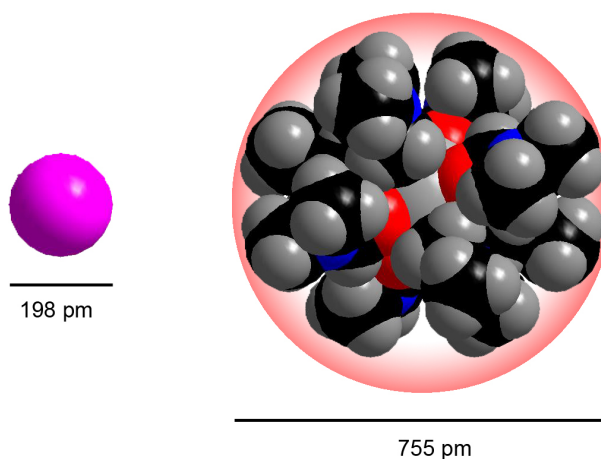


Figure 4.9.: Van-der-Waals radii of I^- (left) and $[\text{Er}(\text{DMF})_8]^{3+}$ (right) to scale.

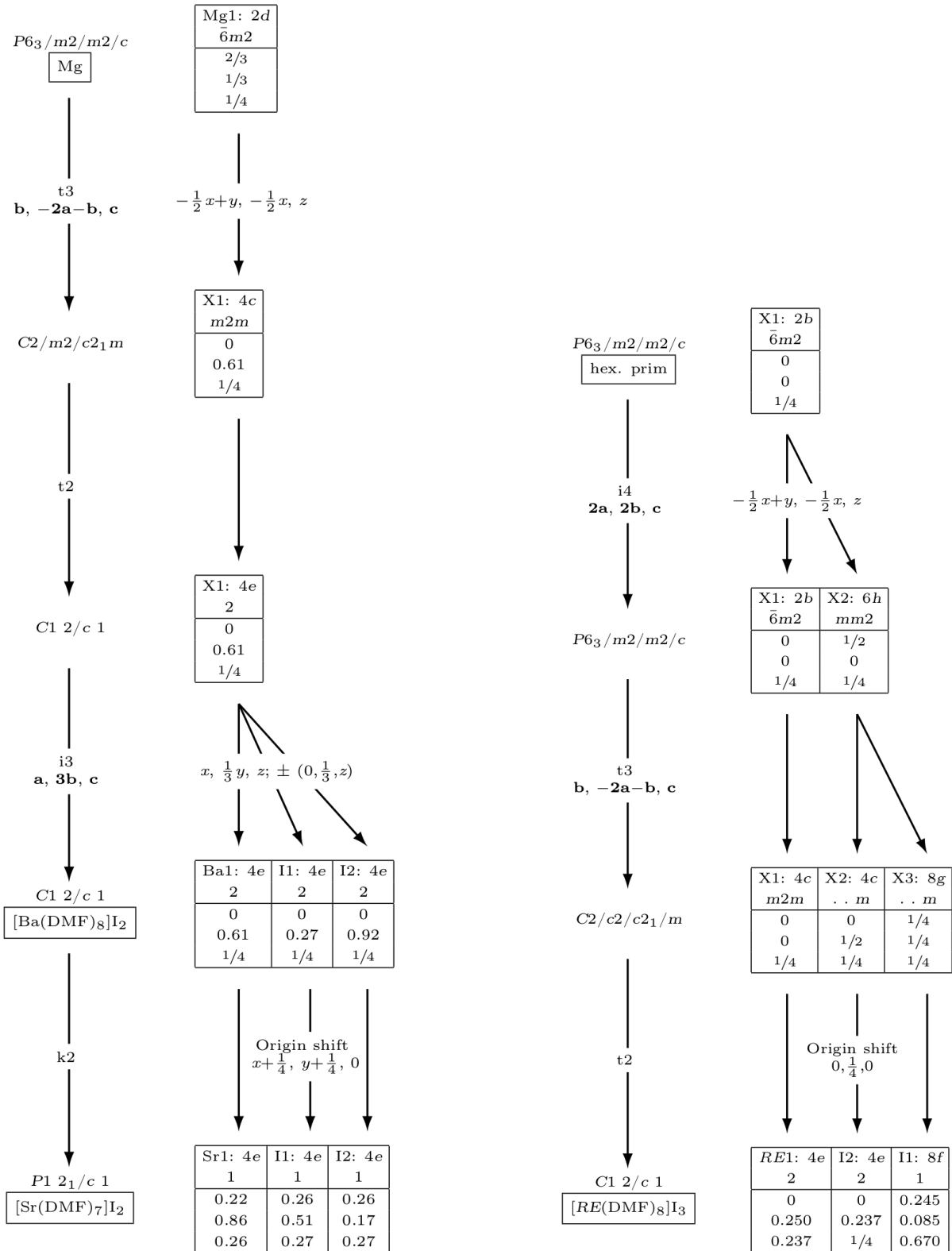


Figure 4.10.: Group-subgroup relation between the Mg structure type, [Ba(DMF)₈]I₂ and [Sr(DMF)₇]I₂ (left) and the hexagonal primitive structure and the [RE(DMF)₈]I₃ structures (RE = Sm, Gd, Er, Yb, right). Values are exemplarily taken from RE = Sm.

Klassengleiche reduction of index 2 including origin shift leads to $P2_1/c$ ($[\text{Sr}(\text{DMF})_7]\text{I}_2$) and thus free x and z coordinates (Sr1, I1 and I2) which differ only little from the ideal value of $1/4$ (see Figure 4.10).

$[\text{RE}(\text{DMF})_8]\text{I}_3$ ($RE = \text{Nd, Sm, Eu, Gd, Er, Yb}$) crystallise as decorated hettotypes of the hexagonal primitive packing, the symmetry relation is depicted in a Bärnighausen tree (figure 4.10 right and Figure 4.11). First, the hexagonal primitive packing is doubled in a and b direction quadrupling the volume and introducing the $6h$ position. A *translationengleiche* reduction of index 3 leads to an orthorhombic C cell and splitting of the $6h$ position into $4c$ and $8g$. $C2/c$ as final space group type is reached by *translationengleiche* reduction (index 2) including an origin shift. Atomic positions vary only little from the ideal starting values.

$[\text{Zn}(\text{DMF})_2]\text{I}_2$ crystallises as decorated hettotype of a hexagonal primitive packing (see Figure 4.13). Centroids of $[\text{Zn}(\text{DMF})_2]\text{I}_2$ molecules form hexagonal layers stacked along the crystallographic b axis in an $-A-B-A-B-$ sequence. The layers are undulated in the b direction, a result of the higher spatial demand of DMF versus iodide. A further representation of the distortion shows in the monoclinic angle of 111.33° .

$[\text{Cd}(\text{DMF})_6][\text{CdI}_4]$ crystallises as complex salt $[\text{CdI}_4]^{2-}[\text{Cd}(\text{DMF})_6]^{2+}$. The packing of $[\text{CdI}_4]^{2-}$ forms the motif of a cubic primitive packing, as does the packing of $[\text{Cd}(\text{DMF})_6]^{2+}$. Both motifs are interpenetrating in a decorated variant of the CsCl structure type. Figure 4.13 (right) shows this relation. Distortions originate from the different spatial requirements of the respective complex ions.

$[\text{Sc}(\text{DMF})_6](\text{I}_3)_3$ does not form a decorated variant of a simple structure. Due to the fact that triiodide ions (I_3^-) are elongated and far from spherical, simple packing is not possible without severe distortions straining the concept applied above too much. The topology of the packing of $[\text{Sc}(\text{DMF})_6]^{3+}$ and I_3^- ions can better be rationalised in another way. I_3^- are oriented almost parallel to one another forming "strings" approximately along the $[10\bar{1}]$ direction. In between the $[\text{Sc}(\text{DMF})_6]^{3+}$ ions are located. The octahedra are also aligned in the $[10\bar{1}]$ direction. Together, both structural units form a tetragonal rod packing (see Figure 4.14).

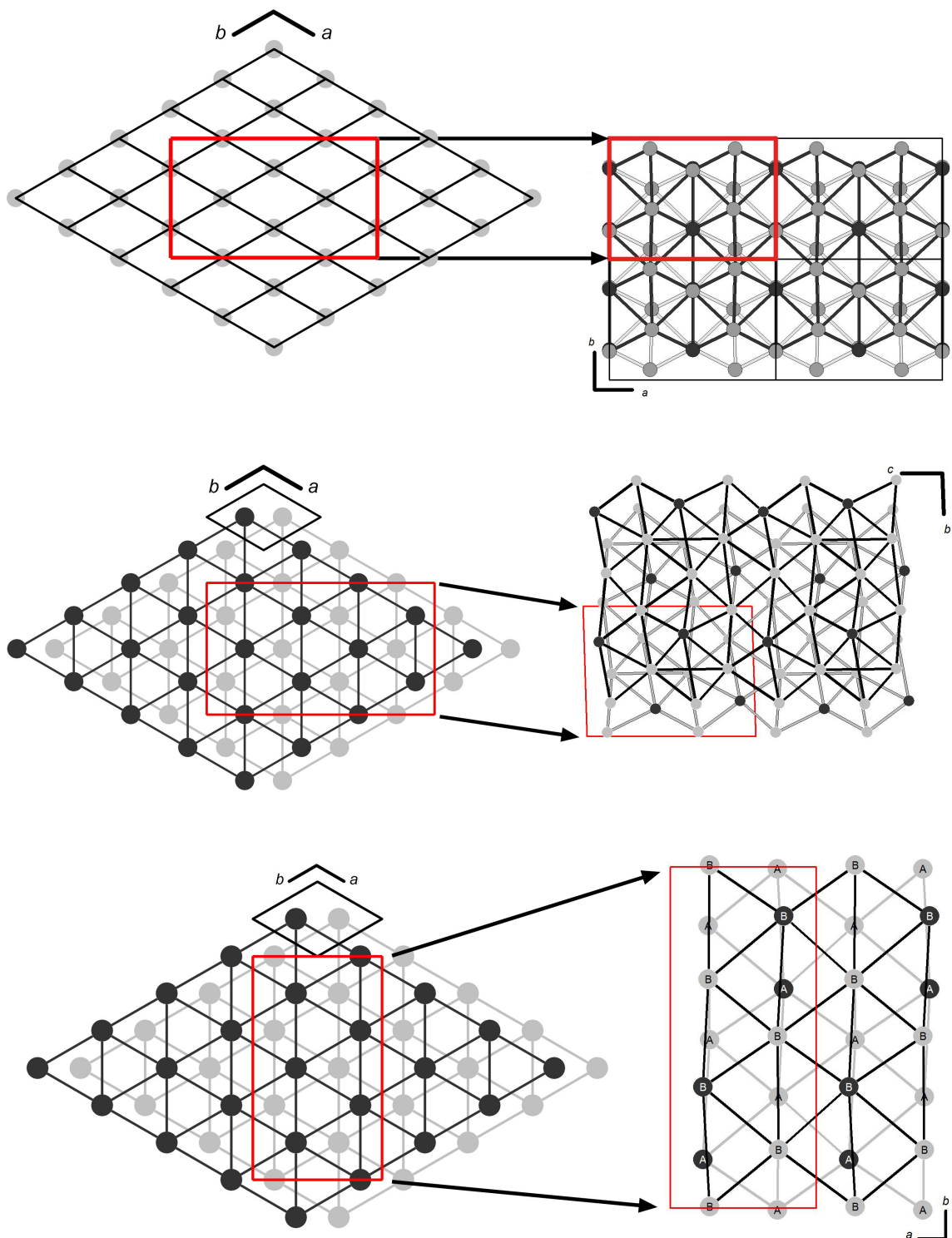


Figure 4.11.: **Top:** Relation between the hexagonal primitive packing (left) and the packing of centroids in $[RE(DMF)_8]I_3$ ($RE = Nd, Sm, Eu, Gd, Er, Yb$; right; dark grey: RE^{3+} , light grey: I^-). **Center:** Relation between the hexagonal closest packing (left) and the packing of centroids in $[La(DMF)_9]I_3$ (right). Dark grey: $[La(DMF)_9]^{3+}$, light grey: I^-). **Bottom:** Relation between a hexagonal closest packing (left) and the packing of centroids in $[Sr(DMF)_7]I_2$ (right). Dark grey: Sr^{2+} , light grey: I^-).

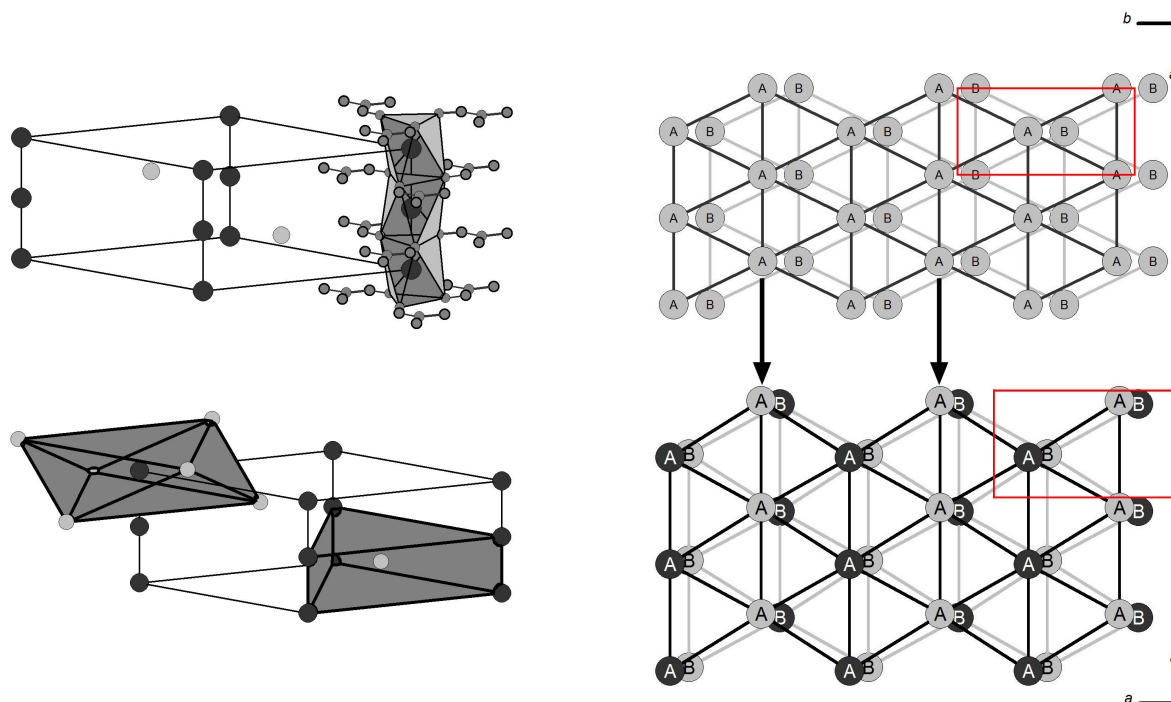


Figure 4.12.: **Top left:** Face-sharing stacking of octahedra around Na in $[\text{Na}(\text{DMF})_3]\text{I}$. **bottom left:** Centroids of $[\text{Na}(\text{DMF})_3]\text{I}$ as NiAs structure type. **Right:** Relation between the α -U structure type (top) and the packing of centroids in $[\text{Li}(\text{DMF})_4]\text{I}$.

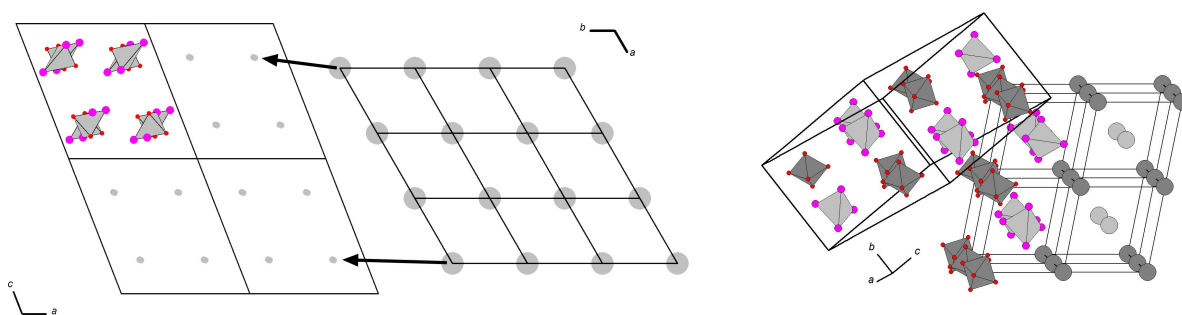


Figure 4.13.: **Left:** Relation between the hexagonal primitive packing and the packing of centroids in $[\text{Zn}(\text{DMF})_2\text{I}_2]$. **Right:** Relation between the CsCl structure type and the packing of centroids in $[\text{Cd}(\text{DMF})_6][\text{CdI}_4]$. Light grey: $[\text{Cd}(\text{DMF})_6]^{2+}$, dark grey: $[\text{CdI}_4]$, magenta: iodide, red: oxygen atom of DMF (omitted for clarity).

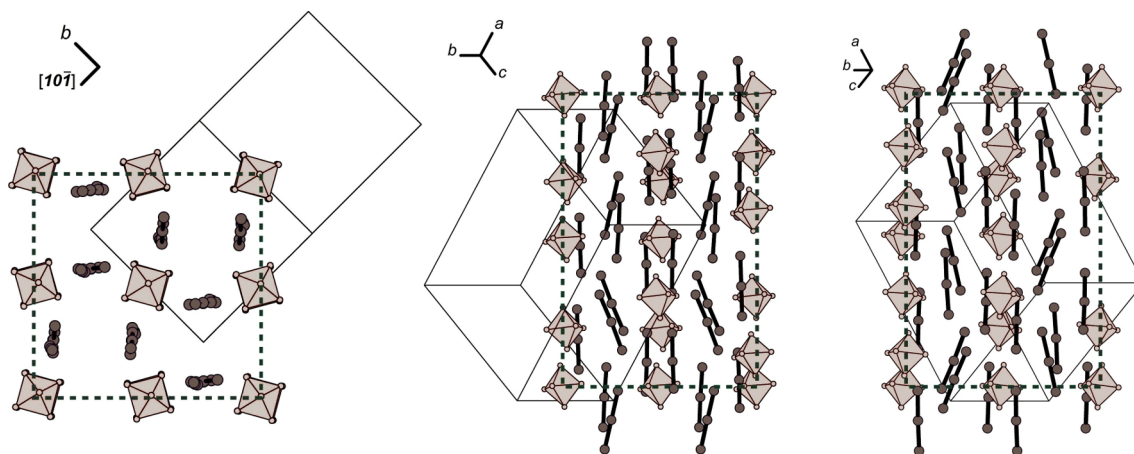


Figure 4.14.: Rod packing of $[\text{Sc}(\text{DMF})_6](\text{I}_3)_3$ along three perpendicular directions. The monoclinic unit cell is shown in black, the unit cell of an idealised tetragonal rod packing in dashed black. Dark grey: Iodine; light grey: polyhedra around Sc.

4.2.2. Amalgams

General aspects of amalgams, crystal structures and phase diagrams

Phase diagrams alkali metal – mercury are characterised by a dystecticum at the composition AHg_2 ($A = Na, K, Rb, Cs$) followed by a steep slope of the liquidus curve towards the melting point of Hg.^[18] In between AHg_2 and liquid Hg only Rb–Hg and Cs–Hg show additional dystectica (at ≈ 80 at% Hg), all other phases decompose peritectically. Generally, formation of mercury-rich amalgams is favourable among heavy alkali metals indicative for the general trend towards increased formation of mercury-rich amalgams with increasing atomic number of the electropositive metal (see Table 1.1). An exception is the Li–Hg system (dystecticum at LiHg), which in general shows different features than the other systems: All three known Li amalgams derive from simple structure types and do not exhibit extended mercury sublattices.^[18] A possible cause are the similar metallic radii of Li (152 pm) and Hg (150 pm), enhancing the formation of close sphere packings with high density. Because of their structural simplicity and their accessibility for NMR studies (7Li , ^{199}Hg), Li amalgams were chosen for the examination and quantification of the electron transfer within a polar metallic bonding, see chapters 3.4.2 and 4.3.2.

Phase diagrams alkaline earth metal – mercury exhibit a dystecticum AHg , followed by a steep slope of the liquidus curve towards the melting point of mercury. Additional dystectica are Mg_2Hg , AHg_2 ($AE = Ca, Sr, Ba$) and Ba_7Hg_{31} (formerly noted as $BaHg_4$ ^[18]), all other phases decompose peritectically. The obvious trend is alike to the alkali metal amalgams: Heavier alkaline earth metals tend to form mercury-rich amalgams whereas light alkaline earth metal amalgams form mercury-poor amalgams (see Table 1.2). Mercury-rich amalgams usually show peritectic behaviour. Up to now there are no amalgams known of the lightest alkaline earth metal Be and solubilities of the elements are very low, indicating very small interactions.^[18]

Phase diagrams rare earth metal – mercury are mostly speculative, no full evaluation of any system has been performed.^[38–52] An overview of known and assumed crystal structures and thermochemical analyses is given in Table 1.3. All rare earth metals form amalgams $REHg$ and $REHg_3$, most of the latter have been prepared in this thesis. In addition, most RE metals form amalgams $REHg_2$, with the exception of Sc, Tm and Lu. Thermoanalytical studies were also carried out with the educt composition $REHg_4$,^[53] the values reported most likely point towards the respective $RE_{11}Hg_{45}$ compounds. Amalgams previously reported with compositions " $REHg_{6.5}$ " were found to have general sum formula $RE_{11-x}Hg_{55+x}$ and were observed for $RE = Eu, Yb$. For $RE = La-Nd$ and Tb, no evidence for those structures have been found, thermoanalytical data might again refer to $RE_{11}Hg_{45}$ compounds.

A trend in most A –Hg systems ($A =$ alkali, alkaline earth and rare earth metals except Li, Be and Mg) is the tendency to form small or extended, negatively polarised mercury sublattices $[Hg_x]^{\delta-}$. The degree of condensation is roughly a function of mercury content with few exceptions. As a general rule mercury-rich compounds form more complex structures as indicated by complexity measures (see below). Coordination numbers

of the electropositive metals are frequently high, e.g. CN=16 (Frank-Kasper, capped augmented tetrahedron, reoccurring structural feature), CN=20 (BaHg₁₁) and CN=32 (surrounding the "extended metal" Mg(NH₃)₆ in Mg(NH₃)₆Hg₂₂).^[54]

REHg₂ amalgams: SmHg₂

SmHg₂ was synthesised by distillation (see chapter 3.3.5). It crystallises in the AlB₂ structure type (*P6/mmm*) and thus differs from the reported structure (CeCd₂ structure type, *P3̄m1*).^[55] Both models show sixfold rings of Hg stacked along *c* (see Figure 4.15). In *P6/mmm* the Sm atoms are located between two sheets of Hg, in *P3̄m1* the Sm atoms center Hg hexagons. In the latter structure the Hg sheets are slightly puckered.

Other REHg₂ phases (*RE* = Dy, Ho, Er) were reported to crystallise with the AlB₂ structure type, too.^[56] In this case, the compounds were synthesised in vacuum, whereas SmHg₂ was synthesised in an argon atmosphere. No publication lists the exact temperatures or pressures applied. However, it can be assumed that two modifications for SmHg₂ exist, formation seems to be dependent on synthesis conditions, especially temperature and pressure.

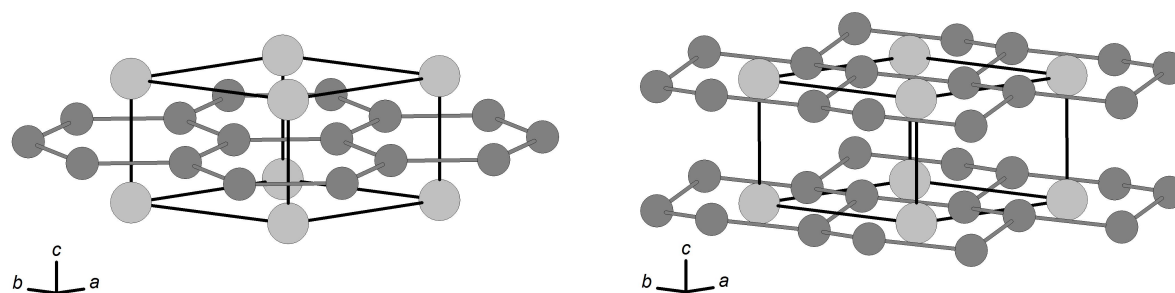


Figure 4.15.: Comparison of the two structure models for SmHg₂. **Left:** Structure as refined in this work (*P6/mmm*); **Right:** Structure model from literature (*P3̄m1*).^[55]

REHg₃ amalgams

The 1:3 compounds of *RE* with Hg (*RE* = rare earth metal) were first synthesised in 1963.^[56–58] The crystal structures were assigned to the Ni₃Sn structure type on the basis of powder diffraction patterns. No single crystal or Rietveld refinements were performed. In this work the 1:3 crystal structures of *RE* with Hg (*RE* = Sc, Y, La, Gd, Dy, Ho, Er, Tm, Yb, Lu) were reproduced and analysed by Rietveld refinement, for details see chapter 3.3.5. All refinements show good agreement with lattice parameters from literature.^[56–58]

All rare earth metals form compounds REHg₃ (Ni₃Sn structure type).^[38–52] From La to Lu the lattice parameters decrease in accordance with the lanthanide contraction. Eu and Yb differ significantly from the trend indicating the RE²⁺ oxidation state rather than RE³⁺ observed for the rest of the lanthanides. Mössbauer measurements on EuHg,

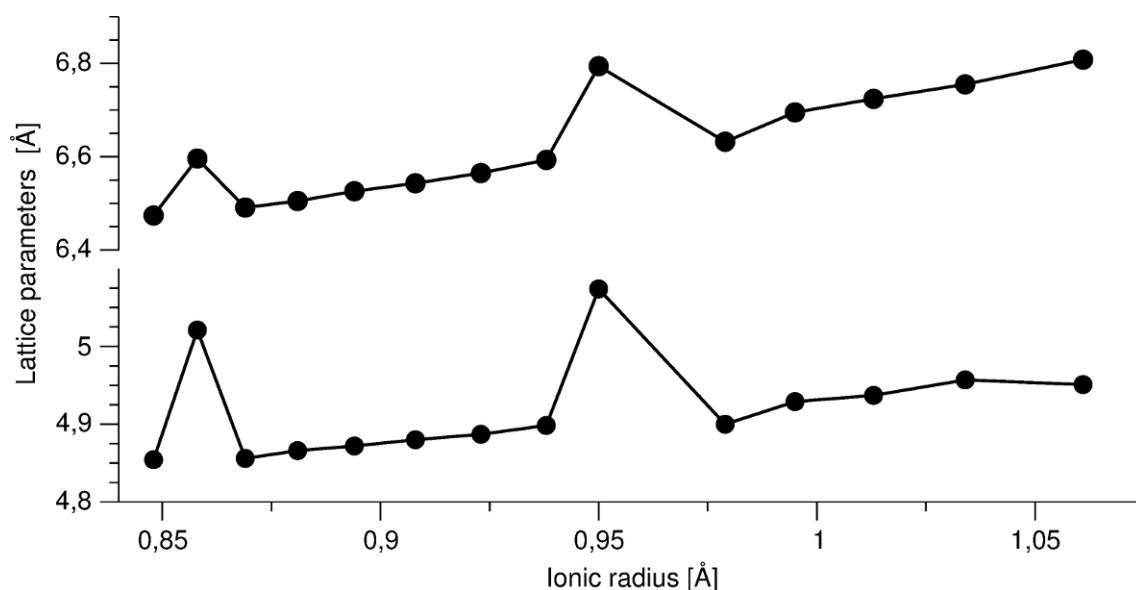


Figure 4.16.: Relation between lattice parameters (top: a , bottom: c) of $REHg_3$ and the respective ionic radii of the trivalent ions. Yb and Eu show large deviations and support the assumption of predominantly divalent species in the amalgams.

$EuHg_2$ and $EuHg_3$ confirmed oxidation state +2 for Eu in each compound, corroborating the observed trend.^[58,59]

Further mercury-rich amalgams of rare earth and alkaline earth metals

Some mercury-rich amalgams of rare earth metals form structures $A_{11-x}Hg_{55+x}$ and $A_{11}Hg_{45+x}$, the former are also observed for the alkaline earth metals Ca and Sr.^[60] Ca, Sr, Eu and Yb readily exhibit oxidation state +2, other rare earth metals do not, as can be seen from atomic radii and molar volumes of the elements. Sm and Tm also exhibit 2+ valence states, albeit at larger standard potentials (Sm: -1.55 V, Tm: -2.3 V) and show no pronounced differences in atomic radii and molar volumes. It seems that formation of $RE_{11-x}Hg_{55+x}$ depends on bivalency and might have electronic reasons. However, up to now quantum mechanical calculations cannot account for numerous mixed occupancies of the crystal structures or exact modelling of the f -electrons within reasonable computational time.

A way of rationalising the occurrence of mercury-rich amalgam structures is illustrated in Figure 4.17. Metallic radii are plotted against atomic number in a structure field diagram. The lower part (brown) contains elements forming amalgams $A_{11}Hg_{45+x}$ including all rare earth metals with exception Eu and Yb. The green part contains elements forming amalgams $A_{11-x}Hg_{55+x}$, notably Na, Eu, Yb, Ca and Sr. Coincidentally, and in accordance with the description above, mostly bivalent elements are found here with the exception of Na. As $Na_{11}Hg_{52}$ shows a very complex crystal structure (large unit cell, low symmetry, mixed positions) it might be seen as lower boundary of ionic radius. Sr clearly is the upper perimeter, showing formation of $A_{11-x}Hg_{55+x}$ alongside with AHg_{11} (blue field). Elements with highest radii form AHg_{11} (except Cs). Cs with highest atomic radius forms the unique Cs_2Hg_{27} structure, the Hg-richest of all known amalgams.

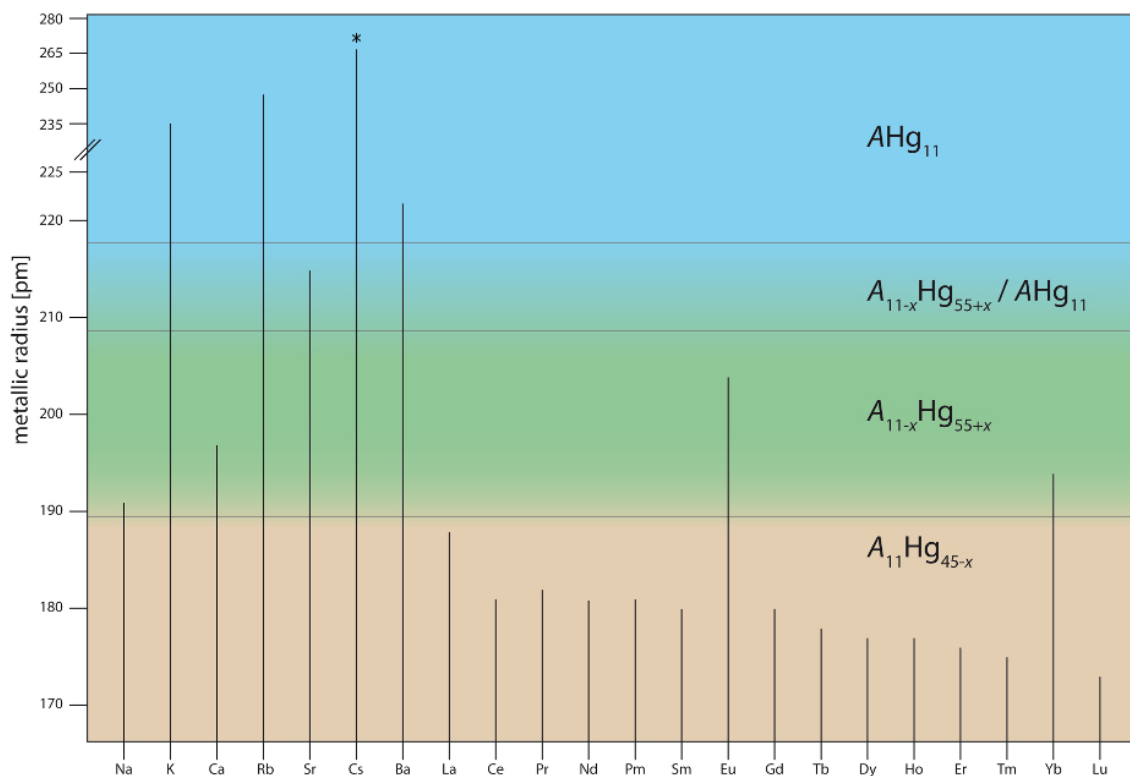


Figure 4.17.: Structure-field diagram for mercury-rich amalgams AHg_{11} , $A_{11-x}Hg_{55+x}$ and $A_{11}Hg_{45+x}$. *: Cs forms an amalgam Cs_2Hg_{27} .^[14]

The crystal structures of $A_{11-x}Hg_{55+x}$ ($A = Na, Eu, Yb, Ca, Sr$) can be derived from the $Gd_{14}Ag_{51}$ aristotype by lowering the symmetry (from $P6/m$ to $P\bar{6}$) and introducing several disorder phenomena (see chapter 3.3.2). Only Yb shows no disorder phenomena, all atomic positions are fully occupied by one element (see chapter 3.3.4). In $Ca_{11-x}Hg_{55+x}$ and $Sr_{11-x}Hg_{55+x}$, the position centring the Frank-Kasper polyhedron is of mixed occupancy. In addition to that, $Eu_{10}Hg_{55}$ shows a Hg chain along the crystallographic c axis with constrained underoccupation (see chapter 3.3.1). The crystal structure of $Na_{11}Hg_{52}$ is the most complex. It crystallises in a $3 \times 3 \times 1$ superstructure of $Gd_{14}Ag_{51}$ with 132 crystallographically independent positions, one of which shows mixed occupancy.

Complexity measures (see chapter 4.2) for the compounds $A_{11-x}Hg_{55+x}$ ($A = Na, Eu, Yb, Ca, Sr$) are compiled in Table 4.3. The aristotype crystallises with higher symmetry and thus is significantly less complex than the other compounds. Amalgams of Yb, Ca/Sr and Eu crystallise with lower symmetry and thus higher complexity than $Gd_{14}Ag_{51}$. Despite the differences of their crystal structures and the numerous disorder phenomena, their complexities lie in the same order of magnitude (250–275). Next higher in symmetry is a (not yet fully characterised) Na–K amalgam with an estimated complexity of ~ 1000 . Due to its $2 \times 2 \times 1$ superstructure (in comparison to $Gd_{14}Ag_{51}$), its unit cell content is quadrupled and so is the information content. Highest in complexity is $Na_{11}Hg_{52}$ with a value close to ~ 4000 which is considerably larger than expected even for the $3 \times 3 \times 1$ supercell with ninefold unit cell content. The difference can be explained by increased value of IG, the information content of each atomic position. Due to its large unit cell and low symmetry, each atom can account for more information which then translates

Table 4.3.: Complexity values for compounds derived from the $\text{Gd}_{14}\text{Ag}_{51}$ and the $\text{La}_{11}\text{Hg}_{45}$ family. IG is the bit per atom, IG_{Bits} the total information content of the unit cell, IG_n the normalised information content.

Compound	SG	IG	IG_{Bits}	IG_n
$\text{Gd}_{14}\text{Ag}_{51}$ ^[61]	$P6/m$	3.101	210.850	0.509
$\text{Yb}_{11}\text{Hg}_{54}$	$P\bar{6}$	3.986	259.111	0.662
$\text{Ca}_{11}\text{Hg}_{54}$ ^[60]	$P\bar{6}$	4.141	269.156	0.640
$\text{Eu}_{10}\text{Hg}_{55}$ ^[62]	$P\bar{6}$	4.233	275.159	0.703
Na-K-Hg	$P\bar{6}$	5.466	1197	0.703
$\text{Na}_{11}\text{Hg}_{52}$ ^[16]	$P\bar{6}$	6.942	3936.056	0.759
$\text{La}_{11}\text{Hg}_{45}$	$F\bar{4}3m$	3.797	425.287	0.558
$\text{Nd}_{11}\text{Hg}_{44.5}$	$F\bar{4}3m$	3.757	417.043	0.553
$\text{Sm}_{11}\text{Hg}_{44.5}$	$F\bar{4}3m$	3.757	417.043	0.553

onto the value of IG_{Bits} . It is noteworthy that $\text{Na}_{11}\text{Hg}_{52}$ is the most complex binary inorganic compound known so far.^[63,64]

Classification of KHg_6

Particularly the K–Hg system shows a great variety of mercury-rich amalgams with a striking lack of mercury-poor amalgams beyond KHg . In contrast to various Na-rich amalgams, formation of isolated $\text{Hg}^{\delta-}$ atoms is disfavoured, a trend that inflicts the heavier Rb–Hg and Cs–Hg systems, too. In this work KHg_6 was synthesised and its crystal structure and physical properties discussed (see chapter 3.4.1). A revised phase diagram is proposed, see Figure 4.18. Green phases are newly assigned from literature data: K_2Hg_7 together with K_3Hg_{11} (formerly KHg_3) and K_7Hg_{31} (formerly KHg_4). KHg_6 was synthesised in this work and is shown in red.

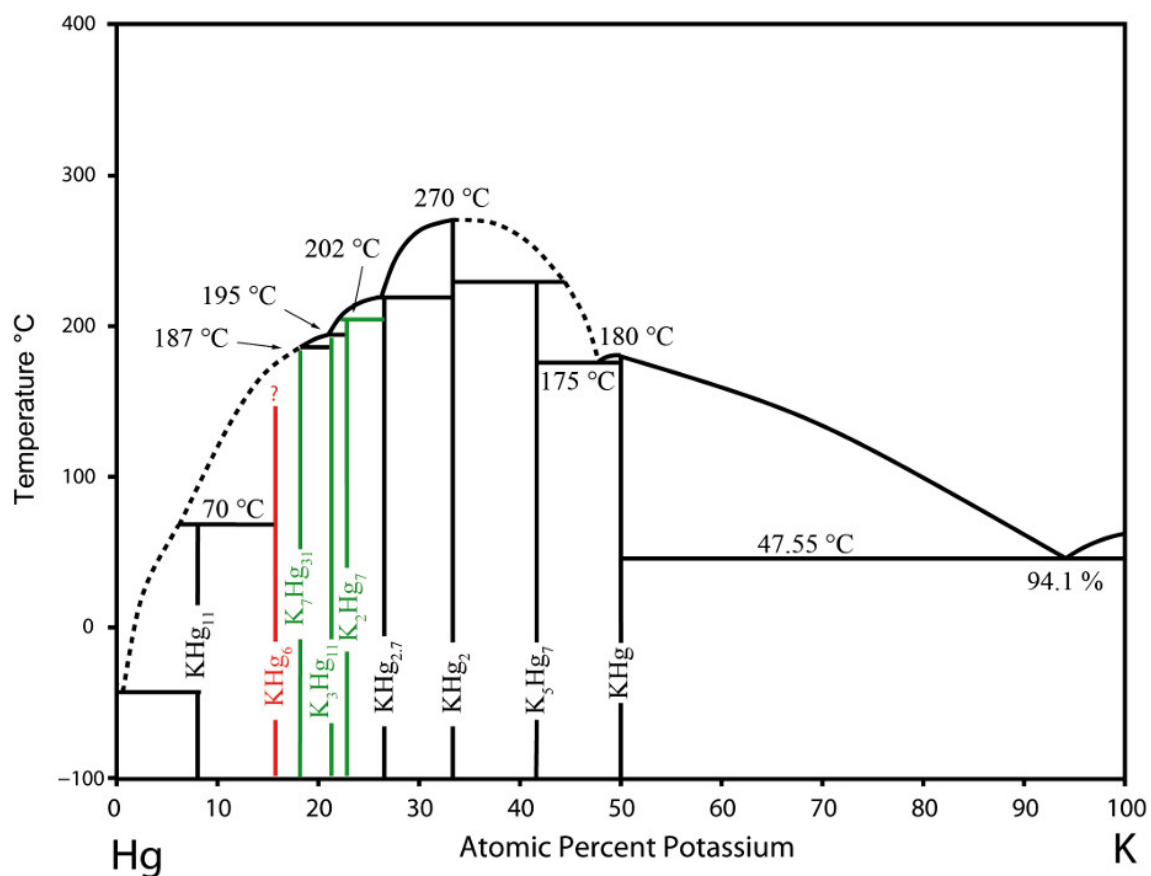


Figure 4.18.: Revised phase diagram for K–Hg. The original phase diagram was taken from Massalski.^[18] Green phases are newly assigned from literature data, the red phase (KHg₆) was synthesised in this work.

4.3. Polar Intermetallics – Aspects of Chemical Bonding

4.3.1. What is a Polar Metal?

In this work the term "polar metal" is used to describe the gradual transition from a metallic bond to an ionic bond, equivalent to the "polar covalent bond" in between covalent and ionic bonding (see chapter 1.3)

Essential for the formation of a polar metallic bond in the sense of a gradual transition from a metallic bond to an ionic bond is the interplay of a high electronegativity difference (ΔEN) of the electropositive partner combined with a high (endothermic) electron affinity (EA) of the noble partner. In general, there are two extremes which do not result in a polarised metal-metal bonding: 1) If ΔEN is too low, typical intermetallic phases without pronounced electron transfer will form. The structures are mostly dominated by dense packing of atoms, e.g. Hume-Rothery and Frank-Kasper phases, their properties are typically good ductility, opacity and high metallic conductivity. 2) If ΔEN is high and the noble element has a negative (exothermic) electron affinity, Zintl phases will form. They can be rationalised to a great extent with ionic binding concepts and are usually brittle, transparent, semiconducting and dissolve in polar aprotic solvents.

A "polar metallic bonding" forms if ΔEN is high enough for a considerable electron transfer from the less electronegative to the noble metal, combined with a positive electron affinity of the latter. This does not result in the formation of distinct Zintl anions (which in this case are thermodynamically unstable) but in the formation of extended, negatively polarised networks with embedded cations of the less noble metal. The only noble metal with a positive electron affinity is Hg ($E^\circ = +0.8$ V, EA = 1.45 V)^[17] and thus amalgams of less noble metals with high Hg content often show metallic conductivity with comparably high resistances and Ioffe-Regel saturation of the specific resistance at low temperatures. Strong scattering of conduction electrons at the periodic Coulomb potentials lead to typical "bad metal" behaviour.

Another definition of "polar metals" comes from the combination of ionic and metallic motifs in the sense of a "chemical twin". In this case a composite structure of ionic oxo(nitrido)metallate ions and excerpts of metal structures is formed, combining properties of classical salts and metals.^[65]

4.3.2. Polarity in Amalgams

Structural differences as the result of increasing Hg content lead to severe changes in the band structures of the amalgams (see chapter 1.3 and Figure 4.19). Hg-poor amalgams show isolated Hg atoms, Hg states are localised without strong Hg–Hg interactions. If small Hg clusters form (squares, cubes) observed bond angles are about 90° , indicating mainly σ_p binding interactions.

Increasing Hg content leads to involvement of Hg6s states into the chemical bonding and thus to dispersion of the respective states. If more Hg–Hg contacts form, Hg5d states show increasing dispersion, too. For amalgams crystallising in CsCl structure type it is

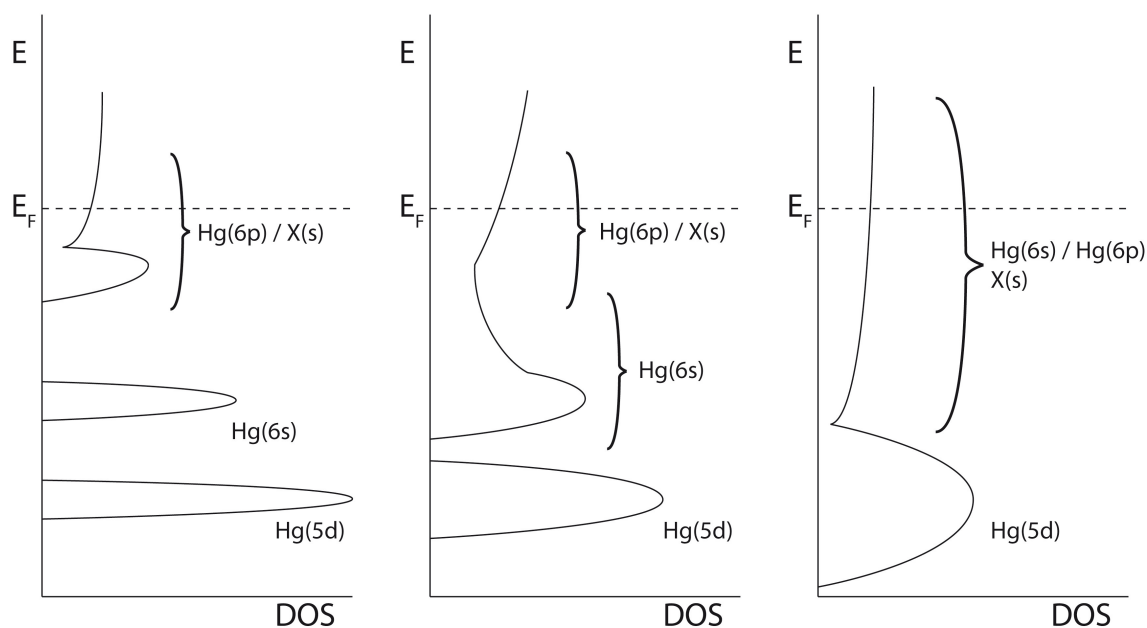


Figure 4.19.: Schematic view of the trend of the DOS with increasing Hg content (from left to right). Hg-poor amalgams show strong localisation of low lying states which broaden with increasing Hg content. X = Alkali metal.

possible that the interlaced $X^+ [Hg_8]^{δ-}$ motifs lead to strong coulomb interactions. High melting points of XHg phases are the result, supporting this assumption.

A further increase in Hg content leads to formation of negatively polarised mercury frameworks and to increasing dispersion of Hg5d states and an increasing mixing of Hg6s and Hg6p states. The change in respective orbital (band) energies, similar to a molecular orbital diagram, was verified by NMR and band structure investigations of simple Li amalgams, which is the topic of the following chapter 4.3.2.

Quantification of polarity in Li Amalgams

The elements Li and Hg have NMR-active nuclei: ${}^6\text{Li}$, ($I = 1$, natural abundance 7.42%); ${}^7\text{Li}$ ($I = \frac{3}{2}$, natural abundance 92.58%); ${}^{199}\text{Hg}$ ($I = \frac{1}{2}$, natural abundance 16.84%) and ${}^{201}\text{Hg}$ ($I = \frac{3}{2}$, natural abundance 13.22%).^[66] Exhibiting a receptivity greater than five times that of ${}^{13}\text{C}$, ${}^{199}\text{Hg}$ has great potential for NMR studies.^[66] In this chapter we show that NMR studies can, to an extent, provide an experimental quantification of electron transfer in a polar metallic bond by comparison of Knight shift measurements.

Here, the assessment of electron correlations in bad metals is discussed. The understanding of this substance class heavily relies on the degree of polarity and thus on the degree of electron transfer between Li and Hg which can directly be monitored by NMR. Nuclear magnetic resonance for both ${}^{199}\text{Hg}$ and ${}^7\text{Li}$ show a distinct trend: With increasing mercury content, the Li signal shifts to lower ppm values, whereas the Hg signal shifts to higher ppm values. The valence electron densities for Li and Hg can be evaluated by band structure calculations and subsequently compared to the NMR results.

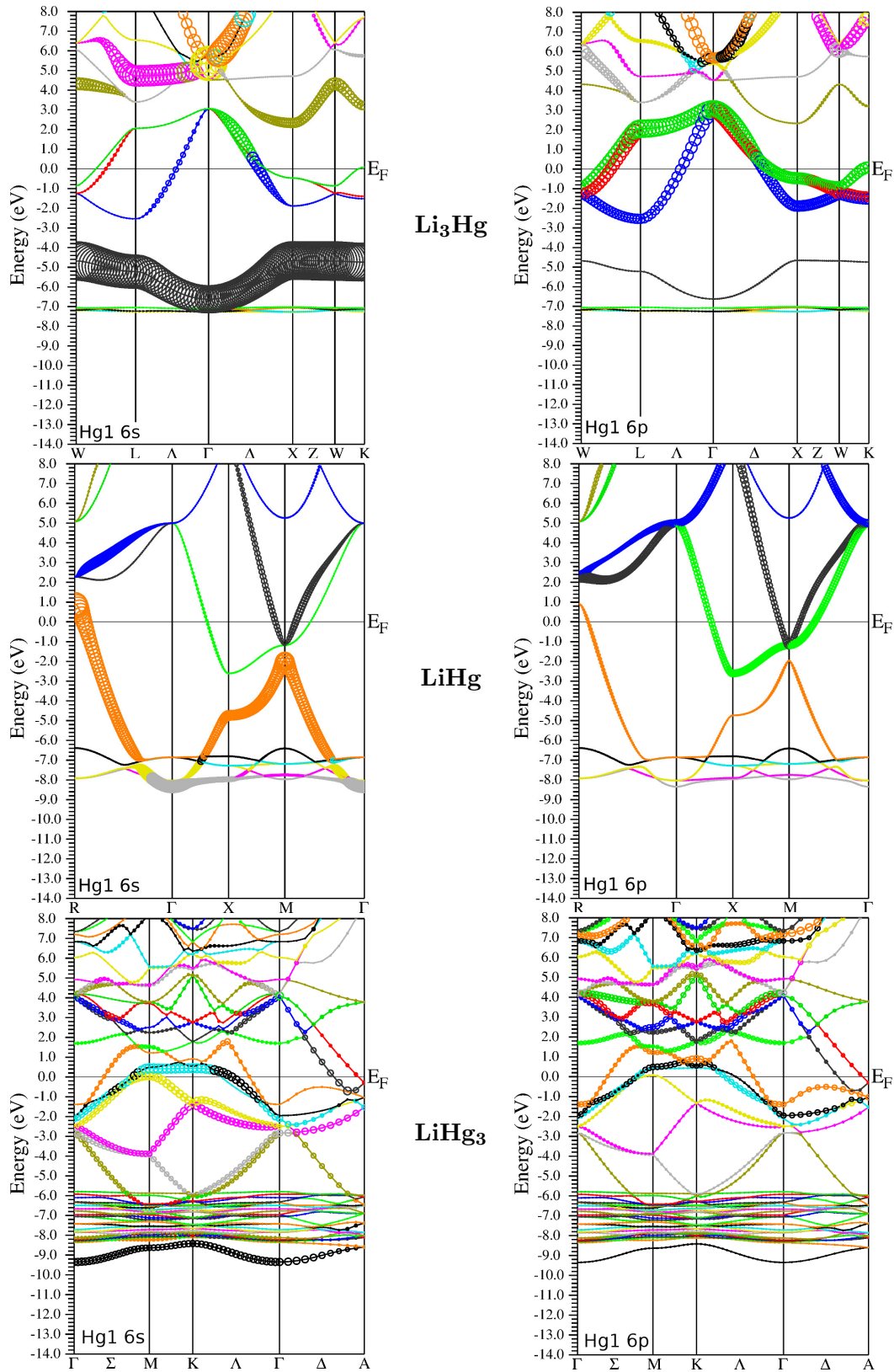


Figure 4.20.: Fat-band plots of the three Li amalgams Li_3Hg , LiHg and LiHg_3 . **Left:** emphasis on Hg6s bands, **right:** emphasis on Hg6p bands.

The total density of states (tDOS) and partial densities of states (pDOS) for the Li amalgams were calculated (see Figure 4.21) in the range of -10 to $+2$ eV, relative to Fermi level. In addition, band structures for the Li amalgams were calculated (see Figure 4.20) and plotted in fat-band mode with emphasis either on Hg6s bands or Hg6p bands. All three compounds are metals, but the electronic structures differ significantly indicating changes in the chemical bonding situations from Hg-poor to Hg-rich compound (Li_3Hg vs. LiHg_3).

Li₃Hg: The band structure of Li_3Hg exhibits a narrow band of Hg5d states from -7 to -7.5 eV, between -4.5 and -6.5 eV, Hg6s states occur. From -2.5 to -4.5 eV a band gap is located. Above the gap, from the Fermi level to -2.5 eV, Hg6p and Li2s states dominate the tDOS. In accordance to the low electron transfer from Li to Hg (in the case of full electron transfer three electrons from Li would have to be transferred to Hg), the partial density of states (pDOS) for Li contributes considerably to the total DOS at Fermi level. The two crystallographically different Li sites do not differ with respect to their electron transfer ability and give only one signal in the NMR spectrum (203.2 ppm, see Figure 3.25). As can be seen from the fat-band plots

(see Figure 4.20, top), Hg6s states are low in energy and clearly separated from Hg6p states, in accordance with the scheme shown in Figure 4.19. In first approximation, only s electrons contribute to the Knight shift and thus only a small shift is observed for ^{199}Hg in Li_3Hg (1680 ppm). Li_3Hg shows low polarity in terms of small δ in $[\text{Li}^{\delta+}]_3[\text{Hg}^{\delta-}]$.

LiHg: In LiHg , Hg5d states are located in the range of -6 to -8 eV. Compared against Li_3Hg they are broadened, indicating stronger Hg-Hg interactions than in Li_3Hg . Closure of the band gap through mixing of Hg6s and d states occurs. Fat band plots (see Figure 4.20, middle) show considerable broadening of Hg6s states and mixing with Hg5d states at low energies. Hg6s states are no longer only located at low energies but spread to Fermi level. The separation of Hg6s and Hg6p states is no longer as clear as in Li_3Hg , significant mixing is observed. Hg6s electron density at Fermi level is higher than in Li_3Hg which can be observed in a Knight shift of 4500 ppm (see Figure 3.25). Hg states dominate the total DOS, and distinct features from the Li states hardly can be observed. The Li-pDOS shows a decrease of the density of Li2s electrons at Fermi level and results in a lower Knight shift for ^7Li (101.7 ppm). Thus, electron transfer from Li is increased in comparison to Li_3Hg with a higher δ in $[\text{Li}^{\delta+}][\text{Hg}^{\delta-}]$.

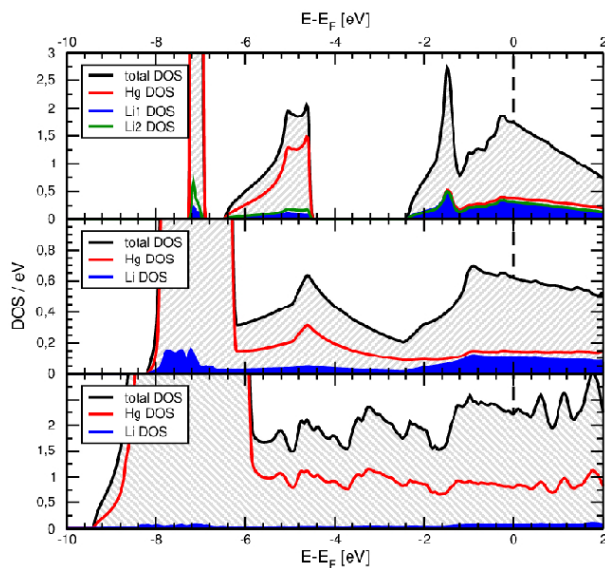


Figure 4.21.: tDOS and pDOS for Li_3Hg (top), LiHg (centre) and LiHg_3 (bottom).

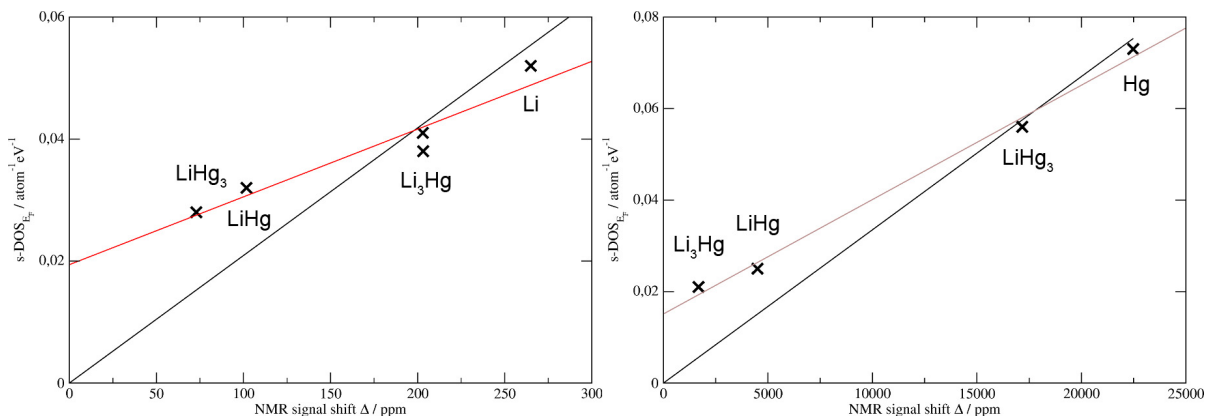


Figure 4.22.: Partial electronic density of states of the s -like electrons at the Fermi level (s -DOS(EF)) versus NMR signal shift of the Li (left) and Hg (right) atoms. In both cases, the solid black lines represent the linear dependency expected for the correlation of s -electron density and the Knight shift. Colored lines show the regression.

LiHg₃: This compound exhibits a DOS typical for Hg-rich amalgams. Low in energy, between -6 and -9.5 eV, broad Hg5d states indicate strong binding interactions between Hg atoms. The strength of the interaction is also visible in strong mixing of Hg6s and Hg6p states, resulting in broad diffuse states between -6 eV

and Fermi level. Fat band plots (see Figure 4.21, bottom) also show very strong mixing of Hg6s and Hg6p states with a very high density of Hg6s states at Fermi level (especially between M and K point, see Figure 4.20). This leads to a high Knight shift for ^{199}Hg (17172 ppm). The electron transfer from the Li atom to three Hg atoms is near-complete but some contribution of Li2s states to the total DOS at Fermi level remain, resulting in a Knight shift of 72.9 ppm for ^7Li (see figure 3.25. This indicates a considerable but incomplete electron transfer in the sense of highly polarised metal-metal bonding (high δ in $[\text{Li}^{\delta+}][\text{Hg}^{\delta-}]_3$).

Table 4.4.: pDOS values at Fermi level for s and p bands as a result of band structure calculations.

Compound	Li s -DOS	Hg s -DOS	Hg p -DOS
Li	0.052	—	—
Li ₃ Hg	0.041 / 0.038	0.021	0.198
LiHg	0.032	0.025	0.119
LiHg ₃	0.028	0.056	0.077
Hg	—	0.073	0.028

The correlation between NMR shift and pDOS is shown in Figures 4.22 and 4.23. The density of Li2s states is non-zero at the atomic core site. These electrons contribute more to the Knight shift than p or d conduction electrons.^[67,68] As a consequence, the Knight shift is in a first approximation proportional to the partial s electron density at Fermi level.^[69] In Figure 4.22 the observed correlation of the s DOS at Fermi level with the NMR shift is shown. For ^7Li measurements, elemental Li has the highest shift and thus the highest s electron density at Fermi level. With increasing Hg content, Li transfers its electron with increased efficiency in the series Li₃Hg–LiHg–LiHg₃, resulting in the lowest shift (72 ppm) for LiHg₃, indicating the "most positive" $\text{Li}^{\delta+}$.

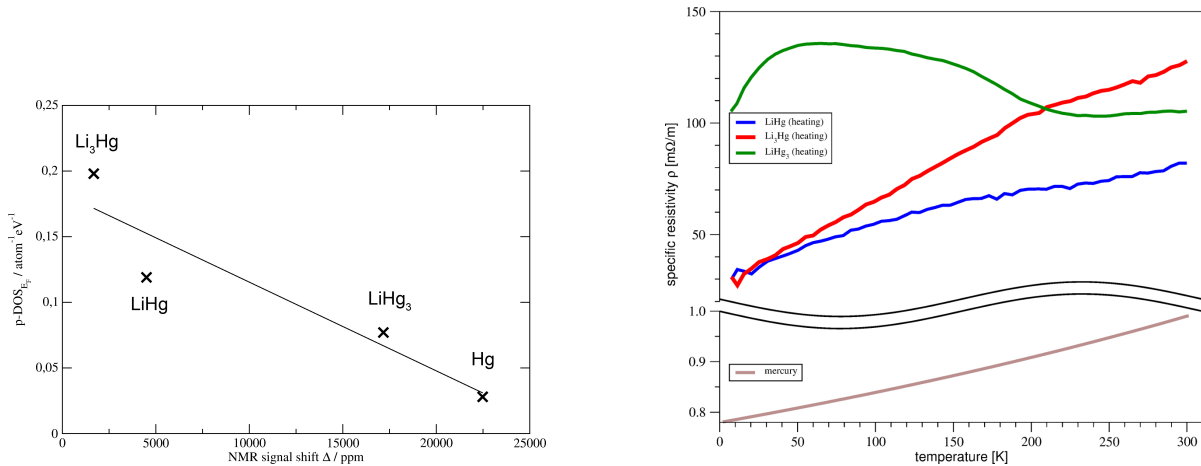


Figure 4.23.: **Left:** Partial electronic density of states of p electrons at the Fermi level ($p\text{-DOS}(E_F)$) versus NMR signal shift of the Hg atoms. Solid black line represents linear regression. **Right:** Measured specific resistances for the three Li amalgams and for mercury in comparison.

A complementary trend is observed for ^{199}Hg measurements. Elemental Hg shows the highest shift (22480 ppm) and thus the highest s electron density at Fermi level. With increasing Li content, more and more "electron pressure" is put on Hg resulting in a lower shift in the series $\text{LiHg}_3\text{--LiHg--Li}_3\text{Hg}$. However, this cannot solely be attributed to different δ in $[\text{Hg}^{\delta-}]$. It is rather illustrating the shift in the energies of the $\text{Hg}6s$ and $\text{Hg}6p$ bands and their mixing. Amalgams with low Hg content generally show little interaction of the Hg atoms and thus s and p states are separated and localised with small dispersions. As the Hg content increases, interactions become stronger and dispersion of bands is observed. Mixing of $\text{Hg}6s$ and $\text{Hg}6p$ as well as broadening of those states are the result. The increasing pDOS of $\text{Hg}6s$ electrons at Fermi level can directly be observed by Knight shift measurements and supports the results from band structure calculations. Similarly, the partial density of states of the $\text{Hg}6p$ states at Fermi level decreases in the series $\text{Li}_3\text{Hg--LiHg--LiHg}_3$ (see Figure 4.23). This also is directly correlated to a higher mixing of $\text{Hg}6s$ and $\text{Hg}6p$ with increasing Hg content.

The observed scattering of the data points relates to the fact that the NMR signal shift is not only dependent on the s DOS. For a full description, chemical shielding and other effects would also have to be taken into account. However, with the methods available today this is not viable for the systems in question. Elements up to atomic number 55 (Cs) have been examined and require the use of extensive k -meshes ($\approx 2 \times 10^6$ k -points in the BZ).^[70]

The following conclusion can be drawn: LiHg_3 shows the highest electron transfer *per Li atom*. This may be seen as the "most polar" of the Li amalgams. Li_3Hg shows the least electron transfer *per Li atom*. This may be seen as the "least polar" of the Li amalgams. However, as Knight shift measurements only correlate with s electron density at Fermi level, and Hg has significant amount of p electron density at Fermi level, too, no such conclusions can be drawn for the total electron count on the Hg atoms. The assignment of highest and lowest polarity is strongly corroborated by measurements of specific electric conductance, see Figure 4.23.

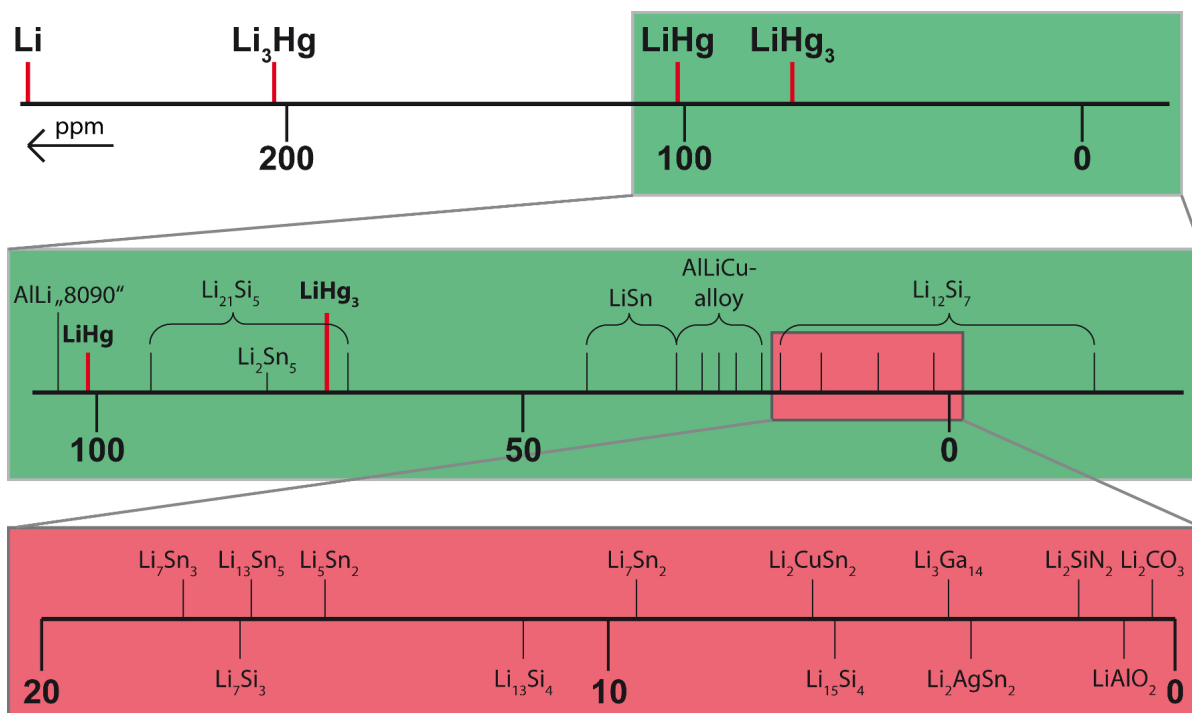


Figure 4.24.: ${}^7\text{Li}$ NMR shifts of selected metallic, semiconducting and ionic (incl. Zintl phases) Li compounds. Data acquired in this work is indicated by red lines. The scheme shows accumulation of shifts in the ionic bonding realm near 0 ppm. Semiconducting and metallic behaviour is observed above ≈ 5 ppm with the exception of Zintl phases up to ≈ 94 ppm. References can be found in Table 4.5.

A broader context for the Li signals of the amalgams is shown in Figure 4.24. The Figure shows signals for ${}^7\text{Li}$ as reported in literature (see Table 4.5) and also the signals of three lithium amalgams. The latter are equally spread with equal distribution, indicating pronounced differences in their electronic states.

Highest Knight shifts are observed for elemental Li and Li_3Hg . In the immediate vicinity, no compounds are located, closest is the AlLi 8090 alloy next to LiHg. Between LiHg and LiHg_3 two compounds are located: $\text{Li}_{21}\text{Si}_5$ and Li_2Sn_5 . $\text{Li}_{21}\text{Si}_5$ exhibits Zintl phase characteristics as well as Hume-Rothery phase characteristics, indicative for a non-classical Zintl phase.^[79] In contrast, Li_2Sn_5 was reported to be of metallic lustre and to deform rather than break under pressure thus exhibiting mostly metallic features. LiHg_3 shows metallic characteristics, too (metallic lustre, opacity) but conductance measurements show no linear dependence of the resistance with temperature as would be expected for classical metals. While showing signals in similar regions of the ppm scale, lithium amalgams, silicides and stannides behave differently, mainly due to different electron affinities of the binding partner and due to different Li to Hg/Sn/Si ratios.

Between 0 and 50 ppm, the majority of reported Li compounds are located. The closer the NMR signal is to 0 ppm, the "more ionic" the lithium compound is with Li_2CO_3 as example for a highly ionic compound. Generally speaking, the closer the signal is to 0 ppm, the more influence the chemical environment – that is the chemical shift – has and the higher the shift the more contributions originate from the Knight shift.

Table 4.5.: Chemical shift of the various Li compounds used in the Li ppm scale.

Sum formula	Li Wyckoff number	chemical shift	Reference	
Li ₂ CO ₃	8 <i>f</i>	0.4	[71]	
LiAlO ₂	4 <i>b</i>	0.9	[71]	
Li ₂ SiN ₂	8 Li sites exchanged	1.7	[72]	
Li ₂ AgSn ₂	8 <i>e</i>	3.6	[73]	
Li ₃ Ga ₁₄	18 <i>h</i>	4	[74]	
Li ₁₅ Si ₄	12 <i>a</i> , 14 <i>e</i> exchanged	6	[75]	
Li ₂ CuSn ₂	8 <i>e</i>	6.4	[73]	
Li ₇ Sn ₂	6 Li sites exchanged	9.5	[76]	
Li ₁₃ Si ₄	7 Li sites exchanged	11.5	[75]	
Li ₅ Sn ₂	3 Li sites exchanged	14.3	[76]	
Li ₁₃ Sn ₅	7 Li sites exchanged	16	[76]	
Li ₇ Si ₃	8 Li sites exchanged	16.5	[75]	
Li ₇ Sn ₃	7 Li sites exchanged	17.5	[76]	
Li ₁₂ Si ₇	not assigned	-17.0		
	not assigned	1.8		
	not assigned	8.3	[77]	
	not assigned	15.0		
	not assigned	19.8		
	13 sites, exchanged	18.5	[75]	
AlLiCu		22		
		25		
		mixture of phases, for details see reference	27	[78]
			29	
			32	
			32	
LiSn	4 <i>b</i>	32	[76]	
	8 <i>e</i>	42.5	[76]	
Li ₂₁ Si ₅	not assigned	70.5		
	not assigned	93.7	[75]	
LiHg ₃	2 <i>c</i>	72.9	this work	
Li ₂ Sn ₅	4 <i>h</i>	80	[76]	
LiHg	1 <i>b</i>	101.7	this work	
AlLi alloy 8090		104.5	[71]	
Li ₃ Hg	4 <i>b</i> , 8 <i>e</i>	203.2	this work	
Li	2 <i>a</i>	265.1	this work	

Electric conductance in polar metals

Scattering of conduction electrons, e.g. on strong local Coulomb fields (i.e. ionic moieties), leads to typical "bad metal" behaviour. Electric conductances are generally low and deviate from linear temperature dependence expected for a typical (good) metal. Instead, conductances converge towards Ioffe-Regel saturation, a typical indication for polar metallic bonding due to a small free path length of the conduction electrons.

Specific resistance measurements have been carried out for Gd₁₄Ag₅₁ as example for a good metal (see chapter 3.3.2), KHg₆ (see chapter 3.4.1, Figure 2) and all Li amalgams (Li₃Hg, LiHg, LiHg₃, this chapter, Figure 3.26).

Gd₁₄Ag₅₁ shows a decrease of specific resistance with decreasing temperature. The relation is linear in the measured temperature interval. Together with an overall low resistance, this indicates good metallic behaviour.

KHg₆ shows a decrease of specific resistance with decreasing temperature. The overall resistance in comparison to a good metal is high. Furthermore, linear dependence of the resistance with respect to temperature is only given for a small temperature interval (0 to 50 K), at higher temperatures Ioffe-Regel saturation is observed, indicative for a typical "bad metal". The findings are supported by band structure calculations.^[80]

The Li amalgams Li₃Hg, LiHg and LiHg₃ differ in their electric behaviour as a result of Li content and thus polarity of metal-metal bonding. Li₃Hg and LiHg show bad metal behaviour and exhibit lower specific resistances than LiHg₃. At temperatures above 20 K, the thermal behaviour of the resistances deviates from linearity and converges in a Ioffe-Regel saturation. LiHg₃ shows a complicated behaviour even at low temperatures, not indicating typical metallic or "bad metal" behaviour. At temperatures higher than 50 K, it follows more or less the signature of a semiconductor, constituting the upper border of a polar metal-metal bonding.

4.3.3. Structures Derived from the BaHg₁₁ Structure Type

Amalgams with composition AHg_{11-x}In_x (A = K: $x \approx 1$, Rb: $x \approx 6$) have been synthesised and analysed by powder X-ray diffraction methods as stated in chapter 3.4.3. Both crystallise in the cubic crystal system in space group $Pm\bar{3}m$ with the BaHg₁₁ structure type.

KHg_{11-x}In_x ($x \approx 1$) can best be described by constructing a set of concentric endohedral polyhedra around Hg1 on $(\frac{1}{2}, \frac{1}{2}, \frac{1}{2})$. The first coordination sphere is an undistorted cuboctahedron (CN = 12), consisting of a mixed Hg/In position (75:25). It is surrounded by an octadecahedron (CN = 32, all Hg), which is surrounded by a cuboctahedron of K atoms. This description can be shortened to Hg@(Hg/In)₁₂@Hg₃₂@K₁₂, see Figure 4.25. The polyhedra describe the whole structure as all atoms take part, however, the large K cuboctahedra cannot be packed without leaving large octahedra surrounding (0,0,0) empty.

The lattice parameters of KHg_{11-x}In_x differ significantly from those reported for KHg₁₁ by $\Delta a = +0.0812(3)$ Å leading to $\Delta V = +2.5\%$. This is in accordance with a larger atomic radius of In in comparison to Hg and serves as indication for incorporation of In on at least one atomic position. Analysis of interatomic distances was carried out in comparison to KHg₁₁. Distances between Hg4 and surrounding atoms increase: $\Delta_{\text{Hg1-Hg4}} = +0.095$ Å, $\Delta_{\text{Hg2-Hg4}} = +0.026$ Å and $\Delta_{\text{Hg4-Hg4}} = +0.095$ Å. This directly leads to an expanded cuboctahedron and in turn to a larger octadecahedron. The latter distorts by shifting Hg2 towards the centre of the unit cell, leaving $\Delta_{\text{Hg2-Hg3}} = -0.007$ Å almost unchanged but dispersing Hg3 atoms slightly ($\Delta_{\text{Hg3-Hg3}} = 0.081$ Å). Overall, this supports the incorporation of In on the Hg4 position.

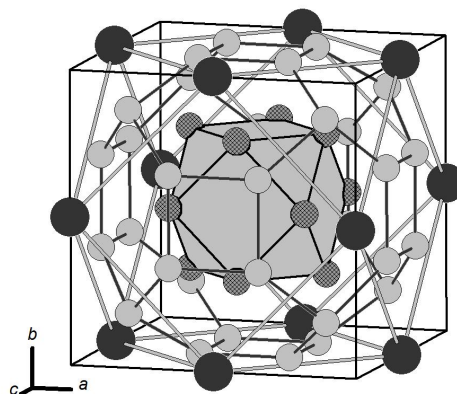


Figure 4.25.: Set of concentric endohedral polyhedra Hg@Hg/In₁₂@Hg₃₂@K₁₂ of which the structure of KHg_{11-x}In_x is built. K: black; Hg: grey; Hg/In: grey gids.

To assess the mixed position, DFT calculations were performed for KHg₁₁ and the hypothetical compound KHg₇In₄ (assuming 100 % In on the Hg4/In4 position). The exchange and correlation functional of Perdew, Burke and Ernzerhof [28] with a generalised gradient approximation (GGA) was applied. The muffin-tin radii were set to 132.3 pm (2.5 a. u.) and the number of basis functions was determined by the value of $R_{\text{mt}} \cdot K_{\text{max}} = 8$ with K_{max} as the largest k vector. The separation energy was set to -6 Ry. 1331 k points in the Brillouin zone (56 thereof in the irreducible Brillouin zone) were calculated in a 11x11x11 Monkhorst-Pack grid. The respective plots of the density of states are compiled in Figure 4.26.

The band structure of KHg_{11} is discussed first, the incorporation of In into the structure and its implications later on. Low in energy (-9 to -6 eV), $\text{Hg}5d$ states are located, showing considerable dispersion indicative for strong Hg-Hg interactions. Between -6 and 0 eV, mixing of s , p and d states is observed. $\text{K}4s$ states do not contribute much to the total DOS. Those findings are in accordance to other mercury-rich amalgams, e.g. XHg_6 ($X = \text{K}, \text{Ba}$), $\text{Ba}_3\text{Hg}_{11}$, $\text{Cs}_2\text{Hg}_{27}$. Incorporation of In on the $\text{Hg}4/\text{In}4$ site does not lead to drastic changes in the total DOS. The small pseudo-bandgap at Fermi level is closed in the tDOS and the respective pDOS of Hg, In and K atom positions. As the In-In contacts are few, the dispersion of $\text{In}4d$ bands is small. Akin to Hg, s and p states of In mix considerably with p states predominantly at Fermi level. Overall, no electronic reason for In to be incorporated at this particular site can be seen from those calculations.

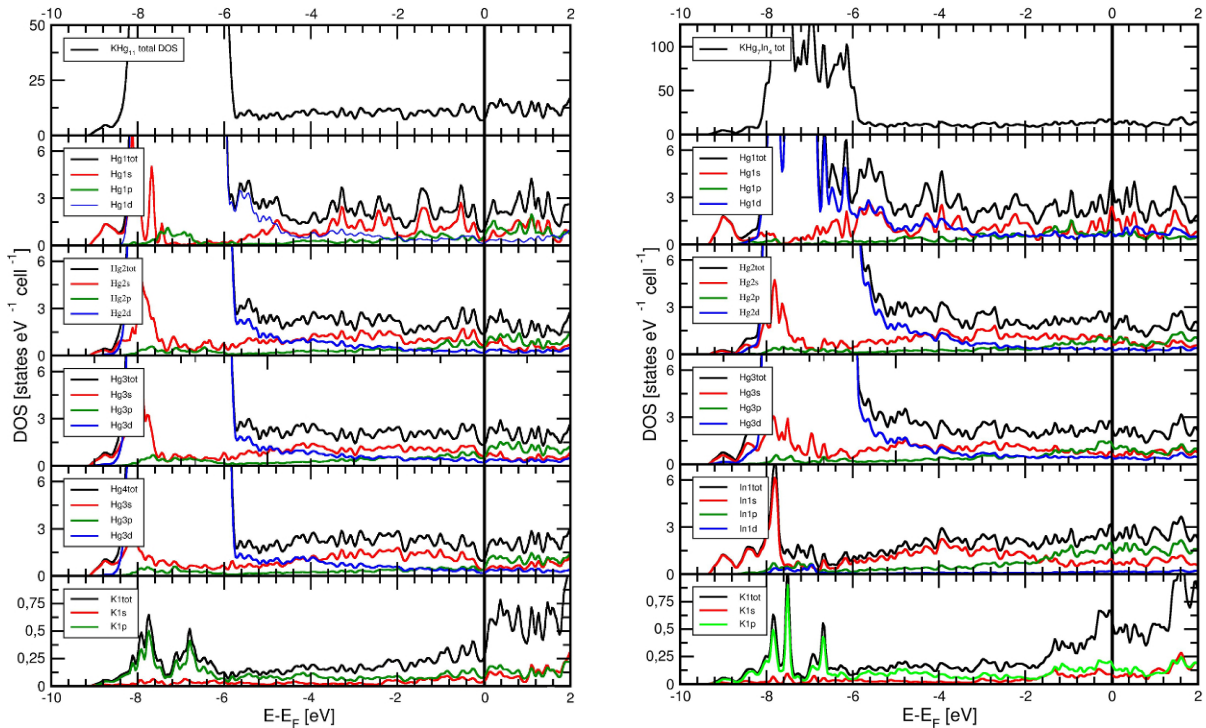


Figure 4.26.: **Left:** Plot of the total density of states in KHg_{11} and the partial densities of states for atoms $\text{Hg}(1) - \text{Hg}(4)$ and $\text{K}1$ are shown. **Right:** Plot of the total density of states of the hypothetical compound KHg_7In_4 and the partial densities of states for atoms $\text{Hg}1 - \text{Hg}3$, $\text{In}1$ and $\text{K}1$ are shown.

KIn_4 was obtained as side product in the synthesis of KHg_{10}In . The lattice parameters observed for KIn_4 differ from the reported by $\Delta a = +0.073$ Å and $\Delta c = +0.387$ Å. This could be indicative for incorporation of Hg in the compound (presumably on the In positions) with the metallic radius of Hg slightly smaller than that of In. Due to the low phase fraction of KIn_4 not enough data was collected to refine mixed occupancy.

$\text{RbHg}_{11-x}\text{In}_x$ ($x \approx 6$) ($Pm\bar{3}m$, $a = 9.7538(3)$ Å) crystallises in the BaHg_{11} structure type, all Hg positions are mixed with In in varying amounts (see Table 3.29). The lattice parameters differ by $\Delta a = +0.046(3)$ Å leading to $\Delta V = +1.4\%$. In contrast to $\text{KHg}_{11-x}\text{In}_x$, the expansion is smaller, despite the higher incorporation of In into the crystal structure. The interatomic distances are also enlarged but a pronounced distur-

tion as seen for $\text{KHg}_{11-x}\text{In}_x$ is absent. This might be due to the uniform incorporation of In on all Hg positions.

Bader charges – a measure for polarity?

The method of calculating Bader charges (AIM: atoms in molecules) is a method for the topological analysis of molecular and atomic electron densities.^[81] Space is separated into sub-volumes, centred by atoms (Bader basins), and an arbitrary spatial charge distribution is calculated. Resulting values are often (incorrectly) taken as absolute charges of atoms in solids, whereas they should be regarded as a spatial charge state. The inconsistencies originate from the definition of an "atom" in the AIM theory which is not unambiguous. One wedge of space is allocated to one atom only, covalent/metallic binding interactions are substantially neglected. The theory also neglects vibrational effects.^[82] Despite this limitation it is useful in a comparative sense, e.g. calculation of charge distributions, allocation of cations/anions and general trends of electron transfer. In this work, Bader charges were calculated for KHg_6 (chapter 3.4.1), $\text{Cs}_2\text{Hg}_{27}$ (see Table 4.6), $\text{La}_{11}\text{Hg}_{45}$ (chapter 3.3.3) and $\text{Li}_3\text{Ga}_{13}\text{Sn}$ (chapter 4.3.4).

The structure of KHg_6 features a large sublattice of $[\text{Hg}_6]^{\delta-}$. Bader charges indicate no distinct differences between Hg atoms showing similar negative polarisation. Electron transfer from K is near complete, which can also be seen from the low partial *s*-DOS of K at Fermi level.

The situation in $\text{Cs}_2\text{Hg}_{27}$ is different. Its structure is composed of a large $[\text{Hg}_{104}]^{\delta-}$ cluster surrounded by $\text{Cs}^{\delta+}$, leading to only marginally different charge distribution among Hg atoms. Some atoms can be regarded as near neutral (Hg3/4), one as slightly positive (Hg2), the rest shows equal charge distribution (Hg1/5–7). Thus, the view of a "cationic space webbing with anionic filling" is flawed from an electronic point of view, albeit useful for a more general and intuitive description of the structure.

Positive charges in $\text{La}_{11}\text{Hg}_{45}$ (see chapter 3.3.3) are equally distributed among the La atoms, negative charges equally among Hg atoms. The structure can be described in various ways, emphasizing structural relations to closest packed structures. Distribution of La atoms in a Hg sublattice is uniform, no pronounced formation of $[\text{Hg}]^{\delta-}$ clusters is observed.

Bader charges calculated for $\text{Li}_3\text{Ga}_{13}\text{Sn}$ (see chapter 3.5.2) show localisation of positive charge on Li atoms and negative charge on Ga and Sn atoms. Although differences between Ga and Sn would be expected from structure and electron counting rules (Wade), no obvious differences are observed. This might be due to artificial ordering of mixed

Table 4.6.: Bader charges calculated for $\text{Cs}_2\text{Hg}_{27}$.

Atom	Bader charge	site multiplicity	Charge incl. multiplicity
Cs1	+0.75	12	+9
Hg1	-0.12	48	-5.76
Hg2	+0.16	24	+3.84
Hg3	-0.04	24	-0.96
Hg4	+0.03	24	+0.72
Hg5	-0.14	24	-3.36
Hg6	-0.14	16	-2.24
Hg7	-0.17	2	-0.34
Hg total			-8.1
Cs total			+9
Diff. total			0.9
Diff. %			10

Ga/Sn and underoccupied Li positions for the calculation, necessary because WIEN2k does not feature calculations including disorder phenomena.

To conclude, Bader charges serve as comparative values, addressing structural features and the trend of electron transfer. Absolute charges cannot be calculated with this method, making other experiments (e.g. Knight shift measurements) essential for deeper insight into polarity of intermetallic phases. In all amalgams for which Bader charges have been calculated a clear trend points towards uniform distribution of the negative charge in the Hg sublattice. No concentration of charge on individual Hg atoms is observed, corroborating the picture of polar metallic bonding getting more pronounced in the Hg-rich phases due to more efficient delocalisation of a negative charge on a larger Hg sublattice.

4.3.4. Polarity in $\text{Li}_3\text{Ga}_{14}$ and $\text{Li}_3\text{Ga}_{13}\text{Sn}$

Electrolysis of a LiI solution on a Ga cathode leads to formation of $\text{Li}_3\text{Ga}_{14}$ (see chapter 3.5.1), electrolysis on a Ga/Sn cathode to formation of $\text{Li}_3\text{Ga}_{13}\text{Sn}$ (see chapter 3.5.2). $\text{Li}_3\text{Ga}_{14}$ was previously synthesised by melting a mixture of elemental Li and Ga in high Ga surplus.^[31,83] Cooling to 100 °C followed by filtration through glass wool separating $\text{Li}_3\text{Ga}_{14}$ from Ga melt yielded single crystals.

Structural elements are $[\text{Ga}_{12}]$ icosahedra packed in a cubic closest packing (see Figure 3.33). They are interconnected either directly via *exo*-bonds or by tetrahedrally coordinated $[\text{Ga}_2]$ dumbbells. Li atoms are located in voids of this packing, see also chapter 3.5.2. Electron counting shows $\text{Li}_3\text{Ga}_{14}$ to be a metal: The Ga_{12} icosahedra represent Wade clusters with 36 electrons. For a *closo* cluster $N + 1 = 13$ electron pairs corresponding to 26 electrons are necessary. 10 electrons are available for *exo*-bonds. As each icosahedron vertex shows a two-electron-two-centre *exo*-bond, accounting to 12 electrons, the Ga_{12} icosahedron must bear the charge -2 . The Ga atoms in the dumbbells are fourvalent and thus the dumbbell has also a charge of -2 . In one unit cell with $Z = 3$ the overall charge on the Ga sublattice is -12 . The lithium atoms are located on $18h$ positions and are half-occupied, yielding 9 electrons in total and leading to a non-electron precise metallic phase.

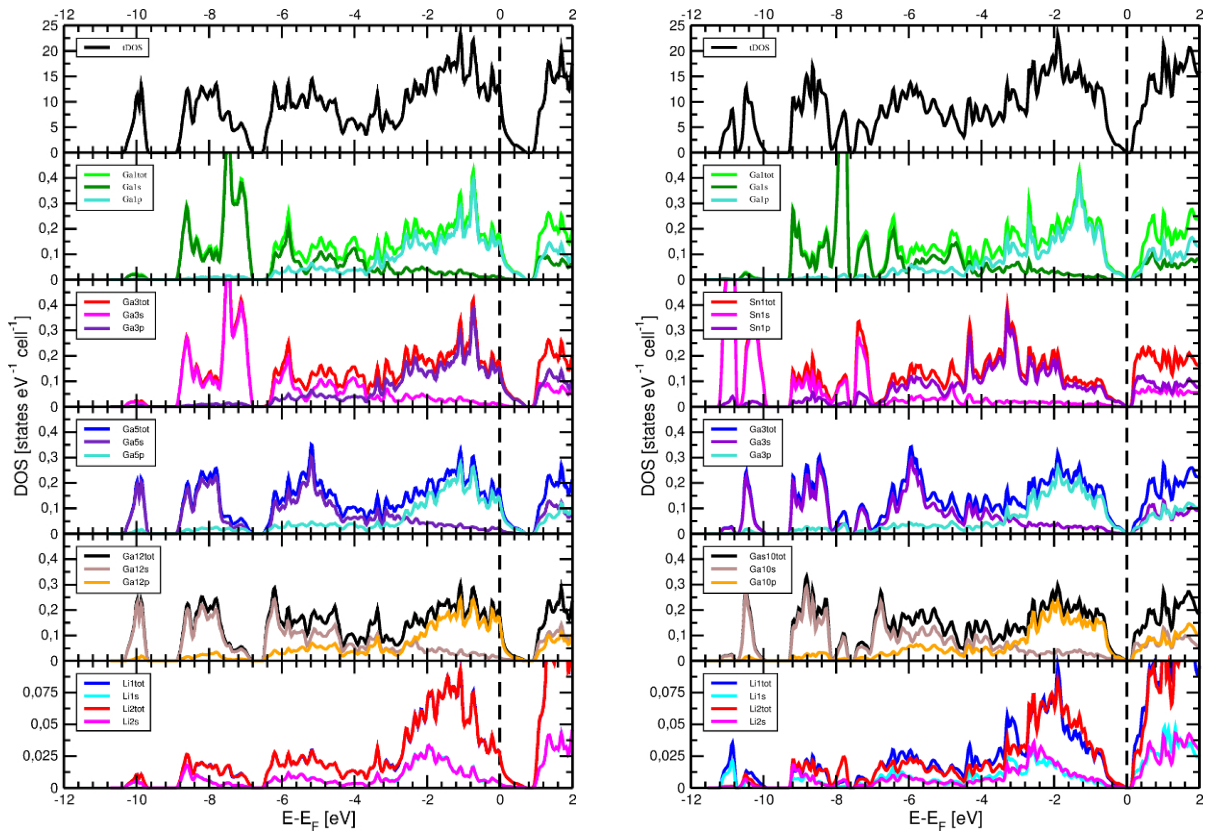


Figure 4.27.: **Left:** Plot of the total density of states in $\text{Li}_3\text{Ga}_{14}$ and the partial densities of states for atoms Ga(1) and Ga(3) (dumbbell), Ga(5) and Ga(12) (icosahedron), Li(1) and Li(2). **Right:** Plot of the total density of states in $\text{Li}_3\text{Ga}_{13}\text{Sn}$ and the partial densities of states for atoms Ga(1) (dumbbell), Sn(1) (dumbbell), Ga(3) and Ga(10) (icosahedron) also Li(1) and Li(2).

If Sn is present in the electrode material, $\text{Li}_3\text{Ga}_{13}\text{Sn}$ forms as product (see chapter 3.5.2). Here, the Sn atoms are located on dumbbell positions with an occupation factor of 0.5. Applying electron counting rules, no changes for the icosahedron (12 skeletal electrons and -2 charge) are expected. Dumbbell positions have only one Ga with a charge of -1 left. Sn as tetrel has a valency of 4 and thus no charge. This reduces the electron demand per unit cell from $12e^-$ to $9e^-$ which is in accordance with a half-occupied Li 18h position. $\text{Li}_3\text{Ga}_{13}\text{Sn}$ therefore should show a band gap and semiconducting behaviour. Band structure calculations support the electron counting, see below and Figure 4.27.

The half-occupied position for lithium and the mixed occupancy of Ga(3)/Sn(3) are crucial for the position of the Fermi energy with respect to the DOS. Both were modelled by symmetry reduction by enlargement of the unit cell and reducing the symmetry to $R3m$. This orders the underoccupied Li position into fully occupied positions and voids, and also leads to a split of the "dumbbell" position Ga(3)/Sn(3) (mixed-occupation of Ga3 with 1:1 Ga:Sn). A detailed Bärnighausen tree is shown in Figure 4.30.

Calculations with full lithium occupation ($\text{Li}_6\text{Ga}_{14}$, less resource consuming) resulted in a band structure with Fermi energy significantly above a pseudo-band gap (see Figure 4.28). Decreasing the symmetry to account for the underoccupation ($\text{Li}_3\text{Ga}_{14}$, calculated in $R3m$) results in a similar band structure but with the band gap above Fermi energy.

As can be seen in Figure 4.27 (calculation for $\text{Li}_3\text{Ga}_{14}$), the band structure shows distinct features. The lowest-lying states (-10.5 to -9.5 eV) result mainly from Ga atoms forming the icosahedra. States slightly higher in energy originate from Ga atoms constituting the icosahedra as well as the dumbbells. All aforementioned features show high s contributions. From -6.5 eV up to -4 eV s -states are prevalent and p -states are prevalent above -3 eV. Higher in energy at $+0.6$ eV a band gap is located. Li shows little contribution to the total DOS. Only s -states are present spreading

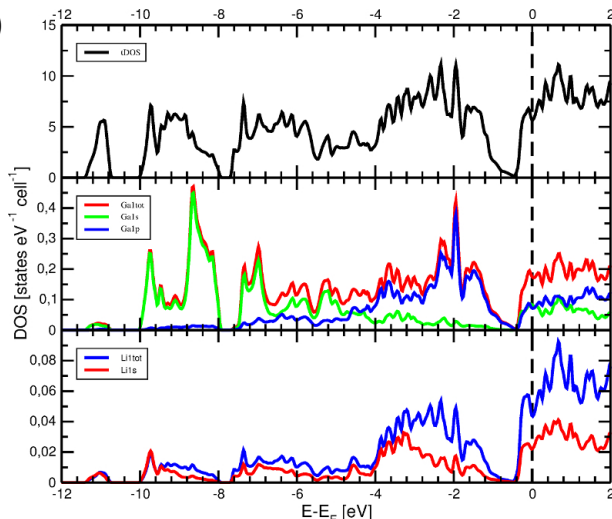


Figure 4.28.: Plot of the total density of states of the hypothetical $\text{Li}_6\text{Ga}_{14}$ structure and the partial densities of states for atoms Ga(1) and Li(1).

Table 4.7.: Bader charges calculated for $\text{Li}_3\text{Ga}_{13}\text{Sn}_1$

Atom	Bader charge	Site multiplicity	Charge incl. multiplicity
Ga1	-0.297	3	-0.891
Ga2	-0.266	3	-0.798
Ga3	-0.181	9	-1.629
Ga4	-0.127	9	-1.143
Ga5	-0.146	9	-1.314
Ga6	-0.096	9	-0.864
Ga7	-0.266	9	-2.394
Ga8	-0.140	9	-1.260
Ga9	-0.243	9	-2.187
Ga10	-0.122	9	-1.098
Sn1	-0.338	3	-1.014
Sn2	-0.249	3	-0.747
Li1	+0.854	9	+7.686
Li2	+0.858	9	+7.722
Ga + Sn total			-15.339
Li total			+15.408
Diff. total			0.069
Diff. %			0.4

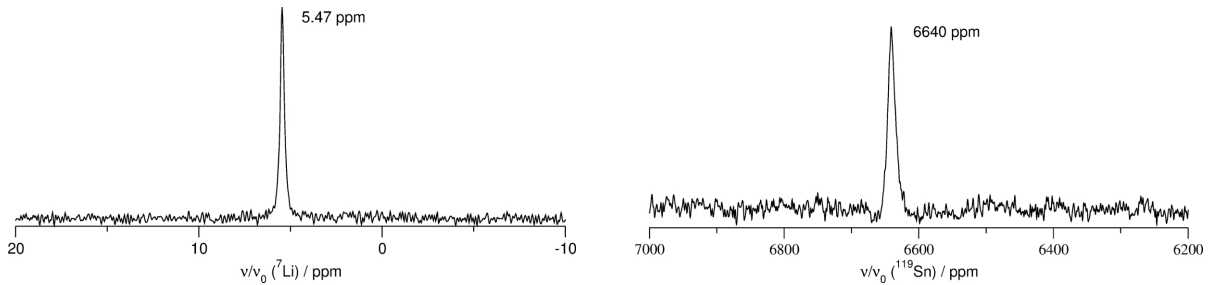


Figure 4.29.: ${}^7\text{Li}$ and ${}^{119}\text{Sn}$ NMR signals for $\text{Li}_3\text{Ga}_{13}\text{Sn}_1$.

over the whole energy range with a maximum at -1.5 eV. The two crystallographically independent Li positions behave about the same.

The band structure of $\text{Li}_3\text{Ga}_{13}\text{Sn}$ (calculated in $R3m$, see Figure 4.27) shows features similar to the band structure of $\text{Li}_3\text{Ga}_{14}$. Notable differences are additional, low-lying states introduced by tin s -bands, compression of the s -band of Ga1 at -8 eV results in a high local DOS. Sn largely shows the same features as Ga. The introduction of two additional electrons by the incorporation of Sn raises the Fermi level to the aforementioned band gap thus forming a semiconductor with a small band gap. Similarly to the band structure of $\text{Li}_3\text{Ga}_{14}$, Li shows no large contribution to the band structure. However, the two crystallographically independent sites show small differences.

Bader charges calculated for $\text{Li}_3\text{Ga}_{13}\text{Sn}$ are compiled in Table 4.7. They do not represent absolute charges in electrons but are unitless and as such serve as relative values suitable for direct comparison of charges in one compound/calculation. The total difference in positive and negative charges is $+0.069$ (0.4%) indicating good quality of the calculated scf-process. However, there are no distinct differences between Ga atoms or Ga and Sn atoms, Li atoms appear to be similar to each other, too. One would have expected lower charges for Sn atoms as they count as ± 0 for Wade cluster calculation. The discrepancy might be due to the ordered model employed for calculation in contrast to the true disordered model from single crystal refinement (see also precession images in Figure 3.32).

Solid state NMR measurements for $\text{Li}_3\text{Ga}_{14}$ were carried out before and show a shift of 4 ppm for ${}^7\text{Li}$.^[74] Almost no contribution of Knight shift is observed, electron density for Li at Fermi level is thus negligible and Li can be regarded as prevalently ionic. In NMR measurements on $\text{Li}_3\text{Ga}_{13}\text{Sn}$ (${}^7\text{Li}$, ${}^{71}\text{Ga}$, ${}^{119}\text{Sn}$) the ${}^7\text{Li}$ and ${}^{119}\text{Sn}$ resonances of the compound were observed (see Figure 4.29). ${}^{71}\text{Ga}$ only showed resonance for elemental Ga (4486 ppm, side phase, not observed in Rietveld refinement). ${}^7\text{Li}$ shows resonance at 5.47 ppm, indicative for largely ionic Li without pronounced contributions of Knight shift, similar to the parent compound $\text{Li}_3\text{Ga}_{14}$. ${}^{119}\text{Sn}$ shows resonance at 6640 ppm, significantly differing from resonance in elemental Sn (see Table 4.8). Lower Knight

Table 4.8.: Isotropic Knight shift data of ${}^{119}\text{Sn}$ for elemental Sn and $\text{Li}_3\text{Ga}_{13}\text{Sn}_1$.

Compound	isotropic Knight shift [ppm]	
Sn	7090 ± 70	Ref ^[84]
Sn	7570	Ref ^[85]
Sn	7130 ± 20	Ref ^[86]
Sn mean	7263	
$\text{Li}_3\text{Ga}_{13}\text{Sn}_1$	6640	this work

shift means lower s electron density at Fermi level. From band structure calculations $\text{Li}_3\text{Ga}_{13}\text{Sn}$ is expected to be a semiconductor and thus Knight shift measurements are highly temperature dependent. At present, no temperature-dependent measurements have been carried out. Electric resistance measurements are required to confirm semi-conducting behaviour for $\text{Li}_3\text{Ga}_{13}\text{Sn}$.

As can be seen from band structure calculations as well as NMR investigations, Li exhibits a high positive charge in both $\text{Li}_3\text{Ga}_{14}$ and $\text{Li}_3\text{Ga}_{13}\text{Sn}$. The negative charge is equally distributed between the Ga atoms (and Sn atoms if present). Thus we conclude that these compounds show high polarity in the sense that the electron transfer from the Li atoms is near-complete in accordance with the exothermic electron affinities of Ga and Sn.

References

- [1] J. J. Berzelius, *Föreläsningar i Djurkemi*, Carl Delen, Stockholm (1806).
- [2] H. Davy, *Philos. Trans. R. Soc. London*, **97**, 1–56 (1807).
- [3] A. Volta, *Philos. Trans. R. Soc. London*, **90**, 403–431 (1800).
- [4] H. N. McCoy, H. S. Morris, P. W. Selwood, *Inorganic Syntheses*, volume 2 of *Inorganic Syntheses*, John Wiley & Sons, Inc., Hoboken, NJ, USA, 2 edition (1946).
- [5] T. Moeller, H. E. Kremers, *Industrial & Engineering Chemistry Analytical Edition*, **17(12)**, 798–800 (1945).
- [6] E. E. Jukkola, L. F. Audrieth, B. S. Hopkins, *J. Am. Chem. Soc.*, **56(2)**, 303–304 (1934).
- [7] J. W. Neckers, H. C. Kremers, *J. Am. Chem. Soc.*, **50(4)**, 950–954 (1928).
- [8] J. K. Marsh, *J. Chem. Soc.*, **53(9)**, 398 (1942).
- [9] J. K. Marsh, *J. Chem. Soc.*, **53(9)**, 523 (1942).
- [10] J. K. Marsh, *J. Chem. Soc.*, **53(9)**, 8–10 (1943).
- [11] J. K. Marsh, *J. Chem. Soc.*, **53(9)**, 531–335 (1943).
- [12] H. N. McCoy, *J. Am. Chem. Soc.*, **63(2)**, 7–8 (1937).
- [13] H. N. McCoy, R. P. Hammond, *J. Am. Chem. Soc.*, **64(4)**, 1009–1009 (1942).
- [14] C. Hoch, A. Simon, *Z. Anorg. Allg. Chem.*, **634(5)**, 853–856 (2008).
- [15] C. Hoch, A. Simon, *Z. Anorg. Allg. Chem.*, **632(14)**, 2288–2294 (2006).
- [16] C. Hoch, A. Simon, *Angew. Chem.*, **124(13)**, 3316–3319 (2012); b) C. Hoch, A. Simon, *Angew. Chem. Int. Ed.*, **51(13)**, 3262–3265 (2012).
- [17] J. H. Simons, R. P. Seward, *J. Chem. Phys.*, **6(12)**, 790 (1938).
- [18] T. B. Massalski, *Binary Alloy Phase Diagrams*, ASM International, Materials Park,

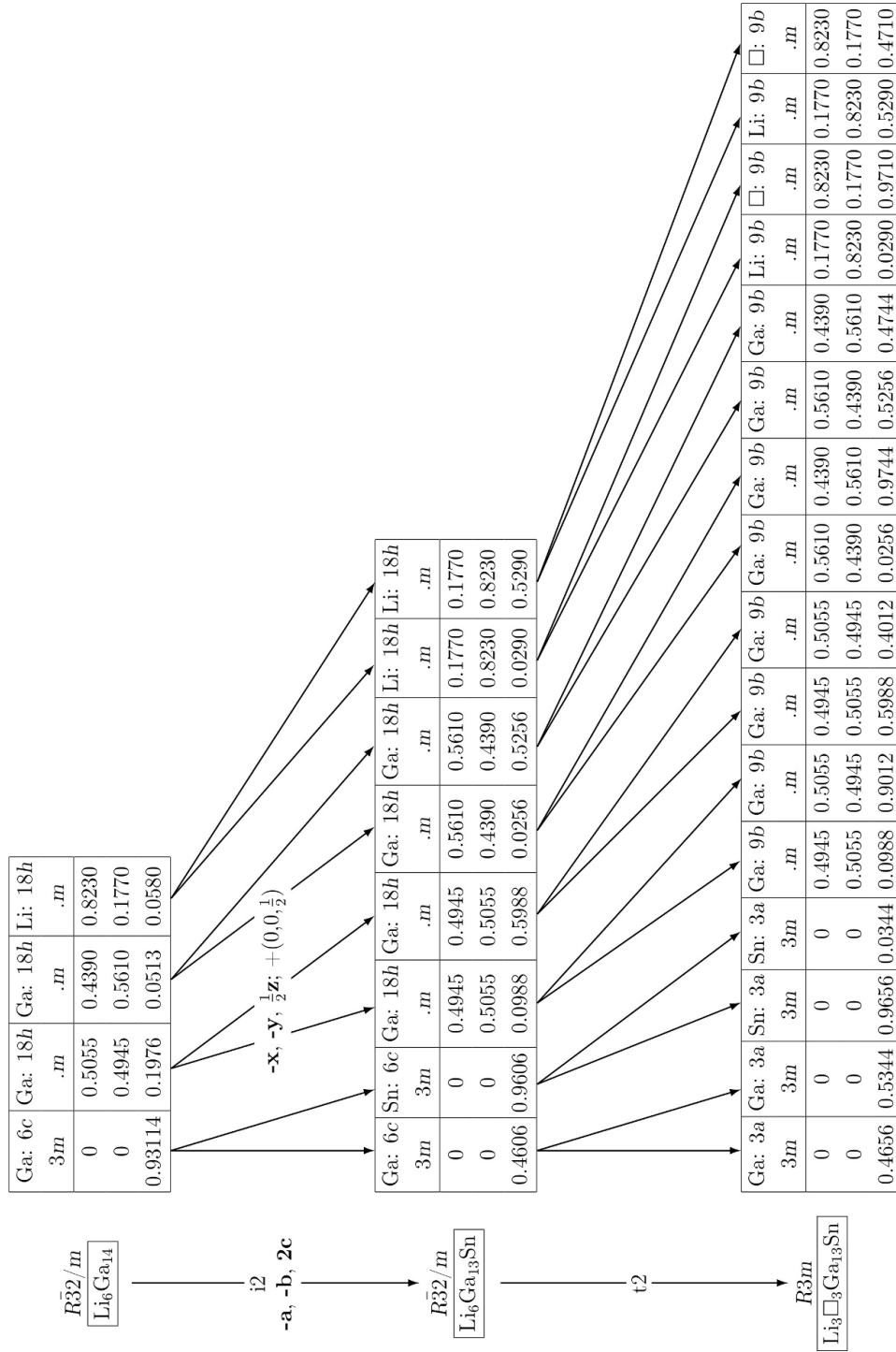


Figure 4.30.: Group-subgroup relation between $\text{Li}_6\text{Ga}_{14}$, $\text{Li}_3\text{Ga}_{14}$ and $\text{Li}_3\text{Ga}_{13}\text{Sn}$ utilised as base for quantum mechanical calculations. The first step [i2] duplicates the c axis and thus leads to ordering of the 6c position in Ga_2 and Sn_2 dumbbells. The second step [t2] reduces the symmetry with splitting of the Li 18h positions and subsequent ordering of fully occupied positions and voids.

Ohio, USA, 2nd edition (1990).

- [19] W. Müller, H. Schäfer, *Z. Naturforsch. B*, **28(5-6)**, 246–248 (1973).
- [20] G. El, G. I. Oleksiv, K. PI, *Sov. Phys. - Crystallogr.*, **9(3)**, 269 (1964).
- [21] W. Müller, *Z. Naturforsch. B*, **29b**, 304–307 (1974).
- [22] J. Stöhr, H. Schäfer, *Z. Anorg. Allg. Chem.*, **474(3)**, 221–225 (1981).
- [23] J. Blessing, *Synthesis and Study of Ternary Phases of Li with Elements of Group 3 and 4*, Phd-thesis, Cologne (1978).
- [24] Corina Lupu, Jiang-Gao Mao, J. Wayne Rabalais, and Arnold M. Guloy, J. James W. Richardson, *Inorg. Chem.*, **42(12)**, 3765–3771 (2003).
- [25] G. Jang, *J. Crys. Growth*, **141(3-4)**, 399–403 (1994).
- [26] O. Genser, J. Hafner, *Phys. Rev. B*, **63(14)**, 1–15 (2001).
- [27] D. A. Hansen, L. J. Chang, *Acta Crystallogr. B*, **25(11)**, 2392–2395 (1969).
- [28] W. Blase, G. Cordier, R. Kniep, *Z. Anorg. Allg. Chem.*, **619**, 1161–1166 (1993).
- [29] U. Frank, W. Müller, *Z. Naturforsch. B*, **30(5-6)**, 316–322 (1975).
- [30] M. Wiking, J. Stöhr, *Z. Naturforsch. B*, **32(6)**, 631–636 (1977).
- [31] C. Belin, R. G. Ling, *J. Solid State Chem.*, **45(2)**, 290–292 (1982).
- [32] U. Frank, W. Müller, H. Schäfer, *Z. Naturforsch. B*, **30(1-2)**, 1–5 (1975).
- [33] M. L. Huber, A. Laesecke, D. G. Friend, *NIST Interagency/Internal Report (NIST-IR) - 6643*, pp. 1–56 (2006).
- [34] S. Krivovichev, *Acta Crystallogr. A*, **68**, 393–8 (2012).
- [35] S. V. Krivovichev, *Angew. Chem. Int. Ed.*, **53(3)**, 654–61 (2014); b) S. V. Krivovichev, *Angew. Chem.*, **126(3)**, 666–674 (2014).
- [36] J. K. Burdett, C. Mariani, J. F. Mitchell, *Inorg. Chem.*, **33(9)**, 1848–1856 (1994).
- [37] S. E. Lister, I. Radosavljevic Evans, J. A. K. Howard, A. Coelho, J. S. O. Evans, *Chem. Commun.*, **(22)**, 2540 (2004).
- [38] C. Guminski, *J. Phase Equilib.*, **14(1)**, 97–99 (1993).
- [39] C. Guminski, *J. Phase Equilib.*, **14(3)**, 382–387 (1993).
- [40] C. Guminski, *J. Phase Equilib.*, **16(1)**, 86–91 (1995).
- [41] C. Guminski, *J. Phase Equilib.*, **16(1)**, 73–76 (1995).
- [42] C. Guminski, *J. Phase Equilib.*, **16(2)**, 181–185 (1995).
- [43] C. Guminski, *J. Phase Equilib.*, **16(1)**, 77–80 (1995).
- [44] C. Guminski, *J. Phase Equilib.*, **16(2)**, 186–192 (1995).

- [45] C. Guminski, *J. Phase Equilib.*, **16(3)**, 276–276 (1995).
- [46] C. Guminski, *J. Phase Equilib.*, **16(5)**, 448–453 (1995).
- [47] C. Guminski, *J. Phase Equilib.*, **16(6)**, 526–526 (1995).
- [48] C. Guminski, *J. Phase Equilib.*, **16(5)**, 454–458 (1995).
- [49] C. Guminski, *J. Phase Equilib.*, **14(3)**, 391–392 (1993).
- [50] C. Guminski, *J. Phase Equilib.*, **16(2)**, 193–196 (1995).
- [51] C. Guminski, *J. Phase Equilib.*, **16(5)**, 459–459 (1995).
- [52] C. Guminski, *J. Phase Equilib.*, **16(4)**, 348–352 (1995).
- [53] W. Lugscheider, H. R. Kirchmayr, *Z. Metallkd.*, **57**, 725 – 728 (1966).
- [54] I.-C. Hwang, T. Drews, K. Seppelt, *J. Am. Chem. Soc.*, **122**, 8486–8489 (2000).
- [55] A. Iandelli, A. Palenzona, *J. Less-Common Met.*, **15(3)**, 273–284 (1968).
- [56] H. R. Kirchmayr, *Monatsh. Chem.*, **95(6)**, 1667–1670 (1964).
- [57] E. Laube, H. Nowotny, *Monatsh. Chem.*, **94(5)**, 851–858 (1963).
- [58] A. Palenzona, *J. Less-Common Met.*, **10(4)**, 290–292 (1966).
- [59] S. J. Lyle, W. A. Westall, *J. Less-Common Met.*, **99(2)**, 265–272 (1984).
- [60] A. V. Tkachuk, A. Mar, *Inorg. Chem.*, **47(4)**, 1313–8 (2008).
- [61] D. M. Bailey, G. R. Kline, *Acta Crystallogr. B*, **27(3)**, 650–653 (1971).
- [62] F. Tambornino, C. Hoch, *Z. Anorg. Allg. Chem.*, **641(3-4)**, 537–542 (2015).
- [63] W. Hornfeck, C. Hoch, *Acta Crystallogr. B*, **71(6)**, 752–767 (2015).
- [64] S. Krivovichev, *Private Communication* (2014).
- [65] M. Wörsching, F. Tambornino, S. Datz, C. Hoch, *Angew. Chem. Int. Ed.*, **55**, 1–5 (2016); b) M. Wörsching, F. Tambornino, S. Datz, C. Hoch, *Angew. Chem. Int. Ed.*, **11**, 1–6 (2016).
- [66] R. K. Harris, E. D. Becker, S. M. Cabral De Menezes, R. Goodfellow, P. Granger, *Concepts in Magnetic Resonance Part A: Bridging Education and Research*, **14(5)**, 326–346 (2002).
- [67] A. Abragam, *The Principles of Nuclear Magnetism*, International series of monographs on physics, Clarendon Press (1961).
- [68] C. P. Slichter, *Principles of Magnetic Resonance*, Lecture Notes in Computer Science, Springer (1996).
- [69] M. D’Avezac, N. Marzari, F. Mauri, *Phys. Rev. B*, **76(16)**, 1–12 (2007).
- [70] R. Laskowski, P. Blaha, *J. Phys. Chem. C*, **119**, 19390–19396 (2015).

- [71] Y. Ba, J. A. Ripmeester, *Mag. Res. Chem.*, **40(1)**, 81–86 (2002).
- [72] S. Pagano, M. Zeuner, S. Hug, W. Schnick, *Eur. J. Inorg. Chem.*, **2(12)**, 1579–1584 (2009).
- [73] F. Winter, S. Dupke, H. Eckert, U. C. Rodewald, R. Pöttgen, *Z. Anorg. Allg. Chem.*, **639(15)**, 2790–2795 (2013).
- [74] M. Tillard-Charbonnel, C. Belin, M. H. Herzog-Cance, *Eur. J. Solid State Inorg. Chem.*, **25**, 329 (1988).
- [75] B. Key, R. Bhattacharyya, M. Morcrette, V. Sezne, J.-M. Tarascon, C. P. Grey, *J. Am. Chem. Soc.*, **131**, 9239–9249 (2009).
- [76] E. Bekaert, F. Robert, P. E. Lippens, M. Ménétrier, *J. Phys. Chem. C*, **114(14)**, 6749–6754 (2010).
- [77] T. K.-J. Köster, E. Salager, A. J. Morris, B. Key, V. Seznec, M. Morcrette, C. J. Pickard, C. P. Grey, *Angew. Chem. Int. Ed.*, **50(52)**, 12591–12594 (2011).
- [78] C. Lee, D. White, B. H. Suits, P. A. Bancel, P. A. Heiney, *Phys. Rev. B*, **37(15)**, 9053–9056 (1988).
- [79] R. Nesper, H. G. von Schnering, *J. Solid State Chem.*, **70(1)**, 48–57 (1987).
- [80] F. Tambornino, C. Hoch, *J. Alloys Compd.*, **618**, 299–304 (2015).
- [81] R. F. W. Bader, *Atoms in Molecules*, John Wiley & Sons, Ltd, Chichester, UK (2002).
- [82] P. Cassam-Chenai, D. Jayatilaka, *Theor. Chem. Acc.*, **105**, 213–218 (2001).
- [83] J. Stöhr, H. Schäfer, *Rev. Chim. Miner.*, **19**, 122 (1982).
- [84] B. R. McGarvey, H. S. Gutowsky, *J. Chem. Phys.*, **21(12)**, 2114 (1953).
- [85] N. Bloembergen, T. Rowland, *Acta Metall.*, **1(6)**, 731–746 (1953).
- [86] E. Jones, D. Llewelyn Williams, *Phys. Lett.*, **1(3)**, 109–110 (1962).

5. Conclusion

In this thesis polar intermetallic compounds have been investigated. They are characterised by an incomplete electron transfer from an electropositive to an electronegative metal. On selected examples, the impact of introducing Coulombic contributions in a metallic matrix on the physical properties have been demonstrated. Main objectives have been the development of new synthetic methods towards the synthesis of this class of intermetallics with special focus on amalgams as model systems. A plethora of structures of coordination compounds (educts for electrolysis), various amalgams and some selected related Hg-free compounds have been elucidated. Furthermore, DFT calculations have been performed to get insight into bonding modes of the compounds and to better understand fundamental structure-property relations. Additional analytical methods (electric conductance, magnetometry) have been employed to characterise the impact of polarisation of metal-metal bonding on some physical properties.

This chapter gives a brief review of the key results presented in this thesis.

5.1. DMF Solvates of Metal Iodides as Educts for Electrocrystallisation

Solvates of metal iodides with *N,N*-dimethyl formamide (DMF) as ligand have been prepared as educts for subsequent preparative electrolysis. Their structures have been elucidated with single crystal X-ray diffraction. With the concept of hierarchical variants, most of these structures can be rationalised as decorated variants of simple structure types, e.g. hcp, ccp, NiAs, or hexagonal primitive packing. Symmetry reductions are the result of different spatial demands of iodide ions and DMF ligands, together with the point group of the latter. Group-subgroup relations have been evaluated with Bärnighausen trees for selected examples to illustrate the topological relations.

5.2. Electrolysis on Unary, Binary and Ternary Reactive Cathodes

Electrolyses with elemental Hg or Ga cathode materials have been performed and yielded the Hg- and Ga-richest phases of the respective intermetallic systems. The amalgams LiHg_3 , KHg_{11} , KHg_6 , $\text{Cs}_3\text{Hg}_{20}$, $\text{Ca}_{11-x}\text{Hg}_{54+x}$, $\text{Eu}_{10}\text{Hg}_{55}$ and ErHg_3 were synthesised. The gallides $\text{Li}_3\text{Ga}_{14}$ and NaGa_4 were synthesised. The principal reaction mechanisms have been evaluated and put into context with an alternative distillation method (yielding $\text{La}_{11+x}\text{Hg}_{45-x}$ and $\text{RE}_{11}\text{Hg}_{45}$ with $\text{RE} = \text{Sm}, \text{Nd}$) and classical solid state syntheses.

Electrolysis on binary systems as cathode materials can yield a single ternary compound, two binary compounds or one binary compound plus one element. The first case has been observed for the electrolysis of LiI on a GaSn eutectic cathode (yielding $\text{Li}_3\text{Ga}_{13}\text{Sn}$) and NaI on a GaSn eutectic (yielding $\text{K}_8\text{Ga}_8\text{Sn}_{38}$). The latter case has been observed for electrolysis of CsI on a Hg/In (1:1) cathode yielding the new binary main group element compound CsIn_{12} whereas Hg served as inert solvent under the given conditions. Formation of two binary compounds has not been observed on the systems employed, but is likely to occur with other educt materials.

Electrolysis on a ternary cathode materials has been investigated with GaInStan and yielded a mixture of $\text{Li}_3\text{Ga}_{13}\text{Sn}$, LiGa, LiIn and In. Principal reaction pathways have been evaluated and a rational pathway for the subsequent formation of the products has been assessed. In principle, formation of a single quaternary product is possible but not in the Li–Ga–Sn–In system for thermodynamic reasons.

The distillation method is complementary to electrocrystallisation at low temperatures. A mercury surplus is distilled off in vacuo after reaction in Hg flux. This method can be performed in a temperature range of 100 – 300 °C and allows for good crystallisation of the products as has been shown for $\text{La}_{11+x}\text{Hg}_{45-x}$ and $\text{RE}_{11}\text{Hg}_{45}$ ($\text{RE} = \text{Sm}, \text{Nd}$). The horizontal pathway through the x, T -phase diagram is similar to electrocrystallisation, but the mechanism is different: the former relies on stepwise *increasing* the amount of the more electronegative element in the cathode material, whereas the latter relies on *decreasing* the mercury surplus in the distillation residue.

5.3. Crystal Structures of Hg-rich Amalgams

Crystal structures of Hg-rich amalgams are complicated and often exhibit mixed and/or underoccupied positions as shown for $\text{RE}_{11+x}\text{Hg}_{45-x}$, structures deriving from the $\text{Gd}_{14}\text{Ag}_{51}$ aristotype and KHg_6 . Reoccurring motifs are Frank-Kasper polyhedra, closest sphere packings and cation-centred polyhedra, the latter emphasising ionic binding contributions.

Crystal structures with the common aristotype $\text{Gd}_{14}\text{Ag}_{51}$ as well as the aristotype itself have been examined. The structures show different disorder phenomena, which have been evaluated crystallographically and on the basis of complexity measures. We have shown that the $\text{Gd}_{14}\text{Ag}_{51}$ structure type crystallises with space group $P6/m$ by single crystal and powder X-ray structure analysis combined with TEM investigations. Six symmetry equivalent, half-occupied and mutually exclusive Ag positions cannot be resolved by symmetry reduction and thus are intrinsic to this structure type.

This disorder is resolved in amalgam crystal structures (hettotypes of $\text{Gd}_{14}\text{Ag}_{51}$) by symmetry reduction to $P6$. However, additional disorder phenomena, mixed and underoccupied positions, are introduced in most of them with the exception of $\text{Yb}_{14}\text{Hg}_{51}$ crystallising in a fully ordered structure. Quantification of individual disorder phenomena has become possible by employing the concept of complexity measures. Singular mixed/underoccupied positions do not greatly increase complexity (e.g. $\text{Yb}_{14}\text{Hg}_{51}$ is only little less complex than $\text{Eu}_{10}\text{Hg}_{55}$). A larger effect is observed when superstructures with longer translation periods form.

5.4. Evaluation of Polarity in Amalgams and Related Phases

Polar metals are characterised by an incomplete electron transfer from an electropositive metal to an electronegative metal. This leads to strong local Coulomb fields from few cations in an overall metallic lattice. Hg-rich amalgams serve as model systems as few electrons from an electropositive element delocalise over a large Hg sublattice.

NMR Knight shift studies have been carried out on the three Li amalgams Li_3Hg , LiHg and LiHg_3 as both ^7Li and ^{199}Hg are NMR-active nuclei. With increasing Hg content the electron transfer increases. Thus LiHg_3 features the most positive partial charge on $[\text{Li}^{\delta+}]$. In this sense it is the most polar of the Li amalgams, followed by LiHg and Li_3Hg as the least polar. These investigations are corroborated by electric conductivity measurements of the model compounds Li_3Hg , LiHg , LiHg_3 and KHg_6 with respect to Hg and $\text{Gd}_{14}\text{Ag}_{51}$ as metallic references. Polar metals show linear dependence of resistance with temperature only at low temperatures (LiHg : ≤ 20 K, KHg_6 : ≤ 50 K). Further increase of the polarity leads to complicated behaviour even at low temperatures and to semiconducting characteristics at only slightly higher temperatures (LiHg_3 : $T \geq 50$ K).

DFT calculations have been performed to monitor the electron transfer *ab initio*. Bader charges have proven as viable concept but are prone to intrinsic errors as Bader basins are allocated arbitrarily and the computed charges are not absolute. Better results are obtained by correlation of the partial density of states at Fermi level with observed NMR Knight shift measurements. Knight shifts for both ^7Li and ^{199}Hg can be rationalised by shifting the electronic bands in energy to assume energetically more favoured positions and occupying them.

6. Outlook

Electrocrystallisation has proven a promising synthetic method for intermetallic compounds, especially polar metals and compounds with low peritectic decomposition temperatures. Thus far, only few electrode materials have been tested: Hg, Ga, Ga/Sn and Hg/In eutectics and GaInStan. Other viable systems are a great number of multinary systems compiled in chapter 3.5.1. Depending on the electrolyte, different scenarios for product formation can be expected as has been discussed above. For higher melting eutectics with melting points close to or above the boiling point of DMF, the solvent would have to be changed. One option consists of ionic liquids as they are thermally stable up to very high temperatures, conduct electricity very well and are commercially available. Preliminary experiments were unsuccessful as many ionic compounds decompose at higher terminal voltages. In addition, solubility of their iodides is low or the iodides of the cations of the respective ionic liquid form stable/insoluble salts. An ionic liquid with a redox-active organic anion instead of iodine has to be developed in combination with large cations with low charge (e.g. Cs^+) as their polarisability favours low melting points.

An approach complimentary to the use of multinary cathode materials with an electrolyte containing only one cation would be the use of a unary cathode material together with a multinary mixture of electrolytes containing two or more different cations. According to Nernst equation concentrations would have to be chosen so that the cations present in this mixture exhibit the same electrochemical potential and hence dissolve simultaneously in the reactive cathode. Preliminary experiments with a solution of KI and NaI in DMF electrolysed on a Hg cathode show indications of a ternary Na-K amalgam crystallising in a hettotype structure of the $\text{Ga}_{14}\text{Ag}_{51}$ structure type. However, due to the extreme sensitivity of the systems with respect to reaction conditions and air/moisture in combination with highly anisotropic crystal shape and very high absorption coefficients, up to now no reliable crystal data could be acquired. Use of synchrotron radiation for both single crystal and powder X-ray measurements are clearly indicated and should be carried out in the future.

Furthermore, the electrolytic process could be used for preparation of metal-rich compounds comprising larger, cluster-like ionic units in the metallic matrix. Examples have already been given by tetramethyl ammonium amalgam and $[\text{Mg}(\text{NH}_3)_6]\text{Hg}_{22}$. The resulting amalgams share features of intercalation compounds and ordinary intermetallics, and have highest polarity within all metallic compounds. Extension of this interesting field seems possible in different ways: Cluster compounds like e.g. MoCl_2 ($\text{Mo}_6\text{Cl}_{12}$) are of interest as the four *exo*-chloride atoms can be exchanged to yield $\text{Mo}_6\text{Cl}_8\text{I}_4$. This DMF-soluble cluster compound might result in incorporation of $[\text{Mo}_6\text{Cl}_8]^{4+}$ clusters in a reactive cathode material. Also conceivable is the use of the isostructural MoI_2 (Mo_6I_{12}),

with a $[\text{Mo}_6\text{I}_8]^{4+}$ -core. Experiments in this direction are currently being performed in the group.

The presented apparatus for electrocrystallisation should be modified by adding a reference electrode. This enables direct measurement of electrode potentials *in situ*, in contrast to merely adjusting the terminal voltage. Electrochemical decomposition of DMF and onset of electrocrystallisation can thus be determined reliably, and electrochemical quantification of product formation would be possible. This is especially useful for multi-component electrolytes as the respective potentials have to be equilibrated with great precision.

Electrocrystallisation and distillation method for amalgam synthesis yield the mercury-richest amalgams under the respective synthesis conditions. Those amalgams have been shown to exhibit a plethora of structural features including mixed/ underoccupied positions and superstructures. Numerous amalgams of lanthanide metals with the approximate composition $RE\text{Hg}_{6.5}$ are reported, mainly on the basis of thermoanalytical data. The structures for $RE = \text{Eu}$ and Yb could be determined, it is likely that other structures can be elucidated by those means, too. Emphasis lies on synthesis at low temperatures as the compounds are increasingly sensitive.

Combining synthesis, NMR Knight shift measurements and *ab initio* calculations have been proven useful for the quantification of polarity in amalgams and polar intermetallics in general. This method has yet to be expanded over a lot more exemplary structures and to be combined with other methods, such as e.g. determination of the molar heat. However, solid state NMR on many metals is difficult due to usually high quadrupole moments (nuclear spin $I \geq 5/2$). Further complication is expected for studies on rare earth metal amalgams. NMR measurements are hampered by electronic and magnetic effects. Those may be overcome by a dilution series of amalgams on an inert substrate making magic angle spinning available even for metallic compounds, leading to narrow line widths and an overall improved signal-to-noise ratio. The support by *ab initio* calculations is also possible for all alkali and alkaline earth metal amalgams. Necessary relativistic corrections for Hg in combination with large unit cells and low symmetry make the calculations time and resource consuming. Calculations for rare earth metal amalgams are even more complicated. Parallelisation on supercomputing clusters combined with modified exchange correlation potentials and Hubbard U correction should be used for accurate modelling of (magnetically active) *f* electrons. To corroborate band structure calculations, a combination of XPS and XAFS is indicated to experimentally confirm the calculations.

A. Crystallographic Data

Crystallographic data for [Li(DMF)₄]I and [Na(DMF)₃]I

Table A.1.: Coefficients U_{ij} (pm²) of the anisotropic atomic displacement parameters for [Li(DMF)₄]I and [Na(DMF)₃]I. U_{ij} is defined as $\exp\{-2\pi^2[U_{11}(ha^*)^2+\dots+2U_{12}hka^*b^*]\}$. Standard deviations in units of the last digit are given in parentheses.

[Li(DMF) ₄]I						
Atom	U_{11}	U_{22}	U_{33}	U_{23}	U_{13}	U_{12}
I1	0.0962(3)	0.0950(2)	0.0792(2)	-0.0055(2)	0.00933(15)	0.0049(2)
O1	0.127(3)	0.101(2)	0.107(3)	0.014(2)	0.001(2)	0.032(2)
N1	0.075(2)	0.080(2)	0.069(2)	-0.0002(2)	0.004(2)	0.006(2)
C1	0.118(4)	0.110(4)	0.115(4)	0.018(3)	0.002(4)	0.023(3)
C2	0.111(4)	0.157(6)	0.081(3)	-0.015(3)	0.013(3)	0.023(4)
C3	0.098(3)	0.090(3)	0.074(3)	0.002(2)	0.013(3)	0.003(2)
O3	0.120(3)	0.096(2)	0.066(2)	-0.007(2)	0.018(2)	0.012(2)
N3	0.082(2)	0.076(2)	0.066(2)	-0.007(2)	0.011(2)	0.004(2)
C7	0.127(4)	0.081(3)	0.112(4)	-0.003(3)	0.019(3)	0.018(3)
C8	0.080(3)	0.075(2)	0.085(3)	-0.003(2)	0.014(2)	0.002(2)
C9	0.103(3)	0.114(4)	0.076(3)	-0.006(3)	0.016(3)	0.001(3)
O5	0.094(2)	0.154(4)	0.141(3)	0.002(3)	0.054(3)	-0.002(2)
N5	0.081(2)	0.084(2)	0.080(2)	-0.003(2)	0.024(2)	0.001(2)
C13	0.095(3)	0.093(3)	0.084(3)	0.008(2)	0.018(3)	-0.004(2)
C14	0.125(4)	0.122(4)	0.084(3)	0.006(3)	-0.007(3)	0.024(3)
C15	0.108(4)	0.164(6)	0.126(5)	-0.010(4)	0.059(4)	-0.002(4)
O7	0.084(2)	0.135(3)	0.068(2)	-0.002(2)	-0.008(2)	0.0006(2)
N7	0.074(2)	0.097(3)	0.065(2)	-0.008(2)	-0.001(2)	-0.002(2)
C22	0.077(3)	0.085(3)	0.076(3)	-0.007(2)	0.008(3)	0.004(2)
C23	0.112(4)	0.116(4)	0.069(2)	-0.010(2)	-0.001(3)	-0.001(3)
C24	0.077(3)	0.191(6)	0.088(3)	-0.007(4)	-0.001(3)	-0.006(3)
Li1	0.071(4)	0.102(5)	0.058(3)	0.000(3)	0.003(3)	0.010(3)
[Na(DMF) ₃]I						
Atom	U_{11}	U_{22}	U_{33}	U_{23}	U_{13}	U_{12}
N1	0.050(2)	0.0268(17)	0.056(2)	0	0	0.013(2)
C1	0.088(4)	0.034(2)	0.063(4)	0	0	0.026(2)
O1	0.039(2)	0.0422(13)	0.073(2)	0	0	0.0250(12)
C2	0.048(3)	0.045(3)	0.107(5)	0	0	0.012(2)
C3	0.041(2)	0.051(2)	0.036(2)	0	0	0.025(2)
I1	0.0615(2)	U_{11}	0.0540(3)	0	0	0.03074(11)
Na1	0.0362(5)	U_{11}	0.0483(12)	0	0	0.0181(3)

Table A.2.: Selected interatomic distances for [Li(DMF)₄]I [Å]. Standard deviations in units of the last digit are given in parentheses.

Atom 1	atom 2	distance [Å]	Atom 1	atom 2	distance [Å]	Atom 1	atom 2	distance [Å]			
O1	C3	1.221(2)	N3	O3	2.232(2)	C15	O5	3.540(2)			
	Li1	1.908(2)		N3	3.682(2)		C2	3.64(2)			
	N1	2.259(2)		C8	3.707(2)		C24	3.96(2)			
	C2	2.773(2)		O3	3.868(2)		O7	C22	1.217(2)		
	O3	3.026(2)		C7	3.878(2)		Li1	1.916(2)			
	O5	3.104(2)		C7	N3		1.439(2)	N7	2.242(2)		
	O7	3.204(6)			C8		2.413(2)	C24	2.769(2)		
	C8	3.211(2)			C9		2.467(2)	O5	3.085(2)		
	C1	3.557(2)			O3		2.755(2)	O3	3.152(2)		
C23	3.753(2)	C7	3.458(2)		O1	3.204(6)					
N1	C3	1.302(2)	C8	C8	3.637(2)	C23	C23	3.548(2)			
	C2	1.422(2)		C3	3.673(2)		C9	3.552(2)			
	C1	1.440(2)		N3	3.878(2)		C23	3.691(2)			
	O1	2.259(2)		C23	3.962(2)		C23	3.830(2)			
	O3	3.723(2)		O3	3.990(2)		N7	3.863(2)			
	Li1	3.937(2)		C9	O3		1.211(2)	N7	3.864(2)		
	C1	3.971(2)			N3		1.322(2)	C13	3.960(2)		
	C1	N1			1.440(2)		C9	2.404(2)	N7	C22	1.313(2)
		C3			2.398(2)		C7	2.413(2)		C23	1.439(2)
C2		2.446(2)	Li1		2.826(2)	C24	1.452(2)				
O1		3.557(2)	O1	3.211(2)	O7	2.242(2)					
C14		3.646(2)	C7	3.637(2)	C22	3.707(2)					
O3		3.699(2)	N3	3.707(2)	C22	3.755(2)					
C8		3.733(2)	C1	3.733(2)	N7	3.834(2)					
C1		3.74(2)	C3	3.872(2)	N7	3.834(2)					
N1		3.971(2)	C9	N3	1.443(2)	O7	3.863(2)				
C2	N1	1.422(2)		C8	2.404(2)	O7	3.864(2)				
	C3	2.368(2)		C7	2.467(2)	C22	O7	1.217(2)			
	C1	2.446(2)		O3	3.536(2)		N7	1.313(2)			
	O1	2.773(2)		O7	3.552(2)		C23	2.406(2)			
	O5	3.575(2)	C24	3.663(2)	C24		2.410(2)				
	C15	3.64(2)	O3	3.755(2)	Li1		2.878(2)				
	C13	3.848(2)	O5	C13	1.205(2)		O5	3.447(2)			
	C24	3.931(2)		Li1	1.892(2)		C24	3.67(2)			
	C3	Li1		3.99(2)	N5		2.237(2)	N7	3.707(2)		
O1		1.221(2)		C14	2.768(2)		N7	3.755(2)			
N1		1.302(2)		O7	3.085(2)	C24	3.88(2)				
C2		2.368(2)	O1	3.104(2)	C23	N7	1.439(2)				
C1		2.398(2)	O3	3.197(2)		C22	2.406(2)				
Li1		3.065(2)	C22	3.447(2)		C24	2.465(2)				
C7		3.673(2)	C15	3.540(2)		O3	3.541(2)				
C8		3.872(2)	C2	3.575(2)		O7	3.548(2)				
O5		3.916(2)	C3	3.916(2)		O7	3.691(2)				
O3	3.974(2)	N5	C13	1.313(2)		O1	3.753(2)				
O3	C8		1.211(2)	C14		1.421(2)	O7	3.830(2)			
	Li1		1.948(2)	C15		1.445(2)	C7	3.962(2)			
	N3		2.232(2)	O5	2.237(2)	C24	N7	1.452(2)			
	C7		2.755(2)	C13	O5		1.205(2)	C22	2.410(2)		
	O1	3.026(2)	N5		1.313(2)		C23	2.465(2)			
	O7	3.152(2)	C14		2.391(2)		O7	2.769(2)			
	O5	3.197(2)	C15		2.40(2)		C9	3.663(2)			
	C9	3.536(2)	Li1		3.04(2)		C22	3.67(2)			
	C23	3.541(2)	C2		3.848(2)		C22	3.88(2)			
C1	3.699(2)	O7	3.960(2)		C2		3.931(2)				
N1	3.723(2)	C14	N5		1.421(2)		C15	3.96(2)			
C9	3.755(2)		C13		2.391(2)	Li1	O5	1.892(2)			

N3	N3	3.868(2)	C15	C15	2.44(2)	O1	O1	1.908(2)
	C3	3.974(2)		O5	2.768(2)		O7	1.916(2)
	C7	3.990(2)		C1	3.646(2)		O3	1.948(2)
	C8	1.322(2)		N5	1.445(2)		C8	2.826(2)
	C7	1.439(2)		C13	2.40(2)		C22	2.878(2)
	C9	1.443(2)		C14	2.44(2)		C13	3.04(2)

Table A.3.: Selected angles for $[\text{Li}(\text{DMF})_4]\text{I}$ [$^\circ$]. Standard deviations in units of the last digit are given in parentheses.

Atom 1	atom 2	atom 3	angle [$^\circ$]	Atom 1	atom 2	atom 3	angle [$^\circ$]	
O1	Li1	O3	38.790	O5	O7	O1	62.341	
	Li1	O5	35.063		O7	O3	60.196	
	Li1	O7	33.187		O1	O3	57.385	
	O3	O3	O5	62.853	O7	Li1	O5	35.616
		O3	O7	60.711		Li1	O3	35.699
O5		O7	58.550	Li1		O1	33.029	
Li1		O1	37.843	O5		O3	61.653	
Li1		O7	35.021	O5		O1	59.110	
O5	Li1	O5	33.093	Li1	O3	O1	56.860	
	O1	O7	62.429		O5	O1	109.527	
	O1	O5	59.763		O5	O7	108.236	
	O7	O5	58.151		O5	O3	112.688	
	Li1	O7	36.148		O1	O7	113.784	
O5	Li1	O1	35.410	O1	O3	103.368		
	Li1	O3	34.219	O7	O3	109.280		

Table A.4.: Selected interatomic distances for $[\text{Na}(\text{DMF})_3]\text{I}$ [\AA]. Standard deviations in units of the last digit are given in parentheses.

Atom 1	atom 2	distance [\AA]	Atom 1	atom 2	distance [\AA]	Atom 1	atom 2	distance [\AA]			
N1	C3	1.318(4)	O1	O1	3.3650(8)	C3	Na1	3.415(4)			
	C2	1.439(8)		O1	3.3650(8)		Na1	3.415(4)			
	C1	1.442(7)		C2	3.499(6)		O1	3.556(2)			
	O1	2.275(3)		C3	3.556(2)		O1	3.556(2)			
	C3	3.377(2)		C3	3.556(2)		C2	3.739(3)			
	C3	3.377(2)		C1	3.574(7)		C2	3.739(3)			
	N1	3.681(2)		N1	3.798(2)		C1	3.927(4)			
	N1	3.681(2)		N1	3.798(2)		C1	3.927(4)			
	O1	3.798(2)		C2	3.871(2)		Na1	O1	2.432(2)		
	O1	3.798(2)		C2	3.871(2)			O1	2.432(2)		
	C1	C1		3.963(4)	C2			N1	1.439(8)	O1	2.432(2)
		C1		3.963(4)				C3	2.400(6)	O1	2.432(2)
	C1	N1		1.442(7)				C1	2.469(9)	O1	2.432(2)
		C3		2.404(5)				O1	2.794(4)	O1	2.432(2)
C2		2.469(9)	O1	3.499(6)		Na1		3.2631(4)			
C2		3.573(8)	C1	3.573(6)		Na1		3.2631(4)			
O1		3.574(5)	C3	3.739(3)		C3		3.415(4)			
C1		3.702(3)	C3	3.739(3)		C3		3.415(3)			
C1		3.702(3)	O1	3.871(2)		C3		3.415(4)			
C3		3.927(3)	O1	3.871(2)		C3		3.415(3)			
C3		3.927(3)	Na1	3.983(4)		C3		3.415(4)			
O1		N1	3.963(2)	Na1		3.983(4)		C3	3.415(4)		
		N1	3.963(2)	C3		O1	1.236(6)	C2	3.983(5)		
		C3	1.236(6)			N1	1.318(6)	C2	3.983(4)		
		N1	2.275(5)		C2	2.400(6)	C2	3.983(4)			
		Na1	2.432(2)		C1	2.404(8)	C2	3.983(6)			
	Na1	2.432(2)	C3		3.313(2)	C2	3.983(6)				

C2	2.794(7)	C3	3.313(2)	C2	3.983(5)
O1	3.124(2)	N1	3.377(2)		
O1	3.124(4)	N1	3.377(2)		

Table A.5.: Selected angles for $[\text{Na}(\text{DMF})_3]\text{I}$ [$^\circ$]. Standard deviations in units of the last digit are given in parentheses.

Atom 1	atom 2	atom 3	angle [$^\circ$]	Atom 1	atom 2	atom 3	angle [$^\circ$]
O1	Na1	Na1	84.250(2)	Na1	O1	O1	155.187(2)
	Na1	O1	50.035(3)		O1	O1	119.025(2)
	Na1	O1	50.035(3)		O1	O1	87.527(2)
	Na1	O1	127.533(1)		O1	O1	79.929(3)
	Na1	O1	46.236(1)		O1	Na1	47.875(1)
	Na1	O1	50.035(3)		O1	Na1	132.125(1)
	Na1	O1	50.035(3)		O1	O1	79.929(3)
	Na1	O1	46.236(1)		O1	O1	79.929(3)
	Na1	O1	127.533(1)		O1	O1	87.527(2)
	O1	O1	60.000(8)		O1	Na1	132.125(1)
	O1	O1	80.386(3)		O1	Na1	47.875(1)
	O1	O1	80.386(3)		O1	O1	79.929(3)
	O1	O1	94.056(6)		O1	O1	155.187(2)
	O1	O1	94.056(6)		O1	Na1	132.125(1)
Na1	O1	O1	151.736(1)	O1	Na1	47.875(1)	
	O1	O1	79.929(3)	O1	O1	119.025(2)	
	O1	O1	119.025(2)	O1	Na1	132.125(1)	
	O1	O1	87.527(2)	O1	Na1	47.875(1)	
	O1	O1	155.187(2)	O1	Na1	47.875(1)	
	O1	O1	79.929(3)	O1	Na1	132.125(1)	
	O1	Na1	47.875(1)	Na1	Na1	180.000	
	O1	Na1	132.125(1)				

Crystallographic data for [La(DMF)₉]I₃

Table A.6.: Selected interatomic distances for [La(DMF)₉]I₃ [Å]. Standard deviations in units of the last digit are given in parentheses.

Atom 1	atom 2	distance [Å]	Atom 1	atom 2	distance [Å]	Atom 1	atom 2	distance [Å]
La1	O17	2.324(2)	La1	O19	2.529(2)	La2	O26	2.481(2)
	O16	2.425(2)		O15	2.540(2)		O21	2.513(2)
	O11	2.498(2)		O18	2.550(2)		O29	2.514(2)
	O12	2.511(2)	La2	O25	2.412(2)		O23	2.516(2)
	O13	2.517(2)		O22	2.424(2)		O27	2.536(2)
O14	2.520(2)	O28	2.464(2)	O24	2.617(2)			

Table A.7.: Selected angles for [La(DMF)₉]I₃ [°]. Standard deviations in units of the last digit are given in parentheses.

Atom 1	atom 2	atom 3	angle [°]	Atom 1	atom 2	atom 3	angle [°]
La1	O17	O16	85.8(2)	La2	O25	O22	77.8(2)
	O17	O11	132.8(2)		O25	O28	138.3(2)
	O17	O12	141.9(2)		O25	O26	79.8(2)
	O17	O13	136.9(2)		O25	O21	73.3(2)
	O17	O14	73.8(2)		O25	O29	140.7(2)
	O17	O19	71.1(2)		O25	O23	136.5(2)
	O17	O15	71.0(2)		O25	O27	84.8(2)
	O17	O18	73.7(2)		O25	O24	68.6(2)
	O16	O11	141.0(2)		O22	O28	70.0(2)
	O16	O12	73.0(2)		O22	O26	75.2(2)
	O16	O13	83.2(2)		O22	O21	136.1(2)
	O16	O14	138.0(2)		O22	O29	139.1(2)
	O16	O19	135.8(2)		O22	O23	87.3(2)
	O16	O15	69.8(2)		O22	O27	137.6(2)
	O16	O18	69.1(2)		O22	O24	69.5(2)
	O11	O12	71.9(2)		O28	O26	67.0(2)
	O11	O13	70.5(2)		O28	O21	113.2(2)
	O11	O14	70.3(2)		O28	O29	69.8(2)
	O11	O19	69.0(2)		O28	O23	68.5(2)
	O11	O15	120.5(2)		O28	O27	136.8(2)
O11	O18	112.5(2)	O28	O24	120.5(2)		
O12	O13	72.4(2)	O26	O21	67.6(2)		
O12	O14	141.3(2)	O26	O29	96.0(2)		
O12	O19	102.6(2)	O26	O23	135.4(2)		
O12	O15	126.3(2)	O26	O27	139.0(2)		
O12	O18	69.3(2)	O26	O24	136.5(2)		
O13	O14	87.1(2)	O21	O29	69.1(2)		
O13	O19	138.6(2)	O21	O23	135.8(2)		
O13	O15	66.0(2)	O21	O27	71.6(2)		
O13	O18	137.8(2)	O21	O24	126.1(2)		
O14	O19	71.3(2)	O29	O23	70.9(2)		
O14	O15	68.9(2)	O29	O27	72.9(2)		
O14	O18	134.5(2)	O29	O24	127.2(2)		
O19	O15	130.9(2)	O23	O27	79.2(2)		
O19	O18	68.48(59)	O23	O24	67.9(2)		
O15	O18	126.8(2)	O27	O24	68.1(2)		

Crystallographic data for $[RE(DMF)_8]I_3$ with $RE = Sm, Gd, Er, Yb$

Table A.8.: Coefficients $U_{ij} / \text{\AA}^2$ of the anisotropic atomic displacement parameters for $[Sm(DMF)_8]I_3$, $[Gd(DMF)_8]I_3$, $[Er(DMF)_8]I_3$ and $[Yb(DMF)_8]I_3$. U_{ij} is defined as $\exp\{-2\pi^2[U_{11}(ha^*)^2 + \dots + 2U_{12}hka^*b^*]\}$. Standard deviations in units of the last digit are given in parentheses.

Atom	U_{11}	U_{22}	U_{33}	U_{23}	U_{13}	U_{12}
Sm1	0.0593(6)	0.0490(4)	0.0475(5)	0	0.0123(4)	0
Gd1	0.02900(8)	0.03278(8)	0.02466(8)	0	0.00586(5)	0
Er1	0.02995(12)	0.02975(12)	0.02397(13)	0	0.00534(8)	0
Yb1	0.0378(3)	0.0316(3)	0.0244(2)	0	0.01093(16)	0
I1	0.1037(9)	0.0882(7)	0.0835(8)	-0.0027(5)	0.0229(6)	-0.0115(6)
	0.0707(2)	0.0754(2)	0.0586(2)	-0.00191(14)	0.01635(13)	-0.01276(14)
	0.0692(2)	0.0694(2)	0.0566(2)	-0.00179(14)	0.01532(14)	-0.01141(14)
	0.0781(5)	0.0704(5)	0.0565(4)	-0.0013(3)	0.0223(3)	-0.0110(3)
I2	0.0937(11)	0.0819(9)	0.0648(9)	0	0.0142(7)	0
	0.0672(2)	0.0641(2)	0.04405(17)	0	0.0103(2)	0
	0.0661(2)	0.0596(2)	0.0423(2)	0	0.0092(2)	0
	0.0732(6)	0.0631(6)	0.0416(4)	0	0.0153(4)	0
O1	0.113(8)	0.070(5)	0.073(6)	-0.028(5)	0.051(6)	0.002(5)
	0.081(2)	0.0474(13)	0.059(2)	-0.0130(12)	0.0353(15)	0.0041(12)
	0.072(2)	0.0419(13)	0.049(2)	-0.0095(12)	0.0281(14)	0.0034(12)
	0.080(4)	0.041(3)	0.051(3)	-0.011(3)	0.033(3)	0.000(3)
O2	0.120(9)	0.065(5)	0.056(6)	0.013(4)	0.001(6)	0.018(5)
	0.073(2)	0.0455(12)	0.0461(14)	0.0143(11)	0.0035(12)	0.0115(12)
	0.069(2)	0.0422(13)	0.039(2)	0.0107(11)	0.0032(13)	0.0098(12)
	0.081(4)	0.042(3)	0.034(3)	0.009(2)	0.010(3)	0.006(3)
C1	0.056(8)	0.055(6)	0.078(10)	0.022(6)	-0.001(7)	-0.004(6)
	0.053(2)	0.041(2)	0.050(2)	0.0072(14)	0.001(2)	-0.0019(13)
	0.049(2)	0.035(2)	0.049(3)	0.005(2)	0.001(2)	-0.006(2)
	0.056(5)	0.039(5)	0.046(5)	0.005(4)	0.007(4)	-0.002(4)
C2	0.073(9)	0.050(6)	0.089(10)	-0.015(6)	0.026(8)	0.002(6)
	0.052(2)	0.0394(14)	0.046(2)	-0.0084(13)	0.0160(14)	-0.0034(13)
	0.048(2)	0.038(2)	0.043(2)	-0.006(2)	0.010(2)	-0.003(2)
	0.053(5)	0.041(5)	0.041(4)	-0.008(3)	0.019(4)	-0.002(4)
N1	0.076(7)	0.055(5)	0.054(6)	-0.001(4)	0.014(6)	0.007(5)
	0.057(2)	0.0414(13)	0.0364(13)	-0.0037(11)	0.0125(12)	0.0053(11)
	0.056(2)	0.038(2)	0.035(2)	-0.0064(12)	0.0108(14)	0.0032(13)
	0.068(4)	0.041(4)	0.035(3)	-0.003(3)	0.020(3)	0.006(3)
N2	0.094(9)	0.062(6)	0.060(7)	0.008(5)	0.011(6)	0.005(6)
	0.064(2)	0.0490(15)	0.0433(15)	0.0134(13)	0.0044(13)	0.0102(13)
	0.063(2)	0.047(2)	0.040(2)	0.0116(14)	0.007(2)	0.011(2)
	0.071(5)	0.047(4)	0.038(3)	0.013(3)	0.011(3)	0.012(4)
O3	0.071(7)	0.089(6)	0.091(8)	0.007(5)	0.037(6)	0.020(5)
	0.0516(14)	0.068(2)	0.054(2)	0.004(2)	0.0266(12)	0.0140(12)
	0.048(2)	0.060(2)	0.049(2)	0.0063(13)	0.0218(13)	0.0111(12)
	0.051(3)	0.058(4)	0.045(3)	0.007(3)	0.028(3)	0.013(3)
C3	0.118(13)	0.059(7)	0.073(10)	-0.001(6)	0.021(9)	0.004(8)
	0.075(3)	0.056(2)	0.053(2)	0.0050(18)	0.012(2)	0.011(2)
	0.076(3)	0.047(2)	0.050(3)	0.0034(19)	0.012(2)	0.011(2)
	0.084(7)	0.043(5)	0.050(5)	0.004(4)	0.017(5)	0.013(5)
O4	0.088(8)	0.083(6)	0.080(7)	0.002(5)	-0.006(6)	0.008(6)
	0.053(2)	0.082(2)	0.051(2)	-0.004(2)	-0.0134(12)	0.0198(14)
	0.051(2)	0.068(2)	0.047(2)	-0.0050(14)	-0.0098(13)	0.0166(14)
	0.052(4)	0.064(4)	0.042(3)	-0.005(3)	-0.007(3)	0.013(3)
C4	0.076(10)	0.067(7)	0.075(9)	-0.021(6)	0.050(8)	-0.012(7)
	0.045(2)	0.048(2)	0.041(2)	-0.0072(13)	0.0168(13)	-0.0059(13)
	0.048(2)	0.040(2)	0.038(2)	-0.007(2)	0.011(2)	-0.007(2)
	0.057(5)	0.037(4)	0.038(4)	-0.010(3)	0.019(4)	-0.011(4)

C5	0.071(9)	0.050(6)	0.082(10)	0.013(6)	0.018(8)	-0.005(6)
	0.050(2)	0.044(2)	0.043(2)	0.0089(13)	-0.0011(14)	-0.0033(13)
	0.050(2)	0.035(2)	0.043(2)	0.0010(2)	-0.001(2)	-0.005(2)
	0.063(6)	0.033(4)	0.042(4)	0.003(3)	0.010(4)	-0.013(4)
N3	0.061(7)	0.065(6)	0.056(7)	0.002(5)	0.016(5)	0.001(5)
	0.0400(13)	0.0487(14)	0.0410(14)	-0.0021(11)	0.0143(11)	-0.0028(11)
	0.038(2)	0.045(2)	0.038(2)	-0.0017(13)	0.0118(13)	0.0005(12)
N4	0.044(4)	0.045(4)	0.039(3)	0.001(3)	0.018(3)	-0.002(3)
	0.058(7)	0.076(6)	0.065(8)	0.019(5)	-0.002(6)	0.000(5)
	0.0403(13)	0.053(2)	0.0417(14)	0.0096(12)	-0.0037(11)	0.0003(11)
	0.042(2)	0.047(2)	0.039(2)	0.0073(13)	-0.0023(14)	0.0010(13)
C6	0.045(4)	0.050(4)	0.037(3)	0.005(3)	0.000(3)	0.000(3)
	0.067(9)	0.128(12)	0.062(9)	0.011(8)	0.010(8)	0.013(9)
	0.048(2)	0.084(3)	0.063(2)	0.017(2)	-0.001(2)	0.012(2)
	0.048(2)	0.083(3)	0.061(3)	0.016(2)	0.000(2)	0.012(2)
C7	0.059(6)	0.089(8)	0.058(6)	0.018(5)	0.005(5)	0.005(5)
	0.072(10)	0.115(12)	0.093(12)	-0.006(9)	0.027(9)	0.003(9)
	0.040(2)	0.103(3)	0.061(2)	0.001(2)	0.009(2)	0.006(2)
C8	0.041(2)	0.096(3)	0.057(3)	0.000(2)	0.009(2)	0.005(2)
	0.053(6)	0.094(8)	0.063(6)	0.006(6)	0.019(5)	0.001(5)
	0.113(14)	0.086(9)	0.085(12)	0.013(8)	0.035(10)	0.024(9)
	0.066(2)	0.080(3)	0.057(2)	0.017(2)	0.033(2)	0.013(2)
C9	0.064(3)	0.074(3)	0.054(3)	0.015(2)	0.031(2)	0.013(2)
	0.081(7)	0.071(6)	0.052(5)	0.013(5)	0.038(5)	0.017(5)
	0.092(12)	0.098(10)	0.082(12)	0.000(8)	0.004(10)	0.017(9)
	0.072(3)	0.077(3)	0.051(2)	-0.013(2)	-0.008(2)	0.003(2)
C10	0.071(3)	0.070(3)	0.048(3)	-0.010(2)	-0.008(2)	0.006(2)
	0.087(7)	0.071(6)	0.046(5)	-0.014(5)	-0.004(5)	0.006(6)
	0.17(2)	0.117(13)	0.084(13)	0.031(10)	0.033(13)	0.067(14)
	0.179(8)	0.125(6)	0.085(4)	0.038(4)	0.053(5)	0.102(5)
C11	0.172(7)	0.099(4)	0.076(5)	0.034(3)	0.045(5)	0.088(5)
	0.158(13)	0.108(11)	0.071(8)	0.025(7)	0.046(8)	0.079(10)
	0.15(2)	0.077(9)	0.074(11)	-0.012(8)	0.043(11)	-0.009(10)
	0.104(4)	0.066(2)	0.045(2)	-0.011(2)	0.030(2)	0.013(2)
C12	0.099(4)	0.058(2)	0.042(3)	-0.009(2)	0.026(2)	0.010(2)
	0.102(8)	0.061(6)	0.041(5)	-0.014(4)	0.033(5)	0.007(6)
	0.106(13)	0.104(10)	0.055(9)	0.024(8)	0.011(9)	0.000(9)
	0.084(3)	0.070(3)	0.047(2)	0.017(2)	0.006(2)	0.008(2)
	0.087(3)	0.062(3)	0.046(3)	0.016(2)	0.006(2)	0.006(2)
	0.087(7)	0.063(6)	0.046(5)	0.012(4)	0.010(5)	-0.003(5)

Crystallographic data for [Sc(DMF)₆](I₃)₃

Table A.9.: Coefficients U_{ij} (\AA^2) of the anisotropic atomic displacement parameters for [Sc(DMF)₆](I₃)₃. U_{ij} is defined as $\exp\{-2\pi^2[U_{11}(ha^*)^2 + \dots + 2U_{12}hka^*b^*]\}$. Standard deviations in units of the last digit are given in parentheses.

Atom	U_{11}	U_{22}	U_{33}	U_{23}	U_{13}	U_{12}
Sc1	0.071(2)	0.056(2)	0.077(2)	0.001(2)	-0.010(2)	0.006(2)
I1	0.1389(13)	0.1190(12)	0.1004(10)	0.0007(9)	0.0209(9)	0.0051(10)
I2	0.1117(11)	0.1021(11)	0.1372(13)	0.0010(10)	-0.0199(9)	0.0018(9)
I3	0.1155(10)	0.0683(8)	0.0846(8)	0.0012(7)	-0.0033(7)	-0.0089(7)
I4	0.1194(12)	0.1266(13)	0.1194(11)	0.0123(10)	0.0205(9)	-0.0163(10)
I5	0.159(2)	0.254(3)	0.272(3)	0.049(2)	0.072(2)	0.026(2)
I6	0.0975(10)	0.0989(11)	0.190(2)	0.0336(11)	-0.0378(10)	-0.0157(8)
I7	0.332(4)	0.201(2)	0.176(2)	-0.022(2)	0.005(2)	0.048(2)
I8	0.156(2)	0.1128(12)	0.1416(13)	0.0205(11)	0.0075(11)	0.0032(11)
I9	0.1337(11)	0.0767(9)	0.0925(9)	-0.0014(8)	-0.0208(8)	0.0076(8)
O4	0.100(9)	0.071(8)	0.075(8)	-0.009(7)	-0.006(7)	0.009(6)
O3	0.079(8)	0.093(8)	0.089(9)	0.000(7)	0.010(7)	0.032(7)
O2	0.098(9)	0.073(8)	0.109(9)	0.002(8)	0.004(7)	-0.014(7)
O6	0.089(9)	0.128(11)	0.093(9)	0.020(8)	0.020(8)	0.010(8)
O5	0.086(8)	0.083(8)	0.086(9)	-0.005(7)	-0.012(7)	-0.015(6)
O1	0.103(9)	0.062(7)	0.081(8)	-0.002(7)	-0.019(6)	0.002(7)

Table A.10.: Selected interatomic distances for [Sc(DMF₆)(I₃)₃] [\AA]. Standard deviations in units of the last digit are given in parentheses.

Atom 1	atom 2	distance [\AA]	Atom 1	atom 2	distance [\AA]	Atom 1	atom 2	distance [\AA]
Sc1	O6	2.024(2)	I8	I9	2.902(2)	O2	O5	2.947(2)
	O3	2.048(2)		I7	3.967(3)	O6	Sc1	2.024(2)
	O2	2.083(2)	I9	I8	2.902(2)		O4	2.898(2)
	O4	2.086(2)		I2	2.944(2)	O2	O2	2.939(2)
	O1	2.088(2)	O4	Sc1	2.086(2)	O1	O1	2.971(2)
	O5	2.096(2)		O3	2.866(2)		O5	2.994(2)
I1	I3	2.948(2)		O6	2.898(2)	O5	Sc1	2.096(2)
I2	I9	2.944(2)		O2	2.925(2)		O3	2.914(2)
I3	I4	2.916(2)		O1	2.970(2)		O2	2.947(2)
	I1	2.948(2)	O3	Sc1	2.048(2)		O1	2.968(2)
I4	I3	2.916(2)		O2	2.853(2)		O6	2.994(2)
	I5	3.912(3)		O4	2.866(2)	O1	Sc1	2.088(2)
I5	I6	2.896(3)		O1	2.894(2)		O3	2.894(2)
	I4	3.912(3)		O5	2.914(2)		O5	2.968(2)
I6	I5	2.896(3)	O2	Sc1	2.083(2)		O4	2.970(2)
	I7	2.926(3)		O3	2.853(2)		O6	2.971(2)
I7	I6	2.926(3)		O4	2.925(2)			
	I8	3.967(3)		O6	2.939(2)			

Table A.11.: Selected angles for [Sc(DMF₆)(I₃)₃] [$^\circ$]. Standard deviations in units of the last digit are given in parentheses.

Atom 1	atom 2	atom 3	angle [$^\circ$]	Atom 1	atom 2	atom 3	angle [$^\circ$]
Sc1	O6	O3	177.1(4)	O3	O1	O5	61.4(3)
	O6	O2	91.3(4)	O2	Sc1	O3	45.7(3)
	O6	O4	89.6(4)		Sc1	O4	45.4(3)
	O6	O1	92.4(4)		Sc1	O6	43.5(3)
	O6	O5	93.1(4)		Sc1	O5	45.3(3)
	O3	O2	87.3(4)		O3	O4	59.4(3)
	O3	O4	87.7(4)		O3	O6	89.2(4)
	O3	O1	88.7(4)		O3	O5	60.2(3)
	O3	O5	89.3(4)		O4	O6	59.2(3)
	O2	O4	89.0(4)		O4	O5	90.8(4)
	O2	O1	176.1(4)		O6	O5	61.1(4)

Sc1	O2	O5	89.6(4)	O6	Sc1	O4	46.1(2)
	O4	O1	90.7(4)		Sc1	O2	45.1(3)
	O4	O5	176.9(4)		Sc1	O1	44.6(3)
	O1	O5	90.3(4)		Sc1	O5	44.3(3)
I3	I4	I1	178.19(6)	O4	O2	60.1(3)	
I4	I3	I5	157.29(6)	O4	O1	60.8(3)	
I5	I6	I4	130.72(8)	O4	O5	90.3(4)	
I6	I5	I7	177.07(9)	O2	O1	89.7(4)	
I7	I6	I8	153.52(9)	O2	O5	59.5(4)	
I8	I9	I7	172.78(7)	O1	O5	59.6(3)	
I9	I8	I2	178.57(7)	O5	Sc1	O3	44.6(3)
O4	Sc1	O3	45.5(3)		Sc1	O2	44.9(3)
	Sc1	O6	44.3(3)		Sc1	O1	44.7(3)
	Sc1	O2	45.4(3)		Sc1	O6	42.4(3)
	Sc1	O1	44.66(2)		O3	O2	58.2(3)
	O3	O6	89.8(4)		O3	O1	58.9(3)
	O3	O2	59.0(3)		O3	O6	87.0(4)
	O3	O1	59.4(3)		O2	O1	89.6(4)
	O6	O2	60.6(3)		O2	O6	59.2(3)
	O6	O1	60.8(3)		O1	O6	59.7(3)
	O2	O1	90.0(4)	O1	Sc1	O3	45.0(3)
O3	Sc1	O2	46.8(3)		Sc1	O5	44.9(3)
	Sc1	O4	46.6(3)		Sc1	O4	44.60(2)
	Sc1	O1	46.1(3)		Sc1	O6	42.9(3)
	Sc1	O5	45.9(3)		O3	O5	59.6(3)
	O2	O4	61.5(3)		O3	O4	58.4(3)
	O2	O1	93.0(4)		O3	O6	87.9(4)
	O2	O5	61.4(3)		O5	O4	89.5(4)
	O4	O1	62.0(3)		O5	O6	60.5(3)
	O4	O5	92.6(4)		O4	O6	58.3(3)

Crystallographic data for [Zn(DMF)₂I₂]

Table A.12.: Coefficients U_{ij} (\AA^2) of the anisotropic atomic displacement parameters for [Zn(DMF)₂I₂]. U_{ij} is defined as $\exp\{-2\pi^2[U_{11}(ha^*)^2 + \dots + 2U_{12}hka^*b^*]\}$. Standard deviations in units of the last digit are given in parentheses.

Atom	U_{11}	U_{22}	U_{33}	U_{23}	U_{13}	U_{12}
Zn1	0.0656(3)	0.0539(4)	0.0647(3)	-0.0030(3)	0.0331(3)	-0.0005(3)
I1	0.0780(3)	0.1044(4)	0.0764(3)	-0.0162(2)	0.0116(2)	0.0034(2)
I2	0.0897(3)	0.0589(2)	0.0882(3)	-0.0075(2)	0.0312(2)	-0.0100(2)
C1	0.148(6)	0.107(6)	0.123(6)	-0.015(5)	0.093(5)	-0.014(5)
C2	0.289(14)	0.077(6)	0.31(2)	0.040(7)	0.241(14)	0.014(7)
C3	0.092(4)	0.075(4)	0.091(4)	0.015(3)	0.052(3)	0.012(3)
N1	0.110(4)	0.078(3)	0.108(4)	0.019(3)	0.076(3)	0.007(3)
O1	0.104(3)	0.064(3)	0.102(3)	0.003(2)	0.067(2)	-0.003(2)
C4	0.099(4)	0.078(4)	0.100(5)	-0.032(4)	0.040(4)	-0.021(4)
C5	0.058(3)	0.061(3)	0.072(3)	-0.003(3)	0.028(2)	-0.002(2)
C6	0.101(5)	0.117(6)	0.147(7)	-0.051(5)	0.053(5)	0.024(4)
O2	0.060(2)	0.058(2)	0.079(2)	-0.012(2)	0.031(2)	0.005(2)
N2	0.068(2)	0.058(3)	0.062(2)	-0.010(2)	0.030(2)	0.002(2)

Table A.13.: Selected interatomic distances for $[\text{Zn}(\text{DMF})_2\text{I}_2]$ [Å]. Standard deviations in units of the last digit are given in parentheses.

Atom 1	atom 2	distance [Å]	Atom 1	atom 2	distance [Å]	Atom 1	atom 2	distance [Å]
Zn1	O1	1.994(2)	C3	N1	1.300(2)	C5	O2	1.238(2)
	O2	2.001(2)		C1	2.37(2)		N2	1.288(2)
	I2	2.5284(7)		C2	2.43(2)		C4	2.378(2)
	I1	2.5383(9)		Zn1	2.875(2)		C6	2.40(2)
	C3	2.875(2)		O2	3.302(2)		Zn1	2.882(2)
I1	C5	2.882(2)	N1	N1	3.675(2)	C6	I1	3.765(2)
	Zn1	2.5383(9)		C1	3.869(2)		C4	3.84(2)
	O2	3.687(2)		C3	3.913(7)		I2	3.892(2)
	O1	3.690(2)		C2	3.92(2)		N2	1.473(2)
	C5	3.765(2)		I2	3.974(2)		C5	2.40(2)
I2	C2	3.796(2)	O1	C3	1.300(2)	O2	C4	2.487(2)
	C4	3.875(2)		C1	1.41(2)		O2	3.581(2)
	Zn1	2.5284(7)		C2	1.47(2)		I2	3.865(2)
	O1	3.642(2)		O1	2.224(2)		O1	3.957(2)
	O2	3.700(2)		C3	3.675(2)		C5	1.238(2)
C1	C6	3.865(2)	C4	N1	3.819(2)	N2	Zn1	2.001(2)
	C5	3.892(2)		C3	1.200(2)		N2	2.246(2)
	C3	3.974(2)		Zn1	1.994(2)		C4	2.763(2)
	N1	1.41(2)		N1	2.224(2)		O1	3.070(2)
	C3	2.37(2)		C1	2.75(2)		C3	3.302(2)
C2	C2	2.46(2)	C4	O2	3.070(2)	C4	C6	3.581(2)
	O1	2.75(2)		C2	3.56(2)		I1	3.687(2)
	O1	3.808(2)		I2	3.642(2)		I2	3.700(2)
	O2	3.814(2)		I1	3.690(2)		C1	3.814(2)
	C3	3.869(2)		C1	3.808(2)		C5	1.288(2)
C3	N1	1.47(2)	C4	C6	3.957(2)	C4	C4	1.440(2)
	C3	2.43(2)		N2	1.440(2)		C6	1.473(2)
	C1	2.46(2)		C5	2.378(2)		O2	2.246(2)
	O1	3.56(2)		C6	2.487(2)		C4	3.914(2)
	I1	3.796(2)		O2	2.763(2)			
C3	C2	3.86(2)		C5	3.84(2)			
	C3	3.92(2)		I1	3.875(2)			
	O1	1.200(2)		N2	3.914(2)			

Table A.14.: Selected angles for $[\text{Zn}(\text{DMF})_2\text{I}_2]$ [°]. Standard deviations in units of the last digit are given in parentheses.

Atom 1	atom 2	atom 3	angle [°]	Atom 1	atom 2	atom 3	angle [°]
Zn1	O1	O2	100.3(2)	O1	Zn1	O2	39.8(2)
	O1	I2	106.6(2)		Zn1	I2	41.67(2)
	O1	I1	108.4(2)		Zn1	I1	40.73(2)
	O2	I2	109.00(2)		O2	I2	66.26(2)
	O2	I1	108.07(2)		O2	I1	65.3(2)
	I2	I1	122.10(2)		I2	I1	74.39(2)
I1	Zn1	O2	31.05(2)	O2	Zn1	O1	39.72(2)
	Zn1	O1	30.84(2)		Zn1	I1	40.87(2)
	O2	O1	49.17(2)		Zn1	I2	40.24(2)
I2	Zn1	O1	31.63(2)	O1	I1	I1	65.4(2)
	Zn1	O2	30.75(2)		O1	I2	64.31(2)
	O1	O2	49.42(2)		I1	I2	73.75(2)

Crystallographic data for [CdI₄][Cd(DMF)₆]

Table A.15.: Coefficients U_{ij} (\AA^2) of the anisotropic atomic displacement parameters for [CdI₄][Cd(DMF)₆]. U_{ij} is defined as $\exp\{-2\pi^2[U_{11}(ha^*)^2+\dots+2U_{12}hka^*b^*]\}$. Standard deviations in units of the last digit are given in parentheses.

Atom	U_{11}	U_{22}	U_{33}	U_{23}	U_{13}	U_{12}
I1	0.01145(11)	0.01720(13)	0.01339(12)	0.00707(8)	0.00155(9)	-0.00226(7)
I2	0.01656(13)	0.01462(13)	0.0272(2)	0.00301(9)	0.01366(11)	-0.00336(8)
C1	0.021(2)	0.023(2)	0.021(2)	-0.003(2)	0.011(2)	0.001(2)
C2	0.022(2)	0.024(2)	0.048(3)	0.002(2)	0.025(2)	0.004(2)
N1	0.018(2)	0.027(2)	0.0148(14)	-0.0047(13)	0.0103(12)	-0.0042(13)
O1	0.0199(14)	0.0160(13)	0.0213(14)	-0.0028(11)	0.0084(12)	0.0054(11)
O2	0.035(2)	0.022(2)	0.036(2)	0.0023(14)	0.025(2)	0.0008(14)
C3	0.019(2)	0.027(2)	0.019(2)	-0.002(2)	0.011(2)	0.000(2)
C4	0.018(2)	0.019(2)	0.0135(15)	0.0017(12)	0.0088(13)	0.0059(13)
C5	0.021(2)	0.013(2)	0.025(2)	-0.0025(14)	0.0107(17)	-0.0009(13)
C6	0.023(2)	0.025(2)	0.020(2)	-0.005(2)	0.011(2)	-0.004(2)
N2	0.0149(13)	0.0160(14)	0.0134(13)	-0.0014(10)	0.0084(11)	-0.0038(10)
O3	0.0167(13)	0.0171(14)	0.0153(12)	-0.0030(10)	0.0026(11)	0.0020(10)
C7	0.014(2)	0.017(2)	0.017(2)	-0.0030(13)	0.0062(13)	-0.0038(12)
N3	0.0113(13)	0.021(2)	0.0139(13)	-0.0018(11)	0.0041(11)	-0.0028(11)
C8	0.020(2)	0.033(3)	0.023(2)	-0.010(2)	0.004(2)	0.006(2)
C9	0.020(2)	0.020(2)	0.025(2)	0.011(2)	0.006(2)	0.002(2)
Cd1	0.00792(13)	0.00797(14)	0.00977(14)	0.000	0.00380(11)	0.000
Cd2	0.0135(2)	0.0115(2)	0.0113(2)	-0.00061(11)	0.00420(13)	0.00330(11)

Crystallographic data for Eu₁₂C₉₂H₂₂₀O₆₀N₂₈I₁₂ and Nd₁₂C₉₂H₂₂₀O₆₀N₂₈I₁₂

Table A.16.: Coefficients U_{ij} / \AA^2 of the anisotropic atomic displacement parameters for [RE₁₂(DMF)₂₄(μ_3 -COOH)₈(μ_3 -OH)₁₆]₁₂ · 4DMF (RE = Nd, Eu). U_{ij} is defined as $\exp\{-2\pi^2[U_{11}(ha^*)^2+\dots+2U_{12}hka^*b^*]\}$. Standard deviations in units of the last digit are given in parentheses.

Atom	U_{11}	U_{22}	U_{33}	U_{23}	U_{13}	U_{12}
Nd1	0.03180	U_{11}	0.04250	0.00420	-0.00100	0.00100
Eu1	0.0313(3)	U_{11}	0.0455(7)	0.0011(6)	-0.0011(6)	0.0018(5)
Nd2	0.03260	0.04450	0.05660	-0.050	-0.01340	0.040
Eu2	0.0457(5)	0.0324(4)	0.0661(6)	0.0176(4)	-0.0022(6)	-0.0013(4)
I1	0.08240(4)	U_{11}	0.04290(7)	0	0	0
I1	0.08370(11)	U_{11}	0.0427(2)	0	0	0
I2	0.12520(3)	0.14420(2)	0.0974(2)	0	0	-0.0350(12)
I2	0.10910(13)	U_{11}	0.1030(2)	-0.0150(13)	0.03240(13)	-0.0324(2)
I3	0.17900(3)	U_{11}	0.100(2)	0.0450(11)	0	0
I3	0.12870(2)	0.1410(2)	0.09700(2)	0	0	-0.02200(3)
I4	0.09050(4)	U_{11}	0.0995(2)	-0.00700(11)	0.02350(7)	-0.02350(6)
I4	0.16700(2)	U_{11}	0.10400(3)	0.02900(5)	0	0

Crystallographic data for Yb₁₁Hg₅₄

Table A.17.: Coefficients $U_{ij} / \text{\AA}^2$ of the anisotropic atomic displacement parameters for Yb₁₁Hg₅₄. U_{ij} is defined as $\exp\{-2\pi^2[U_{11}(ha^*)^2 + \dots + 2U_{12}hka^*b^*]\}$. Standard deviations in units of the last digit are given in parentheses.

Atom	U_{11}	U_{22}	U_{33}	U_{12}	U_{13}	U_{23}
Hg1	0.0222(4)	0.0163(3)	0.0172(3)	0.0004(3)	0.0013(3)	0.0098(3)
Hg2	0.0179(4)	0.0221(4)	0.0374(5)	0.0023(3)	0.0013(3)	0.0095(3)
Hg3	0.0341(5)	0.0231(4)	0.0189(3)	-0.0017(3)	-0.0016(3)	0.0156(4)
Hg4	0.0183(3)	0.0181(3)	0.0177(3)	0.0007(3)	0.0025(3)	0.0047(3)
Hg5	0.0190(4)	0.0199(4)	0.0262(3)	-0.0048(3)	-0.0019(3)	0.0113(3)
Hg6	0.0211(3)	0.0161(3)	0.0153(3)	0.0001(2)	0.0000(2)	0.0082(3)
Yb1	0.0138(5)	0.0151(5)	0.0151(4)	0	0	0.0068(4)
Yb2	0.0195(6)	0.0158(6)	0.0153(5)	0	0	0.0094(5)
Hg7	0.0170(5)	0.0212(5)	0.0180(4)	0	0	0.0017(4)
Yb3	0.0136(5)	0.0160(6)	0.0147(4)	0	0	0.0067(5)
Hg8	0.0270(6)	0.0273(6)	0.0313(6)	0	0	0.0168(5)
Hg9	0.0209(5)	0.0268(6)	0.0239(5)	0	0	0.0115(5)
Hg10	0.0182(5)	0.0207(5)	0.0218(4)	0	0	0.0079(4)
Yb4	0.0134(4)	= U_{11}	0.0142(5)	0	0	0.0067(2)
Hg11	0.0205(4)	= U_{11}	0.0274(7)	0	0	0.0103(2)
Hg12	0.0206(4)	= U_{11}	0.0288(7)	0	0	0.0103(2)
Hg13	0.0136(5)	= U_{11}	0.0249(8)	0	0	0.0068(2)
Hg14	0.0238(7)	= U_{11}	0.0361(12)	0	0	0.0119(3)

Crystallographic data for Li₃Ga_{14-x}Sn_x with $x \approx 1$

Table A.18.: Coefficients $U_{ij} / \text{\AA}^2$ of the anisotropic atomic displacement parameters for Li₃Ga_{13-x}Sn_x. U_{ij} is defined as $\exp\{-2\pi^2[U_{11}(ha^*)^2 + \dots + 2U_{12}hka^*b^*]\}$. Standard deviations in units of the last digit are given in parentheses.

Atom	U_{11}	U_{22}	U_{33}	U_{23}	U_{13}	U_{12}
Ga1	0.0040(12)	U_{11}	0.0035(14)	-0.0011(5)	0.0011(5)	0.0028(12)
Ga2	0.0041(14)	U_{11}	0.0046(16)	0.0003(5)	-0.0003(5)	0.0025(12)
Ga3	0.0025(17)	U_{11}	0.027(3)	0.	0	0.0013(8)
Sn3	0.0025(17)	U_{11}	0.027(3)	0	0	0.0013(8)
Li1	0.00(3)	-0.03(3)	2.0(16)	-0.2(2)	-0.11(10)	-0.017(14)

Table A.19.: Selected interatomic distances for $\text{Li}_3\text{Ga}_{13-x}\text{Sn}_x$ [Å]. Standard deviations in units of the last digit are given in parentheses.

Atom 1	atom 2	distance [Å]	Atom 1	atom 2	distance [Å]	Atom 1	atom 2	distance [Å]	
Ga1	Ga1	2.438(2)	Ga 2	Ga2	2.667(2)	Sn3 Ga3	Li2	3.2(2)	
	Ga2	2.597(2)		Li2	2.78(7)		Li2	Li2	2.5(2)
	Ga2	2.597(2)		Li2	2.78(7)		Ga2	2.78(9)	
	Ga2	2.613(2)		Li2	2.7(2)		Ga2	2.78(9)	
	Ga1	2.666(2)		Li2	2.7(2)		Ga2	2.79(9)	
	Ga1	2.666(2)		Li2	3.8(2)		Ga2	2.79(9)	
	Li2	2.9(2)		Sn3 Ga3	Ga2		2.586(2)	Sn3 Ga3	2.9(2)
	Li2	2.9(2)			Ga2		2.586(2)	Ga1	2.9(2)
	Li2	3.0(2)			Ga2		2.587(2)	Ga1	2.9(2)
	Li2	3.0(2)			Sn3 Ga3		2.65(3)	Ga1	3.00(7)
Ga2	Sn3 Ga3	2.587(2)	Li2	2.9(2)	Ga1	3.00(7)			
	Ga1	2.597(2)	Li2	2.92(8)	Sn3 Ga3	3.2(2)			
	Ga1	2.597(2)	Li2	2.92(8)	Li2	3.4(2)			
	Ga1	2.613(2)	Li2	3.2(2)	Li2	3.4(2)			
	Ga2	2.667(2)	Li2	3.2(2)	Ga2	3.8(2)			

Table A.20.: Standardised fractional atomic coordinates and equivalent isotropic displacement parameters / pm^2 for $\text{Li}_3\text{Ga}_{13-x}\text{Sn}_x$ from powder X-ray diffraction data. Standard deviations in units of the last digit are given in parentheses. Thermal displacement factors were constrained for the mixed occupied position and not refined for the Li position.

Atom	Wyckoff number	x	y	z	B_{iso}
Ga1	18h	0.437(2)	0.552(2)	0.049(2)	2.13(2)
Ga2	18h	0.5027(2)	0.4973(2)	0.1968(2)	1.63(8)
Ga3	6c	2/3	1/3	0.2534(4)	2.1(2)
Sn3	6c	2/3	1/3	0.2534(4)	2.1(2)
Li1	18h	0.2525(5)	0.4475(11)	0.02(4)	0.7

B. Performed Experiments

Table B.1.: Experiments Frank Tambornino

No.	Type of experiment	Target compound	Result
FT001	electrolysis	CaI ₂ · 6DMF	phase pure product obtained
FT002	electrolysis	Ca–amalgam	no product obtained
FT003	electrolysis	ScI ₃ · xDMF	educt isolated
FT004	electrolysis	ScI ₃ · xDMF	educt isolated
FT005	electrolysis	ScI ₃ · xDMF	ScI ₃ · DMF isolated
FT006	electrolysis	Ca–amalgam	no product obtained
FT007	electrolysis	NdI ₃ · 8DMF	phase pure product obtained
FT008	electrolysis	CaI ₂ · 6DMF	phase pure product obtained
FT009	electrolysis	KHg ₁₁	product obtained
FT010	electrolysis	KHg ₁₁	product obtained
FT011	electrolysis	KHg ₆	mixture of KHg ₁₁ and KHg ₆
FT012	electrolysis	Ca–amalgam	no product obtained
FT013	electrolysis	FeI ₂ · 6DMF	no product obtained
FT014	electrolysis	Ca–amalgam	no product obtained
FT015	electrolysis	KHg ₆	mixture of KHg ₁₁ and KHg ₆
FT016	electrolysis	Nd–amalgam	electrolysis did not start, no product obtained
FT017	electrolysis	KHg ₆	mixture of KHg ₁₁ and KHg ₆
FT018	electrolysis	KHg ₆	mixture of KHg ₁₁ and KHg ₆
FT019	electrolysis	KHg ₁₁	phase pure product obtained
FT020	thermochemical synthesis with seeds from FT017	KHg ₆	phase pure product obtained
FT021	electrolysis	EuI ₃ · 8DMF	phase pure product obtained
FT022	electrolysis	Mg–amalgam	no product obtained
FT023	electrolysis	Mg–amalgam	no product obtained
FT024	electrolysis	MgI ₂ · 6DMF	phase pure product obtained
FT025	electrolysis	Nd–amalgam	electrolysis did not start, no product obtained
FT026	electrolysis	Mg–amalgam	no product obtained
FT027	electrolysis		not performed
FT028	electrolysis	Mg–amalgam	no product obtained
FT029	electrolysis	Mg–amalgam	no product obtained
FT030	electrolysis	Fe–amalgam	deposition of Fe in Hg matrix, no compound formation
FT031	electrolysis	EuI ₃ · 8DMF	phase pure product obtained

FT032	electrolysis	Mg–amalgam	no product obtained
FT033	electrolysis	CaHg ₂	unidentified product isolated
FT034	electrolysis	ErI ₃ · 8DMF	phase pure product isolated
FT035	electrolysis		not performed
FT036	electrolysis	Eu ₁₀ Hg ₅₅	product obtained, high Hg _(lq) content
FT037	HP synthesis	WC and Hg	educt isolated
FT038	electrolysis	Eu ₁₀ Hg ₅₅	product obtained, high Hg _(lq) content
FT039	electrolysis	Eu ₁₀ Hg ₅₅	product obtained, high Hg _(lq) content
FT040	electrolysis	Er–amalgam	product isolated, not identifiable
FT041	electrolysis	Eu ₁₀ Hg ₅₅	product obtained, high Hg _(lq) content
FT042	electrolysis	Ca _{11-x} Hg _{54+x}	phase pure product isolated
FT043	solvate	DyI ₃ · xDMF	
FT044	electrolysis	Ca _{11-x} Hg _{54+x}	phase pure product isolated
FT045	solvate	LaI ₃ · 9DMF	phase pure product obtained
FT046	solvate	SmI ₃ · xDMF	no product isolated
FT047	electrolysis		not performed
FT048	solvate	ScI ₃ · xDMF	Sc(I ₃) ₃ · 6DMF obtained
FT101	DFT	test Al	successful convergence
FT102	thermo.	ErHg	Hg distilled off
FT103	thermo.	TbHg	elemental Tb in bulk with liquid Hg
FT104	tempering	Er _x Hg _y	microcrystalline powder, unknown
FT105	electrolysis	La amalgam	no product obtained
FT106	electrolysis	La amalgam	no product obtained
FT107	thermo.	La amalgam	La ₁₁ Hg ₄₅ and LaHg
FT108	electrolysis	LiHg ₃	phase pure product
FT109	electrolysis	KHg ₁₁	phase pure product
FT110	thermo.	LaHg	phase pure LaHg ₃ , microcrystalline
FT111	solvate	EuI ₃ · 8DMF	phase pure product
FT112	tempering	KHg ₆	phase pure product
FT113	thermo.	LaHg	La obtained
FT114	distillation	La ₁₁ Hg ₄₅	phase pure product
FT115	thermo.	KHg ₆	KHg ₁₁ and minor amounts of KHg ₆
FT116	electrolysis	La amalgam	"LaHg ₆ ", microcrystalline
FT117	thermo.	ErHg	no product obtained
FT118	distillationi	ErHg ₃	phase pure ErHg ₃ , microcrystalline powder
FT119	thermo.	LiHg	phase pure product obtained

FT120	electrolysis	Na/K amalgam	microcrystalline powder, unknown
FT121	single crystal analysis	Na/K amalgam from FT120	no single crystal isolated
FT122	solvate	MoCl ₂ in var. solvents	soluble in DMF, hot acids
FT123	DFT	Cs ₉ AlO ₄	calculation successful
FT124	electrolysis	Dy amalgam	no product obtained
FT125	electrolysis	Dy amalgam	no product obtained
FT126	solvate	TiI ₄ in DMF	decomposition of DMF
FT127	solvate	ZnI ₂ · xDMF	single crystals obtained
FT128	electrolysis	Mg amalgam	no product obtained
FT129	solvate	MgI ₂ · 6DMF	product obtained
FT130	electrolysis	KHg ₁ from NMP solution	insufficient solution of KI in NMP
FT131	solvate	TiI ₄ in DMF	decomposition of DMF
FT132	solvate	TiI ₄ in DMF	decomposition of DMF
FT133	electrolysis	Cd amalgam	solid solution of Cd in Hg
FT134	electrolysis	Ag amalgam	Ag ₇ NO ₁₁ single crystals
FT135	distillation	ErHg ₃	phase pure product
FT136	DFT	Cs ₂ Hg ₂₇	successful convergence, Bader charges calc.
FT137	electrolysis	Ag ₂ O ₃	no product obtained
FT138	distillation	La amalgam	La ₁₁ Hg ₄₅ phase pure
FT139	DTA		no data collected
FT140	DFT	Cs ₁₀ AlO ₅	no convergence, problem too large
FT141	DFT	Li amalgams	successful convergence, band structures obtained
FT142	distillation	Ce amalgam	ampoule burst, no product obtained
FT143	tempering	"LaHg ₆ " from electrolysis	decomposition into LaHg ₃ and Hg
FT144	distillation	La ₁₁ Hg ₄₅	phase pure product
FT145	tempering	"LaHg ₆ " from electrolysis	decomposition into LaHg ₃ and Hg
FT146	tempering	"LaHg ₆ " from electrolysis	decomposition into LaHg ₃ and Hg
FT147	tempering	"LaHg ₆ " from electrolysis	decomposition into LaHg ₃ and Hg
FT148	thermo.	Li _{0.9} Hg _{1.1}	no product obtained
FT149	thermo.	Li _{0.8} Hg _{1.2}	phase pure product
FT150	thermo.	Li _{0.9} Hg _{1.1}	phase pure product
FT151	thermo.	Li _{1.1} Hg _{0.9}	phase pure product
FT152	thermo.	Li _{1.2} Hg _{0.8}	phase pure product
FT153	electrolysis	Sm amalgam	"SmHg ₆ ", microcrystalline powder, unknown

FT154	thermo.	$\text{Li}_{0.85}\text{Hg}_{1.15}$	phase pure product
FT155	thermo.	$\text{Li}_{0.95}\text{Hg}_{1.05}$	phase pure product
FT156	thermo.	$\text{Li}_{1.05}\text{Hg}_{0.95}$	phase pure product
FT157	electrolysis	Er amalgam	no product obtained
FT158	electrolysis	KHg_{11}	phase pure product
FT159	solvate	Te iodide in DMF	no product obtained
FT160	—	InHg	metallic InHg solution obtained
FT161	electrolysis	K on InHg in glass spoon	$\text{KHg}_{11-x}\text{In}_x$ obtained
FT162	electrolysis	Sm amalgam	no product obtained
FT163	electrolysis	K on InHg in copper spoon	$\text{KHg}_{11-x}\text{In}_x$ obtained
FT164	electrolysis	Ce amalgam	passivation, no product obtained
FT165	solvate	$\text{YbI}_2 \cdot x\text{DMF}$	solution obtained, no crystalline product
FT166	electrolysis	Yb amalgam	passivation, no product obtained
FT167	electrolysis	Yb amalgam	passivation, no product obtained
FT168	electrolysis	KHg_{11}	phase pure product
FT169	NMR	Li amalgams	NMR data obtained
FT170	thermo.	YbHg	$\text{Yb}_{14}\text{Hg}_{51}$, poor quality
FT171	solvate	$\text{YbI}_2 \cdot x\text{DMF}$	solution obtained, no crystalline product
FT172	thermo.	Hg phosphide	no product obtained
FT173	distillation	YHg_3	phase pure product
FT174	electrolysis	Yb amalgam	passivation, no product obtained
FT175	electrolysis	Ag_2O_3	very little product obtained.
FT176	thermo.	YbHg_2	phase pure product, high amount of Hg remnant
FT177	DFT	$\text{Cs}_2\text{Hg}_{27}$ with Au	successful convergence, DOS-plots
FT178	thermo.	Li_6Hg	Li_3Hg obtained, phase pure
FT179	thermo.	Hg phosphide	no product obtained
FT180	thermo.	$\text{LiHg}_{0.75}\text{Ga}_{0.25}$	product crystallises in CsCl type, poor quality
FT181	thermo.	$\text{LiHg}_{0.75}\text{Sc}_{0.25}$	product crystallises in CsCl type, poor quality
FT182	thermo.	$\text{LiHg}_{0.75}\text{Au}_{0.25}$	no product obtained
FT183	thermo.	$\text{LiHg}_{0.75}\text{Au}_{0.25}$	no product obtained
FT184	electrolysis	CsI on HgIn electrode	CsIn_{12}
FT185	solvate	Dy iodide in DMF	oxidation of iodide through air contact
FT186	electrolysis	Na/K amalgam	microcrystalline powder, unknown
FT187	electrolysis	$\text{Li}_3\text{Ga}_{14}$	phase pure product

FT188	thermo.	CeHg	no product obtained
	FT189 – FT200	not performed	
FT201	distillation	YbHg ₃	phase pure product
FT202	electrolysis	Gd amalgam	no product obtained
FT207	electrolysis	Na/K amalgam	low quality sample
FT208	electrolysis	Cs on InHg	CsIn ₁₂
FT209	DFT	Li ₃ Ga ₁₄	successful convergence
FT210	tempering	Na/K amalgam	no improvement in quality from FT207
FT211	electrolysis	Cd on InHg	mixture of Cd/In and Cd _x In _y Hg _z
FT212	electrolysis	Cs on InHg	CsIn ₁₂
FT213	electrolysis	Rb on InHg	RbHg _{11-x} In _x
FT214	distillation	TmHg ₃	phase pure product
FT215	DFT	Li ₃ Ga ₁₃ Sn ₁	successful convergence
FT217	electrolysis	Yb amalgam	Yb ₁₄ Hg ₅₁ , poor quality
FT218	distillation	DyHg ₃	phase pure product
FT219	distillation	HoHg ₃	phase pure product
FT220	electrolysis	Cs on InHg	CsIn ₁₂
FT222	electrolysis	Cs on InHg	CsIn ₁₂

Table B.2.: Experiments Jonathan Sappl

No.	Target compound	Result
FTJS01	Cd ₅₁ Ca ₁₄	Cd
FTJS02	Cd ₅₁ Ca ₁₄	product obtained
FTJS03	Cd ₅₈ Sr ₁₃	Cd and CdO
FTJS04	Ag ₅₁ Tb ₁₄	Ag ₅₁ Tb ₁₄
FTJS05	Ag ₅₁ Gd ₁₄	Ag ₅₁ Gd ₁₄
FTJS06	Cd ₅₈ Sr ₁₃	no product obtained
FTJS07	Ag ₅₁ Y ₁₄	Ag ₅₁ Y ₁₄
FTJS08	Ag ₅₁ Ce ₁₄	Ag ₅₁ Ce ₁₄
FTJS09	Cd ₅₈ Sr ₁₃	product obtained
FTJS10	Cd ₅₁ Ca ₁₄	CaO and CaCd ₆
FTJS11	Ag ₅₁ Eu ₁₄	product obtained
FTJS12	Ag ₅₁ Sc ₁₄	product obtained
FTJS13	Ag ₅₁ Yb ₁₄	product obtained
FTJS14	Cd ₅₁ Eu ₁₄	product obtained
FTJS15	Cd ₅₁ Ca ₁₄	product obtained

Table B.3.: Experiments Trung Minh Cong

No.	Cathode material / electrolyte / temperature [°C]	Target compound	Result
FTTC01	Hg / LiI / r.t.	LiHg ₃	phase pure LiHg ₃
FTTC02	Ga / KI / 50	KGa ₄	product not identifiable
FTTC03	Galinstan / LiI / r.t.	explorative	LiGa, Li ₃ Ga ₁₄ , LiIn, In
FTTC04	Ga / LiI / 55	Li ₃ Ga ₁₄	Li ₃ Ga ₁₄ , side phases (n.i.)
FTTC05	Ga / KI / 55	KGa ₄	no product isolated
FTTC06	Galinstan / CsI / r.t.	explorative	no product isolated
FTTC07	Ga / FeI ₂ / 55	FeGa ₄	passivation of electrode
FTTC08	Ga / LiI / 75	Li ₃ Ga ₁₄	Li ₃ Ga ₁₄
FTTC09	Galinstan / CsI / r.t.	explorative	CsOH · H ₂ O, side phases (n.i.)
FTTC10	Galinstan / CsI / r.t.	explorative	CsOH · H ₂ O, side phases (n.i.)
FTTC11	Ga / KI / 55	KGa ₄	no product isolated
FTTC12	Galinstan / CsI / r.t.	explorative	passivation of electrode

Table B.4.: Experiments Felix Pultar

No.	Type of experiment	Target compound	Result
FXP01		Ga–Sn alloy	product obtained
FXP02	electrolysis	dry KI	product obtained
FXP03	electrolysis	Ga ₈ Sn ₈ Sn ₃₈	no product obtained
FXP04	electrolysis	1M KI solution in DMF	product obtained and used
FXP05	electrolysis	Ga ₈ Sn ₈ Sn ₃₈	no product obtained
FXP06	electrolysis	1M CsI	product obtained
FXP07	electrolysis	Ga–Sn alloy	product obtained
FXP08	electrolysis	dry DMF	product obtained and used
FXP09	electrolysis	Cs ₈ Ga : 8Sn ₃₈	no product obtained
FXP10	electrolysis	dy DMF	product obtained and used
FXP11	electrolysis	Ga–Sn alloy	product obtained
FXP12	electrolysis	KGa ₄	no product obtained
FXP13	electrolysis	NaI · 3DMF	product obtained
FXP14	electrolysis	NaGa ₄	no product obtained
FXP15	electrolysis	dry KI	product obtained
FXP16	electrolysis	NaGa ₄	product obtained
FXP17	electrolysis	NaGa ₄	product obtained
FXP18	electrolysis	NaGa ₄	electrolysis discontinued
FXP19	electrolysis	dry DMF	product obtained
FXP20	electrolysis	K ₈ Ga ₈ Sn ₃₈	product obtained, not identifiable
FXP21	electrolysis	BaI ₂ · 8DMF	product obtained
FXP22	electrolysis	dry KI	product obtained
FXP23	electrolysis	Ba ₈ Ga ₁₆ Sn ₃₀	no product obtained
FXP24	electrolysis	BaGa ₄	no product obtained
FXP25	electrolysis	Ga–Sn alloy	product obtained

FXP26	electrolysis	Ba–Ga–Sn–In alloy	no product obtained
FXP27	electrolysis	dry CsI	no product obtained
FXP28	electrolysis	$\text{Na}_x\text{Cs}_{8-x}\text{Sn}_{44}\square_2$	$\text{Cs}_8\text{Sn}_{44}\square_2$ obtained
FXP29	electrolysis	$\text{K}_8\text{Ga}_8\text{Sn}_{38}$	product obtained
FXP30	electrolysis	dry KI	product isolated
FXP31	electrolysis	–	not performed
FXP32	electrolysis	$\text{K}_8\text{Ga}_8\text{Sn}_{38}$	product obtained
FXP33	electrolysis	dry KI	product obtained
FXP34	electrolysis	KI · 3DMF	phase pure KI obtained
FXP35	electrolysis	dry CsI	product obtained
FXP36	electrolysis	dry DMF	product obtained

Table B.5.: Experiments Philipp Bielec

No.	Type of experiment	Target compound	Result
FTPBO1	electrolysis	$\text{EuI}_3 \cdot 8\text{DMF}$	product obtained
FTPBO2-A	electrolysis	$\text{EuI}_3 \cdot x\text{Acetonitrile}$	educt isolated
FTPBO2-B	electrolysis	$\text{EuI}_3 \cdot x\text{Cyclohexanone}$	educt isolated
FTPBO2-C	electrolysis	$\text{EuI}_3 \cdot x\text{Acetonitrile}$	no product obtained
FTPBO3	electrolysis	solvation study of $\text{Nd}_{12}\text{C}_{92}\text{H}_{220}\text{O}_{60}\text{N}_{28}\text{I}_{12}$	no solvation
FTPBO4	electrolysis	$\text{EuI}_3 \cdot x\text{DiGlyMe}$	educt isolated
FTPBO5	electrolysis	$\text{EuI}_3 \cdot x\text{Acetone}$	no product obtained
FTPBO6	electrolysis	$\text{EuI}_3 \cdot 8\text{DMF}$	product isolated
FTPBO7	electrolysis	$\text{EuI}_3 \cdot x\text{DiGlyMe}$	no product obtained
FTPBO8	electrolysis	$\text{EuI}_3 \cdot [18]\text{crown}[6]$	$\text{Eu}_{12}\text{C}_{92}\text{H}_{220}\text{O}_{60}\text{N}_{28}\text{I}_{12}$
FTPBO9	HP synthesis	EuI_3	blow out, no product
FTPBO10	electrolysis	EuCl_3	$\text{EuCl}_3 \cdot 6\text{H}_2\text{O}$
FTPBO11	electrolysis	$\text{Eu}_{12}\text{C}_{92}\text{H}_{220}\text{O}_{60}\text{N}_{28}\text{I}_{12}$	no product isolated
FTPBO12	electrolysis	EuI_3	blow out, no product
FTPBO13	electrolysis	$\text{EuI}_3 \cdot x\text{Acetone}$	I_2 elusion
FTPBO14	electrolysis	EuI_3	no product
FTPBO15	electrolysis	$\text{EuI}_3 \cdot x\text{Acetone}$	$\text{Na}(\text{C}_3\text{H}_6\text{O})_3\text{I}_2$ and $\text{Eu}(\text{H}_2\text{O})_4(\text{C}_3\text{H}_6\text{O})_4\text{I}_3$
FTPBO16	electrolysis	$\text{EuI}_3 \cdot 8\text{DMF}$	product obtained
FTPBO17	electrolysis	EuI_3	EuI_2

Table B.6.: Experiments Kuno Schwärzer

No.	Target compound	Result
FTKS01	CeHg	unknown product
FTKS02	CeInHg	CeIn ₃ /CeHg ₃ mixture
FTKS03	CeHg ₃	Ce ₁₁ Hg ₄₅ /CeHg ₃ mixture
FTKS04	GdHg ₃	oxygen contamination, discarded
FTKS05	LuHg ₃	product isolated
FTKS06	CeHg	unknown product
FTKS07	YHg ₃	product isolated
FTKS08	CeInHg	CeIn ₃ /unknown side phase
FTKS09	YbHg ₃	Yb ₁₁ Hg ₅₄ isolated
FTKS10	GdHg ₃	product isolated
FTKS11	TbHg ₃	experiment discarded
FTKS12	CeHg	product/minor amounts CeHg ₂ isolated
FTKS13	EuHg ₃	Eu ₁₀ Hg ₅₅ isolated
FTKS14	SmHg ₃	Sm ₁₁ Hg _{44.5} isolated
FTKS15	NdHg ₃	oxygen contamination, mixed Nd-oxide
FTKS16	TbHg ₃	unknown product
FTKS17	CeHg	product/minor amounts CeHg ₂ isolated
FTKS18	CeRuHg	Ru/Ce ₂ O ₃ /CeRu ₂ isolated
FTKS19	CeMoHg	Mo/Ce ₂ O ₃ isolated
FTKS20	CeNiHg	Ni/Ce ₂ O ₃ /Ce ₁₁ Hg ₄₅ isolated
FTKS21	CeIrHg	educt isolated
FTKS22	NdHg ₃	Nd ₁₁ Hg _{44.5} isolated
FTKS23	CeCoHg	CeHg/CeCo ₅ isolated
FTKS24	CeHg	product/minor amounts CeHg ₂ isolated
FTKS25	CeFeHg	educt isolated
FTKS26	CePdHg	experiment discarded
FTKS27	CdHg ₃	unknown product
FTKS28	CePtHg	Pt ₂ Ce/Ce ₁₁ Hg ₄₅ isolated
FTKS29	CeRuHg	CeRu ₂ /CeHg ₂ /CeHg ₃ /Ce ₂ O ₃ isolated
FTKS30	NdHg ₃	Nd ₁₁ Hg _{44.5} isolated
FTKS31	YbHg ₃	Yb ₁₄ Hg ₅₁ isolated
FTKS32	CeHg ₃	Ce ₁₁ Hg ₄₅ /CeHg ₃ /unknown phase isolated
FTKS33	TbHg ₃	TbHg ₂ isolated
FTKS34	EuHg ₃	Eu ₁₀ Hg ₅₅ isolated
FTKS35	SmHg ₃	SmHg ₂ isolated

Table B.7.: Experiments Arthur Haffner

No.	Target compound	Result
AH01	$[\text{Gd}(\text{DMF})_8]\text{I}_3$	product isolated
AH02	$[\text{Nd}(\text{DMF})_8]\text{I}_3$	product isolated
AH03	$[\text{Nd}(\text{DMF})_8]\text{I}_3$	product isolated
AH04	$[\text{Yb}(\text{DMF})_8]\text{I}_3$	product isolated
AH05	$\text{Nd}_{12}\text{C}_{92}\text{H}_{220}\text{O}_{60}\text{N}_{28}\text{I}_{12}$	$\text{Nd}(\text{COOH})_3$ isolated
AH06	$\text{Nd}_{12}\text{C}_{92}\text{H}_{220}\text{O}_{60}\text{N}_{28}\text{I}_{12}$	$\text{Nd}(\text{COOH})_3$ isolated
AH07	$[\text{}^6\text{Li}(\text{DMF})_4]\text{I}$	product isolated
AH08	$\text{Nd}_{12}\text{C}_{92}\text{H}_{220}\text{O}_{60}\text{N}_{28}\text{I}_{12}$	no product isolated
AH09	–	not performed
AH010	$\text{Nd}_{12}\text{C}_{92}\text{H}_{220}\text{O}_{60}\text{N}_{28}\text{I}_{12}$	$\text{Nd}(\text{COOH})_3$ isolated
AH011	$\text{Gd}(\text{COOH})_3$	product isolated
AH012	$\text{Nd}_{12}\text{C}_{92}\text{H}_{220}\text{O}_{60}\text{N}_{28}\text{I}_{12}$	$[\text{Nd}(\text{DMF})_8]\text{I}_3$ isolated
AH013	$\text{Nd}(\text{COOH})_3$	product isolated
AH014	$\text{Nd}_{12}\text{C}_{92}\text{H}_{220}\text{O}_{60}\text{N}_{28}\text{I}_{12}$	no product isolated
AH015	$\text{Nd}_{12}\text{C}_{92}\text{H}_{220}\text{O}_{60}\text{N}_{28}\text{I}_{12}$	$\text{Nd}(\text{COOH})_3$ isolated
AH016	$\text{Nd}_{12}\text{C}_{92}\text{H}_{220}\text{O}_{60}\text{N}_{28}\text{I}_{12}$	no product isolated
AH017	$\text{NdI}_3 \cdot x\text{TTHF}$	no product isolated
AH018	$\text{GdI}_3 \cdot x\text{TTHF}$	no product isolated
AH019	$\text{SrI}_3 \cdot x\text{TTHF}$	no product isolated

Table B.8.: Experiments Sabine Hübner

No.	Type of experiment	Target compound	Result
FTSH01	electrolysis	KHg_{11}	KHg_{11}
FTSH02	electrolysis	$\text{Cs}_2\text{Hg}_{27}$	$\text{Cs}_2\text{Hg}_{27}$
FTSH03	electrolysis	$\text{Cs}_2\text{Hg}_{27-x}\text{Au}_x$	no product isolated
FTSH04	electrolysis	$\text{Cs}_2\text{Hg}_{27-x}\text{Au}_x$	$\text{Cs}_2\text{Hg}_{27}$
FTSH05	electrolysis	$\text{Cs}_2\text{Hg}_{27-x}\text{Au}_x$	no product isolated
FTSH06	electrolysis	$\text{Cs}_2\text{Hg}_{27-x}\text{Au}_x$	$\text{Cs}_3\text{Hg}_{20}$
FTSH07	electrolysis	$\text{Cs}_2\text{Hg}_{27-x}\text{Au}_x$	YYY
FTSH08	electrolysis	$\text{Cs}_2\text{Hg}_{27-x}\text{Au}_x$	YYY
FTSH09	electrolysis	In-amalgam	product isolated
FTSH10	electrolysis	$\text{Cs}_2\text{Hg}_{27-x}\text{Au}_x$	no product isolated
FTSH11	electrolysis	In-amalgam	CsIn_{12}
FTSH12	electrolysis	$\text{Cs}_2\text{Hg}_{27-x}\text{Au}_x$	$\text{Cs}_3\text{Hg}_{20}$

Table B.9.: Experiments Tobias Giftthaler

No.	Cathode material	Electrolyte	Result
FTSTG01	GaInStan	NaI	product isolated
FTSTG02	Ga ₁₁ Sn ₂	LiI	liquid product isolated
FTSTG03	GaInStan	NaI	no product isolated
FTSTG04	Ga ₁₁ Sn ₂	LiI	product isolated
FTSTG05	GaInStan	RbI	no product isolated
FTSTG06	GaInStan	RbI	liquid product isolated
FTSTG07	GaInStan	CaI ₂	no product isolated
FTSTG08	Ga	NdI ₃	no product isolated
FTSTG09	Ga	NdI ₃	no product isolated
FTSTG10	Ga ₁₁ Sn ₂	LiI	product isolated
FTSTG11	GaInStan	NaI	liquid product isolated
FTSTG12	Ga ₁₁ Sn ₂	LiI	no product isolated
FTSTG13	Ga ₁₁ Sn ₂	LiI	product isolated
FTSTG14	Ga ₁₁ Sn ₂	LiI	product isolated
FTSTG15	Ga ₄ Sn	LiI	product isolated
FTSTG16	GaInStan	NaI	liquid product isolated
FTSTG17	Ga ₁₃ Sn	LiI	product isolated

C. Curriculum Vitae

Personal Details

Name	Frank Tambornino
Date of Birth	
Place of Birth	Bocholt
Nationality	German

EDUCATION

PhD Inorganic Chemistry

LMU Munich (Germany) 03/2013 – 12/2016
THESIS - Electrolytic synthesis and structural chemistry of intermetallic phases with polar metal-metal bonding
Advisor: Dr. C. Hoch & Prof. W. Schnick

Master of Science Chemistry

LMU Munich, (Germany) 10/2010–03/2013
THESIS - Synthesis and characterisation of mercury-rich amalgams by preparative electrolysis
Advisor: Dr. C. Hoch & Prof. W. Schnick, grade 1.0, overall grade 1.12

Bachelor of Science Chemistry and Biochemistry

LMU Munich, (Germany) 10/2007–10/2010
THESIS - New energetic materials based on 3,5-diamino-1*H*-1,2,4-triazole
Advisor: Prof. T. M. Klapötke, grade 1.0, overall grade 1.6

High school Diploma (Abitur)

St. Georg Gymnasium, Bocholt (Germany) 08/1998–05/2007
overall grade: 2.0

Elementary school

Grundschule Biemenhorst, Bocholt (Germany) 08/1994–08/1998

PROFESSIONAL EXPERIENCE

Research Assistant

05/2013 – Now

Department of Chemistry, LMU Munich

- Synthesis and structural investigations on mercury-rich amalgams of alkali, alkaline earth and lanthanide metals.
- Development of isothermal preparative electrolysis methods on reactive (inter)metallic cathode materials including mercury, gallium, indium, tin.
- Structural elucidation (single crystal/powder X-ray diffraction) and characterisation (conductivity, band-structure calculation with WIEN2k, magnetic properties, ss-NMR) of intermetallic compounds.

Assistant Lecturer

10/2013 – 10/2015

Department of Chemistry, LMU Munich, Munich

- Planning, preparation and co-conduction of the lecture "Introduction to general and inorganic chemistry" (first semester lecture, 6h/week) with Prof. W. Schnick.
- Design and execution of educational experiments for this lecture with >600 students.

Jr. Supervisor

Various courses 2009 – Now

Department of Chemistry, LMU Munich

- Supervisor for advanced students (6-8th semester students, 8 in total, 1on1 supervision, 40h/week for 8 weeks), 2013–Now.
- Advanced inorganic synthesis lab course (4th semester students, 27h/week for 4 weeks), summer terms 2010–13.
- Basic lab course (1st semester students, 15h/week for 10 weeks), 2009.

Research Internships

Prof. U. Wille, University of Melbourne (Australia) 09 – 12/2011

- Synthesis and characterization of DiMeCSTMIO as a potential fluorophore for polymer degradation studies

Prof. T. Bein, LMU Munich (Germany) 06 – 08/2011

- Organometallic functionalization and post-synthesis modification of mesoporous MCM-41

Prof. D. Johrendt, LMU Munich (Germany) 02 – 06/2011

- Synthesis and structure of layered iron arsenides and LaSSb

Jr. researcher

03 – 04/2008

Ab-solut chemistry GmbH, Rhede

- Development of decoating technologies through plasma (CO, N₂, CO₂ plasma) and chemical etching

Alternative civilian service

08 – 10/2007

Fraunhofer-Institute UMSICHT, Oberhausen, Department: Materials and interaction

- Dispersion of carbon nanotubes in supercritical CO₂ for insertion into polymer materials

HONORS and AWARDS

GDCh travel scholarship (2016)

Römer Prize for outstanding research (Master's thesis) 2013.

Best Poster Presentation (Terrae Rarae 2013).

Best Chemistry Abitur Prize, Fonds der Chemischen Industrie (2007).

Best Biology Abitur Prize, Fonds der Chemischen Industrie (2007).

PUBLICATIONS

12. **F. Tambornino**, J. Sappl, F. Pultar, T. M. Cong, S. Hübner, T. Giftthaler, C. Hoch, "Electrocrystallization – a synthetic method for new intermetallic phases with polar metal-metal bonding", *Inorg. Chem.* (2016), *in print*.
doi: 10.1021/acs.inorgchem.6b02068.
11. M. Wörsching, **F. Tambornino**, S. Datz, C. Hoch, "Chemical Twinning of Salt and Metal in the Subnitridometalates $\text{Ba}_{23}\text{Na}_{11}(\text{MN}_4)_4$ with $M = \text{V}, \text{Nb}, \text{Ta}$ ", *Angew. Chem.* **128**, 11026–11030 (2016), doi:10.1002/ange.201605113; *Angew. Chem. Int. Ed.* **55** (2016), 10868–10871, doi:10.1002/anie.201605113.
10. **F. Tambornino**, K. Schwärzer and C. Hoch, "Synthesis and characterization of $\text{La}_{11+x}\text{Hg}_{45-x}$ and $\text{RE}_{11}\text{Hg}_{44.5}$ ($\text{RE}=\text{Nd}, \text{Sm}$) as hettotypes of the $\text{Sm}_{11}\text{Cd}_{45}$ structure type", *J. Solid State Chem.*, **242**, 162–169 (2016).
doi:10.1016/j.jssc.2016.07.001.
9. A. Schmidt, P. Köstler, **F. Tambornino** and T. Bein, "Efficient Functionalization of Mesoporous MCM-41 with Aromatic Organo-Lithium Reagents", *Micropor. Mesopor. Mat.* **223**, 219–224 (2016). doi:10.1016/j.micromeso.2015.10.015.
8. A. Marchuk, S. Wendl, N. Imamovic, **F. Tambornino**, D. Wiechert, P.J. Schmidt, W. Schnick, "Nontypical Luminescence Properties and Structural Relation of $\text{Ba}_3\text{P}_5\text{N}_{10}\text{X} : \text{Eu}^{2+}$ ($\text{X} = \text{Cl}, \text{I}$): Nitridophosphate Halides with Zeolite-like Structure", *Chem. Mater.* **27**, 6432–6441 (2015). doi:10.1021/acs.chemmater.5b02668.
7. **F. Tambornino**, C. Hoch, "The Mercury-richest Europium Amalgam, $\text{Eu}_{10}\text{Hg}_{55}$ ", *Z. Anorg. Allg. Chem.* **641**, 537–542 (2015). doi:10.1002/zaac.201400561.
6. **F. Tambornino**, C. Hoch, "Bad metal behaviour in the new Hg-rich amalgam KHg_6 with polar metallic bonding", *J. Alloys Compd.* **618**, 299–304 (2015).
doi:10.1016/j.jallcom.2014.08.173.
5. **F. Tambornino**, J. Sappl, C. Hoch, "The $\text{Gd}_{14}\text{Ag}_{51}$ structure type and its relation to some complex amalgam structures", *J. Alloys Compd.* **618**, 326–335 (2015).
doi:10.1016/j.jallcom.2014.08.017.
4. **F. Tambornino**, P. Bielec, C. Hoch, "Redetermination of $[\text{EuCl}_2(\text{H}_2\text{O})_6]\text{Cl}$ ", *Acta Cryst.* **E70**, i27 (2014). doi:10.1107/S1600536814010307.
3. **F. Tambornino**, C. Hoch, "The new potassium amalgam KHg_6 ", *Z. Kristallogr. Suppl.* **32** (2013).
2. **F. Tambornino**, C. Hoch, "The Hg-richest europium amalgam, $\text{Eu}_{10}\text{Hg}_{55}$ ", *Z. Kristallogr. Suppl.* **32** (2013).
1. R. Frankovsky, H. Luetkens, **F. Tambornino**, A. Marchuk, G. Pascua, A. Amato, H.-H. Klauss, D. Johrendt, "Short-range magnetic order and effective suppression of superconductivity by manganese doping in $\text{LaFe}_{1-x}\text{Mn}_x\text{AsO}_{1-y}\text{F}_y$ ", *Phys. Rev. B* **87**, 174515 (2013). doi:10.1103/PhysRevB.87.174515.

PRESENTATIONS

17. "Unexpected complexity in polar metals: Amalgams", Poster, Antwerp summer school on aperiodic crystals, 07/2016.
16. "Aktuelle Forschung" (Recent research), oral presentation, Group Seminar AK Schnick 12/2015.
15. "The $\text{Ag}_{51}\text{Gd}_{14}$ structure type and its relation to some amalgam structures", Poster and oral presentation, Young crystallographers meeting at STOE, Darmstadt, 09/2015.
14. "Probing the electronic structures of lithium amalgams with solid-state NMR", Poster, ECSSC - 15th European Conference on Solid State Chemistry, Vienna (Austria), 08/2015.
13. "Synthese und Struktur von $\text{La}_{11}\text{Hg}_{45}$ " (Synthesis and structure of $\text{La}_{11}\text{Hg}_{45}$), oral presentation, Hirscheegg-Seminar on solid state chemistry 06/2015.
12. "Demixing of multinary metallic liquids during electrolysis - synthesis of CsIn_{12} ", Poster, Annual Meeting of the German Crystallographic Society, Göttingen (Germany) 2015.
11. "Vergälltes Gallium" (Spoilt Gallium), oral presentation, "Hemdsärmelkolloquium" inorganic chemistry (Munich), 02/2015.
10. "Komplex-Chemie" (Complex-Chemistry), oral presentation, Group Seminar AK Schnick 11/2014.
9. "Festkörper-NMR an Li-Amalgamen" (Solid state NMR on Li-amalgams), oral presentation, Hirscheegg-Seminar on solid state chemistry 06/2014.
8. "NMR-Untersuchungen an Lithium-Amalgamen" (NMR-Investigations on Lithium-amalgams), oral presentation, Obergurgl-Seminar on inorganic chemistry, Obergurgl (Austria) 01/2014.
7. "Metalliodid-Solvate: Nebenprodukte mit Eigenleben" (Metaliodide-solvates: side products with independent existence), oral presentation, Group Seminar AK Schnick 01/2014.
6. "Structural investigation of a dodeca-nuclear Neodymium complex", Poster, XXV. Tage der Seltenen Erden - Terrae Rarae, Stuttgart (Germany) 12/2013.
5. "The $\text{Ag}_{51}\text{Gd}_{14}$ structure type and its relation to some amalgam structures", Poster, XII international conference on crystal chemistry of intermetallic compounds, Lviv (Ukraine) 09/2013.
4. "Quecksilberreiche Amalgame von unedlen Metallen" (Mercury-rich amalgams of non-precious metals), oral presentation, Group Seminar AK Schnick 07/2013.
3. "Quecksilberreiche Amalgame von unedlen Metallen" (Mercury-rich amalgams of non-precious metals), oral presentation, Hirscheegg-Seminar on solid state chemistry, Hirscheegg (Austria) 05/2013.
2. "The New Potassium Amalgam KHg_6 ", Poster, Annual Meeting of the German Crystallographic Society, Freiberg (Germany) 03/2013.
1. "The Hg-Richest Europium Amalgam, $\text{Eu}_{10}\text{Hg}_{55}$ ", Poster, Annual Meeting of the German Crystallographic Society, Freiberg (Germany) 03/2013.